CONF-770602-

Proceedings of the TOPICAL CONFERENCE on

HEAVY-ION COLLISIONS

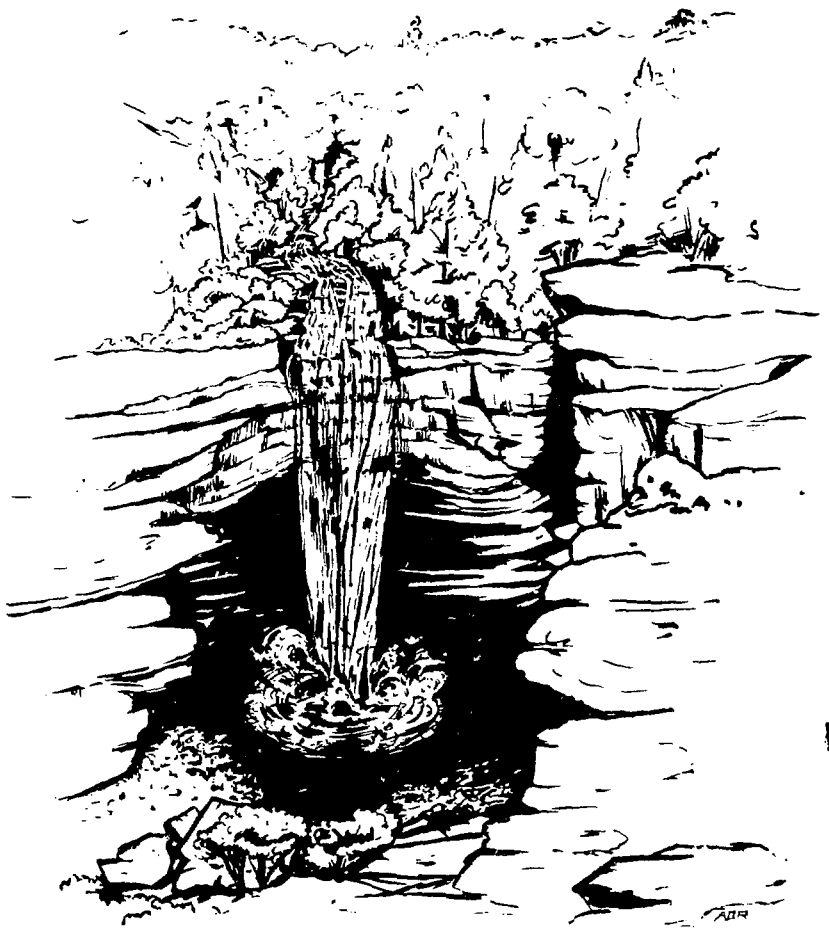

FALL CREEK FALLS STATE PARK, TENNESSEE

JUNE 13-17, 1977

sponsored by OAK RIDGE NATIONAL LABORATORY OPERATED BY UNION CARBIDE CORPORATION FOR THE ENERGY RESEARCH AND DEVELOPMENT ADMINISTRATION

Printed in the United States of America. Available from
National Technical Information Service
U.S. Department of Commerce
5285 Port Royal Road, Springfield, Virginia 22161
Price: Printed Copy $15.50; Microfiche $3.00

CONF-770602

PROCEEDINGS OF THE TOPICAL CONFERENCE ON HEAVY ION COLLISIONS

Fall Creek Falls State Park
Pikeville, Tennessee

June 13-17, 1977

Organizing Committee

E. C. Halbert
J. A. Maruhn
V. Maruhn-Rezwani
J. B. McGrory

Date Published: October 1977

Sponsored by
OAK RIDGE NATIONAL LABORATORY
Oak Ridge, Tennessee 37830
operated by
UNION CARBIDE CORPORATION
for the
ENERGY RESEARCH AND DEVELOPMENT ADMINISTRATION
Contract No. W-7405-eng-26

FOREWARD

This publication contains manuscripts of invited talks and contributed abstracts which formed the substance of a Topical Conference on Heavy Ion Collisions held at Fall Creek Falls Inn, Fall Creek Falls State Park, Pikeville, Tennessee from June 13 through June 17, 1977. Many of the contributed abstracts were discussed in short oral presentations during the plenary sessions or in more specialized afternoon workshops.

The manuscripts of the invited talks and contributed papers are reproduced here as submitted by the authors, without additional editing. The abstracts are arranged in alphabetic order of the first author's name, except for the last three abstracts, which form a sequence of three closely related reports.

The publication of these Proceedings was accomplished with the assistance of the Graphic Arts and Technical Publications sections of Oak Ridge National Laboratory. In particular, the cover was drawn by Alice D. Richardson. The budgetary and logistics work for the meeting was done with the assistance of the Conference Office of Oak Ridge National Laboratory, in particular, Sandra Vaughan. Finally, we are especially grateful to Althea Tate, of the ORNL Physics Division, for her expert handling of many clerical and administrative details of the conference.

The Organizing Committee

1. A. J. Cole
2. R. Dayras
3. D. K. Scott
4. R. K. Smith
5. H. H. Heckman
6. J. V. Maher
7. S. E. Vigdor
8. M. L. Halbert
9. D. G. Raich
10. J. J. Griffin
11. J. R. Huizenga
12. W. T. Pinkston
13. R. Y. Cusson
14. K. K. Kan
15. M. Buenerd
16. R. Arvieu
17. D. Sperber
18. W. Greiner
19. O. Bohigas
20. J. Randrup
21. E. Schopper
22. N. K. Glendenning
23. C. M. Ko
24. A. Tate
25. V. Maruhn
26. R. G. Stokstad
27. J. B. Natowitz
28. M. Divadeenam
29. F. Plasil
30. K. A. Sage
31. G. R. Satchler
32. D. Shapira
33. A. Zucker
34. J. Gomez del Campo
35. W. A. Friedman
36. J. B. McGrory
37. J. W. Negele
38. M. A. Deleplanque
39. S. J. Krieger
40. D. G. Sarantites
41. K. L. Wolf
42. J. A. Vrba
43. H. Schultheis
44. O. Zohni
45. R. Schultheis
46. A. Gobbi
47. S. Ayik
48. K. T. R. Davies
49. E. C. Halbert
50. F. Schussler
51. H. Weidenmüller
52. D. Agassi
53. K. Cordell
54. S. T. Thornton
55. C. Noack
56. F. E. Obenshain
57. T. A. Welton
58. P. Lichtner
59. A. R. Bodmer
60. C. Leclercq-Willain
61. C. Ngô
62. K. Pruess
63. H. Hofmann
64. P. Möller
65. W. Scheid
66. J. A. Maruhn
67. M. Gyulassy
68. M. Berlanger

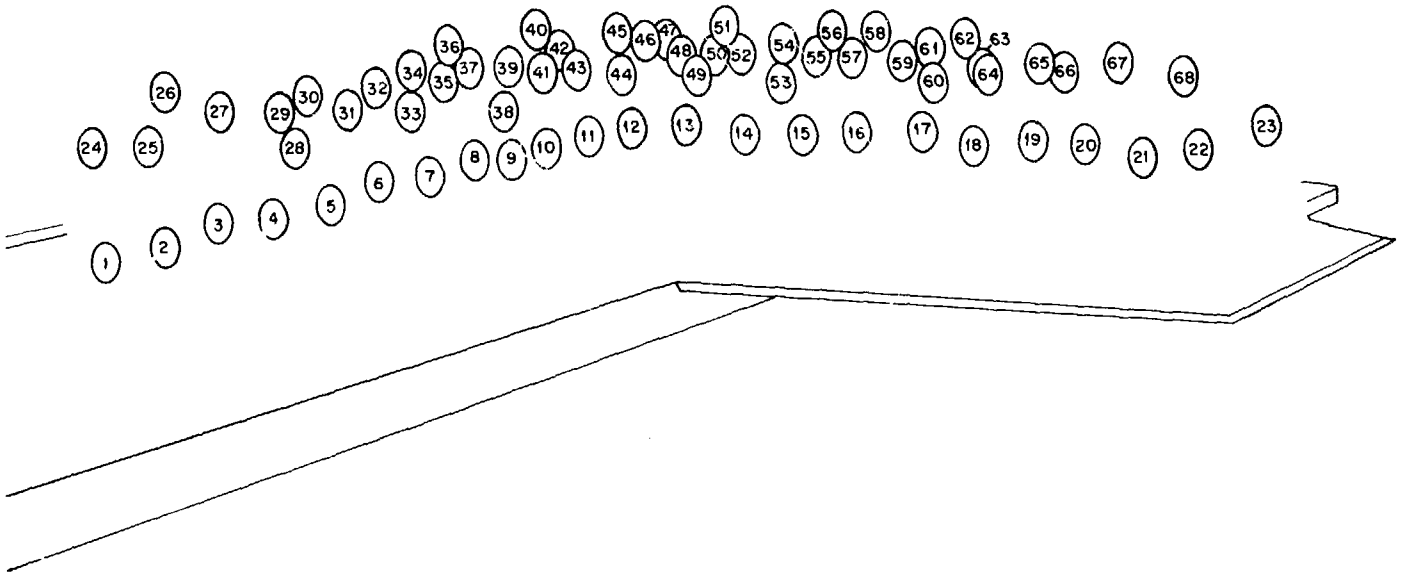

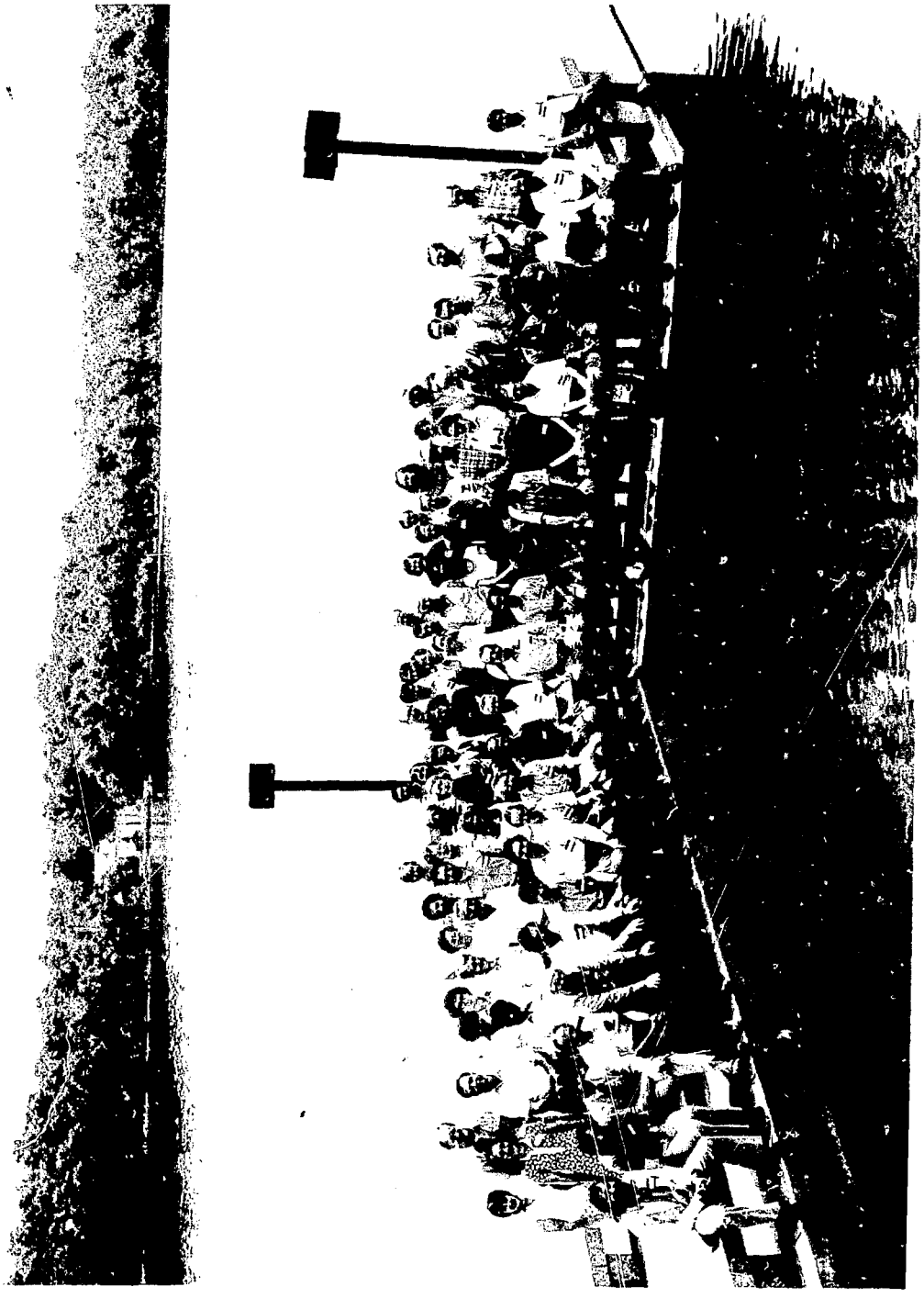

TABLE OF CONTENTS

NUCLEAR FERMI DYNAMICS: PHYSICAL CONTENT VERSUS THEORETICAL APPROACH

James J. Griffin†*
Department of Physics and Astronomy
University of Maryland, College Park, Maryland 20742 U.S.A.

ABSTRACT

Those qualitative properties of nuclei, and of their energetic collisions, which seem of most importance for the flow of nuclear matter in these collisions are listed and briefly discussed. It is suggested that nuclear matter flow is novel among fluid dynamical problems. The name, Nuclear Fermi Dynamics, is proposed as an appropriate unambiguous label. The Principle of Commensurability, which suggests the measurement of the theoretical content of an approach against its expected predictive range is set forth and discussed. Several of the current approaches to the nuclear matter flow problem are listed and subjected to such a test. It is found that the Time-Dependent Hartree-Fock (TDHF) description, alone of all the major theoretical approaches currently in vogue, incorporates each of the major qualitative features within its very concise single mathematical assumption.

Some limitations of the conventional TDHF method are noted, and one particular defect is discussed in detail: the Spurious Cross Channel Correlations which arise whenever several asymptotic reaction channels must be simultaneously described by a single determinant. A reformulated Time-Dependent-$\mathcal{S}$-Matrix Hartree-Fock Theory is proposed, which obviates this difficulty. It is noted that the *structure* of TD-$\mathcal{S}$-HF can be applied to a more general class of non-linear wave mechanical problems than simply TDHF.

Physical requirements minimal to assure that TD-$\mathcal{S}$-HF represents a sensible reaction theory are utilized to prescribe the definition of acceptable asymptotic channels. That definition, in turn, defines the *physical range* of the TD-$\mathcal{S}$-HF theory as the description of collisions of certain mathematically well-defined objects of mixed quantal and classical character, the "TDHF droplets."

†Work supported by U. S. Energy Research and Development Administration.
*The TD-$\mathcal{S}$-HF reformulation is a collaborative effort with Drs. P. Lichtner and M. Dworzecka. Dr. T. Tamura and Dr. Kit-Keung Kan have also recently studied the physical content of TDHF. We appreciate conversations with them and a prepublication copy of their work.

INTRODUCTION

This report comprises four subsections, with subtitles as follows:

IA. IB. Nuclear Fermi Dynamics and the Commensurability Critique. For example,

II. One Limitation of Conventional Numerical TDHF: Spurious Cross Channel Correlations, which suggests the

III. Reformulation of the Theory into TD-λ-HF, whence one defines

IV. "Channels" in the TD-λ-HF Theory and its Physical Range: the collisions of the (mixed quantum-classical) "TDHF Droplets."

I.A. NUCLEAR FERMI DYNAMICS

RELEVANT PROPERTIES OF NUCLEI

In part I, we discuss briefly three nuclear properties and two circumstances of nuclear heavy ion collisions which promise to be of qualitative significance in the description of the matter flow during such collisions. Table I lists these items and identifies them briefly. Of the three, the SMALL and FINITE properties are two which are unique to nuclei and promise to set nuclear matter dynamics apart from the flow of matter in other physical systems.

The nucleus is said to be "small" by virtue of the fact that the dimensionless size parameter, R/λ (where λ is the mean free path of a nucleon inside the nucleus) is less than one(*), for a substantial range of low nuclear temperatures(†).

The long mean free path is, of course, the result of the Fermi statistics of nucleons and the resulting Pauli exclusion principle. This same property provides the theoretical validation of the shell model description of nuclear structure [5-6]. We believe, therefore, that it warrants prime consideration in the construction of any theory of nuclear matter flow.[7].

---

* This mean free path, λ, can be estimated to be $\sim$13 Fm for neutrons incoming with 10 MeV kinetic energy on the basis of the imaginary part of the optical model inside the nucleus as fit to measurements by Greenlees and Bechetti. [1]. Such a value is qualitatively substantiated by the theoretical calculations of Vinh-Mau and Bouyssy [2].

† Kind, et al., [3] have calculated as a function of temperature the mean path of a nucleon in a nuclear degenerate Fermi gas of temperature, T, and report that the mean free path exceeds the nuclear radius for temperature up to about 7MeV, for incoming nucleon energies up to 35 MeV. Collins, [4] is currently re-analyzing this problem.

The SMALLNESS of nuclei, on the other hand, offers a substantial obstacle to any assumption of local equilibrium in any small volume inside the nucleus, and would seem to exclude the possibility of a

(Text continues on following page).

****

TABLE I: SALIENT FEATURES OF NUCLEAR FERMI DYNAMICS

A. Three Nuclear Properties

1. FERMI → SMALL, $R/\lambda < 1$; implies

   No Local Equilibrium
   Collisions of Particles with Walls are Crucial

2. FINITE-A, GRANULAR; implies

   STRUTINSKY GENERALIZED SHELL EFFECTS on
   POTENTIAL, INERTIAL, and DISSIPATIVE parameters

3. LIQUID-SELF-BOUND:

   System responds self-consistently to its own motion.

B. Two Circumstances

1. NON-EQUILIBRIUM ↔ DISSIPATIVE

   Suppressed degrees of freedom serve as dissipative sink

2. MASS-DYNAMICAL ↔ GLOBAL

   Matter flow substantially alters average field during process.

hydrodynamical description(*) via equations of the Navier-Stokes type. For such theories deal with intensive variables which are assumed to vary smoothly across the nucleus.

In addition, NUCLEAR SMALLNESS focuses one's attention on the collisions of nucleons with the walls of the nucleus, since these are the *only* collisions left when the mean free path becomes very large. This qualitative feature [7] is elevated to an exclusive role in the "wall formula" recently recommended by W. J. Swiatecki [10], and plays an important part in the various other one body approaches to dissipation [11-13].

The second property listed is the FINITE-A, or GRANULARITY property of nuclei which arises from the discreteness of their quantum description. This property leads to spherical [14] and generalized [15] shell deviations of the nuclear collective potential energy from its smooth liquid drop value. It arises from the fact that A ($\sim 10^2$) particles allow substantial relative fluctuations from a smooth average as compared with a true many-body system ($A \to \infty$). For macroscopic systems with $A \sim 10^{23}$, e.g., the generalized shell corrections would be much smaller, relatively, and the smooth liquid drop limit much more nearly realized.

We already know that in nuclear physics these generalized shell corrections are sufficient to effect qualitative alterations on the process of nuclear deformation in reaction processes. Especially in the case of fission they supply the currently accepted basis for understanding the mass asymmetry of the fission of heavy nuclei at low and moderate excitation energy [16-19].

(*) We reserve the word *Hydrodynamical* for *water*-like matter flows, well described by the Navier-Stokes equation. The label, *Fluid Dynamical*, on the other hand, denotes the broadest class of matter flow problem, unrestricted to any particular dynamical equation. It should also be noted that the conservation laws (of matter, energy and momentum) must prevail for any physical system [8], and impose upon any dynamical theory a certain general structure sometimes referred to (we think, imprecisely) as "hydrodynamics." The usage here would replace "hydro" by "fluid," except when the tensors involved in the expressions of the conservation laws exhibit the properties (especially locality) which are assumed in the Chapman-Enskog [9] derivation of the Navier-Stokes equations.

In adition, it has been shown that the inertial tensor for nuclear mass flow will also exhibit Strutinsky-type structure in N, Z, and deformation[20]which can be understood as effecting a locally compressible flow for the nuclear matter[21]. Finally, one must anticipate that in a theory which calculates dissipative parameters from microscopic properties, such parameters also will reflect the effects of Strutinsky's generalized shells(*). Thus, the fact that the nucleus is a GRANULAR system will influence the potential, inertial and the dissipative parameters - which is to say, every aspect - of the ultimate description of nuclear Fermi dynamics.

The third property listed, that the nucleus is a self-bound liquid, emphasizes the fact that as nuclear matter flows the average binding field alters in accordance with the matter distribution. The nuclear flow shares this particular property with other physical liquids, but not with gases,nor with the flow of electrons in an atom, where a strong external field (the Coulomb field of the nuclear charge) is unresponsive to the flow of the electron matter.

RELEVANT CIRCUMSTANCES OF NUCLEAR HEAVY ION COLLSIONS

In addition to the above three nuclear properties, two circumstances of the nuclear heavy ion reactions seem essential. The first is that the colliding system is initially extremely DIS-EQUILIBRIZED - containing, in fact, all of its free energy in the single degree of freedom describing the distance between the two nuclei about to collide. One can therefore be certain that, immediately upon collision, this energy will begin flowing into other degrees of freedom, with a strong tendency towards equilibration. The theoretical description of the subsequent motion, since practical considerations require it to involve some number of dynamical variables less than the complete set, will involve from time to time the transfer of energy, momentum, or other physical quantities into degrees of freedom which are being suppressed in the theory. Such transfers which leave the limited space of the retained variables must be considered "dissipation." We therefore expect to deal ultimately in this problem not simply with one "dissipation" but, rather, with several alternative possible dissipative schemes,

(*) Recent work by Koonin and Randrup [13] to be discussed in this conference relates the dissipation kernel to the trajectories of classical particles. These in turn are connected with the degeneracies of a wave mechanical system by Bloch, Balian et al [22]. Thus already one specific path for describing the influence of generalized shells upon dissipation parameters is available.

corresponding to the various numbers of explicit degrees of freedom which we may wish to retain in a particular description, the remainder of which, having been suppressed, provide the sinks for the dissipated quantities.

The second important circumstance of hard(*) nuclear heavy ion collisions arises from the fact that the substantial mass flow can occur in such reaction processes on a short time scale, and can, therefore, imply substantial readjustment of the average shell-model field during the time of the collision. This requirement of a knowledge of the nuclear shell model properties over a finite region of nuclear shapes (including shapes describing ruptured configurations) we refer to as the GLOBAL property of such collisions. We contrast it with the fact that traditional nuclear structure studies generally require no more than a knowledge of nuclear properties (and one or two derivatives) at an equilibrium point. This GLOBAL-MASS-DYNAMICAL property may, as the description of nuclear heavy ion collisions moves forward, come to place demands upon our mathematical capacity, which can not be met with the techniques currently available. But it is also possible that the dissipative processes in nuclear Fermi dynamics will be so dominant over the mass flow properties as to substantially alleviate, and even qualitatively alter, the Fermi dynamical problem into a dissipation-dominated process, rather than a kinetic-dominated mass flow problem. This expectation has been vigorously advanced by W. J. Swiatecki, in particular [23].

COMPARISON AMONG SOME CURRENT THEORIES

In Table II, we tabulate four current theoretical approaches to nuclear heavy ion collisions, Time-Dependent Hartree-Fock[24], Navier-Stokes Hydrodynamics [25], Transport Theory [26] (including [10] the "window formula") and the "wall formula" [10], and the five features just discussed. A "Yes" is entered for each feature which a given theory meets; a "No" for each feature which a given theoretical approach omits. In a few cases neither a Yes nor a No seems adequate:

(*) The emphasis throughout this talk is upon the matter flow, and therefore the "soft" long-distance collisions of heavy ions are not the focus of attention.

TABLE II: QUALITATIVE PROPERTIES INCORPORATED INTO VARIOUS THEORIES

Property: \ Theory:	*TIME DEPENDENT HARTREE-FOCK*	*NAVIER-STOKES HYDRODYNAMICS*	*TRANSPORT THEORY (including window Formula)*	*WALL FORMULA*
SMALL-FERMI ($\lambda > R$)	Yes	No	--(a)	Yes?(b)
FINITE A (Genalized Shells)	Yes	No	No	No
LIQUID (Self-bound)	Yes	Yes	No	No
GLOBAL MASS-DYNAMICAL	Yes	Yes	No	--(c)
NON-EQUILIBRIUM DISSIPATIVE	Yes	Yes	Yes	Yes

a)b)c) refer to notes so labelled in the discussion in the text.

(a) The transport theory description of energy charge and mass equilibrization between two fragments in deep inelastic contact might describe systems with long mean free paths or short mean free paths by incorporating their respective effects into its phenomenological transport coefficients;

(b) The wall formula [10](which is an extension of the piston model [11] to the complete 4π nuclear solid angle) incorporates the long mean free paths by omitting all collisions *except* those with the wall. On the other hand, it is a classical description and incorporates no further effects of the Pauli exclusion effects upon the Fermi particles. Therefore the response: "Yes?."

(c) The wall formula is narrowly aimed at dissipation. Therefore it does not imply, nor exclude, any particular matter flow description.

We emphasize that the successful incorporation of all the important qualitative physical aspects into a single concise assumption, which the Time-Dependent Hartree-Fock method achieves, is no assurance that the resulting description will adequately describe observed nuclear data. Indeed, Commensurability, as discussed below, might dim one's hope to get so much from so little. Even so, the TDHF is of great interest, precisely because of the very economy of its assumptions, as a theorists' theory, to teach one how to look at problems in Fermi dynamics and what reasonably to expect from them. It is for this reason, rather than from an expectation of any successful confrontation between TDHF and observed data, that we devote some considerable discussion to this model below.

I.B. COMMENSURABILITY IN THE ASSESSMENT OF DESCRIPTIONS OF COMPLICATED PHENOMENA

We note that one can formulate the present outlook consciously into a method of assessment of theories for complicated processes such as the present physical problem poses. This method employs The Principle of Commensurability[27],stated as follows:

A sound theoretical model should only yield information commensurate with its input and its structure.

We consider this statement to be self-evident. However, it implies immediately the practical corollary that models which give too much may be erroneous, or may involve hidden assumptions. In addition it leads one to evaluate theoretical models, and especially complicated

models, by emphasizing the "commensurability" between the input, the structure and the predictive capacity of the model. Such an evaluation can be helpful in focussing the search for limitations and/or shortcomings in any proposed theoretical description.

Finally, for a model characterized completely by *mathematical* assumptions, the principle of commensurability suggests the question: What is the *physical* range of the model? This question becomes the more difficult (and its answer the more useful), the more concise and compact is the assumptive mathematical basis of a given model. In particular, as Table I illustrates forcefully, the single-determinant assumption of the Time-Dependent Hartree-Fock description provides an appropriate specific example of a very concise assumptive axiomatic basis for a model, which is able (cf. Table II) to incorporate an impressive range of appropriate physical property, but whose *physical* implications are not immediately transparent.

II. LIMITS OF THE TDHF DESCRIPTION OF COMPLEX REACTIONS: SPURIOUS CROSS CHANNEL CORRELATIONS

CONVENTIONAL TDHF DESCRIPTION

We turn now to a discussion of the numerical Time-Dependent Hartree-Fock method [24] which so economically and completely incorporates the qualitative features of Nuclear Fermi dynamics into the single assumption that the exact solution will be approximated as

$$\Psi \sim \Phi \ , \text{ a single determinant} \ . \tag{1}$$

This assumption, imposed as a restriction on the variational principle whose unrestricted variation yields the Time-Dependent Schrödinger Equation,

$$i\hbar\dot{\Psi} = H\Psi \tag{2}$$

leads to the *Time-Dependent Hartree-Fock Equation,* [28]

$$i\hbar\dot{\Phi}(t) = \mathcal{H}^{HF}(\Phi(t)) \cdot \Phi(t) \ . \tag{3}$$

to describe the time evolution of the determinantal wave function. Then the specification that

$$\Phi(t)\Big|_{t=t_i} = \Phi_o \tag{4}$$

gives the initial condition, whence equation (3) specifies the solution $\Phi(t)$ for all subsequent times.

Thus the TDHF problem, once posed and once subjected to initial conditions, *appears to be* an axiomatically complete structure whose predictions are inexhorable and unalterable. Indeed it is this very compact and closed character of the TDHF problem which enhances its interest for theoretical analysis. For, once the initial values are given and the method of propagation forward in time is prescribed, one seems committed to a specific outcome and is allowed, apparently, no freedom for reinterpretation or creative restructuring of the physical content of the description. One could easily be persuaded that substantial phenomenological success in such a tightly constrained theoretical realm should be considered as very significant. (By Commensurability, on the other hand, one expects that such a drastic simplification of the Schrödinger theory could not fail to lose some essential features of the nuclear physics.)

In spite of its apparent rigidity, we shall here propose a reformulation of the TDHF description for problems involving reaction from and into asymptotic reaction channels. For, as a reaction theory, the TDHF is not so inflexible as it might at first seem. In fact, its basic assumption that the wave function shall be a single determinant can be imposed on reactions in more than one way. We propose here a reformulated method which is physically more reasonable than the more direct method used so far in numerical analyses by the TDHF method.

We should mention also the practical basis for great current interest in Numerical TDHF: the fact that the numerical solution of the TDHF problem with nuclear model forces of the Skyrme type [29,30] was shown in recent years to be possible and became therefore the object of substantial effort, and that it continues to command considerable attention [24]. Thus, TDHF is now a practical object for numerical experiment.

We emphasize that in spite of the remarkable incorporation of the main qualitative nuclear properties into the TDHF method (as exhibited in Table II), the method is still an *approximate* method. Its restriction to a single determinant limits the accuracy of TDHF in each of the three phases of its time dependent description [27]:

(i) The specification of the initial wave function $\Psi_i(t_i)$ by a single determinant approximation is inexact, and inflexible;

(ii) its propagation forward in time to and through the collision by $\mathcal{H}^{HF}$ instead of H_{EXACT} is approximate (omitting, e.g., some two-nucleon correlations);

*Items (i) and (ii) are discussed further in references[31-32].

(iii) the post-breakup determinant, $\Phi(t)$ $(t >> 0)$, is too simple to describe the many channels of the exact outgoing state, and, to date, lacks any specific proposed interpretation.

SPURIOUS CROSS CHANNEL CORRELATIONS

Here we focus upon the third item, and a remedy for the incommensurability between the single TDHF determinant and the outgoing multichannel state of the true Schrödinger system. In particular, we argue that, after the collision and breakup into two spatially separate densities, the TDHF wave function involves *spurious cross-channel correlations*, because it attempts to describe [33]a "coherent superposition of outgoing channels." The available reaction channels correspond to different pairs of nuclei, and/or for each pair a range of possible excited states, which, if they were allowed to propagate independently, would surely be found at large distances to be separating with a variety of relative velocities. But in TDHF only one relative velocity (that prescribed by the relative velocity of the separating potential wells) enters, even though the wave function must purport to describe all channels.

We show now that the single determinantal limitation of the Hartree-Fock description, and the consequent calculation of the single self-consistent potential by means of that single determinant, results for a multi-channel situation in contributions to the potential energy which do not occur in the asymptotic channels of the exact linear Schrödinger theory and which, therefore, we label "spurious." These spurious interactions exert a distorting influence on the physical content of the final phase of the reaction - a phase which ought to be very simple since it involves merely the translation in space of well-separated fragments which have been formed from the reaction process.

Consider $\Phi(t)$ of the Time-Dependent Hartree-Fock description to be expanded in a complete set of exact channel wave function, Ψ_f, for the Schrödinger problem:

$$\Phi(t) = \sum_f w_f \Psi_f(t) \text{ for } t >> 0 . \qquad (5)$$

[Never mind here the complication that the coefficients w_f must surely depend on time.] In particular, if the reaction were initiated as $^{16}O + {}^{16}O$, then one label, f, should denote, e.g., the $^{28}Si + {}^{4}He$ channel. Then consider the (direct term of the) Hartree-Fock potential

$$V_{HF}(\vec{r}) = \int V(\vec{r}_1-\vec{r}_2)\ \rho(\vec{r}_2)\ d^3\vec{r}_2 \tag{6}$$

$$= |w_{O-O}|^2\ V_{HF}^{O-O} + |w_{Si-He}|^2[V_{HF}^{Si-He} + V_{HF}^{He-Si}] \tag{7}$$

Here V_{HF}^{O-O} denotes the self-consistent potential for a 32 x 32 determinant built by anti-symmetrizing two 16 x 16 subdeterminants each describing ^{16}O in its Hartree-Fock ground state well separated in space. This is exactly the potential which arose in the incoming channel of this same reaction. On the other hand, V_{HF}^{Si-He} is the self-consistent potential for a 32 x 32 determinant built from a 4 x 4 determinant describing the ^4He ground state and a 28 x 28 determinant for ^{28}Si. Equation (7) demonstrates the fact that *the Hartree-Fock potential even in the asymptotic region, is a mixture of potentials for the several channels it attempts to describe.*

A very similar argument shows that only channels which *happen to have* the same relative velocity as the separation velocity of the two parts of the Hartree-Fock Potential can have even a possibility of adequate description by the conventional TDHF.

We conclude from the existence of these spurious cross channel correlations in the late stages of a multi-channel process as described by TDHF, that *the TDHF description, as conventionally applied, is not able to provide a self-consistent propagation in time for any one of several outgoing open channels in the final stages of a reaction process.* Only in the trivial case of a single channel (mass *and* energy elastic) collision will the outgoing TDHF state provide the best single determinant description of any particular pair of separating fragments.

From these considerations we are led to propose the following reformulation of the conventional TDHF description,- the TD-$\mathcal{S}$-HF description,- which obviates these spurious cross channel correlative effects in the final stages of the reaction.

III. THE TIME-DEPENDENT-$\mathcal{S}$-MATRIX HARTREE-FOCK DESCRIPTION OF MANY-PARTICLE REACTIONS

We first make a simple renotation of the Time-Dependent Hartree-Fock wave function evolved from the initial state, i, by the Hartree-Fock propagation forward in time. Let

$$\Phi(t) = \Phi_i^{(+)}(t) = U_i^{(+)}(t,t_i)\ \Phi_i^{(0)}(t_i) \tag{8}$$

be the familiar TDHF solution where the propagator U_i represents the (nonlinear) Hartree-Fock process of propagating the wave function $\Phi_i^{(0)}$ forward in time from the initial time t_i to the time t. Analogously, we define the wave function

$$\Phi_f^{(-)}(t) = U_f^{(-)}(t,t_f)\Phi_f^{(0)}(t_f) \tag{9}$$

to be the wave function evolved backwards in time via a similar, but time-reversed TDHF process from $\Phi_f^{(0)}(t_f)$.

THE (TIME-DEPENDENT) CURLY-$\mathcal{S}$ MATRIX

We then construct the following analog of the scattering matrix:

$$\mathcal{S}_{fi}(t) = \langle \Phi_f^{(-)}(t) | \Phi_i^{(+)}(t) \rangle \ . \tag{10}$$

Were the wave functions $\Phi_f^{(-)}$ and $\Phi_i^{(+)}$ to be replaced by the exact solutions, $\Psi_f^{(-)}$ and $\Psi_i^{(+)}$, to the Schrödinger equation, this integral would yield the (time-independent) S-matrix element which gives the amplitude for the wave packet evolved from the initial state, i, to be found in the state which will evolve to the final state, f. We therefore consider $\mathcal{S}_{fi}(t)$ to be the amplitude that the TDHF "state," $\Phi_i^{(+)}(t)$, is found at time t to be the TDHF "state," $\Phi_f^{(-)}(t)$, which will *evolve under TDHF to the final state* $\Phi_f^{(0)}$ *at* $t = t_f$, *without spurious cross channel correlations with channels other than f*. Then we propose that[+]

$$\bar{\mathcal{S}}_{fi} = \frac{1}{2T}\int_{-T}^{+T} dt\, \mathcal{S}_{fi}(t) \tag{11}$$

(*) The time derivative of $\mathcal{S}$ in equation (6) can be estimated from those of Φ_i, Φ_f to be of order $(\hbar)^{-1}$ times of the difference between the corresponding matrix elements of the two distinct Hartree-Fock Hamiltonians, H_i and H_f, at time, t. Since their diagonal elements are ~ -8 A $\simeq 10^3$MeV, this derivative might easily have a magnitude as large as (100 MeV)/$\hbar \simeq 10^{23}$/sec. We therefore consider any attempt to utilize $\mathcal{S}(t)$, unaveraged in time, as futile.

(+) The physical implications of equation (11) should not depend upon the value of the parameter, T, which must therefore be chosen large enough to include all times during which transitions from i can occur to any channel, f. One hopes that for a range of values of T larger than this minimum value, the relative physical transition amplitudes will be insensitive to the specific value of T. (This question is discussed in more detail in reference [34]).

describes the (relative) amplitude that the TDHF state i which evolves from $\Phi_i^{(0)}$ at $t = t_i << 0$ will be found in the state, $\Phi_f^{(0)}$, at $t = t_f >> 0$.

Normalized (since there is no structural compulsion for unitarity in this theory) for the incoming channel i, this becomes

$$\hat{\mathcal{S}}_{fi} = \mathcal{S}_{fi} / [\sum_f \mathcal{S}^*_{fi} \mathcal{S}_{fi}]^{1/2} , \qquad (12)$$

the operational analog of the unitary S matrix in the TD-$\mathcal{S}$-HF theory. Equation (12) completes the required reformulation of the time-dependent reaction theory within the Hartree-Fock framework.

Note that the result (11) applies independent of the particular prescription for the time evolution operations, $U^{(\pm)}$, in equations (8) and (9). It represents therefore an alternative to the use of equation (8) alone, not just for the Hartree-Fock problem, but for any approximate description of the time evolution of a reaction process by means of a wave function to which the statistical interpretation of quantum mechanics, equation (10), is expected to apply.

We note the following features of TD-$\mathcal{S}$-HF:

1. The once only multi-outgoing-channel TDHF calculation of $\Phi_i^{(+)}(t)$ is replaced by one time-reversed incoming calculation of $\Phi_f^{(-)}(t)$ *for each final channel.*

2. A time integral of the overlap

$$\langle \Phi_f^{(-)} | \Phi_i^{(+)} \rangle = \mathcal{S}_{fi}(t) \qquad (13)$$

yields the (unnormalized) $\mathcal{S}_{fi}$, and normalization yields $\hat{\mathcal{S}}_{fi}$, the S-matrix analog.

3. *No spurious cross channel correlations* enter into $\mathcal{S}_{fi}$: separated configurations are propagated only by single-channel self-consistent Hartree-Fock Hamiltonians.

It is remarkable that this reformulation of the TDHF description for multi-channel processes is able still to conform to the requirement that each wave function at each moment be described as a single determinant. Still, it obviates the spurious correlation difficulty of a single determinantal description of a multi-channel physical situation - a difficulty which seems inescapable in the straightforward time-integration of the TDHF equation from the initial incoming state to a

postbreakup time. Since here a time-reversed calculation is used to propagate each of the outgoing configurations backwards into the interaction region, spurious cross channel correlations never enter in the description of well-separated fragments.

In addition, the new theory exhibits a structure symmetric in time, which fits naturally with the time reversal invariance of the scattering theory and provides a framework which requires for both initial and final states precise labels which are appropriate for the elementary objects which the scattering process describes. In contrast, the direct TDHF method, in which only the nearly unique initial state needs to be constructed, allows one to evade the question of what labels are required to characterize its asymptotic states.

We turn next to a consideration of what these labels should comprise, and obtain therefrom a statement of what a "channel" in the TD-$\mathcal{S}$-HF description is to specify. The sought after result is a clear and concise definition of the *physical range* of the TD-$\mathcal{S}$-HF.

IV. "CHANNELS" IN THE TD-$\mathcal{S}$-HF REFORMULATION

MINIMAL REQUIREMENTS OF A REACTION THEORY

To have a reasonable reaction theory, we need at least to be sure that our predictions are (a) specific and unambiguous, and (b) that they do not depend upon the distance of the measurement apparatus from the collision region. In Schrödinger theory, these conditions follow at once from the superposition principle, which in turn is guaranteed by the linearity of the theory. For non-linear theories like TD-$\mathcal{S}$-HF or TDHF, however, even such basic properties are not automatic, and cannot be guaranteed unless they have been specifically built into the theory.

Within the TD-$\mathcal{S}$-HF framework, we can attempt to guarantee these requirements by the choice of "reaction channels." Alternatively, one could say that these conditions require a certain specific choice for these channels. Then its rational structure determines the theory's *physical range*, as discussed above. We follow such an approach here.

Specifically, we demand that an asymptotic channel, (f), specify

(i) completely, two well-separated sub-determinants at some (arbitrary) large standard initiation distance R_0 and at the time t_f for the initiation of the channel reaction; and that

(ii) the subdeterminants so specified must translate in time and space under TDHF propagation *without change* of their internal structure.

APPLICATION TO HARTREE-FOCK

We note that condition (ii) can be satisfied only by the Hartree-Fock ground state, or by another state which is stationary with respect to variation of the Hartree-Fock determinantal wave function. Unfortunately, the set of states composed of all such stationary states for a given exact Hamiltonian are not orthogonal. (Their inclusion would imply, according to equation (10), spontaneous transitions to other channels, even in the far asymptotic region.) They would therefore seem to be unsuitable labels for the identification of a set of excitations for the initial (or final) nuclear projectile and target.

Thus the literal imposition of condition (ii), together with the proposed interpretation of $\mathcal{S}_{fi}(t)$ in equation (10), would require that we restrict the range of Hartree-Fock theory to mass and energy elastic scattering of the Hartree-Fock ground state, to the set of (orthogonal) Hartree-Fock ground states corresponding to all the different mass division of a given A-nucleon system, or to some other arbitrarily selected subset of orthogonal stationary states. Such a restriction would trivialize the theory unacceptally(*).

However, the requirement of stability for the asymptotic channel amplitudes against spontaneous change during free translation can be met, perhaps adequately, by requiring that it prevail not instant by instant, but instead only on a time averaged basis. Thus the demand that

$$\lim_{t\to\infty} \frac{1}{2\tau}\int_{t-\tau}^{t+\tau} dt\, \mathcal{S}_{fi}(t) = 0 \qquad (14)$$

for

$$t-\tau >> +T \quad \text{or} \quad t+\tau << -T \qquad (14a)$$

insures that asymptotic stability of the channel amplitudes on a time-averaged basis.

(*) Note that a Gram-Schmidt orthonormalization of the Hartree-Fock stationary states is self-defeating here, because linear combination of stationary states are not stationary in general, as a result, again, of the non-linearity of the Hartree-Fock problem.

Therefore, we here adopt this alternative: That the condition (ii), requiring no change of the internal wave function as it translates freely in space, be applied not as an exact condition, at every time, but instead only on a time-averaged basis. Then

(iii) *Cyclic, self-consistent oscillations* of the subdeterminants for target and projectile become acceptable in the asymptotic reaction channels, since such oscillations imply no change in the *time-averaged* intrinsic structure as the system translates.

We then arrive at the following set of labels for describing the channel wave function(*) $\Phi_f^{(0)}(t_f)$ as follows:

$$(f) = (A_1, S_1, A_2, S_2, \vec{R}_f, \vec{V}_f, t_f; \varepsilon_{\lambda_1}, \phi_{\lambda_1}, \varepsilon_{\lambda_2}, \varepsilon_{\lambda_2}) \ . \tag{15}$$

This set of labels describes:

1. A single $(A_1+A_2) \times (A_1+A_2)$ determinant constructed by anti-symmetrizing:

2. An $(A_1 \times A_1)$ determinant describing the $S_1{}^{th}$ stationary solution of the isolated A_1-particle Hartree-Fock system , and

3. An analogous $(A_2 \times A_2)$ determinant centered at time $t = t_f$ at some fixed (large!) standard distance, $\vec{R}_f$, in the center of mass frame from the center of mass of A_1.

4. Each subdeterminant at the time t_f describes

   (a) a Hartree-Fock stationary state, labelled S_i, which is

   (b) translating at velocity, $\vec{V}_f$, (relative to its partner in the center-of-mass frame), and

   (c) vibrating (in small TDHF self-consistent oscillations) at its various R.P.A. normal frequencies, ω_λ, with amplitudes ε_λ, and

   (d) at time $t = t_f$ has phase angles, ϕ_λ, for these oscillations.

(*) We restrict ourselves to small amplitudes in the TDHF vibrations, where their properties have been extensively studies. See especially reference [35].

We thus arrive at the conclusion that THE PHYSICAL RANGE of TD-$\mathcal{A}$-HF is the collisions of "TDHF Droplets", where a *"TDHF Droplet" is completely defined dynamically by its Hartree-Fock stationary states and the classical self-consistent TDHF oscillations*(*) *thereof*. That is, the TDHF droplet is completely defined(+) by its spectrum of Hartree-Fock stationary states and of its R.P.A. normal modes.

We note that this statement of the physical content of the TD-$\mathcal{A}$-HF scattering theory indicates that that theory is a description of droplets which exhibit a discrete spectrum of stationary states(++), in addition to a set of classical oscillations. We say "classical," since the small amplitude TDHF self-consistent oscillations around a stationary state are allowed to have arbitrary amplitude and phase, since the Time-Dependent Hartree-Fock Theory compels no discretization for these vibrational amplitudes. Of course, one might wish in some cases to quantize these classical vibrations to obtain (in the multi-boson, harmonic oscillator approximation) eigenenergies spaced at intervals, $h\omega_\lambda$ where ω_λ is the frequency of a given R.P.A. mode. Such a decision would represent an addition (indeed, perhaps, a most reasonable one) to the theory, not required by its intrinsic structure.

Thus, we conclude the TDHF mathematics describes the approach, the interaction (including possible mass exchange), and the separation of TDHF droplets, whose stable points are prescribed by the stationary solutions of the Hartree-Fock equations, and whose normal mode frequencies for small amplitude oscillation are prescribed by the R.P.A. frequency spectra of oscillations around the stationary states.

In other words, the TDHF description of nuclear scattering processes replaces the nuclei by a very special kind of fluid droplet, which exhibits both stationary states of discrete energy and self-consistent vibrations around them of continuous energy.

(*) See footnote on preceding page.

(+) The question whether the droplet is thereby *overspecified* is open.

(++) The realization that *all* Hartree-Fock stationary states *must* be considered on an equal basis, and *could* be incorporated under condition (c), occurred after this talk was presented, partly, indeed, stimulated by a question from Dr. S. Krieger on this point. This question is discussed further in reference [34].

Each pair of droplets is specified by the list of numbers, (15), which suffice to characterize uniquely the single determinantal "channel" wave functions at large separation distances (i.e., the dynamical behavior of the determinants as isolated systems) and appropriate translational properties. We thus arrive at the remarkable result that the TD-ℓ-HF reaction theory describes the collision such mixed classical-quantum mechanical TDHF droplets in terms of a *wave mechanical amplitude*, ℓ, calculated from the overlap of two determinantal wave functions. This remarkable result seems sufficiently intriguing to warrant further attention.

V. SUMMARY

To recapitulate the content of this paper we recall that in order to remove the *spurious cross channel correlations*, we were led to reformulate the TDHF reaction theory into the TD-ℓ-Matrix-HF Theory.

The resulting structure overflows the limits of its origins and emerges as a general scheme, equation (11), for extracting reaction amplitudes from (non-linear) time dependent theories for which the superposition principle does not apply, but where the wave function at each instant can still be assumed to define the amplitudes for the results of measurements defined by a complete linearly independent set of wave functions, according to equation (10).

Then certain minimal requirements for the reaction theory to make physical sense prescribes certain properties for the asymptotic channels, which in the small amplitude limit for TDHF vibrations(*), can be satisfied by channels which can be defined by the set of labels (15).

The resulting definition of reaction channels in the new TD-ℓ-HF theory defines its physical range to be the collision of "TDHF droplets", those objects whose structure when isolated is described by the TDHF theory. One thus arrives at the very commensurable conclusion that precisely the physical content of the self-consistent TDHF description of an isolated nucleus can be incorporated into the TD-ℓ-HF theory of reactions - no more, and no less. This clear qualitative characterization of the physical implications of the single determinantal assumption for reaction theories should be useful in measuring the achievements of and in prescribing the expectations for the TD-ℓ-HF reaction theory.

(*) New knowledge of the large amplitude cyclic TDHF vibrations of an isolated TDHF droplets could require alteration of this channel definition without undermining the essential proposal for TD-ℓ-HF; namely, that equation (11) defines the (relative) transition amplitudes for reaction.

REFERENCES

[1] F.D. Becchetti and G.W. Greenlees, Phys. Rev. 182, (1969)1190.

[2] N. Vinh Mau and A. Bouyssy, Inst. de Physique Nucleaire (Orsay, France). Report IPNO/TH - 75 (May 1975).

[3] A. Kind and G. Patergnani, Nuovo Cimento X (1953) 1375.

[4] M. Collins, private communication

[5] W. Bethe and J. Goldstone, Proc. Roy. Soc. (London)A238 (1957) 551; J. Goldstone, Proc. Roy. Soc. (London)A239 (1957) 267.

[6] L.C. Gomes, J.D. Walecka, and V.F. Weisskopf, Ann. Phys. (N.Y.) 3 (1958) 241.

[7] K.K. Kan and J.J. Griffin, Phys. Rev. C15 (1977) 1126; Rev. Mod. Phys. 48 (1976) 467; K.K. Kan, U. Md. Thesis, 1975; and papers to be published.

[8] G.E. Uhlenbeck and G.W. Ford, Lectures in Statistical Mechanics, Chapter VI, (Amer. Math. Soc., Providence, R.I., 1963).

[9] S. Chapman and T.G. Cowling, The Mathematical Theory of Non Uniform Gases, 2nd Ed. (Cambridge U. Press, 1955) follows the method of Enskog's Uppsala Dissertation (1917).

[10] W.J. Swiatecki, 4x50 Conference (Copenhagen, May 1976), unpublished.

[11] D.H.E. Gross, Proc. Conf. on Heavy Ions, High Spin States and Nuclear Structure in Trieste, 1973. (Int'l. Atomic Energy Agency SMR-14/6, 1975), and Nucl. Phys. A240 (1975) 472.

[12] H. Hofmann and P.J. Siemens, Nucl. Phys. A257 (1976) 165.

[13] J. Randrup and S. Koonin, in these proceedings.

[14] W. Myers and W.J. Swiatecki, Nucl. Phys. 81 (1966)1.

[15] V.M. Strutinsky, Nucl. Phys. A95 (1967) 420: A122 (1969)1. See also M. Brack et al., Rev. Mod. Phys. 44 (1972) 320, and references cited therein.

[16] V.V. Paskevich, Nucl. Phys. A169 (1971) 275.

[17] P. Moller and S.G. Nilsson, Phys. Lett. 31B (1970) 283.

[18] H.C. Pauli and T. Ledergerber, Phys. Lett. 34B (1971) 264.

[19] M. Mustafa, H.W. Schmidt, and U. Mosel. Phys. Lett. 28 (1972) 1536 and Phys. Rev. C7(1973) 1519.

[20] J.J. Griffin, Proceedings of the Second International Atomic Energy Symposium on Physics and Chemistry Fission, Vienna, Austria, 1969 (IAEA, Vienna) p.3; and Nucl. Phys. A 170, 395 (1971).

[21] J.J. Griffin and K.K. Kan, 1974, In Proceedings of the Third International Atomic Energy Agency Symposium on Physics and Chemistry of Fission, Rochester, New York, 1973 (IAEA, Vienna), Vol. 1, p. 533.

[22] C. Bloch and R. Balian, Ann. of Physics (USA) 69 (1972) 76, and earlier work cited therein.

[23] W.J. Swiatecki, private communication.

[24] P. Bonche, S.E. Koonin and J.W. Negele, Phys. Rev. C (1976) 1126; S.E. Koonin, Phys. Rev. Lett. 61B 227 (1976); V. Maruhn-Rezwani, K.T.R. Davies and S.E. Koonin, Phys. Lett. (1977); R.Y. Cusson, R.K. Smith and J.A. Maruhn, Phys. Rev. Lett. 36 (1976) 134.

[25] C.T. Alonso, in Proc. Int'l. Conf. on Drops and Bubbles (Cal. Inst. of Tech., 1974) 139.

[26] W. Nörenberg, Z. Phys. A274 (1975) 241 and A276 (1976) 84; J.de Physique, 37 (1976) Colloque C-5, Suppl. No. 11. (Proc. European Conf. on Nucl. Phys. with Heavy Ions, Caen,(France), September, 1976); H. Weidenmuller, in these proceedings.

[27] J.J. Griffin and P.C. Lichtner, Proc. Int'l. Workshop on Gross Properties of Nuclei and Nuclear Excitations IV, Hirschegg, Austria, Jan. 1976. [Inst. for Kernphysik, T.W. Darmstadt Report AED - Conf - 76-015-000]; and U. Md.-Technical Report 76-096 [ORO-4856-51], 1976.

[28] P.A.M. Dirac, Proc. Cambridge Phil. Soc. 26 (1930) 376.

[29] T.H R. Skyrme, Phil. Mag 1 (1956)1043; Nucl. Phys. 9 (1959) 659.

[30] D. Vautherin and D.M. Brink, Phys. Rev. C5 (1972) 626 and C7 (1973) 6.

[31] P.C. Lichtner and J.J. Griffin, Phys. Rev. Lett. 37 (1976) 1521.

[32] P. Lichtner and M. Dworzecka and J.J. Griffin, to be published.

[33] V. Maruhn-Rezwani, K.T.R. Davies and S.E. Koonin, preprint, to be published in Phys. Lett. (1977). (This view of the interpretation of the post break-up T.D.H.F. wave function is noncontroversial, and widely shared among researchers interested in T.D.H.F).

[34] J.J. Griffin, P.C. Lichtner and M. Dworzecka, The T.D.H.F. Method, to be published.

[35] D.J. Rowe, in Nuclear Collective Motion, (Methuen, Ltd, London, EC4, 1970).

CONF-770602--1

HEAVY ION REACTIONS - AN EXPERIMENTAL VISTA*

R. G. Stokstad

Oak Ridge National Laboratory
Oak Ridge, Tennessee 37830

ABSTRACT

Examples of recent experiments in the areas of fusion and deep-inelastic scattering are presented and discussed. Emphasis is placed on the importance of individual nucleons in the fusion process, the effects of high angular momentum, and our understanding of compound nuclear decay. Experiments on deep inelastic scattering are entering a new stage in which important parameters of the reaction mechanism are now open to investigation. Primarily through coincidence measurements, direct information on the angular momentum transferred in a collision and on the time scale of decay is being obtained.

I. INTRODUCTION

The rate at which our understanding of heavy-ion reaction mechanisms increases is astounding and exciting. It would be impossible to keep up with, let alone contribute effectively to, this rapidly developing field without the personal communication and interaction provided by topical conferences.

This meeting at Fall Creek Falls will emphasize, in the words of our organizing committee, "theoretical descriptions." I note however that about half of the scheduled talks are to be delivered by experimentalists. This recognizes, I believe, that we are ultimately concerned with theoretical descriptions of experimental data. If the necessary data do not exist, then we must acquire them. (The completion of GSI, the scheduled upgrading of the Bevelac, and the accelerator projects at Daresbury, Caen and Oak Ridge represent a strong commitment to this.) If new measurements exist, but the theoretical descriptions have not been brought to the level of a quantitative comparison, then this is also a challenge to be met. The interfacing of these two complementary approaches to "understanding" is one of the reasons why we are here. The talks you will hear from my experimentalist colleagues in the coming sessions will provide a broad view of what is new and exciting in current experimental work. In a real sense, it is the sum of all these presentations which will constitute the "vista" provided by experimental studies of heavy-ion collisions.

*Work supported by U.S. Energy Research and Development Administration under contract with the Union Carbide Corporation.

I have selected a number of experiments which illustrate the kinds of information now being obtained in the areas of fusion and deep inelastic scattering. As you will see, these experiments involve reactions throughout the periodic table and bombarding energies ranging over more than two orders of magnitude.

Much of the data you will see is not yet published, and I refer you to the acknowledgements for recognition of those who have very kindly communicated their results prior to publication.

Figure 1 outlines the physics I wish to cover. I have opted to mention a large number of experiments, describing only their essential features and results, rather than concentrating on only a few. (Regrettably, it is not possible to describe some of the elegant and sophisticated experimental techniques which have made some of these results possible.)

FUSION

MICROSCOPIC ASPECTS

ANGULAR MOMENTUM LIMITATIONS

COMPOUND NUCLEUS DECAY

DEEP INELASTIC SCATTERING

ALIGNMENT AND ANGULAR MOMENTUM TRANSFER

TIME SCALE AND MECHANISMS FOR DECAY

FIG. 1. Topics to be discussed.

Section IV gives a summary which attempts to tie this altogether.

II. FUSION

A. Microscopic Aspects

Even though the fundamental constituents of the nucleus are protons and neutrons, surprisingly little is known about the importance of individual nucleons in processes such as fusion. Perhaps this should be taken as an indication that the effects of individual nucleonic motion are not of importance in determining the fusion cross section, and that macroscopic and collective variables are all that matter. Macroscopic properties (radii, deformation, potentials, etc.) may be derived from microscopic models, however, and such calculations provide a motivation for the experiments I will discuss. The two-center shell model calculations of Glas and Mosel (GL 74), for example, suggest that the fusion cross section might depend on which shell model orbitals are occupied, and hence on the valence nucleons of the target and projectile. Figure 2 shows the energies of shell model configurations for the two-center ^{16}O-^{16}O system as a function of the separation between the centers of the oscillator wells. Nuclear interactions leading to fusion occur at level crossings and are estimated with the Landau-Zener approximation. If we argue that the

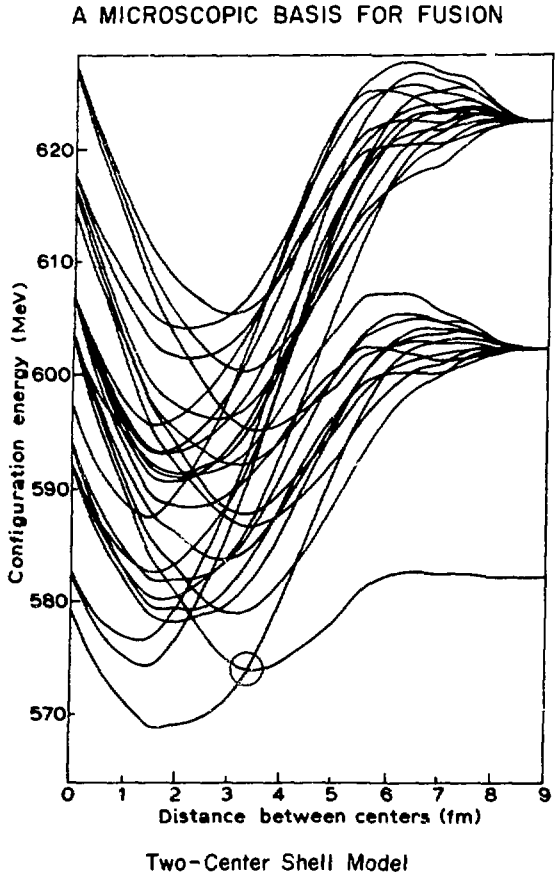

FIG. 2. Configuration energies calculated with the two-center shell model as a function of the separation of the centers. At distances less than 3.4 fm, the lowest energy configuration is the ^{32}S ground state, at larger distances it is the ^{16}O-^{16}O ground state. Fusion is initiated at such level crossings (Gl 74,76).

first level crossing (circled in Fig. 2) in some way determines a critical radius for fusion, then changes in the fusion cross section might be observed as individual nucleons are added or subtracted from the target or projectile. To be considered as evidence for microscopic processes in fusion, we require that these changes be in addition to those expected on the basis of changes in Coulomb barrier or macroscopic "$A^{1/3}$-type" changes in radius.

Recent experimental results on fusion cross sections have much to say on this question. Figure 3 illustrates the characteristic energy regions for fusion. This one-dimensional classification is valid for relatively light heavy-ion systems for which the dynamical path for fusion lies inside the saddle point for fission (Mö 76). In region 1, for small values of σ_{fus}, penetration of the Coulomb barrier is the mechanism governing the order of magnitude of the cross section. In region 2, direct reactions begin to compete, and σ_{fus} can experience a maximum value and then decrease slowly. We shall consider each of these regions in turn but will postpone the discussion of the third region to Section IIB.

The high currents and availability of low energy Van de Graaff accelerators has enabled the measurement of fusion cross sections covering the extreme range of tens of nanobarns to $\sim$ 1 barn. Recently, systematic studies of a large number of systems have become available (St 76, Cu 76, Hi 76, 77b). Typical experimental results are shown in Fig. 4 for the ^{12}C + ^{13}C system (Da 76b). The fusion cross section is

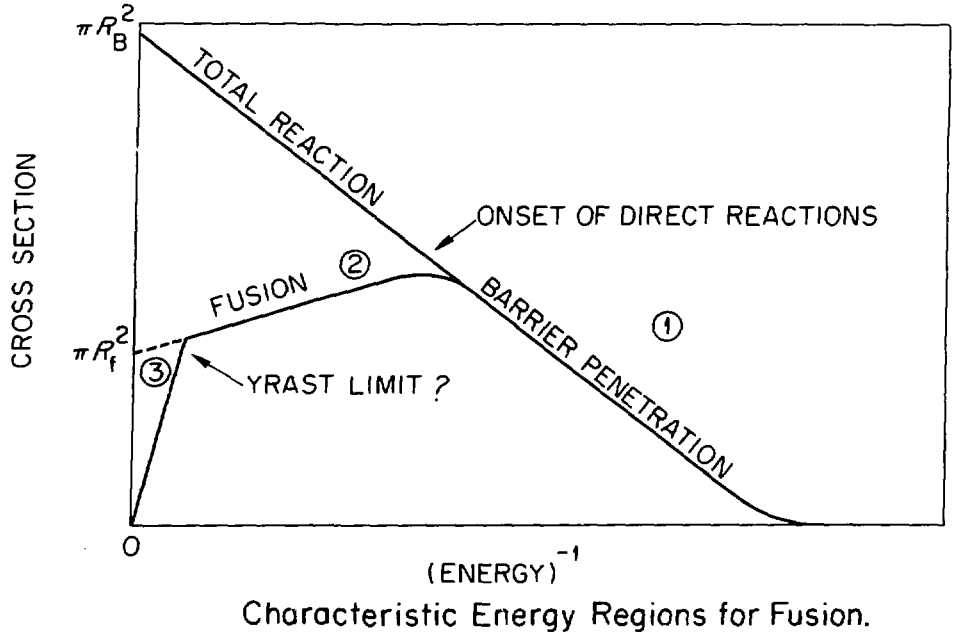

FIG. 3. Schematic representation of the fusion cross sections and total reaction cross section as a function of the reciprocal of the bombarding energy.

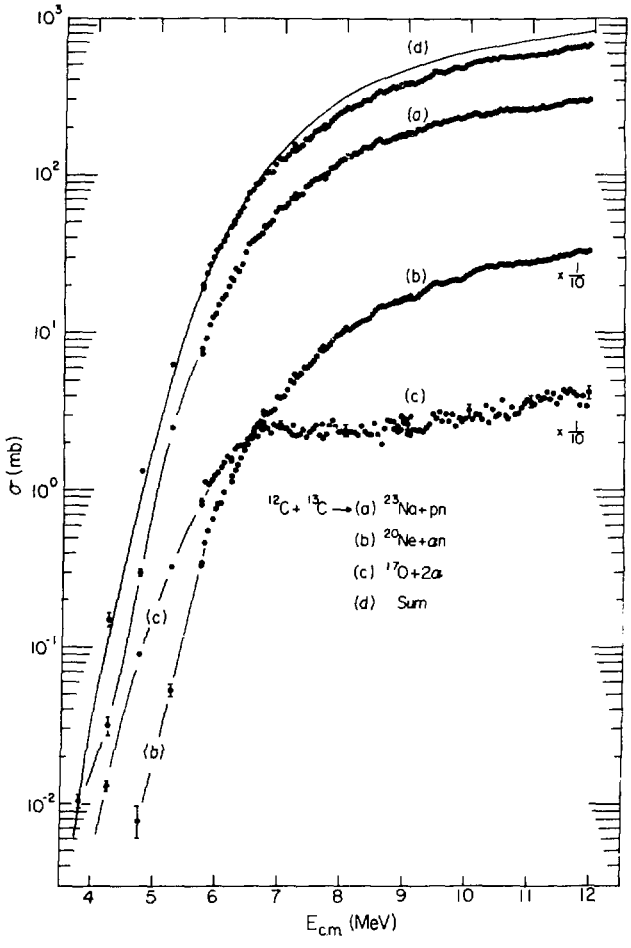

FIG. 4. Energy dependence of evaporation-residue cross sections for ^{12}C + ^{13}C at sub-Coulomb bombarding energies. The full drawn curve is an optical model calculation for the fusion cross section, coupled with a statistical model calculation for branching to the observed residues (Da 76b).

deduced from the observation of discrete γ-ray lines in the residue of the compound nucleus. The full curve which is compared with the sum of the cross sections to all bound states in ^{23}Na, ^{20}Ne and ^{17}O represents the effect of barrier penetration as given by an optical model calculation of the entrance channel transmission coefficients and a statistical model calculation of the decay of the compound nucleus. It is the deviation of the cross section from this prediction which is of interest. In the following presentation of the experimental results, the total fusion cross section was first deduced from experiment and was then divided by the cross section calculated with the optical model using a single set of parameters.* The energy scale in the center of mass has been shifted by an amount $E_{Coul} = \frac{Z_1 Z_2 e^2}{R}$ where $R = 1.7(A_1^{1/3} + A_2^{1/3})$ fm.

Figures 5 and 6 present the quantity $R = \sigma_{fusion}/\sigma_{opt.mod.}$ vs. $E_{c.m.} - E_{Coul}$ for 14 heavy-ion systems with projectiles and targets in the 1p shell. In Fig. 5 we see that the cross sections involving the isotopes of ^{10}B and ^{11}B are all reproduced very well by the "standard" optical model. There is perhaps a small decrease in R(E) at the lower energies for $^{14}N + ^{10}B$, but it is not marked. Given our operational definition above, one would not cite any evidence for microscopic effects based on a comparison of the lower six excitation functions shown in Fig. 5. The energy dependence for $^{16}O + ^{9}Be$ (Sw 77b), however is quite different, with R rising by a factor of 2 from the lowest to the highest energy. It is interesting to note that this system, as does $^{12}C + ^{9}Be$ (Cu 77), has a direct reaction channel involving neutron transfer to the heavy partner which far exceeds the fusion cross section at low energies. In Fig. 6 the values of R for systems involving projectiles and targets both with masses $\geq$ 12 are shown. The difference between Fig. 5 and Fig. 6 is striking. A general feature for the systems in Fig. 6 is that R decreases at lower energies even though the detailed behavior in all systems is by no means identical. (The narrow resonances in $^{12}C + ^{12}C$ and to a lesser extent in $^{16}O + ^{12}C$ are noteworthy, but that is another story; we are concerned here with the energy-averaged behavior of the data.) The average energy dependence of R for $^{16}O + ^{14}N$ is quite different from that of $^{16}O + ^{16}O$. The systems $^{14}N + ^{12}C$, $^{13}C + ^{12}C$ and $^{12}C + ^{12}C$ are all different. The differences referred to can be quite large also, up to factors of two.

The message of Figs. 5 and 6 is simply stated. The addition or subtraction of one or two nucleons from the projectile or target can

*V = 50 MeV, W = 10 MeV, r_o = 1.27 fm, a = 0.4 fm; matching radius = 15a + the larger of R or D, where R is the nuclear radius and D is the distance of closest approach.

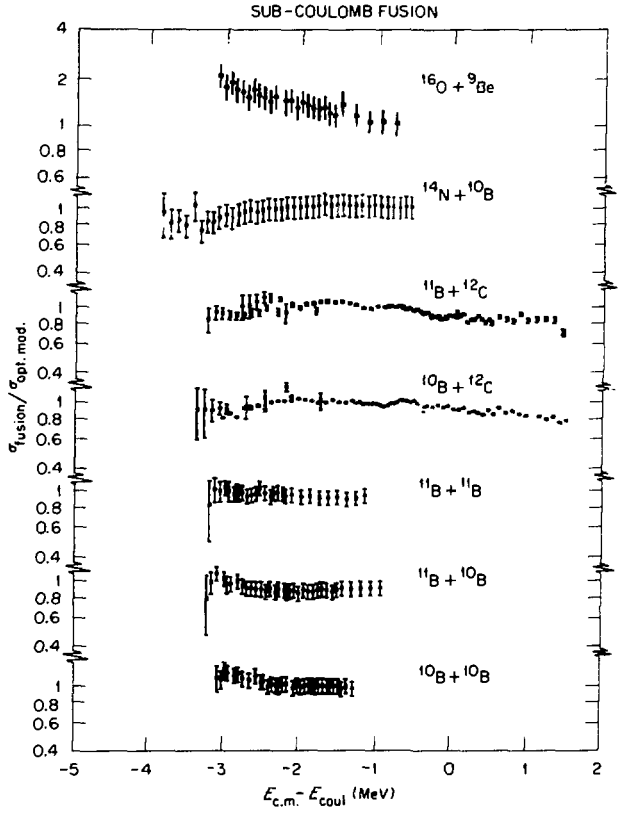

FIG. 5. The ratio of measured fusion cross sections to a standard optical model prediction for sub-Coulomb energies. The energy scale in each case has been shifted such that 0 MeV corresponds to $E_{c.m.} = Z_1 Z_2 e^2/R$ MeV where $R = 1.7(A_1^{1/3} + A_2^{1/3})$ fm. The experimental data are taken from: $^{10}B + ^{10}B$, $^{11}B + ^{10}B$, $^{11}B + ^{11}B$ (Hi 76); $^{10}B + ^{12}C$, $^{11}B + ^{12}C$ (Da 76, Hi 77b); $^{14}N + ^{10}B$ (Hi 77b); $^{16}O + ^{9}Be$ (Sw 77b).

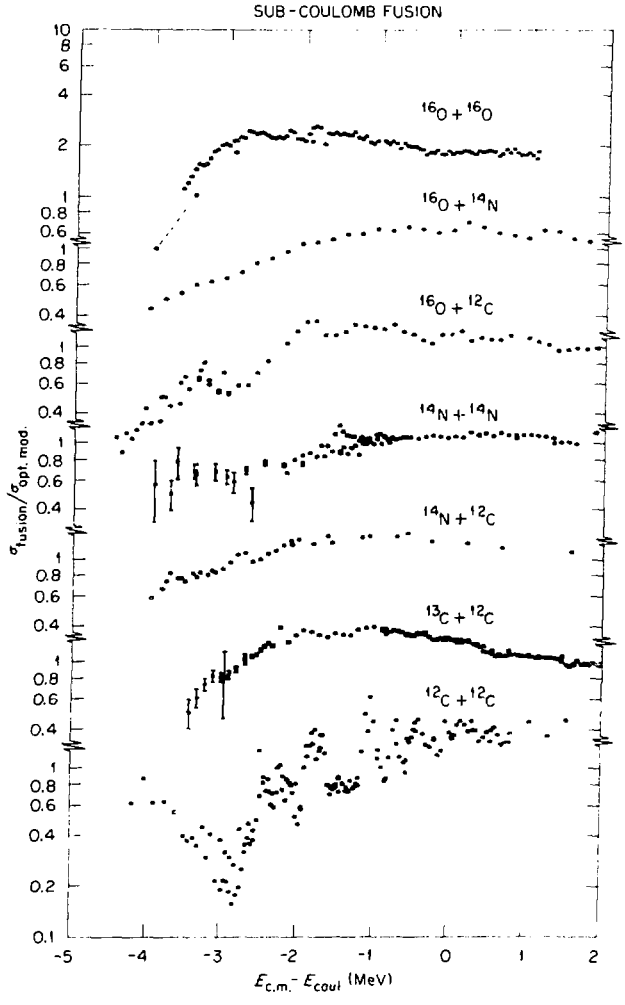

FIG. 6. The ratio of measured fusion cross sections to a standard optical model prediction for sub-Coulomb energies. The energy scale in each case has been shifted such that 0 MeV corresponds to $E_{c.m.} = Z_1 Z_2 e^2/R$ MeV where $R = 1.7(A_1^{1/3} + A_2^{1/3})$ fm. The experimental data are taken from: $^{12}C + ^{12}C$ (Ma 73); $^{12}C + ^{13}C$ (Da 76b); $^{14}N + ^{12}C$, $^{14}N + ^{16}O$ (Sw 77a); $^{12}C + ^{16}O$ (Cu 76); $^{14}N + ^{14}N$ (Sw 76c); $^{16}O + ^{16}O$ (Sp 74).

have a profound effect upon the energy dependence for fusion. This is a strong indication that the valence nucleons play an important role in the mechanisms leading to fusion. At present there is no qualitative or quantitative explanation for the disparate results shown in Figs. 5 and 6. Quantitative microscopic calculations for comparison with these data are needed. In one case (Wi 77), a folding model calculation of the real potential for the different systems has been made. The imaginary potential was taken to be a Woods Saxon with W = 10 MeV, r_o = 1.27 fm, and a = 0.4 fm. This procedure yields values of $R = \sigma_{\text{folded potential}}/\sigma_{\text{opt.mod.}} \simeq 1$ for all reactions. Thus, the microscopic effects may well be contained in the imaginary potential.

The real interaction potentials for $^{12}C + ^{12}C$ and $^{16}O + ^{16}O$ have been calculated in the two-center shell model (Pr 70) and in the TDHF approximation (Ma 76, Ko 77). Generally, the calculations now available are for closed shell systems or even-even nuclei and comparisons with the low energy data has not been extensive. Recently, a macroscopic treatment of the potentials has been presented (Ar 76). Phenomenological comparisons with the data for the α-conjugate systems are found in refs. Ch 77, Mi 72 and Fo 75.

In summary, the experimental results shown in Figs. 5 and 6 together with those to be discussed next provide an excellent opportunity for testing microscopic calculations of the fusion process.

The value of σ_{fus} in region 2 of Fig. 3, the energy region over the Coulomb barrier, provides another opportunity for observing the effects of individual nucleons on the fusion process. The experimental technique used in this region differs in that the residues of compound nucleus decay are observed directly with a ΔE-E counter telescope. This technique can be sufficiently precise that the rather small changes in the fusion cross section associated with the $A^{1/3}$ dependence of the nuclear radius can be observed, even with the addition of only one nucleon. Figure 7 shows measurements of σ_{fus} for $^{16,17,18}O + ^{27}Al$ just above the Coulomb barrier (Ei 77). The straight lines represent fits to the data using the classical expression $\sigma_{fus} = \pi R_B^2 (1 - \frac{V_B}{E_{c.m.}})$. The small changes (∿ 5-10%) in the fusion cross section in this energy region are consistent with the increase in size of the oxygen nucleus as neutrons are added.

A more dramatic change in behavior of the fusion cross section at energies well above the Coulomb barrier is illustrated in Fig. 8 (Vi 76, Sp 76a,b). When the small resonances in the $^{12}C + ^{16}O$ data are averaged by fitting the data with, e.g., the expression of Glas

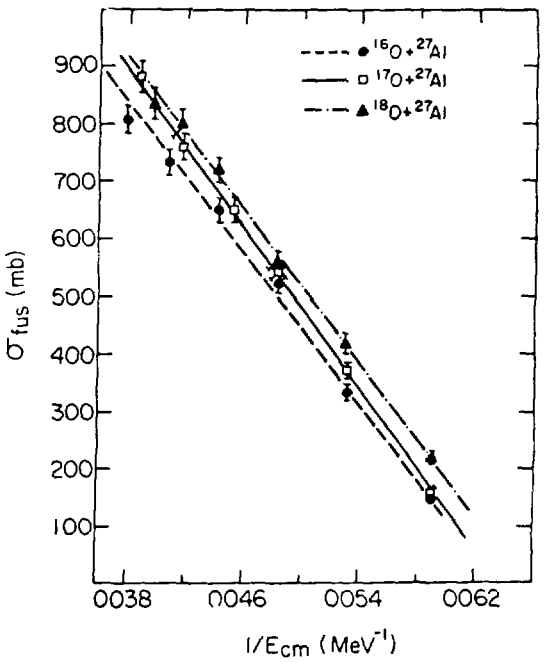

FIG. 7. Fusion cross sections for $^{16,17,18}O + ^{27}Al$ (Ei 77). The straight lines are fits to the data. The differences between the cross sections for the different projectile isotopes reflect in large part the $A^{1/3}$ dependence of the oxygen radius.

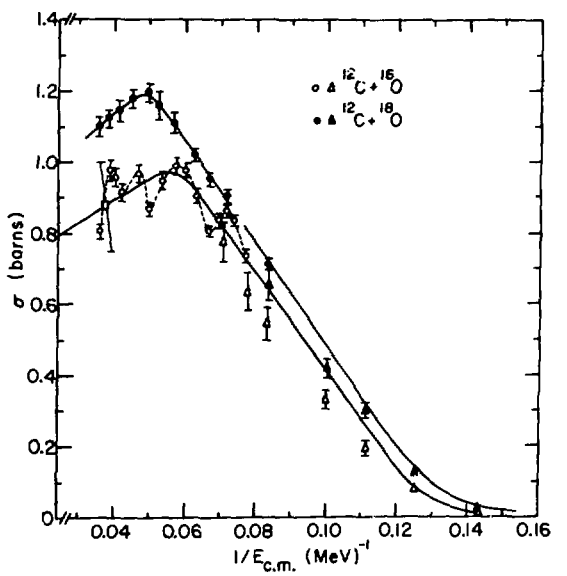

FIG. 8. Fusion cross sections for $^{12}C + ^{16}O$, $^{12}C + ^{18}O$ (Vi 76, Sp 76a, Sp 76b, Ei 77). The curved lines are fits to the data using the formula of Glas and Mosel (Gl 75).

and Mosel (Gl 75), a difference of about 200 mb or 20% in the value of the maximum fusion cross section is noted. (We would expect an increase of $\lesssim$ 5% based on the $A^{1/3}$ change in radius of ^{18}O-^{16}O.) Systematic studies of the value of $\sigma_{fus}(max)$ in this mass region led to the suggestion that the 200 mb increase was associated with the addition of one or more nucleons in the s-d shell (Sp 76b). The addition of nucleons into a major oscillator shell presumably could cause an abrupt change in the mean-square radius. Figure 9 summarizes the experimental data currently available for the maximum fusion cross section in the region above the Coulomb barrier. The correlation of the abrupt change in the fusion cross section of $\sim$ 200 mb with the introduction of a nucleus in the s-d shell is upset by the recent measurement of the ^{15}N + ^{12}C fusion cross section (Co 76). This value is $\sim$ 15% larger than that of ^{14}N + ^{12}C and much closer to the value prevalent when one of the reaction partners is in the s-d shell.

It appears that the manner in which valence nucleons affect the magnitude and the energy dependence of the fusion cross section for these light heavy ions is yet to be understood. Perhaps the role played by these nucleons is complex - indeed, the complexity of Fig. 2 suggests this - and coupling to direct reactions or collective modes of motion may be important (Pe 76).

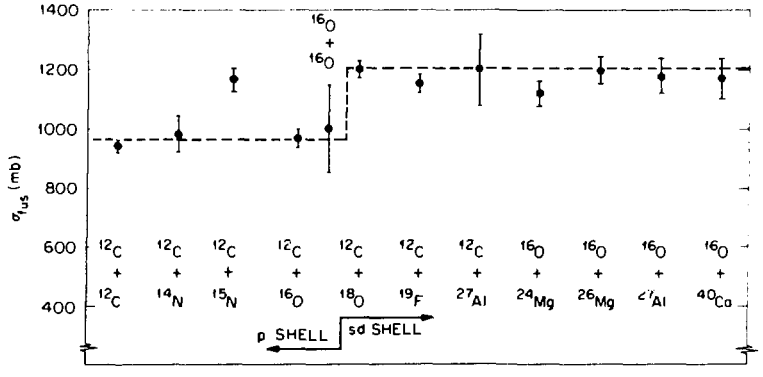

FIG. 9. Measured values of the maximum fusion cross section for different systems. Cases in which both the projectile and target are in the p shell are in the left hand portion of the figure, as indicated. The apparent systematics $\sigma_{fus} \sim 1000$ mb for p shell nuclei and $\sigma_{fus} \sim 1200$ mb for s-d shell targets, is upset by the large value of σ_{fus} for ^{15}N + ^{12}C. The experimental data are taken from: ^{12}C + ^{12}C ^{12}C + ^{16}O, ^{18}O + ^{12}C, ^{12}C + ^{19}F, ^{16}O + $^{24,26}Mg$ (Vi 76, Sp 76a, Sp 76b, Sc 77, Ta 77), ^{12}C + ^{14}N (Co 76, St 77, Sc 77), ^{12}C + ^{15}N (Co 76, Sc 77); ^{12}C + ^{27}Al (Be 76), ^{16}O + ^{16}O (We 76), ^{16}O + ^{27}Al (Ba 77). Unpublished values and their errors are preliminary and subject to revision.

B. Angular Momentum Limitations

A macroscopic view of the fusion process enables an "understanding" of the gross behavior of σ_{fus} in regions (1) and (2) (Fig. 3) in terms of a barrier. At low energies, it is the Coulomb barrier. At high energies, region 2, it is predominantly the centrifugal barrier. The degree of penetration required for fusion is determined by a hypothetical critical radius (Ga 74, Gl 75) which is nearly equivalent to an energy dependent critical angular momentum (Ba 73). This approach and somewhat more sophisticated one dimensional calculations (Gr 74) have been extremely successful in reproducing experimental data over a wide range of energy and mass for which the dynamical path to fusion lies inside the saddle point for fission. There remains the possibility of an additional limitation on the fusion mechanism, however, which has been harder to detect experimentally. This limit would occur in region 3 of Fig. 2, and is a Yrast limit. That is, the compound nucleus cannot be formed if, at that excitation energy, a state with angular momentum J does not exist. This "absolute" upper limit on the angular momentum is usually calculated with the rotating liquid drop model (Co 74). Previous measurements where the angular momentum introduced at the critical radius approaches that of the liquid drop limit are described in refs. Na 75, Br 76b, and Vi 76.

Results of a recent experiment (St 77) in which both the effect of penetration to a critical radius and, apparently, that of a Yrast limit are present are shown in Fig. 10. At the right hand portion of the figure (low bombarding energies) the beginning of the drop in σ_{fus} is just on scale. In the region $0.012 \leq E^{-1} \leq 0.05$ ($180 \geq E \geq 43$ MeV), σ_{fus} varies linearly with E^{-1}, consistent with penetration to a critical radius. At the highest bombarding energy, $E_{^{14}N}$ = 248 MeV, a significant decrease in the value of σ_{fus} of about 200 mb is observed.

Two dimensional TDHF calculations (Ma 77) have been performed and compared to these data. The theoretical cross sections for σ_{fus} decrease from about 1150 mb at $E^{-1}_{c.m.} = 0.02$ to 900 mb at $E^{-1}_{c.m.} = 0.009$.

The results of Fig. 10 may be plotted in a different manner by converting σ_{fus} to a critical angular momentum J using the sharp cutoff relation $\sigma_{fus} = \pi \lambda\!\!\!^{-2} (J + 1)^2$ and plotting the results versus excitation energy in ^{26}Al ($E^* = E_{c.m.}$ + 15 MeV separation energy). The maximum angular momentum for which fusion occurs is seen to change only very little with excitation energy for the two highest energy data points. The solid vertical line at $J_{max} = 26.6\ \hbar$ represents the prediction of the rotating liquid drop model, which is consistent with the experimental data. The trend of the experimental results in Fig. 11 suggests that the maximum angular momentum which a ^{26}Al

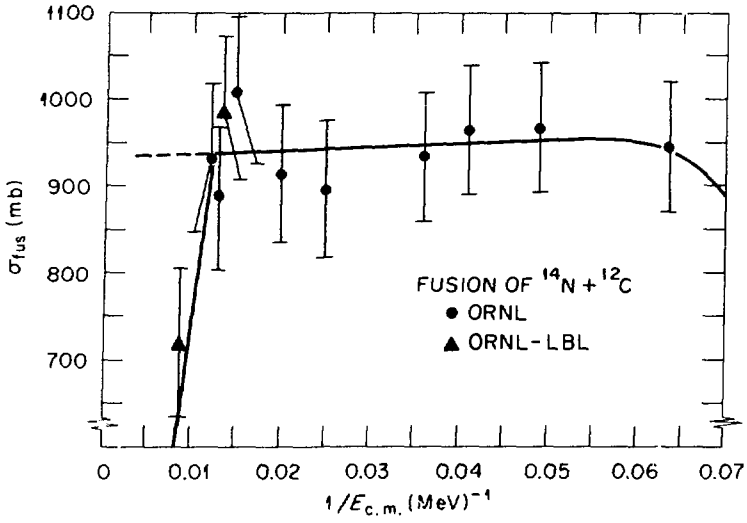

FIG. 10. The fusion cross section for ^{14}N + ^{12}C at ^{14}N bombarding energies from 34 MeV to 248 MeV. The solid line for $0.012 \leq E_{c.m.} \leq .05$ is a straight line fit to the data in that region. The solid line for $E_{c.m.} < 0.012$ corresponds to the fusion cross section expected for a Yrast limit of $\sim$ 27 $\hbar$ (St 77).

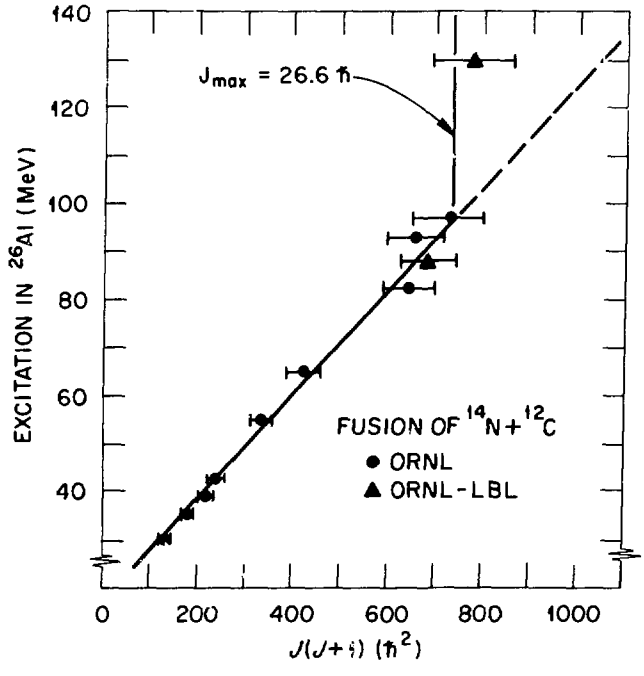

FIG. 11. The critical angular momenta for ^{12}C + ^{14}N deduced from the measured values of σ_{fus} using $\sigma_{fus} = \pi\lambda^2(J+1)^2$, (St 77). The angular momentum corresponding to the liquid drop limit (Co 74) J_{max} = 26.6 $\hbar$, is shown.

compound nucleus may have (at any excitation energy) has been observed and is $\sim$ 1 $\hbar$/nucleon.

C. Compound Nucleus Decay

Several important properties of the compound nucleus become accessible through the measurement and analysis of the decay products. Such quantities are the temperature, distribution of angular momenta and moments of inertia and the degree of equilibration. Analysis of the reaction products usually involves comparison of the data with the predictions of an evaporation calculation, i.e. a statistical model. Significant progress has been made both in the range and quality of experimental data and the sophistication of the computer codes used for the analysis (Pü 77, Go 77, Hi 77). As an example, the mass distributions obtained from the fusion of ^{19}F and ^{27}Al are shown for four different bombarding energies in Fig. 12 (Pü 77). The experimental data were obtained with a time-of-flight spectrometer as described in ref. Pü 75. The main decay mode leading to several of the residual masses is indicated. The production of lighter residues and the increased importance of multiple α-particle emission as the bombarding energy is increased is immediately apparent. That the increased α-particle emission is associated with higher angular momentum rather than higher excitation energy is illustrated in Fig. 13 in which calculated mass distributions as a function of compound nucleus angular momentum are presented. Thus, the residues corresponding to α-particle emission probe the region of the energy-angular momentum plane nearer the Yrast line of the compound nucleus. Analysis of the relative intensity of these products indicates that the compound nuclei in this mass region and their immediate daughters are quite deformed at high excitation energy and angular momenta (Pü 77, see also St 77).

The mass distribution obtained from the decay of a much heavier system, ^{151}Tb, formed in the reaction ^{65}Cu + ^{86}Kr (716 MeV) is shown in Fig. 14 (Br 76b, Br 76c, Pl 77). An evaporation calculation (Pl 75, Pl 77) reproduces the distribution of residues rather well.

Since a large amount of experimental data on the mass and/or charge distributions of evaporation residues is available it is of interest to examine the systematics of a simple quantity such as the average amount of mass evaporated versus excitation energy. (This has been done for the case of ^{151}Tb, Pl 77). In Fig. 15, results from some 14 different compound systems are shown. The ordinate is $\Delta A = A_{C.N.} - \bar{A}_{residue}$ where A is the average mass of the evaporation residues. In cases where Z-distributions were measured, the conversion to mass was made using the N/Z ratio appropriate for nuclei near the most probable Z-value. Several features of this plot are of interest. Typical values of the excitation energy removed per mass unit range from $\sim$ 7-12 MeV/amu.

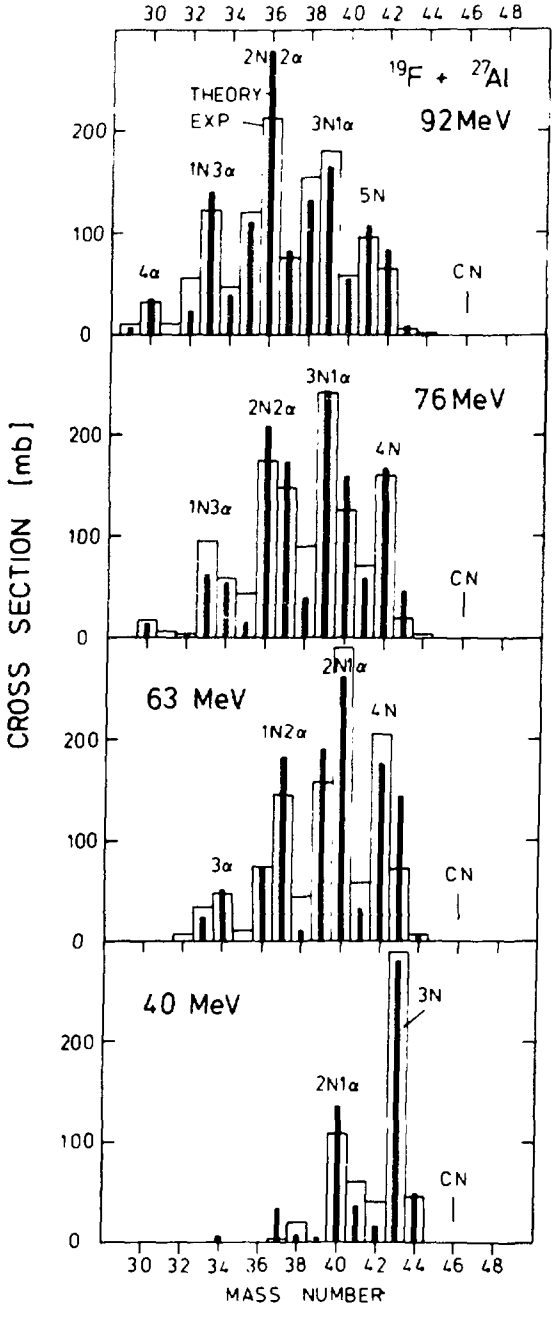

FIG. 12. Measured and predicted mass distributions for the evaporation residues of $^{19}F + ^{27}Al$ (PU 77).

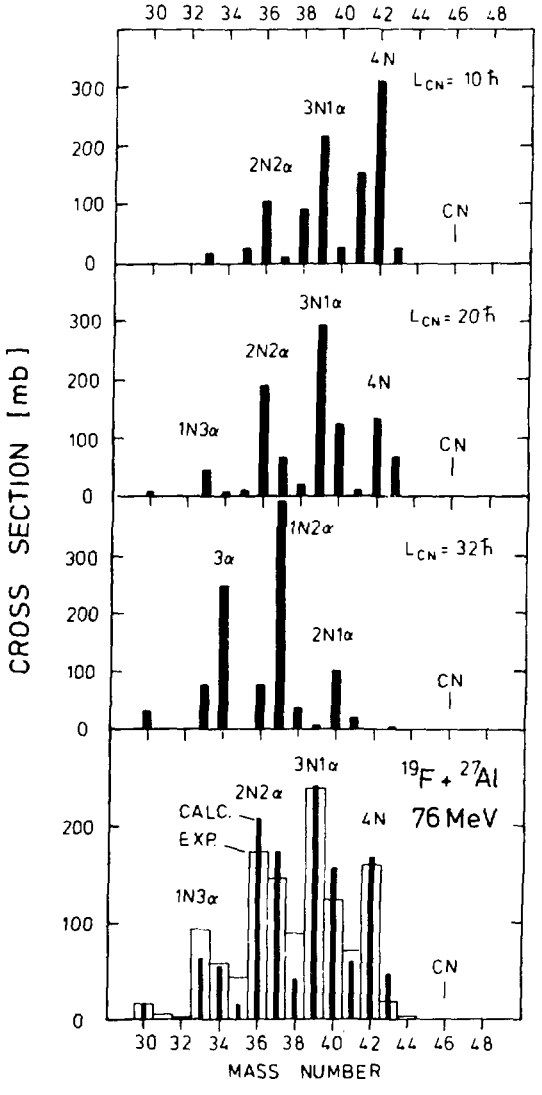

FIG. 13. The predicted distribution of residues for different angular momenta of the compound nucleus (Pü 77).

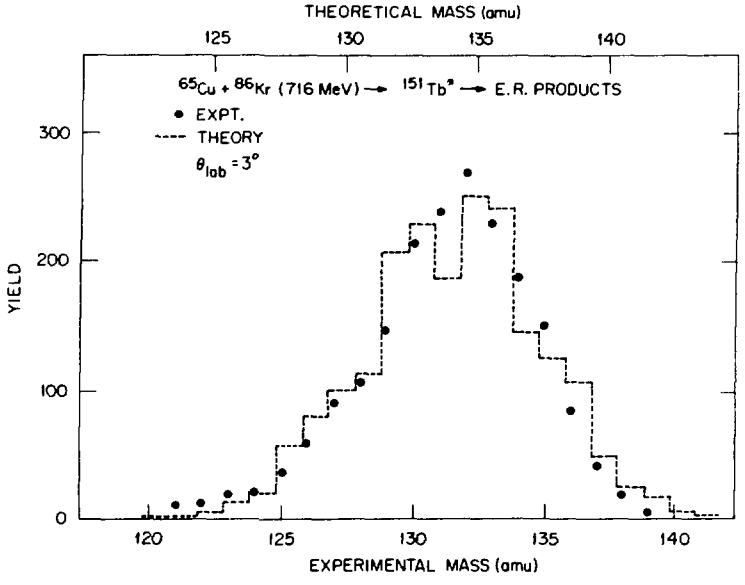

FIG. I4. Measured and predicted mass distributions for the evaporation residue products of ^{151}Tb (Br 76c, Pl 77).

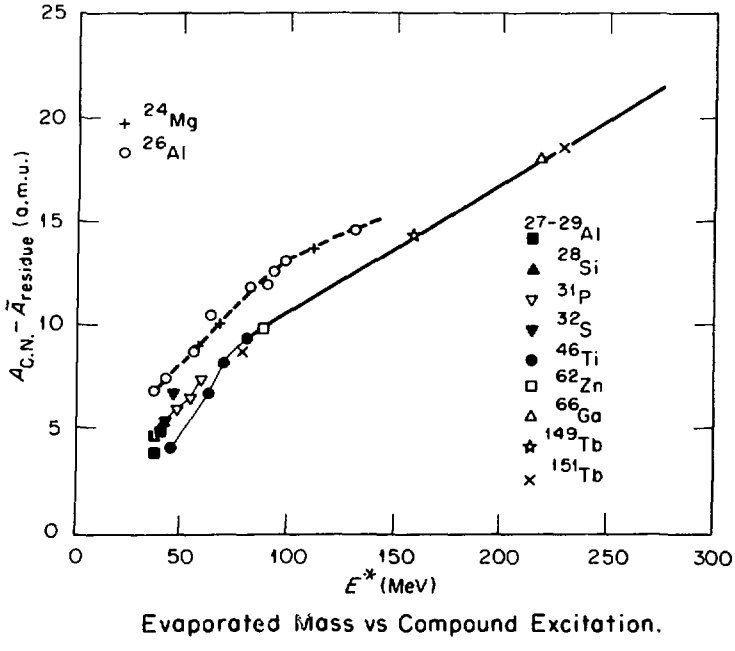

FIG. 15. The average evaporated mass (in amu) versus compound nucleus excitation energy for a variety of compound nuclei produced in heavy ion reactions. Very light systems evaporate more mass per unit excitation energy than do heavier systems. This can be attributed to the larger angular momenta with which the heavier nuclei are produced. The data are taken from ^{24}Mg (Na 75), ^{26}Al (St 77), $^{27-29}$Al (Co 76b), ^{28}Si (We 76), ^{31}P (Pü 75, Ko 77b), ^{32}S (We 76), ^{46}Ti (Pü 77), ^{62}Zn (Co 77), ^{66}Ga (Na 75), ^{149,151}Tb (Br 76b, Pl 77).

These values are reasonable considering separation energies, temperatures and the fact that α-particles as well as nucleons are emitted. Systematic trends are also evident. The heavier nuclei, e.g. A $\gtrsim$ 40 tend to lie on one curve whereas lighter compound nuclei emit, on the average, more mass per unit excitation energy. There are two reasons why a heavier system should emit fewer particles to remove a given amount of excitation energy. Both reasons are connected with the fact that they are formed (in these heavy ion reactions) with much larger angular momenta. High angular momentum and heavy nuclei favor γ-ray emission which means less mass is evaporated. The main reason, however, is that the removal of angular momentum requires particles to be emitted with energies greater than the sum of the Coulomb repulsion and thermal energies. Since each particle then carries off on the average more energy, fewer particles are emitted in removing a given amount of excitation energy. Statistical model calculations reproduce these trends fairly well.

It appears that, over a wide range of compound nuclear masses, excitation energies, and angular momenta, the decay of the compound nucleus can be adequately explained on the basis of an equilibrated nucleus and statistical decay. This statement has a practical significance which is in addition to the obvious importance of understanding the decay of the compound nucleus. It facilitates the comparison of theoretical calculations of heavy-ion reactions, in which large amounts of energy are converted into excitation of the fragments, to results obtained in the laboratory. The excited reaction products will emit some number of particles before being detected and this must be taken into account as best as possible before comparing theoretical calculations with experiment.

Of course, a general statement such as the one beginning the foregoing paragraph cries out for an exception. It is well known (Bl 75) that, for nucleon and α-particle induced reactions, light particles are emitted from the compound system before equilibrium is attained. This pre-equilibrium emission is identified as a departure from the predictions for equilibrium decay. In particular, an excess number of particles appears with higher-than-average kinetic energies. Evidence for such pre-equilibrium emission (from the compound system) in heavy-ion induced reactions is scant and probably reflects the fact that the excitation energy is more easily spread over a larger number of nucleons in a heavy ion reaction. A possible exception is illustrated in Fig. 16 (Sa 77). The top row of the figure shows the probability of emitting x neutrons depending on whether the same compound nucleus is formed in the reactions ^{20}Ne + ^{150}Nd or ^{12}C + ^{158}Gd. Below is shown the average number γ-rays <M> emitted as a function of x. The ^{20}Ne results are consistent with statistical expectations. Assuming that the neutrons have a statistical distribution of energies, then the average number of γ-rays should increase as fewer neutrons are emitted. This behavior is also observed for ^{12}C + ^{158}Gd at lower bombarding energies. At an excitation

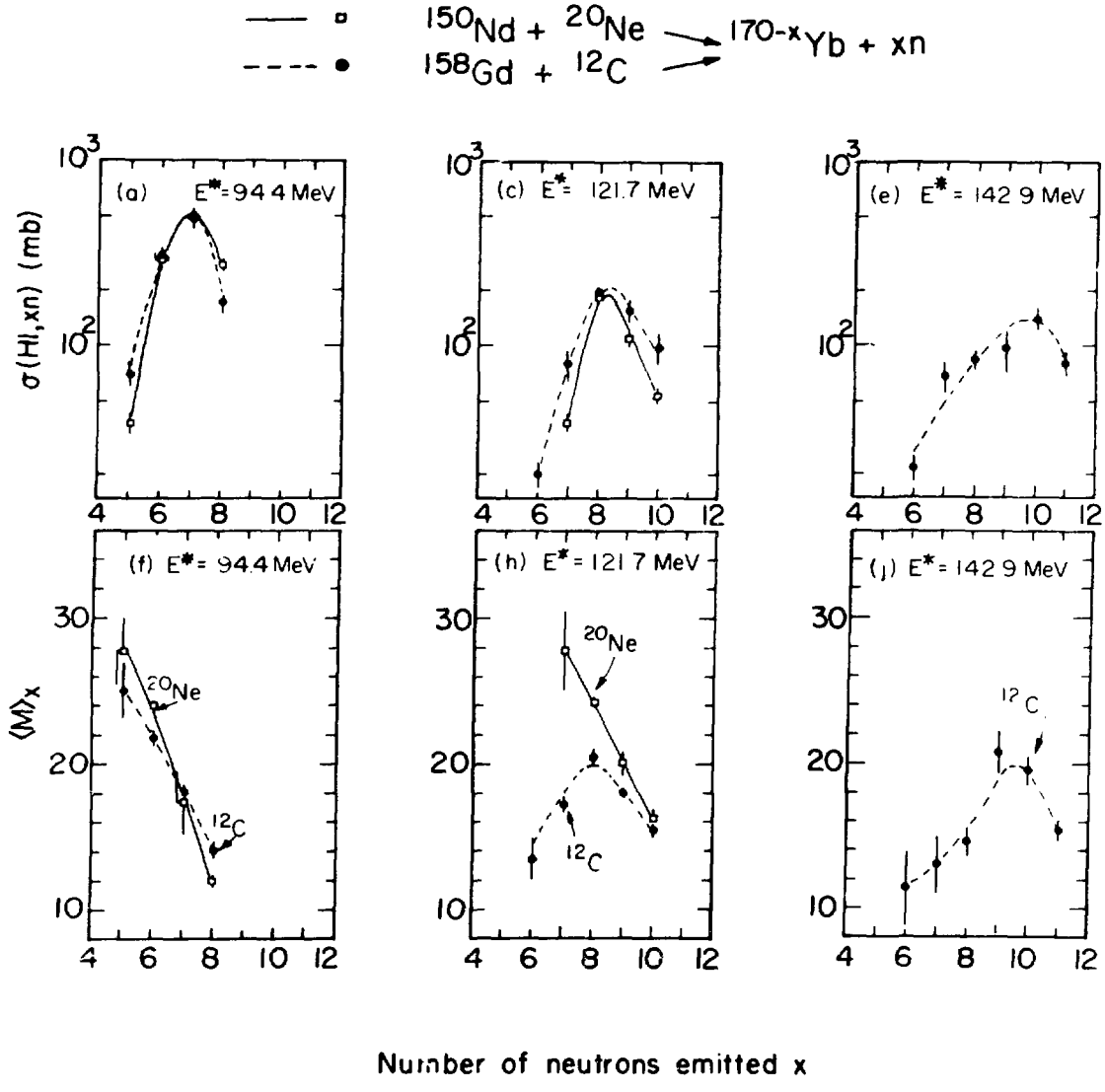

FIG. 16. Heavy-ion xn cross sections and γ-ray multiplicities for the reactions ^{12}C + ^{158}Gd and ^{20}Ne + ^{150}Nd (Sa 77). The decrease in $\langle M \rangle_x$ for small values of x observed for high energy ^{12}C bombardment suggests pre-equilibrium emission of neutrons.

energy of 121.7 MeV, however, one observes that $\langle M \rangle_x$ decreases with decreasing x. Part of this effect may arise from the opening of αxn channels which compete with the 7n and 6n channels, lowering the average compound nucleus angular momentum associated with these decays. However, it seems likely that the neutrons associated with the 6n and 7n decays now have a higher average kinetic energy (and most likely carry off more angular momentum). A plausible explanation for this is that the first neutron emitted had an anomalously large energy and therefore was emitted before equilibrium was attained. This could be verified by measuring the neutron spectra in coincidence with the residues. The cross section associated with this effect is of the order of 100 mb/sr.

The observation and further study of pre-equilibrium phenomena in heavy ion reactions is important in that it probes the early stages of compound nucleus formation. It is not clear how successful in these cases will be the theories developed for nucleon induced reactions, nor is it clear what are the best approximations to be made in treating the heavy-ion case. (The experimental results for ^{4}He projectiles and ^{12}C projectiles at the same MeV/nucleon are different.) The study, both experimental and theoretical, of pre-equilibrium emission in heavy ion reactions is thus at an early stage and should prove an exciting area in the future as the region of bombarding energy between 20 and 200 MeV/nucleon becomes accessible.

III. DEEP INELASTIC SCATTERING

Since the phenomenon of deep inelastic scattering began to attract attention in the early 1970's, an extremely large amount of experimental and theoretical work has been done. The basic features of the process have been established and the dependence of these features on the bombarding energy and charges of projectile and target has been mapped. The subject has been reviewed at the Caen Conference (Ga 76, Mo 76) and recently by Schröder and Huizenga (Sc 77b).

Most of the information gained so far in deep inelastic scattering is based on measurements of the energy, angle, and charge (or mass) of one of the fragments. These "first generation" experiments have been extremely productive. In the last year or two experiments have become more complex as more detailed questions are asked about the reaction mechanism. I want to select two aspects of the reaction mechanism and present, briefly, a number of recent experiments which focus on them. First we will consider the (spin) alignment of the fragments after collision and the amount of angular momentum transfer. The second aspect deals with the time scale of the collision and the mechanisms by which the damped energy is ultimately dissipated. The first topic is of relevance to theory insofar as the transfer of angular momentum is induced by nonconservative forces, i.e. by friction or viscosity, and this is of very current interest. The second aspect relates to the degree of equilibration of the rotating

di-nuclear complex (RDC) as we like to call the projectile-target system up to the point of scission. Simple and graphic questions are: Does the RDC emit particles before it scissions? Are there local hot spots (e.g. at the walls or in the neck) or does the system achieve a uniform temperature?

We ask what experiment can tell us.

A. Alignment and Angular Momentum Transfer

1) Particle experiments

In a simple classical picture of the deep inelastic reaction in which a portion of the angular momentum of relative motion is transferred to intrinsic degrees of freedom, the two fragments produced in the collision should have their angular momenta aligned perpendicular to the reaction plane defined by the beam and one of the fragments. The particles emitted by an excited fragment should exhibit an angular correlation which is indicative of this alignment. In particular, particles should be preferentially emitted in the reaction plane if the nucleus is aligned perpendicular to this plane. The situation is illustrated schematically in Figs. 17a and 17b. In Fig. 17a we

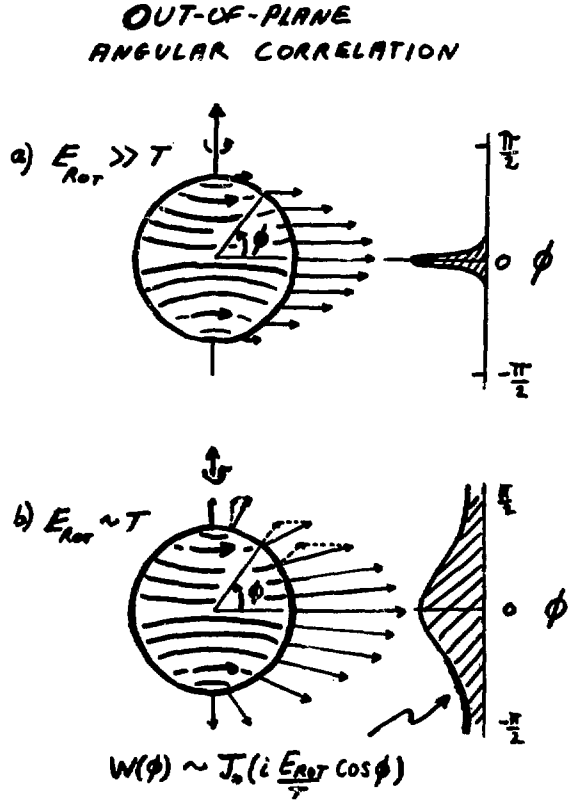

FIG. 17. (a) Particles released from the surface of a rotating sphere, all move in the equatorial plane provided their rotational velocity greatly exceeds the average radial velocity associated with their temperature. The angle of emission with respect to the equatorial plane is denoted by ϕ. (b) When the temperature and rotational energy are comparable, the out-of-plane correlation is broadened. The dashed arrows denote the components of the velocity due to temperature and the centrifugal force. The correlation function is given by Ericson and Strutinsky (Er 58).

consider a cold, rotating nucleus. The centrifugal force on any particle is parallel to the equatorial plan of the rotating nucleus which also lies in the reaction plane. If the nucleus has a temperature T, the emitted particles will have a radial velocity component which will smear out the sharp correlation of Fig. 17a and produce a correlation like that shown in Fig. 17b. Ericson and Strutinsky have derived the indicated expression for the angular correlation (Er 58). The quantity determining the anisotropy is the ratio of the emitted particles' rotational energy to the temperature of the compound nucleus.

An experiment to measure the angular correlation and intensity of alpha particles in coincidence with the projectile-like fragment has been made by Ho et al. (Ho 77), for the reaction ^{58}Ni + ^{16}O (96 MeV). The experimental configuration is illustrated schematically in Fig. 18. The heavy-ion detector was at an angle of 35° with respect to the beam. The out-of-plane correlation was measured by moving the α-particle detector in a plane which cuts the reaction plane at angles of $\theta_\alpha = 35°$ for $\phi_\alpha = 0°$, and $\theta_\alpha = -145°$ for $\phi_\alpha = 180°$. The results are shown in Fig. 19 for α-particles in coincidence with carbon ions (solid points) and oxygen ions (open circles). (The data have been converted to the rest frame of the heavy fragment.) There is a clear out-of-plane correlation. The correlation is not symmetric about $\phi_\alpha = 90°$, however, as would be expected for equilibrium decay; we shall return to this point in Section IIIB. An analysis of the portion of the correlation from $\phi_\alpha = 90°$ to $\phi_\alpha = 180°$ yields a ratio of rotational energy to temperature which implies a spin J of 13 ħ for a temperature T = 2 MeV. (Complete alignment of J perpendicular to the reaction plane is assumed in deriving a value of J.) This value for the temperature is consistent with statistical model predictions and the shapes of the α-spectra (for $\phi_\alpha > 90°$). The value of 13 ħ agrees with results obtained from the measured γ-ray multiplicity (Al 75). Regardless of the precision with which the transferred angular momentum can be deduced by this procedure, the results shown in Fig. 19 demonstrate that the spin of the heavy fragment produced in this deep inelastic collision is aligned.

Light-particle emission is not the only possible mode of decay. In systems much heavier than mass 60, fission is an important de-excitation mechanism, and has the advantage of a well-developed theory of angular correlation and of previous experimental study (Va 73). This has been exploited in a recent experiment by Dyer et al. (Dy 77) in which a ^{209}Bi target was bombarded by 610 MeV ^{86}Kr ions. The experimental arrangement is shown schematically in Fig. 20. The angular correlation of one of the fission fragments in coincidence with the projectile-like fragment was measured both in plane and out of plane. Classical arguments similar to those applied in the previous example tell us that the fission fragments should be most intense in the reaction plane provided that the target-like fragment has a large angular momentum perpendicular to the reaction plane before scission.

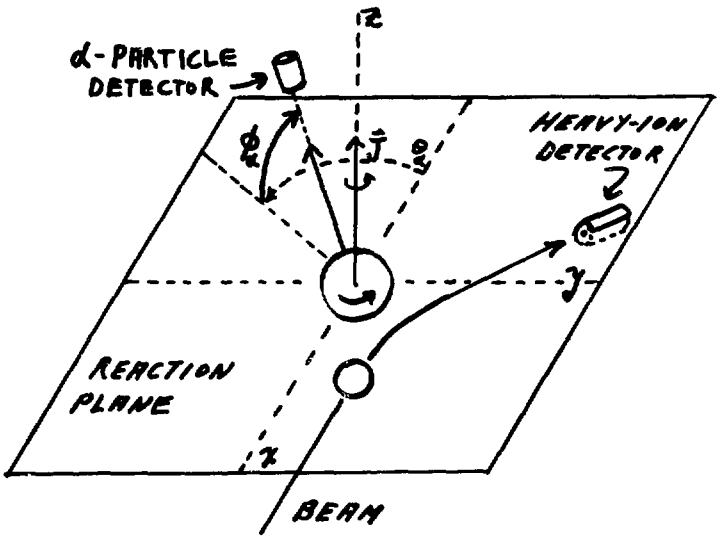

FIG. 18. Schematic representation of the experimental arrangement used to measure the correlation between α-particles and projectile-like fragment in the reaction ^{58}Ni + ^{16}O (96 MeV) (Ho 77). Note that ϕ_α is the polar angle between the emitted α-particle and the reaction plane.

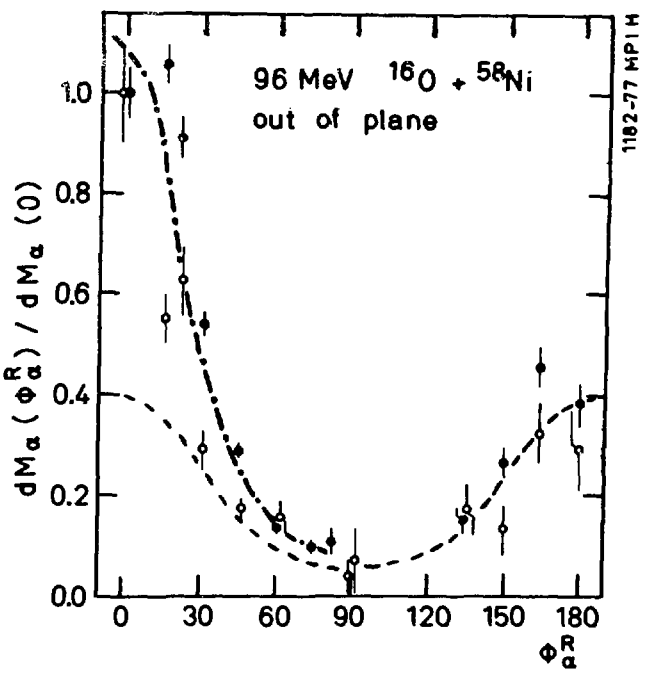

FIG. 19. The measured out-of-plane correlation. The angle ϕ_α^R corresponds to the angle ϕ in Fig. 18, but evaluated in the rest frame of the heavy fragment. The ordinate is the differential α-particle multiplicity (coincident α-particles per projectile-like fragment detected at 35°). The dashed lines are to guide the eye.

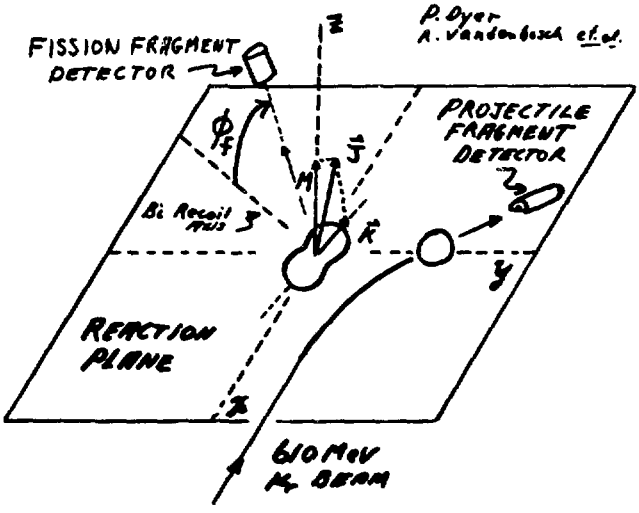

FIG. 20. Schematic diagram of the experimental arrangement used to measure the angular correlation of fission fragments in coincidence with the krypton-like fragment in the reaction $^{209}Bi + ^{86}Kr$ (610 MeV) (Dy 77).

The out-of-plane angular correlation for the fission fragments depends now on an additional quantum number K, the projection of the total angular momentum on the symmetry axis of the fissioning nucleus at scission. Thus we have

$$W^J_{MK}(\phi) \propto (2J + 1) \mid d^J_{MK}(\phi) \mid^2$$

and

$$\text{yield} \propto \sum_{JMK} P(J)\, P(M)\, P(K)\, W^J_{MK}(\phi) \ .$$

The distributions P(K), P(M) and P(J) represent the probability for finding the system with these quantum numbers and are obtained as follows.

i) P(K): This is a property of the fissioning nucleus and

$$P(K) \propto \exp\left(-\frac{K^2}{2K_o^2}\right) .$$

K_o can be inferred from previous fission fragment angular correlation experiments.

ii) P(M): The alignment of the system is determined by the reaction mechanism. As a first estimate, complete alignment perpendicular to the reaction plane is assumed, M = J.

iii) P(J): The probability that the target-like fragment has total angular momentum J. The determination of this is the goal of the experiment. Assuming that the amount of angular momentum transferred, J, is proportional to the initial orbital angular momentum, ℓ, one has for deep inelastic collisions of Kr + Bi, $P(J) \propto 2J + 1$. This is because the partial cross section $\sigma_\ell^{D.I.} \propto 2\ell+1$. This distribution has an upper limit J_{max} which is the quantity to be determined by comparison with the data.

In Fig. 21 both the out-of-plane and in-plane angular correlations are shown. The in-plane counting rate is $\sim$ 25 times more intense than the rate perpendicular to the reaction plane. There is a slight in-plane correlation which should not be present if the system is completely aligned with M = J. An analysis has been made of both correlations allowing for less than complete alignment and other factors such as nonequatorial collisions and the existence of a lower limit (J_{min} = 18 $\hbar$) on the angular momentum transferred in deep inelastic collision. The result is shown by the dotted lines and yields a value of J_{max} = 58 $\hbar$. Dyer et al. are able to conclude that the maximum angular momentum transferred is between 50 and 70 $\hbar$. J_{max} is estimated to be about 68 $\hbar$ in the limit that the Kr and Bi stick together and 39 $\hbar$ is the rolling limit. Thus the angular momentum transfer is larger than the rolling limit, less than (but consistent with) the sticking limit, and indicates that tangential friction is very important. A calculation of J_{max} has been made for this system by Gross et al. (Gr 75) and their prediction, J_{max} = 38 $\hbar$, underestimates the transferred angular momentum. Agreement with experiment would presumably require increasing the tangential component of the friction. In any case, this experimental value for the transferred angular momentum represents an important datum for testing models for friction or viscosity in deep inelastic reactions. (The foregoing discussion is based on ref. Dy 77.)

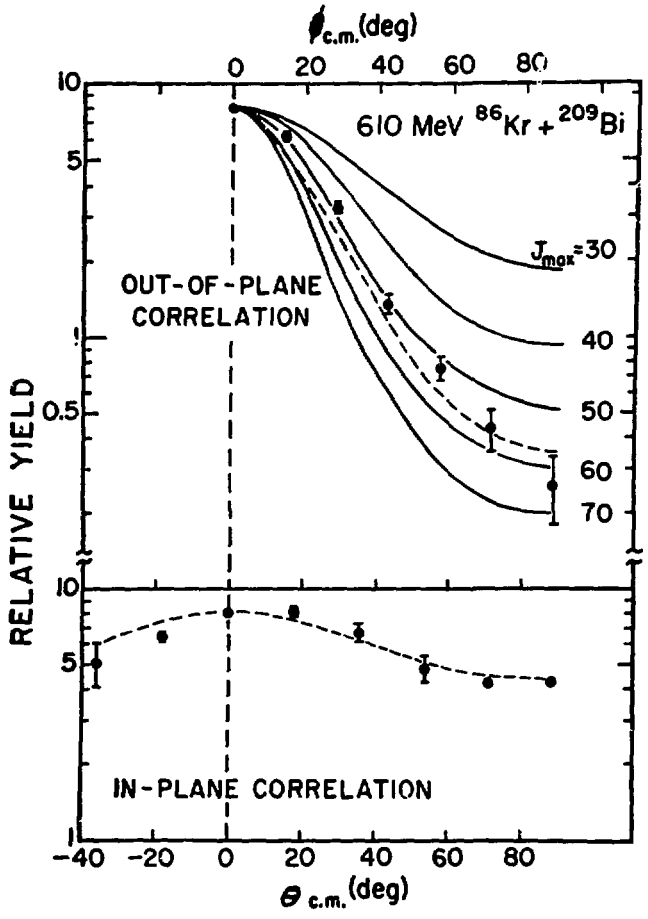

FIG. 21. The measured in-plane and out-of-plane correlation (Dy 77). Predictions of the out-of-plane correlation for various values of the maximum transferred angular momentum are shown. The dashed line is a simultaneous fit to both correlations which allows for some degree of non-alignment ($M \neq J$).

2) γ-ray experiments

After the excited fragments produced in the deep inelastic collision no longer have sufficient energy available for particle decay, γ-ray emission begins and completes the deexcitation process. The relative importance of γ-ray emission (in terms of the amount of excitation energy and angular momentum removed) varies with the mass and angular momentum of the excited fragment. In heavy nuclei where neutron emission is favored, γ-rays can carry away most of the angular momentum. Thus, the properties of the deep inelastic reaction products after scission can be reflected in the γ-ray emission. The problem, however, is how quantitatively to relate the experimental observations to the properties of the deep inelastic fragments before particle emission began.

Let us sidestep this problem for the moment, however, and first discuss two experiments which demonstrate that the residual nuclei can still be aligned when γ-ray emission commences. If the α-particle detector in the schematic diagram of Fig. 18 is replaced by a Ge-Li detector, the angular correlation for specific γ-ray transitions in the heavy fragment can be measured as a function of the species and energy of the light fragment. This has been done for the reaction $^{27}Al + ^{16}O$ (100 MeV) by Van Bibber et al. (Va 77). Gamma-ray yields obtained in plane ($\phi_\gamma = 0$, solid data points) and out of plane ($\phi_\gamma = \frac{\pi}{2}$, open circles) are shown in Fig. 22. The γ-ray angular correlations expected for a nucleus aligned perpendicular to the reaction plane depend on the multipolarity of the radiation and are quite different for $\lambda = 1$ and $\lambda = 2$. Note in Fig. 22 that the yields of $\lambda = 2$ transitions $^{12}C(2^+ - 0^+)$ and $^{24}Mg(2^+ - 0^+)$ are largest for $\phi_\gamma = 0$ while the M1 transition $^{31}P(\frac{3^+}{2} - \frac{1^+}{2})$ is most intense perpendicular to the reaction plane. Although not all the E2 and M1 transitions in other nuclei observed in this work show the same pronounced anisotropy, these data are sufficient to demonstrate that some alignment exists. This experiment also shows that γ-ray angular correlations measured with a detector which records all γ-rays will in general be attenuated because E2 and M1 transitions will be summed.

The second experiment to be mentioned shows not only that the fragments retain alignment but are also polarized in the direction perpendicular to the reaction plane. The goal of the experiment, by Trautman, de Boer et al. (Tr 77), was to measure the direction of rotation of the fragments for quasielastic and deep inelastic scattering and thereby test the negative-angle-scattering proposal of Wilczynski (Wi 73). γ-rays emitted in stretched transitions, regardless of multipolarity, will be circularly polarized in the direction of the angular momentum of the emitting nucleus. The amount of polarization varies as the cosine of the angle between the direction of the nuclear spin and the direction of the γ-ray. The direction of

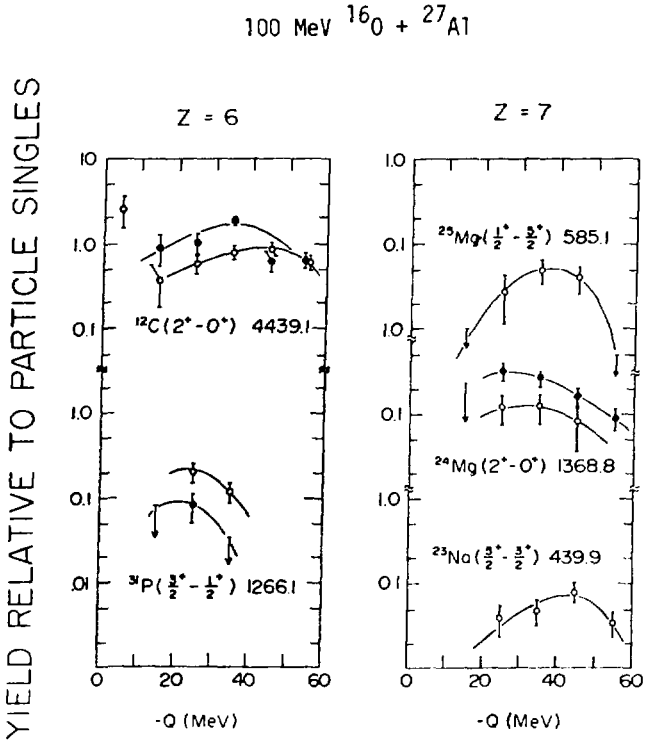

FIG. 22. The yield of specific γ-ray transitions in coincidence with Z = 6 and Z = 7 ions produced in the scattering of ^{16}O (100 MeV) by ^{27}Al (Va 77). The solid points represent the yield in the reaction plane, the open points perpendicular to the reaction plane. -Q is the energy lost in the collision.

the circular polarization can be measured by scattering the emitted γ-rays from the polarized electrons in magnetized iron. (The cross section for compton scattering at forward angles is larger if the electrons and γ rays are polarized in opposite directions.) Two polarimeters were employed in a symmetric configuration normal to the plane defined by two heavy ion counters at ± 35° with respect to the beam. (One reason for this is that the experimental effect to be measured is small, of the order of one percent, because only 2 out of the 26 electrons in an ion atom are polarized, and a very efficient system is needed.) The apparatus they used is sketched in Fig. 23. The reaction was Ag + ^{40}Ar (∿ 300 MeV) and was measured at GSI. They observed an asymmetry in the count rate which was of opposite sign for the quasielastic and deep inelastic components indicating that the fragments produced in the quasielastic and deep inelastic collisions spin in opposite directions. This confirms that deep inelastic scattering in this reaction is associated with a negative classical deflection angle. The degree of polarization was much larger for the quasielastic component than for the deep inelastic. This suggests that particle emission and other possible mechanisms we shall mention later contribute to a loss of polarization and alignment.

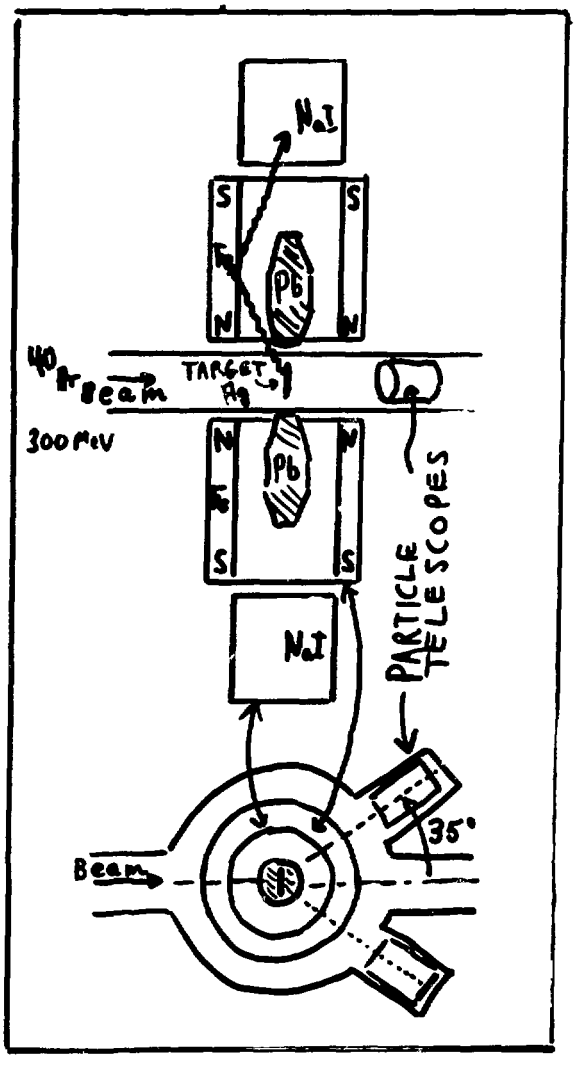

FIG. 23. Schematic diagram of the apparatus used by Trautmann, de Boer et al. (Tr 77) to measure the circular polarization of γ-rays emitted in quasi-elastic and deep inelastic reactions.

We return now to the question of relating γ-ray emission to the properties of the fragments before particle emission began.

The paths followed by the nuclei on the way to their ground states, and by the experimenter on the way back to the initial conditions, are illustrated in Fig. 24. The compound system is the rotating dinuclear complex which then separates into a heavy and a light fragment each having an average excitation energy and angular momentum. After particle emission ceases, an average number of γ-rays $\bar{M}_H$ and $\bar{M}_L$ are emitted by the heavy and light fragment, respectively. The sum of these two multiplicities is observed in coincidence with the light fragment as recorded by a counter telescope. The problem of working backwards from the observed average γ-ray multiplicity and average γ-ray energy to the quantities of interest involves estimating or measuring the effects of particle emission. Statistical model estimates can be made for very heavy nuclei which decay only by neutron emission. In lighter systems this procedure would seem less reliable and the empirical approach is preferred. One measures the multiplicities for evaporation residues in which the E^* and J (of Fig. 24) are known. A functional dependence of M_γ on E^* and J can

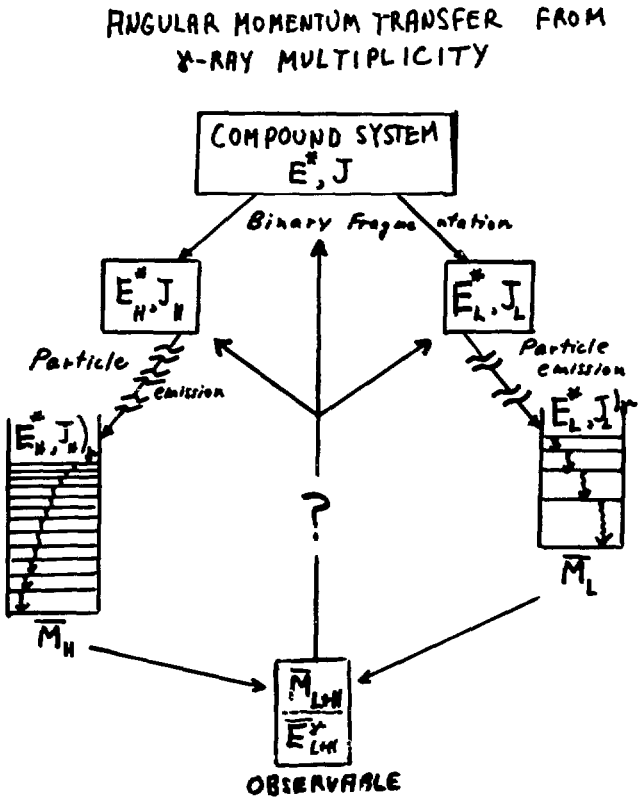

FIG. 24. Illustration of the various stages of decay in a deep inelastic reaction. In order to deduce the transferred angular momentum $J_L + J_H$ from the measured multiplicity $\bar{M} = \bar{M}_L + \bar{M}_H$, a correction for the amount of angular momentum removed by particle emission must be made.

thus be deduced. The crucial assumption is that the decay of the deep inelastic fragment follows the same rules as that of a compound nucleus.

Measurements of the average γ-ray multiplicity, $\bar{M}_\gamma$, have been made on a number of systems (Al 75, Ish 76, Bo 76, Gl 77, Pe 77, Da 77) (see Pe 77 for a recent review). The manner in which the various authors have estimated the effects of particle emission has varied, but the end results have generally yielded values of the angular momentum transfer in between those corresponding to rolling and sticking. Several examples are as follows.

The value of $\bar{M}_\gamma$ in the reaction $^{14}N + {}^{93}Nb$ at $E_{^{14}N} = 120$ MeV has been measured by Ishihara et al. (Ish 76). The results are shown in Fig. 25 for both the deep inelastic component and the quasielastic component as a function of the mass of the light product. The dashed line is a prediction of M_γ assuming the reaction partners reach a stage in which their surfaces stick together and the system undergoes rigid rotation before scissioning. The solid line pertains to quasi-elastic reactions in which the exchange of mass is assumed responsible for a transfer of angular momentum. In relating the transferred

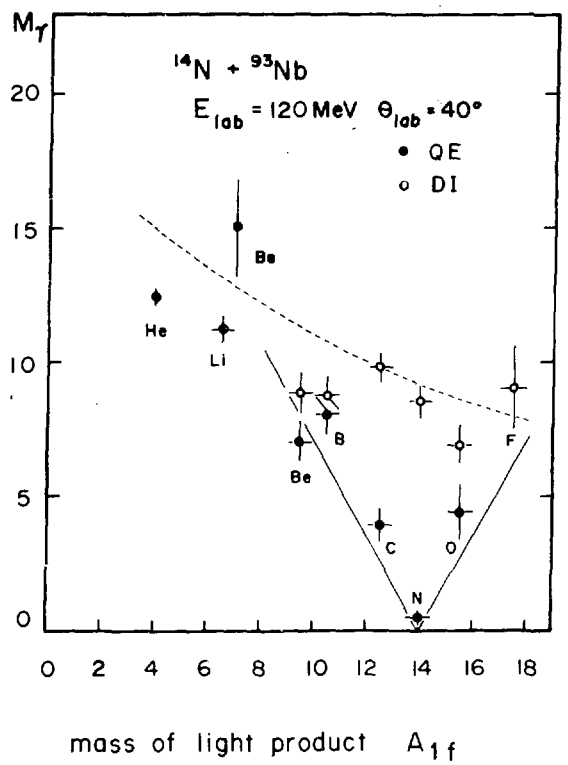

FIG. 25. Measured γ-ray multiplicity for the reaction $^{14}N + ^{93}Nb$ (Ish 76).

angular momentum J to the γ-ray multiplicity, the equation $J = 2.4\ M_\gamma$, was used. A portion of this amount, $J = 1.7\ M_\gamma$ represents the angular momentum associated with γ ray emission alone whereas the remainder $J = 0.7\ M_\gamma$ corresponds to the angular momentum carried off by particle emission. The latter was estimated with a statistical model.

Qualitatively similar results were obtained for a somewhat heavier system, Ag + ^{20}Ne (175 MeV) by Glässel et al. (Gl 77). Figure 26 shows the multiplicity measured as a function of the light-fragment atomic number for several scattering angles. The more damped the energy of a reaction product, the higher the multiplicity. M_γ increases in general for larger scattering angles suggesting that the compound system has lived longer and therefore had more time to approach a sticking limit. The agreement for smaller values of Z is better with a sticking limit obtained from a lower initial orbital angular momentum (50 ħ). This is interpreted as a consequence of the lower Z reaction products being preferentially produced by lower ℓ-waves. The relationship between M_γ and transferred angular momentum in this case is assumed to be $J = 2\ M_\gamma$, the argument being that γ-ray multipolarities less than 2 are offset by the neglect of the angular momenta carried off by neutrons. The results, again, lie in between the rolling and sticking limits.

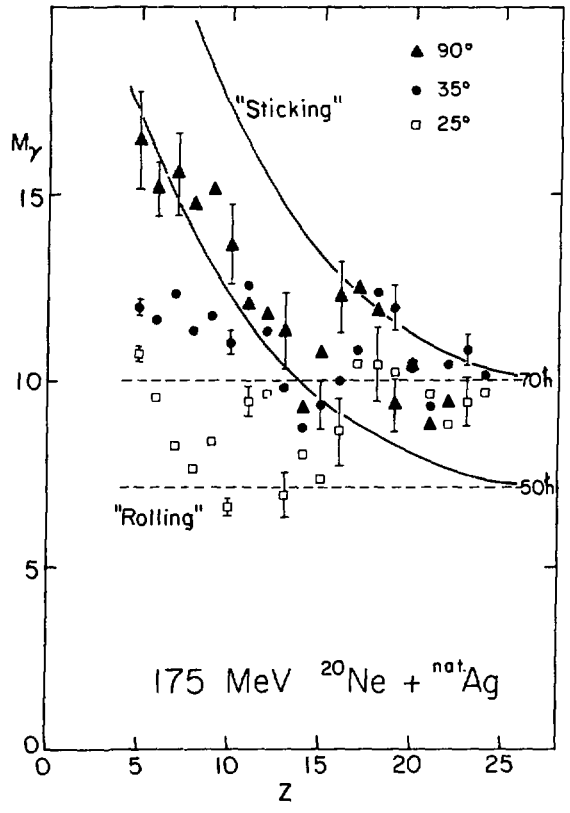

FIG. 26. Measured values of M_γ for the deep inelastic products produced at angles of 90°, 35° and 25° in the reaction Ag + ^{20}Ne (175 MeV) (Gl 77).

The results for a much heavier system, Au + Cu (443 MeV) are shown in Figs. 27 and 28 (Be 76b, Pe 77). The value of M_γ as a function of the energy of particles detected at 49° is given in Fig. 27. The multiplicity increases as a function of energy loss through the range of events corresponding to partial and complete damping. In Fig. 28 the value of M_γ measured at two angles is plotted versus mass asymmetry and compared with various sticking model predictions assuming $J = 2\ M_\gamma$. The prediction includes the effect of deformation at the scission point. The initial orbital angular momentum $\ell_i = 124$ is near the weighted average of angular momenta over the range $\ell_i = 0$ (assuming no fusion) to $\ell_i = 175$ (the maximum ℓ-value contributing to the deep inelastic collision). The value $\ell_i = 175/2$ is shown for additional reference.

In the reaction ^{58}Ni + ^{40}Ar (280 MeV), the measured multiplicities are below the rolling limit if $J = 2\ M_\gamma$ and no correction for particle emission is made (Bo 76). These authors have also measured the α-particle multiplicity and suggest that the amount of angular momentum removed by particle emission together with a more realistic calculation of the transferred angular momentum (i.e. one including deformation) would bring theory and experiment much closer together.

While most of our information on angular momentum transfer has come from coincidence experiments observing the decay products of

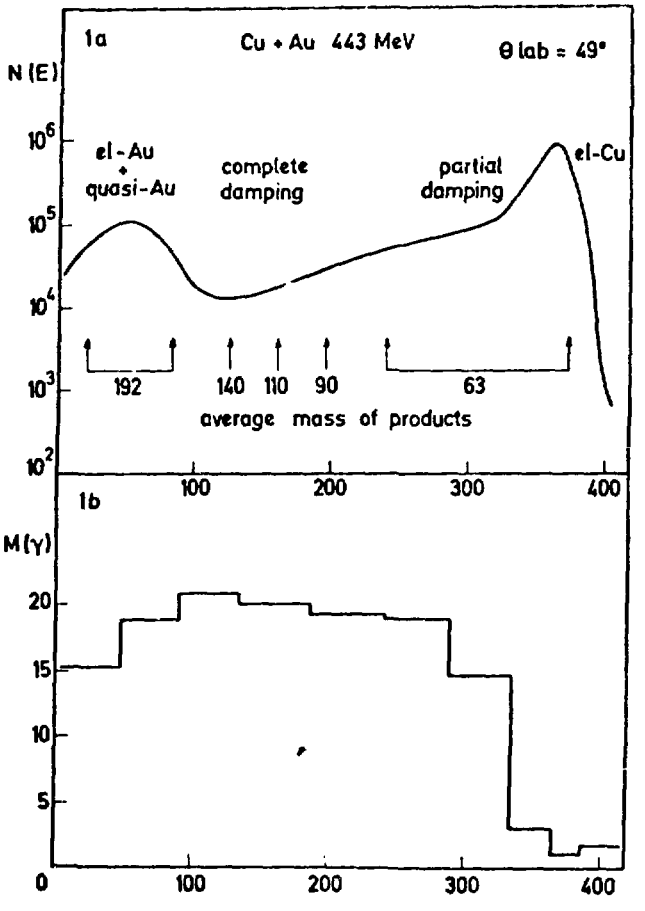

FIG. 27. Measured values of M_γ for deep inelastic products produced in the reaction Au + Cu (443 MeV) (Be 76b, Pe 77).

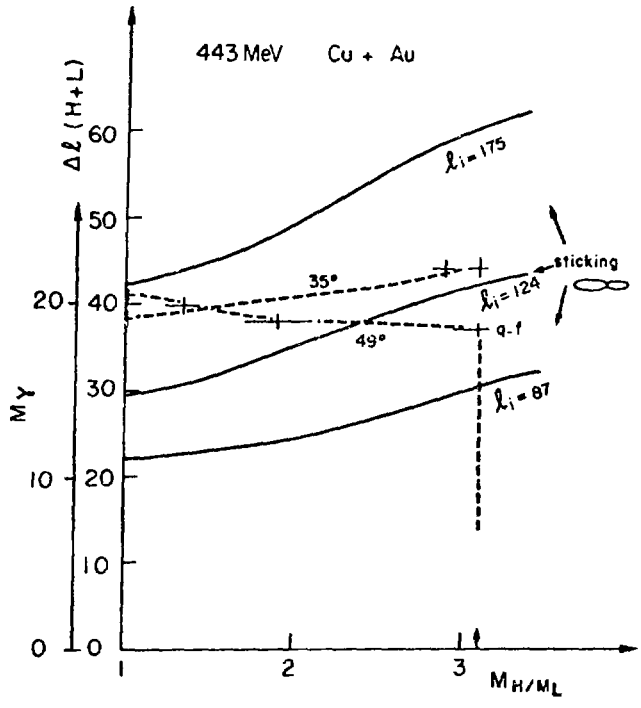

FIG. 28. The multiplicity of the deep inelastic products as a function of the masses of the reaction products (Be 76b, Pe 77). Predictions of the sticking model for various initial orbital angular momenta are shown.

the primary fragments, it should be noted that there is one experiment in which angular momentum transfer has been deduced from the measurement of the total kinetic energies of the primary fragments as a function of bombarding energy. This has been done by Braun-Munzinger et al. (Br 76, Co 77b). The analysis assumes that the Coulomb separation energy is independent of bombarding energy and that the amount of transferred angular momentum (which reduces the rotational portion of the total kinetic energy) is proportional to the initial orbital angular momentum. The deduced constant of proportionality agrees well with the sticking model.

The measurements of the average γ-ray multiplicity described above are valuable in that they provide (albeit with accompanying assumptions and uncertainties) a measure of the amount of angular momentum transfer. Measurements of the angular correlation of the γ-rays, averaged over all γ-ray energies, in principle give information on the degree of alignment, but it is here that things begin to be more complicated than the foregoing descriptions of the experiments and their interpretations would suggest. Measurements of the out-of-plane γ-ray angular correlation averaged over all γ-ray energies) for the reactions $^{14}N + {}^{93}Nb$ (Ish 76), Ar + Ni (Bo 76), and Cu + Au (Pe 77) indicate a rather small anisotropy, i.e. the out-of-plane count rate is generally ∿ 80-90% of the in-plane count rate. Perrin

and Peter (Pe 77) suggest (particularly for the heavy system Cu + Au) that this lack of alignment may arise from sources other than M1-E2 mixed multipolarity or misalignment caused by particle emission. Making the analogy with fission, the fragments at scission can, through bending, wriggling, or twisting modes of motion (Ni 65), induce angular momenta in the primary fragments which are not in the plane of the reaction defined by the beam and one of the fragments. For the first two modes of motion, the induced angular momentum would be perpendicular to the direction of the separating fragments; in the third case, it would parallel this direction. Measurements of angular correlations of discrete γ-rays in the spontaneous fission of ^{252}Cf by Wolf and Cheifitz (Wo 76) suggest that twisting is not an important mode of motion and that bending and/or wriggling dominate. The results of Dyer et al. (Dy 77), (Fig. 21) should enable an upper limit to be placed on these bending and wriggling contributions and it would be very interesting to see what a quantitative analysis would yield. However the induction of additional angular momenta in the fragments through dynamical processes at scission does not imply that current analyses of γ-ray multiplicity experiments overestimate the amount of angular momentum transferred through friction in the portion of the reaction leading up to scission. This is because the average angular momentum (i.e. the first moment of the distribution) obtained after averaging the vector sum of the aligned component and the induced component over all directions of the induced angular momentum would not be much different than that due to the aligned component alone. The second moment, or width, of the angular momentum distribution would be very different, however. This brings us to the consideration of higher moments of the multiplicity distribution.

Just as the average number of γ-rays reflects an average angular momentum, the distribution of the number of γ-rays about the average reflects a distribution in angular momenta. Knowledge of the distribution of angular momenta in the reaction products is very desirable. Higher moments of the multiplicity have been reported for compound nucleus decay (Ha 75, Sa 76) and used to deduce spin distributions.

In the case of deep inelastic collisions, the second and third moments of the γ-ray multiplicity have been measured by Dayras et al. (Da 77) for the reaction $^{63}Cu + ^{20}Ne$ (164 MeV). Data were also obtained for the evaporation residues produced in the reaction $^{63}Cu + ^{12}C$ (130 MeV). The results are shown in Fig. 29. The moments of the γ-ray multiplicity are in each case evaluated at a single scattering angle and over a narrow energy window at the peak intensity of the deep inelastic yield for each atomic number. (In this portion of the spectrum, the contribution from reactions induced on carbon and oxygen contaminants in the target is small). One would expect that the width of the multiplicity distribution would be less in the case of the deep inelastic collision; the argument is as follows. The evaporation residues contain angular momenta from 0 to ℓ_{crit} and, for a $(2\ell+1)$ triangular

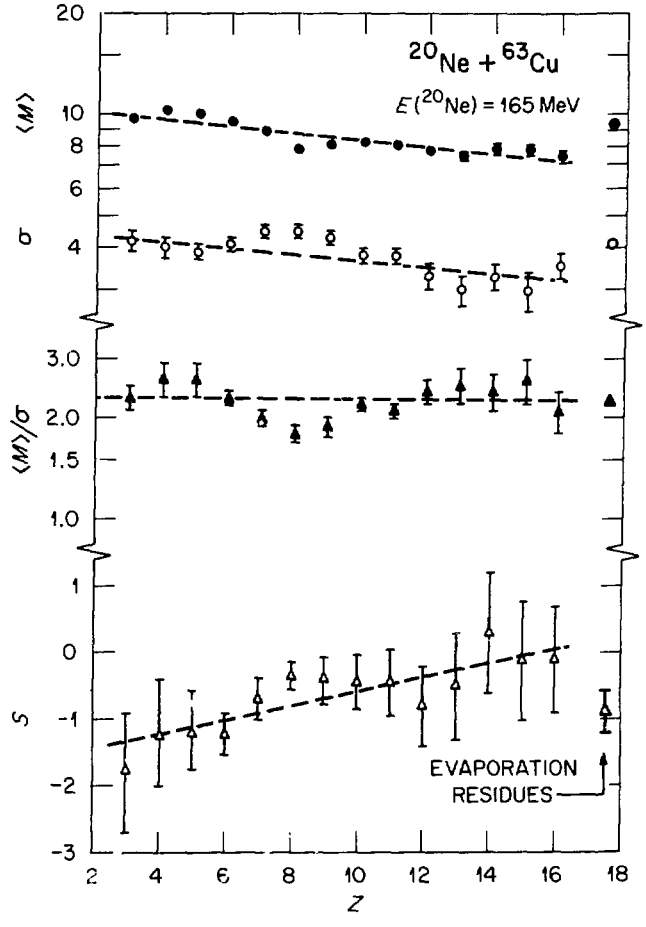

FIG. 29. The multiplicity M, width σ, and skewness S measured for the deep inelastic scattering of ^{63}Cu + ^{20}Ne (164 MeV), (Da 77). The straight lines are to guide the eye. The projectile-like fragments with atomic number Z were detected at 20° lab. M, σ, and S are evaluated for those particles having energies at the peak of the deep inelastic yield. The trend of M to decrease with Z is in agreement with the sticking model. Also shown are the results for evaporation residues produced in the fusion of ^{63}Cu + ^{12}C (130 MeV). Note that the limit of M, σ, and S as Z decreases approaches that of compound nucleus decay. The quantities M, S and σ are defined in ref. Sa 76.

distribution, we would expect $\frac{\langle M \rangle}{\langle \sigma \rangle} \sim \sqrt{8} \sim 2.8$. We observe a value of 2.3 and attribute the discrepancy to additional broadening arising from particle emission and statistical cascades. In the case of deep inelastic scattering we would expect a narrower distribution of angular momenta varying from f x ℓ_{crit} to f x ℓ_{gr} where f represents the fraction of angular momentum transferred. Indeed, this should represent an upper limit on the width since we have selected a narrow angular and energy region of deep inelastic products and, if anything, this would narrow the range of impact parameter. Neglecting broadening from particle emission and from other effects such as statistical cascades, a variance $\sigma^2 \approx 0.6$ would be expected for the multiplicity distribution. Assuming the broadening of the distribution by the effects mentioned above can be derived from the value deduced from the evaporation residues, a variance of $\sigma^2 \sim 7.6$ is predicted. Yet this value is only about one half of the measured variance. For example, $\sigma^2_{experimental} = 15$ for deep inelastic products with Z = 5. This implies an additional broadening of the transferred angular momentum distribution. Possible explanations for this are as follows.

i) The distribution of initial angular momenta contributing to deep inelastic scattering is much broader than $\ell_{crit} \rightarrow \ell_{gr}$. Even if this were the case, however, the selection of reaction products at a given energy and scattering angle should correspond to a narrow population of initial angular momenta. This follows provided that the angular momentum transfer J is proportional to the initial orbital angular momentum, J = f x ℓ.

ii) The constant f in the relation J = f x ℓ_i is not a constant but has itself a distribution. This would imply statistical processes in the transfer of angular momentum, a proposition which does not seem unreasonable.

iii) There are additional angular momenta induced at scission (the bending and wriggling just discussed) which would certainly broaden the angular momentum distribution while not greatly affecting the average value. This possibility has been suggested by Perrin and Peter (Pr 77).

iv) We have assumed that the excited fragments produced in the deep inelastic collision reach equilibrium and decay in the same manner as compound nuclei produced in fusion reactions. This assumption may not be valid.

The last item introduces another (and our last) topic. What in fact are the modes of decay by which the deep inelastic complex and its fragments rid themselves of excess energy and angular momentum?

B. Time Scale and Mechanisms for Decay

The length of time for which the system produced in a heavy-ion collision holds together is a basic parameter. Although it cannot be measured directly, (at least not for the short time scales of deep inelastic collisions) it can be inferred from analyses of the reaction products and orbit calculations (see, e.g. Bo 75) and from correlations of energy loss and mass transfer (Hu 76). However, rough estimates of the time scale can be made using very simple arguments.

Considering the rotational motion, we have an angular velocity ω, and an angle of rotation θ through which the fragments remain in contact.

$$\tau_{DI} = \theta/\omega$$

We can estimate a rotational energy, an orbital angular momentum ℓ, and a moment of inertia, $\mathfrak{J}$ and use

$$\omega = 2E_{ROT}/\hbar\ell$$

or

$$\omega = \hbar\ell/\mathfrak{J}$$

to obtain ω. For example, we could take $\ell \approx \frac{5}{7} \ell_{gr}$ corresponding to rolling fragments and $E_{ROT} = E_{c.m.} - E_{coul} + Q$. A typical angle θ would be ~ 1 radian for a forward peaked reaction.

Considering the radial motion, the time for the fragments to move together and apart is governed by the Coulomb force f and the radial velocity, v_{rad} (Mo 76)

$$\tau_{DI} = -\frac{2\mu\, v_{rad}}{f_{coul}} = \frac{\sqrt{2}\ \hbar\ell}{E_{coul}} \ .$$

Most of the reactions studied experimentally thus far have collision times in the range of 4-20 (10^{-22} sec).

We can also make estimates of the time it takes an equilibrated excited nucleus to emit a particle (proton, neutron or α-particle). An empirical fit to measured widths of compound nuclei in the mass range A = 20 - 100 yields (St 74)

$$\Gamma \text{ (MeV)} = 14 \exp\left(-4.69 \sqrt{A/E^*}\right)$$

where E^* is the excitation energy of a nucleus with mass A. Relating the temperature T to the excitation energy as $E^* = aT^2$ where a = A/7.5,

we have

$$\tau_{part} \simeq 0.5 \exp (13/T)$$

where T is in MeV and τ_{part} is in units of 10^{-22} sec. An excitation energy of 1.2 MeV/A yields a temperature of 3 MeV and a lifetime $\sim 40 \times 10^{-22}$ MeV sec.

Figure 30 relates ω, τ, E^*/A and T for an angular rotation of 1 radian. We see from this figure that if local temperatures of $\sim$ 3-5 MeV, i.e. excitation energies of $\sim$ 1 - 4 MeV per nucleon should be produced in a deep inelastic collision, then the lifetime for particle emission will be sufficiently short that the complex will eject light particles before it scissions. We say local temperatures because total center-of-mass bombarding energies in most experiments are less than $\sim$ 7 MeV/$A_{projectile}$ and therefore the achievement of, say, 3 MeV/A nucleon in some region requires a pronounced concentration of energy, i.e. what might be called a "hot spot".

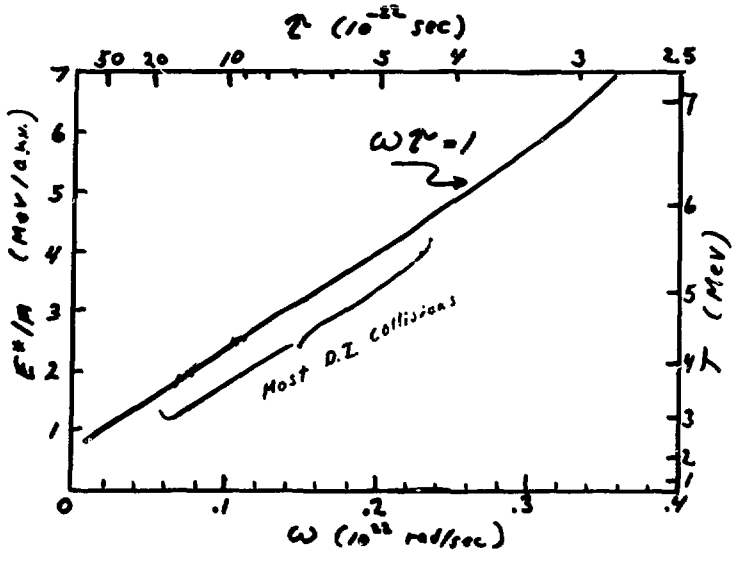

FIG. 30. Relationship of the excitation energy/nucleon and equivalent temperature to the lifetime τ against particle decay of a system in statistical equilibrium. ω is the angular velocity of the rotating dinuclear system. Given either abscissa (τ or ω), either of the ordinates then yields the temperature or excitation energy/amu for which the lifetime against statistical particle emission is equal to the lifetime τ of the dinuclear complex or to the time it takes the system to rotate one radian. Most deep inelastic collisions studied to date have lifetimes in the region indicated.

Experimental evidence for such phenomena would consist of a departure of observed yields (energy distributions, angular distributions) from what would be expected if equilibrium had been attained.

In the experiment by Ho et al. (see Figs. 18, 19) a departure from equilibrium manifests itself by an excess yield of α-particles at forward angles. This appears in the out-of-plane correlation shown in Fig. 19 and also in Fig. 31, which presents the yield of α-particles in the reaction plane. There is a strong peaking of the yield at forward angles, in contrast to the isotropic angular distribution which would have been expected in the classical picture of emission from a completely equilibrated and aligned rotating nucleus. Using the simple expression we have just given ($\omega = \hbar\ell/\mathcal{J}$) and $\theta = 2\sigma_\theta$ where σ_θ is the experimental standard deviation of the angular distribution in Fig. 31, the result is $\tau_\alpha \leq 20 \times 10^{-22}$ sec independent of whether it is the deep inelastic complex with 33 units of angular momentum (before scission) which emits the α-particle or an excited ^{58}Ni fragment with 12 units of (transferred) angular momentum. In Fig. 30 we see that such a lifetime corresponds to a local temperature of $\approx$ 3.3 MeV. A statistical analysis of the α-particle energy spectra (intensity $\propto$ exp(- E_α/T) yields temperatures of 3-4 MeV for the α-particles emitted

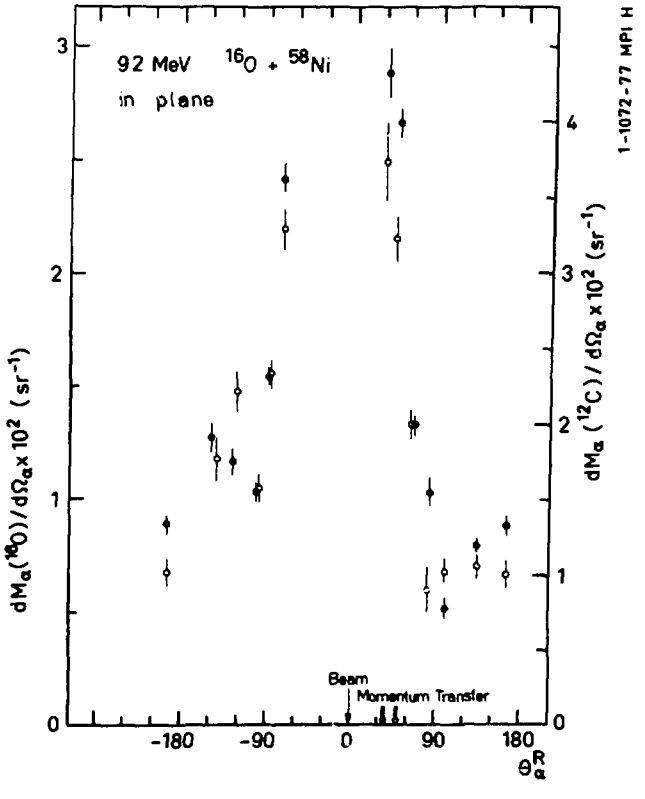

FIG. 31. The in-plane angular correlation of α-particles in coincidence with carbon ions (solid points) or oxygen ions (open circles) detected at -35° lab (Ho 77). The angle with respect to the beam is measured in the frame of the heavy residual nucleus. The strong forward peaking is not consistent with an isotropic decay of an equilibrated residual nucleus.

in the forward hemisphere and a temperature, as we have already noted, of 2 MeV for particles emitted in the back hemisphere. Thus, these features of the reaction (angular distributions and shapes of energy spectra) suggest emission of α-particles either before scission of the deep inelastic system or immediately thereafter and before the heavy fragment had time to equilibrate. Note that the fraction of the alpha particle yield corresponding to preequilibrium emission is ∿ 50%. However, this does not represent a major fraction of the total decay since the α particle multiplicity itself is only ∿ 10% (for detected O) and ∿ 20% (for detected C).

A kinematic analysis of the most probable α-particle energy indicates that this energy is independent of angle if it is calculated in the rest frame of the heavy fragment. Provided that this would not also be the case if the rest frame of the dinuclear complex (i.e. $^{16}O + ^{58}Ni$) were used instead, this suggests that the α-particles are emitted after scission. (This analysis also rules out projectile breakup as an important mechanism.) To explain these features, Ho et al. propose the formation of a local hot spot with a temperature of T ≈ 3.5 MeV, and an area covering ∿ 20% of the sphere to explain the observed angular correlation, energy spectra and α-particle multiplicities.

Mechanisms for the production of preequilibrium α-particles have been discussed recently by Gross and Wilcyznski (Gr 77). In their model, a strong radial friction induces α-particle emission on the opposite side of the nucleus from where projectile and target first come into contact. Such a picture could be consistent with the data of Ho et al.

Other experiments of this type have been reported by Harris et al. (Ha 77), $^{27}Al + ^{16}O$ (65 MeV), and Ishihara et al. (Ish 76b) $^{93}Nb + ^{14}N$ (95 MeV). They all have in common the fact that anisotropic in-plane correlations between the emitted light particle (p or α) and the light fragment are observed.

The emission of light charged particles in a deep inelastic collision involving much heavier nuclei is being studied by a group at the SuperHilac (Al 77). Krypton-like products are detected at a forward angle of 36° or 42° and light charged particles are observed with a counter telescope at angles varying from 81° to 315° in the reaction plane. The approach is to use the knowledge (including empirical systematics) of compound nucleus decay to identify that portion of the α-particle yield consistent with decay of equilibrated Kr and Au fragments. The purpose of the experiment, then, is to determine the amount, if any, and properties of charged particle emission which might correspond to preequilibrium emission.

The velocity-vector diagram of Fig. 32 shows how the kinematics of the reaction is used to identify the evaporation products. The

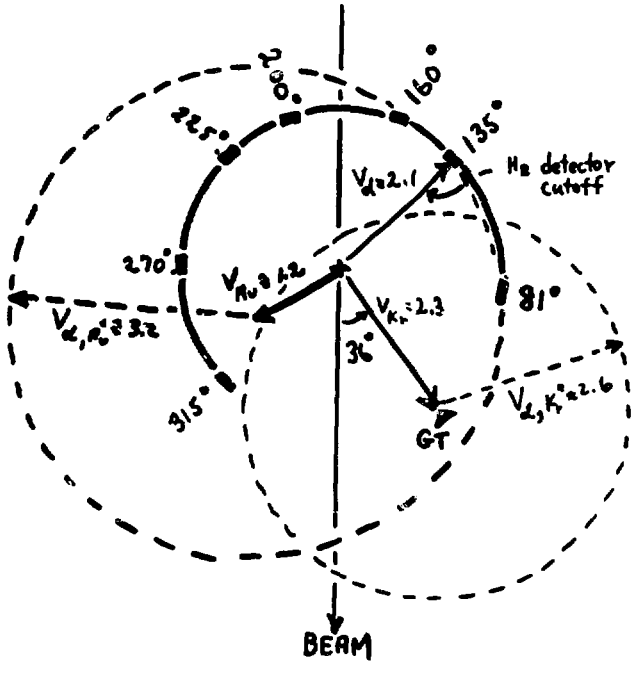

FIG. 32. Velocity vector diagram illustrating the kinematics for statistical α-particle emission in the reaction Au + ^{86}Kr (724 MeV) (Al 77). The scattered Kr ion is detected at 36° by a gas telescope (GT) and has an average velocity of 2.3 cm/ns. An alpha particle evaporated from the Kr would have a velocity of 2.6 cm/ns. Only the solid state telescope positioned at 81° could therefore detect α-particles evaporated from Kr. A similar kinematic circle for the α-particle evaporated from the Au fragment is also shown.

threshold for detection of an α-particle in this experiment is ∿ 9 MeV or ∿ 2.1 cm/ns. The average velocity of an evaporated α particle is the sum of its velocity relative to the Kr or Au which emitted it and the velocity of the Kr or Au. Because of the higher Coulomb barrier, α-particles evaporated from the Au-like fragment can be well above the threshold in the detectors located at 200°-315°. α-particles evaporated from the Kr will only be observed in the detector at 81°.

The following results are preliminary. The α-spectra observed at 225° and 270°, when transformed to the frame of the Au fragment, are just what one expects for evaporation of α's from an excited but equilibrated Au-like nucleus. This evaporation portion is subtracted bin by bin from the spectra at other angles. The α-spectra at 81°, when transformed to the Kr frame, is entirely consistent with α-evaporation from a Kr-like fragment. This evaporation spectrum is then subtracted from the spectra at other angles. (The subtraction is done in individual energy bins because of the 9 MeV threshold.) At angles other than 81°, 225°, and 270° there is a significant number of events left over after subtraction of the evaporation component. These α-particles have a higher average energy than that expected for evaporation from either of the fragments - in fact, this energy is ∿ 40 MeV, slightly above the Coulomb barrier for Z = 36 + 79 = 115. Figure 33 shows the measured energy-integrated yields above threshold in the various detectors before and after subtraction of the evaporation component vs. the average center-of-mass angle between the α-particle and the detected Kr fragment. The magnitude of the total yield at some angles is affected by the 9 MeV threshold. The preequilibrium yield is not strongly affected since the energies are higher. The preequilibrium α-particles are preferentially observed at angles near 90° and 270°, i.e. normal to the direction of motion of the Au and Kr fragments. This is illustrated schematically in Fig. 34 and is a situation similar to that encountered in fission where fast α particles appear to be ejected at scission at right angles to the neck focussed by the Coulomb force of the two fragments. In the present case, however, the α-particle energies are higher (Va 73). Although there is some evidence for the preequilibrium emission of protons in this experiment, (when the heavy-ion detector was at 42°) it does not seem to be as large a portion of the yield as is the case with the α-particles.

The experiments on ^{16}O + Ni and Kr + Au which we have just discussed indicate that the emission of light particles can occur on the same time scale as the deep inelastic collision. In both experiments there is evidence that this "preequilibrium" emission takes place at or immediately after the point at which the two fragments separate. (Preequilibrium decay does not happen exclusively, however. Many of the events correspond to the excited fragments reaching equilibrium before decay.) The preequilibrium particles are the means we have for studying the properties of nuclear systems under extreme conditions of temperature.

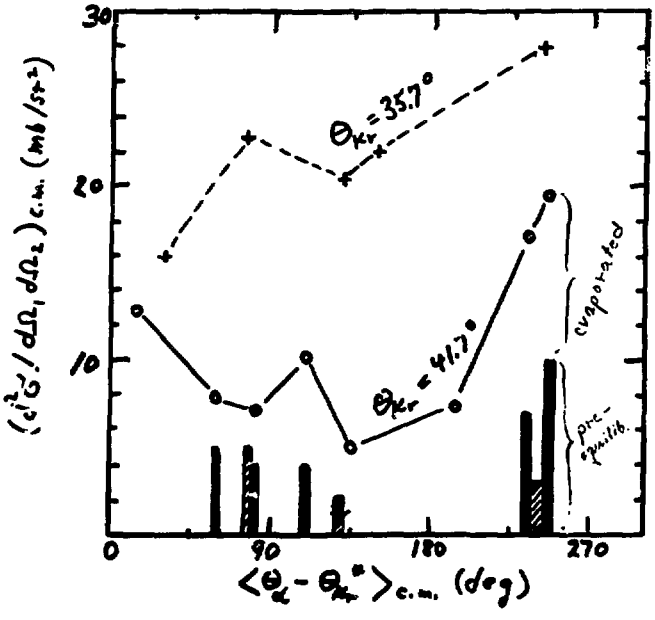

FIG. 33. Preliminary results of coincidence measurements (A1 77) with the gas telescope at 35.7° and at 41.7°. The circles and crosses represent the total number of α's above the detector threshold. The lines are only to guide the eye. The abscissa is the average center-of-mass angle between the emitted α and the Kr-like fragment. The vertical bars represent the α-particle yield remaining after the contribution due to evaporation from either fragment has been subtracted (solid bars, 41.7°; hatched bars, 35.7°). There is a preference for α-particles to be emitted at nearly right angles to the direction of the Kr ion.

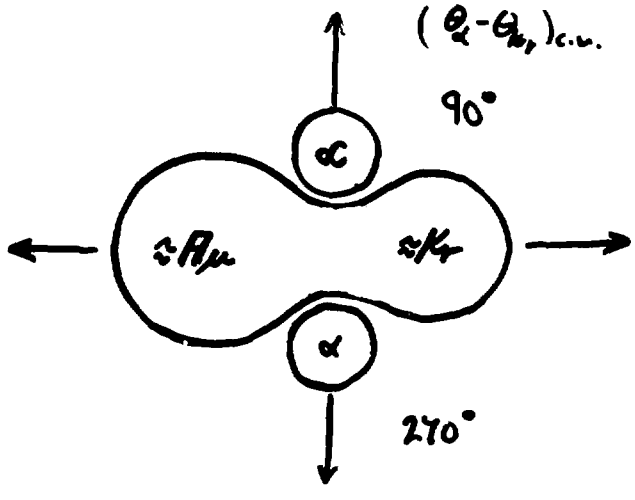

FIG. 34. Illustration of the emission of α-particle at right angles to the axis of symmetry at scission. The Coulomb forces of the two main fragments can "focus" the alpha particles to angles near 90°.

IV. SUMMARY AND CONCLUSIONS

We have just seen the results of a very large number of experiments. What are their distinguishing features, what do they tell us about heavy-ion collisions and how do they relate to nuclear theory?

A. Fusion

The process of fusion represents the most complex of heavy-ion collision processes in that the final state has all degrees of freedom excited in a statistical way. Phenomenologically, however, fusion has been the process most easily described with a small number of degrees of freedom and very few parameters. We wish to extend our knowledge of fusion beyond the stage of phenomenology and proceed further toward the final state. The initial stages of fusion as the two ions approach must involve low nuclear densities and therefore only a few nucleons. We ask whether the nature of the fusion process is such that the valence nucleons affect the outcome. Microscopic calculations suggest this might happen. Experiments on the fusion of light heavy ions at sub-Coulomb energies show in some cases pronounced changes in the energy dependence of σ_{fus}. These changes occur with variations of one or two units in the mass number of the colliding system (Figs. 5, 6). Microscopic calculations of the complex potential as well as of the real potential will probably be necessary to understand the changes in behavior from system to system.

Fusion cross sections measured at energies above the Coulomb barrier at the point where direct reactions become an important part of the reaction cross section also show large variations with mass number of the colliding system (Fig. 9). These variations, of the order of 200 mb, are much larger than variations in $A^{1/3}$. Until the measurement of σ_{fus} for $^{15}N + ^{12}C$ there was an apparent systematic dependence of σ_{fus} on the shell closure at ^{16}O. These experimental data on fusion cross sections both above and below the Coulomb barrier provide an opportunity for testing microscopic theories of heavy-ion fusion.

In heavy-ion systems studied with projectiles of $A < 40$ the most important factor limiting fusion has been the dynamics of the entrance channel. These dynamical requirements for fusion have been condensed into a one dimensional prescription - penetration to a critical radius. By measuring σ_{fus} at a sufficiently high bombarding ($E_{^{14}N} \gtrsim 18$ MeV/A) it has been possible to observe a decrease in σ_{fus} indicating a limitation more restrictive than penetration to a critical radius (Fig. 10). The maximum angular momentum with which it has been possible to form ^{26}Al (Fig. 11) is consistent with value predicted by the rotating liquid drop model. Because the number of nucleons in a system as light as ^{26}Al, is relatively small, microscopic calculations are more manageable and economical. Differences between macroscopic and microscopic treatments can be explored in a system for which such differences are more likely, and for which there is an experimental result.

The distribution of residues of the compound system can be calculated rather well (Fig. 12). These calculations suggest that highly excited compound nuclei undergo rigid rotation for large angular momenta and are deformed. This is consistent with measurements of the critical angular momentum as a function of excitation energy. Statistical calculations are of value in identifying non-compound processes such as preequilibrium decay (Fig. 16) and enable the understanding of systematic features of the compound nucleus decay over a wide mass region (Fig. 15). Preequilibrium emission of particles in fusion reactions seems to be much more prevalent for reactions induced by α-particles or lighter ions. Nevertheless, some evidence for such effects seems to be emerging (Fig. 16). The cross sections associated with preequilibrium decay are not a major fraction of the overall reaction cross section.

B. Deep Inelastic Scattering

Deep inelastic scattering and fusion differ mainly in the degree to which the initial kinetic energy of relative motion is converted into internal degrees of freedom. The initial stages of each of these processes are probably similar. The two types of reactions are sometimes distinguished in that the deep inelastic collision results in a binary fragmentation whereas fusion need not. The sharpness of this distinction diminishes as the size of the projectile-like fragment decreases (or if the compound nucleus fissions). The deep inelastic reaction offers the possibility to probe the early and middle stages of a reaction in which frictional or viscous forces convert kinetic energy to heat; the light fragment may be thought of as the probe. Energy loss is not the only result of the nonconservative forces - angular momentum is transferred as well and enables one to distinguish different components of the frictional force (i.e. radial friction and tangential friction). The study of angular momentum transfer is of great importance for further understanding of heavy ion collisions, and a number of experimental methods have been brought to bear on this problem.

The preferential emission of charged particles in the reaction plane shows the fragments to be aligned as a result of the collision (Fig. 19). An estimate of the transferred angular momentum can be obtained through knowledge of the temperature and moment of inertia of the emitting nucleus. The angular correlation of fission fragments produced in the reaction Kr + Bi has enabled a determination of the angular momentum transfer for a heavy system (Fig. 21). The results indicate a coefficient of tangential friction larger than that used in a global set of calculations (Gr 75). The deduction of a coefficient of friction from a deep inelastic scattering measurement requires a theoretical treatment of the entire scattering orbit.

The angular momentum transfer has been deduced from measurements of the average number of γ-rays emitted. Because the γ-rays appear after particle emission (Fig. 24) corrections for the excitation energy

and angular momentum removed by particles have to be applied. In spite of these difficulties a number of features of the reaction have emerged. In one (particularly light) system $^{16}O + ^{27}Al$ evidence for fragment alignment has been obtained from the angular correlation of discrete γ-ray lines (Fig. 22). Measurements on a number of systems (Figs. 25-28) suggest that the compound system lives sufficiently long for the frictional forces to bring the system to nearly rigid rotation (sticking limit) before scission occurs. Measurements of the higher moments of the distribution of γ-rays for a deep inelastic collision reveal a broader distribution of γ-rays than is suggested by an analysis assuming similar decay mechanisms for the compound nucleus ^{75}Br and the fragments produced in the deep inelastic collision of $^{20}Ne + ^{63}Cu$ (Fig. 29).

The time scale for deep inelastic collisions can be roughly estimated on general grounds. We expect that the ejection of particles before the fragments have equilibrated or even before scission may occur if high local temperatures ($T \sim 3$-6 MeV) are produced (Fig. 30). Although the bulk of the decay process can be accounted for by equilibrium mechanisms, there is some experimental evidence for such preequilibrium processes. These measurements are still few in number and much further work is necessary. However, measurement of the angular correlation between α-particles and the projectile-like fragment (Figs. 31,33) indicates the emission of α-particles on a time scale comparable to or shorter than that of the lifetime of the compound system. In one case $^{16}O + ^{58}Ni$ the particles are ejected preferentially in the forward direction, in the other case, Kr + Au, they appear perpendicular to the direction of the separating fragments. These "preequilibrium" particles are probes for studying nuclear matter under extreme conditions of temperature.

ACKNOWLEDGEMENTS

Many people responded swiftly and generously to a request for their latest experimental results. Without their cooperation and help it would not have been possible to present such a breadth of current experimental information. (Unfortunately it was not possible because of length restrictions to include all of the interesting contributions I received.) I should like to express my thanks to Drs. J. M. Alexander, T. Cormier, B. Cujec, J. de Boer, M. Deleplanque, P. Dyer, P. Glässel, A. Gobbi, M. Lefort, F. Plasil, F. Pühlhofer, D. Sarantites, J. P. Schiffer, Z. Switkowski, K. Van Bibber, and J. P. Wurm, for information they sent me which has been incorporated in this article. Dr. Roland Dayras acted as critic in a number of stimulating conversations on the experiments described herein and is also thanked for a careful reading of the manuscript. Finally, I would especially like to thank Mrs. Christine Wallace for her help in preparing the camera-ready manuscript.

REFERENCES

Al 75) R. Albrecht, W. Dünnweber, G. Graw, H. Ho, S. G. Steadman, and J. P. Wurm, Phys. Rev. Lett. 34, 1400 (1975).

Al 77) J. M. Alexander, private communication; J. M. Miller, G. Catche, D. Logan, M. Rajagopalan, J. M. Alexander, M. Kaplan, and M. S. Zisman, work in progress.

Ar 76) M. Arnould and W. M. Howard, Nucl. Phys. A274, 295 (1976).

Ba 73) R. Bass, Phys. Letters 47B, 139 (1973); Nucl. Phys. A231, 45 (1974).

Ba 77) B. Back et al., preprint (1977).

Be 76) R. R. Betts, W. A. Lanford, M. H. Mortensen, and R. L. White, Proc. Symp. on Macroscopic Features of Heavy Ion Collisions, Argonne Natl. Lab. 1976 (ANL/PHY-76-2), unpublished, p. 443.

Be 76b) M. Berlanger, M. A. Deleplanque, C. Gerschel, F. Hanappe, M. Leblanc, J. F. Mayault, C. Ngô, D. Paya, N. Perrin, J. Peter, B. Tanain, and L. Valentin, J. Phys. Lettres 37, L-323 (1976).

Bl 75) M. Blann, Ann. Rev. Nucl. Sci. 25, 123 (1975).

Bo 75) J. P. Bondorf, J. R. Huizenga, M. I. Sobel, and D. Sperber, Phys. Rev. C 11, 1265 (1975).

Bo 76) R. Boch, B. Fischer, A. Gobbi,* K. Hildenbrand, W. Kohl, V. Lynen, I. Rode, H. Stelzer, G. Auger, J. Galin, J. M. Lagrange, R. Albrecht, and B. B. Back. *Presented at the IX Masurian School in Nuclear Physics, Mikolaiki, August 1976. See also Proc. Caen Conf., p. 167 (1976).

Br 76) P. Braun-Munzinger, T. M. Cormier, and C. K. Gelbke, Phys. Rev. Lett. 37, 1582 (1976).

Br 76b) H. C. Britt, B. H. Erkkila, R. H. Stokes, H. H. Gutbrod, F. Plasil, R. L. Ferguson, and M. Blann, Phys. Rev. C 13, 1483 (1976).

Br 76c) H. C. Britt, B. H. Erkkila, P. D. Goldstone, R. H. Stokes, F. Plasil, R. L. Ferguson, and H. H. Gutbrod, Proc. Symp. on Macroscopic Features of Heavy-Ion Collisions, Argonne Natl. Lab. 1976 (ANL/PHY-76-2), unpublished, p. 491.

Ch 77) P. R. Christensen and Z. E. Switkowski, Nucl. Phys. A280, 205 (1977).

Co 74) S. Cohen, F. Plasil, W. T. Swiatecki, Ann. Phys. (N.Y.) 82, 557 (1974).

Co 76) M. Conjeaud, S. Gary, S. Harar, and J. P. Wieleckzo, European Conf. on Nuclear Physics with Heavy Ions, Caen, 1976, p. 116.

Co 76b) J. P. Coffin, P. Engelstein, and P. Wagner, Proc. European Conf. on Nuclear Physics with Heavy Ions, Caen, 1976, p. 127.

Co 77) T. M. Cormier, E. R. Cosman, A. J. Lazzasini, H. E. Wegner, J. D. Garrett, and F. Pühlhofer, Phys. Rev. C 15, 654 (1977).

Co 77b) T. M. Cormier, P. Braun-Munzinger, P. M. Cormier, J. W. Harris, and L. L. Lee, Jr., to be published in Phys. Rev. C.

Cu 76) B. Cujec and C. A. Barnes, Nucl. Phys. A266, 461 (1976).

Cu 77) B. Cujec, private communication.

Da 76) R. A. Dayras, R. G. Stokstad, Z. E. Switkowski, and R. M. Wieland, Nucl. Phys. A261, 478 (1976).

Da 76b) R. A. Dayras, R. G. Stokstad, Z. E. Switkowski, and R. M. Wieland, Nucl. Phys. A265, 153 (1976).

Da 77) R. A. Dayras, R. G. Stokstad, M. L. Halbert, D. C. Hensley, C. B. Fulmer, R. Robinson, A. H. Snell, D. G. Sarantites, and L. Westerberg, ORNL Physics Division 1976 Ann. Report.

Dy 77) P. Dyer, R. J. Puigh, R Vandenbosch, T. D. Thomas, and M. S. Zisman, to be published (1977), private communication.

Ei 77) Y. Eisen, I. Tserruya, Y. Eyal, Z. Fraenkel, and M. Hillman, Weizmann Institute of Science Preprint WIS 77/19-Ph. See also Y. Eyal, M. Beckerman, R. Chechik, Z. Fraenkel, and H. Stocker, Phys. Rev. C 13, 1527 (1976).

Er 58) T. Ericson and V. M. Strutinski, Nucl. Phys. 8, 284 (1958).

Fo 75) W. A. Fowler, G. R. Caughlan, and B. A. Zimmerman, Ann. Rev. Astron. and Astrophys. 13, 69 (1975).

Ga 74) J. Galin, D. Guerreau, M. Lefort, and X. Tarrago, Phys. Rev. C 9, 1018 (1974).

Ga 76) J. Galin, Proc. European Conference on Nuclear Physics with Heavy Ions, Caen, 1976; J. de Physique C5-37, 83 (1976).

Gl 74, 76) D. Glas and U. Mosel, Phys. Letters 49B, 301 (1974); Nucl. Phys. A264, 268 (1976).

Gl 75) D. Glas and U. Mosel, Nucl. Phys. A275, 429 (1975).

Gl 77) P. Glässel, R. S. Simon, R. M. Diamond, R. C. Jared, I. Y. Lee, L. G. Moretto, J. O. Newton, R. Schmitt, and F. S. Stephens, Phys. Rev. Lett. 38, 331 (1977).

Go 77) J. Gomez del Campo, LILITA - A Monte-Carlo Hauser-Feshbach Computer Code, Phys. Rev. Lett. 36, 1529 (1976).

Gr 74) D. H. E. Gross and H. Kalinowski, Phys. Letters 48B, 302 (1974).

Gr 75) D. H. E. Gross, H. Kalinowski, and J. N. De in "Classical and Quantum Mechanical Aspects of Heavy-Ion Collisions," H. L. Harney, P. Braun-Munzinger and C. K. Gelbke, Eds., Lecture Notes in Physics, Vol. 33, p. 194 (Springer-Verlag) 1975.

Gr 77) D. H. E. Gross and J. Wilczynski, Phys. Letts. 67B, 1 (1977).

Ha 75) G. B. Hageman, R. Broda, B. Herskind, M. Ishihara, S. Ogaza, and H. Ryde, Nucl. Phys. A245, 166 (1975).

Ha 77) J. W. Harris, T. M. Cormier, D. F. Geesaman, L. L. Lee, Jr., R. L. McGrath, and J. P. Wurm, preprint; Proc. Symposium on Macroscopic Features of Heavy-Ion Collisions, Argonne, Vol. II, p. 609 (1976).

Hi 76) M. D. High and B. Cujec, Nucl. Phys. A259, 513 (1976).

Hi 77) M. Hillman and Y. Eyal, JULIAN - A Monte-Carlo Hauser-Feshbach Computer Code, Proc. European Conf. on Heavy Ions, Caen (1976), p. 109.

Hi 77b) M. D. High and B. Cujec, Nucl. Phys. A278, 149 (1977).

Ho 77) H. Ho, R. Albrecht, W. Dünnweber, G. Graw, S. G. Steadman, J. P. Wurm, D. Disdier, V. Rauch, and F. Scheibling, preprint. Proc. European Conf. on Nuclear Reactions with Heavy Ions, Caen, p. 159.

Hu 76) J. R. Huizenga, J. R. Birkelund, W. U. Schröder, K. L. Wolf, and V. E. Viola, Jr., Phys. Rev. Lett. 37, 885 (1976).

Ish 76) M. Ishihara, T. Numao, T. Fukada, K. Tanaka, and T. Inamura, IPCR-Cyclotron Report 35, May 1976, Proc. Argonne Symposium, 1976.

Ish 76b) M. Ishihara, K. Kamitsubo, T. Shimoda, T. Fukada, T. Motobayashi, T. Ohi, and I. Kohno, Proc. Caen Conf. Communications, p. 157.

Ko 77) S. E. Koonin, K. T. R. Davies, V. Maruhn-Rezwani, H. Feldmeier, S. J. Krieger, and J. W. Negele, Phys. Rev. C 15, 1359 (1977).

Ko 77b) B. Kohlmeyer, W. Pfeffer, and F. Pühlhofer, preprint.

Ma 73) M. Mazarakis and W. E. Stephens, Phys. Rev. C 7, 1280 (1973).

Ma 76) J. A. Maruhn, R. Y. Cusson, and R. K. Smith, Nucl. Phys. A270, 471 (1976).

Ma 77) V. Maruhn-Rezwani, K. T. R. Davies, and S. E. Koonin, Phys. Letters 67B, 134 (1977).

Mi 72) G. J. Michaud and E. W. Vogt, Phys. Rev. C 5, 350 (1972).

Mö 76) P. Möller and J. R. Nix, Nucl. Phys. A272, 502 (1976).

Mo 76) L. G. Moretto and R. Schmitt, Proc. European Conference on Nuclear Physics with Heavy Ions, Caen, 1976; J. Physique C5-37, 109 (1976).

Na 75) M. N. Namboodiri, E. T. Chulick, J. B. Natowitz, R. A. Kenefick, Phys. Rev. C 11, 401 (1975). M. N. Namboodiri, E. T. Chulick, J. B. Natowitz, Nucl. Phys. A263, 491 (1976). J. B. Natowitz, E. T. Chulick, M. N. Namboodiri, Phys. Rev. Lett. 31, 643 (1973).

Ni 65) J. R. Nix and W. J. Swiatecki, Nucl. Phys. 71, 1 (1965).

Pe 76) D. Pelte and U. Smilansky, European Conference on Nuclear Physics with Heavy Ions, Caen, 1976, p. 103.

Pe 77) N. Perrin and J. Peter, Institut de Physique Nucleaire Orsay Preprint IPNO-RC-77-02, presented at Winter School on Nuclear Physics Zakopane (Poland) 2/77.

Pl 75) F. Plasil and M. Blann, Phys. Rev. C 11, 508 (1975).

Pl 77) F. Plasil, paper presented at the Winter Meeting on Nuclear Physics, Bormio, Italy, Jan. 17-21, 1977, unpublished.

Pr 70) K. Preuss and W. Greiner, Phys. Letters 33B, 197 (1970).

Pü 75) F. Pühlhofer, W. Pfeffer, B. Kohlmeyer, and W. F. W. Schneider, Nucl. Phys. A244, 329 (1975).

Pü 77) F. Pühlhofer, Nucl. Phys. A280, 267 (1977).

Sa 76) D. G. Sarantites, J. H. Barker, M. L. Halbert, D. C. Hensley, R. A. Dayras, E. Eichler, N. R. Johnson, and S. A. Gronemeyer, Phys. Rev. C 14, 2138 (1976).

Sa 77) D. G. Sarantites, J. H. Barker, L. Westerberg, R. A. Dayras, M. L. Halbert, and D. C. Hensley, to be published.

Sc 77) J. P. Schiffer, private communication.

Sc 77b) W. U. Schröder and J. R. Huizenga, to be published in Annual Review of Nuclear Science, Vol. 27. University of Rochester preprint UR-NSRL-144.

Sp 74) H. Spinka and H. Winkler, Nucl. Phys. A233, 456 (1974).

Sp 76a) P. Sperr, S. Vigdor, Y. Eisen, W. Henning, D. G. Kovar, T. R. Ophel, and B. Zeidman, Phys. Rev. Lett. 36, 405 (1976).

Sp 76b) P. Sperr, T. H. Braid, Y. Eisen, D. G. Kovar, F. W. Prosser, J. P. Schiffer, S. L. Tabor, and S. Vigdor, Phys. Rev. Lett. 37, 321 (1976).

St 74) R. G. Stokstad, Proc. Int. Conf. on Reactions between Complex Nuclei, Nashville, Tenn., Vol. II, p. 327, North Holland Co. (1974).

St 76) R. G. Stokstad, Z. E. Switkowski, R. A. Dayras, and R. M. Wieland, Phys. Rev. Lett. 37, 888 (1976).

St 77) R. G. Stokstad, R. A. Dayras, J. Gomez del Campo, P. H. Stelson, C. Olmer, M. S. Zisman, preprint. R. G. Stokstad, J. Gomez del Campo, J. A. Biggerstaff, A. H. Snell, and P. H. Stelson, Phys. Rev. Lett. 36, 1529 (1976).

Sw 76c) Z. E. Switkowski, R. G. Stokstad, and R. M. Wieland, Nucl. Phys. A274, 202 (1976).

Sw 77a) Z. E. Switkowski, R. G. Stokstad, and R. M. Wieland, Nucl. Phys. A279, 502 (1977).

Sw 77b) Z. E. Switkowski, Shiu-Chin Wu, J. C. Overly, and C. A. Barnes, Caltech preprint LAP-157 (1976).

Ta 77) S. L. Tabor, D. F. Geesaman, W. Henning, D. G. Kovar, K. E. Rehm, and F. W. Prosser, Jr., BAPS 22, 630 (1977).

Tr 77) W. Trautmann, J. de Boer, W. Dünnweber, G. Graw, R. Kopp, C. Lauterbach, H. Puchta, and U. Lynen, work in progress; J. de Boer, private communication.

Va 73) R. Vandenbosch and J. R. Huizenga, Nuclear Fission, Academic Press, N.Y. (1973).

Va 77) K. Van Bibber, R. Ledoux, S. G. Steadman, F. Videbaek, G. Young, and C. Flaum, Phys. Rev. Lett. 38, 334 (1977).

Vi 76) S. Vigdor in Proc. Symp. on Macroscopic Features of Heavy Ion Collisions Argonne Nat. Lab. 1976 (ANL/PHY-76-2), unpublished, p. 95.

We 76) A. Weidinger, F. Busch, G. Gaul, W. Trautmann, and W. Zipper, Nucl. Phys. A263, 511 (1976).

Wi 73) J. Wilczynski, Physics Letters 47B, 484 (1973).

Wi 77) R. M. Wieland, R. G. Stokstad, and G. R. Satchler, private communication.

Wo 76) A. Wolf and E. Cheifetz, Phys. Rev. C 13, 1952 (1976).

OVERVIEW OF THE TIME DEPENDENT MEAN-FIELD THEORY*

J. W. Negele†
Center for Theoretical Physics, Massachusetts Institute of Technology, Cambridge, Massachusetts 02139

I. Introduction

The microscopic theory of the dynamics of self-bound composite systems is of fundamental importance to a variety of areas of theoretical physics. For example, one of the outstanding problems of particle physics is to replace the "shell model" theory of quarks confined within a phenomenological bag or well with a microscopic theory arising from interactions between the quarks, and the primary impediment is our present ineptitude with relativistic many-body theory. Turning to more tractable non-relativistic applications, the potentially fascinating investigation of finite drops of liquid He^3 and He^4 is presently limited by a lack of sufficient experimental data. Thus, nuclear physics, possessing a rich phenomenology of collective and single-particle properties, and being confined to the context of non-relativistic many-body theory, provides an ideal and unique opportunity to explore a systematic, microscopic dynamical theory.

The time-dependent mean field approximation is one possible starting point for such a theory and, if successful, offers the possibility of providing a unified description of such diverse phenomena as nuclear ground states, rotational and vibrational excited states, large amplitude collective motion, fusion, compound nucleus formation, fission, fragmentation, and dissipation.

a. The Mean Field Approximation for Stationary States

To elucidate the essential features of the time-dependent problem, it is useful to recall some salient aspects of conventional many-body perturbation theory. Assume that in the fully interacting ground state each particle has probability ε for excitation out of its unperturbed shell-model orbital. Then, the shell model wave function has exponentially small overlap with the exact wave function $(1 - \varepsilon)^N \sim e^{-N\varepsilon}$, although

---

*This work is supported in part through funds provided by ERDA under Contract EY-76-C-02-3069.*000.

†Alfred P. Sloan Foundation Research Fellow.

it yields expectation values of few body operators valid to order ε. We hence give up all pretense of calculating the wave function, and instead, develop perturbation expansions for observables of interest like the energy and density.

Due to the strong repulsion between nucleons at short range, standard perturbation theory is reorganized in terms of an effective interaction, which sums all virtual rescatterings between two interacting nucleons in the presence of the surrounding particles. The mean field approximation with this effective interaction, often loosely referred to as the Hartree Fock (HF) approximation, yields an excellent description of ground state and single particle energies, radial density distributions in spherical nuclei, and shapes of deformed nuclei throughout the periodic table[1]. For simplicity in subsequent discussions, however, we will henceforth drop the crucial distinction between the true two-body interaction and the effective interaction.

There are seven features of the stationary state mean field theory which are particularly relevant to our discussion of the time-dependent theory:

1) The intuitive argument of Hartree suggests that the motion of each particle should be governed by the mean field of the others.

2) The theory avoids arbitrary parameterization of the shell model potential by oscillator or Woods-Saxon wells.

3) Instead, the system and H uniquely specify the energy, shape, and radial distribution.

4) Single particle equations may be derived variationally from $\delta\langle|H|\psi\rangle/\langle\psi|\psi\rangle$. Restricting ψ to be a Slater determinant replaces the Schrodinger equation by the coupled set of single particle equations $(T + W)\phi_\alpha = \varepsilon_\alpha\phi_\alpha$, where T is the kinetic energy and W is the instantaneous mean field.

5) The structure of linear quantum mechanics has been replaced by a system of coupled non-linear equations.

6) The single particle wave functions in (4) provide an optimal basis for systematic perturbation corrections.

7) The theory has unavoidable semiclassical aspects. The localized center of mass wave function represents a wave packet of momentum eigenstates and a deformed HF wave function must be understood as a wave packet of angular momentum eigenstates.

b. The Time-Dependent Mean Field Approximation

Each of these seven features has a precise analog in the time-dependent theory:

1) Intuitively, the mean field is the most obvious

mechanism to communicate collective information.

2) The theory avoids arbitrary selection of collective and intrinsic variables and the need for parameterizing shapes.

3) Instead, the initial conditions and H uniquely specify the dynamics.

4) Single particle equations may be derived variationally from the stationarity of the action

$$\delta\langle\psi(t)\,|\,i\frac{\partial}{\partial t} - H\,|\,\psi(t)\rangle .$$

Restricting ψ to be a Slater determinant replaces the time-dependent Schrodinger equation by the coupled set of single particle equations

$$i\frac{\partial}{\partial t}\,\phi_\alpha(\vec{r},t) = (T + W)\,\phi_\alpha(\vec{r},t) .$$

5) Linear quantum mechanics has again been replaced by a system of coupled non-linear equations.

6) The basis of time dependent single particle wave functions provides an optimal basis and definition of reaction channels. In contrast to the usual optical model description in terms of ground states of the scattering nuclei, no one-particle one-hole amplitudes remove probability from the entrance channel.

7) As before, the initial conditions represent a wave packet for the impact parameter and orientation of two interacting nuclei. The final state evolved by the equations of motion approximates the final wave packet evolving from the original packet.

Thus, the time-dependent mean field approximation, or time dependent Hartree Fock approximation[2] (TDHF), is the obvious generalization of the mean field theory to dynamics. The equations automatically conserve energy and maintain orthonormality of the single particle wave functions, thus incorporating the Pauli principle exactly. In the limit of infinitesimal deviations away from the ground state, TDHF is equivalent to the random phase approximation (RPA), so it is already known to be reliable in one important limit[3].

As stressed previously for stationary states, this approximate time-dependent perturbation theory can, at most, yield valid expectation values for few body operators. In this regard, we encounter one crucial new feature in the time-dependent case. Whereas experimentalists are generally content to restrict their attention to few body operators such as energies and density distributions when dealing with stationary states, in treating nuclear reactions they insist on far too much specificity and confront theorists with S-

matrix elements representing the overlap of two complete many body wave functions. Thus, in the context of TDHF, we must give up all pretense of describing such data, and rather restrict ourselves to addressing mean values such as multiplicities, mean excitation energies, dispersion in proton and neutron number and similar quantities.

c. Single Particle Propagation in the Mean Field

The essential features of TDHF dynamics are most easily understood by considering the propagation of single particle wave functions in the collective mean field. Colliding slabs of matter provide an adequately realistic system which is particularly simple to visualize: wave functions for transverse plane waves decouple completely and one simply considers a one-dimensional wave function evolving in a rather smooth, time-dependent well of maximum depth of about 50 MeV[4]. At low energies, orbitals from the left and right wells bounce back and forth in the compound slab potential at different velocities -- ranging from almost zero for the most-bound orbitals to the fermi velocity for the least-bound. Under these conditions, randomization occurs quickly and the excited compound slab remains intact. At higher energies, sufficient translational motion is superimposed upon the single particle motion that the orbitals of one slab traverse the potential of the other as a group and actually emerge from the far side, giving rise to break-up of the compound slab into two excited final state fragments. The density and two single particle wave functions for such a case at a c.m. energy of 2.5 MeV per particle are shown in Figs. 1 and 2. As is evident, considerable reflection and orbital distortion still occur at this energy, yielding significant dissipation which is highly suggestive of the strong dissipation observed in heavy ion reactions at comparable energies. Precisely when the transition from compound-slab to break up occurs is a delicate question subject to significant influence by single particle motion.

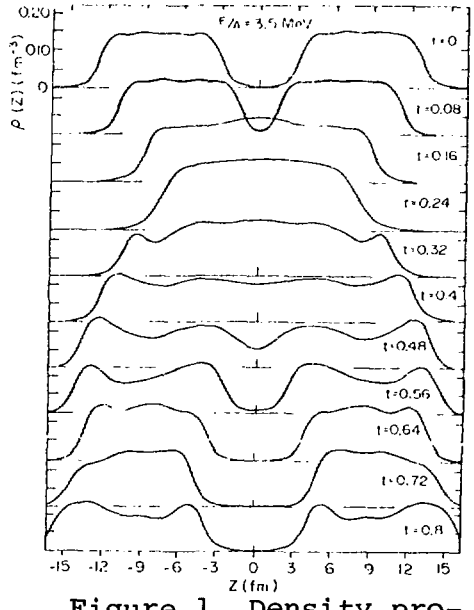

Figure 1. Density profiles $\rho(z,t)$ for E/A = 3.5 MeV. (Ref. 4).

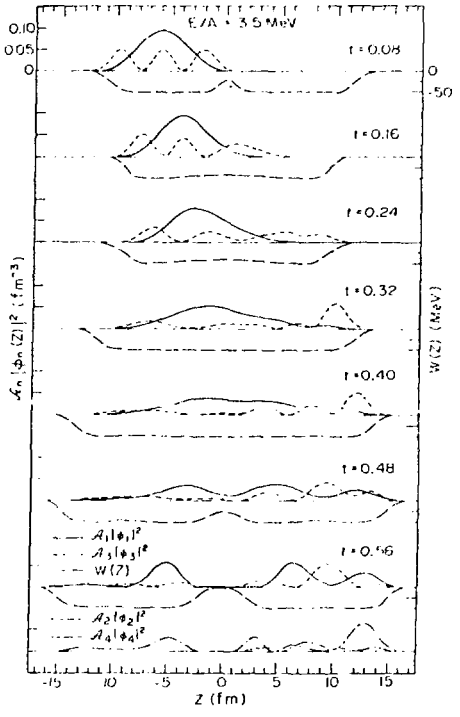

Figure 2. Contributions of individual single-particle orbitals to the density at various times for the $\mathcal{A}_1 = \mathcal{A}_2 = 1.4$ fm^{-2} system at E/A = 3.5 MeV. In the seven upper graphs, the solid and short-dashed lines denote the contributions of the lowest and third lowest orbitals originating in the left-hand slab. The contributions of the second and fourth orbitals originating in this left slab are shown at t=0.56 in the lowest graph. In all cases, the long-dashed curves denote the one-body potential W(z,t). (Ref. 4).

If there happens to be an excess of particles in the neck region at the instant when scission should occur, it is inhibited; if single particle effects generate a depletion, it should be enhanced.

Such single particle resonance effects in slab collisions are quite obvious in the plot of the ratio of final translational kinetic energy to the incident translational kinetic energy in Figure 3, where fusion is indicated by a ratio of zero. The recent discovery[5,6] of resonances in the fusion cross sections in light ion reactions on ^{12}C thus cries out as a significant test of the mean field theory. As shown in

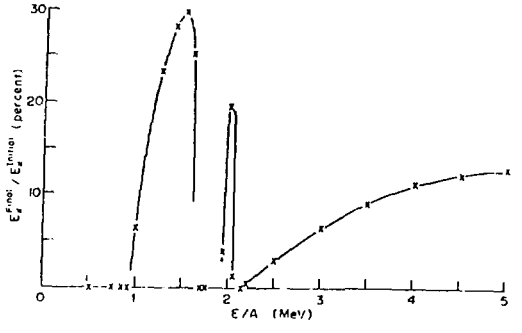

Figure 3. The ratio of final translational kinitic energy to initial translational energy as a function of E/A for the 1.4 fm^{-2} plus 1.4 fm^{-2} system. Calculated points are denoted by a cross. A value of zero denotes fusion. (Ref. 4).

Figs. 4 and 5, dramatic fusion cross section fluctuations are observed with ^{16}O and ^{12}C projectiles in the energy regime studied in Fig. 3, and structureless cross sections occur for ^{18}O and ^{19}F. If the theory is in fact successful in reproducing this phenomenology, it should give significant insight into the mechanism whereby the valence nucleons in ^{18}O and ^{19}F increase and smooth the fusion cross sections.

Another important feature evident in slab collisions is single particle emission, arising from excitation of high momentum components in the single particle orbitals of one nucleus due to the rapid passage of the potential generated by the other nucleus. Fig. 6 shows the density during a 2.4 MeV per particle c.m. collision on a logarithmic scale, and the corresponding velocity distribution. At $t=0.32\times10^{-21}$ sec., the dashed line shows a high energy particle distribution at about one percent of the central density beginning to emerge from the compound slab. By the time scission occurs, the solid line shows the high energy tail clearly separating with particle velocities ranging well above the incident velocity of 21.5 fm/10^{-21}sec. Roughly 2/3 of the probability comes from the least bound single particle orbital,

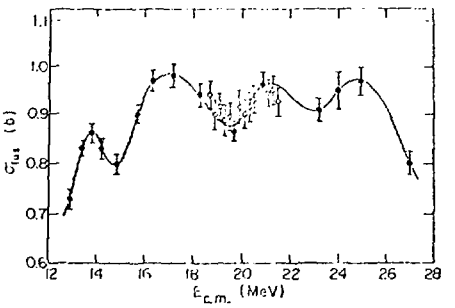

Figure 4. Total fusion cross section for ^{16}O + ^{12}C as a function of the c.m. energy. (Ref. 5).

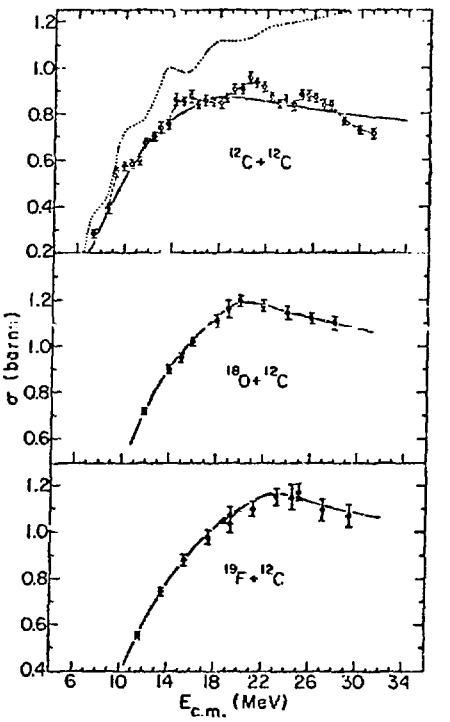

Figure 5. Total fusion cross section for $^{12}C+^{12}C$, $^{18}O+^{12}C$, and $^{19}F+^{12}C$, as a function of the c.m. energy. (Ref. 6).

1/4 from the next and the remaining 1/12 from the deepest two levels. In a more realistic calculation, George Bertsch[7] has calculated the probability that the $Y_{\ell 0}$ component of a $p^{1}/_{2}$ orbital in ^{14}N is excited above 10 or 20 MeV by the passage of a ^{16}O potential, with the results shown in Figure 7. It should be quite interesting to compare the angular and energy distributions from such calculations with experimental results.

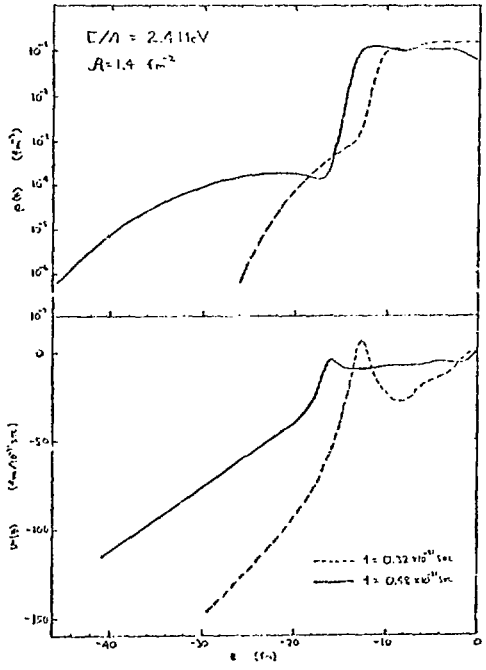

Figure 6. Density and velocity profiles showing the emergence of high energy particles after a slab collision at 2.4 MeV per particle in the c.m.

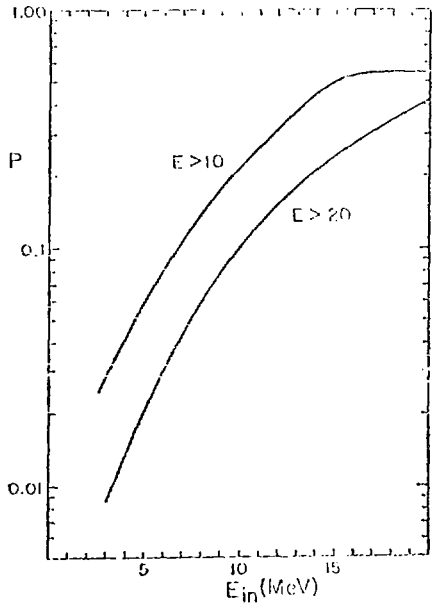

Figure 7. The probability P for escape of a $p^{1}/_{2}$ particle in ^{14}N with energy E after colliding with ^{16}O at incident lab energy E_{in} (Ref. 7).

d. Relation to Hydrodynamics

Although the time dependent mean field approximation and hydrodynamics obey the same mass, energy, and momentum conservation equations, they differ fundamentally with respect to equilibration. In the mean-field theory, equilibration arises slowly from repeated collisions with the edges of the

potential, whereas in hydrodynamics, one imposes from the outset the assumption of complete instantaneous local equilibration.

During collisions, the shapes of intermediate configurations in the two theories may differ significantly. In head-on hydrodynamic collisions, longitudinal momentum is immediately equilibrated in the transverse direction, leading to transverse motion which produces either an oblate configuration or transverse mass ejection. In contrast, the mean field theory produces very little transverse momentum, yielding a prolate compound system. This system is elongated by the pressure of high longitudinal momentum components, and only gradually broadens from an increasing transverse pressure.

The central density in a high energy collision may rise far above twice nuclear density in a hydrodynamic theory, depending on the details of the equation of state and possible inclusion of relativistic kinematics. In the mean field theory, single particles in one nucleus experience significant scattering from the mean field of the other nucleus, since the potential at twice nuclear density is roughly 100 MeV more repulsive than at nuclear density with our interaction. However, at sufficiently high energy, the nuclear density at most doubles, corresponding to intuitively plausible interpretation. As already discussed, the interpenetrating fragments still experience a strong pulse from each other, leading to excitation and subsequent particle emission and fragmentation.

One means of visualizing the degree of equilibration during an interaction is to plot the one body density matrix

$$\tilde{\rho}(z,s) \frac{e^{-imvs}}{\rho(z)} \sum_{\alpha} \psi_{\alpha}\left(z + \frac{s}{2}\right) \psi_{\alpha}\left(z - \frac{s}{2}\right)$$

where we have normalized to the density at c.m. coordinate z and removed the overall phase associated with the local mean velocity v. The density matrix as a function of relative coordinate s is displayed in Fig. 8 during and after a slab collision. At the earliest time, $\tilde{\rho}$ agrees quite well with the Slater density ρ_{SL}, since that region of the nucleus has not yet been disturbed by the reaction. At later times, $\tilde{\rho}$ differs significantly from a thermal density matrix for a hot fermi gas, either by virture of a large imaginary part or because the overshoot beyond the first zero is much too large. Thus, during the relevant interaction time, collisions at this and other energies we have investigated are not fully equilibrated.

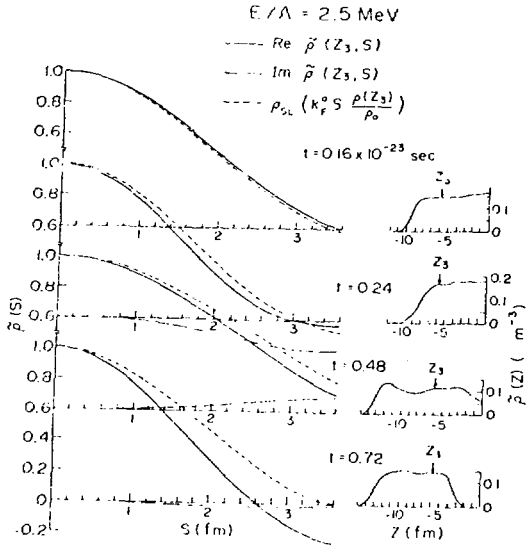

Figure 8. Normalized one-body density matrices for E/A=2.5 MeV. The left-hand plots present the one-dimensional Fermi gas results (short-dashed curves) and real and imaginary parts of the calculated density matrices (solid and long-dashed curves) at the position z_3 denoted on the density distributions graphed on the right. (Ref. 4).

II. An Exactly Soluble Model

A number of the conceptual questions one might raise concerning the time dependent mean field theory may be investigated quantitatively for the exactly soluble problem of bosons in one dimension interacting with attractive δ-function forces.(8) This model problem directly confronts the question of final state interpretation and whether the approximation degrades in time. In at least this one controlled case, one can see whether there is trouble because the time dependent variational principle is a stationary, rather than minimum principle. Finally, the model provides a testing ground for any qualitative arguments or conjectured criteria regarding regions of validity of the theory.

With the Hamiltonian

$$H = -\frac{1}{2} \sum_{i=1}^{N} \frac{d^2}{dx_i^2} - v \sum_{i<j=1}^{N} \delta(x_i - x_j)$$

the exact ground state is(9,10)

$$\psi_N = N!\sqrt{(N-1)!\ v^{N-1}}\ e^{-\frac{v}{2}\sum_{i<j}|x_i-x_j|}$$

with energy

$$E_N = -\frac{N(N^2-1)v^2}{24}$$

and one-body density[11]

$$\rho_N(x) = v(N!)^2 \sum_{n=1}^{N-1} (-1)^{n+1} \frac{n\, e^{-vnN|x|}}{(N+n-1)!\,(N-n-1)!}$$

$$\xrightarrow[N\to\infty]{} \frac{N^2 v}{4\cosh^2(\frac{Nvx}{2})} \{1 + \mathcal{O}(\tfrac{1}{N}) + \ldots\}$$

The scattering of N particles by N particles yields no breakup.[10] From the exact elastic scattering phase shift, one obtains the time delay

$$\Delta = \frac{1}{NK}\frac{\partial}{\partial K}\delta(K)$$

$$= -\frac{4v}{NK}\sum_{m=1}^{N-1}\frac{m}{4K^2+m^2v^2} - \frac{2v}{K(4K^2+N^2v^2)}$$

$$\xrightarrow[N\to\infty]{} -\frac{4}{NvK}\ \ell n\ N + \mathcal{O}(\tfrac{1}{N})$$

Turning now to the mean field theory, assuming the product wave function

$$\Psi_N^H = \sqrt{N}\prod_{i=1}^{N}\phi(x_i)$$

yields the Hartree equation

$$\{-\frac{1}{2}\frac{d^2}{dk^2} - v(N-1)|\phi|^2 - \varepsilon\}\ \phi = 0$$

The solution

$$\phi = \frac{\sqrt{(N-1)v}}{2\cosh\{\frac{(N-1)vx}{2}\}}$$

yields the Hartree energy[11]

$$E_N^H = \frac{-N(N-1)^2v^2}{24}$$

and one body density[11]

$$\rho_N^H(x) = \frac{N(N-1)v}{4\cosh^2\{\frac{(N-1)vx}{2}\}}$$

Thus, as one can also prove from a diagrammatic analysis[8], the energy and one-body density are asymptotically exact in the large N limit. The time-dependent Hartree equation for $2N$ particles occupying the single particle wave function ϕ is

$$\{i\frac{\partial}{\partial t} + \frac{1}{2}\frac{d^2}{dx^2} + (2N-1)v|\phi|^2\}\phi = 0$$

which is exactly soluble[13]. The resulting time delay is

$$\Delta T^H = \frac{-4}{(2N-1)vK}\ell n[1 + \frac{(2N-1)^2v^2}{16\,K^2}]$$

$$\to -\frac{4}{NvK}\ell nN + \mathcal{O}(\frac{\ell nN}{N^2})$$

which agrees with the exact result in the large N limit.

It is important to note that we have only characterized the final state in terms of few-body operators. The time-delay, for example, may be extracted from the one-body density, and the mean number of particles and final translational kinetic energy are expectation values of one-body operators. It is certainly true that in the large N limit, the Hartree wave function has negligible overlap with the exact wave function and the "lifetime"[14] of the determinant $(\langle H^2\rangle - \langle H\rangle^2)^{-1/2}$ is zero. Thus for this model problem we have only substantiated quantitatively in the large N limit the modest claim stated at the outset that the mean field theory applies to the expectation values of few-body operators.

III. Applications to Nuclear Systems

a. The Role of Symmetries

Before discussing specific applications, it is useful to review an important fact associated with symmetries in the mean field theory: Any symmetry of the wave function which

occurs in the mean field is preserved in time. For example, if one selects an initial condition with reflection, inversion, spin, isospin, or axial symmetry, this symmetry will be preserved in time. Such solutions are very special. Not only are they especially cheap to calculate because they evolve in a limited space but for the same reason they also have much less freedom for randomization and thus dissipation and equilibration. The essential fact to bear in mind is that in considering a realistic ensemble of initial conditions, these special symmetric cases receive negligible weight. Thus, although those of us cursed with impoverished computer budgets must often restrict ourselves to such symmetric cases, we must at least be alert to the possible unrealistic consequences of such symmetries.

A case in point is the restriction to axial symmetry. Macroscopically, one recognizes that the realistic shapes sketched in Fig. 9 must be replaced by rather different shapes

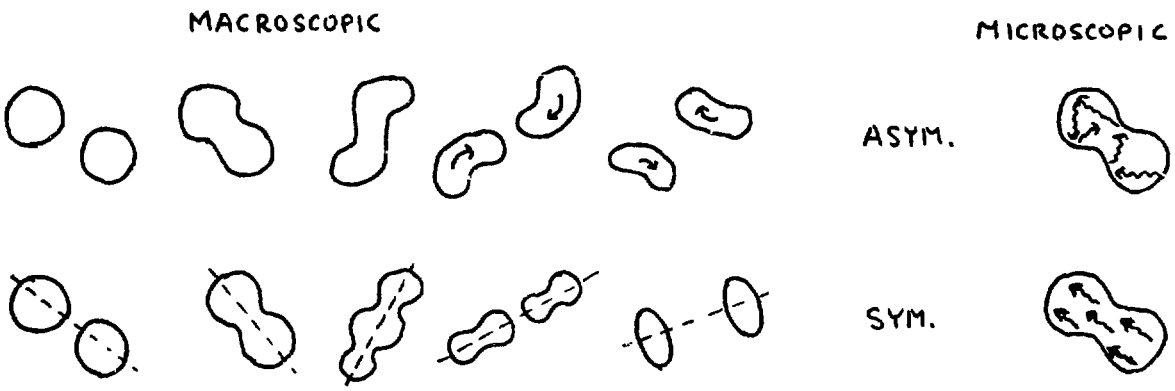

Figure 9. Sketch of macroscopic and microscopic consequences of axial symmetry.

if one postulates axial symmetry with respect to the axis joining the centers of two interacting nuclei. Since such deformation modes are reasonably soft, one may expect such macroscopic restrictions to be benign. Microscopically, however, as also sketched in Fig. 9, single particle orbitals bouncing around on non-closed random trajectories may be expected to exhibit considerably greater dissipation than the periodic longitudinal trajectories imposed by axial sym-

metry. We shall subsequently see suggestive recent evidence that this is the case.

Even with this caveat, it is a non-trivial question how to implement the axial symmetric hypothesis in a dynamical theory. A particularly appealing variational formulation by H. Feldmeier arose from discussion at Oak Ridge last year.(15)

One assumes the variational wave function

$$\Psi = e^{-iL_y\eta}\, e^{i\sum_i \chi(r_i,z_i,\phi_i)}\, \mathcal{A}\, \pi\psi_\lambda(r_i,z_i)e^{im_\lambda\phi_i}$$

which is axially symmetric in an intrinsic frame that may be freely rotated by an angle η and which has a collective velocity potential χ. Using the periodicity of χ, the action is

$$S=\int d^3r\, dt\{H(\psi_\lambda^*\psi_\lambda)-i\sum\psi_\lambda^*\frac{\partial}{\partial t}\psi_\lambda + \frac{1}{2m}\rho|\nabla\chi|^2 - \dot{\eta}\rho\hat{e}_y\cdot rx\nabla\chi\}$$

Variation with respect to η yields

$$\frac{d}{dt}\int d^3r\ \rho\hat{e}_y\cdot rx\nabla\chi = 0 \rightarrow \langle Ly\rangle = \text{const} \equiv L$$

and variaton with respect to $\langle Ly\rangle$ yields

$$\eta = \frac{\partial}{\partial\langle Ly\rangle}\ \frac{1}{2m}\int\rho|\nabla\chi|^2$$

Thus, L is the dynamical variable conjugate to η and all other degrees of freedom in χ are static degrees of freedom (16,17). Defining

$$\theta = a\chi$$

then

$$L = \int\rho e_y\cdot rx\ \frac{\nabla\theta}{a}$$

and

$$S = \int d^3r\, dt\ \{H(\psi_\lambda^*\psi_\lambda) - i\Sigma\psi_\lambda\frac{\partial}{\partial t}\psi_\lambda + \frac{L^2}{[\int\rho\hat{e}_y\cdot rx\nabla\theta]^2}\frac{\rho}{2m}|\nabla\theta|^2 - \dot{\eta}L\}$$

Thus, the equation of motion is in canonical form with

$$\mathcal{H} = \int H(\psi_\lambda^*\psi_\lambda) + \frac{L^2}{2}\cdot\frac{\frac{1}{m}\int\rho|\nabla\theta|^2}{[\int\rho\hat{e}_y\cdot rx\nabla\theta]^2}$$

The Hamiltonian equations $\dot{\eta} = \frac{\partial H}{\partial L}$ and $\dot{L} = \frac{\partial H}{\partial \eta}$ simply reproduce the previous equation of motion, and we define the coefficient of $\frac{L^2}{2}$ as the inverse of the moment of inertia. This moment of inertia corresponds to irrotational flow and attains the proper form in the limit of two nuclei passing by and for a spherical nucleus. Modification of the usual TDHF equations is straightforward. Variaton with respect to $\delta\psi^*$ yields an additional potential for the evolution the single particle wave functions:

$$\frac{L^2}{2m}\left\{\frac{|\nabla^2\theta|^2}{[\int\rho e_y\cdot rx\nabla\theta]^2} - \frac{\int\rho|\nabla\theta|^2}{[\int\rho\hat{e}_y\cdot rx\nabla\theta]^2}\ 2\hat{\theta}_y\cdot rx\nabla\theta\right.$$

Variation with respect to $\delta\theta$ yields an equation which determines the velocity field at each time:

$$2\nabla\cdot\rho\nabla\theta = \frac{\int\rho|\nabla\theta|^2}{\int\rho e_y\cdot rx\nabla\theta}\ 2e_y\cdot rx\nabla\rho \equiv 2am\eta e_y\cdot rx\nabla\rho$$

As an alternative to this formulation, one may postulate a Hamiltonian functional with a physically plausible moment of inertia. For example, Koonin[18] has suggested the use of

$$I_{rigid} = m\int d^3r\ \rho(r)\ [z^2+\tfrac{1}{2}r^{\prime 2}]$$

and

$$I_{point} = m\,\frac{A_1+A_2}{A_1+A_2}\ R^2$$

at appropriate stages of a reaction. Note that these two prescriptions make physically different assumptions about the post-scission rotation of two fragments, as sketched in Fig. 10.

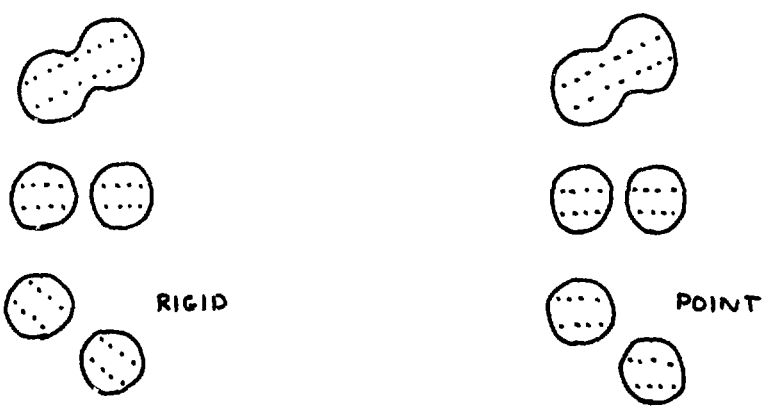

Figure 10. Comparison of rigid and point post-scission moment of inertia assumptions.

b. Collisions

The time evolution of a collision of ^{40}Ca on ^{40}Ca is displayed with contour plots of the density at evenly spaced time intervals in Fig. 11.

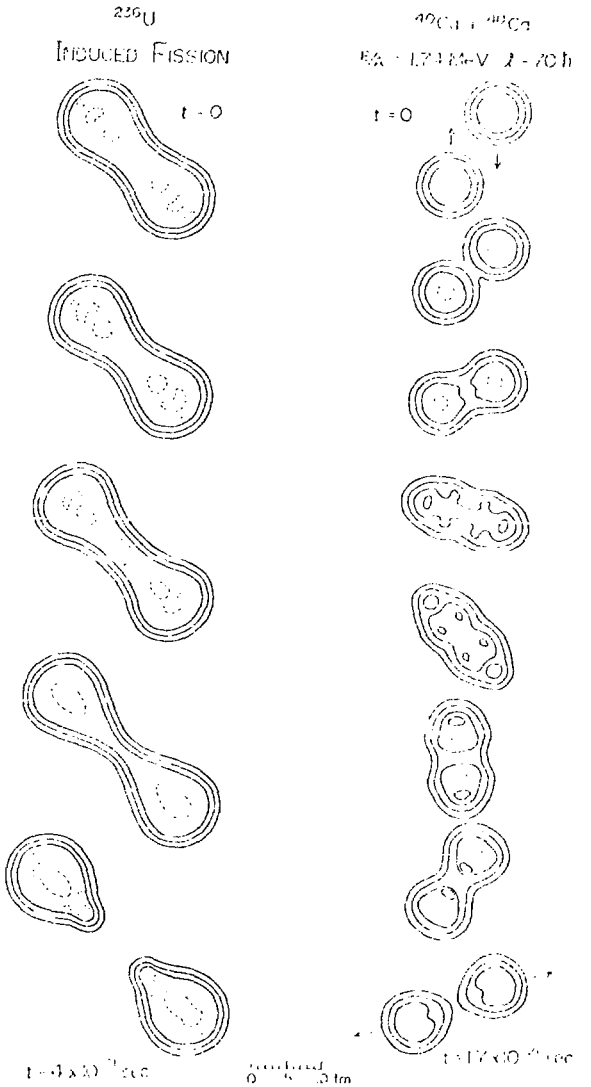

Figure 11. Contour plots of the nuclear density at evenly spaced time intervals during induced fission and a heavy-ion collision. The outermost three solid lines denote densities of 0.02, 0.08, and 0.14 fm^{-3} and thus display the shape and extent of the surface. Interior density fluctuations are shown by dashed and solid lines which denote densities of 0.16 and 0.14 fm^{-3} respectively.

Corresponding calculations[18] at a variety of impact parameters for ^{16}O and ^{40}Ca are summarized on the polar plots in Fig. 12. The familiar behavior of nearly elastic peripheral Coulomb trajectories, dissipative orbiting trajectories and highly dissipative central collisions is qualitatively reproduced. The resulting deflection functions and energy loss curves are shown in Fig. 13. In ^{16}O, the final energy is comparable to the Coulomb energy for most interior impact

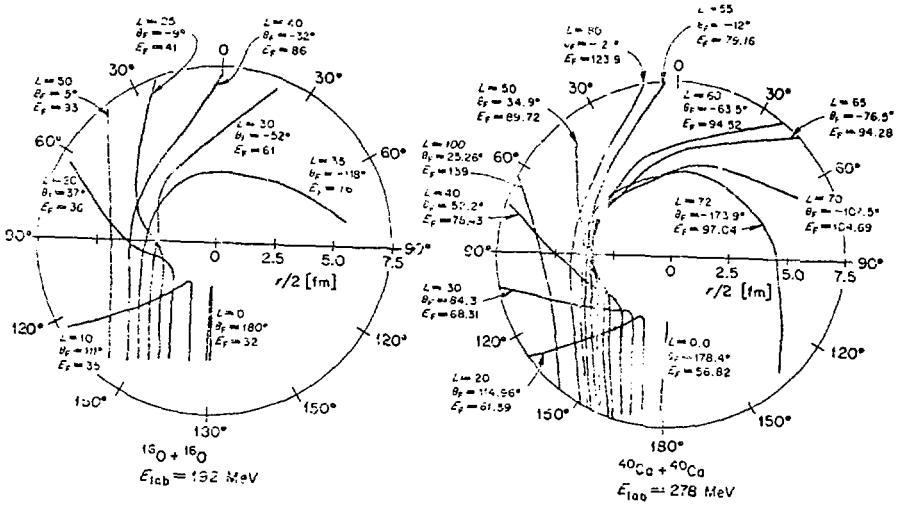

Figure 12. Polar plot of trajectories for representative $^{16}O + ^{16}O$ and $^{40}Ca + ^{40}Ca$ reactions.

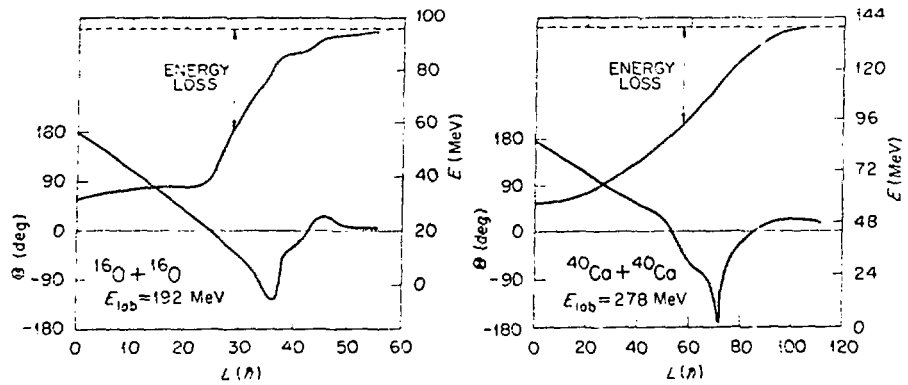

Figure 13. The deflection and energy-loss functions for the reactions of Fig. 12. The dotted line represents elastic scattering. (Ref. 18).

parameters, so not much more dissipation is required for fusion. In the case of ^{40}Ca, however, near the orbiting impact parameter the axially symmetric calculation yields significantly less dissipation than observed experimentally.(19) Roughly averaging over all interior impact parameters yields about 70% of the required dissipation.

In this connection, it is interesting to report preliminary three dimensional results for similar collisions by Flocard and Weiss.[20] For $^{16}O + {}^{16}O$ at a lower energy of 110 MeV in the lab, fusion occurs between ℓ = 13 and 29ħ. This is qualitatively consistent with the earlier remark that the non-closed three dimensional trajectories in an arbitrary shaped well for non-central collisions should randomize and dissipate significantly more than for the closed longitudinal trajectories for central collisions. In the case of ^{40}Ca, which is directly comparable to the axially symmetric calculation of Fig. 13, a three dimensional calculation appears to fuse at ℓ=30 and 70ħ. Hence, preliminary evidence is strongly suggestive that the remaining 30% of the dissipation may be accounted for in three dimensions. Clearly exactly comparable systems and forces should be compared in detail to quantitatively assess the limitations of axial symmetry.

The distribution in particle number in the $^{40}Ca + {}^{40}Ca$ calculation is compared with experiment in Fig. 14. Even when corrected for evaporation, it is evident that the number dispersion is significantly less than observed experimentally. It will be particularly interesting to see to what extent this is also the result of imposing axial symmetry.

A more complete comparison between theory and experiment is afforded by $^{14}N + {}^{12}C$. Results for the angular distribution for direct inelastic reaction products and fusion cross sections in an axially symmetric calculation[21] are shown in Figures 15 and 16. The discrepancy at large angles arises from the fact that the fusion channel is not being adequately described.

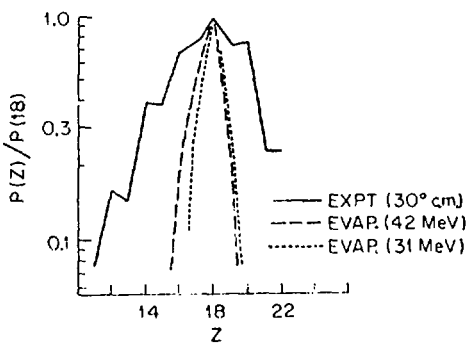

Figure 14. Fragment charge distribution relative to Z=18 for final states measured in Ref. 19 and calculated due to evaporation. (Ref. 18).

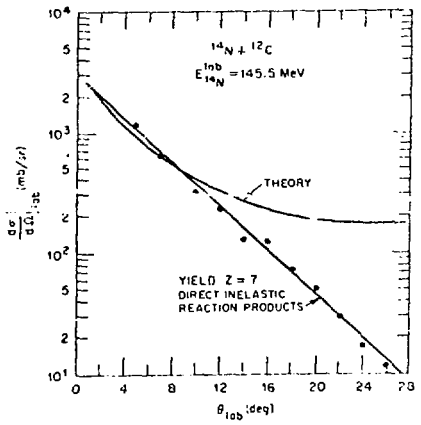

Figure 15. Theoretical and experimental cross sections for direct inelastic products. The ^{14}N bombarding energy is 145.5 MeV and the data are the yield for Z=7. (Ref. 21).

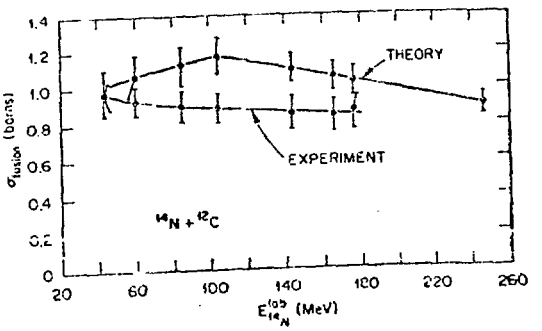

Figure 16. Experimental and theoretical fusion cross section for $^{14}N + ^{12}C$ as a function of incident ^{14}N energy. (Ref. 21).

c. Fission

Induced fission near threshold is an ideal application of the mean field theory, because the initial condition is conceptually well specified and because fission systematics offer a quantitative test of dissipation. After excitation, a fissioning nucleus is understood to rattle around statistically until it finally happens to gather essentially all of its excitation energy in the fission degree of freedom. After progressing up the fission barrier, its most likely path is to pass slowly past the saddle point configuration before beginning its decent to scission. Thus, the appropriate initial condition is to release a constrained static HF solution slightly beyond the saddle point. Since the saddle point is rigorously independent of the form of the constraint, the initial condition is essentially unique.

The results of such a fission calculation[22] are shown in Fig. 11, and represent the first such microscopic calculation of fission. Unfortunately, the calculation falls somewhat short of the intended definitive test of the mean-field theory, again because of the limitations of axial symmetry.

By symmetry, the Hamiltonian does not connect different angular momentum projection and parity subspaces, so in contrast to the case with finite axial asymmetry, level crossing occurs, as sketched in Fig. 17. Hence, an axially symmetric initial condition slightly beyond the saddle point would become trapped forever in a concave upward well. Clearly, then, some tractable technical device must be chosen to introduce matrix elements to prevent level crossing. The most simple device to accomplish this effect is to assume constant gap pairing,[23] However, it must be understood from the outset that one deals with an effective gap Δ or pairing strength G which actually is intended to mock up the average effect of symmetry breaking mean field matrix elements as well as the residual interaction.

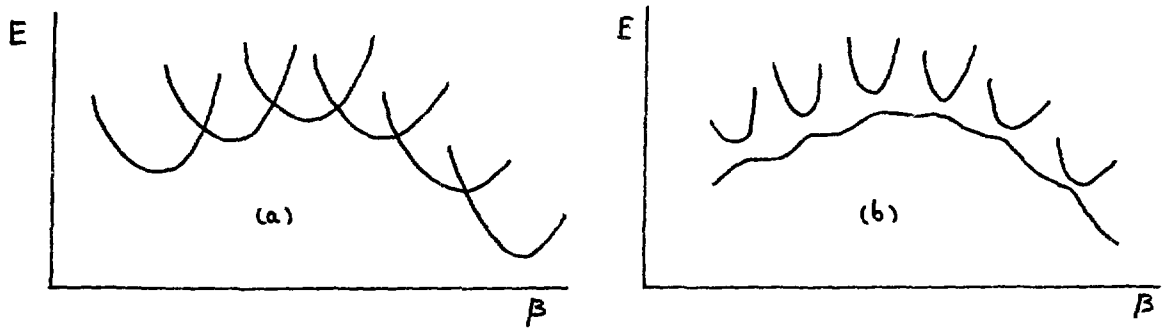

Figure 17. Sketch of the energy as a function of deformation for an axially symmetric determinant (a) and with axial asymmetry and/or pairing (b).

The equations of motion derived from applying the time dependent variational principle to a BCS wave function with the assumption of a constant gap are very simple.(23) The single particle wave functions evolve according to

$$i\,\dot{\phi}_\ell = (\mathcal{H}-\varepsilon_\ell)\,\phi$$

and the u_ℓ's and v_ℓ's are determined by

$$i(v_\ell{}^2) = \Delta[(u_\ell v_\ell) - (u_\ell v_\ell)^*]$$

$$i(u_\ell v_\ell) = 2\,u_\ell v_\ell(\varepsilon_\ell-\lambda) + \Delta(2v_\ell{}^2-1)$$

where

$$\varepsilon_\ell = \int \phi_\ell{}^*\,\mathcal{H}\,\phi_\ell$$

and the lagrange multiplier λ is defined to conserve particle number

$$\lambda = [\Delta N + \sum_{\ell>0}(\varepsilon_\ell\{u_\ell v_\ell + u_\ell v_\ell{}^*\} - \Delta)]/\sum_{\ell>0}(u_\ell v_\ell + u_\ell v_\ell{}^*)$$

The sequence of densities obtained with Δ = 2.0 MeV have already been presented in Fig. 11. Particularly salient features are the fact that the time scale is rapid, essentially an order of magnitude fastor than with the classical one-body dissipation formula(24) and that the neck is much more elongated than with one-body dissipation. Shapes close to the scission point for Δ = 6.0 and Δ = 0.7 MeV are shown in Fig. 18.

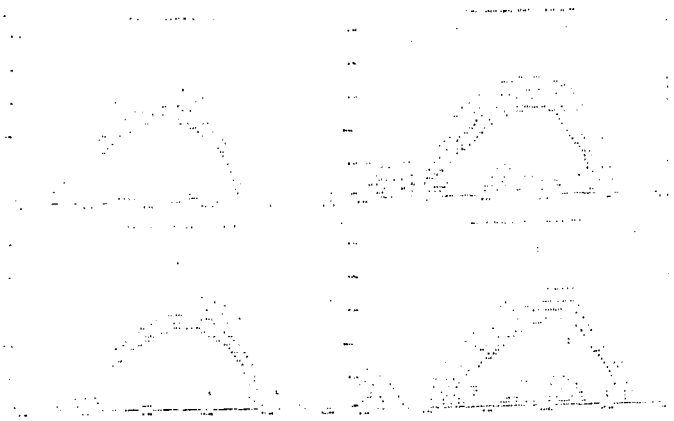

Figure 18. Pre-scission and post-scission configurations for ^{236}U with Δ = 6.0 MeV (left frames) and with Δ = 0.7 MeV (right frames).

Here one observes that the formation of an alpha-like cluster at the neck arises when the matrix element is sufficiently weak that the relevant central orbitals are not completely depopulated.

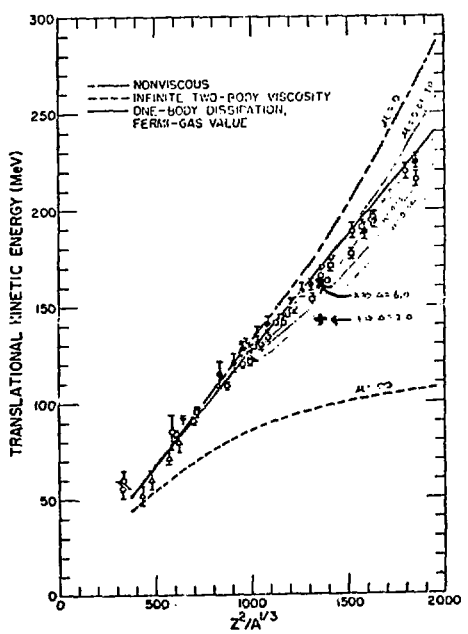

Figure 19. Final fragment translational kinetic energy as a function of fissility, with TDHF fission results for ^{236}U denoted by X for Δ = 6.0 MeV and + for Δ = 2.0 MeV. (Ref. 24).

The dissipation for various values of Δ is displayed in Fig. 19. Unfortunately, dissipation is completely dominated by the strength of Δ, with weak matrix elements yielding far too much dissipation (i.e., probability is trapped in highly excited orbitals) and very strong pairing (Δ=6.0) required to agree with the experimental result. In the space employed in this calculation, Δ=2 MeV corresponds to a two-body matrix element $G \approx 0.28$ MeV. For comparison, 23/A yields $G \approx 0.1$ and realistic reaction matrix elements yield values ranging from 0 to 0.4 MeV in this region of the periodic table.

Because of the phenomenological nature of Δ, the present calculation does not provide a definitive test of the mean field theory. However, the results do appear both plausible and encouraging. Because of the neglect of axial asymmetry, the effective matrix element should be larger than specified by the residual interaction, and a factor of two is not unreasonable. Averaging over a wave packet of asymmetric initial conditions roughly corresponds to averaging over Δ with an appropriate weighting function. Occasionally, for almost symmetric initial conditions, the effective Δ should be very small, leading to an α particle from the neck which is observed experimentally roughly one time in 600. The particle number dispersion in the fragments has not yet been calculated, but provides another possible test of the theory. Thus, fission provides a rich opportunity for future investigations.

d. Pion Condensation in Heavy Ion Collisions

The time-dependent mean field theory is also capable of describing other interesting dynamics which have yet to be observed experimentally. There is abundant theoretical evidence that slightly beyond nuclear density, nuclear matter becomes unstable with respect to spin-isospin fluctuations with a wave length on the order of several fermis.[26] Such fluctuations, often obscured by unnecessarily fancy pion condensation language, are quite adequately described by TDHF (in fact they are usually calculated in the RPA approximation). Thus, TDHF affords the ideal framework for describing both the heavy-ion collision giving rise to dense matter and the ensuing dynamics of spin-isospin modes of the short-lived dense intermediate state, and such calculations are presently under way.

The pion propagator in the nuclear medium is sketched in Fig. 20. Near threshold, the pions between particle hole have ω=0 and thus may be replaced by static potential interactions. Thus, the growth of the spin-isospin instability corresponding to pion condensation may be described by adding

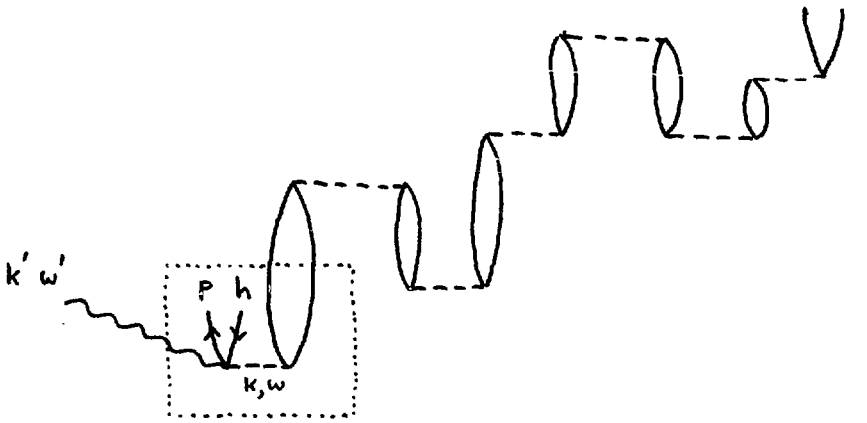

Figure 20. Pion propagator in the RPA approximation.

the following terms to the effective Hamiltonian:

$$-\frac{f^2}{\mu^2}\int\int d^3r_1 d^3r_2 \nabla^k \left(\sum_{\alpha\,\alpha}\psi^*_\alpha(1)\tau_1^j\sigma_1^k\psi_\alpha(1)\right)\frac{e^{-\mu r_{12}}}{r_{12}}\nabla^\ell\left(\sum_{\beta\beta}\psi^*_\beta(2)\tau_2^j\sigma_2^\ell\psi(2)\right)$$

$$+ g_o\int d^3r \sum_{\alpha\,\alpha}\psi^*_\alpha(1)\tau_1^j\sigma_1^k\psi_\alpha(1)\sum_\beta\psi_\beta{}^*(2)\tau_2^j\sigma_2^k\psi_\beta(2)$$

To determine whether the spin isospin density source term leads to a unique signature in the observed distribution of emitted pions, one simply constructs an effective operator of the form indicated in the box in Fig. 20. An off-mass shell pion characterized by k, ω is allowed to scatter from all occupied states h and one sums over all final states p such that an on-mass shell pion is emitted with k' and ω'. Integrating the instantaneous emission throughout the interaction should give a first approximation to the observable effects of a pion condensate.

The essential question, of course, is whether the high density region lasts long enough during collisions for significant growth of such instabilities. The present theory appears to be the only formulation which simultaneously treats the dynamics of the nuclear matter distribution and the instability, and thus offers a unique opportunity for investigating the possibility of observing pion condensation in laboratory experiments.

IV. Open Questions

It should be evident from this brief overview that investigations of the time-dependent mean field theory to date have raised a number of challenging problems and questions.

Experimentally, the most crucial question is to think of observables corresponding to expectation values of few body operators which can definitively distinguish the mean field theory from other approximations. It is one thing for theorists in their fairy tale world to draw pictures showing how different intermediate density shapes look in TDHF and hydrodynamics, but quite another to design an experiment which can discriminate between the two cases. The key features to consider in comparing the mean field theory with other approximations are the relatively small transverse momentum transfer, the dominance of single particle effects in appropriate regimes, and the lack of complete equilibration during the interaction time.

Another open question concerns the limitations of symmetry restrictions, such as axial symmetry, relative to the limitations of the mean field theory. Although fragmentary three dimensional results exist,[20,27] what is definitely required is a thorough systematic investigation of two and three dimensional calculations of identical collisions with identical forces. (For zero impact parameter, the results should be identical, allowing a direct check on the separate technologies.) Only in this way can one determine, in Jim Griffin's language, when the additional expense of three dimensional calculations is in fact commensurable with the additional physics.

The criteria for validity of the mean field theory have yet to be clarified. Simple estimates of the decay time for the end caps of two fermi spheres of interacting matter suggest that at 2.5 MeV per particle in the c.m., slabs would interpenetrate 10 fm before significant decay occurs.[28] This is certainly not the whole story, however, as indicated by the surprising result that for the boson model discussed above, the approximation was asymptotically exact at all energies without any Pauli effects. Thus, more complete and precise criteria are needed.

Another possibility for future work is to find viable approximations to TDHF which clearly separate collective, statistical, and single particle effects. To the extent to which a collection of single particle orbitals bouncing aroung in a well is purely statistical, TDHF codes are the worlds most expensive random number generators. Thus, a clean separation of statistical aspects of the problem would be most welcome.[29] Several notes of caution, however, appear warranted. What is required is a theoretically sound, systematic reduction of the TDHF theory. Thus, unmotivated ansätze

like time dependent Thomas-Fermi are not likely to be very instructive. Furthermore, we have demonstrated that in many cases, TDHF is not statistical during the relevant time scale, so at the least, some viable criteria and restrictions for application of statistical approximations are required.

The most essential problem, in many respects, is the formulation of a practical general theory such that the mean field theory is a first approximation which can be systematically improved. In this context, the generator coordinate method appears unsuitable since although certain specific generalizations of the trial wave function appear natural, there is no practical scheme for systematic generalization. A coupled-channel formulation in the mean-field basis has the advantage of utilizing an optimal definition of the entrance channel, but the complete coupled-channel problem is as intractable as ever, and we have no guidance as to how to systematically expand the space of included channels. The most promising alternative appears to be the systematic truncation of some appropriate hierarchy of equations, such as the time-dependent generalization of the e^S hierarchy[30] or the Martin-Schwinger Greens function equations,[31] both of which yield the mean field theory in lowest order. One complication is to choose truncations which are number, energy, and momentum conserving order by order. Although, in the Greens function language, well known conserving approximations exist,[32] the computational difficulty relative to alternative methods is significant. In any event, an appropriate systematic formulation of corrections appears crucial to our ultimate understanding of the theory.

In conclusion, I believe many exciting possibilities lie ahead. The ultimate goal is far more than simply fitting this angular distribution or reproducing that fusion cross section. Rather, we are embarking on a fundamental investigation of the dynamics of self-bound composite systems, and I am optimistic that the mean-field theory is an appropriate first step.

References

1. J. W. Negele, Phys. Rev. C1, 1260 (1970); X. Campi and D. W. L. Spring, Nucl. Phys. A194, 401 (1972).
2. P. A. M. Dirac, Proc. Cambridge Phil. Soc. 26, 376 (1930).
3. G. F. Bertsch and S. F. Tsai, Phys. Rep. 18, 125 (1975).
4. P. Bonche, S. Koonin, and J. W. Negele, Phys. Rev. C13, 1226 (1976).
5. P. Sperr, S. Vigdor, Y. Eisen, W. Henning, D. G. Kovar, T. R. Ophel, and B. Zeidmann, Phys. Rev. Lett. 36, 405 (1976).
6. P. Sperr, T. H. Braid, Y. Eisen, D. G. Kovar, F. W. Prosser, J. P. Schiffer, S. L. Tabor, and S. Vigdor, Phys. Rev. Lett. 37, 321 (1976).
7. G. F. Bertsch, 1977 Les Houches Lectures and private communication; G.F. Bertsch and J.W. Negele,to be published.
8. B. Yoon and J. W. Negele, Center for Theoretical Physics Preprint (1977).
9. H. A. Bethe, Z. Physik 71, 205 (1931).
10. J. McGuire, J. Math. Phys. 6, 432 (1965).
11. F. Calogero and A. Degasperis, Phys. Rev. All, 265 (1975).
12. C. N. Yang, Phys. Rev. Lett 19, 1312 (1967).
13. V. E. Zakharov and A. B. Shabot, Soviet Phys. JETP 34, 62 (1972).
14. P. C. Lichtner and J. J. Griffin, Phys. Rev. Lett. 37, 1521 (1976).
15. H. Feldmeier, contributed paper to this conference and to be published.
16. A. K. Kerman and S. E. Koonin, Ann. Phys. 100, 332 (1976).
17. A. K. Kerman and N. Onishi, Nucl. Phys. A281, 373 (1977).
18. S. E. Koonin, K. T. R. Davies, V. Maruhn-Rezwani, H. Feldmeier, S. J. Krieger, and J. W. Negele, Phys. Rev. C15, 1359 (1977).
19. P. Colombani, N. Frascuria, J. L. Jacmart, M. Rion, C. Stephan, H. Doubre, N. Poffe, and J. C. Roynette, Phys. Lett. 55B, 45 (1975).
20. H. Flocard and M. Weiss, private communication.
21. V. Maruhn-Rezwani, K. T. R. Davies, and S. E. Koonin, Phys. Lett. 67B, 134 (1977).
22. S. Koonin, J. W. Negele, P. Møller, J. R. Nix, A. Sierk, and H. Flocard, to be published.

References (continued)

23. J. Blocki and H. Flocard, Nucl. Phys. A273, 45 (1976).

24. A. J. Sierk and J. R. Nix, Proceedings of Symposium on Macroscopic Features of Heavy Ion collisions, Argonne (1976).

25. J. W. Negele, Nucl. Phys. A143, 225 (1970).

26. M. Gyulassy, Invited paper to this conference.

27. R. Y. Cusson, R. K. Smith, and J. A. Maruhn, Phys. Rev. Lett. 36, 1116 (1976).

28. G. F. Bertsch, Phys. Rev. C15, 713 (1977).

29. H. A. Weidenmuller, Invited paper to this conference.

30. K. H. Lührmann, Ann. Phys. 103, 253 (1977) and references therein.

31. P. C. Martin and J. Schwinger, Phys. Rev. 115, 1342 (1959).

32. G. Baym, Phys. Rev. 127, 1391 (1962).

QUANTAL THEORY OF HEAVY ION SCATTERING IN A THREE-DIMENSIONAL TDHF MODEL

R.Y. Cusson, Duke University, Durham, North Carolina 27706

Introduction

Heavy Ion inelastic collisions have been described[1] as collisions of two bodies moving along classical trajectories with elastic and frictional forces. This picture is more accurate for a heavy system such as Ar+Th (Fig. 1) than for a lighter system such as $^{14}N+^{12}C$ or $^{16}O+^{16}O$, which are currently being studied[2]. Fig. 1 illustrates what can be obtained from such a classical picture. The ordinate

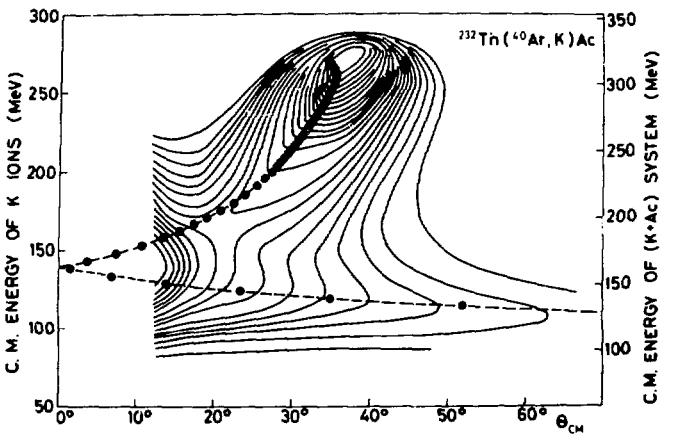

Figure 1

is the cm kinetic energy of the projectile-like K ion and the abcissa shows the cm angle of this ion. The contour lines show constant values of the double differential cross-section $d^2\sigma/d\Omega dE$, while the open dots represent the classical values of outgoing energy and angle for a given incoming cm angular momentum ℓ, ranging from about 250 $\hbar$ at high energy to $\ell \sim 180\ \hbar$ at the highest (near-orbital) angle. The cm orbital angular momentum is related classically to the impact parameter b and the incoming energy by the usual kinematic relations

$$\ell = \mu v b , \quad v = \sqrt{\frac{2}{m}\frac{E_\ell}{A_p}} \qquad (1)$$

where μ is the reduced mass, v the relative velocity, E_ℓ the laboratory energy and m A_p the total mass of the projectile. Although the classical trajectory does seem to follow the ridges in the yield contours, it does not explain the height of the yield contour nor the energy width of those ridges. It also leaves open the possibility of interference between trajectories of different energies (different ℓ-values) and same scattering angle. The main purpose of the present work[2] is to take this classical model one step further and to study semiquantal expressions of the form

$$\frac{d^2\sigma}{d\Omega dE} = |f(\theta,E)|^2$$

where $f(\theta,E)$ is a scattering amplitude expressed as a sum over partial waves; it also involves the classical deflection function $\theta(\ell)$, the energy loss function $\bar{E}_\ell$ and some additional information regarding the energy width of the scission doorway states. It will be convenient to take $\theta(\ell)$ and $\bar{E}_\ell$ from a 3-dimensional TDHF calculation but one could also obtain them from other physical models such as hydrodynamic[3] or potential scattering with friction[1].

Since the approach to heavy ion scattering involves the use of classical $\theta(\ell)$ and $\bar{E}_\ell$ functions, it removes the usual objections concerning the use of the TDHF scheme on the grounds that it yields only a classical prescription for the motion of the cm of the two ions. This therefore enhances the value of TDHF calculations of the trajectories and should eventually allow a detailed test of our ability to predict correct trajectories. After describing briefly the fast fourier transform and predictor corrector method used to solve the TDHF equations for the reactions $^{14}N+^{12}C$ and $^{16}O+^{16}O$ at 8 MeV/A we show the resulting plot of $d^2\sigma/d\Omega dE$. We find some interesting explanations for the fact that, for these lighter systems, the yield surfaces appear rather different from those of heavier systems such as in Fig. 1. We also compare the present results with data from ORNL[4] for the reaction $^{14}N+^{12}C$ at 145 MeV bombarding energy. Reasonable agreement is found in view of the approximations made.

We end with a mention of further calculations which are suggested by the present developments, such as hydro-

dynamic approaches to the solution of the equation of motion $i\dot{\rho} = [H,\rho]$, prefusion neck formation at energies near the Coulomb barrier[5], multi-Slater determinant theories from variational principles[6] and other topics of interest.

II. Quantal Expression for $d^2\sigma/d\Omega dE$.

Let us first consider the usual partial wave expansion for the elastic scattering of spin zero fragments. The cross section is $d\sigma/d\Omega = |f(\theta)|^2$ with

$$f(\theta) = \sum_{\ell=0}^{\ell_c} \frac{(2\ell+1)}{2ik} (e^{2i\delta_\ell} - 1)P_\ell(\cos\theta) \quad , \qquad (2)$$

where $E = \frac{\hbar^2}{2\mu} k^2$ is the cm total kinetic energy and δ_ℓ is the elastic phase shift so that $e^{2i\delta_\ell}$ is the scattering S matrix. If there is some absorption $e^{2i\delta_\ell}$ is replaced by $e^{2i\delta_\ell}C_\ell$, where C_ℓ is the amplitude for remaining in the elastic channel. The cut-off angular momentum ℓ_c is large enough that $\delta_{\ell_c} = 0$. If the Coulomb phase shift is included in δ_ℓ, the introduction of a cut-off ℓ_c means that $f(\theta)$ will be correct only for angles $\theta \tilde{>} 1/\ell_c$.

Our aim is to modify Eq. (2) so that it will describe $f(\theta,E)$ the amplitude for scattering at an angle θ and outgoing kinetic energy E smaller than the incoming energy E_i. We begin this by noting that the various partial waves are allowed to interfere in Eq. (2) because they are coming out at the same energy and θ but not ℓ is observed. If we were dealing with inelastic scattering such that each partial wave has a different energy <u>eigenvalue</u>, each ℓ would be an independent <u>channel</u> and the sum over ℓ would be <u>outside</u> the square. The actual situation in heavy ion scattering is intermediate between these two limiting cases, namely each partial wave can be thought of as having a certain mean energy $\bar{E}_\ell$ and mean width Γ. Thus if we detect particles at energy E there is an amplitude

$$g_\ell(E) \propto \frac{1}{E-\bar{E}_\ell - i\Gamma/2} \quad , \tag{3}$$

for observing a state with an angular momentum ℓ and mean energy $\bar{E}_\ell$. For each angular momentum ℓ we are saying that there is a scattering doorway state which can be represented as the two ion configurations at the instant of scission. The lifetime τ of this scission configuration should obey the uncertainty relation $\Gamma\tau \cong \hbar$. By inspection of the time development of semi-classical TDHF heavy ion scattering we see that τ is of the order of 10 fm/c (1 fm/c = 3.3 x 10^{-24} s.). In the work we will discuss here we have therefore used Γ = 20 MeV. We should keep in mind that Γ could be adjusted to fit experiment and could even depend on the angular momentum ℓ. The amplitude $g_\ell(E)$ should be normalized so that

$$\int_{-\infty}^{+\infty} dE\,|g_\ell(E)|^2 = 1 \quad . \tag{4}$$

The extension of Eq. (2) to take into account the amplitude $g_\ell(E)$ can now be carried out. As discussed above, the procedure for doing this can not be to use a multichannel theory where states of different final energy are represented by independent channels, since states of different ℓ values are <u>not</u> energy eigenstates. We use a different formulation. We simply allow the various partial waves to interfere according to the amplitude $g_\ell(E)$, by setting

$$f(\theta,E) = \sum_{\ell=0}^{\ell_c} \frac{2\ell+1}{2ik}\, e^{2i\delta_\ell} C_\ell g_\ell(E) P_\ell(\cos\theta) \quad . \tag{5}$$

We have neglected the sum $\sum_{\ell=0}^{\ell_c} \frac{2\ell+1}{2ik} \times 1 \times P_\ell(\cos\theta)$ which contributes to elastic diffraction scattering and whose effect is appreciable only at angles $\theta \lesssim 1/\ell_c$. We need to stay backward of these angles to avoid the diffraction effects. The expression (5) includes the amplitude C_ℓ for remaining in the direct inelastic channel. The probability that the scattering be exactly elastic or that the system will undergo complete fusion is thus $1-C_\ell^2$. For the lighter systems with compound atomic number $\lesssim 100$, $1 - C_\ell^2$ is dominated by the complete fusion cross section, so we set

$$\sigma_f = \frac{\pi}{k_i^2} \sum_{\ell=0}^{\ell_c} (2\ell+1)(1-C_\ell^2) \quad . \tag{6}$$

The expression (5) is expected to be meaningful for reactions which are described mainly by the semiclassical liquid drop scattering with friction. For such systems the most probable result of a scattering at a given impact parameter (or ℓ value) is an inelastic deflection by some angle $\theta(\ell)$. Our scattering cross section should therefore converge to the classical cross section expressions[7] vs. $\theta(\ell)$. We can insure this by using the quantal approximation

$$\delta_\ell \cong -\frac{1}{2} \int_{\ell+1/2}^{\infty} \theta(\ell)\, d\ell \quad . \tag{7}$$

The Eqs. (3,5,7) now allow us to obtain the double differential scattering amplitude $f(\theta,E)$ in terms of three functions of ℓ, $\theta(\ell)$, $\bar{E}_\ell$ and C_ℓ. For very heavy systems such as the one of Fig. 1, the complete fusion cross section is negligible because of liquid drop instabilities[8] and, neglecting all other channels, we can then set $C_\ell = 1$.

The functions $\theta(\ell)$ and $\bar{E}_\ell$ will be obtained from a TDHF calculation for $^{16}O+^{16}O$ and $^{14}N+^{12}C$. The only way we could obtain C_ℓ from TDHF would be to add a fusion channel which would be represented by at least one more Slater determinant. A multi-Slater determinant theory could be worked out from the variational principle[6]. Here we follow a simpler procedure. We consider a model in which complete fusion would take place whenever enough collective energy is lost by nucleon emission to prevent the fragments from coming out. The internal excitation energies of the fragments we will be dealing with is less than 20 MeV so the most probable event is single nucleon evaporation. We have used the statistical model formula of Eberhard, et al.[9] to calculate an instantaneous width Γ_o for single nucleon emission. This Γ_o depends on the instantaneous internal excitation energy $E_x(t)$ and on the level density parameter, among other things. The energy $E_x(t)$ is extracted from the TDHF runs and the level density parameter was adjusted to yield reasonable results for σ_f and $d^2\sigma/d\Omega dE$. These will be described in the next sections. Having obtained $\Gamma_o(t)$ we then compute C_ℓ as

$$C_\ell = \exp\{ - \frac{1}{2\hbar} \int_{t_i}^{t_f} \Gamma_o(E_x(t))dt\} \qquad (8)$$

where t_i and t_f are the contact and scission times during which complete fusion can take place. We will return later to the possibility of observing complete fusion (capture) in the single Slater determinant theory itself. For now we discuss some of the features of our 3-dimensional TDHF calculation.

III. Three-Dimensional TDHF Calculations.

The TDHF method for computing the semi-classical orbit and energy loss function $\theta(\ell)$ and $\bar{E}_\ell$ consists in solving the time dependent Hartree-Fock equations

$$\left\{ - \frac{\hbar^2}{2m} \nabla^2 + v_N(\underset{\sim}{r}) + v_c(\underset{\sim}{r}) \right\} \psi_\lambda(\underset{\sim}{r},t) = +i\hbar \frac{\partial \psi_\lambda(\underset{\sim}{r},t)}{\partial t} \qquad (9)$$

where v_c is the Coulomb potential and v_N is the nuclear single-particle average potential and is taken from the simplified Skyrme interaction as

$$v_N(\underset{\sim}{r}) = -a\rho(\underset{\sim}{r}) + b\rho^2(\underset{\sim}{r}) \qquad (10)$$

with a = 817.5 MeV fm^3 and b = 3241.5 MeV fm^6. $\rho(r)$ is the total density given by

$$\rho(\underset{\sim}{r},t) = \sum_{\lambda=1}^{A/4} 4 \, |\psi_\lambda(\underset{\sim}{r},t)|^2 \quad . \qquad (11)$$

The factors of 4 are incorporated because we assume spin and isospin saturation. This expression for ρ comes from the assumption that the total wave function of the $A_1+A_2=A$ compound system is a single Slater determinant. This forces the cm of the clusters to move along classical orbits. Thus the TDHF method is quantized and microscopic in its description of the internal motion but it is classical in the external motion of the clusters. The method also neglects two body residual collisions which may contribute to the overall viscosity. Only the single particle viscosity is included in the model. The consequences of

that will be discussed later. An effective charge of 1/2 is assumed for all particles and only the direct part of the Coulomb potential is considered.

The initial wavefunctions should be the self-consistent solutions of the HF equations for the initial clusters. We have approximated these by oscillator wavefunctions with $\hbar\omega$=37.55 MeV/$A^{1/3}$. The occupied orbits for the ^{16}O clusters are (n_x,n_y,n_z) = (0,0,0), (1,0,0), (0,1,0), (0,0,1). For ^{14}N and ^{12}C, the three p-shell orbits are given constant occupation of 10/3 and 8/3 respectively instead of 4 as in ^{16}O. The complete initial single particle wavefunctions have the form

$$\psi_\lambda(\underset{\sim}{r},t=0) = e^{i\underset{\sim}{k}_\lambda\cdot\underset{\sim}{r}}\,\phi_\lambda(\underset{\sim}{r}) \ , \qquad (12)$$

where $\underset{\sim}{k}_\lambda$ is the appropriate initial momentum of the cluster nucleons and $\phi_\lambda(\underset{\sim}{r})$ is the real oscillator wavefunction.

The Hamiltonian in Eq. (11) is time dependent so that the solutions are not just of the form

$\exp[-i\int \frac{H}{\hbar}\,dt]\psi_\lambda(\underset{\sim}{r},t=0)$, because $[H(t_1),H(t_2)] \neq 0$. These are the familiar time ordering difficulties of scattering theory. An accurate solution of the equation can be obtained by using the predictor-corrector method[10] consisting of the following two steps

1) predictor of order n(n=6 in this work):

$$\psi_\lambda(t+n\Delta t) = \psi_\lambda(t+(n-1)\Delta t) + \Delta t \sum_{k=0}^{n-1} p_k^n \dot{\psi}^\circ_\lambda(t+k\Delta t), \qquad (13)$$

2) correctors of order n:

$$\psi_\lambda(t+q\Delta t) = \psi_\lambda(t+(q-1)\Delta t) + \Delta t \sum_{k=1}^{n} c_k^{qn} \dot{\psi}^\circ_\lambda(t+k\Delta t). \qquad (14)$$

$$1 \leq q \leq n$$

The time step used here was Δt = 1.25 fm/c and the derivative $\dot{\psi}$ is just $-i/\hbar H\psi$, as given by Eq. (9). The kinetic

energy is diagonal in momentum space whereas the potential is diagonal in coordinate space. An accurate method of generating ψ consists in using the Fast Fourier Transform (FFT) algorith[11] to transfer back and forth from coordinate to momentum space using the finite Fourier transform relation

$$\psi_\lambda(k_\ell,t) = \frac{1}{N\sqrt{\Delta x}} \sum_{m=0}^{N-1} \psi_\lambda(x_m,t)\, e^{-2\pi i m\ell/N}, \qquad (15)$$

in one dimension with $-N/2 \leq \ell \leq N/2+1$. The values of the coordinate x_m and momentum k_ℓ on their respective grids are given by

$$x_m = m\,\Delta x,\ k_\ell = \frac{2\pi}{\Delta x}\frac{\ell}{N} \quad . \qquad (16)$$

We have used $\Delta x = 1$ fm, and $N_x = 16 = 2^4$, $N_y = N_z = 24 = 3x2^3$. The y,z plane is taken to be the scattering plane. With these parameters the norm and total energy were conserved to about 1 part in 10^3 during a complete collision.

All the calculations were started at an initial separation of 10 fm for the cm of the clusters and were stopped when the separation of the clusters was again about 10 fm. Classical Coulomb trajectories were matched before and after these points. The final kinetic energy is obtained by computing the total momentum of the individual clusters after separation. This gives us $\bar{E}_\ell$. The final angle after matching to Coulomb orbits gives $\theta(\ell)$. The initial ℓ is used to determine the initial impact parameter according to Eq. (1) and the final internal spin was neglected, so that ℓ was assumed to be the total orbital angular momentum both before and after the collision. More complex expressions[12] for $f(\theta,E)$ will be needed if the internal spin is included. The loss of kinetic energy is assumed to go to internal energy. By computing the collective kinetic energy vs time an internal energy E_x vs time is also obtained so that C_ℓ can be computed from Eq. (8).

IV. Results.

Before we present our results for the double differential cross section $d^2\sigma/d\Omega dE$ it is of interest to look at the density and velocity fields as a function of time.

The Figs. (2-a,b,c) show some density contours for 9 different times into the collision. The reaction is $^{14}N+^{12}C$ at E_ℓ/A_p = 8 MeV and an impact parameter b=1 fm, which corresponds to $\ell = 4\hbar$. The ^{14}N fragment is initially on top. The contours show equal values of the integrated density

$$\rho_I(y,z) = \int dx \rho(x,y,z) \quad . \tag{17}$$

The increment from one contour line to the other is about 0.15 nucleons/fm^2. The field of arrows corresponding to each density represents the velocity field $\underset{\sim}{v}(\underset{\sim}{r})=\underset{\sim}{J}(\underset{\sim}{r})/\rho(\underset{\sim}{r})$ (and not the current as labelled in the figures) in the scattering plane x=0. The velocity $v_x(x=0,y,z)$ vanishes and v_y and v_z are shown by the arrows, on a grid, at every fermi. The third frame at T=70 fm/c is already past the maximum compression point since the velocity arrows have already changed sign. From the fifth frame on (T=110fm/c) we see that the system does not fuse and that the heavy fragment is now in the bottom. This type of scattering is called vibrational instability scattering and has been observed in the scattering of classical liquid drops[13]. A neck of about 0.4 nucleons/fm^2 forms around T=110 fm/c and survives until T $\tilde{=}$ 160 fm/c. The neck breaks off (scission) from T = 160 to T = 80 fm/c and at T = 190 fm/c one can observe a fairly complex internal velocity field.

We next show in Fig. (3-a,b,c) a different type of event corresponding to rotational instability scattering in the classical case and to deep inelastic scattering for the reaction of Fig. 1. We study the case $^{16}O+^{16}O$ at E_ℓ/A_p = 8 MeV and b = 5 fm which corresponds to $\ell \tilde{=} 25\hbar$ and is slightly above the orbiting value. From T = 60 fm/c to T = 150 fm/c there is a quite well defined $\underset{\sim}{v}=\underset{\sim}{w}x\underset{\sim}{r}$ quasi-stationary rigid rotational velocity pattern. The density shape is correspondingly stable. However from T = 180 fm/c on the necking instability sets in and at T = 320 fm/c the fragments have come apart and the usual internal octupole vibrations can be seen.

The Fig 4 shows the cm deflection function $\theta(\ell)$ in degrees for $^{14}N+^{12}C$ at E_ℓ/A_p = 8 MeV. The grazing angle occurs at $\ell = 28\hbar$ and is about 9.4°. The deflection angle then becomes negative so that there is a possibility of Franhofer interference between the positive and negative angle orbits. A single quasi-orbiting angular momentum

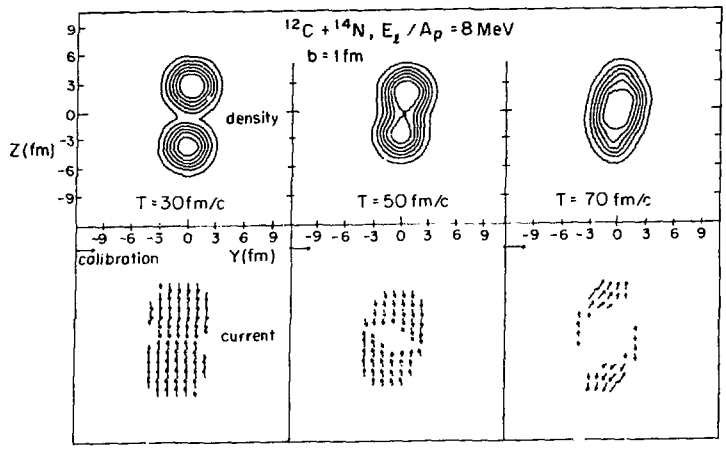

Figure 2a

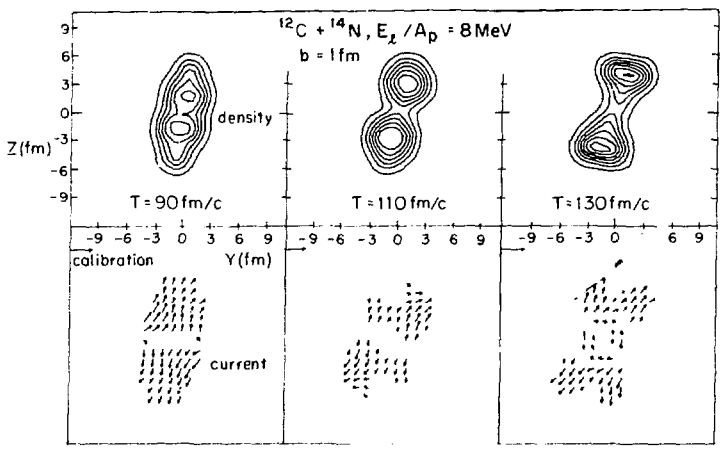

Figure 2b

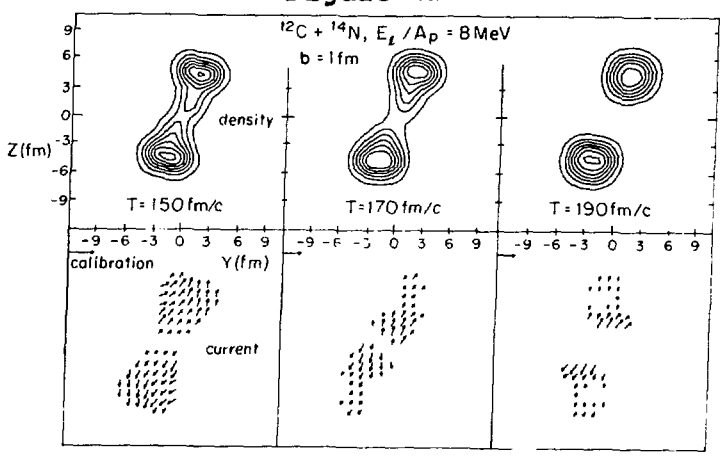

Figure 2c

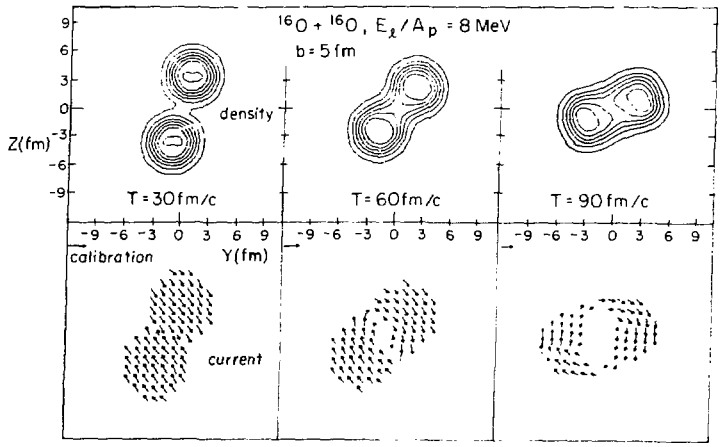

Figure 3a

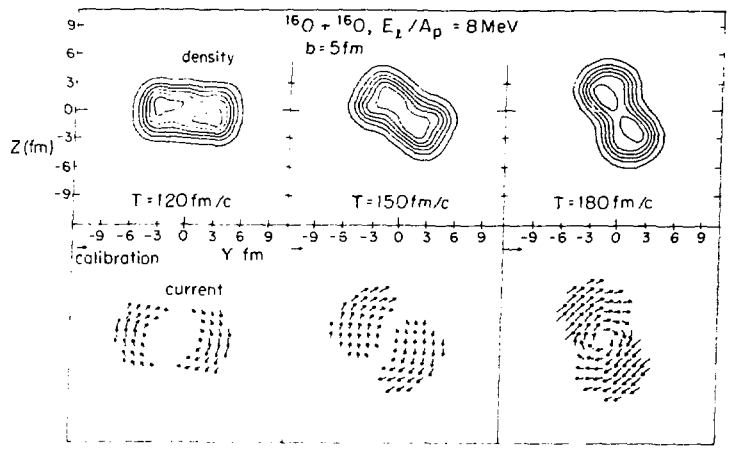

Figure 3b

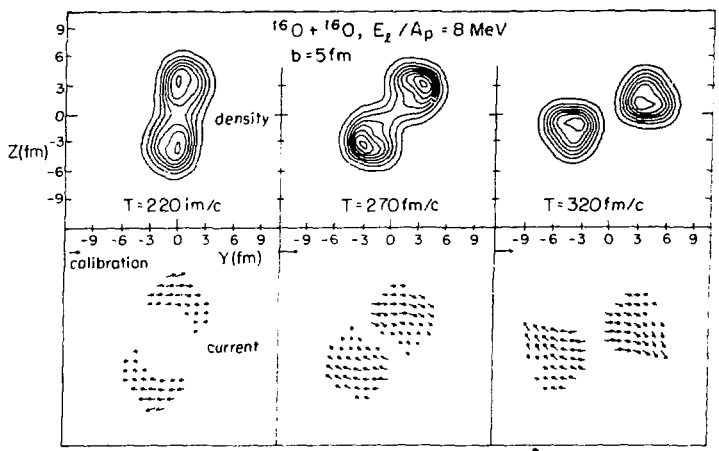

Figure 3c

of $\ell \cong 18\hbar$ is present and the deflection comes back to zero as $\ell \to 0$. Such a curve is quite similar to what we would get from ordinary ℓ-independent potential scattering.

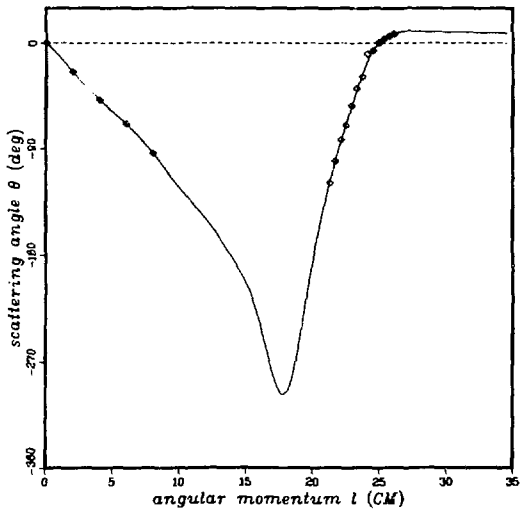

Figure 1

The Fig. 5 shows the percentage cluster kinetic energy loss after the scattering, in the cm, as a function of the cm angular momentum (solid line). Most of the energy is lost before the orbital ℓ is reached. The dotted curve shows the amplitude C_ℓ for remaining in the TDHF channel. It has a zero at the orbiting angular momentum but it rises again at lower ℓ values because of the vibrational instability. We can get an estimate of the amount of complete fusion cross-section lost to vibrational instability by computing first the complete fusion cross-section with the curve as shown inserted in Eq. (6) for σ_f; this gives σ_f = 860 mb. We can also compute σ_f assuming that C_ℓ is zero for $\ell < 18$. This gives σ_f = 1030 mb. The experimental complete fusion cross-section[14] for $^{14}N+^{12}C$ at this energy is 900 ± 100 mb.

The Fig. 6 shows the laboratory double differential cross-section $d^2\sigma/d\Omega dE$, with the vertical axis in mb/MeV-sr and the two horizontal axes being the laboratory scattering angle in degrees and the final laboratory kinetic energy of the heavy (Nitrogen-like) fragment.

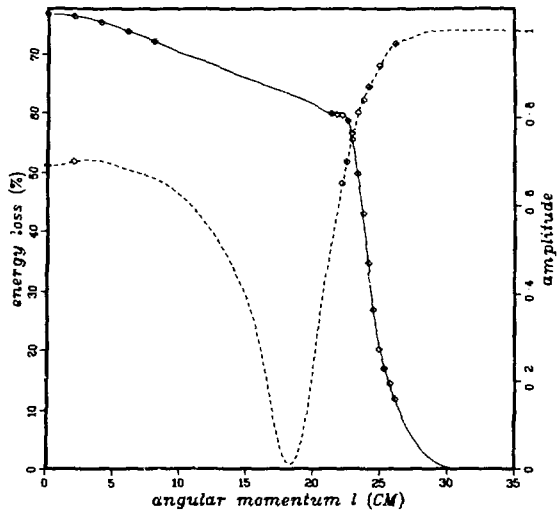

Figure 5

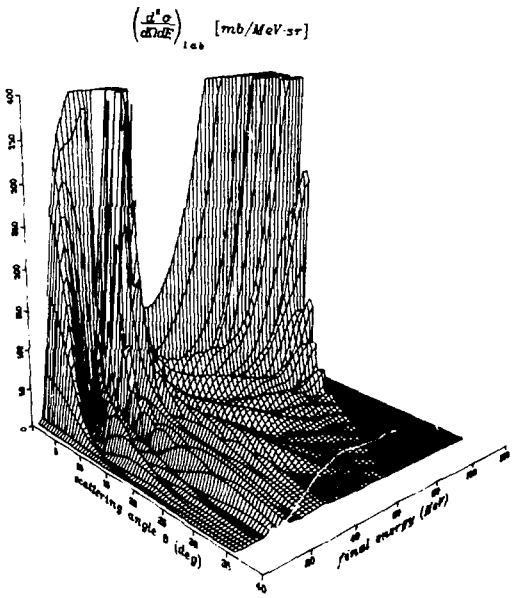

Figure 6

The low energy peak receives most of its contribution from the vibrational instability scattering. This was verified by plotting a similar cross-section in Fig. (7) but with

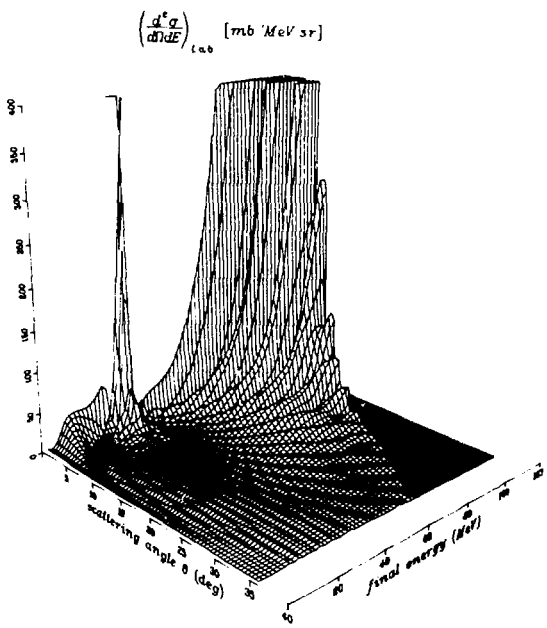

Figure 7

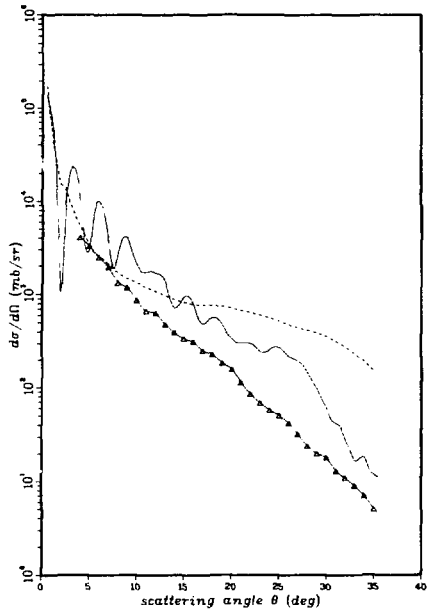

Figure 8

$C_\ell = 0$ for $\ell < 18$. The yield is then attenuated by about 1 order of magnitude at low energies ($E_{lab} < 50$ MeV). In this instance the vibrational instability falls in the same energy range as the residues of the fused system after evaporation and is therefore difficult to detect. The high energy peak ($E_{lab} > 50$ MeV) comprises both the positive and negative parts of the orbit. This system is not heavy enough and does not loose enough energy to separate these two parts of the orbits. In fact they interfere with each other. This is illustrated in Fig. (8), where we show as a solid line the energy integrated cross-section from 50 MeV on up (to eliminate the vibrational part) as a function of the laboratory scattering angle θ_{lab} of the heavy fragment, in degrees. The vertical axis of that figure is in mb/sr. The strong oscillations at forward angles have the form $\sin^2(kR\theta)$, with $kR \cong \ell_{grazing}$. The exponential damping at larger angles is again a quantal effect and comes from the absorbtion of the flux into the complete fusion channel ($C_\ell \to 0$) near $\ell_{orbital}$. The dotted line shows the integrated cross-section for the vibrational part at

E_{lab} < 50 MeV. The triangles represent unpublished experimental data from ORNL on the direct inelastic scattering of ^{14}N on ^{12}C at $E_\ell/A_p(^{14}N) \simeq 10$ MeV/A. The data are summed over Z values near Z=7. The absence of oscillations at forward angles probably means that the sum over the final spins of the fragments, which was neglected here, is incoherent. The slope of the exponential is in reasonable agreement with the calculation, but the calculated cross-section is too large by about a factor of 2. The normalization of $d\sigma/d\Omega$ is very sensitive to the details of the amplitude C_ℓ. A more detailed comparison must await a better calculation of C_ℓ. The present result nonetheless represents a considerable improvement over the $1/\sin\theta$ result that one would obtain by using the classical formula b db/d $\cos\theta$ for the direct inelastic scattering cross-section.

V. Prospects for Future Calculations.

There are two main directions which our efforts should take. The first one is to compute the deflection and energy loss functions for heavy systems such as in Fig. (1). The complete fusion cross-section is negligible there so that one should have a better comparison with experiment. The energy loss is also larger with respect to the doorway state width of about 20 MeV so that the positive and negative angle parts of the trajectories can be resolved. Recent developments in Berkeley, Livermore, and ORNL show promise of being able to handle up to about 100 orbits, in 3-dimensions, with a reasonable amount of computing time. The second direction is to include more than one Slater determinant in order to account for the dominant complete fusion cross-section in the systems with compound atomic numbers $\leqslant 100$. The TDHF equations of motion for these more complex configurations can in principle be derived from time-dependent variational principles[6].

Some calculations of interest are:

i) Hydrodynamic approach where the TDHF equations for the wavefunctions are replaced by coupled equations for $\rho, \underset{\sim}{J}, T_{ij}$, etc.

ii) The low energy behaviour of the complete fusion cross-section depends on the dynamics of the neck formation prior to fusion. This dynamic can be studied in the TDHF model.

iii) The dynamics of fission from states of the compound system which lie above the fission barrier can be studied in the single Slater determinant theory.

iv) The effects of the spin of the final fragments on the scattering can be studied.

v) In the more distant future we can expect to study the relation between heavy ion scattering and the conventional shell model spectroscopy of the fragments and on the compound system; for instance one could study the shell corrections to the complete fusion cross-section in the p and s-d shells.

References

1. K. Siwek-Wilczynska and J. Wilczynski, Nucl. Phys. A264 (1976) 115.
2. R.Y. Cusson, J.A. Maruhn and W.H. Meldner (Annals of Physics (N.Y.), to be published).
3. J.A. Maruhn, this conference.
4. R. Stokstad, ORNL data (unpublished).
5. W.M. Howard, R. Cusson and M. Arnould (to be published).
6. A.K. Kerman and S.E. Koonin, Ann. Phys. (N.Y.) 100 (1976) 332.
7. K.W. Ford and J.A. Wheeler, Ann. Phys. 7 (1959) 259.
8. S. Cohen, F. Plasil and W.J. Swiatecki, Annals of Physics (N.Y.) 82 (1974) 557.
9. K.A. Eberhard, P. von Brentano, M. Böhning, and R.O. Stephen, Nucl. Phys. A125 (1969) 673.
10. I.S. Berezin and N.P. Zhidkov, "Computing Methods", (Pergamon Press, New York, 1965) Vol. II, p. 352ff.
11. R.C. Singleton, IEEE Transactions Audio Electroacoustics 17 (1969) 93.
12. R.A. Broglia, S. Landowne, R.A. Malfliet, V. Rostokin and Aa. Winther, Phys. Lett. 11C (1974) 1.
13. J.R. Adams, N.R. Lindblad, and C.R. Hendricks, J. Appl. Phys. 39 (1968) 5173.
14. R.G. Stockstad, J. Gomes del Campo, J.A. Biggerstaff, A.H. Snell and P. Stelson, Phys. Rev. Lett. 36 (1976) 1529.

PREPARED FOR THE FALL CREEK FALLS MEETING ON HEAVY ION COLLISIONS

Heavy Ion Reactions at 15 to 20 MeV/Nucleon*

J. B. Natowitz

Cyclotron Institute and Department of Chemistry, Texas A&M University,

College Station, Texas 77840

Abstract

A survey is presented of the experimental information presently available for nuclear reactions induced by 15 to 20 MeV/amu ^{12}C, ^{14}N and ^{16}O projectiles. Fusion, fission-like and fragmentation reactions are discussed.

*Work supported in part by the U. S. ERDA and the Robert A. Welch Foundation.

Introduction

This paper is a survey of the current information on the nuclear reactions induced by ^{12}C, ^{14}N and ^{16}O projectiles with kinetic energies of 15 to 20 MeV/nucleon. Such projectiles are the highest energy "low energy" heavy ion projectiles presently available for experimental studies. In contrast, the lowest energy "high energy" heavy ion projectiles now available have energies $\sim$200 MeV/nucleon.

The particular interest in reaction studies with such projectiles can perhaps best be indicated by use of a schematic classification of nuclear reaction space suggested by W. Swiatecki[1] and presented in Figure 1. The dominant phenomena expected to occur in different regions of the space are indicated by the labeling of those regions. The shaded bands represent transition regions in which the underlying physics describing the nuclear interactions is expected to change qualitatively.

The dark circle on the figure represents the portion of reaction space which is the subject of this paper. In terms of this classification scheme, such reactions mark the point of transition into the region dominated by macroscopic effects[2,3] as the nuclear size increases and into the region where supersonic effects[4,5] should become important as the nuclear velocity increases beyond the average fermi velocity of the nucleons in the nuclei. A major goal of the present survey is to indicate the extent to which the expected transitions are observable in the reactions induced by 15 to 20 MeV/nucleon ^{12}C, ^{14}N and ^{16}O projectiles.

Counter telescopes provide an excellent experimental tool for the simultaneous study of the large variety of reaction mechanisms which are possible when two heavy nuclei collide. An example of the types of data

which may be obtained with such telescopes is presented in Figure 2. The intensities of reaction products emitted at a lab angle of 10° following the reactions of 262 MeV ^{14}N with Ni are represented as a function of ΔE and E, the energies deposited in the transmission and stopping detectors. This angle is near the grazing angle. The relative yields and the energy distributions observed in this figure suggest that at least three qualitatively different types of reaction mechanisms are involved in the collisions of ^{14}N with Ni. The products of highest atomic number, approaching that of the composite system have high yields and low kinetic energies. The energies are comparable to the kinetic energy expected for recoiling compound nuclei produced in total momentum transfer collisions. These products of highest atomic number appear to be primarily evaporation residues of Br nuclei produced in complete fusion reactions.

Products with lower atomic number, intermediate between that of the compound nucleus and of the projectile appear with lower intensities and have narrow distributions in kinetic energy with average energies which are comparable to the Coulomb repulsion energies which would be observed in products of two body breakup of the composite system. Such products then appear to result from fission-like reactions.

The products having atomic number near that of the projectile have large yields and kinetic energy distributions extending to high energies approaching that of the elastically scattered projectile. These observations suggest that such products result from reaction processes which are more direct than those already mentioned.

In Figure 3, a comparison is made of the laboratory angular distributions $d\sigma/d\Omega$ for products selected from each of the qualitatively different

regions of Figure 2. Even in the laboratory frame, with the large center of mass velocity imposed on the distributions there are clear differences in the product angular distributions. The projectile-like products represented by C have very forward peaked angular distributions which gradually decrease in slope at large angles. The evaporation residues represented by Cr have angular distributions which are less strongly forward peaked but decrease more rapidly with increasing angle of observation. Finally, the Si angular distribution, characteristic of the fission like reactions decreases relatively slowly with increasing angle.

The tentative conclusions which were reached about the qualitative differences in the predominant reaction mechanisms leading to products in the different groups are supported by observations of the angular distributions associated with these products. For convenience we shall discuss each of these three types of reactions separately, always recognizing that the dominance of one reaction mechanism does not preclude contributions from others, i.e. that the boundaries between certain types of collision phenomena are not perfectly distinct.

Complete Fusion Reactions

Complete fusion reactions still account for a large fraction of the total reaction cross section for 15 to 20 MeV/amu projectiles. This is evidenced in Figures 4, 5, and 6 where evaporation residue cross section data[6,7,8,9] are presented for the reactions of ^{12}C with ^{12}C, ^{12}C with ^{27}Al and ^{16}O with ^{40}Ca. These data are plotted as a function of $1/E_{cm}$, the reciprocal of the center of mass energy. As has been emphasized by

Glas and Mosel,[10,11] for energies such that $(E_{cm} - V_I) >> \hbar\omega$, where V_I is the potential energy at the interaction distance, R_I, where nuclear reactions first begin to occur and $\hbar\omega$ characterizes the width of the potential barrier, the total reaction cross section, σ_R, may be represented as

$$\sigma_R = \pi R_I^2 \left(1 - \frac{V_I}{E_{cm}}\right). \tag{1}$$

Thus a plot of σ_R versus $1/E_{cm}$ should define a straight line whose slope and intercept determine R_I and V_I. Since fusion is a very probable reaction at least at energies just above the interaction barrier, the fusion cross section is expected to show the same energy dependence initially. Ngo and co-workers have recently presented a convenient parameterization of R_I and V_I in terms of the product of Z_p and Z_T the projectile and target atomic number.[12] Solid lines in Figures 4-6 represent the expected total reaction cross sections based upon that parameterization.

At higher energies, if the probability of fusion is controlled by the necessity to reach the critical fusion distance[13,14] R_F the cross section for fusion σ_F would be

$$\sigma_F = \pi R_F^2 \left(1 - \frac{V_F}{E_{cm}}\right) \tag{2}$$

where V_F is the potential energy barrier at R_F. At high energy then, a plot of the fusion cross section versus $1/E_{cm}$ should produce a different straight line whose slope and intercept define V_F and R_F.

Under the assumption of no dissipation until the critical distance is reached,[15] information on the interaction distance, the critical fusion distance and the nuclear potential at those distances may be extracted. For example, a least squares fit to the $^{12}C + ^{27}Al$ fusion reaction data

of Figure 5 leads to the result that R_F = 5.44 fm and V_F = -11.0 MeV.

This critical distance for fusion is consistent with the large body of data which has accumulated indicating that the critical distance is essentially that distance corresponding to the sum of the half density radii of the two nuclei.[13,14,15,16]

For ℓ = 0, $V_F = V_N + V_C$ where V_N is the potential arising from the nuclear force and V_C is the Coulomb potential energy, assuming that V_C = 1.438 $Z_P Z_T / R_F$ we find V_N = -31.6 MeV at R_F.

In Figure 7, this extracted value of the nuclear potential is compared with several proposed ion-ion potentials derived from liquid drop model arguments.[17,18,19]

The result is in excellent agreement with the semiempirical potential recently proposed by Bass.[19] It should be noted that this potential differs from that originally proposed[15] in that the nuclear potential has been parameterized as

$$V_N = - \frac{C_T C_P}{C_T + C_P} g(s) \qquad (3)$$

where C_P and C_T are the half density radii of the target and projectile nuclei. The function g(s) assumed to be a universal function of s, the distance of separation between the surfaces defined by the half density radii, has been determined from recent experimental data, generally at lower energies than 10 MeV/nucleon. In Figure 8, the derived function g(s)[19] is presented together with a comparison with the function which represents the potential proposed earlier.

In Figures 4-6, fusion cross sections calculated with the Bass potential and with the proximity potential are presented for comparison. The critical distance model provides a useful tool for predicting fusion cross sections.

Figure 9 is presented in order to focus on fusion data obtained for the highest energy ^{12}C, ^{14}N and ^{16}O projectiles for which such measurements have been made. For this purpose we have assumed that fusion reactions occur preferentially for the lowest impact parameter collisions. In that case, the fusion cross section is related to the maximum angular momentum of the fusion product by the sharp cut off approximation expression

$$[\ell(\ell + 1)\hbar^2] = 2\mu E_{cm}\sigma_F \qquad (4)$$

It is the limiting angular momenta derived from the evaporation residue cross section measurements which have been plotted in Figure 9. Once again calculations using the Bass potential are presented for comparison. As indicated previously, the calculations are in good agreement with the data. Of course, if any significant fusion-fission probability exists it should be added to the evaporation residue cross section for such comparisons. In fact, as we shall note in the next section such cross sections are very low in the mass range for which evaporation residue measurements are presented in Figure 9.

For comparison to the experimental data, Figure 9 also contains the predicted ℓ-limit to nuclear stability which arises when the angular momentum dependent fission barrier drops to zero.[21] One would expect that this constitutes a limit to the production of compound nuclei which decay by statistical evaporation processes and signal a rapid increase in fission-like reactions as the angular momentum increases above this value. It is possible that such effects have been observed[22,23] but considerably more data are required to establish this point.

The data presented in Figure 9 indicate the production of compound nuclei with large angular momenta. Such nuclei offer the opportunity to

test other theoretical predictions of the properties of nuclei having high angular momenta. Notable among these is the calculated rapidly increasing deformation as the angular momentum of the nucleus increases.[21] Such deformation should have significant effects on the excitation energy dependence of the yrast line and on level densities and therefore on the de-excitation modes which are followed. Studies of γ-ray emission from some of these nuclei demonstrate that the angular momentum dissipation occurs predominantly in the particle emission cascade[25] and therefore it is probably necessary to focus on studies of the emitted particles, particularly α particles, or on the product yield distribution to study such effects in the light to medium mass region.

Fission-like Reactions

The classical deflection function[26] for the interaction of 262 MeV ^{14}N ions with ^{109}Ag is shown in Figure 10. For this purpose, the Bass ion-ion potential, which was found in the preceding section to be in agreement with the fusion cross-section data, was employed in the calculation . In Figure 11 the trajectories corresponding to partial waves of ℓ = 5 to 200 are depicted. The circle on this figure has a radius equal to the sum of two half-density radii of the target and projectile nuclei.

These figures emphasize the fact that partial waves with ℓ just above ℓ_{fus} interact strongly with the target nucleus. It is natural to associate such trajectories with the reactions in which large kinetic energy losses and large mass transfers are observed, such as those leading to the intermediate-atomic-number products of Figure 2.

Such reactions have been observed in the reactions of 10 to 20 MeV/amu ^{12}C, ^{14}N and ^{16}O projectiles with a variety of targets.[27,28,29] Except at very forward angles, the most probable kinetic energies of the products of these reactions are close to the energies which are expected from Coulomb repulsion.

In Figure 12 are the most probable kinetic energies of products of fission like reactions of 197 MeV ^{12}C with Ni, Y, Ag, Tb and Au targets. For the reactions with Ni, Ag and Au, the trend of kinetic energies calculated assuming two spherical nuclei in contact are also presented. Those energies agree very well with the experimentally determined energies for low Z products but overestimate the kinetic energies of high Z products. The observed energies have not been corrected for mass changes which occur during de-excitation of the primary fragments. Even so the data indicate rather large distortions of the more symmetric dinuclear systems at the time of scission.

For the fission-like reactions of 262 MeV ^{14}N with Ag, product angular distributions corresponding to complete damping are presented in Figure 13.[30] Constant values of $(d\sigma/d\theta)_{cm}$ with angle indicate that the product results from the decay of a system having a lifetime which is comparable to or longer than the rotational period. Such angular distributions are observed for the heavier reaction products and may indicate a fusion-fission reaction mechanism. However for the lighter products, even though the kinetic energy damping is complete, the angular distributions are distinctly forward peaked. The gradual change of the angular distributions with increasing mass transfer has been interpreted as resulting from the evolution of the composite systems along the

mass asymmetry degree of freedom. The great sensitivity of the mass asymmetry potential to the angular momentum of the system is obvious in Figure 14.

There, for the composite system ^{120}I, the mass asymmetry potentials for two rotating spherical nuclei in contact are shown as a function of mass asymmetry and angular momentum. For comparison, the initial asymmetry corresponding to $^{12}C + ^{108}Ag$ is indicated. Such potentials clearly favor fusion into a single spherical nucleus at low angular momentum but increasing possibility of evolution towards a symmetric dinuclear system at high angular momentum. Extensive calculations have been performed using diffusion models to study the evolution of such systems.[31]

Integration over the angular distribution presented in Figure 13 (assuming constant values of $(d\sigma/d\theta)_{cm}$ at angles greater than those for which experimental data are available) leads to a cross section for fission-like reactions producing elements with $10 \leq Z \leq 27$ of 40 mb. This cross section is equivalent to the cross section associated with ~1 partial wave with $\ell \simeq \ell_{fus}$. The reactions are of course not necessarily confined to such a limited ℓ space.

In Figure 15 center of mass angular distributions $(d\sigma/d\theta)_{cm}$ for the reactions of 262 MeV ^{14}N with Ni, Ag and Au targets are compared.[30] The cross sections correspond to the emission at center of mass angles near 35°. The relative importance of deep inelastic collisions decreases with increasing asymmetry of the initial collision. However the fraction of the deep inelastic yield which is accounted for by each element is relatively constant as evidenced by the very similar shapes of the cross section curves in the region of the lighter product elements.

In summary the observation of such reactions appears to signal entrance into the region of macroscopic reaction processes in which dinuclear composite systems evolve towards more symmetric configurations.

Direct Reactions

Reactions leading to products with atomic number near that of the projectile apparently reflect the more peripheral nucleus-nucleus collisions. What is the basic nature of such collisions?

Certainly simple few-nucleon transfer reactions will make a contribution to the cross section for peripheral collisions. However, the evidence is that the cross sections for such transfers are low.[32,33]

Near the grazing angle the center-of-mass kinetic energies of the light products have relatively high kinetic energies and broad energy distributions. These reactions have been termed quasi-elastic or partially damped. Since the most probable energies and the widths of the energy spectra decrease rapidly with increasing angle, these partially-damped collisions may reflect break-up of the composite system in early stages of its evolution before relaxation is complete.[27] Various dynamical models have been proposed to describe the energy damping in such reactions.[34]

Recently, Gelbke and his co-workers at LBL have made an extensive study of the reactions of 315 MeV ^{16}O with several target nuclei.[35] Their investigation of the systematics of light ion production in these reactions discloses several interesting features. In Figure 16 the cross section data which they obtained for the reactions of ^{16}O with ^{208}Pb are compared with similar data taken at projectile energies of 140 MeV and 33.6 GeV by plotting the cross section ratios. Part (a) of the figure shows that as the projectile energy is increased from 140 MeV to

315 MeV the relative probability of producing light fragments increases with increasing removal of nucleons. In contrast, this relative probability remains essentially constant as the projectile energy increases from 315 MeV to 33.6 GeV. These data suggest that a qualitative change in the reaction mechanism takes place between 140 MeV and 315 MeV.

In Figure 17 similar cross section data measured for the interactions of 315 MeV ^{16}O projectiles with other targets are compared with the data for the ^{208}Pb target nucleus. There it will be noted that the production cross sections for light fragments are essentially independent of the target nucleus, that is, factorization is observed to be a valid concept.

Additional information on the reaction mechanism results if the fragment energy spectra, observed at energies near the grazing angle, are investigated. Such energy spectra are presented in Figure 18 for the $^{16}O + ^{208}Pb$ reactions.

There are several energies which might be employed to characterize the products resulting from different reaction mechanisms. Two-body transfer reactions leading to the production of the final nuclei in their ground states will lead to fragments of relatively high final kinetic energies. This energy is designated g.s. in Figure 18. In contrast, two-body reactions leading to the maximum excitation energies of the two product nuclei would lead to fragment kinetic energies representative of the exit channel Coulomb barrier. This energy is designated V_C in the figure. Products of projectile break-up into fragments with velocities equal to that of the initial beam would have energies such as those designated E_p in the plot. For fragments of atomic number close to that of the projectile, energies close to E_p are observed. For lower Z fragments energies significantly lower are observed.

In the projectile frame of reference, a fragment with the beam velocity has a momentum P which is identically zero. At high energies, a fragment produced by the decay of an excited projectile is predicted to have a mean momentum P_o in the fragment frame which is just[36]

$$P_o = - \frac{M_F}{M_P} \frac{1}{V} (E_P^* + E_T^*) \tag{5}$$

where M_F is the mass of the observed fragment, M_P the projectile mass; V, the beam velocity and E_P^* and E_T^* are the excitation energies of the projectile and target nuclei. The projectile excitation energy E_P^* is $E_S + E_K$ where E_S is the separation energy of the projectile into the fragments and E_K is the kinetic energy of the fragments. The latter is expected[36] to be 3/2 T where T is the nuclear temperature.

Further, the distribution of fragment momenta in the projectile frame is of the form[37]

$$N(P) \propto \exp \left[- \frac{(P-P_o)^2}{2\sigma^2} \right] \tag{6}$$

The width $\sigma^2 = \sigma_o^2 \frac{M_F(M_P-M_F)}{M_P-1}$. (7)

Using values T = 7.2 MeV and σ_o = 80 MeV/C which are very close to the corresponding values derived from the reaction data at 33.6 GeV,[38] the Berkeley group have determined the average expected laboratory energies, E_F, and the distributions expected for pure projectile excitation. These results are presented in Figure 18 where they are found to be in very good agreement with the observed distributions, supporting the idea that such reactions might be interpreted as projectile fragmentation. This would be consistent with entry into a qualitatively different region of reactions, at least for peripheral collisions, when 20 MeV/amu heavy ions

are employed as projectiles.

The limiting angular momentum for "central collisions" in the reactions of 315 MeV ^{16}O with ^{208}Pb also appears in Figure 8. This value was derived by subtracting the measured cross section[35] for "peripheral collisions" from the total reaction cross section. This limit is in agreement with the calculated fusion cross section limit but no detailed studies on the mechanisms of the reaction in these central collisions exist.

Since the projectile velocities of 15 to 20 MeV/amu correspond to the theoretical threshold region for the onset of density compression effects[39] some efforts have been made to search for such effects in central collisions at these energies.[40,41] So far these experiments do not provide any evidence for compression.

Summary

Studies of reactions induced by 15 to 20 MeV/amu heavy ion projectiles provide new information on the ion-ion potential, on the effect of angular momentum on the evolution of a nuclear reaction and the subsequent decay of the reaction products, and on the changing character of reaction mechanisms which occur at high energy.

Appendix

Visual presentation of data has long been recognized as a very effective technique for maximizing the transfer of information. The preceding paper, and indeed most of the papers presented in this conference rely heavily upon this method.

Bearing this in mind, it is perhaps useful to emphasize certain limitations inherent in the technique. This is attempted in Figure 19 where a common object has been plotted using various combinations of scales for the ordinate and abcissa. The scales used are linear, log, exponential, square and square root. In this case, the linear-linear plot which appears at the center is perhaps the most useful representation of the data although other combinations of scale might well be chosen to emphasize certain features such as the striking resemblance of a pig to a buffalo (lower right), a monkey (upper right) or a coyote (upper left).

Figure Caption

Figure 19. Pig (Ref. 42).

References

1. R. Stock and A. M. Poskanzer, Comments on Nuclear and Particle Physics VII 41 (1977).

2. S. Cohen and W. J. Swiatecki, Ann. Phys. (N.Y.) 19 67 (1962); W. J. Swiatecki, Lawrence Berkeley Laboratory Report LBL-972 (1972) (unpublished).

3. W. B. Schröder and J. R. Huizenga, University of Rochester Nuclear Structure Research Laboratory Report UR-NSRL-144, to be published in Nuclear Science, Volume 27.

4. A. E. Glassgold, W. Heckrotte and K. M. Watson, Ann. Phys. (N.Y.) 6 (1959).

5. W. Scheid, H. Muller and W. Greiner, Phys. Rev. Lett. 32 741 (1974).

6. P. Sperr, S. Vigdor, Y. Eisen, W. Henning, D. G. Kovar, T. T. Ophel and B. Zeidman, Phys. Rev. Lett. 36 405 (1976).

7. M. N. Namboodiri, E. T. Chulick and J. B. Natowitz, Nucl. Phys. A263 491 (1976).

8. J. B. Natowitz, E. T. Chulick and M. N. Namboodiri, Phys. Rev. C6 2133 (1972).

9. S. E. Vigdor, Proceedings of the Symposium on the Macroscopic Features of Heavy Ion Collisions ANL/PHY-76-2, Vol. I, p. 95, 1976 (unpublished).

10. D. Glas and U. Mosel. Phys. Rev. C10 2620 (1974); Nucl. Phys. A237 429 (1975).

11. U. Mosel. Proceedings of the Symposium on the Macroscopic Features of Heavy Ion Collisions ANC/PHY-76-2, Vol. I, p. 341 (1976) (unpublished).

12. C. Ngo, B. Tamain, J. Galin, M. Beiner, and R. J. L. Lombard, Nucl. Phys. A240 353 (1975).

13. J. Galin, D. Guerreau, M. Lefort, X. Tarrago, Phys. Rev. C9 1018 (1974).

14. C. Ngo, These Universite Paris-Sud (1975) unpublished.

15. R. Bass, Phys. Lett. 47B 139 (1973); Nucl. Phys. A231 45 (1974).

16. W. D. Meyers, Nucl. Phys. A204 465 (1973).

17. J. Wilczynski and K. Siwek-Wilczynska, Phys. Lett. 55B 270 (1975).

18. J. Randrup. W. J. Swiatecki and C. F. Tsang, LBL-3603 (1974) unpublished.

19. R. Bass, to be published.

20. B. Wilkins and G. Igo in Proceedings of the Third Conference on Reactions between Complex Nuclei, Pacific Grove, California (Univ. California Press, Berkeley, 1963) p. 19.

21. S. Cohen, F. Plasil and W. J. Swiatecki, Ann. Phys. (N.Y.) 82 557 (1974).

22. R. L. Kozub, N. H. Lu, J. M. Miller, D. Logan, T. W. Debiak and L. Kowalski, Phys. Rev. C11 1497 (1975).

23. R. G. Stokstad, R. A. Dayras, J. Gomez del Campo, P. H. Stelson, C. Olmer and M. S. Zisman, to be published.

24. R.G. Stokstad, Proceedings of this conference.

25. K. A. Geoffroy and J. B. Natowitz, Phys. Rev. Lett. 37 1198 (1976).

26. Calculated using the program curves of R. Vandenbosch, unpublished.

27. L G. Moretto, S. K. Kataria, R. C. Jared, R. Schmitt and S. G. Thompson, Nucl. Phys. A255 491 (1975).

28. J. B. Natowitz, M. N. Namboodiri and E. T. Chulick, Phys. Rev. C13 171 (1976).

29. R. Eggers, M. N. Namboodiri, P. Gonthier and J. B. Natowitz, to be published.

30. R. Eggers, M. N. Namboodiri, P. Gonthier, L. Adler, P. Kasiraj and J. B. Natowitz, to be published.

31. L. G. Moretto and J. S. Sventek in Proceedings of the Symposium on Macroscopic Features of Heavy Ion Collisions, ANL-PHY-76-2, Vol. I, p. 235 (1976) unpublished.

32. M. Buenerd, C. K. Gelbke, B. G. Harvey, D. L. Hendrie, J. Mahoney, A. Menchaca-Rocha, C. Olmer, and D. K. Scott, Phys. Rev. Lett. 37 1191 (1976).

33. C. Olmer, M. C. Mermaz, M. Buenerd, C. K. Gelbke, D. L. Hendrie, J. Mahoney, A. Menchaca-Rocha, D. K. Scott, M. H. Macfarlane and S. C. Pieper, Phys. Rev. Lett. 38 476 (1977).

34. K. Siwek-Wilczynska and J. Wilczynski, Report No. 910/PL INP, Cracow, 1976.

35. C. K. Gelbke, C. Olmer, M. Buenerd, D. L. Hendrie, J. Mahoney, M. C. Mernaz and D. K. Scott, to be published in Physics Reports.

36. N. Masuda and F. Uchiyama, Phys. Rev. C15 1598 (1972).

37. A. S. Goldhaber, Phys. Lett. 53B 306 (1974).

38. D. L. Greiner, P. J. Lindstrom, H. H. Heckman, B. Cook and F. S. Rieser, Phys. Rev. Lett. 35 152 (1975).

39. C. F. Tsang, private communication.

40. M. N. Namboodiri, E. T. Chulick and J. B. Natowitz, unpublished data.

41. D. L. Hendrie, M. Buenerd, A. Menchaca -Rocha, C. Olmer and D. K. Scott LBL 5075, p. 117 (1975) unpublished.

42. Anonymous.

Figure Captions

Fig. 1 A classification of nuclear reactions according to the qualitatively different phenomena which are expected to be dominant for particular projectile masses (plotted as $A^{1/3}$) and projectile velocities (plotted as energy/amu). The region corresponding to the reactions discussed in the text is indicated by the solid circle.

Fig. 2 Product intensities observed at $\theta_L = 10°$ for identified products of the reactions of 262 MeV ^{14}N with Ni. The data are presented as a function of ΔE and E, the energies deposited in the two detectors of the counter telescope.

Fig. 3 Laboratory angular distributions ($d\sigma/d\Omega$) for C, Si and Cr nuclei produced in the reactions of 262 MeV ^{14}N projectiles with Ni.

Fig. 4 Fusion cross sections for the reactions of ^{12}C with ^{12}C. The data from reference 6 are represented by the thin solid line. A typical data point from that work is represented by the open circle. The solid circles represent data from reference 7 with relative errors indicated. For comparison, total reaction cross sections (heavy solid line) and fusion cross sections (dashed lines) have been calculated as indicated in the text.

Fig. 5 Fusion cross section data for the reactions of ^{12}C with ^{27}Al. The solid circles represent data from reference 8. Relative errors are indicated. The solid squares represent the total reaction cross section measurements of reference 20. For comparison, total reaction cross sections (solid lines) and fusion cross sections (dashed lines) have been calculated as indicated in the text.

Fig. 6 Fusion cross section data for the reactions of ^{16}O with ^{40}Ca. The solid circles represent data from reference 9. For comparison, total reaction cross sections (solid line) and fusion cross sections (dashed line) have been calculated as indicated in the text.

Fig. 7 Nuclear potentials for the interaction of ^{12}C with ^{27}Al. Three different potentials based on liquid drop model considerations are presented. The solid point represents the determination of R_F and V_N from the data in Figure 5 and the assumption that $V_C = 1.438\ Z_P Z_T / R_F$.

Fig. 8 The empirical potential function g(s) suggested by Bass. References to the data employed in determining this function appear in reference 19. The lines labeled 1 and 2 indicate the equivalent function corresponding to the potential proposed in reference 15 assuming 1: r_o = 1.00 fm and 2: r_o = 1.07 fm.

Fig. 9 Sharp cut-off limiting angular momenta derived from evaporation residue cross-section measurements. The points indicate the experimental data. Calculated fusion cross sections as a function of A_{CN} the mass of the compound nucleus are presented for reactions with 197 MeV ^{12}C, 262 MeV ^{14}N and 310 MeV ^{16}O projectiles. The dashed line indicates the theoretical angular momentum at which the fission barrier disappears. The data point for 315 MeV ^{16}O projectiles is derived from the cross section for peripheral collisions.

Fig. 10 Classical deflection function for the interaction of 262 MeV ^{14}N with ^{109}Ag. The solid line indicates the deflection function

calculated assuming the nuclear potential proposed in reference 19. The dashed line indicates the Coulomb deflection function.

Fig. 11 Projectile trajectories corresponding to the deflection function presented in Figure 10. The circle indicated on the figure has a radius equal to the sum of the half density radii of the interacting nuclei.

Fig. 12 Most probable kinetic energies for products of fission-like reactions of 197 MeV ^{12}C projectiles with Ni, Y, Ag, Tb and Au targets. The predicted trend of kinetic energies for the Coulomb repulsion of two spherical nuclei in contact is also shown for the Ni, Ag and Au targets.

Fig. 13 Center of mass angular distributions ($d\sigma/d\theta$) for products of the completely damped collisions of 262 MeV ^{14}N with ^{109}Ag. Statistical error bars are indicated where they are larger than the data points.

Fig. 14 Mass asymmetry potentials calculated for the composite system ^{120}I. The potentials calculated for two spherical nuclei in contact and undergoing rigid rotation are presented as a function of $A_L/(A_H + A_L)$ where A_L is the mass of the light partner and A_H that of the heavy partner. All values are relative to that of the spherical nucleus. The initial asymmetry for $^{12}C + ^{108}Ag$ is indicated by the heavy vertical line on the asymmetry scale.

Fig. 15 Cross sections $(d\sigma/d\theta)_{cm}$ for products of the reactions of completely damped reactions of 262 MeV ^{14}N with Ni, Ag and Au. The center of mass angles vary with product but are near 35°.

Fig. 16 Cross section ratios for light products produced in the interaction of ^{16}O with ^{208}Pb at projectile energies of 140 MeV, 315 MeV and 33.6 GeV. In part (a) the ratios of the isotopic and elemental yields observed at 140 MeV projectile energy to those observed at 315 MeV are plotted. In part (b) the analogous ratios for data taken at 315 MeV and 33.6 GeV are presented. Data are from reference 35.

Fig. 17 A comparison of isotopic and elemental yields of light products produced in the reactions of 315 MeV ^{16}O with ^{94}Zr, ^{197}Au, ^{208}Pb and ^{232}Th.

Fig. 18 Energy spectra of light elements in the reactions of 315 MeV ^{16}O with ^{208}Pb. Expected energies corresponding to various assumptions (see text) are indicated by arrows. The dotted line is the distribution calculated from a projectile fragmentation model.

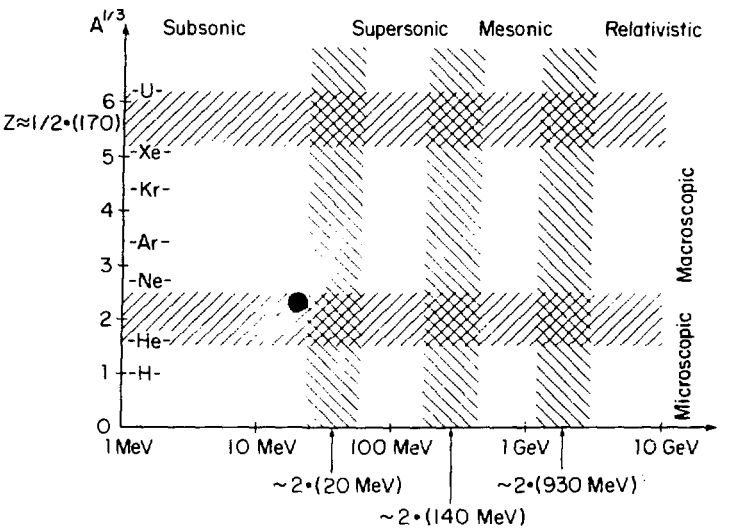
A^1/3
Subsonic
Supersonic
Mesonic
Relativistic
-U-
Z≈1/2•(170)
-Xe-
-Kr-
-Ar-
-Ne-
-He-
-H-
Macroscopic
Microscopic
0
1
2
3
4
5
6
1 MeV
10 MeV
100 MeV
1 GeV
10 GeV
~2•(20 MeV)
~2•(140 MeV)
~2•(930 MeV)

Figure 1

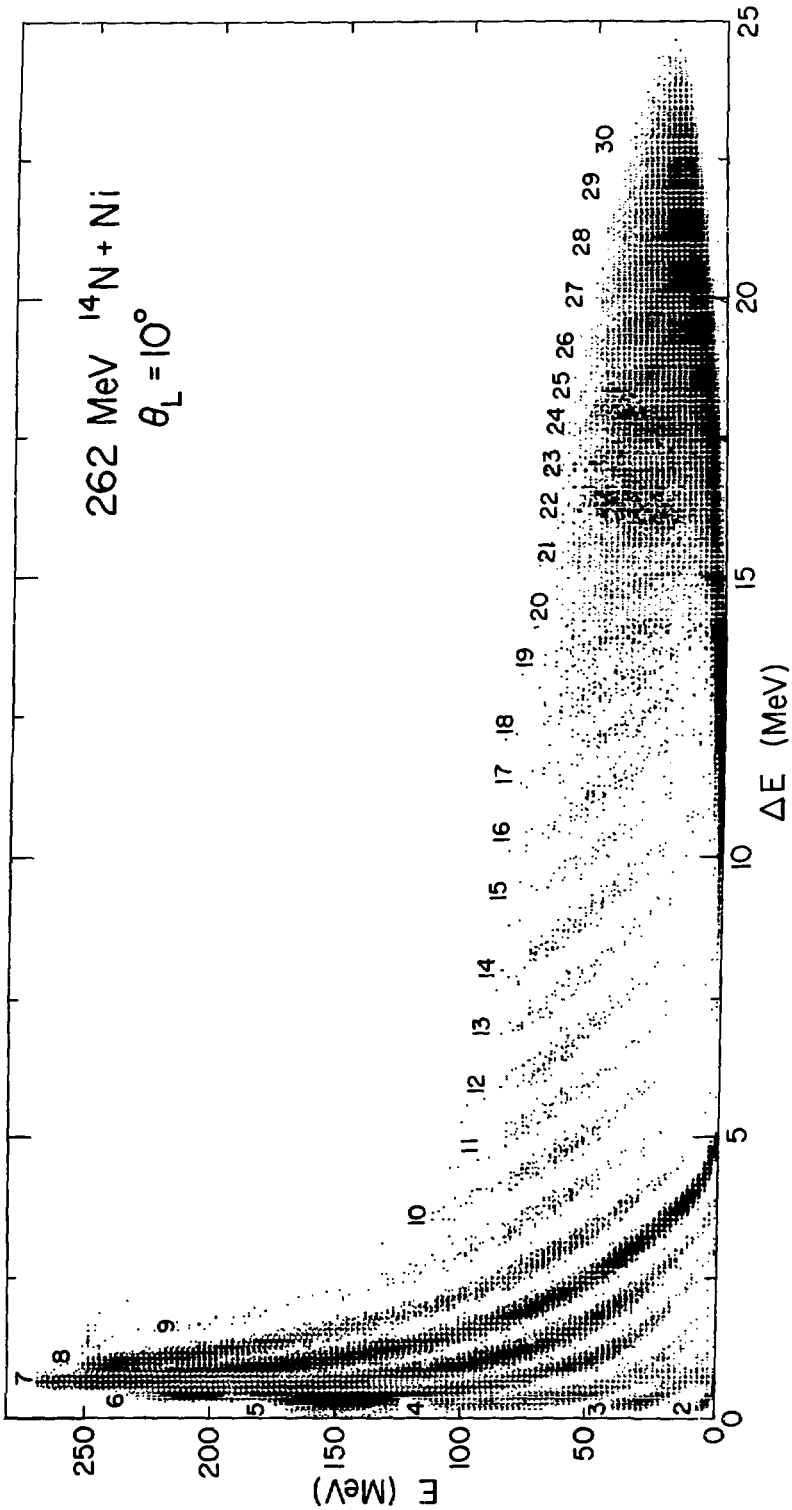
262 MeV ^{14}N + Ni
$\theta_L = 10°$
E (MeV)
ΔE (MeV)
0
50
100
150
200
250
5
10
15
20
25
2
3
4
5
6
7
8
9
10
11
12
13
14
15
16
17
18
19
20
21
22
23
24
25
26
27
28
29
30

Figura 2

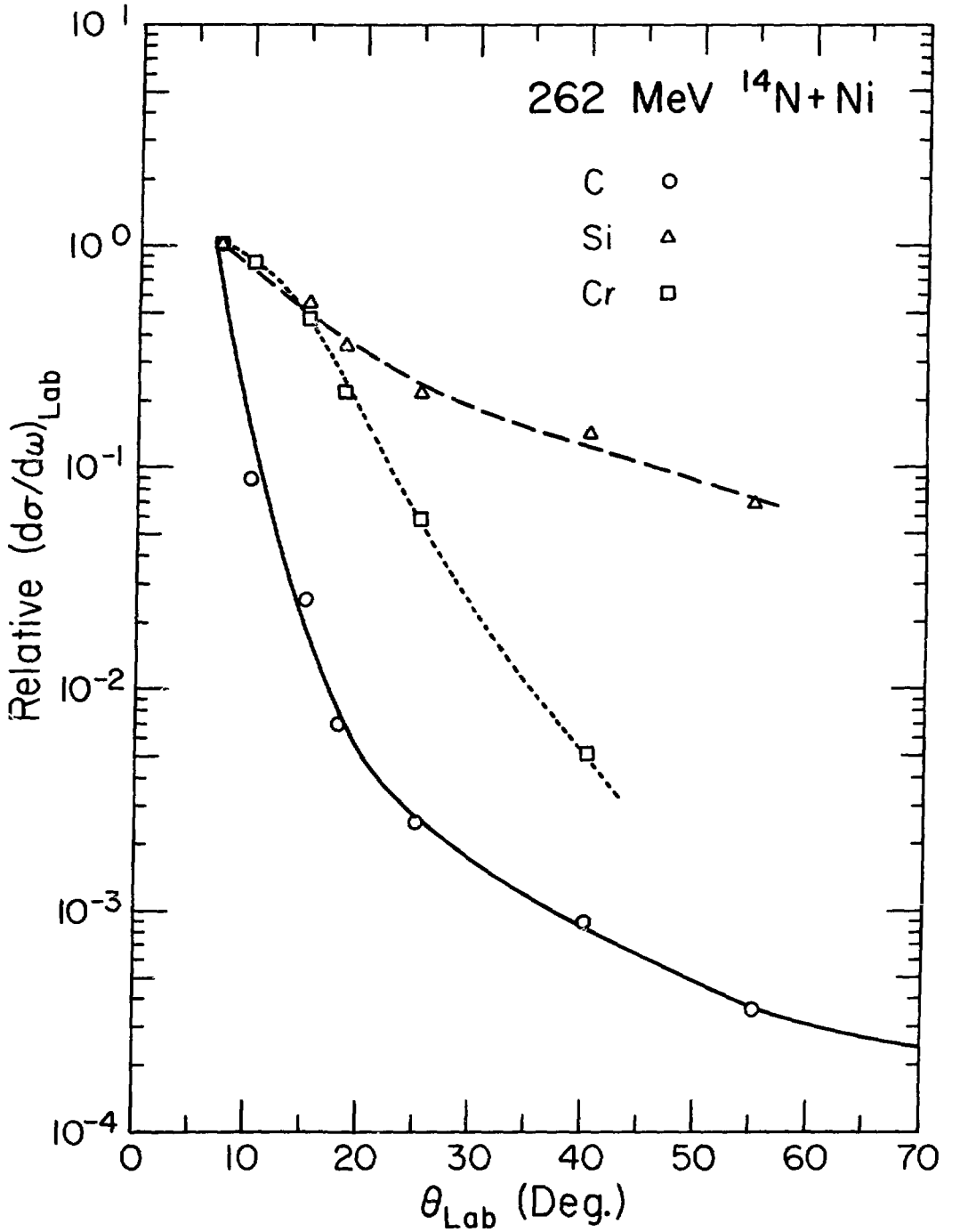
262 MeV ^{14}N+Ni
C
Si
Cr
Relative $(d\sigma/d\omega)_{Lab}$
θ_{Lab} (Deg.)
10^{1}
10^{0}
10^{-1}
10^{-2}
10^{-3}
10^{-4}
0
10
20
30
40
50
60
70

Figure 3

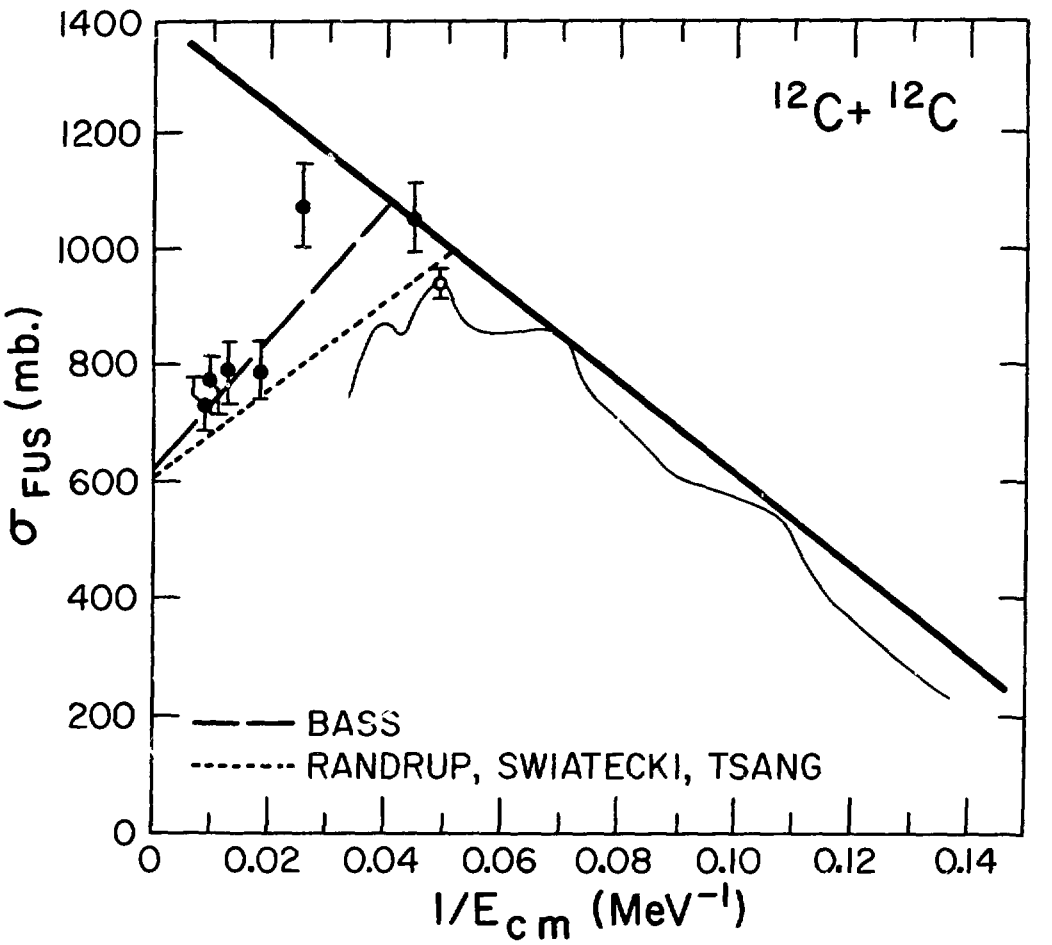
1400
1200
1000
800
600
400
200
0
σ FUS (mb.)
$^{12}C+ ^{12}C$
BASS
RANDRUP, SWIATECKI, TSANG
0
0.02
0.04
0.06
0.08
0.10
0.12
0.14
$1/E_{cm}$ (MeV^{-1})

Figure 4

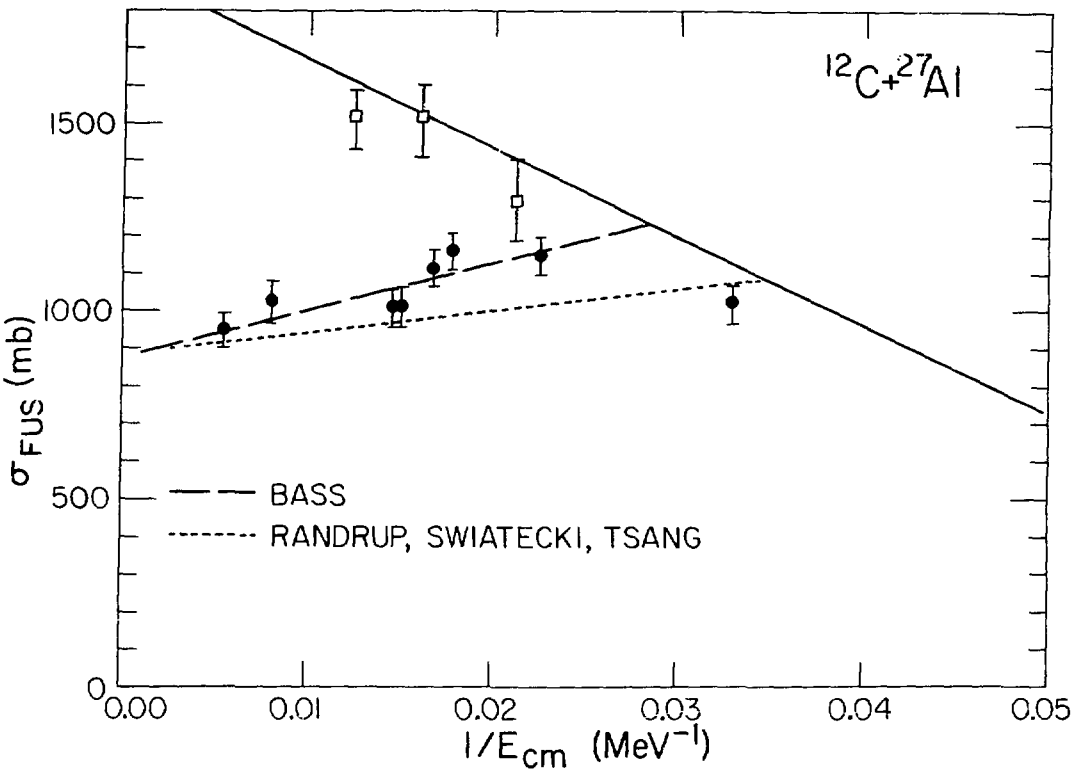
$^{12}C+^{27}Al$
1500
1000
500
0
σ_{FUS} (mb)
BASS
RANDRUP, SWIATECKI, TSANG
0.00
0.01
0.02
0.03
0.04
0.05
$1/E_{cm}$ (MeV^{-1})

Figure 5

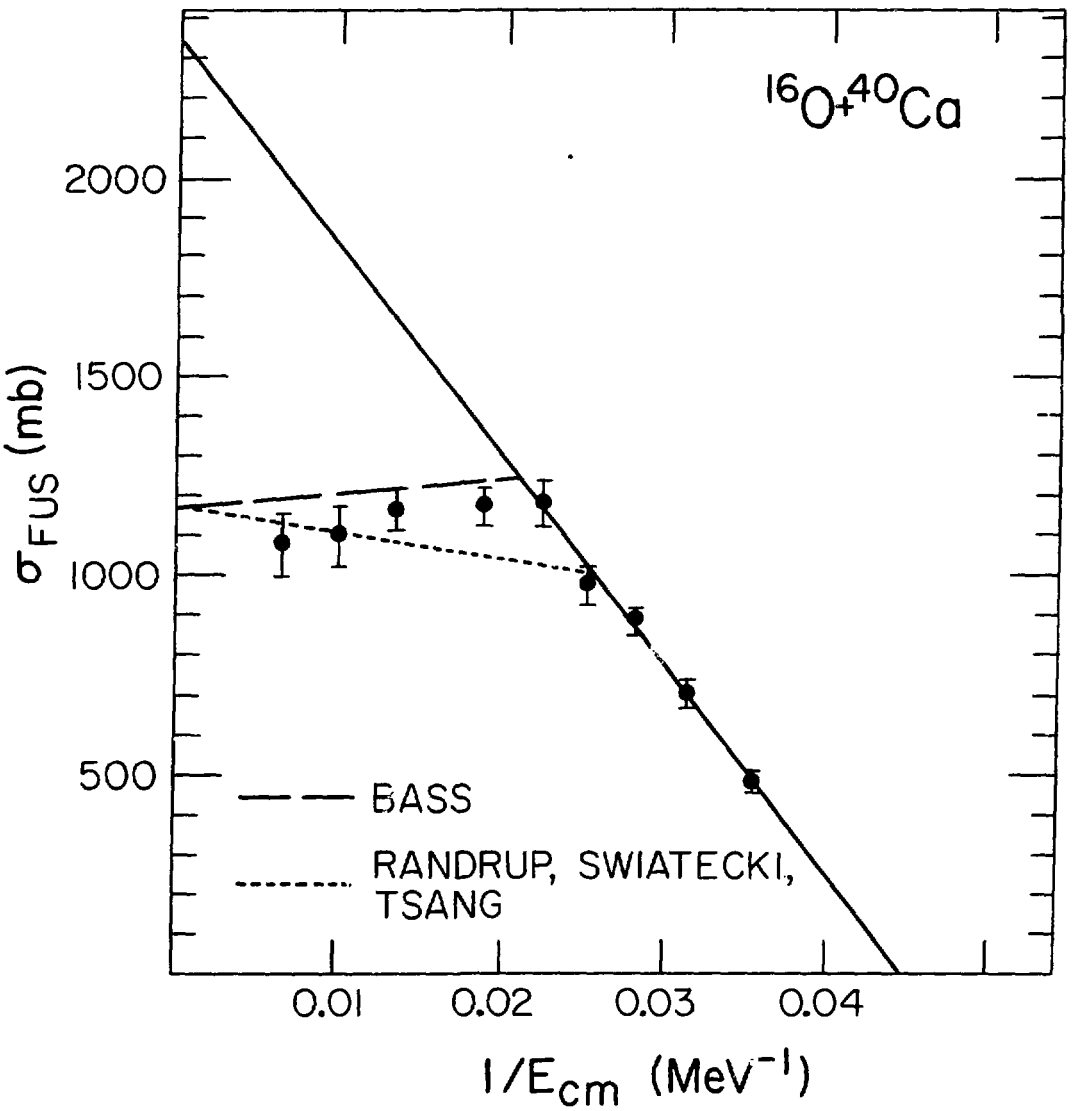
$^{16}O+^{40}Ca$
2000
1500
1000
500
σ_{FUS} (mb)
BASS
RANDRUP, SWIATECKI, TSANG
0.01
0.02
0.03
0.04
$1/E_{cm}$ (MeV^{-1})

Figure 6

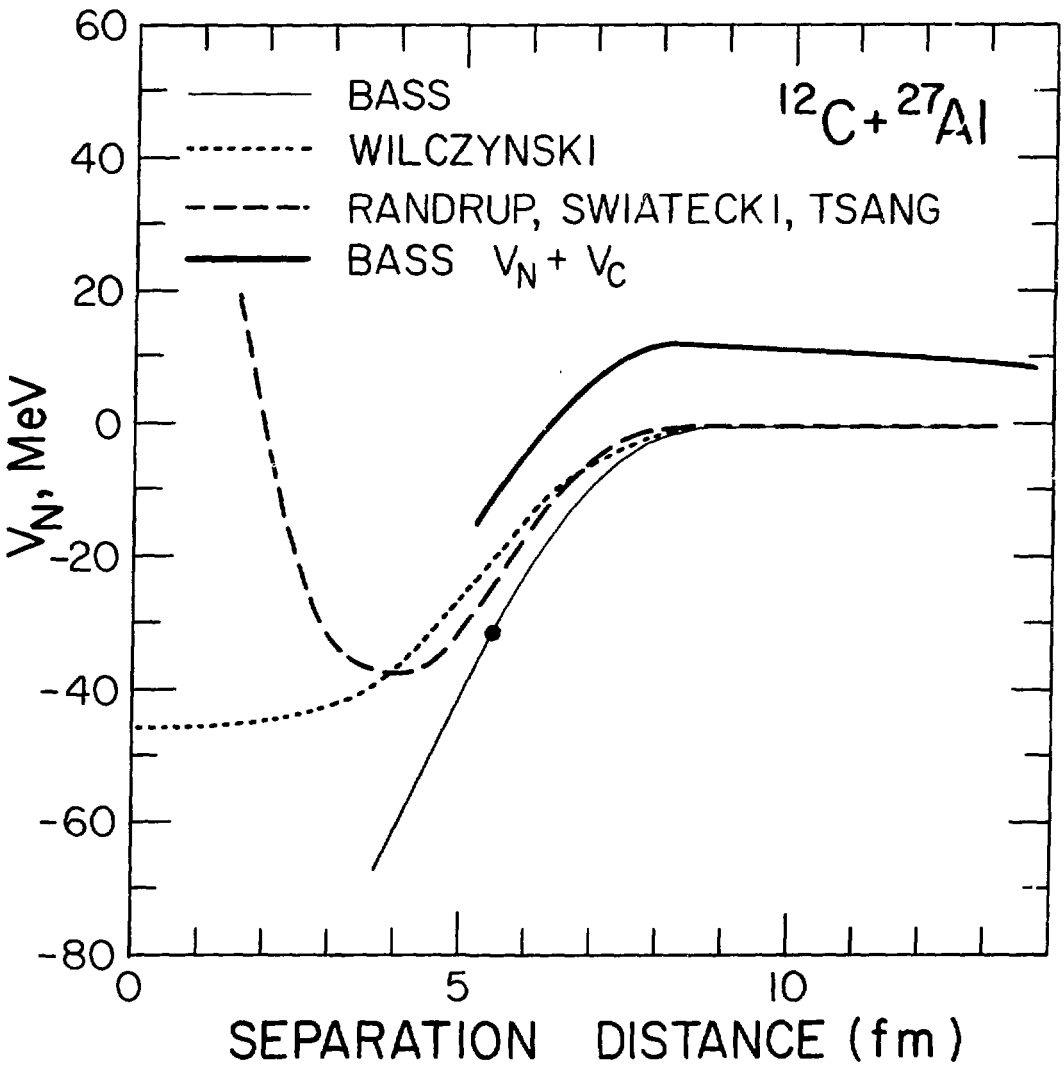
BASS
WILCZYNSKI
RANDRUP, SWIATECKI, TSANG
BASS $V_N + V_C$
$^{12}C + ^{27}Al$
V_N, MeV
60
40
20
0
-20
-40
-60
-80
0
5
10
SEPARATION DISTANCE (fm)

Figure 7

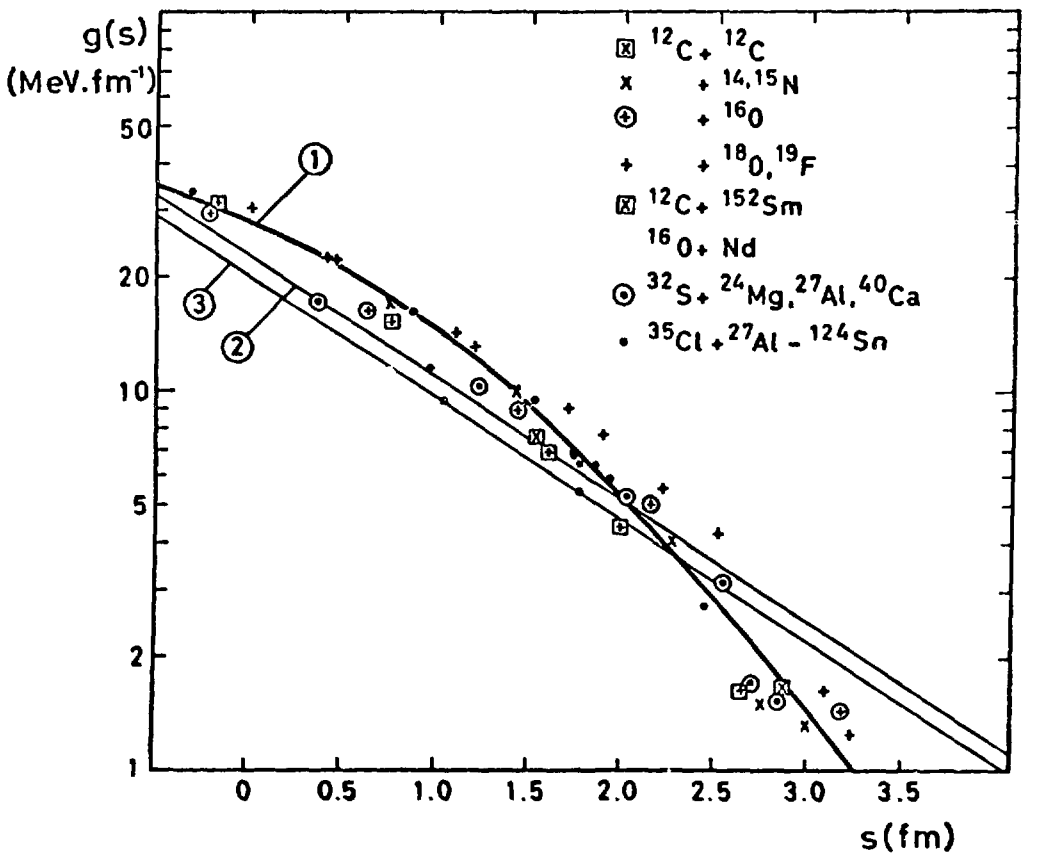
g(s)
(MeV.fm⁻¹)
50
20
10
5
2
1
0
0.5
1.0
1.5
2.0
2.5
3.0
3.5
s(fm)
① ¹²C + ¹²C
+ ¹⁴,¹⁵N
+ ¹⁶O
+ ¹⁸O, ¹⁹F
¹²C + ¹⁵²Sm
¹⁶O + Nd
³²S + ²⁴Mg, ²⁷Al, ⁴⁰Ca
³⁵Cl + ²⁷Al - ¹²⁴Sn
②
③

Figure 8

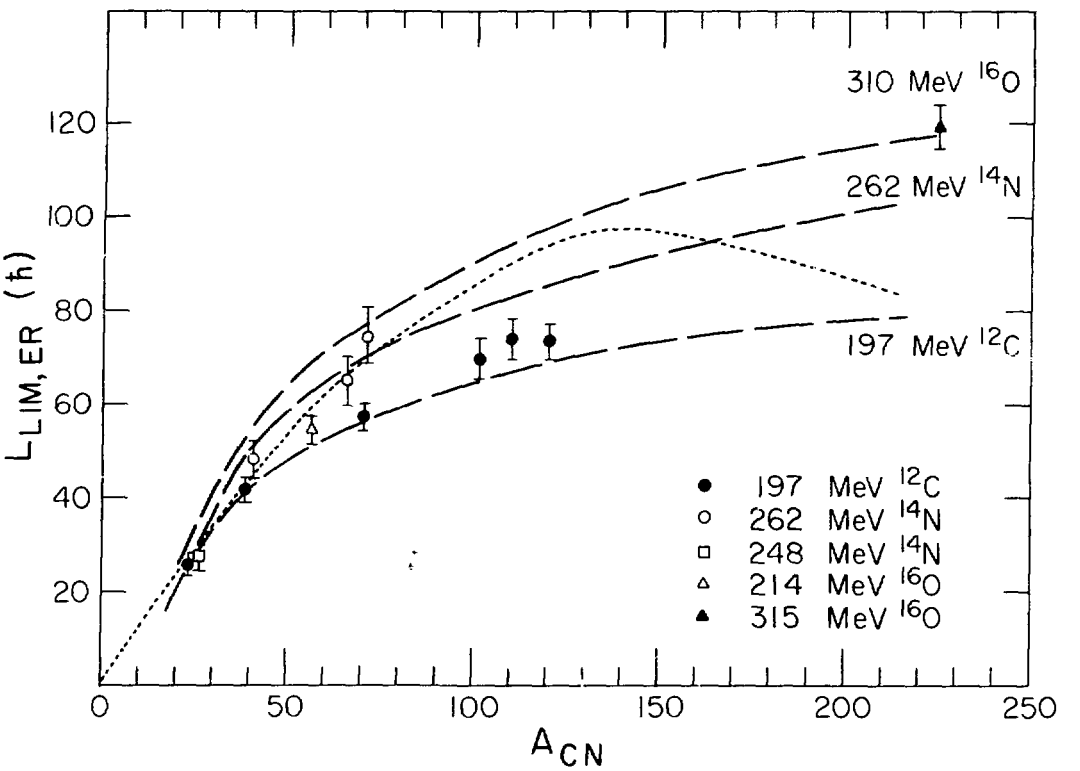
310 MeV ^{16}O
262 MeV ^{14}N
197 MeV ^{12}C
197 MeV ^{12}C
262 MeV ^{14}N
248 MeV ^{14}N
214 MeV ^{16}O
315 MeV ^{16}O
$L_{LIM,ER}$ (ħ)
A_{CN}
0
50
100
150
200
250
20
40
60
80
100
120

Figure 9

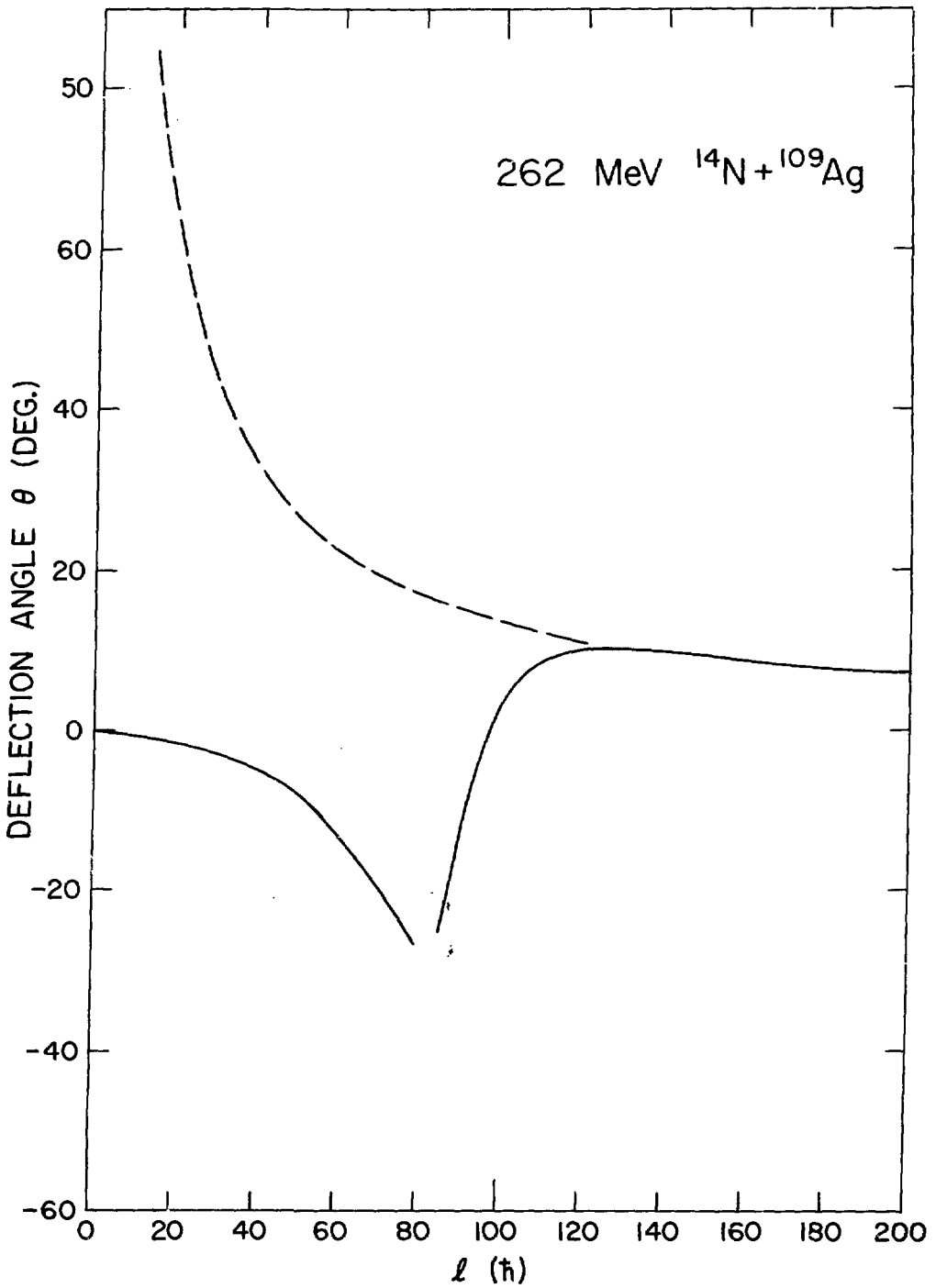
262 MeV $^{14}N + ^{109}Ag$
DEFLECTION ANGLE θ (DEG.)
50
60
40
20
0
-20
-40
-60
0
20
40
60
80
100
120
140
160
180
200
ℓ (ħ)

Figure 10

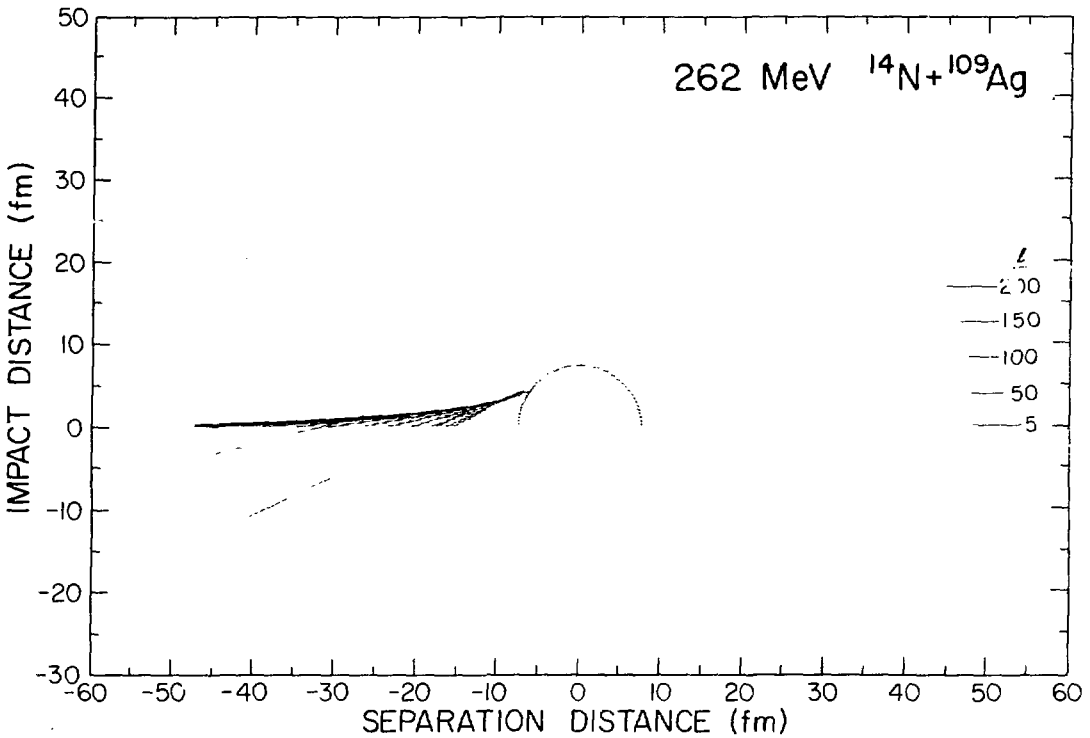
262 MeV $^{14}N+^{109}Ag$
IMPACT DISTANCE (fm)
SEPARATION DISTANCE (fm)
ℓ
200
150
100
50
5
50
40
30
20
10
0
-10
-20
-30
-60
-50
-40
-30
-20
-10
0
10
20
30
40
50
60

Figure 11

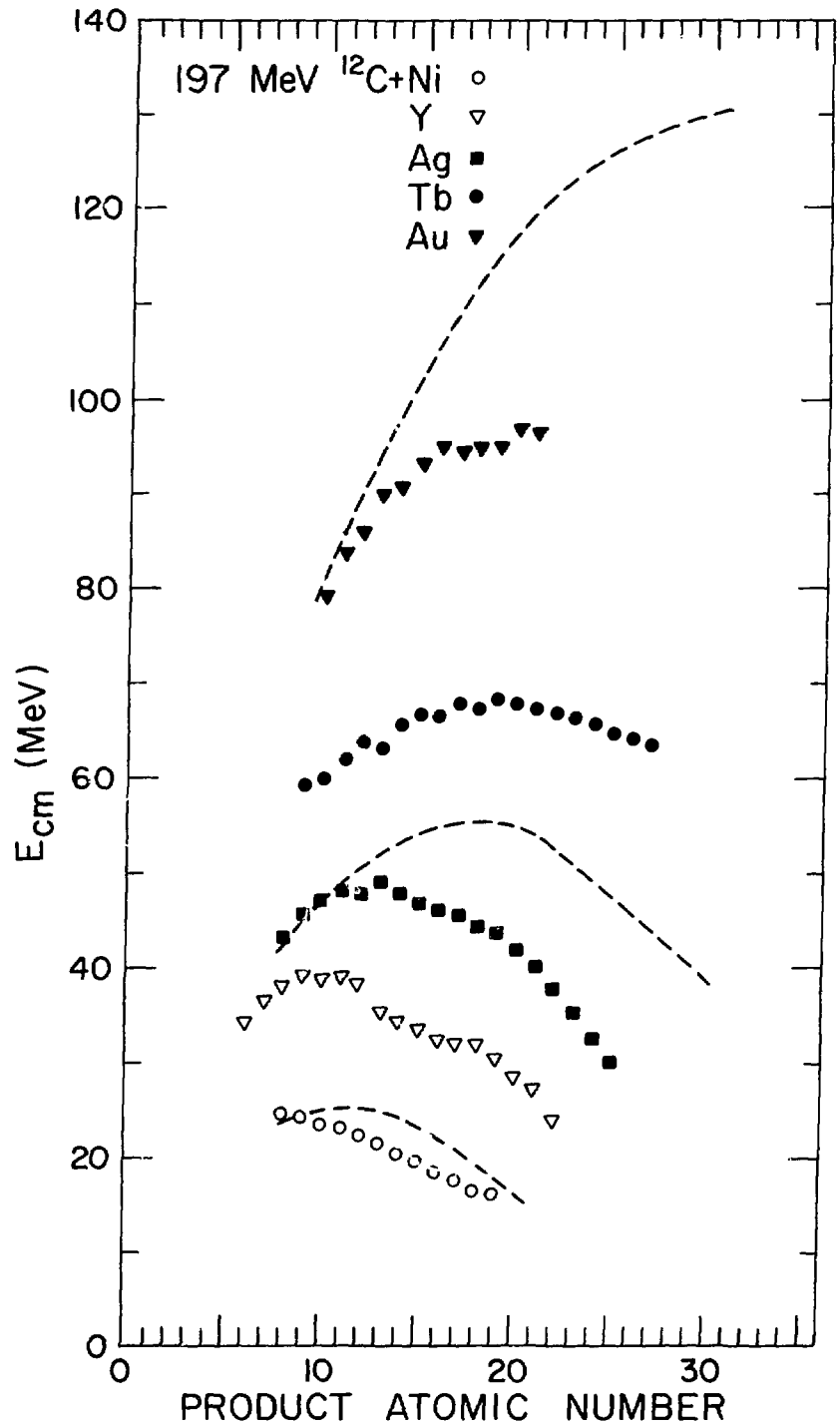
197 MeV ^{12}C+Ni
Y
Ag
Tb
Au
E_{cm} (MeV)
PRODUCT ATOMIC NUMBER
0
20
40
60
80
100
120
140
0
10
20
30

Figure 12

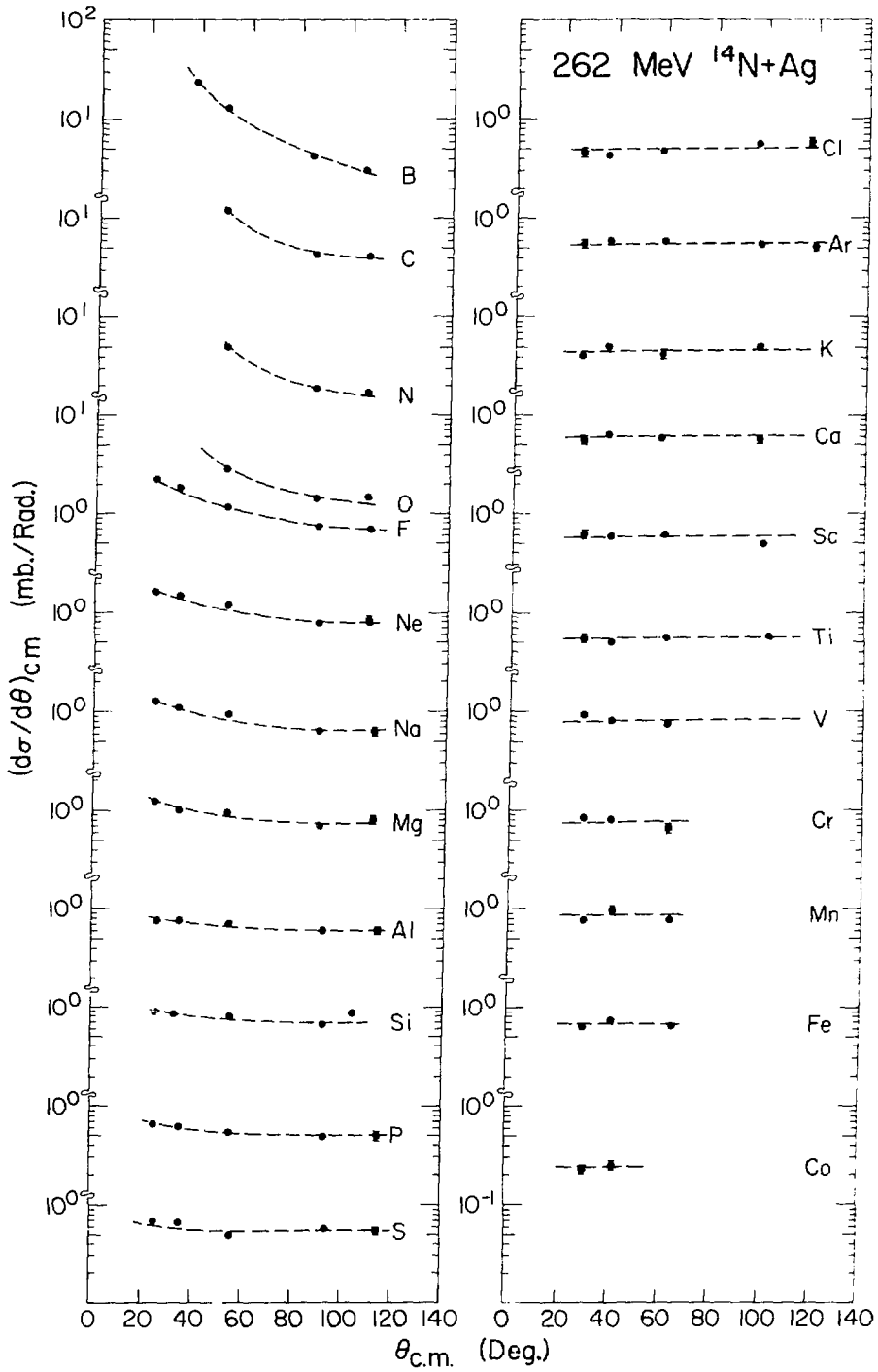
262 MeV ^{14}N+Ag
$(d\sigma/d\theta)_{c.m.}$ (mb./Rad.)
$\theta_{c.m.}$ (Deg.)
B
C
N
O
F
Ne
Na
Mg
Al
Si
P
S
Cl
Ar
K
Ca
Sc
Ti
V
Cr
Mn
Fe
Co

Figure 13

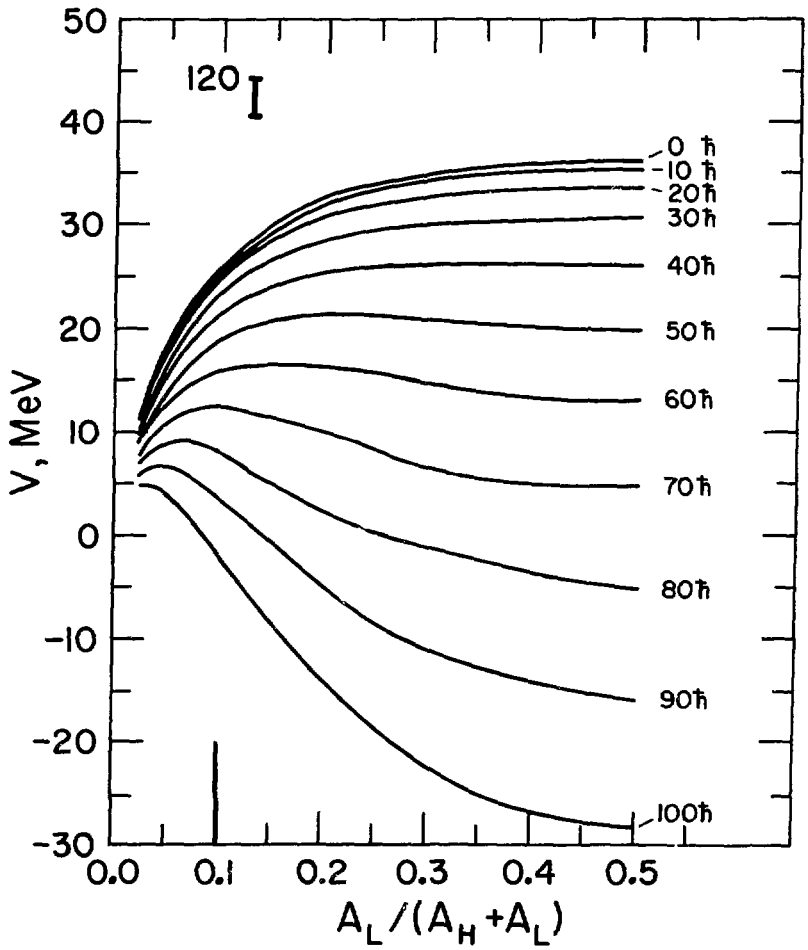
120 I
0 ħ
10 ħ
20ħ
30ħ
40ħ
50ħ
60ħ
70ħ
80ħ
90ħ
100ħ
V, MeV
50
40
30
20
10
0
-10
-20
-30
0.0
0.1
0.2
0.3
0.4
0.5
A_L/(A_H+A_L)

Figure 14

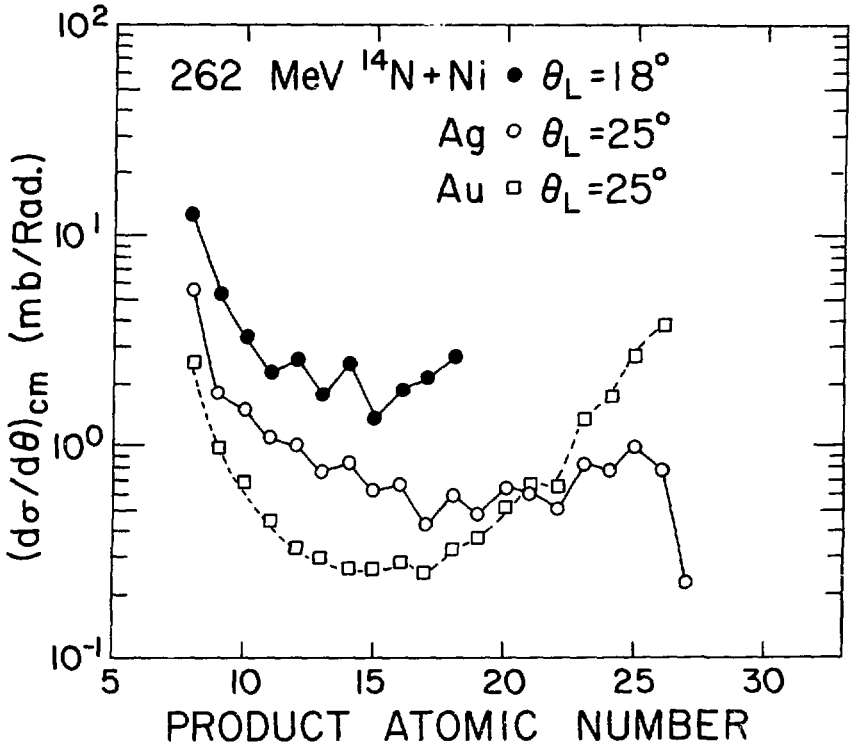
262 MeV ^{14}N+Ni • θ_L=18°
Ag ○ θ_L=25°
Au □ θ_L=25°
$(d\sigma/d\theta)_{cm}$ (mb/Rad.)
10^2
10^1
10^0
10^{-1}
5
10
15
20
25
30
PRODUCT ATOMIC NUMBER

Figure 15

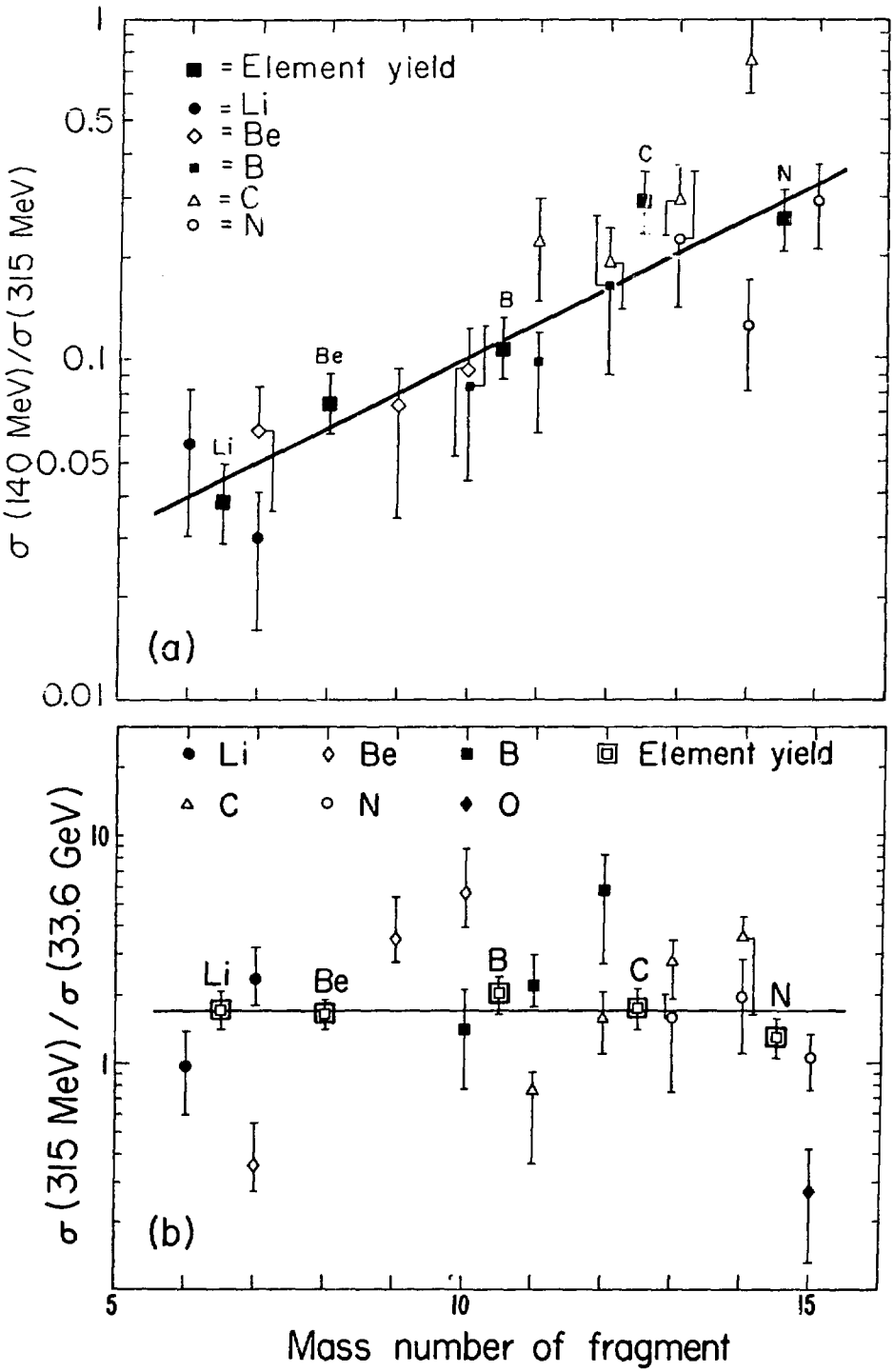
■ = Element yield
● = Li
◇ = Be
▪ = B
△ = C
○ = N
σ (140 MeV)/σ(315 MeV)
1
0.5
0.1
0.05
0.01
Li
Be
B
C
N
(a)
● Li
◇ Be
■ B
▣ Element yield
△ C
○ N
◆ O
σ (315 MeV) / σ (33.6 GeV)
10
1
Li
Be
B
C
N
(b)
5
10
15
Mass number of fragment

Figure 16

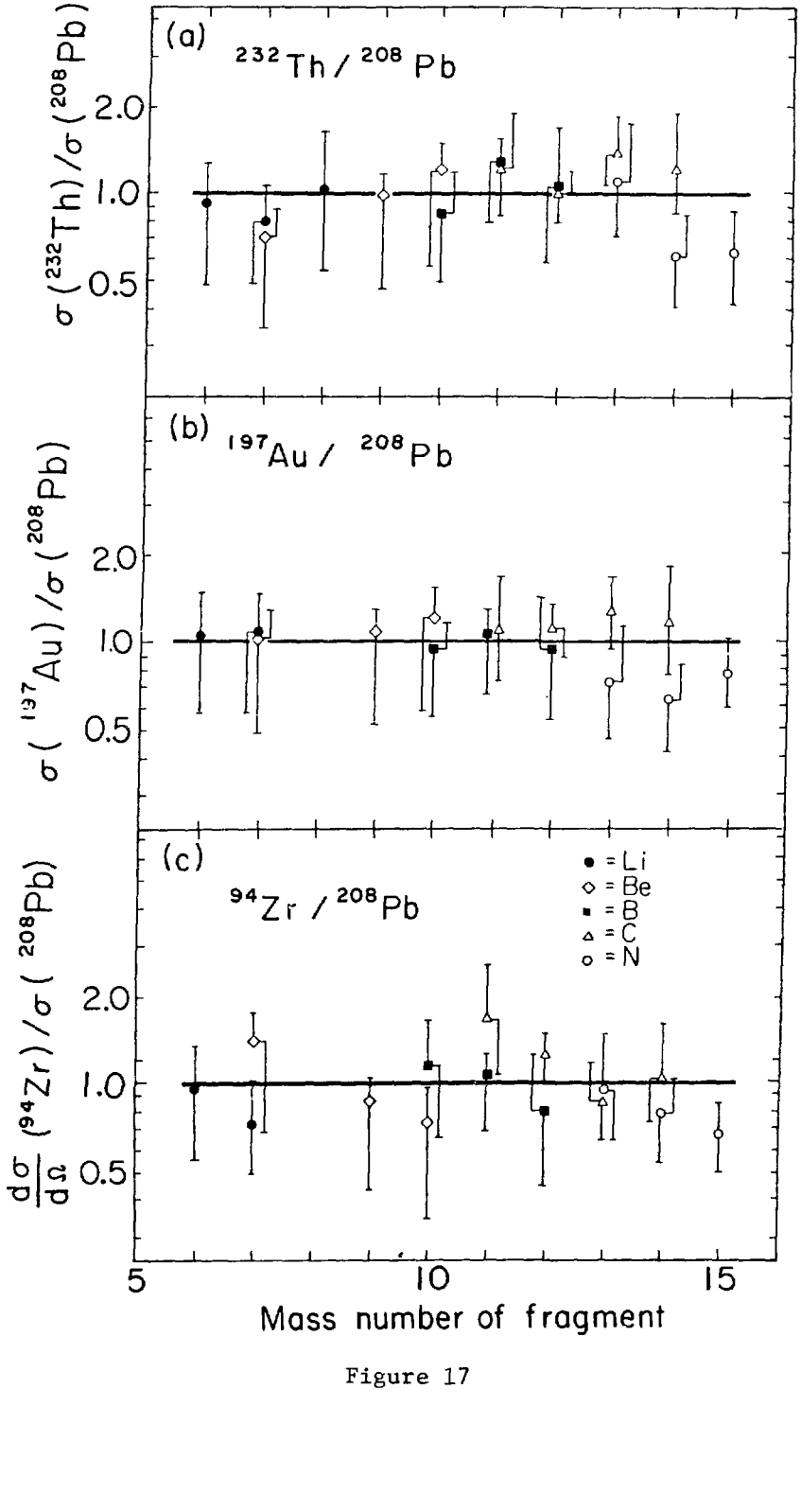
(a) $^{232}Th / ^{208}Pb$
$\sigma(^{232}Th)/\sigma(^{208}Pb)$
(b) $^{197}Au / ^{208}Pb$
$\sigma(^{197}Au)/\sigma(^{208}Pb)$
(c) $^{94}Zr / ^{208}Pb$
$\frac{d\sigma}{d\Omega}(^{94}Zr)/\sigma(^{208}Pb)$
● = Li
◇ = Be
■ = B
△ = C
○ = N
2.0
1.0
0.5
5
10
15
Mass number of fragment

Figure 17

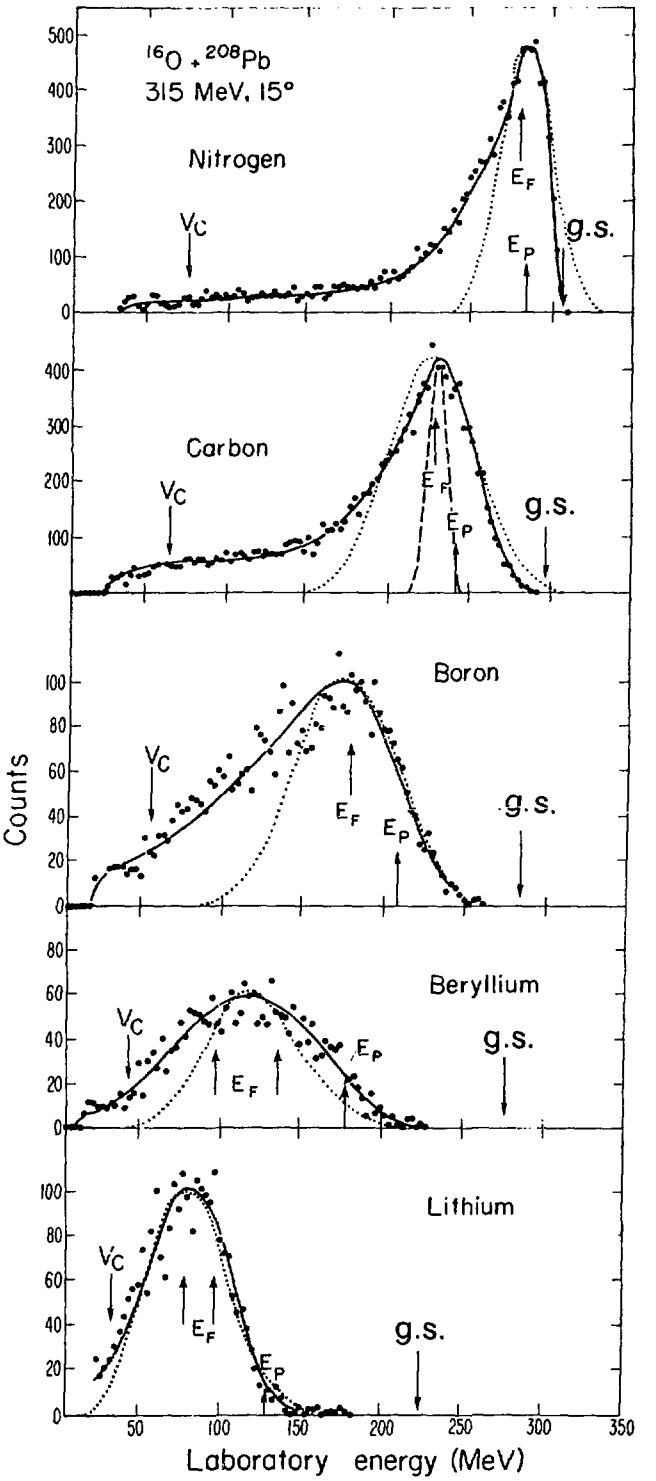
$^{16}O + ^{208}Pb$
315 MeV, 15°
Nitrogen
Carbon
Boron
Beryllium
Lithium
V_C
E_F
E_P
g.s.
Counts
Laboratory energy (MeV)

Figure 18

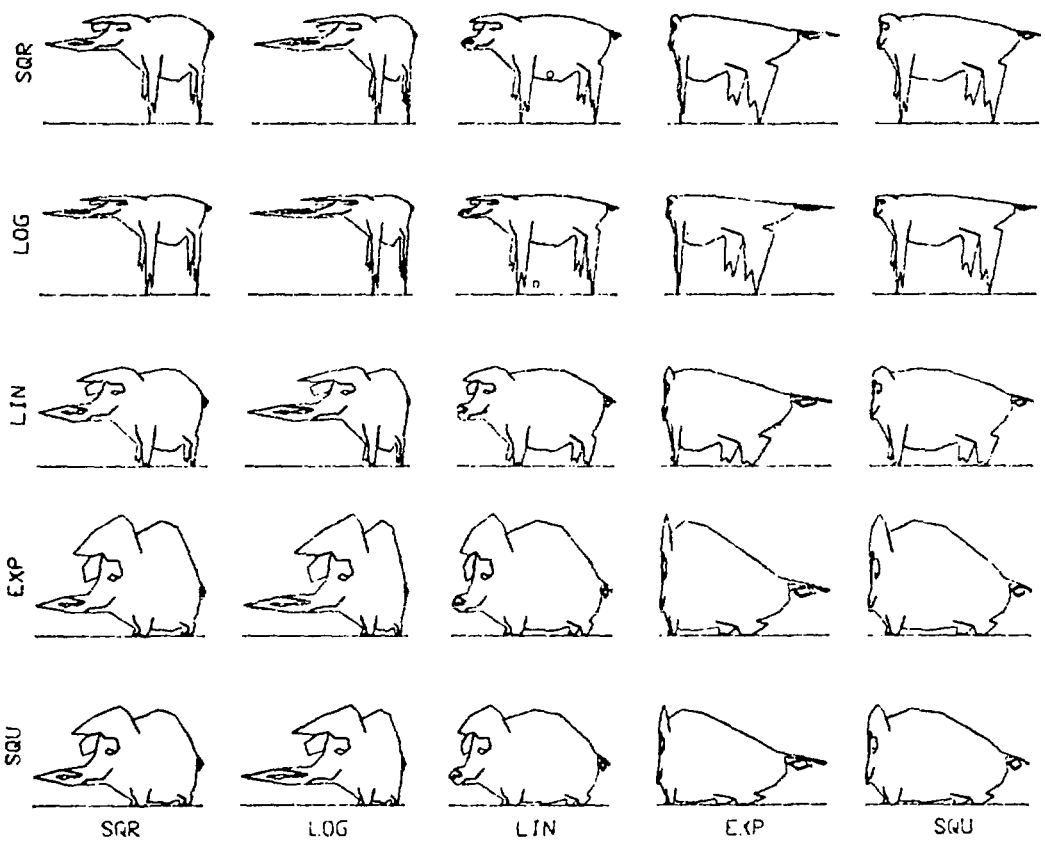

Figure 19

CONF-770602--2

THE FLUID-DYNAMICAL MODEL FOR HEAVY-ION REACTIONS IN THREE DIMENSIONS

J. A. Maruhn
Oak Ridge National Laboratory*
Oak Ridge, Tennessee 37830

I. Introduction

The purpose of this talk is to give a short overview of some of the work that has been done in the area of general fluid dynamical models of heavy-ion collisions, focusing mainly on the very general calculations of three-dimensional collisions performed by the Los Alamos group[1-4] and by our group at Oak Ridge.

A simple characterization of the differences between the two calculations, aside from the technical one of different numerical methods, might be given by stating that the Los Alamos group solves the relativistic Euler equations without full treatment of binding effects, whereas we solve the non-relativistic Navier-Stokes equations with correct treatment of binding. We intend to extend our code to relativistic situations, however.

II. Fluid Dynamics as a Branch of Continuum Mechanics

Before trying to describe nuclei in a fluid-dynamical model, let us take a glance at related branches of classical physics that might be useful for model descriptions of nuclei.

The most general theory encompassing the field is continuum mechanics, which considers all material systems that may be described by macroscopically smooth fields like density ρ, velocity $\vec{v}$, and energy density. The dynamics of these fields is governed by conservation laws, e.g. conservation of mass

$$\frac{\partial \rho}{\partial t} + \nabla \cdot (\rho \vec{v}) = 0$$

and momentum

$$\frac{\partial}{\partial t} (\rho \vec{v}) + \nabla \cdot (\rho \vec{v}\vec{v}) = \nabla \cdot \overleftrightarrow{S},$$

*Research sponsored by the U.S. Energy Research and Development Administration under contract with Union Carbide Corporation.

where $\overleftrightarrow{S}$ is the stress tensor, and a set of constitutive equations depending on the properties of the materials, which serve to complete the macroscopic description. The most familiar example of these is the equation of state; for the two equations given above, we would have to give $\overleftrightarrow{S}$ as a function of ρ and $\vec{v}$ to complete the description.

Let us just mention in passing that there may be several interacting components in a continuum system, such as different chemical compounds or phases. This may be described easily by the use of several fields ρ, $\vec{v}$, etc. An example of a two-component system will be encountered later in the two-fluid model for nuclear collisions.

Continuum mechanics may be subdivided into three branches, depending on the properties of the stress tensor $\overleftrightarrow{S}$:

Solid Mechanics: $\overleftrightarrow{S}$ depends on the deformation only. Example: elastic solids obeying Hooke's law.

Fluid Mechanics: $\overleftrightarrow{S}$ depends only on the rate of deformation. Example: Newtonian fluid.

Rheology: This name covers everything not included in the two special branches mentioned. $\overleftrightarrow{S}$ may depend on the deformation and its time change in any way and may also be modified by the history of the system.

In the following, we shall only be concerned with the special case of a fluid dynamical description. One should, however, always bear in mind that more general models are available in this field and might be considered for describing nuclei.

III. Properties of the Nuclear Fluid

Let us assume for the moment that nuclear matter can be described as a classical fluid (the conditions for this will be discussed later). It is then of utmost interest to examine the properties of this fluid in a collision situation in order to decide how general a dynamical treatment is needed. Some of these decisions may be stated as simple alternatives:

1. Compressible or Incompressible fluid? -- The criterion for this is whether flow velocities are comparable to the speed of sound. For nuclear matter with an incompressibility K (in MeV), the speed of sound is

$$C_S = (K/9m_o)^{1/2}$$

and the projectile energy per nucleon above the Coulomb barrier in the lab system needed to reach such a relative velocity in a

heavy-ion collision is

$$E/A = K/18,$$

so that for the typical range of estimates for K between 150 and 300 MeV we obtain C_S between 0.13c and 0.19c (c is the speed of light) and E/A between 8 MeV and 17 MeV. Apparently compressibility will be important at least in the "intermediate" and "high" energy ranges. It should be mentioned, however, that an incompressible fluid drop must have a sharp surface since the interior density is by definition constant; thus a realistic treatment of the nuclear surface requires a compressible fluid model at any speed.

2. Viscous or Inviscid? -- The experimental data on fission and strongly-damped collisions seem to indicate that viscous effects play an important rôle in nuclear collisions. The introduction of damping into a fluid-dynamical model, however, is not without problems; a microscopic damping caused by one-body dissipation cannot be incorporated easily into the model; on the other hand, even an inviscid fluid shows strong energy dissipation in shock fronts. We shall disregard one-body dissipation and assume the presence of an explicit viscous force in the model equations. We then have to decide whether the fluid is

   Newtonian or Non-Newtonian?, i.e., whether the viscous stress tensor is of the special form

$$S_{ij} = -p\delta_{ij} + \eta(\partial_j v_i + \partial_i v_j - \frac{2}{3}\nabla\cdot\vec{v}\delta_{ij}) + \zeta\nabla\cdot\vec{v}\delta_{ij}$$

   where p is the scalar pressure and η and ζ are the coefficients of viscosity. Since there is no experimental or theoretical information on this point, and since this form is the simplest possible one for a fluid, we shall adopt it for the time being. Whereas ζ is completely unknown, there are estimates on η based on fission calculations. The latest estimate[5] is $\eta \approx 0.03\ \hbar\ \mathrm{fm}^{-3}$. This yields a Reynolds number of

$$\mathrm{Re} = \frac{m_o \rho v d}{\eta} \approx 270\ \frac{v}{c}$$

   where $\rho \approx 0.17\ \mathrm{fm}^{-3}$, $d \approx 10$ fm was used to characterize a nuclear collision. The classical limit for the transition to turbulent flow is for Reynolds numbers of the order of a thousand, so that we are well below this limit. Since a strong dependence of η on temperature cannot be excluded, however, the possibility of turbulence cannot now be dismissed definitely.

3. Thermoconducting or not? -- On the problem of the

thermoconductivity of nuclear matter, there is even less definitive knowledge than on the viscous properties. The calculation of the coefficient of thermoconductivity κ based on a Fermi gas model[6] yields, in the low temperature limit ($kT \ll \varepsilon_F$),

$$\kappa = \frac{7}{48\,\pi\sqrt{2}}\,\frac{\varepsilon_F^{3/2}}{m_o^{1/2}}\,\frac{1}{T}\,\frac{1}{Q_1}\quad,\quad Q_1 \simeq 2.17\ \mathrm{fm}^2$$

$$\eta = \frac{4}{15\,\sqrt{2}\,\pi^3}\,\frac{\sqrt{m_o}\,\varepsilon_F^{5/2}}{k^2T^2}\,\frac{1}{Q_2}\,,\ Q_2 \simeq 1.06\ \mathrm{fm}^2.$$

It should be noted that both quantities become infinite near $T = 0$, which is improbable for nuclei because of their superconducting behaviour near the ground state. (For a more detailed discussion of these problems, see ref. 7.) To get an idea of the importance of thermal conduction, one may compute the Prandtl number

$$Pr = \frac{Cp\eta}{\kappa} = \frac{35}{32}\,\frac{Q_2}{Q_1} \simeq 2$$

where the heat capacity at constant pressure $Cp = \frac{\pi^2}{2}\,k^2T^2/m_o\varepsilon_F$ for a Fermi gas was used. The product of the Reynolds and Prandtl numbers measures the ratio of convective heat transfer to thermal conduction. In our case we have

$$Re\cdot Pr \simeq 500\,\frac{v}{c},$$

so that at moderate velocities convective heat transfer should dominate, at least as far as the pure Fermi gas model is accurate. Since the situation is by no means conclusive, and to allow for heat conduction in model calculations is not expensive, it seems best to provide for that possibility.

IV. Validity of the Fluid Model

There has been some discussion in recent years as to the validity of a fluid dynamical description for the collision of two pieces of nuclear matter[3,8-9]. All of the arguments found, whether presented in favor of or against the fluid model, seem to indicate that the physical quantities concerned are just at the borderline of validity of fluid dynamics. Because of this and of the possibility of additional physical effects like pion condensation, which may change the arguments entirely[10], it may be best to try to use a comparison of experimental data with the model results to obtain information on the validity of the assumptions made. Let us therefore just glance at the basic criteria

and elementary estimates of their validity:

1) Validity of continuum description

"There should be a large number of microscopic degrees of freedom in each volume of macroscopic dimensions" -- In a heavy-ion reaction we may have several hundred nucleons, but only on the average one in a cube of size $(2\ \mathrm{fm})^3$. It thus seems doubtful whether a fluid dynamical description could give details of that scale.

2) Local equilibrium

"The mean free path of the microscopic particles should be small compared to the macroscopic scale" -- Estimates using the free nucleon-nucleon cross section[3] indicate a mean free path of the order of 3 fm, which is only five to ten times smaller than the size of the compound system. This value is for ~ 250 MeV per nucleon; because of Pauli exclusion effects, it increases for lower energies and because of the diminishing nucleon-nucleon cross section also at higher energies.

Barring unknown effects like pion condensation, etc., the fluid dynamical model thus should describe at most the larger-scale effects in a collision. However, one should not forget that the basic quantum mechanical description bears a close resemblance to fluid mechanics[11], and suitable constitutive equations could conceivably make fluid dynamics a viable description in spite of its possible non-validity in the classical sense presented above.

One final aspect of this is whether, if the collision situation does not lead to almost instantaneous equilibration of the two colliding fluids to form one thermally excited mixed fluid, where all the directed motion of the initial system has been transformed into random thermal motion, one might not be better off describing the two ions as made up of two distinguishable kinds of fluid that are allowed to interpenetrate interacting via a drag force that will eventually force formation of one single fluid at equilibrium. Some work done by the Los Alamos group in this "two-fluid" model[4] will be discussed later. One should note, however, that the one-fluid model does not require instantaneous equilibration with infinitely narrow shock fronts; it is known empirically that the macroscopic Navier-Stokes equations work surprisingly well in the description of the internal structure of shock fronts spread over several mean free path lengths.

V. Definition of the Model

In the non-relativistic case the equations of motion used for the fluid-dynamical model are the Navier-Stokes equations, which describe the conservation of particle number,

$$\frac{\partial \rho}{\partial t} + \nabla\cdot(\rho\vec{v}) = 0,$$

momentum,

$$\frac{\partial}{\partial t}(m\rho\vec{v}) + \nabla\cdot(m\rho\vec{v}\vec{v}) = -\nabla\cdot\overleftrightarrow{S} - \rho\nabla V$$

and energy,

$$\frac{\partial}{\partial t}(\rho E) + \nabla\cdot(\rho E\vec{v}) = \nabla\cdot(\kappa\nabla T) - \nabla\cdot(\overleftrightarrow{S}\cdot\vec{v}) - \rho\vec{v}\cdot\nabla V.$$

To complete this set of equations, a number of constitutive equations are needed, viz. the stress tensor $\overleftrightarrow{S}$, the temperature T and the potential V have to be given in terms of $\rho(\vec{r},t)$, $\vec{v}(\vec{r},t)$, and $E(\vec{r},t)$.

To this purpose, we investigate the internal energy per particle of nuclear matter, $\omega(\rho,\sigma)$, where $\sigma(\vec{r},t)$ is the entropy density. ω is related to the total energy per particle E via

$$E = \frac{1}{2}mv^2 + \omega(\rho,\sigma).$$

Thus E determines the magnitude of ω, and standard thermodynamic relations then give the pressure

$$p = \rho^2 \left.\frac{\partial \omega}{\partial \rho}\right|_{\sigma}$$

and the temperature

$$T = \left.\frac{\partial \omega}{\partial \sigma}\right|_{\rho}.$$

The stress tensor is then completed with the Newtonian viscosity as given in Chapter III.

It still remains to fix the functional form of $\omega(\rho,\sigma)$. Since little is known about its behaviour for ρ distinct from the equilibrium density of infinite unclear matter, and for any non-zero σ, one has to proceed with a simple assumption about ω. The choice made by both the Los Alamos and Oak Ridge groups is to split up ω into a ground state (zero-entropy) part ω_0 and a thermal part,

$$\omega(\rho,\sigma) = \omega_0(\rho) + \omega_1(\rho,\sigma).$$

ω_0 is expressed as a polynomial in $\rho^{1/3}$:

$$\omega_0(\rho) = \sum_{i=2}^{n} a_i \rho^{i/3}.$$

In our case, n was taken to be 5, and this allows the determination of the a_i's in terms of the equilibrium density, the equilibrium binding energy per particle, and the incompressibility at equilibrium[12].

For $\omega_1(\rho,\sigma)$, the expression for a Fermi gas at low temperatures is used:

$$\omega_1(\rho,\sigma) = \left(\frac{6}{4\pi}\right)^{2/3} \frac{\hbar^2 c^2}{m^{*} c^2} \sigma^2 \rho^{2/3}.$$

The functional form of ω_1 already determines the maximum non-relativistic shock compression ratio as 4. Relativistically, however, there is no limit on compression ratios obtainable in a shock front[13,14].

Figure 1 shows the binding energy per nucleon, the pressure, and the speed of sound as functions of the nucleon density for an equation of state of the type considered, and at zero entropy. Note that, since below equilibrium density nuclear matter tends to contract rather than to expand, the pressure is negative in this range. Also, sound propagation is possible only at densities where $\partial p/\partial\rho\big|_{\sigma} > 0$, i.e. where matter is stable with respect to density perturbations. Thus, there is no speed of sound at low densities.

Finally, the potential V in the equations of motion is a sum of a Coulomb potential V_c determined via

$$\nabla V_c(\vec{r}) = -4\pi \left(\frac{Ze}{A}\right)^2 \rho(\vec{r})$$

from the nucleon density (equal spatial distributions of protons and neutrons assumed), and a Yukawa part V_y, given by

$$\nabla V_y(\vec{r}) - \alpha^2 V_y(\vec{r}) = -4\pi\beta\rho(\vec{r}).$$

The Yukawa potential has the important advantage of allowing ground states with a non-sharp surface. In the absence of such a potential, equilibrium is guaranteed by the zero pressure at equilibrium matter density, which agrees with the surrounding vacuum pressure on a sharp surface. The Yukawa potential smoothens the surface density. A realistic surface thickness was obtained with the parameters $\alpha = 2.1$ fm^{-1} and $\beta = -280$ MeV fm.

In relativistic calculations, such as done by the Los Alamos group,

the inclusion of potentials causes severe problems, most notably the retardation effect, which would complicate the calculation immensely. Therefore, potentials are not used in those calculations. Since their main advantage is to create a smooth surface, their omission is not expected to be critical at bombarding energies in the 100 MeV to 1 GeV per nucleon range.

VI. Remarks on Numerical Solutions

The use of a purely numerical finite-difference solution to the fluid flow equations may at first seem somewhat of an overkill with its large requirements of computer and programmer time. However, there are important advantages to be gained:

1) Numerical accuracy is the only restriction on the type of solution allowed. There are no additional assumptions about the dynamical behaviour of the system aside from the basic equations of motion and constitutive equation. In particular, there is no restriction on the surface shape, local compression zones, geometry of shock waves, etc.

2) The model can be changed easily; e.g., it is extremely easy to vary the equation of state.

The main drawbacks are that the procedure is very expensive and that the advantages of more analytic solutions are lost; e.g., the dependence of the collision result on parameters such as viscosity or even the impact parameter is not transparent. However, one of the most effective uses of the fully numerical solution might be to find more restricted descriptions like a selection of the most important surface modes. Only a full study of the numerical solution in a wide range of collision situations will provide enough data to extract such information.

VII. Comparison with TDHF

Since a comparison of fluid dynamics and TDHF has been given in an earlier paper in these proceedings[15], I shall only add some late results here, which may help to clarify the situation.

As fluid dynamics is based on the assumption of instantaneous local equilibrium, it is interesting to see whether TDHF approaches local equilibrium during a collision. For this purpose, we have studied the Wigner function for a one-dimensional TDHF collision. In terms of the one-particle density matrix

$$\rho(\vec{r},\vec{r}') = \sum_{i=1}^{A} \psi_i(\vec{r})\psi_i^*(\vec{r}')$$

one may define the associated Wigner function as

$$\omega(\vec{r},\vec{k}) = C \int d^3 r' \; e^{-i\vec{k}\vec{r}'} \; \rho(\vec{r} + \tfrac{1}{2}\vec{r}', \vec{r} - \tfrac{1}{2}\vec{r}')$$

with a constant C (arbitrary for our purpose). Its properties may be summed up as follows:

1) $\omega(\vec{r},\vec{k})$ is a real function of $\vec{r}$ and $\vec{k}$. It is the closest quantum-mechanical counterpart to the classical phase-space distribution function. Because of the uncertainty principle, it is not quite a probability density itself (ω may become negative!) but its integral over a volume in phase space big enough not to violate the uncertainty restriction may be interpreted as a probability. $\int f\omega \, d^3r \, d^3k$ is the expectation value of any function f of $\vec{r}$ or $\vec{k}$ alone, whereas e.g. $\int \vec{r}\cdot\vec{k}\omega d^3r d^3k$ yields the average of the quantum-mechanical expectation values of $\vec{r}\cdot\vec{k}$ and $\vec{k}\cdot\vec{r}$.

Figure 2 shows the results for a collision of two slabs of thickness 2 fm^{-2}. The lower part of each small graph shows the density at a given time, and the upper part contains the Wigner function as a function of k at the center of the collision. Only at the beginning of the collision we show instead the Wigner function at the center of each slab, giving an idea of the equilibrium shape and the relative displacement due to the motion of the slabs. To guide the eye, this curve is then repeated as a dashed line in each graph, but centered at k = 0, since the center of a symmetric collision should have an equilibrium distribution around k = 0. Clearly, the distribution comes closer to something resembling equilibrium in the course of the collision (because of higher density and excitation, it should be wider than the dashed line, though), albeit there is always a division into two humps. However, in the final stage the sides of the distribution have been depleted, because the fast wave functions literally have moved out to the sides to form the fragments. Although these data do not cover all aspects of the equilibration process yet, it seems clear that TDHF does not exhibit strong enough equilibration to resemble the fluid behaviour. The most striking case is the head-on collision of two heavy ions, where TDHF lets the two nuclei pass through each other at higher energy, whereas fluid dynamics will always generate a hot shock zone at the center of the collision that is a very effective dissipation mechanism.

VIII. Relativistic Fluid Dynamics

Let us now take a look at the important results of the Los Alamos group for the relativistic case[3]. The relativistic equations of motion are practically identical with those given in Chapter V without viscosity and thermoconduction; it is mainly in the constitutive equations that relativity plays a role. The equation of state is defined in the local rest frame and takes the form

$$E = m_o + a\left(\frac{\rho}{\rho_o}\right)^{2/3} - b\left(\frac{\rho}{\rho_o}\right) + c\left(\frac{\rho}{\rho_o}\right)^{5/3} + W_1(\rho,\sigma)$$

with W_1 a Fermi-gas thermal energy similar to the one given in Chapter V. The pressure can be defined straightforwardly, and the transformation to the lab frame (primed) is as follows:

$$\rho' = \gamma\rho$$

$$\vec{M}' = \gamma^2 (\rho E+p)\vec{V}'$$

$$\rho'E' = \gamma^2 (\rho E+p) - p.$$

Here $\gamma = (1 - v'^2/c^2)^{-1/2}$, as usual. The need to go forth and back between lab and rest frame introduces some numerical difficulties but no essential problems[2].

The numerical method employed to solve the equations is the Particle in Cell (PIC) method[16]. In this method the fluid density is represented by point particles of given mass (no relation to the nucleon mass) moving in a finite-difference mesh, represented by cells in space, under the influence of the fluid pressure. The fluid aspect enters the method through the averaging over one cell, e.g. the density in a cell is simply obtained by counting the number of particles in the cell, and this density then determines the pressure. The point particles are thus purely fictitious numerical devices, and one should bear this in mind when interpreting the results that may give the impression of a classical interacting particle model as reported elsewhere in this conference[17].

Figure 3 shows the time dependence of the density as represented by the distributions of the numerical particles, as a function of time for different impact parameters in the $^{20}Ne + ^{238}U$ system at 250 MeV per nucleon. The plots are done in the lab system, so that the incident ^{20}Ne-nucleus appears relativistically contracted. Also, because of the absence of potentials, both nuclei have sharp surfaces and a constant density inside.

For the near-central collision (labeled 0.1) the ^{20}Ne nucleus penetrates into the target nucleus and sets off a strong shock wave (clearly visible at 5.1×10^{-23} sec). Subsequently, most of the energy of the projectile is thermalized and the nucleus expands in response to the high thermal pressure. The calculations do not allow for the formation of a residual nucleus since there is no attractive potential and also negative pressures are set equal to zero. Tests allowing for negative pressure yielded small clusters in the final state, but these did not appear to be physically meaningful[2].

For the intermediate impact parameter (0.5) the behaviour is similar. The main difference is that the projectile is not completely absorbed in the target, but part of it flies off, giving a far from isotropic behaviour in the final state. Both projectile and target have been excited so strongly that they expand rapidly.

The peripheral collision (0.9) shows a different behaviour. A small part of the projectile is sheared off by the contact with the target nucleus and sets waves running through it, which, after thermalization, will again cause the target to expand. The projectile itself is also excited. (Its darker shading at $t = 13.5 \times 10^{-23}$ sec does not indicate a higher density; initially the numerical particles were aligned and several of them appeared as one dot only when viewed from above.)

To make a comparison with experiment, one may look at the final state, which always contains an expanding cloud of nucleons, and compute the expected angular distribution, interpreting the fluid density as a probability density for nucleons. Averaging over impact parameters, one then obtains a differential cross section for outgoing nucleons. Under the assumption of equal behaviour of protons and neutrons, a comparison can finally be made to proton-inclusive cross sections (fig. 4). Apparently the general trend of the data is well reproduced, but there is a definite quantitative discrepancy both at very forward angles, where the theoretical cross section is too small, and at backward ones, where it is too large.

This shift of the theoretical yield to backward angles compared to experiment seems to indicate that there is "too much interaction", i.e. too much forward momentum is converted into transverse momentum. Since the assumption of local equilibrium implies a fast conversion of directed into random momentum, this assumption may have to be modified, at least for this energy range.

Thus, the Los Alamos group recently did some two-fluid calculations[4]. The basic concept of the two-fluid model is to describe the two nuclei as distinct fluids which are allowed to interpenetrate without losing their separate identities, but do interact via a drag force, which is proportional to the relative velocity with a strength factor depending on its magnitude and on the density. The strength is adjusted such as to reproduce the stopping length expected from free nucleon-nucleon cross sections.

One problem with this approach is that one would like to have a transition to the regular one-fluid description, whenever the relative velocity of the two fluids becomes small. In this case, for example, there should be only one pressure depending on the total density instead of the two partial pressures. In the calculations this was achieved by interpolation in the relative velocity, but if comparison to experiment makes more refined two-fluid calculations desirable, this aspect deserves some study for a more cogent solution.

The first results of the model are encouraging though they do not appear to completely solve the problems. The cross section in the backward direction is lowered to much better agreement with experiment, but in the forward direction there is no definite improvement. It should be kept in mind, however, that the parameters of the model have not been fitted to these data, but have been taken over from different areas of nuclear physics, so this result may be regarded essentially as a parameter-free calculation.

IX. Low-Energy Results

The calculations by our own group in Oak Ridge have just gotten off the ground, so that we can show only sample results at present.

We utilize the full set of equations given in Chapter V, including viscosity and potentials, but for the non-relativistic case. The numerical method employed is the "flux-corrected transport" method developed by Boris and Book at NRL[18]. Although this method eliminates the most severe problem facing the numerical fluid dynamicist, instability, even in the presence of very steep shock waves, there were still many technical problems, notably the transition to zero density in the surrounding vacuum and the short range of the Yukawa force of < 0.5 fm, which forced us to go to a spatial mesh finer than that limit. In fact, many test calculations were done with a coarser mesh of 0.8 fm separation, and these turned out to be quite adequate in qualitative results, but showed unphysical effects such as squarish deformations in detail. Since these calculations are still quite cheap, they may well be useful for exploring the general behaviour of the system as a function of the various parameters.

For now, however, let us take a glance at the first high-accuracy results obtained with a newly developed code[19]. It works on a cartesian mesh of 64 × 64 × 33 points with a spacing of 0.4 fm, and the physical situation corresponds to a collision of $^{16}O + ^{16}O$ at a relative velocity of 0.2c (corresponding to 18.8 MeV per nucleon in the lab), with an impact parameter of 2 fm. The type of nucleus does not really enter drastically, only the relative surface thickness and the Coulomb effects will change smoothly with mass and/or charge number. The equation of state employed corresponded to an incompressibility of 134 MeV, so that the initial Mach number for this collision is 1.54 for the regions of equilibrium density. It is thus expected that the flow will show the typical phenomena of supersonic flow -- strong compressive effects, shock waves, and the lack of upstream propagation of information.

Figure 5 shows the system close to the initial state. The lower two subgraphs show the density and velocity field viewed facing the collision plane (the density graph actually shows the integral of the density in that direction to give an impression of total thickness, whereas the velocity vectors are plotted in the scattering plane. The two additional graphs show the integrated density from above (upper

left) and from the right (upper right) relative to the scattering plane plot already discussed.

Figure 6 shows the situation at t = 21.6 fm/c. At the center a shock front has formed with very small velocities, and matter has already started to flow out to the sides from there. The rest of the initial nuclei, however, is quite undisturbed, as is characteristic of supersonic flow (there are small internal motions caused by the imperfection of the initial equilibrium).

Figure 7 at 37.1 fm/c has a small part of the initial nuclei still streaming into the collision zone, but there is also now a strong current to the sides. Note that matter from both initial nuclei mixes in each outgoing direction. At the same time, however, as is visible in the top two graphs, the systems expand perpendicular to the scattering plane and thus seem to flatten into a pancake shape.

This development is quite striking in the final fig. 8 at 76.7 fm/c. The system is now very elongated in the scattering plane with the main direction of motion outward. If one had only this viewpoint, one might expect it to fission soon, but the fully 3-dimensional representation shows that it is rather a very flat disk.

At this point, we had to stop the calculation. Whether it will rebound into a prolate shape (as observed in ref. 7), or has lost so much energy that it may rather break up in the oblate form, cannot be decided yet. The upper left graph in fig. 8 seems to show a slight necking-in, but it cannot yet be said whether this will lead to fission.

This, however, leads to an important point on the interpretation of the final state. It is well known from fission calculations[7,20] that the fluid-dynamical model likes to form very long necks. Although it is expected that in the present compressible calculation low-density areas will break up spontaneously because of the negative pressures, the final state may still be quite diffuse and require a long time before final breakup. If this should happen in the calculations, we shall have to try to add some extraneous arguments to be able to extract the final masses, scattering angles, etc. Also, one would have to distrust calculational results that show, e.g., a flat disk with thickness a fraction of a nucleon diameter. Thus, all results should be scrutinized using physical intuition before being accepted as predictions of the model.

The results of a few additional collisions at different impact parameters and relative velocities are shown in table 1. E^* is the thermal energy reached in the final state (in those cases where the system had not separated again, this number is probably still meaningful, because most of the dissipation of energy takes place in the shock waves, and only a few MeV are dissipated later). The ratio of densities gives the maximum compression reached; these numbers are, of course, below the theoretical maximal ratios given in ref. 14.

X. Conclusion

The results presented in this paper have demonstrated that three-dimensional fluid-dynamical calculations are feasible and can be done with sufficient accuracy. The Los Alamos group has already done a comparison to experimental data for proton-inclusive spectra, whereas our calculations are not yet at that stage. Additional experimental data that may provide useful testing grounds are the fusion cross sections and, as far as they are reducible to classical deflection functions, differential cross sections for deep-inelastic collisions at lower energies. One problem one may encounter is that all of these data may not give sufficient information to distinguish between models; e.g., the fusion cross section really tells only the critical impact parameter and can certainly be fitted with the freedom available in fluid dynamics.

In our own calculations, one of the first things we would like to try in the future is to use a more complicated equation of state with a density isomer, and to see how that affects the collision. Among other possible extensions one might think about treating protons and neutrons, or the different spin states, separately, thus again going over to a two- or multi-fluid theory. Also, it is relatively easy to describe the production of additional particles, such as pions, or the excitation of nucleons, again by a many-fluid approach.

The author wishes to thank Drs. T. A. Welton, C. Y. Wong, and J. R. Nix for stimulating discussions and communication of results.

References

1) A. A. Amsden, G. F. Bertsch, F. H. Harlow and J. R. Nix, Phys. Rev. Lett. 35 (1975) 905.

2) F. H. Harlow, A. A. Amsden and J. R. Nix, J. Comp. Phys. 20 (1976) 119.

3) A. A. Amsden, F. H. Harlow and J. R. Nix, LA-UR-77-31.

4) A. A. Amsden, A. S. Goldhaber, F. H. Harlow and J. R. Nix, to be published.

5) K. T. R. Davies, R. A. Managan, J. R. Nix and A. J. Sierk, LA-UR-77-409.

6) S. Tomonaga, Z. Physik 110 (1938) 573.

7) C. T. Alonso, Proc. of the International Colloquium on Drops and Bubbles, Vol. I, p. 139 (California Institute of Technology and Jet Propulsion Laboratory, 1974).

8) M. I. Sobel, P. J. Siemens, J. P. Bondorf and H. A. Bethe, Nucl. Phys. A251 (1975) 502.

9) G. F. Bertsch, Phys. Rev. Lett. 34 (1975) 697.

10) V. Ruck, M. Gyulassy and W. Greiner, Z. Physik 277 (1976) 391.

11) E. Madelung, Z. Physik 40 (1926) 332.

12) K. A. Brueckner, J. R. Buchler, R. C. Clark and R. J. Lombard, Phys. Rev. 181 (1969) 1543.

13) H. G. Baumgardt, J. U. Schott, Y. Sakamoto, E. Schopper, H. Stöcker, J. Hofmann, W. Scheid and W. Greiner, Z. Phys. A273 (1975) 359.

14) C. Y. Wong and T. A. Welton, Phys. Lett. 49B (1974) 243.

15) J. W. Negele, these proceedings.

16) A. A. Amsden, LA-3466.

17) A. Bodmer, these proceedings.

18) J. A. Maruhn and T. A. Welton, to be published.

19) J. P. Boris and D. L. Book, J. Comp. Phys. 20 (1976) 397.

20) See, e.g., L. Wilets, "Theories of Nuclear Fission", Clarendon Press, Oxford, 1964; or R. Vandenbosch and J. R. Huizenga, "Nuclear Fission", Academic Press, N.Y., 1973.

Table 1

Summary of Sample Collision Studies

v_{init}/c	b	$E_{kin}^{(init)}$	E^*	$(\rho/\rho_0)_{max}$
0.1	0.0	37 MeV	28 MeV	1.3
"	2.5	"	13 MeV	1.2
"	5.0	"	6 MeV	1.2
"	6.5	"	4 MeV	1.1
0.2	0.0	146 MeV	66 MeV	1.5
"	2.5	"	61 MeV	1.4
"	5.0	"	30 MeV	1.2
"	6.5	"	9 MeV	1.1
0.4	0.0	586	330 MeV	2.1
"	2.5	"	306 MeV	2.1
"	5.0	"	138 MeV	2.0
"	6.5	"	39 MeV	1.1

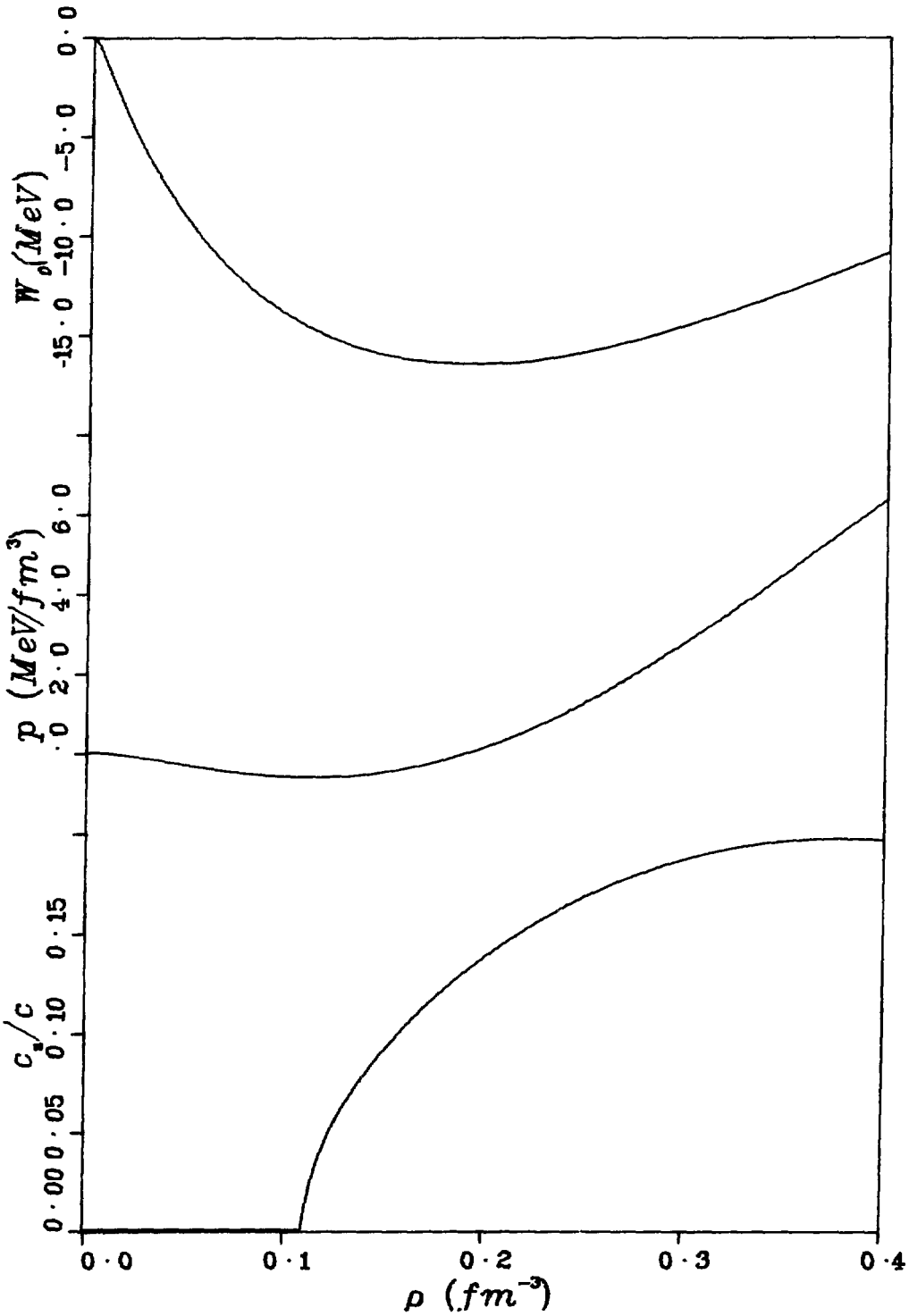

Fig. 1. The Equation of State

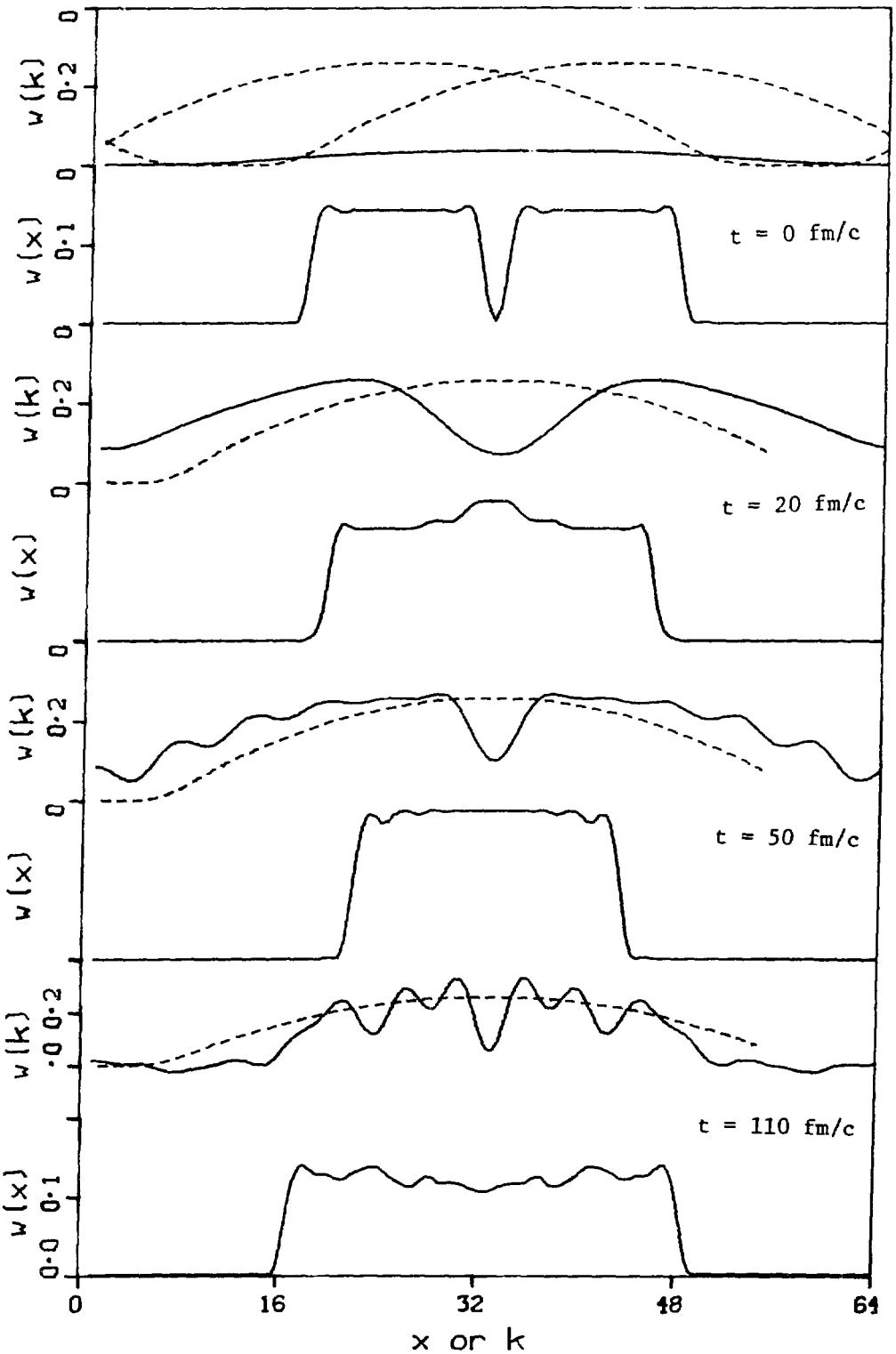

Fig. 2. The Wigner Function in TDHF

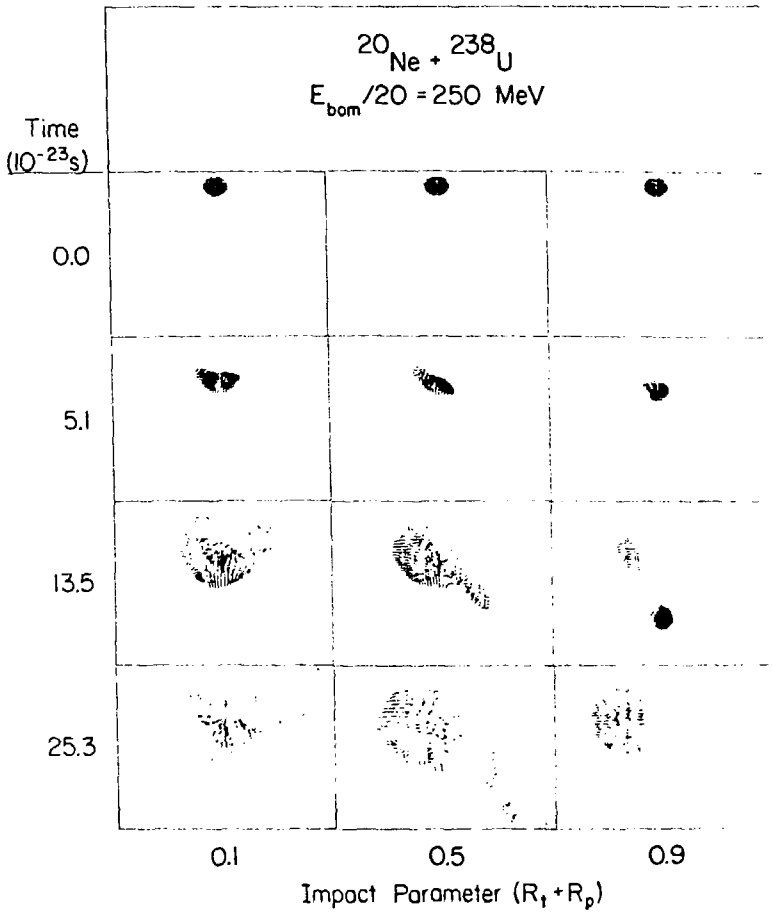

Fig. 3

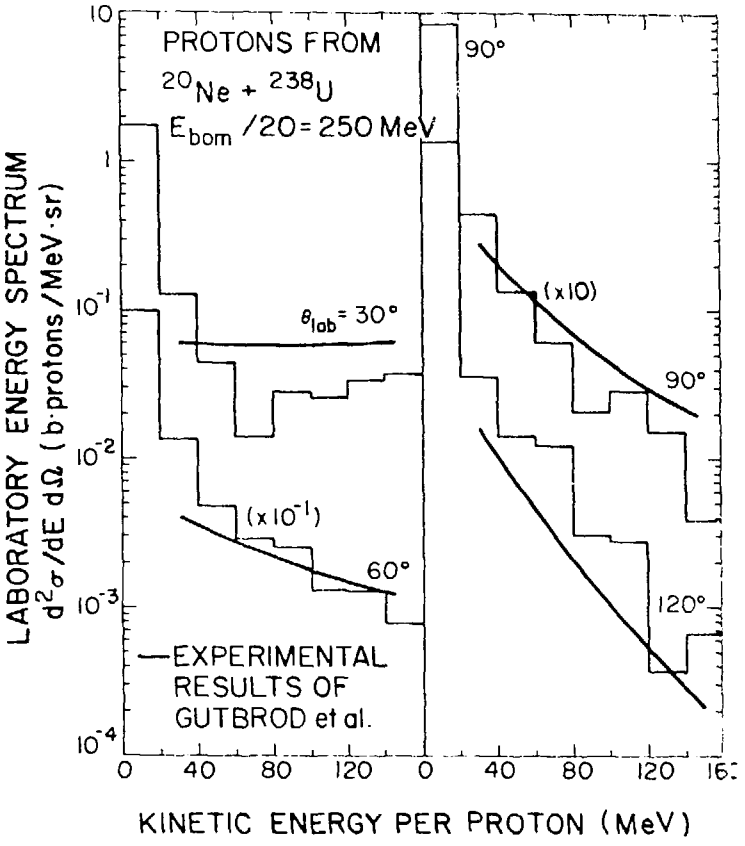

Fig. 4

Results from Ref. 3

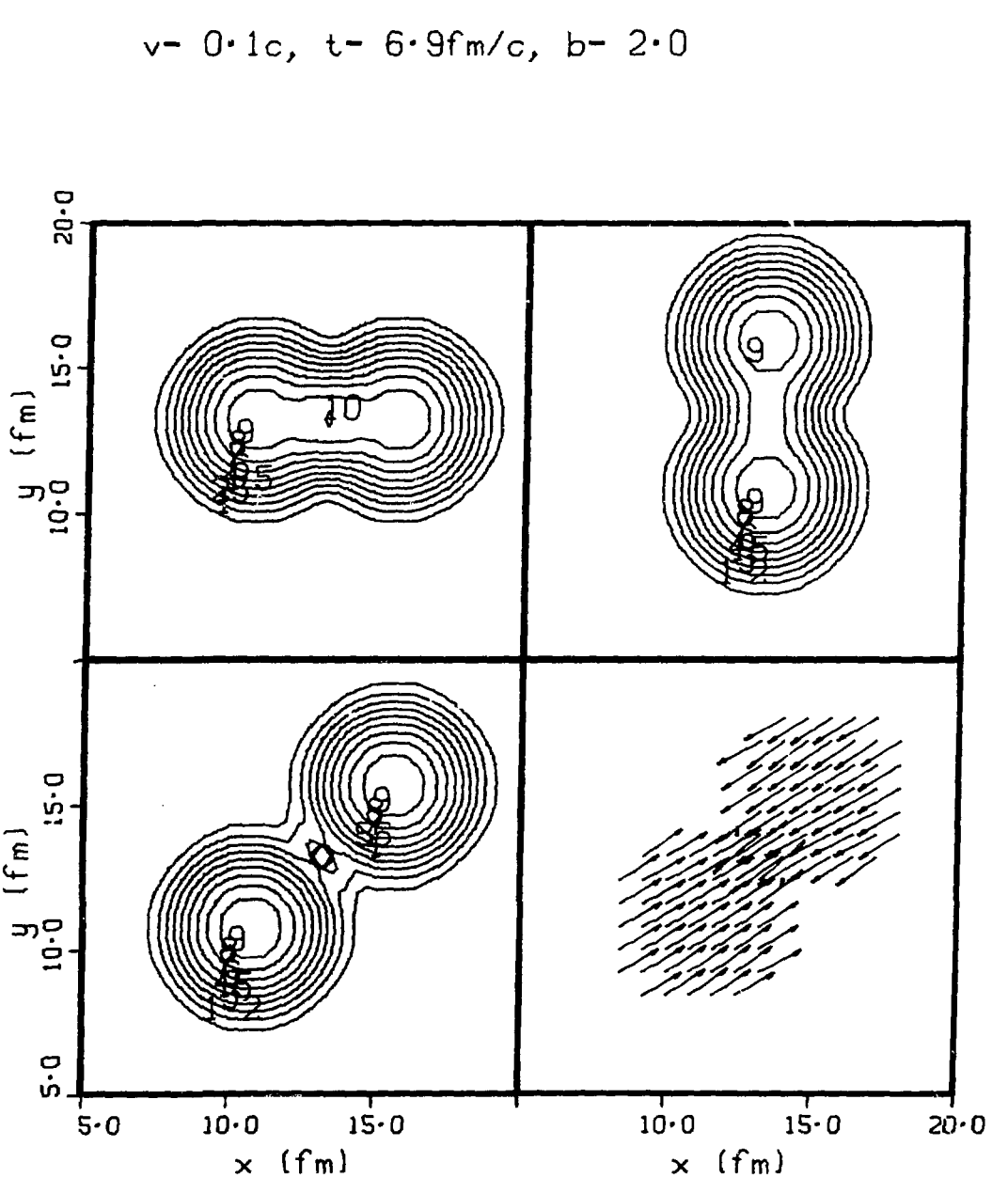
v- 0·1c, t- 6·9fm/c, b- 2·0
20·0
15·0
10·0
y (fm)
10
9
9
9
15·0
10·0
5·0
y (fm)
5·0
10·0
15·0
x (fm)
10·0
15·0
20·0
x (fm)

Fig. 5

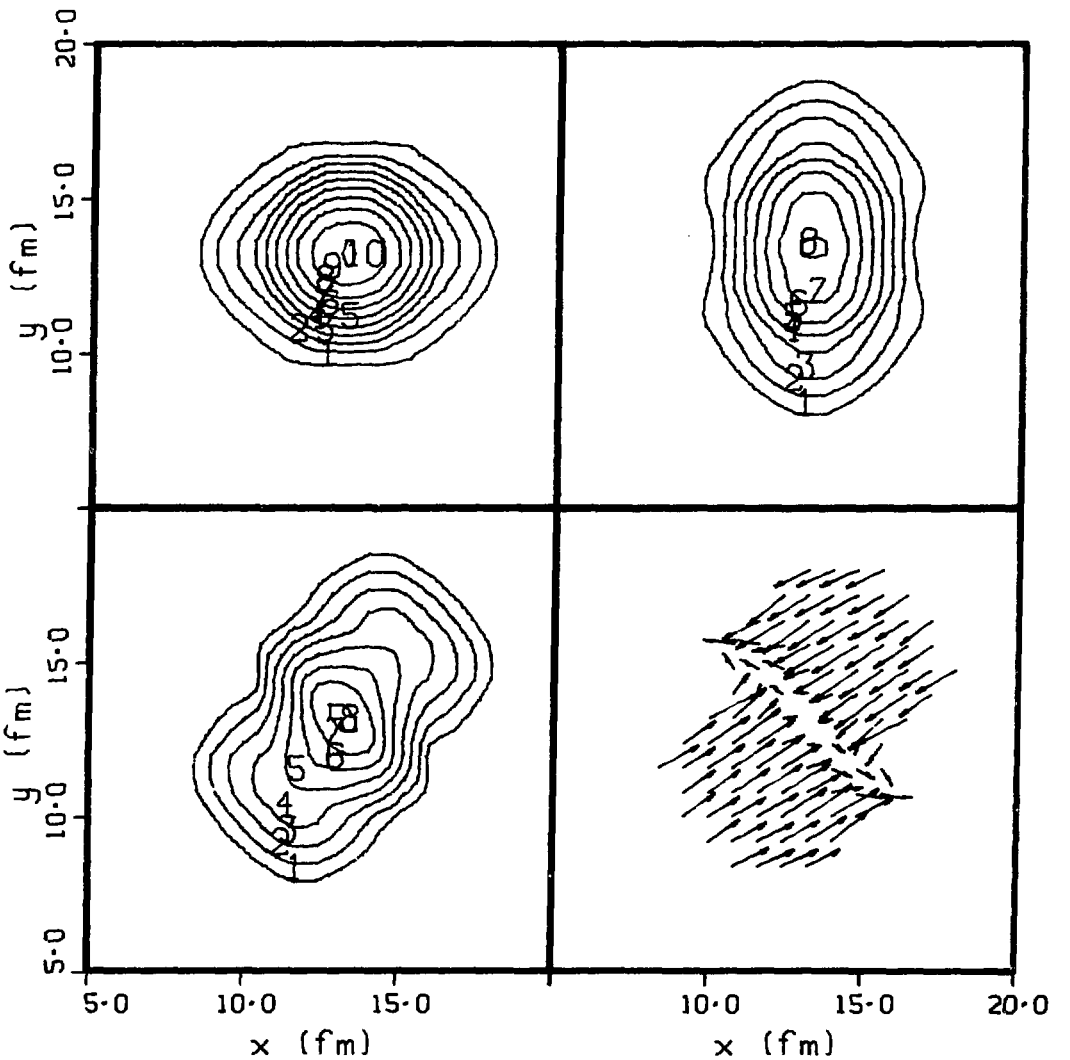

Fig. 6

v= 0·1c, t= 37·1fm/c, b= 2·0

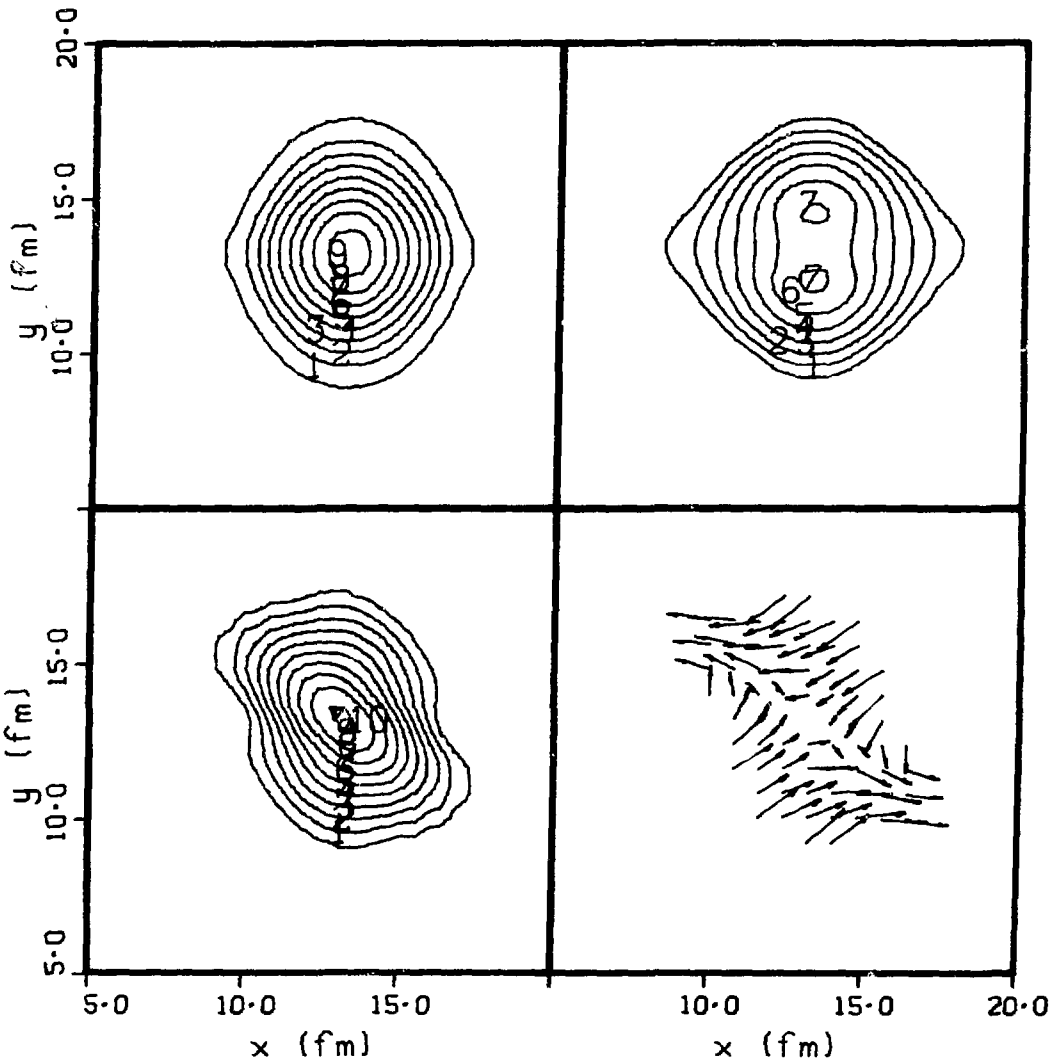

Fig. 7

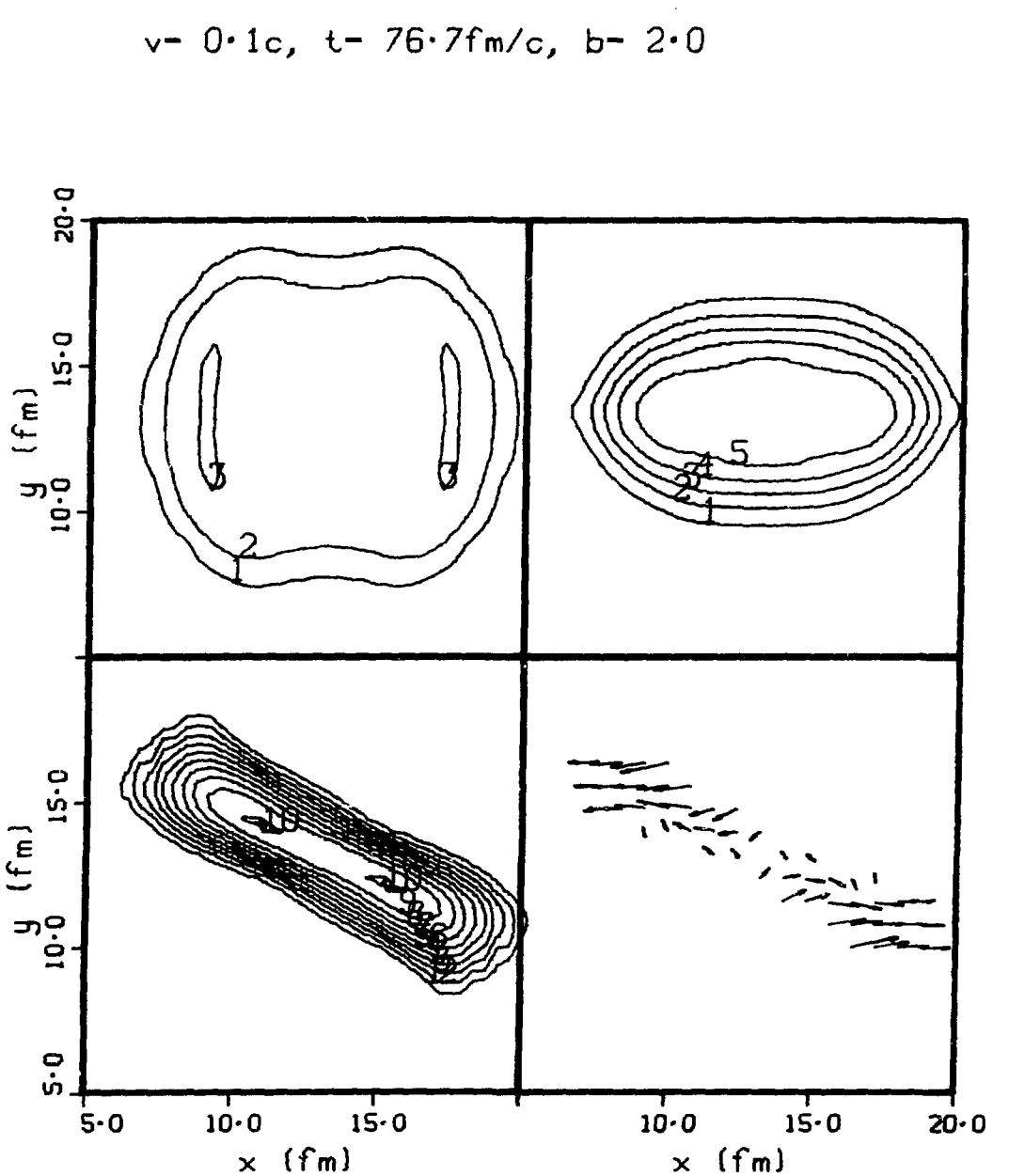
v- 0·1c, t- 76·7fm/c, b- 2·0
20·0
15·0
10·0
y (fm)
5·0
15·0
10·0
y (fm)
5·0
10·0
15·0
x (fm)
10·0
15·0
20·0
x (fm)

Fig. 8

ENERGY DISSIPATION, MASS DIFFUSION AND INTERACTION TIMES FOR HEAVY ION COLLISIONS*,†

J.R. Huizenga, W.U. Schröder**, J.R. Birkelund and W. Wilcke

Departments of Chemistry and Physics and
Nuclear Structure Research Laboratory***
University of Rochester, Rochester, New York 14627

ABSTRACT

Correlations of experimental observables with kinetic energy loss and fragment mass for damped heavy ion reactions are emphasized in this paper. Angular-momentum-dependent interaction times are deduced giving a time scale for the evaluation of nucleon diffusion coefficients. The energy dissipated per nucleon exchange in Kr- and Xe-induced reactions is shown to decrease with increasing kinetic energy loss. These results are compared with predictions of a one-body dissipation mechanism and microscopic transport theory for heavy ion collisions. The relative decrease of energy dissipation due to nucleon exchange with decreasing bombarding energy is a new experimental feature that is unaccounted for by the above theories.

I. INTRODUCTION

There has been a large number of experimental studies of damped reactions involving a range of targets and projectiles.[1] The characteristic experimental features of heavy ion collisions which define this new reaction mechanism are:

a. Binary Process -- The damped reaction mechanism produces two massive primary fragments in the exit channel. However, light particles may be emitted from the intermediate system or, after its breakup, from the target-like or projectile-like primary fragments.

b. Energy Loss -- Damping of the initial relative kinetic energy of the target and projectile nuclei resulting in a range of kinetic energies down to the Coulomb energies for charge centers of highly deformed fragments. The broad energy distribution observed in experiments is the most distinctive property of damped reactions.

c. Nucleon Exchange -- Nucleon diffusion occurs during the short time the two nuclei are in contact. For the heavier ion reactions, the fragment mass distributions are peaked in the vicinity of the projectile and target masses.

d. Angular Distributions -- The angular distributions for products with projectile-like masses have properties of a fast peripheral or direct reaction process. The heavy systems usually rotate less than 180 degrees. Substantial sideways-peaking is observed for a number of systems while a forward rising angular distribution is a characteristic feature of other systems.

e. Angular Momentum Transfer -- The primary fragments resulting from a damped collision may have rather large intrinsic angular momenta.

f. Light Particles and γ-rays -- As stated in (a) light particles (e.g., p, n and α particles) may be emitted from the intermediate system or, after its breakup, from the target-like or projectile-like primary fragments. The emission of γ-rays is mainly confined to the final stages of the fragment de-excitation.

In spite of the large number of experimental studies[1] of heavy ion reactions which report one or more of the characteristic features of damped reactions summarized above, only a relatively small number of studies have been performed where correlations of experimental observables, such as kinetic energy loss and fragment mass, are deduced. Hence, these correlations will be emphasized here. Angular-momentum dependent interaction times are deduced from experimental angular distributions. The angular momentum ℓ is related to the experimental kinetic-energy loss assuming the energy loss to increase monotonically with decreasing ℓ, i.e., increasing overlap of the matter distributions of projectile and target. The progressive increase in the variance of the charge distribution as a function of increasing kinetic energy loss is a feature common to all very heavy ion reactions studied so far. A quantitative correlation between the measured variance of the charge distributions and the amount of kinetic energy loss is employed to calculate the kinetic energy loss associated with the exchange of a single nucleon. The energy dependence of this quantity is compared with different theoretical models. Assuming the above time scale, nucleon diffusion coefficients are deduced from experimental fragment charge distributions.

II. ANGULAR, ENERGY AND MASS DISTRIBUTIONS FROM DAMPED REACTIONS

For illustration of the properties of damped collisions, we choose the $^{209}Bi + ^{136}Xe$ reaction which has been studied extensively. Some of the relevant parameters are listed below.

$$E_{lab} = 1130 \text{ MeV}$$

$$E_{c.m.} = 684 \text{ MeV} \approx 1.6 \times E_{Coul}$$

$$\lambda\!\!\!^{-} = 0.019 \text{ fm}; \qquad 2a = 9.4 \text{ fm}$$

$$\eta = Z_1 Z_2 e^2/\hbar v = a/\lambda\!\!\!^{-} = 245$$

$$\theta_{1/4} = 54^\circ \text{ (c.m.)}$$

$$R_{SA} = 15.2 \text{ fm}$$

$$\sigma_R = 2.8 \text{ b}$$

$$\ell_{max} = 484\hbar$$

The angular distribution of all lighter projectile-like fragments[2] in the total kinetic energy window, $300 \leq TKE \leq 650$ MeV, is shown in Fig. 1. The angular distribution peaks at 50° (c.m.) and is relatively narrow in width. There is no orbiting for this reaction, a phenomenon well known for selected lighter ion reactions. The charge distribution of the lighter fragments[2] for the above energy window and the angular range $25 \leq \theta_{c.m.} \leq 75$ is shown in Fig. 2. The drop of the charge distribution beyond symmetry (Z = 70) is due to experimental detection limits Some contributions to the cross section for the lightest Z fragments is due to sequential fission of the heavy damped fragment. The continual range of total kinetic energy damping for the very heavy ion reactions[3] is illustrated in Fig. 3 where the differential cross section in millibarns per MeV of total kinetic energy loss is plotted versus the total kinetic energy loss. Hence, in speaking of damped heavy ion collisions we refer to a wide range of events with energy losses from a few MeV to hundreds of MeV. The kinetic energy loss indicated by each arrow in Fig. 3 corresponds to a final kinetic energy equivalent to the Coulomb energy at the strong absorption radius R_{SA}.

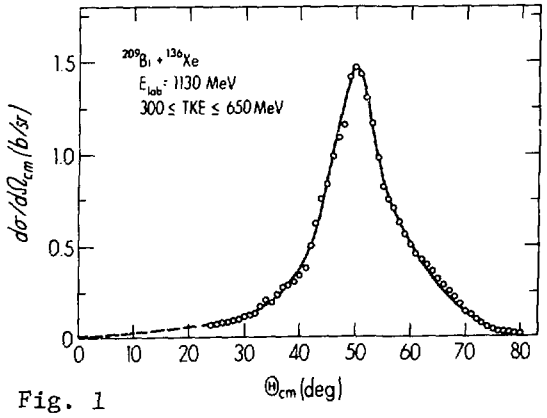

Fig. 1

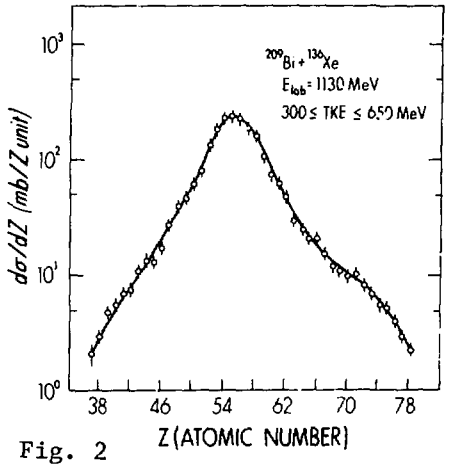

Fig. 2

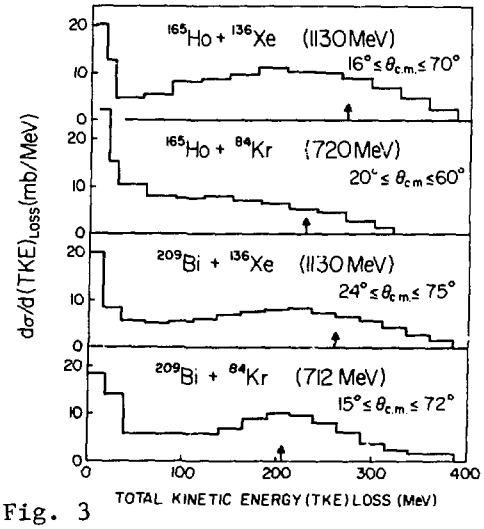

Fig. 3

III. CORRELATION OF EXPERIMENTAL OBSERVABLES IN DAMPED REACTIONS

A. Angular Distributions: Dependence on Mass Exchange and Energy Damping

The angular distributions for damped heavy ion collisions depend on mass (or charge) exchange and energy damping. In Fig. 4 is shown a contour plot of the double-differential cross section $d^2\sigma/d\Omega d(TKE)$ as a function of angle $\theta_{c.m.}$ for the $^{209}Bi + ^{136}Xe$ reaction.[2] Diagrams of this type were first drawn by Wilczyński.[4] For this reaction there is a cross section ridge that moves down in energy at an almost constant angle leading to what is known as strong angular focusing. Depending on the bombarding energy and parameters of the system, the cross section ridge in an energy-angle contour plot may move forward, stay constant or move backward in angle.

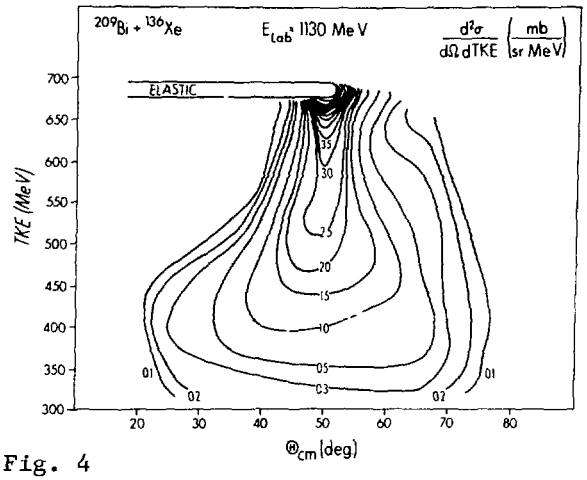

Fig. 4

For some of the lighter systems, an additional ridge at low energies moving backward in angle is observed. This is commonly interpreted as the reflection of the low-energy ridge at negative angles (orbiting).

The angular distributions for fixed TKE bins (50 MeV wide) are shown[2] in Fig. 5. Again one sees that the angular distributions are sideways-peaked for small energy losses and rather flat for large energy losses, although the maximum stays essentially constant at 50° c.m.. The angular distributions for fixed Z bins (3 Z units wide) are displayed in Fig. 6. For fragments near the projectile, the angular distributions are sideways-peaked and become less peaked for fragments far from the projectile. However, it is important to note that the angular distributions for fragments near the projectile change markedly with energy damping in much the same way as illustrated in Fig. 5 for all fragments. This is illustrated in Fig. 7 for Z = 53-55 and energy bins of 50 MeV width.[2] The observed dependence of the angular distribution on the fragment Z is only an apparent correlation which is due to the fact that the energy spectra corresponding to various fragments are somewhat different, as will be discussed below. Hence, the energy loss is a fundamental observable specifying the properties of the reaction. This is also shown in Fig. 8 where the full width at half maximum (FWHM) in the charge distribution is plotted as a

function of $\theta_{c.m.}$ for different final total kinetic energies.[2] Although the FWHM varies considerably for different TKE values, the value of the FWHM for a particular TKE is independent of angle.

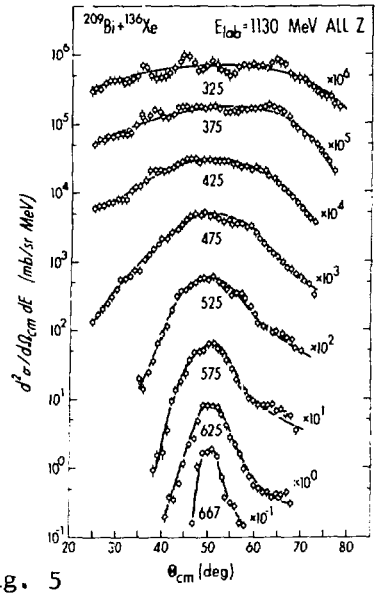

Fig. 5

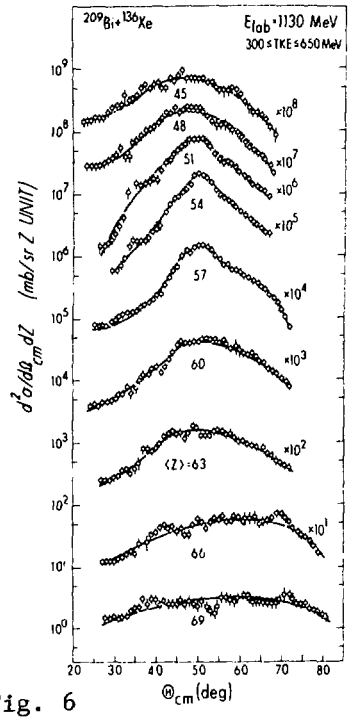

Fig. 6

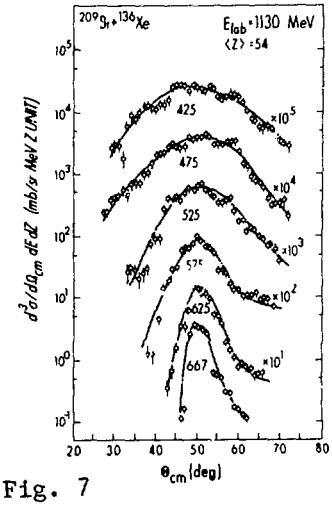

Fig. 7

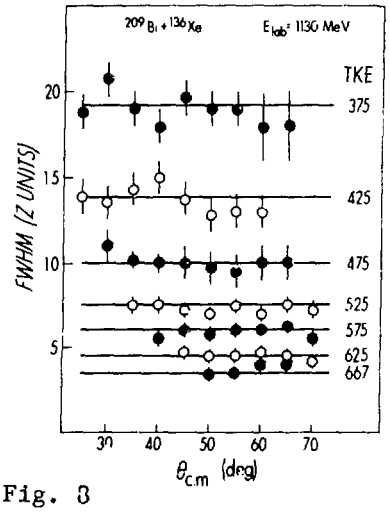

Fig. 8

B. Mass Exchange: Dependence on Energy Damping

There is by now considerable experimental evidence for an intimate correlation between the kinetic energy loss and the angular-momentum dependent interaction time. Hence, it is important to study mass correlations as a function of kinetic energy loss. An alternate parameter to the kinetic-energy loss is the dissipated kinetic energy. The two quantities are related by $E_{diss} = TKE_{loss} + [V_C(f) - V_C(i)]$ and are approximately the same when the differences between the Coulomb energies of the final and initial fragments are small.

The differential cross section $d^2\sigma/dZd(TKE)$ is plotted as a function of total kinetic energy (TKE) for different element bins in Fig. 9 for $^{209}Bi + ^{136}Xe$ reaction. Corrections for the emission of neutrons emitted during the de-excitation of the fragments have also been applied to the data. For Z values near the projectile the spectra contain sizable high-energy components and as Z decreases or increases, the spectra become softer. Hence, the degree of energy damping is a function of the mass of the product. For Z values near the projectile, the spectra contain events of a very wide range of kinetic energies, whereas large net Z transfers are correlated with high degrees of damping. Exit channel Coulomb energies for spherical fragments are indicated by the arrows. It is interesting to notice that (net) stripping and pickup both lead to roughly the same energy spectrum and cross section.

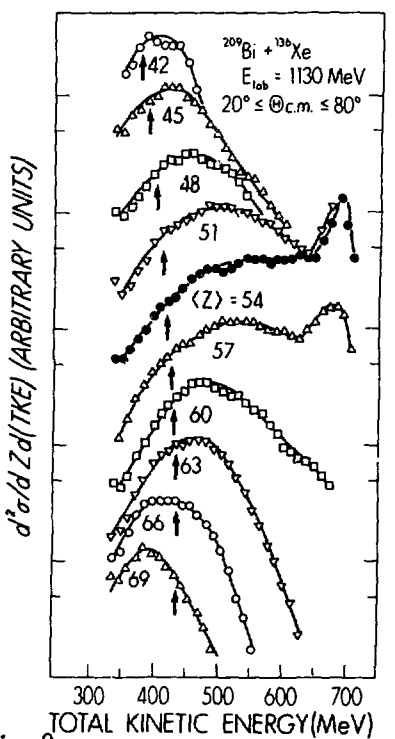

Fig. 9

One of the most informative ways to examine the relationship between the charge (or mass) distribution and the final kinetic energy is a plot of the differential cross section $d^2\sigma/dZd(TKE)$ as a function of Z for different final kinetic energy bins. Such a plot is shown in Fig. 10 where the energy bins are 50 MeV wide. The curves represent gaussian fits to the experimental data. It is readily seen that the width in the charge distribution increases markedly as the kinetic energy decreases. However, the centroid of the charge distribution stays constant at $Z \approx 55$ for a wide range of energy damping.

Such symmetric fragment Z distributions are very suggestive of a diffusive process evolving in time while kinetic energy is lost progressively.

A quantitative correlation between the measured variances of the charge distribution and the amount of kinetic energy loss is shown in Fig. 11 for four different heavy ion reactions.[3] Although the mass distributions are in general angle-dependent, in the case of Xe-induced reactions, the variance is independent of reaction angle for events of the same kinetic energy loss (see Fig. 8). The variance of the charge distribution increases smoothly with increasing total kinetic energy loss. However, the slope of the energy dissipation as a function of variance is largest for small variances and decreases as the variance increases.

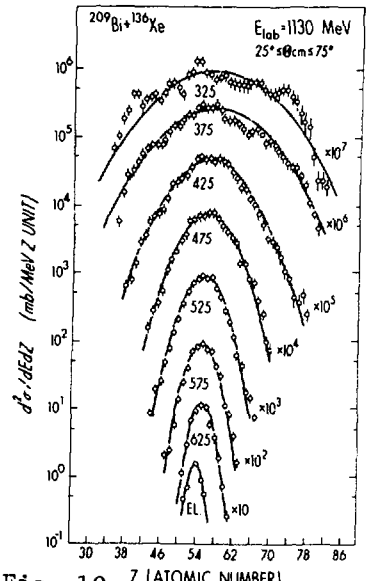

Fig. 10

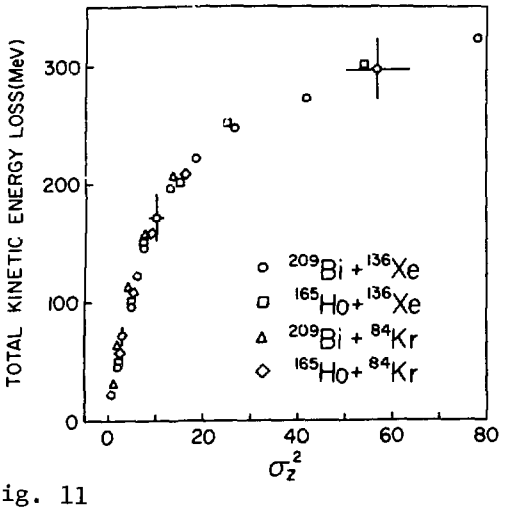

Fig. 11

The observed correlation between energy loss and the variance of the fragment Z distribution is of basic importance for understanding the damped reaction mechanism. Since many reaction channels are open, such reactions are clearly subject to statistical considerations. Regarding nucleon exchange in damped reactions as a random-walk process, the variance of the mass or Z distribution increases as a function of interaction time. Classical dynamical calculations[5,6] suggest that the interaction time increases with decreasing ℓ. The mean rate of nucleon exchange has also to increase with decreasing ℓ because the degree of matter overlap increases. Therefore, different ℓ waves corresponding to different interaction times will certainly lead to different values σ_Z^2 of the variance of the Z distribution. Hence, the σ_Z^2 axis on Fig. 11 represents a macroscopic time or ℓ scale for the damped heavy-ion collisions under consideration. It is conceivable

that in a nucleon exchange process kinetic energy does not always have to be lost but may also be gained, e.g., by decreasing the Coulomb energy. However, the important conclusion to be drawn from the experimental correlation displayed in Fig. 11 is that on the average kinetic energy is lost monotonically with decreasing ℓ and increasing interaction time, at least for a range of low and intermediate energy losses. This relation will be used in the following section to actually deduce the macroscopic time scale of damped heavy-ion reactions.

IV. INTERACTION TIMES OF DAMPED COLLISIONS

Little information is available on the interaction time scale on which heavy-ion collisions occur with various degrees of kinetic energy damping. A knowledge of these interaction times is essential for an understanding of the mass, kinetic energy loss and angular distributions of the reaction products from heavy-ion collisions. Strong focusing of the angular distribution for very heavy-ion reactions (see Fig. 1) suggests an angular-momentum dependence of the interaction time since many impact parameters lead to the same reaction angle.

Experimental evidence on fragment Z distributions, such as presented in the preceding section, suggests that during the time the two constituents of the intermediate double-nucleus system interact with each other, a mass equilibration process proceeds which is accompanied by a damping of the relative kinetic energy into other degrees-of-freedom. Since the equilibration processes are not completed during the short interaction times encountered in collisions between the very heavy ions under consideration, the amount of kinetic energy lost signifies the stage of evolution of the system and, hence, the total interaction time experienced. This view is supported by classical dynamical calculations[5,6] which show that the energy loss is a monotonic function of the initial angular momentum and the total interaction time. Associated with each interaction time is a Z distribution which is characterized by a variance σ_Z^2.

In the present analysis[7] we assume, following the discussion of Fig. 11 in the previous section, a monotonic increase in the total kinetic energy (TKE) loss with decreasing values of the impact parameter (see the first paragraph of IIIB). For simplicity we employ a sharp cutoff model where the cross section for angular momenta up to ℓ_j is given by $\sigma_j = \pi\lambda\!\!\!^{-2}(\ell_j+1)^2$. Using the experimental results on the heavy-ion reaction cross section as a function of TKE loss, $d\sigma/d(\text{TKE loss})$, the angular momentum is related to the TKE loss by

$$\ell_i = \{(\ell_j+1)^2 - \frac{\Delta\sigma_{ij}}{\pi\lambda\!\!\!^{-2}}\}^{1/2} - 1 \qquad (1)$$

where $\Delta\sigma_{ij} = \sigma_j - \sigma_i$ is the cross section in a TKE window $E_i \leq \text{TKE} \leq E_j$.

The procedure for converting energy loss to ℓ is illustrated in Fig. 12. Starting with ℓ_{max} and zero TKE loss, a deflection function is constructed from the experimental data, for a range of the higher ℓ values. Examples of such deflection functions are shown as solid lines in Figs. 13 and 14 for the $^{165}Ho + ^{84}Kr (E_{Lab} = 714$ MeV) and $^{209}Bi + ^{136}Xe$ ($E_{Lab} = 1130$ MeV) reactions, respectively. The plotted angles represent the angles where the cross section is at a maximum for a particular kinetic energy loss. For the first reaction the emission angle of the lighter fragment decreases as ℓ decreases, whereas for the second reaction the emission angle is almost independent of ℓ. For each reaction the energy damping and the variance in the Z distribution both increase as ℓ decreases.

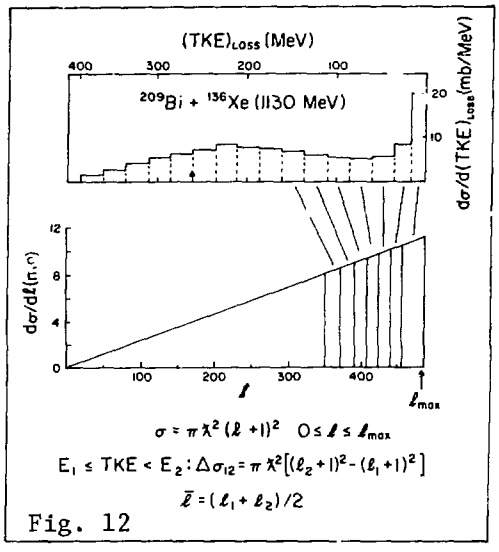

Fig. 12

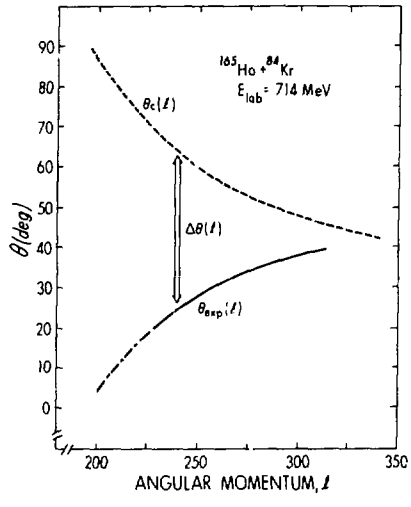

Fig. 13

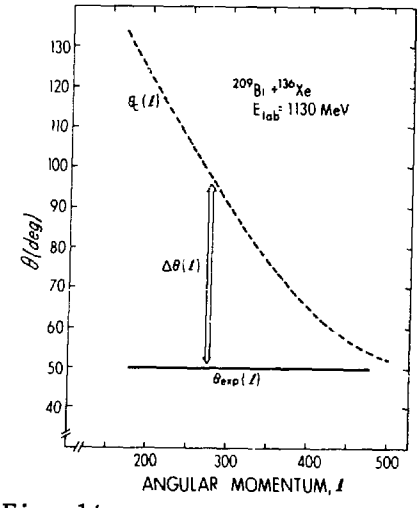

Fig. 14

The angular-momentum-dependent interaction time is calculated with the expression

$$\tau(\ell) = \Delta\theta(\ell)\, \mathcal{I}(\ell)/\hbar\ell \qquad (2)$$

where $\Delta\theta(\ell)$ is the difference between the Coulomb deflection angle $\theta_C(\ell)$ and the actual reaction angle $\theta_{exp}(\ell)$ and $\mathcal{I}(\ell)$ is the moment-of-inertia of the double-nucleus system. The Coulomb deflection angle

is estimated by

$$\theta_c(\ell) = 180^\circ - \theta_1 - \theta_3 \tag{3}$$

where the subscripts refer to the entrance and exit channels, respectively, and

$$\theta_j = +\arccos\frac{1}{\varepsilon_j} - \frac{K_j + R_j}{\varepsilon_j R_j} \quad (\text{for } j = 1 \text{ and } 3) \tag{4}$$

In Equation 4 the parameters ε and K are determined by

$$\varepsilon = \left[1 + \frac{2E\ell^2\hbar^2}{\mu(Z_P Z_T e^2)^2}\right]^{1/2} \tag{5}$$

$$K = \frac{\ell^2\hbar^2}{\mu Z_P Z_T e^2} \tag{6}$$

The above procedure for estimation of $\Delta\theta(\ell)$ is illustrated in Fig. 15. The evaluation of $\tau(\ell)$ requires the adoption of a collision model. Here we present the results of calculations with two rather different models which are labelled as "nonsticking" (NS) and "sticking" (S) collisions. A sticking collision is defined by rigid rotation of the double-nucleus system as a whole. By a NS collision we specify that the entrance and exit channel orbital angular momenta are the same ($\ell_f = \ell_i$) and the moment-of-inertia $\mathcal{I}_{NS} = \mu R^2$ where $\mu = M_1M_2/(M_1 + M_2)$ and R is the contact radius of the double-nucleus system (in the calculation the strong absorption radius R_{SA} is used). In contrast to a nonsticking collision, the final orbital angular momentum is inserted into Eq. 2 for a sticking collision, where $\ell_f = (\mathcal{I}_{NS}/\mathcal{I}_S)\ell_i$ and $\mathcal{I}_S = \mathcal{I}_{NS} + (2/5)(M_1R_1^2 + M_2R_2^2)$. The moment-of-inertia to be substituted into Eq. 2 is again $\mathcal{I}_{NS}$. In the calculations presented, any variation in $\mathcal{I}_{NS}$ with angular momentum or time is neglected. In Figs. 13 and 14, Coulomb deflection functions are shown for the "nonsticking" (NS) model.

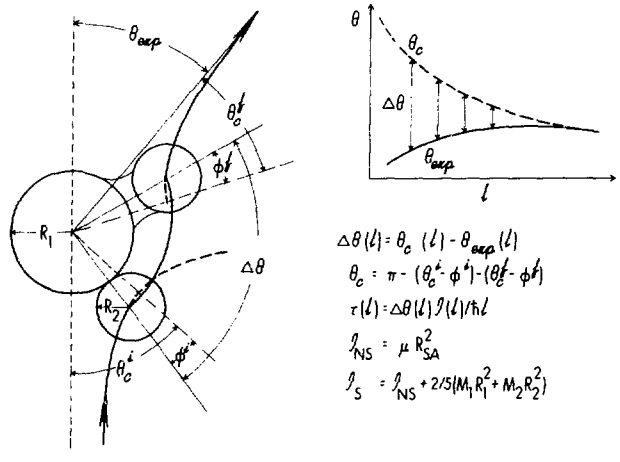

Fig. 15

The above definition of the deflection during the reaction implies that no kinetic-energy loss due to dissipation or dynamical deformation effects occurs at separation distances larger than the strong-absorption radius R_{SA}. The agreement of realistic deflection function calculations with experimental angular distributions for the heavy systems considered here suggests that the deviation of the trajectory with $\ell = \ell_{max}$ from a pure Coulomb trajectory is small. This indicates that all trajectories are similar to Coulomb orbits up to the strong-absorption radius. Hence, for $\ell < \ell_{max}$, the difference between Coulomb and observed deflection is used to evaluate the angle through which the intermediate system rotates during the nuclear interaction.

It should, however, be realized that it is, in principle, impossible to characterize the reaction between very heavy ions by a single deflection function. For such systems there are many intrinsic degrees-of-freedom coupled to the collective motion, and many different reaction paths may lead to similar values of a given experimental observable. Therefore, selecting a certain value of one experimental variable leads to a distribution of values of another variable fluctuating around its mean value. In this sense, the deflection functions derived above represent only average experimental deflection functions.

The angular-momentum-dependent interaction times calculated by the above procedure (see Eq. 2) are displayed in Fig. 16 for the nonsticking model. Multiplication of the angular momentum ℓ by the factor $[10^6(A_T + A_P)^{1/3}/(Z_T + Z_P)^2] \cdot (1/\ell_{max})$ produces straight lines on a semilog plot of approximately the same slope for the three reactions. The angular momentum range for the $^{209}Bi + ^{136}Xe$ reaction shown in Fig. 16 is $120 \leq \ell \leq 430$. For both the sticking and nonsticking models the interaction time is given empirically by the relation $\tau(\ell) = \tau_0 \exp(-\alpha\ell)$. Values of τ_0 and α for the three reactions shown in Fig. 16 are listed in Table 1.

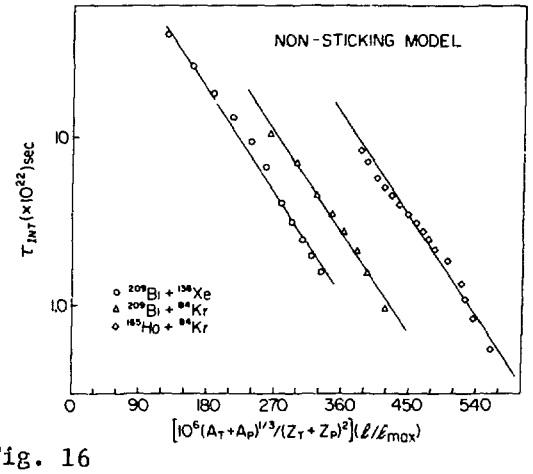

Fig. 16

TABLE 1

Functional parameters of the interaction times as deduced from a fit of the relation $\tau(\ell) = \tau_0 \exp(-\alpha\ell)$ to the data.

Reaction	E(lab)	Model	τ_0(sec)	α
$^{209}Bi + ^{136}Xe$	1130	S	1.86×10^{-20}	0.00974
		NS	2.18×10^{-20}	0.0118
$^{209}Bi + ^{84}Kr$	712	S	5.16×10^{-20}	0.0171
		NS	6.62×10^{-20}	0.0205
$^{165}Ho + ^{84}Kr$	714	S	1.65×10^{-19}	0.0224
		NS	1.62×10^{-19}	0.0244

V. NUCLEON DIFFUSION

The experimental charge distributions shown in Fig. 10 are suggestive of a diffusion process and have been analyzed with a Fokker-Planck equation in terms of the variance σ_Z^2. In its simplest form with one observable x and constant drift and diffusion coefficients, v and D, respectively, the Fokker-Planck equation has Gaussian solutions[8]

$$P(x,t) = (4\pi Dt)^{-1/2} \exp\{-(x-vt)^2/4\ Dt\} \tag{7}$$

The centroid $x_0 = vt$ and the variance $\sigma^2 = 2Dt$ are linear functions of the interaction time. The drift coefficient v_A is related to the diffusion coefficient through the Einstein relation,

$$v_A(A_1) = -\frac{1}{T} D_A \frac{\partial}{\partial A_1} U_\ell(A_1) \tag{8}$$

where U_ℓ denotes the ground-state energy of the combined system with relative angular momentum ℓ and fragmentation A_1. The local temperature T is determined by the excitation energy.

A relationship between experimental values of the total kinetic energy loss and the variance σ_Z^2 of the fragment charge distributions for very heavy damped collisions is shown in Fig. 11. This relationship in conjunction with the experimental cross sections as a function of the total kinetic energy loss is used to calculate angular-momentum-dependent values of the variance $\sigma_Z^2(\ell)$. In the above theory of nucleon diffusion, the value of $\sigma_Z^2(\ell)$ is related to the interaction time $\tau(\ell)$ by

$$\sigma_Z^2(\ell) = 2D_Z(\ell)\tau(\ell) \tag{9}$$

The interpretation of the experimental fragment Z distributions in terms of Eq. 9 is subject to similar observations as made above for the construction of an experimental deflection function. The experimental variance σ_Z^2 of the Z distribution is an average value determined by the range of ℓ waves contributing to a given TKE window. A factorization of σ_Z^2 according to Eq. 9 into mean values of D_Z and τ applies

only if $D_Z(\ell)$ is a slowly varying function of both Z and ℓ because the above analysis suggests that the total interaction time $\tau(\ell)$ is a rapidly varying function decreasing exponentially with increasing ℓ. This requirement on $D_Z(\ell)$ seems, indeed, to be fulfilled as indicated by model calculations and an experimentally observed small drift coefficient v_Z.

The value $\tau(\ell)$ entering Eq. 9 is the mean value of the time during which the nucleon diffusion mechanism operates. In this analysis it is assumed that $\tau(\ell)$ is the total interaction time evaluated by the procedure outlined above. However, it is conceivable that nucleon diffusion occurs only during a part of this time, although there is presently no experimental evidence for such a division of the total interaction time.

Values of $\tau(\ell)$ and $\sigma_Z^2(\ell)$ determined for the $^{165}Ho + ^{84}Kr$ (E_{Lab} = 714 MeV) and the $^{209}Bi + ^{136}Xe$ (E_{Lab} = 1130 MeV) reactions are plotted in Figs. 17 and 18, respectively.[7] The two different sets of values

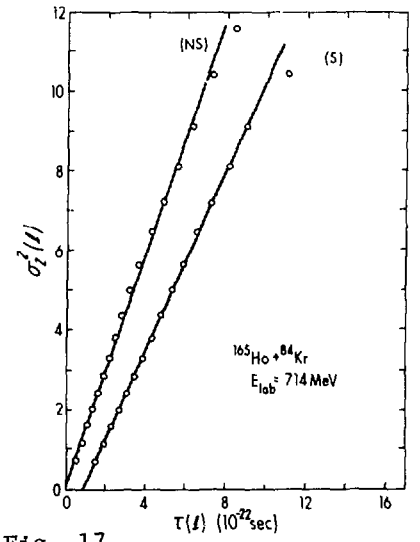

Fig. 17

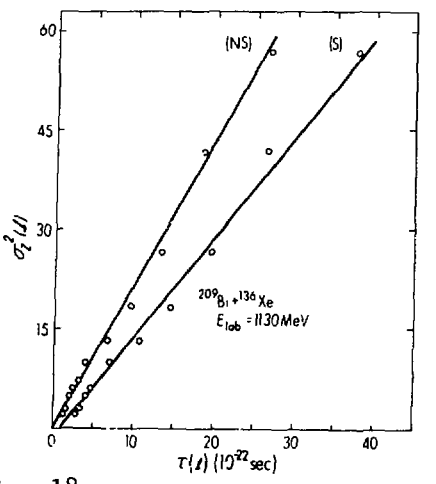

Fig. 18

of $\tau(\ell)$ for each reaction in this figure are based on the above NS and S models. The values of the diffusion coefficients for three heavy ion reactions determined by the slope of the line fitted to the $\sigma_Z^2(\ell)$ vs $\tau(\ell)$ data are given in Table 2 for each of the above two models. The proton number diffusion coefficient does not refer to proton diffusion alone, but to mass diffusion measured by the number of transferred protons. Assuming a conservation of the equilibrium Z/A ratio, the proton number (D_Z) and mass number (D_A) diffusion coefficients are related by $D_Z = (Z/A)^2 D_A$.

Table 2

Proton number (D_Z) and mass number (D_A) diffusion coefficients in units of 10^{22} sec^{-1} for Kr- and Xe-induced reactions.[7] The proton number diffusion coefficient does not refer to proton diffusion alone, but to mass diffusion measured by the number of transferred protons; hence, $D_Z = (Z/A)^2 D_A$ for a constant Z/A ratio. The diffusion coefficients listed in this table are calculated from the slopes of lines drawn through plots of $\sigma_Z^2(\ell)$ vs $\tau(\ell)$ over a range of ℓ values. In the case of the sticking model, for example, the points for the highest ℓ waves do not lie on a line which passes through the origin (see Figs. 17 and 18). Individual values of $D_Z(\ell)$ for the sticking model are ℓ dependent and increase initially as ℓ decreases. The Kr- and Xe-projectile energies (lab) are 714 and 1130 MeV, respectively. The errors in the diffusion coefficients are of the order of 30%. However, the values scale with the contact radius (see Eqs. 2 and 9) which for the reported values is assumed to be the strong absorption radius, R_{SA}.

Reaction	Sticking Model		Nonsticking Model	
	D_Z	D_A	D_Z	D_A
$^{209}Bi + ^{136}Xe$	0.75	4.8	1.1	7.0
$^{209}Bi + ^{84}Kr$	0.62	3.7	0.87	5.3
$^{165}Ho + ^{84}Kr$	0.55	3.2	0.74	4.3

V. MECHANISMS OF KINETIC ENERGY DISSIPATION

In previous sections evidence has been presented to show that kinetic energy loss and mass exchange are strongly correlated. This result is consistent with the view that nucleon diffusion evolves in a continuous fashion as energy is dissipated and supports a close correspondence of the time scales governing energy dissipation and nucleon exchange. In this section we employ the microscopic time scale provided by the nucleon exchange process to study the energy dissipation mechanism.

At the heavy-ion bombarding energies discussed here and moderate excitation energies, one expects that nucleon exchange and particle-hole excitation without nucleon exchange are mediated by the one-body interaction given by the single particle field. Such a mechanism gives rise to classical friction forces proportional to the relative velocity v of the two ions,[10-12]

$$\vec{F} = -k\vec{v} \tag{10}$$

In general, k is an anisotropic tensor dependent on the separation distance of the two ions, which is equivalent to an implicit time dependence of k. The importance of one-body friction in nuclear fission and heavy-ion reactions has been discussed also by other

authors.[13-17] Two-body friction induced by inelastic scattering of individual nucleons of target and projectile, which may also play a role in energy dissipation, has in general a velocity dependence more complicated[18] than that implied by Eq. 10.

The energy loss rate associated with Eq. 10 is

$$-dE/dt = 2(k/\mu)E \tag{11}$$

where μ is the reduced mass. Integration of Eq. 11 with a constant coefficient k gives

$$\ell n(E_0/E) = 2(k/\mu)t \tag{12}$$

where $E_0 = E_{c.m.} - E_B$, $E = E_0 - E_{loss}$ and $E_{c.m.}$ and E_B are the incident c.m. kinetic and Coulomb energies, respectively. Employing the microscopic time scale provided by the nucleon exchange process, namely

$$d\sigma_Z^2/dt = 2D_Z(t) \tag{13}$$

and substituting this relation into Eq. 11 and integrating leads to a relation

$$\ell n(E_0/E) = (k/\mu D_Z)\sigma_Z^2 \tag{14}$$

provided that the ratio (k/D_Z) is independent of time. Hence, a linear relation is predicted between $\ell n(E_0/E)$ and σ_Z^2. Such a plot is shown in Fig. 19 where E_B is calculated at the strong absorption radius. Good agreement between experiment and this simple theory is obtained for energy losses up to 200 MeV. If k/D_Z is the same for Kr- and Xe-induced reactions at a bombarding energy of 8.5 MeV/amu, the slopes of Fig. 19 lead to

$$k/D_Z = (0.9 \pm 0.3) \times 10^{-43} \text{ MeV sec}^2 \text{ fm}^{-2}. \tag{15}$$

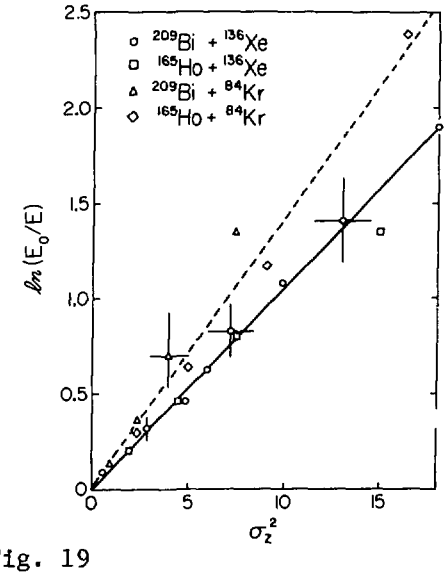

Fig. 19

The result of a constant friction coefficient rather than a strongly varying form factor as suggested by classical dynamical calculations[11,12,19] can be understood as being due to the fact that in the analysis reference was made to a nucleon diffusion mechanism in order to derive a microscopic time scale.[3] Although it is presently not quite clear to what extent the one-body dissipation mechanism applies, the experimental results are consistent with the view that energy dissipation mediated by nucleon exchange and the other possible dissipation mechanisms proceed on a similar microscopic time scale and have a similar

dependence on the separation distance of the two ions and the angular momentum. In principle, a fast dissipation mechanism[20] operating only during a small initial part of the total interaction time cannot be excluded. However, it has to lead to a friction-like relation between the energy loss and the total interaction time which is similar to Eq. 11 in order to fit the data.

An interesting new experimental observation[21,22] is that k/D_Z increases as the bombarding energy decreases. For example, as the bombarding energy is reduced from 1130 to 970 MeV for the $^{209}Bi + ^{136}Xe$ reaction, the value of k/D_Z increases[21] by a factor of more than 2.

Kinetic energy is known to be lost in nucleon exchange between target and projectile.[23] In a simple version of a one-body nucleon exchange process[13], where a nucleon of mass m is assumed to be loosely bound and at rest with respect to the donor nucleus, its relative momentum $\Delta p = mv$ is dissipated in the transfer. The resulting loss of total kinetic energy per nucleon exchange δE_{ex} is then proportional to the kinetic energy available prior to exchange[24],

$$\delta E_{ex} = (m/\mu)(E_{c.m.} - E_B - E_{loss}) = (m/\mu)E \tag{16}$$

where $\delta E_{ex} = (-dE_{ex}/dt)/(dN/dt)$ and dN is the number of exchanged nucleons per unit time dt. Consequently, the energy loss rate for nucleon exchange alone is

$$-dE_{ex}/dt = (m/\mu)E(dN/dt) = k_{ex}v^2 \tag{17}$$

This energy loss rate is equivalent to that due a friction force $F_{ex} = -k_{ex}v$ (see Eq. 10) with a frictional coefficient,

$$k_{ex} = (m/2)(dN/dt) \tag{18}$$

where $(dN/dt) = 2(A/Z)D_Z$. The total number N of nucleon exchanges is obtained from the number $N_Z = \sigma_Z^2$ of protons exchanged by scaling N_Z according to the mass-to-charge ratio, $N = (A/Z)\sigma_Z^2$. This is justified by the experimental observation of a fast equilibration[1] of the mass-to-charge asymmetry degree-of-freedom in damped heavy-ion reactions which indicates that neutron and proton exchange rates are similar. Substitution of dN/dt into Eq. 18 gives

$$(k_{ex}/D_Z) = m\,(A/Z) \tag{19}$$

where m is the nucleon mass. Converting the units of erg sec^2 cm^{-2} to MeV sec^2 fm^{-2}

$$(k_{ex}/D_Z) = 0.1044 \times 10^{-43}\,(A/Z)\ \text{MeV sec}^2\,\text{fm}^{-2} \tag{20}$$

For the $^{209}Bi + ^{136}Xe$ reaction at a bombarding energy of 1130 MeV, it follows that k_{ex}/D_Z is approximately 30% of k/D_Z (see Eq. 15). Hence, energy dissipation caused directly by the nucleon exchange process

represents only a fraction of the total energy dissipation. Furthermore, this fraction decreases as the bombarding energy is reduced.

If one denotes the friction force coefficient due to one-body dissipation processes such as particle-hole excitation without nucleon exchange by k_{nex}, the resulting total energy dissipation rate (in analogy to Eq. 11) is

$$-dE/dt = (2/\mu)(k_{nex} + k_{ex})\, E \tag{21}$$

It may be expected that the rates of one-body processes without and with nucleon exchange represented by the friction coefficients k_{nex} and k_{ex}, respectively, are somewhat different in magnitude. However, since both processes are induced by the same time-dependent single-particle potential, the two friction coefficients are expected to have the same time dependence. This is equivalent to both friction forces having the same spatial form factor. Under this condition, the energy loss rates due to particle-hole excitation and nucleon exchange are proportional to each other. The microscopic time scale corresponding to the nucleon exchange mechanism may then be used to calculate the total energy loss during the time necessary for one-nucleon exchange. Consequently, this <u>total</u> energy loss associated with a single exchanged nucleon, δE, is given by

$$\delta E = -d(E_{nex} + E_{ex})/dN = (m/\mu)[1 + (k_{nex}/k_{ex})]E \tag{22}$$

Similar arguments apply to the case of two-body friction and exchange which, in general, give rise to a more complicated energy dependence.[18]

Experimental results for the energy loss per nucleon exchanged for the reactions[3] $^{165}Ho + ^{84}Kr$, $^{165}Ho + ^{136}Xe$ and $^{209}Bi + ^{136}Xe$ at a bombarding energy of 8.5 MeV/amu and for the reaction[25] $^{197}Au + ^{86}Kr$ at 7.2 MeV/amu are presented in Fig. 20. The values of δE were obtained by differentiating curves of E_{loss} vs N fitted to the experimental data points. The estimated errors are, therefore, correlated. The $^{197}Au + ^{84}Kr$ data were transformed into the center-of-mass system assuming ^{84}Kr-kinematics for all fragments.

The most important observation to be made from the data is that the energy δE dissipated during the time necessary for the exchange of a single nucleon decreases with decreasing available kinetic energy E (i.e. increasing energy loss and total excitation energy of the system). The

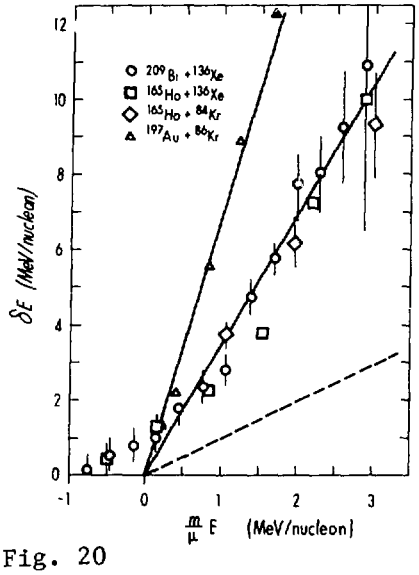

Fig. 20

data points follow a straight line intercepting the abscissa at $(m/\mu)\,E = 0$ as predicted by Eq. 22 over an unexpectedly wide range of available energies. For small available energies the data points deviate from these lines. This indicates that large energy losses may lead to a highly deformed intermediate system. Hence, the Coulomb energy may be much lower than the one in the entrance channel, which is used to calculate the available energy. On the other hand, the one-body mechanism may also lose importance at high excitation energies, where the Pauli principle is less inhibitive for two-body nucleon collisions.

As is indicated by the dashed line in Fig. 20 corresponding to Eq. 16 (or to Eq. 22 with $k_{nex} = 0$), energy dissipation by nucleon exchange alone can account for ~30% of the total energy loss for the 8.5 MeV/amu data and for ~15% for those at 7.2 MeV/amu. The good description of the data by the linear relation predicted by the one-body mechanism suggests that the ratio k_{nex}/k_{ex} is, indeed, constant over a wide range of excitation energies and ℓ values. Although the $^{197}Au + ^{86}Kr$ data[26] exhibit a linear dependence on the available energy, they do not lie on the line determined by the 8.5 MeV/amu reaction data. Studies[21,22] of similar reactions at various bombarding energies indicate that nucleon exchange accounts for a smaller fraction of the total energy loss as the bombarding energy is reduced.

The diffusion model proposed by Nörenberg and collaborators[26-28] treats nucleon exchange and energy loss on the same basis accounting for the dependence of the transport coefficients on excitation energy or energy loss. Noticing that the rates of energy loss and nucleon exchange are determined by the energy drift coefficient v_E and the mass diffusion coefficient D_A according to $dE/dt = -v_E$ and $dN/dt = (2Z/A)D_A$, one obtains[28]

$$\delta E = \frac{A}{Z}\frac{v_E}{2D_A} = \frac{A}{Z}\frac{\Delta^2}{8}\frac{(g_1+g_2)^{1/2}}{(g_1 g_2)^{1/3}}\,(g_1^{1/3}+g_2^{1/3})^2\,E_{loss}^{-1/2} \qquad (23)$$

for the total energy dissipated during the exchange of one nucleon. Here, $\Delta \approx 2.5$ MeV is a mean value of the energy dissipated in one nucleon exchange or particle-hole excitation process, and $g_k = A_k/12$ are the single-particle level density parameters of the two ions.

Theoretical curves represented by Eq. 23 are compared in Fig. 21 with the experimental energy loss per nucleon as a function of energy loss. The level density parameters were calculated for the projectile-target combination of fragments. As can be seen in Fig. 21, the diffusion model can account for the high energy loss observed per nucleon exchange for low values of kinetic energy loss corresponding to small interaction times.[2] However, the predicted functional dependence (Eq. 23) is not supported by the data. It is interesting to notice that on this plot also the $^{197}Au + ^{86}Kr$ data follow the experimental systematics for small values of E_{loss}. If the diffusion model is modified to account for the reaction dynamics employing

velocity-proportional friction forces, the result is quite similar to one-body dissipation.

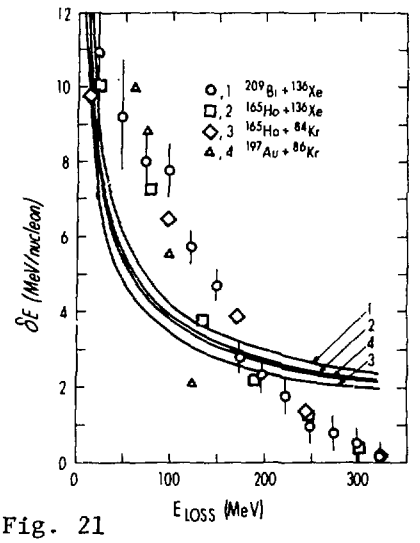

Fig. 21

In conclusion, the observed correlation between nucleon exchange and energy loss suggests that the microscopic time scale provided by the exchange mechanism can be used to study the energy dissipation mechanism in heavy-ion reactions. The experimental energy loss associated with a single nucleon exchange exhibits a linear dependence on the available kinetic energy, as predicted by a one-body dissipation mechanism. The diffusion model can account for high amounts of energy dissipated per nucleon, δE, for low energy losses; however, it does not predict correctly the decrease of δE with increasing energy loss. Neither model accounts directly for the increase of k_{nex}/k_{ex} (or k/D_Z) with decreasing bombarding energy.

Acknowledgments

†The authors acknowledge the contributions of V.E. Viola, Jr. and K.L. Wolf to the results reported in this paper.

*Work supported by the U.S. Energy Research and Development Administration.

**Supported in part by a grant from the German Academic Exchange Service DAAD

***Supported by a grant from the National Science Foundation

References

1. W.U. Schröder and J.R. Huizenga, Ann. Rev. Nucl. Science 27(1977) . References to the literature of damped heavy ion reactions can be found in this review article and, hence, only a limited number of references to results discussed here are included.

2. W.U. Schröder, J.R. Birkelund, J.R. Huizenga, K.L. Wolf, J.P. Unik and V.E. Viola, to be published.

3. J.R. Huizenga, J.R. Birkelund, W.U. Schröder, K.L. Wolf and V.E. Viola, Jr., Phys. Rev. Letts. 37(1976)885.

4. J. Wilzcyński, Phys. Lett. B47(1973)484.

5. D.H.E. Gross, H. Kalinowski and J.N. De, Symposium on Classical and Quantum Mechanical Aspects of Heavy Ion Collisions, Heidelberg, 1974, Springer Verlag, Lecture Notes in Physics 33(1975)194.

6. K. Siwek-Wilczyńska and J. Wilczyński, Nucl. Phys. A264(1976)115.

7. W.U. Schröder, J.R. Birkelund, J.R. Huizenga, K.L. Wolf and V.E. Viola, Jr., Phys. Rev. C16(1977) August issue.

8. W. Nörenberg, Phys. Letts. 52B(1975)289.

9. S. Ayik, B. Schürmann and W. Nörenberg, Z. Physik A279(1976)145.

10. R. Beck and D.H.E. Gross, Phys. Lett. 47B(1973)143.

11. D.H.E. Gross and H. Kalinowski, Phys. Lett. 48B(1974)302.

12. D.H.E. Gross, Nucl. Phys. A240(1975)472.

13. W.J. Swiatecki, Lawrence Berkeley Laboratory Report LBL-4296 (1975); Jour. Phys. C5(1972)45 and private communication.

14. J. Blocki, Y. Boneh, J.R. Nix, J. Randrup, M. Robel, A.J. Sierk and W.J. Swiatecki, Annals of Physics (1977) in press.

15. J. Randrup, preprint 1977.

16. S.E. Koonin, R.L. Hatch and J. Randrup, to be published in Nucl. Phys.

17. S.E. Koonin and J. Randrup, preprint 1977.

18. K. Albrecht and W. Stocker, Nucl. Phys. A278(1977)95.

19. D.H. Gross and H. Kalinowski, 4. Session d'Études Biennale de Physique Nucléaire, La Toussuire, France, 1977.

20. R.A. Broglia, C.H. Dasso and Aa. Winther, Phys. Lett. 61B(1976) 113.

21. W.W. Wilcke, J.R. Birkelund, W.U. Schröder, J.R. Huizenga, A. Mignerey, D.G. Raich, K.L. Wolf and V.E. Viola, to be published.

22. A. Mignerey, D.G. Raich, R.L. Boudrie, K.L. Wolf, V.E. Viola, J.R. Birkelund, W.U. Schroder and J.R. Huizenga, to be published.

23. P.J. Siemens, J.P. Bondorf, D.H.E. Gross and F. Dickmann, Phys. Lett. 36B(1971)24.

24. W.U. Schröder, J.R. Huizenga, J.R. Birkelund, K.L. Wolf and V.E. Viola, Jr., preprint (1977).

25. L.G. Moretto and J.S. Sventek, Proceedings of the Symposium on Macroscopic Features of Heavy-Ion Collisions, Argonne, 1976, Regport ANL/PHY-76-2, p. 235.

26. W. Nörenberg, Z. Physik A274(1975)841.

27. S. Ayik, B. Schürmann and W. Nörenberg, Z. Physik A277(1976)299.

28. S. Ayik, B. Schürmann and W. Nörenberg, Z. Physik A279(1976)145.

DESCRIPTION OF DEEPLY INELASTIC COLLISIONS IN TERMS OF A TRANSPORT EQUATION

Hans A. Weidenmüller[+]

Max-Planck-Institut für Kernphysik, Heidelberg, W. Germany

Abstract. A transport equation for deeply inelastic collisions is derived from a random-matrix model for the form factors for inelastic scattering and transfer reactions. The parametrization of these form factors is discussed. Results in one dimension indicate the importance of quantum fluctuations, and limitations of other approaches to the same problem. Results in three dimensions are compared with the data.

1. Introduction

Reasonably successful fits of friction models to cross-section data[1] and of diffusion models to the observed mass distribution[2] suggest that deeply inelastic collisions (DIC) can perhaps be described in a rather simple way. It may be sufficient to follow the development in time of a few select degrees of freedom (relative motion, shape degrees of freedom and the like) and to describe the coupling of these modes with the multitude of excited states of heavy nuclear systems available at excitation energies exceeding a few MeV by friction and diffusion coefficients, viscosity coefficients etc. This view, if correct, defines the task of the theory. It consists in finding the Hamiltonian for large-scale collective motion of nuclear systems The necessary steps are the following. The relevant collective degrees of freedom have to be identified. The collective Hamiltonian has to be set up by calculating the inertia parameters and potential energies for these modes. In addition, the coupling of these modes to the large number of non-collective intrinsic excitations has to be analysed. Under suitable conditions, this coupling can be expressed in terms of transport coefficients (friction coefficients, diffusion constants etc) the knowledge of which completes the description of large-scale collective motion.

The present paper aims at contributing towards this goal. While methods to calculate energies and inertia parameters for collective nuclear motion have been studied for a long time[3,4], the calculation of transport coefficients has only recently become a challenge for nuclear theorists[5,6]. It is the purpose of this contribution to show

---

[+] Invited paper presented at the Fall Creek Falls Meeting on Heavy-Ion Collisions, Pikeville, Tennessee, June 13-17, 1977.

The author acknowledges partial support for attending the Conference from Oak Ridge National Laboratory.

how such a calculation can be done for realistic values of the relevant input parameters. We pay no attention to some open problems in the theory of inertia parameters[7] and focus attention entirely on the transport properties. The calculation is carried through for a specific choice of the collective variable. Nevertheless, we believe that the techniques developed for this case have general applicability in nuclear physics. The work summarized below was carried through in collaboration with Dan Agassi and Che-Ming Ko[8,9,10]. Some of the numerical results were obtained by David Saloner. The calculation of the second moment of the form factors is presently done jointly with B.R. Barrett and S. Shlomo.

2. Qualitative Description of the Model.

As the collective variable, we choose the distance $\vec{r}$ between the centers of mass of projectile and target. Thereby, we neglect other collective degrees of freedom, particularly shape deformations, which are known[11] to play an important role especially towards the end of the DIC. We assume the two nuclei to remain spherical throughout the collision. This is done not because we consider this a realistic approximation, but because we wish to calculate transport coefficients first in the simplest possible model. The inertia parameter is taken to be the reduced mass μ of projectile and target. Changes of μ due to mass transfer are neglected, and the problem of calculating the inertia parameter ab initio is avoided. The potential $U(r)$ between the two fragments consists of the Coulomb interaction and a real nuclear potential. The latter is taken to be independent of the excitation energy of either fragment. Details of its choice are given in section 5 below.

As the two heavy ions approach each other, they excite one another by Coulomb excitation and, as the nuclear density distributions begin to overlap, by inelastic nuclear scattering and nuclear transfer reactions. The latter two processes soon dominate and can each be described by a matric element of DWBA type. We thus view the DIC essentially and aside from the initial stage (to which we pay no attention in the sequel) as a sequence of a large number of DWBA-type collisions. Each collision term contains the form factor $V_{st}(\vec{r})$ connecting the eigenstates $|s\rangle$ and $|t\rangle$ of intrinsic motion (these two states are products of eigenstates of the intrinsic Hamiltonians of either fragment). At excitation energies exceeding several MeV for either fragment, the states $|s\rangle$ can no longer be described individually and microscopically. Rather, they attain properties which must be described with statistical methods. This is demonstrated by the success of random-matrix models in nuclear spectroscopy in general, and in neutron time-of-flight spectroscopy and preequilibrium decay in particular[12]. Therefore, we replace the detailed description of the behaviour of the form factors $V_{st}(\vec{r})$ by a statistical one, assuming the form factors to have a Gaussian distribution centered at zero. This assumption is consistent with random-matrix models, as is the vanishing of the mean value for $s \neq t$. (The elastic form factors

$V_{ss}(\vec{r})$ are not considered here as they form part of the real nuclear potential contained in $U(r)$.) To specify the distribution of the $V_{st}(\vec{r})$ completely, we only have to give the value of the second moment, $\overline{V_{st}(\vec{r})\, V_{s't'}(\vec{r}')}$. This is done below. We thus view the DIC as a sequence of random collisions of DWBA type, and calculate the mean value of the cross section. This statistical view is in keeping with the general physical principle by which perturbation theory is adequate for weakly interacting systems, statistical mechanics for strongly interacting ones like the nucleus. Note, however, that we avoid introducing a temperature (and thereby assume partial equilibration). We replace the concept of a heat bath and its associated temperature by the statistical assumption on the form factors.

3. Derivation of the Transport Equation.

The distribution of the form factors is specified completely by assuming them to form a Gaussian random-matrix ensemble with mean value zero and second moment

$$\overline{V_{st}(\vec{r})\, V_{s't'}(\vec{r}')} = \left(\delta_{ss'}\delta_{tt'} + \delta_{st'}\delta_{ts'}\right)\left(D_s D_t\right)^{1/2} \sum_{L=0}^{L_{max}} w_L P_L(\hat{r}\hat{r}') \ast$$

$$\ast \exp\left\{-(\varepsilon_s-\varepsilon_t)^2/2\Delta^2\right\} \exp\left\{-(r-r')^2/2\sigma^2\right\} \phi\left\{\tfrac{1}{2}(r+r')\right\}. \quad (3.1)$$

The bar denotes the ensemble average. Space does not permit me to justify the r.h.s. of eq. (3.1) in detail[8]. Calculations based on a shell-model expansion of the states $|s\rangle$ and $|t\rangle$ with B.R. Barrett and S. Shlomo are under way to determine precise values of the parameters w_L, σ and Δ . Suffice it to say that f is related to the overlap of the two mass distributions, Δ = 5 to 7 MeV to the mean energy transfer per collision (roughly given by the harmonic oscillator energy $\hbar\omega$), σ = 2 to 4 fm to the correlation length (roughly given by pi over the inverse Fermi momentum), and $w_L \tilde{=}$ 10 MeV to the strength of a collision in which the angular momentum $\hbar L$ is transferred to intrinsic motion, with $\hbar L_{max}$ the maximum value. Shell-model estimates yield $L_{max} \approx 10$. The quantity D_s is the mean level spacing at the excitation energy ε_s of state $|s\rangle$. The factor $(D_s D_t)^{1/2}$ makes sure that $\overline{V_{st}^2(\vec{r})}\,(D_s D_t)^{-1/2}$ which can be viewed roughly as a spreading width, is independent of excitation energy. (In writing eq. (3.1), we have skipped complications[8] arising from angular-momentum algebra and the Wigner-Eckart theorem). Similarly, eq. (3.1) can be generalized to include mass transfer. Note that all the physics of our model is contained in the assumption (3.1) on the statistics of the form factors, and in the values of the parameters σ, Δ, w_L.

Upon the introduction of the random-matrix model for the form factors, the Hamiltonian for DIC is replaced by an ensemble of random Hamiltonians. In the representation in which the intrinsic Hamiltonians of either fragment are diagonal, this ensemble has the form

$$H_{st} = \left(T_{\vec{r}} + U(r)\right)\delta_{st} + \varepsilon_s \delta_{st} + V_{st}(\vec{r}) \,. \tag{3.2}$$

Here, T_r is the kinetic energy of relative motion, all other symbols were introduced above. It is straightforward to express the scattering matrix (and thus the cross section) formally in terms of H_{st}. In calculating the mean value of the cross section over energy, we use the equality[13] of energy average and ensemble average and determine the latter with the methods described in ref.8). After summation over intrinsic spins, the result can be written as follows. Let T_{ba}, b = a, be the transition matrix leading from the incident channel a to the final channel b. Then,

$$\overline{|T_{ba}|^2} = \sum_{n=1}^{\infty} \overline{|T_{ba}^{(n)}|^2} \,, \tag{3.3a}$$

$$\overline{|T_{ba}^{(n)}|^2} = \sum_{s_1 \cdots s_{n-1}} * \tag{3.3b}$$

$$* \langle \phi_b^{opt(-)} | V_{b s_{n-1}} G_{s_{n-1}}^{opt} \times \cdots \times G_{s_1}^{opt} V_{s_1 a} | \phi_a^{opt(+)} \rangle \langle \phi_a^{opt(+)} | V_{a s_1} G_{s_1}^{opt *} \times \cdots \times G_{s_{n-1}}^{opt *} V_{s_{n-1} b} | \phi_b^{opt(-)} \rangle \,.$$

Eq. (3.3a) shows that $|T_{ba}|^2$ is a sum of terms, each of which describes n collisions of DWBA type leading from state a to state b. Eq. (3.3b) shows the structure of the n-collision term. Here, $\phi_s^{opt(\pm)}$ are the optical-model wave functions with the usual boundary conditions for outgoing (+) or incoming (-) scattered spherical waves, and G_s^{opt} is the optical-model Green function. It is defined by

$$G_s^{opt} = G_s^{o} + \sum_t V_{st} G_t^{opt} V_{ts} G_s^{opt} \,, \tag{3.4a}$$

$$G_s^{o} = \left[E + i\varepsilon - \varepsilon_s - T_{\vec{r}} - U(r)\right]^{-1} . \tag{3.4b}$$

Expanding eq. (3.4a) into a series,

$$G_s^{opt} = G_s^\circ + \sum_t V_{st} G_t^\circ V_{ts} G_s^\circ + \sum_{t_1 t_2} \overline{V_{st_1} G_{t_1}^\circ V_{t_1 s} G_s^\circ V_{st_2} G_{t_2}^\circ V_{t_2 s}} G_s^\circ + \sum_{t_1 t_2} \overline{V_{st_1} G_{t_1}^\circ \overline{V_{t_1 t_2} G_{t_2}^\circ V_{t_2 t_1}} G_{t_1}^\circ V_{t_1 s}} G_s^\circ + \cdots , \qquad (3.4c)$$

we see that G_s^{opt} describes all processes where scattering into intermediate states takes flux out of channel s. The last term shown explicitly in eq. (3.4c) describes a process in which the scattering process $t_1 \to t_2 \to t_1$ takes place before the scattering process $s \to t_1 \to s$ is completed. The term preceding is describes a sequence of two collisions beginning and terminating in channel s. The optical-model wave functions are determined by a Hamiltonian containing T_R, $U(R)$, and the "optical-model potential" $\Sigma_t V_{st} G_t^{opt} V_{ts}$. Returning to eq. (3.3b), we see that each of the two matrix elements appearing on its r.h.s. does have the form expected for an n-fold DWBA collision. The one modification which arises is caused by the fact that the form factors appear pairwise in the matrix element and its complex conjugate, each pair being replaced by its mean value as indicated by the bars. This is a consequence of the random nature of the interaction. It implies that the <u>transfer</u> of energy and angular momentum from relative motion to intrinsic excitation is the <u>same</u> in each collision for the matrix element and its complex conjugate. In other words, this transfer is <u>incoherent</u>. This is demonstrated by the fact that the intermediate state energies $s_1, s_2, \ldots, s_{n-1}$ are the same in both matrix elements, and by the appearance of the Legendre polynomial $P_L(\hat{r}\hat{r}')$ in eq. (3.1). Aside from these incoherent terms, the probability (3.3) of going from channel a to channel b also contains <u>coherent</u> features. Indeed, ϕ_a^{opt} is a coherent sum of all relevant angular-momentum amplitudes, and so are $G_{s_i}^{opt}$, $G_{s_k}^{opt*}$, and $\phi_b^{opt(-)}$. Moreover, in each collision, the angular momentum ℓ before the collision is vector-coupled with the transferred angular momentum L to yield the angular momentum of relative motion $\vec{\ell}' = \vec{\ell} + \vec{L}$ after the collision, just as in any DWBA matrix element. No further restriction exists on the value of ℓ'. In particular, there exists no condition that would force the angular momentum in $G_{s_i}^{opt}$ and in $G_{s_i}^{opt*}$ to be the same, for any $i = 1, \ldots, n$. Therefore, the final angular momenta in $\phi_b^{opt(-)}$ and $\phi_b^{opt(-)*}$ are added <u>coherently.</u> This is necessary to produce the narrow angular distribution peaked in the forward hemisphere often observed in DIC. (An incoherent summation over angular momenta would lead to angular distributions symmetric about 90° c.m.).

We now cast eq. (3.3) into the form of a transport equation which can be solved numerically. We define the mean value of the density matrix,

$$\bar{\varrho}_s(\vec{r},\vec{r}') = |\phi_a^{opt(+)}\rangle\langle\phi_a^{opt(+)}|\,\delta_{sa} + \sum_t G_s^{opt}\,\overline{V_{st}\,\varrho_t\,V_{ts}}\,G_s^{opt*}. \tag{3.5}$$

It is not difficult to see that for large values of $|r|$ and $|r'|$, $\rho_b(\vec{r},\vec{r}')$ becomes proportional to $\overline{|T_{ba}|^2}$. Instead of the density matrix, we introduce the Wigner transform

$$F_s(\vec{R},\vec{k}) = (2\pi)^{-3}\int d^3w\;\bar{\varrho}_s(\vec{R}+\tfrac{1}{2}\vec{w},\vec{R}-\tfrac{1}{2}\vec{w})\exp(-i\vec{k}\vec{w}). \tag{3.6}$$

In the classical limit, F_s can be interpreted as the joint probability density of finding the two heavy ions at a relative distance $\vec{R}$ with relative momentum $\hbar\vec{k}$ and intrinsic excitation energy ε_s. It follows from eqs. (3.3) to (3.6) that F_s obeys the following transport equation[8]).

$$(\hbar^2\mu^{-1}\vec{k}\vec{\nabla}_R - \vec{\nabla}_R U\cdot\vec{\nabla}_k)F_s(\vec{R},\vec{k}) = \sum_t\int d^3R'\int d^3k'\left\{\mathcal{G}_{st}(\vec{R},\vec{k};\vec{R}',\vec{k}')F_t(\vec{R}',\vec{k}') - \mathcal{L}_{st}(\vec{R},\vec{k};\vec{R}',\vec{k}')F_s(\vec{R}',\vec{k}')\right\}. \tag{3.7}$$

The left-hand side of this equation has a simple interpretation. Let us consider for a moment classical trajectories defined by $\mu\dot{\vec{R}} = \hbar\vec{k}$, $\hbar\dot{\vec{k}} = -\vec{\nabla}_R U$. It is easy to check that the l.h.s. of eq. (3.7) is then nothing but $\hbar\frac{d}{dt}F_s(\vec{R}(t),\vec{k}(t))$. More generally, this l.h.s. is the rate of change of $F_s(\vec{R},\vec{k})$ along a classical trajectory. The right-hand side has the form familiar from a Master equation. It consists of a gain term proportional to $\mathcal{G}_{st}$ describing collisions that populate the state $(s,\vec{R},\vec{k})$, and of a loss term proportional to $\mathcal{L}_{st}$ describing collisions that depopulate the same state. Both $\mathcal{G}_{st}$ and $\mathcal{L}_{st}$ can simply be expressed in terms of G_t^{opt} and of $\overline{V_{st}V_{ts}}$. It is intuitively clear why we have termed eq. (3.7) the "probability balance equation". It has to be solved with the boundary condition that the incoming current is known; we look for the asymptotic behaviour of $F_s(\vec{R},\vec{k})$ which directly yields the cross section for DIC.

4. Results in One Dimension

Typical features of the solutions of eq. (3.7) can be exhibited[9]) by suppressing the complications due to angular momentum, and by

replacing $\vec{R}$ and $\vec{k}$ by one-diemsnional quantities z and k, respectively, and by putting $U \equiv 0$. Eq. (3.4a) for G_s^{opt} can be solved in nuclear matter and essentially yields the mean free path λ as a function of w_o, Δ, and σ. One finds[9] that λ is roughly inversely proportional to w_o, and depends weakly on Δ and σ, a typical value of λ being 0.25 to 0.5 fm (see Fig.1). The behaviour of the solutions of eq. (3.7) depends on the ratio σ/λ. For $\sigma < \lambda$ (weak coupling), we find that mean intrinsic excitation energy $\varepsilon(z) = \sum_s \int dk\, \varepsilon_s F_s(z,k)$ and mean kinetic energy $\frac{\hbar^2\langle k^2\rangle}{2\mu} = \sum_s \int dk\, \frac{\hbar^2 k^2}{2\mu} F_s(z,k)$ satisfy energy conservation $\frac{\hbar^2\langle k^2\rangle}{2\mu} + \varepsilon(z) = E$ to a good degree of accuracy. More generally, in this case $F_s(z,k) \approx \delta(\varepsilon_s + \frac{\hbar^2 k^2}{2\mu} - E)\, F_s(k)$ which greatly simplifies the problem and leads to the classical equations of motion studied earlier[14]. Unfortunately, $\sigma > \lambda$ (strong coupling) is the more realistic case, since we expect $\sigma/\lambda \approx 8$. In this regime $F_s(z,k)$ is driven off-shell in the interaction region, the energy conservation relation just given being violated by as much as 60 or 80 MeV for an incident energy of 200 MeV (see Figure 2). This shows that not only statistical fluctuations, but also quantum fluctuations are important for the problem. As a consequence, approximations used in previous treatments of the problem are of questionable validity: The description of the system of internal coordinates in terms of a heat bath cannot rely on local energy conservation to determine the temperature. The use of lowest-order perturbation theory (weak coupling limit) is not justified. The use of classical trajectories and of friction coefficients is meaningful only in this limit. The Einstein relation between drift and diffusion coefficients does not give more than an order-of-magnitude estimate of the latter. Correlation length σ and energy spread Δ must be viewed as independent physical parameters which describe very different aspects of the process.

Aside from these findings, the study of the one-dimensional system also leads to two results which are important for constructing approximate solutions in three dimensions. (i) To within a very good approximation, it is possible to replace the variable $\vec{R}'$ in F_s and F_t on the r.h.s. of eq. (3.7) by $\vec{R}$. (ii) The solution $F_s(\vec{R},\vec{k})$ has nearly Gaussian shape (see Figs.3 and 4),

5. Results in Three Dimensions.

Using the results just described, we have transcribed eq. (3.7) into a system of coupled linear first-order differential equations for the first and second moments of $F_s(\vec{R},\vec{k})$ - all we need to describe a Gaussian. In so doing, we have assumed $F_s(\vec{R},\vec{k})$ to be on shell, in spite of the remarks made above. Our justification is this. The one-dimensional model yields results which show that the fully off-shell results typical for strong coupling lead to cross-sections which can be simulated in terms of a weak-coupling calculation if the parameters are suitably renormalised. In spite of the limitations mentioned at the beginning of section 2, it may be instructive to compare the results obtained in this way with the experimental data. We have extended the theory so as to describe also charge transfer.

We first comment on the input parameters used, and on the dependence of our results on these parameters. For the real nuclear potential, we have used a Woods-Saxon shape with depth V_o = 127 MeV, radius R_o = 12 fm and diffuseness a = 1.415 fm. These last two numbers roughly correspond to the reaction $^{40}Ar + ^{232}Th$, the first DIC observed[15], to which we confine ourselves throughout. The other parameters were chosen Δ = 5 MeV, $w_o \cong w_1 \cong w_2 \cong \ldots$ = 7.2 MeV, σ = 4 fm, L_{max} = 7 . (The approximate equality signs are caused by the introduction of an approximation explained in refs. 8 and 10 the details of which exceed the present frame). For these parameters, the one-dimensional model yields a value $\lambda \cong .25$ fm for the mean free path which was used in the optical-model Green's function (3.4a) in three dimensions. For reasons explained in ref. 10 , the radial friction constant was multiplied by the factor 1.25 . The overlap function f(R) appearing in eq. (3.1) was taken to have Woods-Saxon form, with a radius parameter of 14 fm and the same diffuseness a = 1.415 fm as used above. Another constant was adapted to the mass exchange. For the level density, we used its being proportional to $\exp(2\sqrt{\alpha E})$ with E the excitation energy in MeV and α = 34 MeV^{-1}. These parameters completely determine the calculations. The calculations reported below give the cross section of DIC due to impact parameters < 11 fm. Larger impact parameters give rise to a sharp peak of quasielastic events which we did not calculate.

The distribution function $F_s(\vec{R},\vec{k})$ being Gaussian, it is meaningful to discuss first the mean deflection angle $\Theta(b)$ and the associated mean kinetic energy E(b) after the collision as function of the impact parameter b . Both E(b) and $\Theta(b)$ depend very sensitively upon the details of the overlap function and of the real nuclear potential. This strong dependence implies a similarly strong dependence of the doubly differential cross section for DIC. Therefore, a truly meaningful comparison with the data can only be made if many different energies and masses of projectile and target are considered simultaneously, and a smooth A-dependence of the relevant parameters is used. This we have not done yet. We are confident that shell-model calculations as referred to above will help in reducing very substantially the present ambiguities in the choice of w_L, Δ, σ, and f(R). We hope that the choice of the real nuclear potential can be similarly confined.

Fig.5 shows some of our results. The solid upper curve gives $\Theta(b)$ versus b for the parameters given above. The long-short dashed curve gives $\Theta(b)$ versus b for a slightly different set of parameter values, $w_o \cong \ldots \cong w_L$ = 7 MeV, no multiplicative factor 1.25 in front of radial friction, but a diffuseness a = 1.25 and a radius R_o = 14 fm for the real nuclear potential. We note that the deflection function turns over more steeply. This has the consequence of making the cross section for large energy loss smaller, since it is proportional to $\int bdb$. The reduction can be very substantial. The cross section originating from the full $\Theta(b)$ curve between -10^o and $+10^o$ deflection angle is roughly proportional to $b_1^2 - b_2^2 \cong 121$ mb (we used b_1 = 9.65 fm, b_2 = 9 fm) while for the long-short dashed curve the cross section

between - 10° and + 10° is only proportional to 34.8 mb (b_1 = 9.75 fm, b_2 = 9.58 fm). The lower full curve gives the final kinetic mean energy E(b) for our choice of parameters. Although the curve is roughly the same for both deflection functions shown, the mean kinetic energy at - 10° deflection angle is quite different (180 MeV and 200 MeV) for the two curves. Additional complications arise if other parameters are also varied. Generally speaking, one has to strike a proper balance between keeping the $\Theta(b)$ function from getting too steep on the one hand, and getting too little energy loss on the other. In the integration over impact parameter values, we have used as a lower cutoff $R_<$ the point where $\Theta(b)$ either turns over, or tends to minus infinity. The reason is that we feel smaller b values would mainly contribute to fusion and could not be dealt with anyway with the model developed above.

Some of the results of our calculation are shown in Figs.6 and 7. Fig. 6 gives the doubly differential cross section $d^2\sigma/dEd\Omega$ in mb/(MeV sr) for K ions produced in 388 MeV ^{40}Ar + ^{232}Th, with parameters as given above and $R_<$ = 9 fm . The cross section values are plotted for various c.m. scattering angles versus c.m. kinetic energy in MeV of the reaction products on a linear scale. This was done because our calculations cannot claim an overall accuracy better than a few percent of the peak values. When comparing with the results of ref. 15 , we have to keep in mind that the latter are given in the lab system. Our 9° c.m. data show a peak at ~ 165 MeV c.m. (≈ 220 MeV lab system) with a F.W.H.M. of ~ 110 MeV. Both values are in excellent agreement with ref. 15, and so is - within a factor of two - the peak value of the cross section. The 27° c.m. data show the deep inelastic peak at ~ 100 MeV c.m. (≈ 160 MeV lab) with a value of abt. .15 mb / (MeV sr), and the quasi-elastic peak. The latter is cut off because of our restriction to impact parameter values < 11 fm. At the cut-off value of 220 MeV c.m. (~ 280 MeV lab), the value is 1.8 mb/(MeV sr). Aside from the last value which is perhaps somewhat large by a factor of 3 or so, the agreement again is very good. The 18°c.m. results are in between these two sets of results and show an overall agreement of similar quality. Note the shoulder indicating deeply inelastic contributions. The 36° c.m. results show the quasi-elastic peak at 280 MeV c.m. (≃ 340 MeV lab) with a cross section peak value which is roughly a factor 5 too large. This we attribute to the choice of the surface behaviour of potential and overlap function $f(\bar{R})$ both of which together determine the behaviour near the grazing angle.(Note that at a fixed lab energy of 360 MeV, the experimental cross section changes by two orders of magnitude between 35° and 40° lab!). The deep inelastic component at 36° c.m. is in nice agreement with the data. Note that this component has a tendency to peak at smaller energies with increasing angle, in keeping with the data. In view of the uncertainties in potential and overlap function and of the dependences shown in Fig. 5, we consider the overall agreement excellent.

Fig. 7 gives the same kind of plot for ^{16}O ions produced in the reaction. We see that the deep inelastic peak moves towards smaller mean kinetic energies with increasing c.m. scattering angle. This behaviour as well as the size, position and width of the peak are in rough agreement with the data. The curves plotted show that there is also a mass diffusion contribution to cross section values corresponding to large outgoing energies. This second peak is conspicuously absent in data. We believe that this feature of our calculations as well as the large cross section values shown in Fig. 6 near the quasi-elastic peak must be attributed to the same cause, i.e., too strong friction and too much mass transfer in the outer domain ($b > 10$ fm) of the interaction region. Since these calculations were done, evidence was obtained from the shell-model studies referred to above that the second moment of the form factors decreases monotonically and exponentially for distances > 8 fm, in contrast to the behaviour used in our calculations. This feature would probably change the results of our calculations in the right direction, but it has not yet been incorporated in the programme.

6. Conclusions.

We have shown that a random-matrix model for the nuclear form factors leads to a transport equation for DIC. The parameters in this equation are confined within a fairly narrow margin by shell-model studies. An analysis of the transport equation in one dimension indicates the importance of off-shell effects and limitations of previous theoretical treatments of the problem. Calculations of doubly-differential cross sections in three dimensions show a strong dependence on the input parameters and especially on the real nuclear potential which at present is only poorly known. Save for reactions with a large mass transfer, they yield a very satisfactory agreement with the data. To assess the significance of this agreement, and to obtain solid evidence for or against the participation of other collective modes in DIC, work along the following lines is required. (i) The freedom in choosing the input parameters of the model must be reduced by suitable theoretical studies. (ii) The errors incurred in solving the transport equation approximately must be determined, and better approximations avoiding classical concepts must be found. (iii) The analysis of the experimental results must include a large body of data to cover a wide range of bombarding energies and mass numbers. (iv) The mechanism of large mass transfer must be understood better. Work on these problems is under way.

References

1. R. Beck and D.H.E. Gross, Phys.Lett. 47B (1973) 143
D.H.E. Gross and H. Kalinowski, Phys.Lett. 48B (1974) 302
D.H.E. Gross, Nucl.Phys. A240 (1975) 472
J.P. Bondorf, M.I. Sobel, and D. Sperber, Phys.Lett. 15C(1975)83
J.P. Bondorf, J.R. Huizenga, M.I. Sobel and D. Sperber, Phys. Rev. 11C (1975) 1265
K. Siwek-Wilczynska and J. Wilczynski, Nucl. Phys. A264 (1976)115
H.H. Deubler and K. Dietrich, Phys.Lett. 56B (1975) 241
H.H. Deubler and K. Dietrich, Nucl.Phys. A277 (1977) 493

2. W. Nörenberg, Phys.Lett. 52B (1974) 289
L.G. Moretto and J.S. Sventek, Phys.Lett. 58B (1975) 26

3. M.Brack, J. Damgaard, H.C. Pauli, A. Stenholm-Jensen, V.M. Strutinsky and C.Y. Wong, Revs.Mod.Phys. 44 (1972) 320

4. A. Bohr and B. Mottelson, Nuclear Structure, Vol.II, pp.71 ff. W.A. Benjamin, Inc., Reading 1975

5. H. Hofmann and J.P. Siemens, Phys.Lett. 58B (1975) 417 and Nucl.Phys. A257 (1976) 165, ibid. A275 (1977) 464
H. Hofmann, Phys.Lett. 61B (1976) 243

6. W. Nörenberg, Z.Physik A274 (1975) 241; ibid. A276 (1976) 84; S. Ayik, B. Schürmann, and W. Nörenberg, Z.Physik A277 (1976)299; ibid. A279 (1976) 145; S. Ayik, Phys.Lett. 63B (1976) 22

7. V.M. Strutinsky, Z.Physik A280 (1977) 99

8. D. Agassi, C.M. Ko and H.A. Weidenmüller, Ann.Phys. (N.Y.), in press

9. C.M. Ko, D. Agassi and H.A. Weidenmüller, submitted to Ann.Phys. (N.Y.)

10. D. Agassi, C.M. Ko and H.A. Weidenmüller, in preparation

11. W. Nörenberg, in: European Conference on Nuclear Physics and Heavy Ions, Caen 1976

12. Statistical Properties of nuclei, J.B. Garg, editor , Plenum, New York, London 1972
D. Agassi, H.A. Weidenmüller and G. Mantzouranis, Phys.Lett. 22C (1975) 145

13. J. Richert and H.A. Weidenmüller, Phys.Rev. C, in press

14. C.M.Ko, H.J. Pirner and H.A. Weidenmüller, Phys.Lett.62B(1976)248

15. A.G. Artukh, G.F. Gridnev, V.L. Mikheev, V.V. Volkov and J. Wilczynski, Nucl.Phys. A215 (1973) 91; V.V. Volkov, in: Lecture Notes in Physics, Springer Verlag, Berlin, Heidelberg, New York, Vol. 33, p. 254 (1975)

Figure Captions

Fig.1 $2\eta = \lambda^{-1}$ versus coupling strength w_o in a one-dimensional model for various values of the parameters Δ and σ.

Fig.2 The full thick line gives $\varepsilon(z)$, the long-dashed thick line gives $E - \hbar^2 \langle k^2 \rangle / 2\mu$. The difference between the two curves shows the importance of off-shell effects for strong coupling. For more details, cf. ref.9).

Fig.3 $\int F_s(z,k)dk$ versus $\varepsilon_s \equiv E$ for various values of z .

Fig.4 $\int F_s(z,k)dk$ versus z for various values of ε_s .

Fig.5 Mean deflection function and mean kinetic energy versus impact parameter.

Fig.6 Doubly differential cross section (in mb/(MeV sr)) versus c.m. energy (in MeV) for various c.m. angles and outgoing K ions.

Fig.7 The same as Fig. 6 for outgoing O ions.

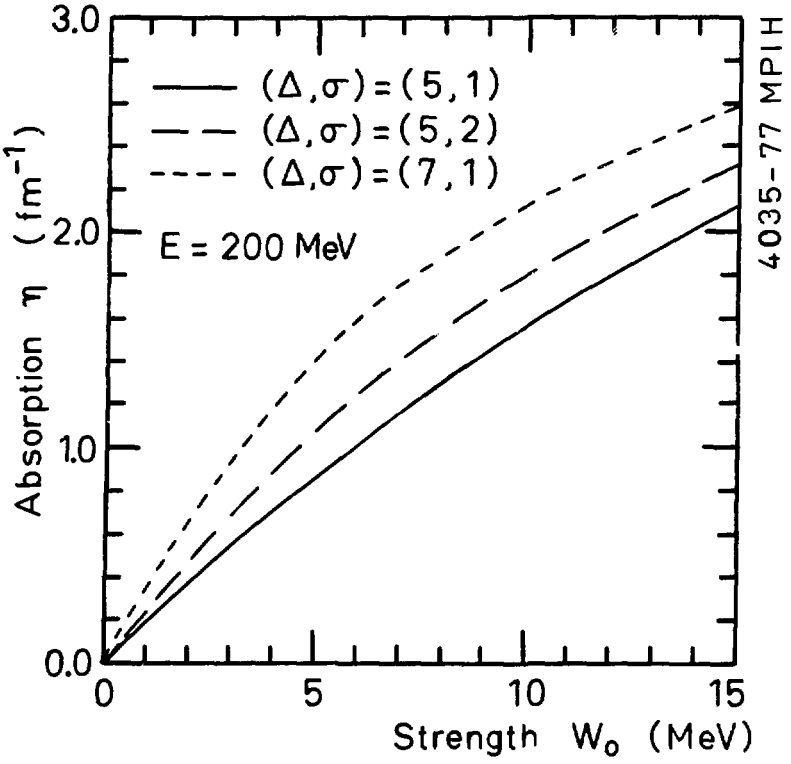
3.0
2.0
1.0
0.0
0
5
10
15
Absorption η (fm⁻¹)
Strength W₀ (MeV)
(Δ,σ)=(5,1)
(Δ,σ)=(5,2)
(Δ,σ)=(7,1)
E = 200 MeV
4035-77 MPIH

Fig. 1

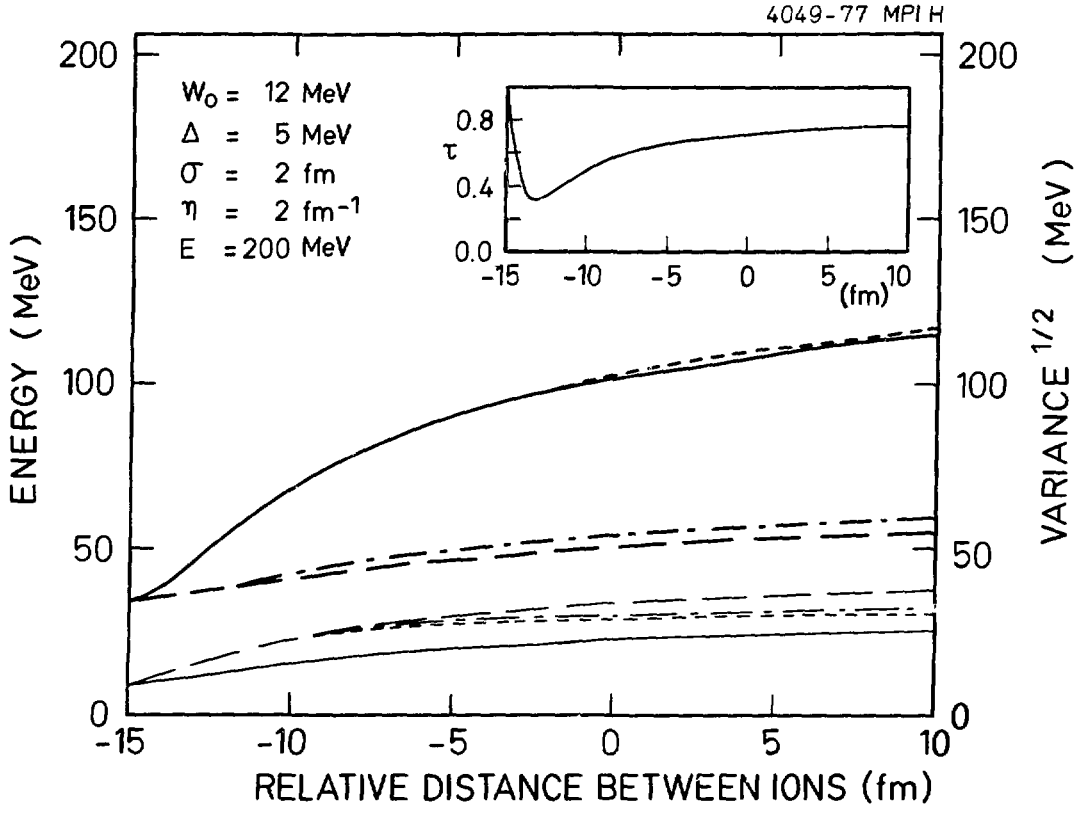
4049-77 MPI H
W_o = 12 MeV
Δ = 5 MeV
σ = 2 fm
η = 2 fm^{-1}
E = 200 MeV
τ
0.8
0.4
0.0
-15
-10
-5
0
5
10
(fm)
200
150
100
50
0
ENERGY (MeV)
VARIANCE $^{1/2}$ (MeV)
RELATIVE DISTANCE BETWEEN IONS (fm)

Fig. 2

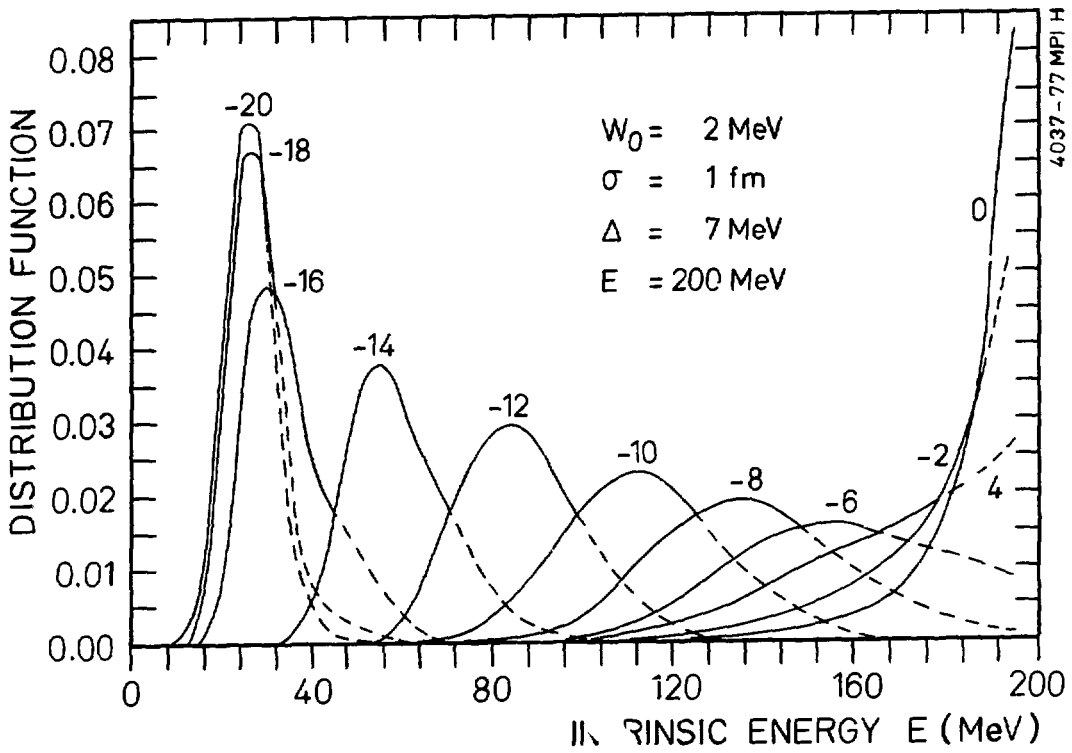
DISTRIBUTION FUNCTION
0.08
0.07
0.06
0.05
0.04
0.03
0.02
0.01
0.00
0
40
80
120
160
200
INTRINSIC ENERGY E (MeV)
-20
-18
-16
-14
-12
-10
-8
-6
-2
0
4
W0 = 2 MeV
σ = 1 fm
Δ = 7 MeV
E = 200 MeV
4037-77 MPI H

Fig. 3

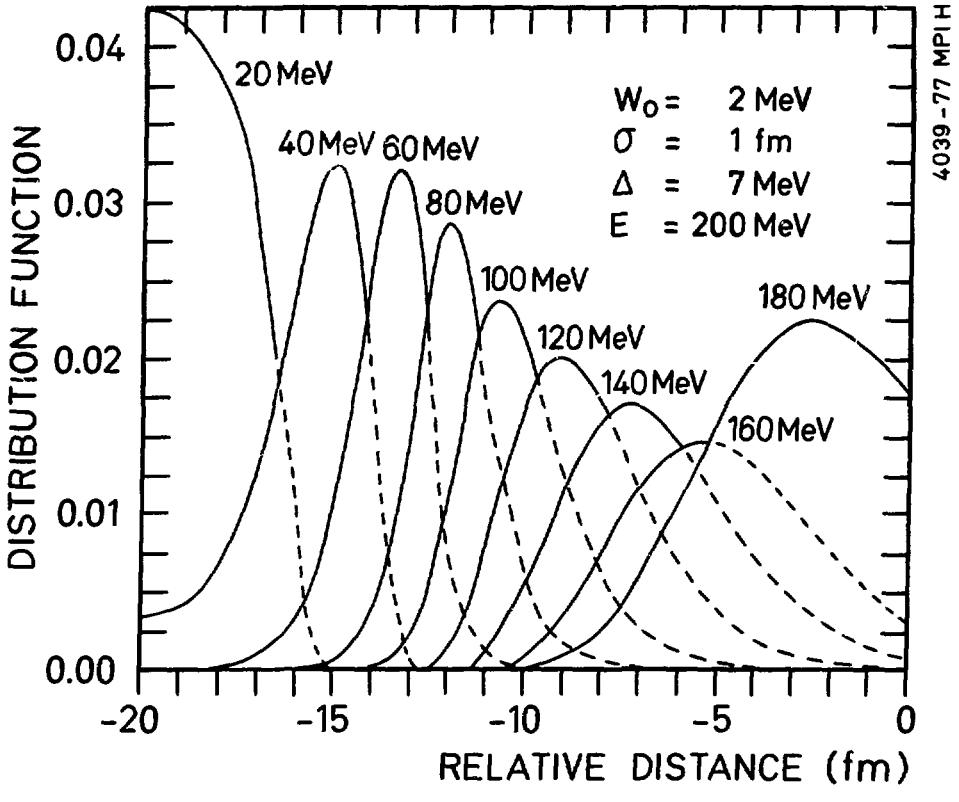
0.04
0.03
0.02
0.01
0.00
DISTRIBUTION FUNCTION
20 MeV
40 MeV
60 MeV
80 MeV
100 MeV
120 MeV
140 MeV
160 MeV
180 MeV
W0 = 2 MeV
σ = 1 fm
Δ = 7 MeV
E = 200 MeV
-20
-15
-10
-5
0
RELATIVE DISTANCE (fm)
4039-77 MPI H

Fig. 4

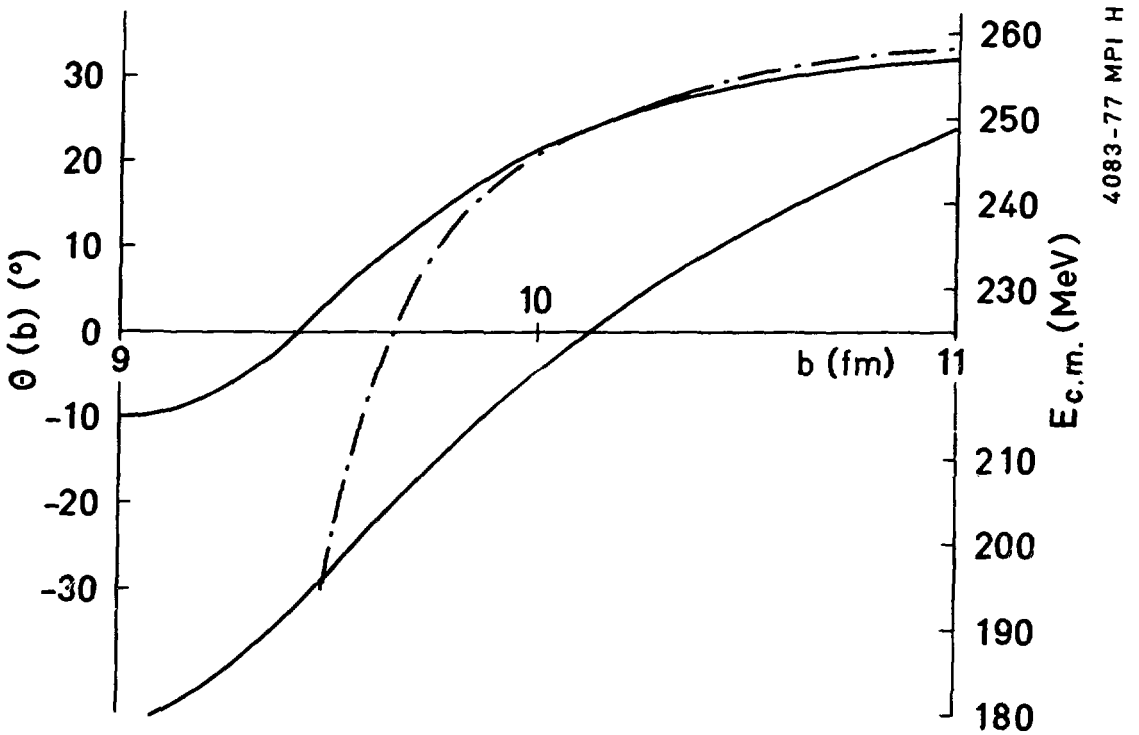
30
20
10
0
-10
-20
-30
Θ (b) (°)
9
10
11
b (fm)
260
250
240
230
210
200
190
180
$E_{c.m.}$ (MeV)
4083-77 MPI H

Fig. 5

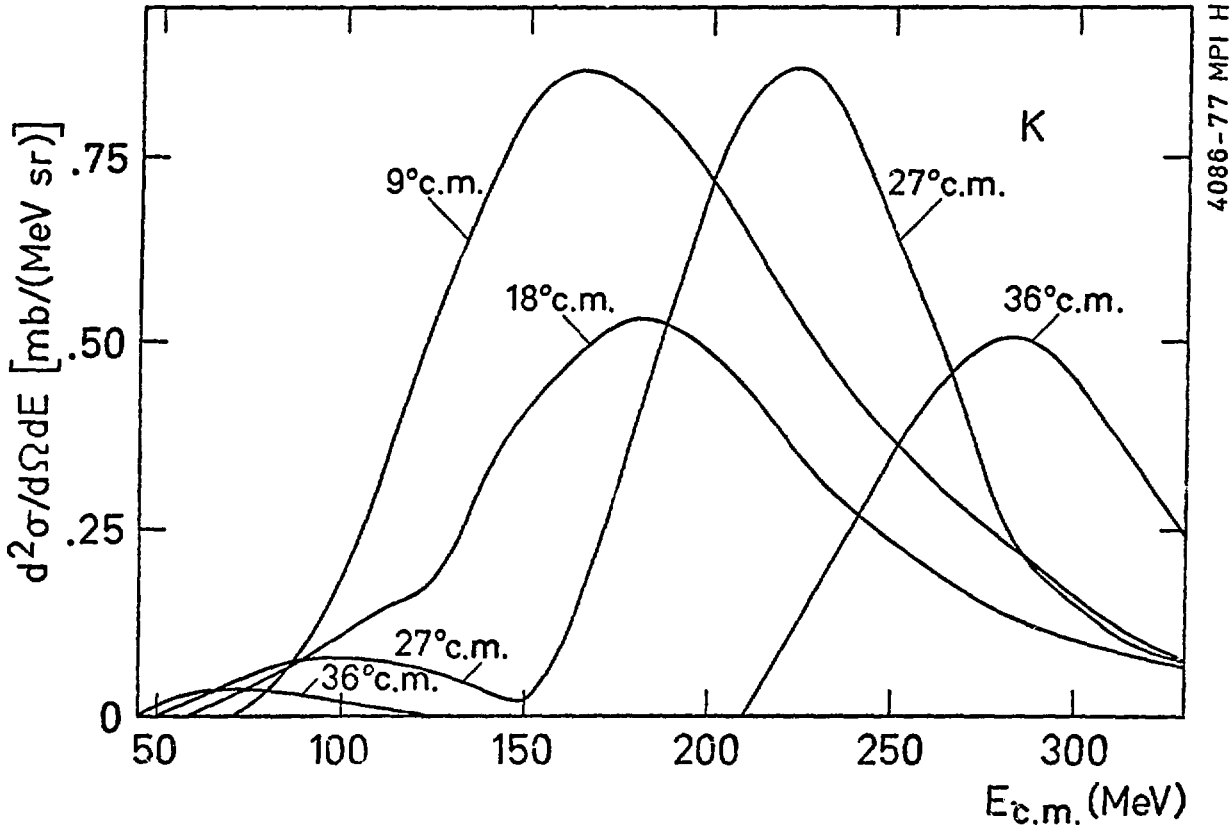
K
9°c.m.
18°c.m.
27°c.m.
36°c.m.
27°c.m.
36°c.m.
$d^2\sigma/d\Omega dE$ [mb/(MeV sr)]
0
.25
.50
.75
50
100
150
200
250
300
$E_{c.m.}$ (MeV)
4086-77 MPI H

Fig. 6

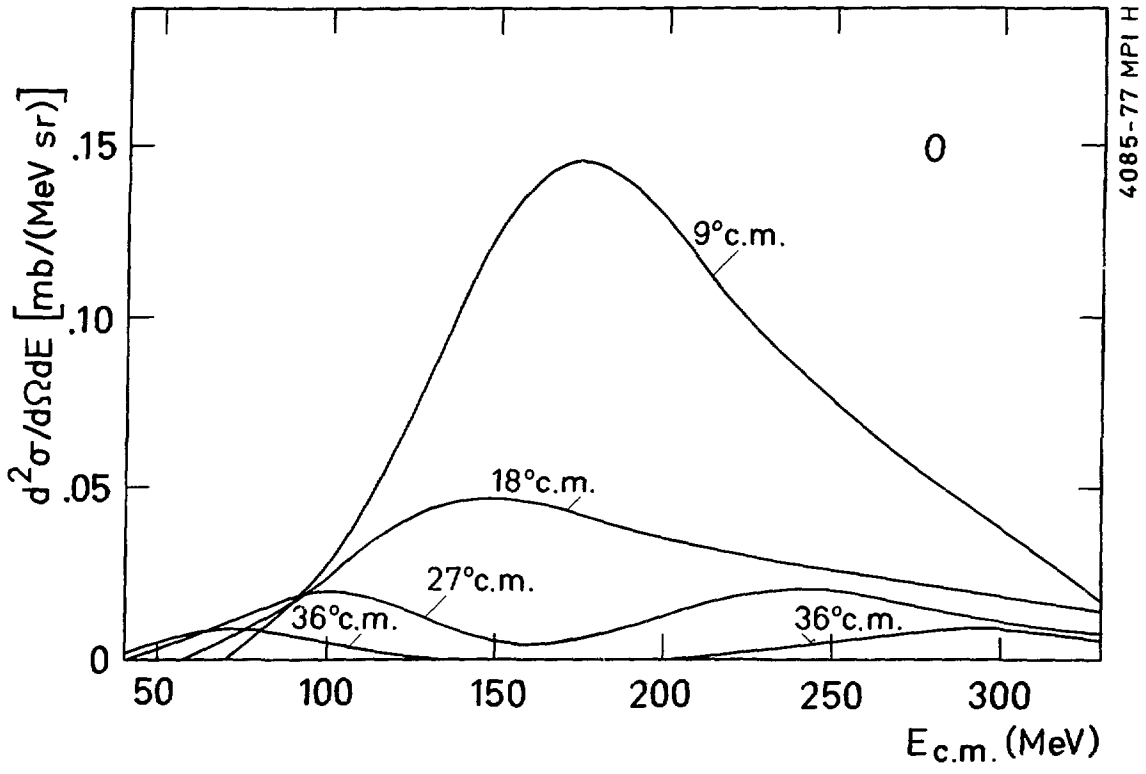
4085-77 MPI H
0
9°c.m.
18°c.m.
27°c.m.
36°c.m.
36°c.m.
$d^2\sigma/d\Omega dE$ [mb/(MeV sr)]
.15
.10
.05
0
50
100
150
200
250
300
$E_{c.m.}$ (MeV)

Fig. 7

Recent Developments in the Theory of Nuclear Dynamics

Jørgen Randrup

NORDITA, Blegdamsvej 17, DK-2100 Copenhagen Ø, Denmark

Invited talk at the Meeting on Heavy-Ion Collisions, Fall Creek Falls State Park, Pikeville, Tennessee, June 13-17, 1977

1. Introduction

In concert with the rapidly accumulating wealth of experimental data on nuclear collisions, the theoretical efforts to understand the nuclear dynamical properties have greatly intensified in recent years. Up to now, only fragments of a full dynamical theory of large-scale nuclear collective motion have been established. Best understood is the nuclear potential energy of deformation which can now be calculated to within a few MeV on a purely microscopic basis or by way of a macroscopic-microscopic method. The efforts devoted to the understanding of the nuclear collective masses have so far yielded only relatively modest results and a quantitatively reliable theory for nuclear inertias is not yet available. Until recently, the third ingredient in a full dynamical theory, namely the dissipation, was largely ignored; the few discussions made of nuclear dissipation were based on the concept of a two-body viscosity, in analogy with ordinary gases and liquids. From its dormant state, the field was recently aroused into whirling development by the realization (1) that the independent-particle model provides a relevant framework for the discussion not only of the nuclear statics but also of the nuclear dynamics. The

dominant dissipation mechanism is then the collision of the individual nucleons with the changing one-body mean field, rather than the collision of two nucleons directly. This talk will present a brief account of the most recent progress in our understanding of the dynamical properties of nuclei, with particular emphasis on the nuclear dissipation mechanism. Substantial parts of the work reported here were carried out in intimate collaboration with S. E. Koonin.

2. Idealized dissipation formulas

Before turning to the general theoretical treatment we shall discuss briefly the nuclear one-body dissipation in two idealized cases, in order to give a feeling for the magnitude and character of this type of damping.

2.1 Wall formula

As was first pointed out by Swiatecki (1), a natural starting point for the discussion of nuclear dynamics is to consider the nucleus as a collection of independent particles confined by a common container whose shape is changing slowly in the course of time.

The collision of the particles with the moving boundary wall gives rise to a velocity-dependent pressure on the wall and hence to an energy dissipation. From elementary kinetic considerations it follows that the dissipation rate is given by the "wall formula" (2)

$$\dot{Q}_{wall} = \rho \bar{v} \oint d^2a \; u(a)^2$$

In order for this expression to be valid over times longer than a typical single-particle transversal time it is necessary to assume the presence of some randomizing agent such that the particles carry no memory with them about past collisions on their journey towards future encounters with the wall. This assumption may conflict with that of a long mean free path and we shall discuss this point in some detail later on.

The constant entering in the dissipation formula is the nuclear mass density ρ times the average nucleonic speed $\bar{v}$; these quantities are well known from nuclear statics. Thus there is no room for introducing an adjustable friction coefficient as is necessary in attempts to calculate the nuclear dissipation on the basis of ordinary hydrodynamical two-body

viscosity. Because of the single-particle nature of the dissipation mechanism the characteristic damping time is of the order $R/\bar{v}$. This time is short compared with the typical duration of the collective motion encountered in fission or deep-inelastic collisions and hence one expects the motion to proceed in a strongly damped manner. Moreover, the wall formula is insensitive to the wave length of the surface velocity field; this is in contrast to ordinary two-body viscosity which preferentially damps distortions of short wave length.

2.1.1 Macroscopic fission

Macroscopic calculations of fission have been carried out with the wall dissipation (2,3). In accordance with expectations the shape evolution is overdamped and leads to relatively compact scission configurations. The results for the fragment kinetic energies (Fig. 1) are in amazing agreement with experiment considering that no parameters have been adjusted; this was a great encouragement at the early stages of the development. However, as will be evident from the discussion later on, the validity of the simple wall formula is yet not clarified and a conclusive comparison with experiment

must await more refined calculations.

2.2 Window formula

Simple estimates can be made in a similar manner for the dissipation occurring in the collision of two heavy nuclei. Here the nuclei are pictured as two separate gases of independent nucleons moving with a small relative velocity and communicating through a small window between them (4). The particles exchanged through the window carry with them and eventually deposit the momentum resulting from the velocity mismatch, thus producing a friction force. The associated dissipation rate may be written (2,5)

$$\dot{Q}_{window} = N\ (2\ u_n^{\ 2} + u_t^{\ 2})$$

where u_n and u_t are the normal and tangential components of the relative velocity $\vec{u}$ between the two nuclei. The friction coefficient $N = \frac{1}{2}\ (N_+ + N_-)$ is the average static flux of mass between the two systems. For a fully open window of cross section σ between two identical systems this mass flux is $N = n_0\sigma$ where $n_0 = \frac{1}{4}\ \rho\bar{v}$ is the bulk flux in ordinary nuclear matter. If the two systems have different composition there will be a net flux $N_+ - N_-$ providing

a driving force in the mass-asymmetry direction and the independent-particle description thus has a bearing on the dynamical mass flow between the two nuclei; even when the net mass flux is zero the random-walk type microscopic exchange of nucleons will cause the mass distribution to spread in time.

2.2.1 Proximity friction

The window formula can be refined to take account of the finite diffuseness of the nuclear surface (5). As the two nuclei approach, the window gradually opens up allowing at first only the most energetic nucleons to be exchanged; consequently, the friction will be a very sensitive function of the separation. Following the same line of argument that led to the nuclear proximity potential (6) one obtains the following expression for the nuclear proximity flux (5)

$$N = 2\pi\, n_0\, \bar{R}\, b\, \Psi\, (\zeta_0)$$

Here b is the surface diffuseness and $1/\bar{R} = 1/C_1 + 1/C_2$ is the mean curvature of the gap between the two nuclei. Furthermore, the dimensionless function $\Psi(\zeta)$ is the incomplete integral of the mass flux per unit area

between two parallel semi-infinite systems of nuclear matter; Ψ is measured in units of n_0 and is a function of the dimensionless surface separation $\zeta = s/b$. This function is displayed in fig. 2 as calculated on the basis of the nuclear Thomas-Fermi model (5-8). The replacement of the simple window formula by the proximity friction is a quantitative improvement analogous to that obtained by replacing the simple surface energy by the proximity potential (6).

2.2.2 Idealized collisions

The effect of the one-body friction can be illustrated by considering the collision of idealized nuclei which are simply spheres interacting with the conservative Coulomb and proximity potential and subject to the proximity friction. This is certainly not an adequate description of a real nuclear collision; in particular the neglect of the intrinsic shape degrees of freedom prevents the neck from developing and the exit channel barrier cannot be reduced relative to that of the entrance channel in conflict with the evidence from the final fragment kinetic energies. However, the simple model of two spheres subject to the proximity friction may provide the injection conditions

for a more refined calculation in a multi-dimensional deformation space. In the present context we shall merely use these idealized collisions to illustrate qualitatively the size of the one-body damping.

For this purpose consider ^{86}Kr on ^{197}Au. Fig. 3 displays the final orbital angular momentum ℓ_f versus the initial angular momentum ℓ_i, for three different bombarding energies. It is seen that the major part of the cross section is associated with fully damped collisions which in this model means that the velocity mismatch at the window vanishes. Only a relatively narrow ℓ-band around grazing leads to partial damping.

The amount of damping in the collision can also be illustrated by plotting the final CM kinetic energy T_{CM} versus the CM scattering angle θ_{CM} as is done in fig. 4. It is apparent that the system dissipates a major fraction of the available energy. The rate of energy dissipation during the approach phase can be estimated by the formula

$$\dot{T} \approx -4\pi\, n_0 \left(\frac{\bar{R}}{\mu}\right) b\, \Psi\, (\zeta_0)\, T$$

where μ is the reduced mass of the two nuclei; the rate typically amounts to ≈ 50 MeV/10^{-22} sec.

From such preliminary comparisons one gains the

impression that the one-body dissipation may in fact dominate nuclear dynamics. However, before a quantitative confrontation with experiment would be meaningful a better theoretical foundation of the one-body dynamics is required. We turn therefore now to the recent progress on this front; the work reported in the following was done in collaboration with S. E. Koonin.

3. Classical theory for one-body dissipation

A classical theory of one-body nuclear dynamics was recently put forth (9). In this approach, one starts out by specifying an appropriate one-body Hamiltonian $H(t)$, varying slowly in time, and then proceeds to solve the classical equations of motion by first-order time-dependent perturbation theory. Assuming that the phase-space distribution $f(\vec{r},\vec{p};t)$ remains close to equilibrium, i.e. $f = f(H)$ only, one can apply the techniques of linear response theory and arrives at the following formula for the dissipation rate

$$\dot{Q}(t) = - \langle \dot{H}(t) \left(\int_0^\infty dt' \, \hat{U}_0 \, (t') \right) \dot{H}(t) \, \frac{\partial f}{\partial H} \rangle$$

The brackets denote the integration over phase space and the evolution operator $\hat{U}_0(t')$ advances a particle along its classical trajectory for a time t'; the subscript indicates that these classical trajectories are to be calculated in the constant field corresponding to the Hamiltonian remaining frozen at its value $H(t)$ at time t.

The above expression lends itself to the following physical interpretation: Particles originating from any point $(\vec{r},\vec{p})$ in the phase space contribute a dissipation rate equal to the product of the initial impulse received $\dot{H}(\vec{r},\vec{p};t)$ and the sum of all impulses received subsequently along the entire (unperturbed) trajectory. The weighting factor $\partial f/\partial H$ ensures that for a Fermi-Dirac distribution only particles near the Fermi surface contribute. These features explicitly indicate the assumptions of a long (infinite) mean-free path and slow collective motion. It is also apparent that the dissipation mechanism has in general a very non-local character.

3.1 Leptodermous systems

For leptodermous systems it is possible to cast the expression for the dissipation rate in a tractable

form. The perturbation then corresponds to a velocity field imposed on the container walls and hence has the form

$$\dot{H} = -u(a)\ \frac{\partial H}{\partial n}$$

where $u(a)$ is the normal velocity of the surface at the point a and $-\frac{\partial H}{\partial n}$ is the normal force generated by the unperturbed container at that point on the surface. Moreover, the time integral can be written as the sum of the separate impulses received by the particle during its successive encounters with the nuclear surface along its trajectory. The first of these impulses gives rise to a local contribution to the dissipation which will turn out to be identical to the wall formula while the subsequent impulses yield the non-local contributions.

In general, the dissipation rate for a leptodermous system can be written in the form of a double surface integral

$$\dot{Q} = \int d^2a \int d^2b\ \ u(a)\ \gamma(a,b)\ u(b)$$

Here the dissipation kernel γ contains all the information about the dissipative properties of the

system; it plays a role analogous to that of the inertial tensor for the collective kinetic energy. By elementary, but somewhat lengthy, calculation it can be shown that the full classical dissipation kernel is given by

$$\gamma(a,b) = \rho\bar{v}\left(\delta^2(a-b) + \frac{4}{\pi}\sum_{\text{paths}} \cos^2\theta_a \cos\theta_b \frac{d^2\Omega_a}{d^2 b}\right)$$

As stated above the first term is recognized as that leading to the wall formula. The non-local contribution to γ is expressed in terms of the classical paths leading from a to b with weights depending on the angles of emission θ_a and absorption θ_b as well as on the focusing properties along the trajectory (expressed by the jacobian $\frac{d^2\Omega_a}{d^2 b}$) .

3.1.1 General properties

The dissipation kernel is independent of the precise profile of the surface region as long as the system remains leptodermous. Furthermore, the dependence on the distribution only enters via the overall strength $\rho\bar{v}$; in particular, the temperature dependence is only very slight (which is in drastic contrast to ordinary viscosity).

The non-local part of γ has a complicated dependence on the nuclear shape and can produce a sizable reduction of the dissipation rate. This is most strikingly brought out when the nucleus is subjected a uniform translation or rotation in which case the non-local contributions counteract completely the local term, resulting in vanishing dissipation.

The derivation of the dissipation formula relies on the assumption that the response function has a rapidly converging long-time behaviour. This behaviour is related to the rate at which the trajectories of the unperturbed Hamiltonian explore the available phase space. For a given trajectory this phase space is limited by the conservation of energy and whichever other single-particle constants of motion are present. It is necessary to modify the above expression for the dissipation kernel to take account of the pathological long-time behaviour arising when special symmetries are present.

3.1.2 Multipole oscillations

The theory is well illustrated by the multipole oscillations of a spherical nucleus. In this simple case the unperturbed trajectories are easily classified

and, for the case of zero temperature, the resulting formula for γ can be written

$$\gamma(\Psi) = \frac{\rho\bar{v}}{R^2 \sin\Psi} \lim_{t\to\infty} \{\delta(\Psi) - \frac{2}{3\pi^2} \frac{v_F}{R} t + \frac{2}{\pi}\Sigma\frac{\sin^3\phi \cos\phi}{n} \theta(t-2n \frac{R}{v_F} \sin\phi)\}$$

Here R is the nuclear radius and Ψ is the angular separation between the two surface points a and b. Furthermore, ϕ is half the angle between the successive reflections of a given trajectory and n is the number of segments. The formula is somewhat modified relative to the general formula above because the spherical symmetry imposes angular momentum conservation on the single-particle orbits which in turn strongly limits the available phase space and consequently violates the assumption of quick randomization.

The associated dissipation is most easily discussed in terms of the Legendre transforms γ_L given by

$$\gamma_L = \frac{2\pi R^2}{\rho\bar{v}} \int_0^\pi d\Psi \sin\Psi P_L(\cos\Psi) \gamma(\Psi)$$

In terms of these coefficients the dissipation rate may be written

$$\dot{Q} = \rho\bar{v}\, R^4 \sum_{LM} |\dot{\alpha}_{LM}|^2\, \gamma_L$$

where the coefficients $\dot{\alpha}_{LM}$ occur in the expansion of the velocity field on spherical harmonics,

$$u = R \sum_{LM} \dot{\alpha}_{LM}\, Y_{LM}$$

The normalization is such that the wall formula alone would yield $\gamma_L = 1$ for all L.

The coefficients γ_L are displayed in fig. 5. As expected, the effect of the non-locality in the dissipation kernel decreases with increasing L. Thus, as L becomes large and the surface velocity field grows increasingly complicated, the wall formula becomes an ever better approximation. The effect of non-locality is largest for the even multipoles where for $L = 0$ and $L = 2$ it completely cancels the local contribution. It is probable that γ_L vanishes for these modes because they preserve the separability of the spherical potential. The vanishing of γ_1 is a manifestation of the translational invariance mentioned above. We note that incompressible, irrotational viscous hydrodynamics gives $\gamma_L \sim L-1$.

In order to illustrate the convergence properties

of the expression for γ we consider in fig. 6 the value of γ_L as a function of the upper limit t, γ_L^t. For the dipole mode, the most striking structure is the persistent "sloshing" with a period equal to the "echo" time $4R/v_F$. If present in nature, this phenomenon would have observable implications for heavy-ion collisions. The gross structure of the octupole function shows a close resemblance with that of the dipole, although the smaller amplitudes and finer micro-structure are both consequences of the more complex surface velocity field. The even multipoles exhibit a faster decay of the gross structure and are quickly reduced to small amplitude oscillations around the asymptotic value.

The response function itself can be obtained directly from γ_L^t by differentiating this function and dividing by t. The relaxation behaviour of γ_L^t is therefore indicative of this property of the response function. For real nuclei, $R/v_F \approx 6$ fm/(8 fm/10^{-22} sec) = 0.75×10^{-22} sec, while typical collective time scales are $\approx 10^{-21}$ sec. Since the γ_L^t can hardly be said to be asymptotic by the time $t = 10\ R/v_F$ (at least for the low multipoles), the short relaxation-time assumption will be marginal at best. However, the

relaxation time is expected to be shorter for shapes less symmetric than the sphere, due to a more efficient randomization of the multiple reflection series.

4. Quantal treatment

The theory described in the preceeding is based on a classical approach. It is therefore devoid of any shell effects. In analogy with the shell-correction method for potential energy surfaces, the classical theory is expected to provide the smooth macroscopic background to which fluctuating quantal corrections must be applied.

The general tools for the quantal treatment of one-body dissipation were established recently (10). On the basis of quantal linear response theory the dissipation rate can be written

$$\dot{Q} = 2\pi \hbar \sum_{nm} f(\varepsilon_n) \; |\langle n|\dot{H}|m\rangle|^2 \; \delta'(\varepsilon_n - \varepsilon_m)$$

Here n,m denote the quantum states and $\varepsilon_n, \varepsilon_m$ their energy. As in the classical formula the occupation probability $f(\varepsilon_n)$ is assumed to depend only on energy.

For a leptodermous system the dissipation kernel following from the above expression can be written, in the case of zero temperature,

$$\gamma(a,b) = \frac{1}{4\pi\ \mu^2}\ (\mathrm{Im}\ \tilde{G}(a,b))^2$$

where $\tilde{G}$ is the double normal derivative of the Green function associated with the potential considered,

$$\tilde{G}(a,b) = (\hat{a}\cdot\vec{\nabla})\ (\hat{b}\cdot\vec{\nabla})\ \ G(a,b;\varepsilon_F)$$

$$G(a,b;\varepsilon_F) = \lim_{\eta\to 0^+} \langle a|\ \frac{1}{\varepsilon_F+i\eta-H}\ |b\rangle$$

In the case of finite temperature a Sommerfeld expansion can be employed involving also the second derivative of G with respect to ε. This allows one to exploit the powerful techniques developed for calculating the Green function.

4.1 Semi-infinite system

In the simple case of a semi-infinite system it is readily found that

$$\gamma = \rho\bar{v}\ \frac{2}{\pi}\ \left(\frac{j_1(ks)}{s}\right)^2$$

in the case of zero temperature. ($\vec{s} = \vec{a} - \vec{b}$.) This expression tends to the classical expression when $ks \to \infty$ but gives in general rise to a spatial smearing due to the finite wave length of the nucleons (fig. 7). This in turn causes a substantial reduction of the dissipation rate when the wave length of the induced surface ripples is comparable to or smaller than the nucleon size (fig. 8). It can also be shown that while the dissipation rate is independent of the surface profile when the wave length of the velocity field is infinite, the dissipation exhibits a decrease as a function of surface diffuseness when the distorting wave length is finite (fig. 9).

Moreover, the semi-infinite geometry can be used to calculate the curvature corrections to the planar dissipation kernel above; this curvature correction depends on the orientation of $\vec{s}$ relative to the local principal system of curvature. In general the curvature reduces the dissipation, and quite appreciably so in realistic cases (fig. 10).

4.2 General shapes

On the basis of the Lippmann-Schwinger equation it is possible to derive an integral equation for the function $\tilde{G}$:

$$\tilde{G}(a,b) = 2\,\tilde{G}_0\,(a,b) + \oint d^2p\;\; K(a,p)\;\tilde{G}(p,b)$$

Here $\tilde{G}_0$ is the double normal derivative of the free Green function G_0 and the integral kernel K is given in terms of G_0 as

$$K(a,b) = -\frac{1}{\mu}\,(\hat{a}\cdot\vec{\nabla})\;G_0(a,b) - \delta(a-b)$$

The above integral equation provides a natural starting point for studying the one-body dissipation of general shapes.

Iteration of the integral equation for $\tilde{G}$ yields an expression for $\tilde{G}$ in terms of multiple surface integrals involving the kernel K and the function $\tilde{G}_0$. The evaluation of these integrals by the stationary-phase method in the limit $kR \gg 1$ results is an expansion for $\tilde{G}(a,b)$ in terms of the classical trajectories between a and b . In the extreme limit $kR \to \infty$ the different paths contribute incoherently and

the classical expression for the dissipation kernel γ is recovered; this is an alternate way of deriving the classical dissipation formula (9).

In fig. 11 is shown the exact quantum-mechanical result for the dissipation coefficient γ_3 corresponding to an octupole oscillation. One notes that while large oscillations occur the average agrees well with the classical value in the limit $kR >> 1$. The quantum oscillations are sensitive to the nuclear temperature and quickly wash out for temperatures exceeding a few MeV. But for smaller temperatures the quantum oscillations can be of the same order as the smooth background. This is contrary to the shell correction to the nuclear potential energy and is a consequence of the fact that only nucleons near the Fermi surface contribute to the dissipation while all of the nucleons contribute to the binding energy. Shell effects may thus substantially affect the dissipative properties of a specific nucleus.

4.2.1 Semi-classical approach to shell effects

The shell effects in the one-body dissipation may be studied in a semi-classical approach (11). A semi-classical treatment of the dissipation can be made by

retaining the phase coherence in the classical path sum for $\tilde{G}$. This permits the different classical paths to interfere and thus produce the quantum oscillations. This approach makes it possible to interpret the shell effects in terms of distinct classical orbits in the potential considered. Preliminary results have been obtained with this simple semi-classical treatment and the approach holds promise for providing a quantitative method for extracting the shell structure in the nuclear dissipation.

5. Discussion

In the preceeding we have discussed the nuclear dissipation in the extreme one-body limit. The approach was based on the application of linear response techniques to the independent-particle description of the nucleus, ignoring all residual inter-nucleon interactions. The entire approach can be carried through in an analogous manner to yield the proper one-body result for the inertial-mass parameters, thus completing the one-body description of the collective nuclear dynamics (9).

For leptodermous systems, the collective kinetic

energy and the rate of energy dissipation for slow but arbitrary collective motion are given in terms of mass and dissipation kernels coupling the velocity of different points on the nucleon surface. In the large-nucleus limit, these kernels are independent of the surface diffuseness of the single-particle potential and are simply and only weakly dependent on the nuclear temperature. For a given nuclear shape, the kernels can be expressed in terms of the classical trajectories for nucleons within the nucleus. These results can also be derived by taking the stationary-phase (large-nucleus) limit of an entirely quantal formulation. Modifications are necessary in case there are special symmetries in the single-particle Hamiltonian. The one-body mass and dissipation coefficients differ significantly from those of incompressible, irrotational hydrodynamics.

The approach rests on the validity of two related assumptions. These are the use of a perturbative treatment and the possibility of a temporally local reduction of the dynamical equations. These questions are intimately related to the self-consistency between the nucleons and the time-dependent nuclear single-particle potential. For collective motion slow in comparison to

the single-particle relaxation time (see Fig. 6 for an estimate of this quantity), reflections of the nucleons within a sufficiently asymmetric nuclear shape will serve to quickly randomize the phase-space distribution function. Consequently, both a perturbative approach about a distribution function characterized by a time-dependent temperature and the local reduction of the generally non-local linear response equations are valid. For relatively rapid collective motion the distribution function does not have sufficient time to relax, so that perturbation theory breaks down and non-linear self-consistency becomes important; a temporally local description then becomes impossible. However, it should be noted that the generally large damping produced by the one-body mechanism is expected to result in slow collective motion, justifying a posteriori this assumption.

If indeed the collective motion is dissipation dominated the nuclear shape will develop in a creeping fashion and the inertial forces will be negligible. Then the dynamical motion is governed by the balancing of the conservative and dissipative forces alone, leading to a first-order equation of motion (2). The validity of such a superdamped nuclear macro-dynamics is

presently an exciting prospect; whether and under which conditions nuclei actually do behave in this simple manner is not yet clear. In order to answer that fundamental question it is necessary to perform more elaborate dynamical calculations, including several collective degrees of freedom simultaneously and, in particular, taking due account of the non-local effects discussed in the preceeding.

References

1. W. J. Swiatecki, Lawrence Berkeley Laboratory Report LBL-4296 (1975)

2. J. P. Błocki, Y. Boneh, J. R. Nix, J. Randrup, M. Robel, A. J. Sierk, W. J. Swiatecki, Lawrence Berkeley Laboratory Report LBL-6100

3. A. J. Sierk and J. R. Nix, Symposium on Macroscopic Features of Heavy-Ion Collisions, Argonne National Laboratory, Argonne, Illinois, (1976) 407

4. W. J. Swiatecki, Jour. Phys. 33 (1972) 45-60

5. J. Randrup, "Nuclear One-Body Proximity Friction", Nordita Preprint 77/7 (1977)

6. J. P. Błocki, J. Randrup, C. F. Tsang, W. J. Swiatecki, Ann. Phys. (1977) (LBL-5014)

7. W. D. Myers and W. J. Swiatecki, Ann. Phys. 55 (1969) 395

8. J. Randrup, Nucl. Phys. A259 (1976) 253

9. S. E. Koonin and J. Randrup, "Classical Theory for One-Body Nuclear Dynamics", The Niels Bohr Institute Preprint (1977)

10. S. E. Koonin, R. L. Hatch, J. Randrup, Nucl. Phys. A277 (1977) 509

11. J. Randrup, V. M. Kolomietz and S. E. Koonin, in preparation

Figure Captions

Fig. 1 Comparison of experimental most probable fission-fragment kinetic energies with results calculated with the wall dissipation formula. This dissipation corresponds to a very overdamped system. The results for infinite two-body viscosity are shown as a dashed line to illustrate the different effects of large dissipation in the two models (2,3).

Fig. 2 The universal proximity flux function $\Psi(\zeta)$ as calculated in the nuclear Thomas-Fermi model (5).

Fig. 3 The final orbital angular momentum ℓ_f as a function of the initial angular momentum ℓ_i for the idealized collision of ^{86}Kr and ^{197}Au, at three different bombarding energies (2)

Fig. 4 The final fragment kinetic energy T_{CM} versus the scattering angle θ_{CM} (both in the center-of-mass system) for the idealized colision of ^{86}Kr and ^{197}Au, at three different bombarding energies. The values of the total angular momentum are indicated (2).

Fig. 5 The dissipation coefficients γ_L for multipole distortions of a sphere, as calculated in the classical one-body theory (9). The open dots indicate the value obtained when only the local term in the dissipation kernel $\gamma(\Psi)$ is retained (the wall formula). The full dots indicate the value resulting when the non-local terms are included.

Fig. 6 Dissipation coefficients γ_L^t for multipole distortions of a sphere, as a function of the upper limit t in the time integral. The marks on the vertical scale are positioned at intervals of 0.5 and the value of all curves is unity at $t = 0$ (9).

Fig. 7 The dissipation kernel $\gamma(s)$ for semi-infinite nuclear matter. The curves are normalized by the zero-temperature value for $s = 0$. The distance scale along the top assumes $k_F = 1.4\ fm^{-1}$ (10).

Fig. 8 The dissipation kernel $\gamma(q)$ for semi-infinite nuclear matter. The curves are normalized by the zero-temperature value at $q = 0$ (10).

Fig. 9 The influence of surface diffuseness on the dissipation kernel. The parameter α is a dimensionless measure of the surface diffuseness (10).

Fig. 10 Curvature effects in the planar dissipation kernel, $\gamma(\vec{s})$, adopting $\kappa_+/k_F = 0.2$, $\kappa_-/k_F = 0.1$. The solid line is the zero-temperature planar result. The hatched region indicates the variation of $\gamma(\vec{s})$ with the orientation of $\vec{s}$ relative to the principal axes of curvature. The lower (upper) limit of this region corresponds to $\vec{s}$ oriented along the axis with the larger (smaller) radius of curvature. The curves are normalized to the planar result at $s = 0$ (10).

Fig. 11 The dissipation coefficient γ_3 for octupole distortion of a sphere of radius R, as calculated in the exact quantal treatment. The complex Fermi energy was taken as $\varepsilon = 40 + 2i$ MeV; results for the temperatures $T = 1,4$ MeV are shown. As indicated, the peaks can be associated with specific single-particle transitions $|n\ell\rangle \rightarrow |n'\ell'\rangle$ (11).

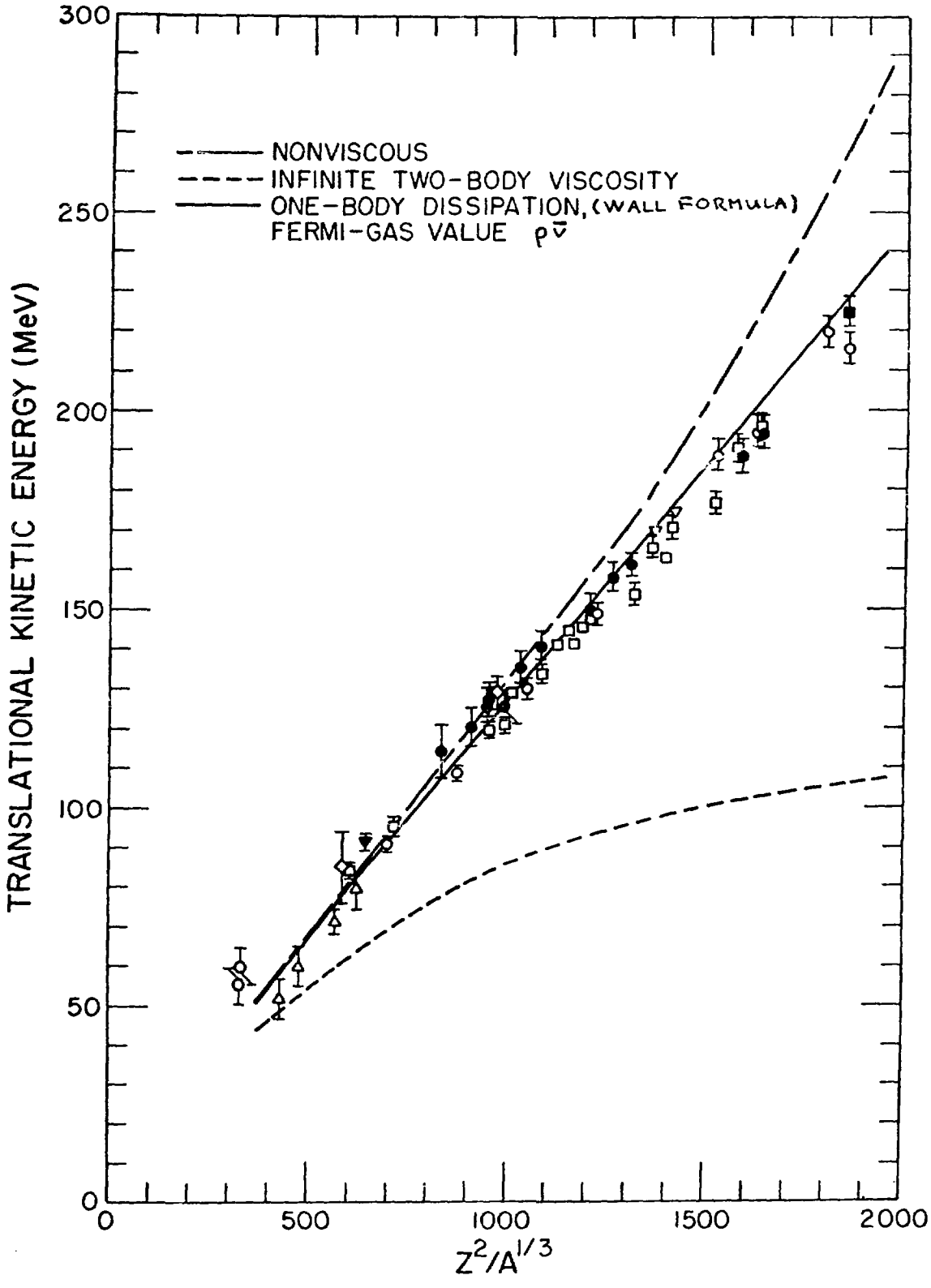
NONVISCOUS
INFINITE TWO-BODY VISCOSITY
ONE-BODY DISSIPATION, (WALL FORMULA)
FERMI-GAS VALUE $p\bar{v}$
TRANSLATIONAL KINETIC ENERGY (MeV)
$Z^2/A^{1/3}$
0
50
100
150
200
250
300
500
1000
1500
2000

Fig. 1

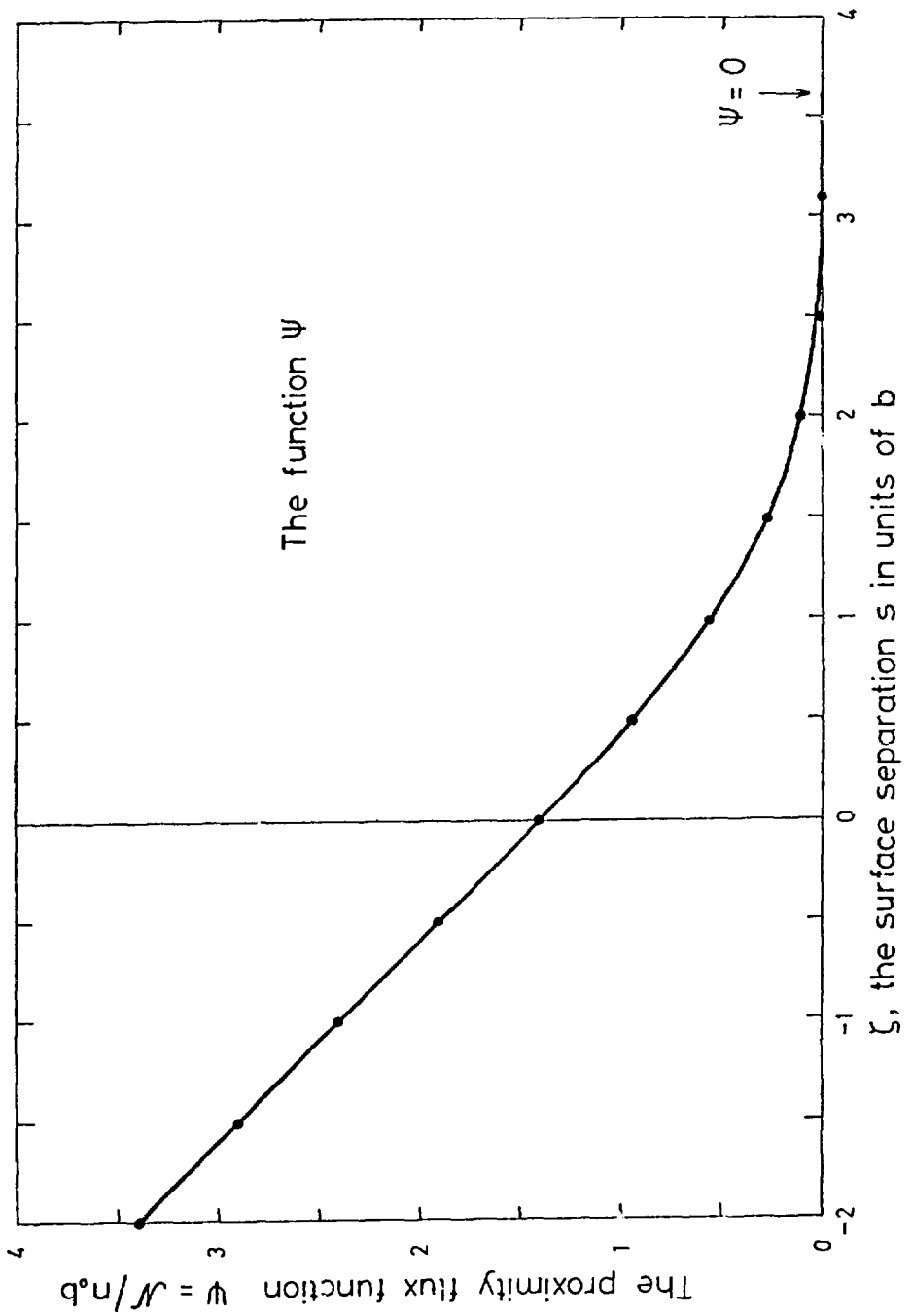
The function Ψ
Ψ = 0
The proximity flux function Ψ = 𝒩/n₀b
ζ, the surface separation s in units of b
4
3
2
1
0
-2
-1
0
1
2
3
4

Fig. 2.

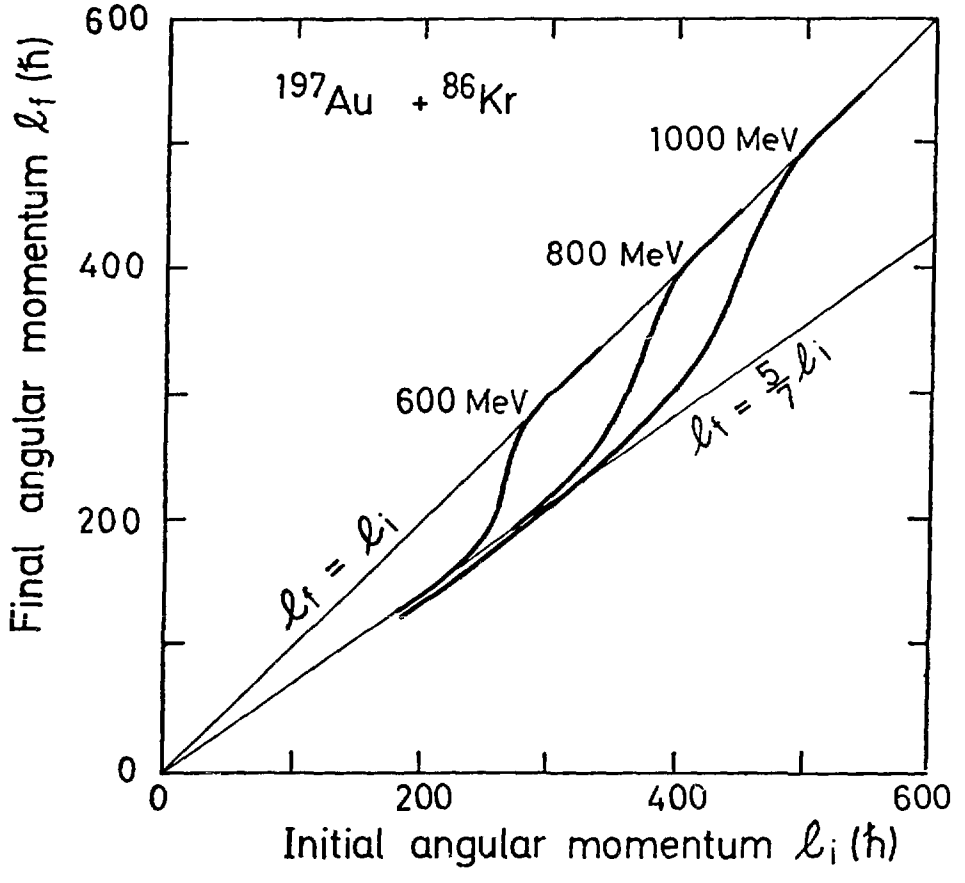
600
400
200
0
0
200
400
600
$^{197}Au + ^{86}Kr$
1000 MeV
800 MeV
600 MeV
$\ell_f = \ell_i$
$\ell_f = \frac{5}{7}\ell_i$
Final angular momentum ℓ_f ($\hbar$)
Initial angular momentum ℓ_i ($\hbar$)

Fig. 3

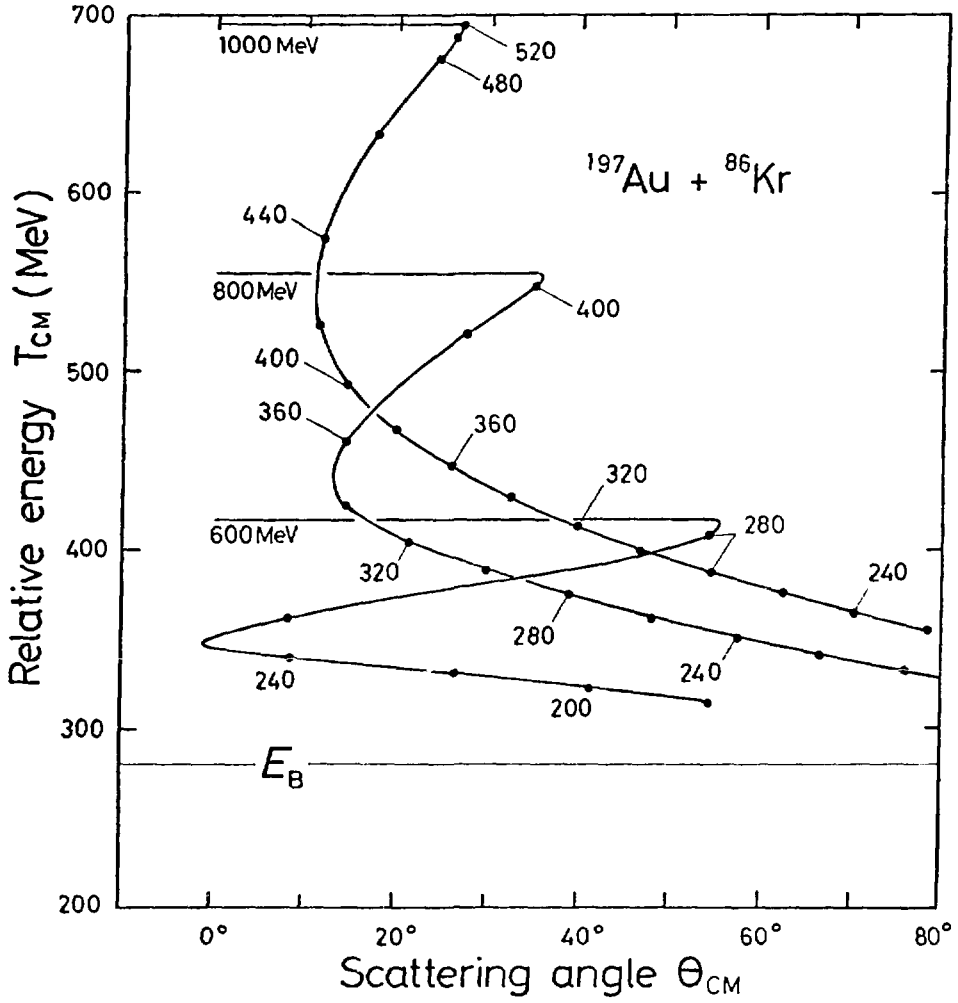
700
600
500
400
300
200
Relative energy T_{CM} (MeV)
0°
20°
40°
60°
80°
Scattering angle Θ_{CM}
$^{197}Au + ^{86}Kr$
1000 MeV
800 MeV
600 MeV
520
480
440
400
400
360
360
320
320
280
280
240
240
240
200
E_B

Fig. 4

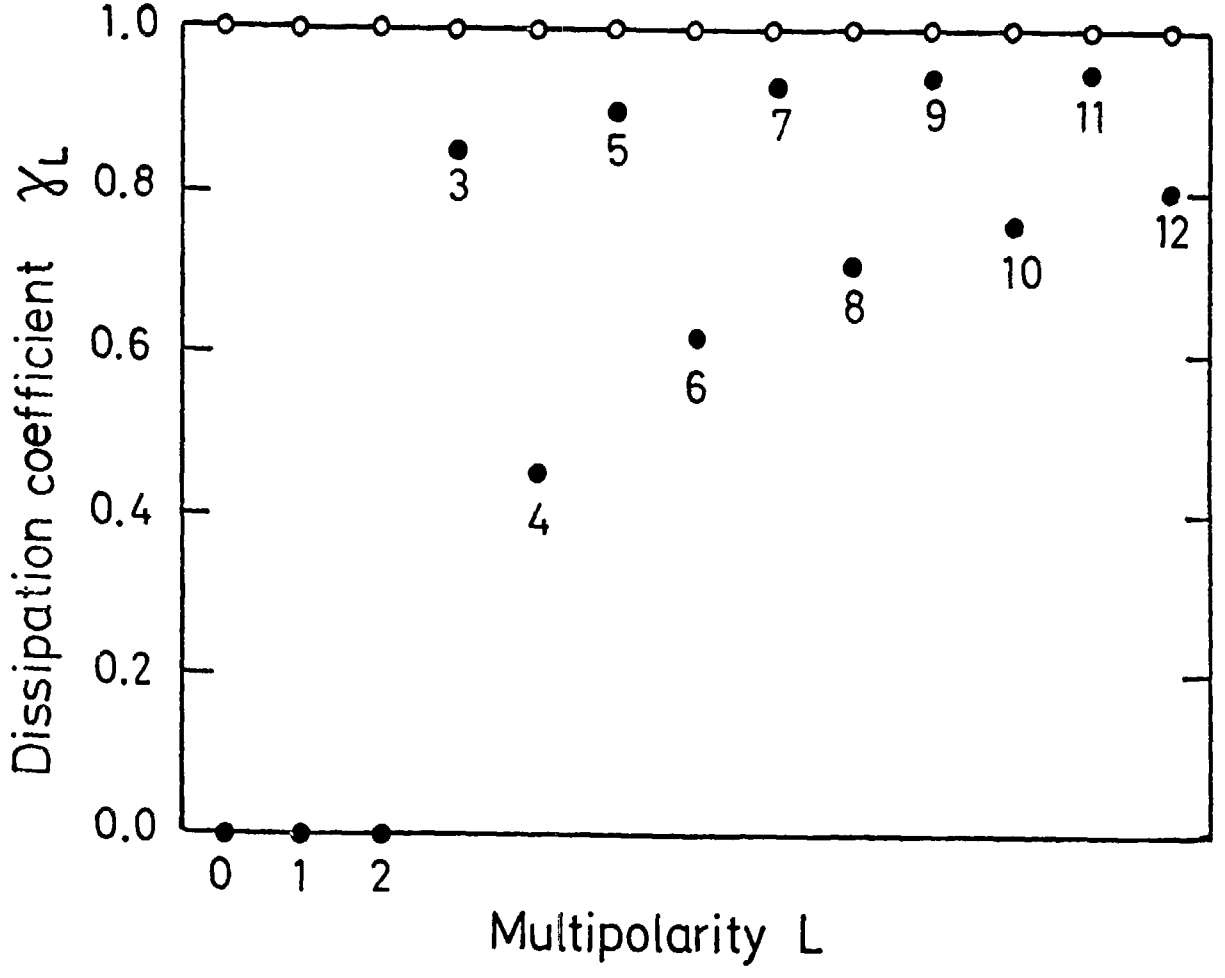
1.0
0.8
0.6
0.4
0.2
0.0
Dissipation coefficient γ_L
0
1
2
3
4
5
6
7
8
9
10
11
12
Multipolarity L

Fig. 5

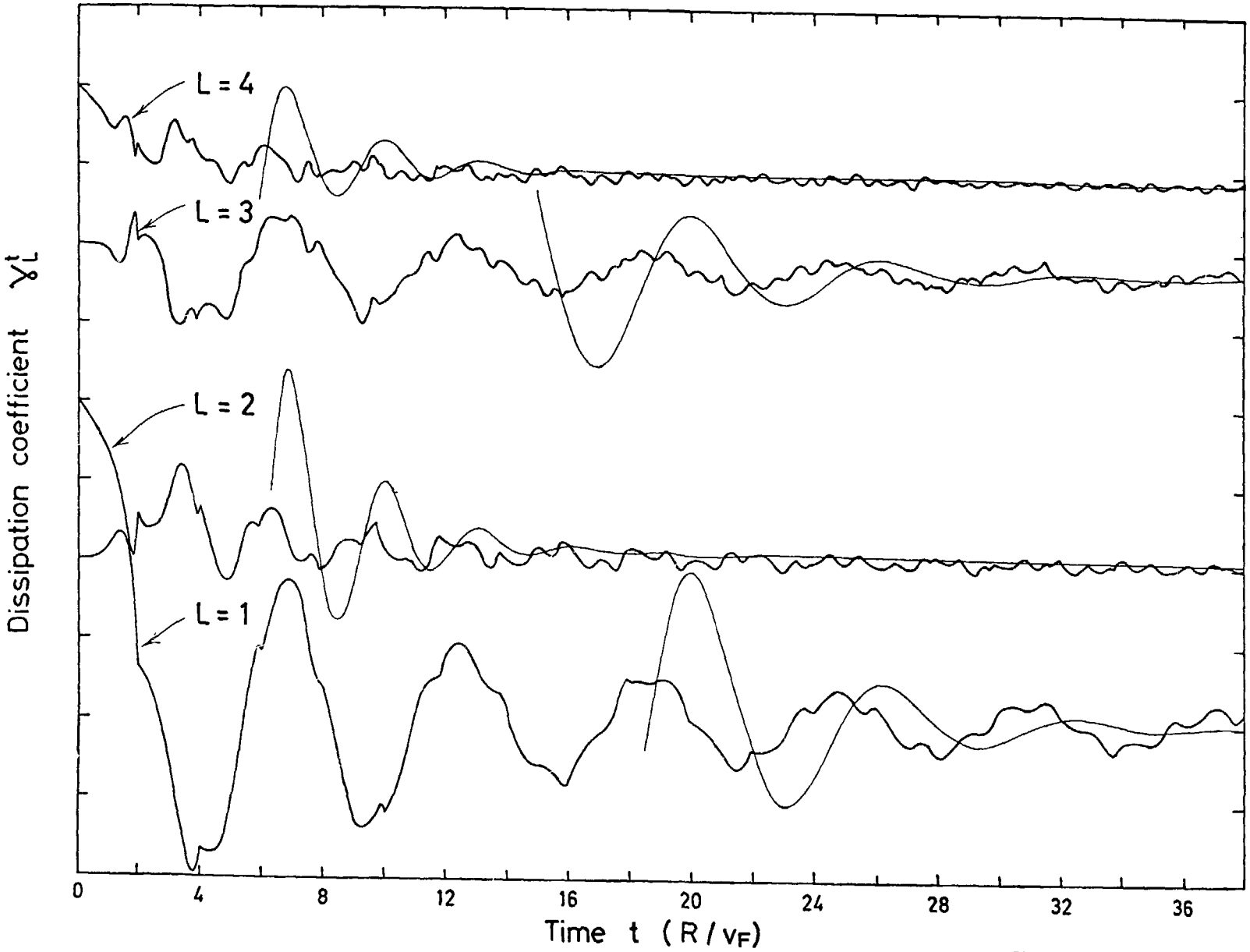
L = 4
L = 3
L = 2
L = 1
Dissipation coefficient γ_L^t
0
4
8
12
16
20
24
28
32
36
Time t (R / v_F)

Fig. 6

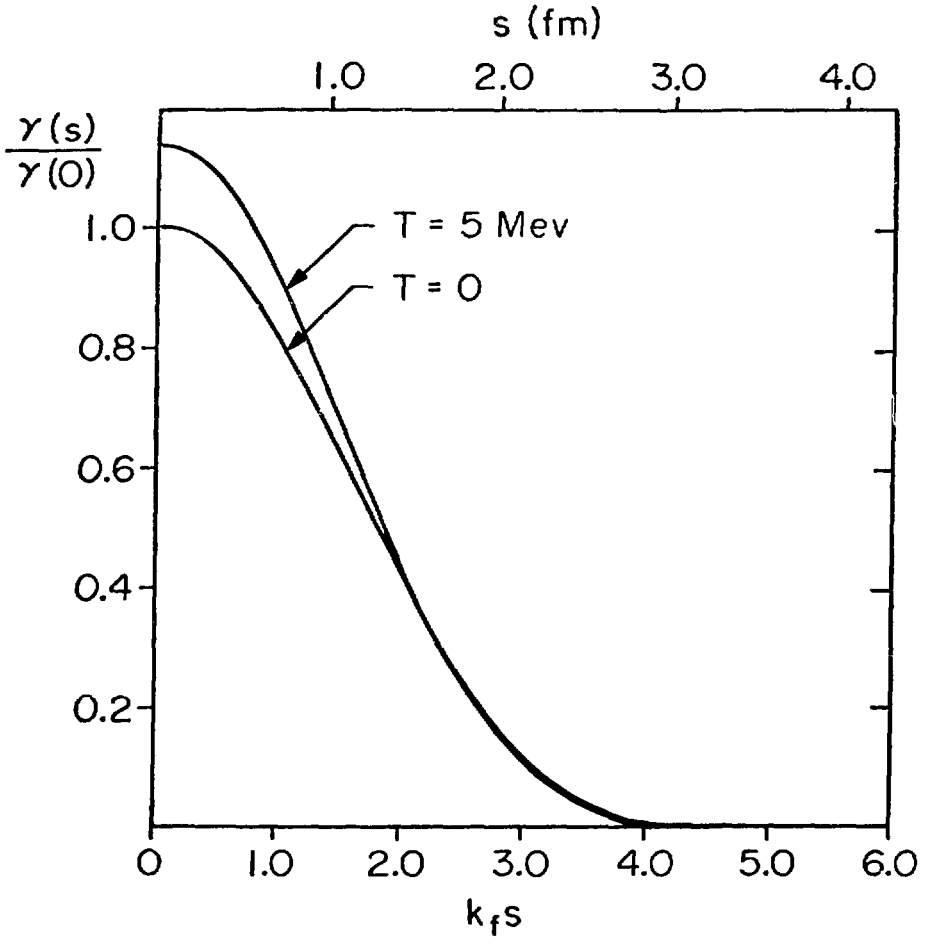

Fig. 7

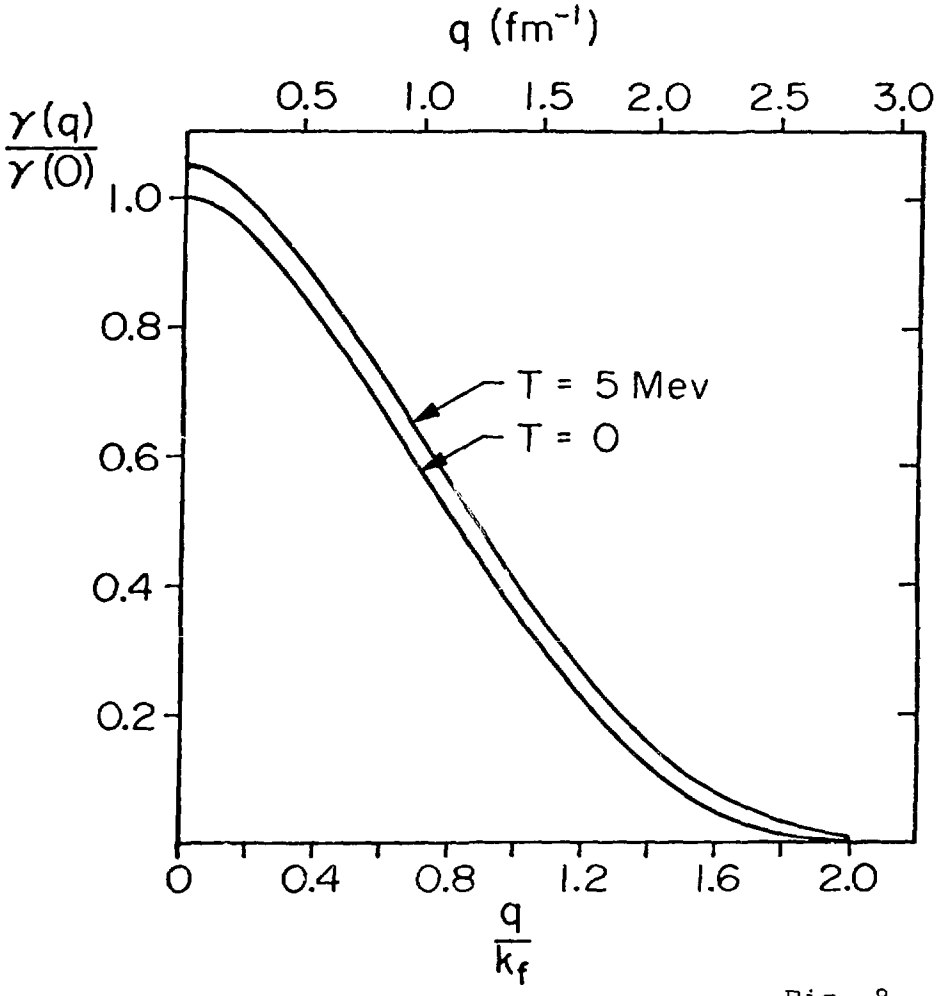
q (fm⁻¹)
0.5
1.0
1.5
2.0
2.5
3.0
γ(q)/γ(0)
1.0
0.8
0.6
0.4
0.2
T = 5 Mev
T = 0
0
0.4
0.8
1.2
1.6
2.0
q/k_f

Fig. 8

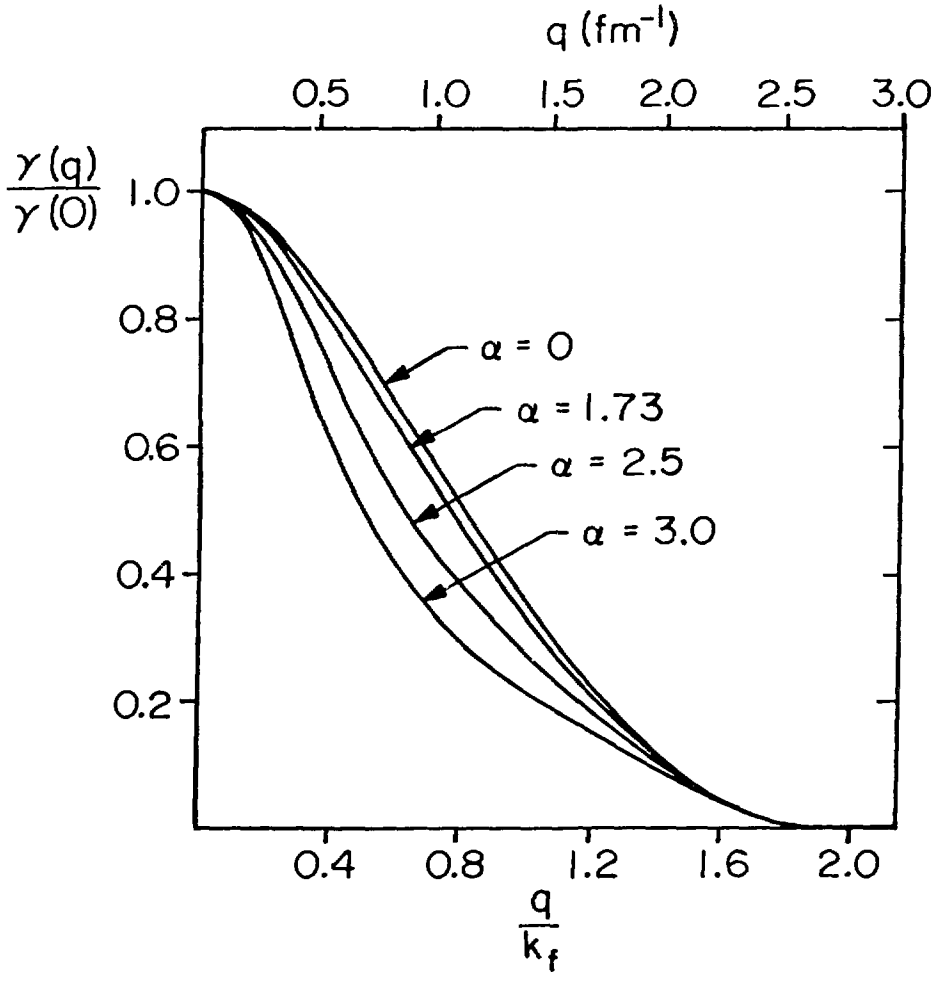
q (fm⁻¹)
0.5
1.0
1.5
2.0
2.5
3.0
γ(q)/γ(0)
1.0
0.8
0.6
0.4
0.2
α = 0
α = 1.73
α = 2.5
α = 3.0
0.4
0.8
1.2
1.6
2.0
q/k_f

Fig. 9

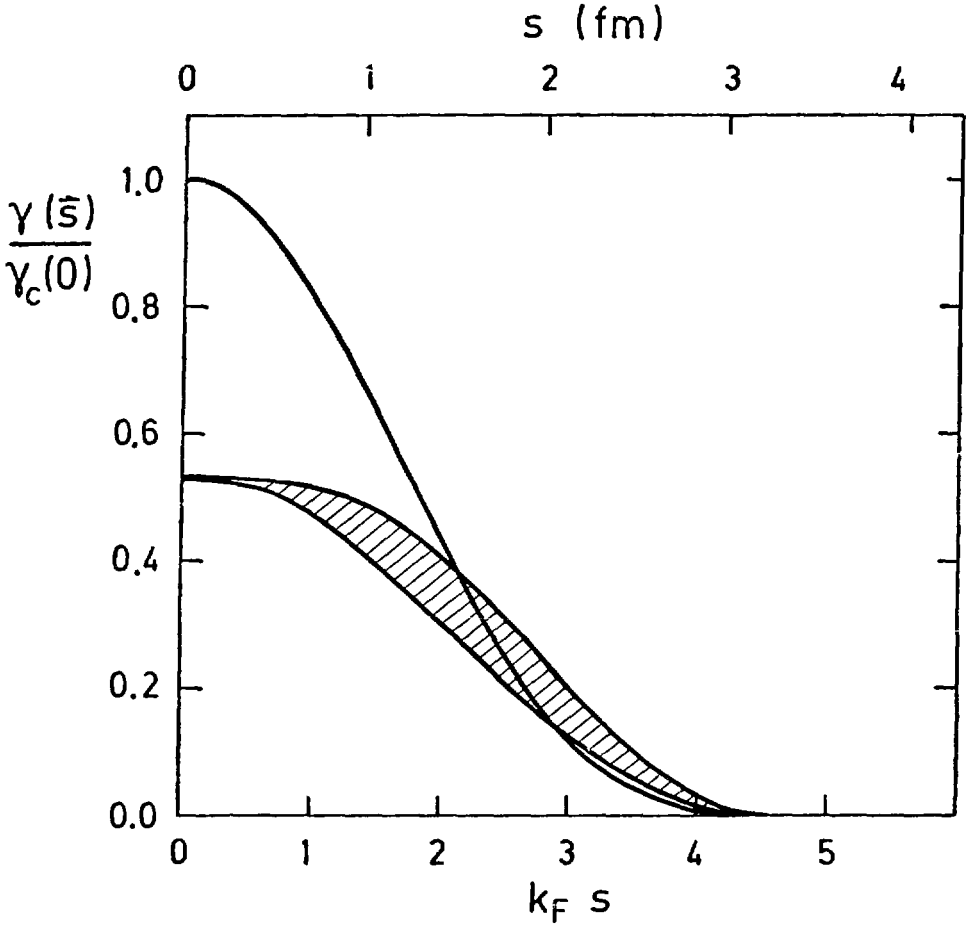
s (fm)
0
1
2
3
4
$\frac{\gamma(\tilde{s})}{\gamma_c(0)}$
1.0
0.8
0.6
0.4
0.2
0.0
0
1
2
3
4
5
k_F s

Fig. 10

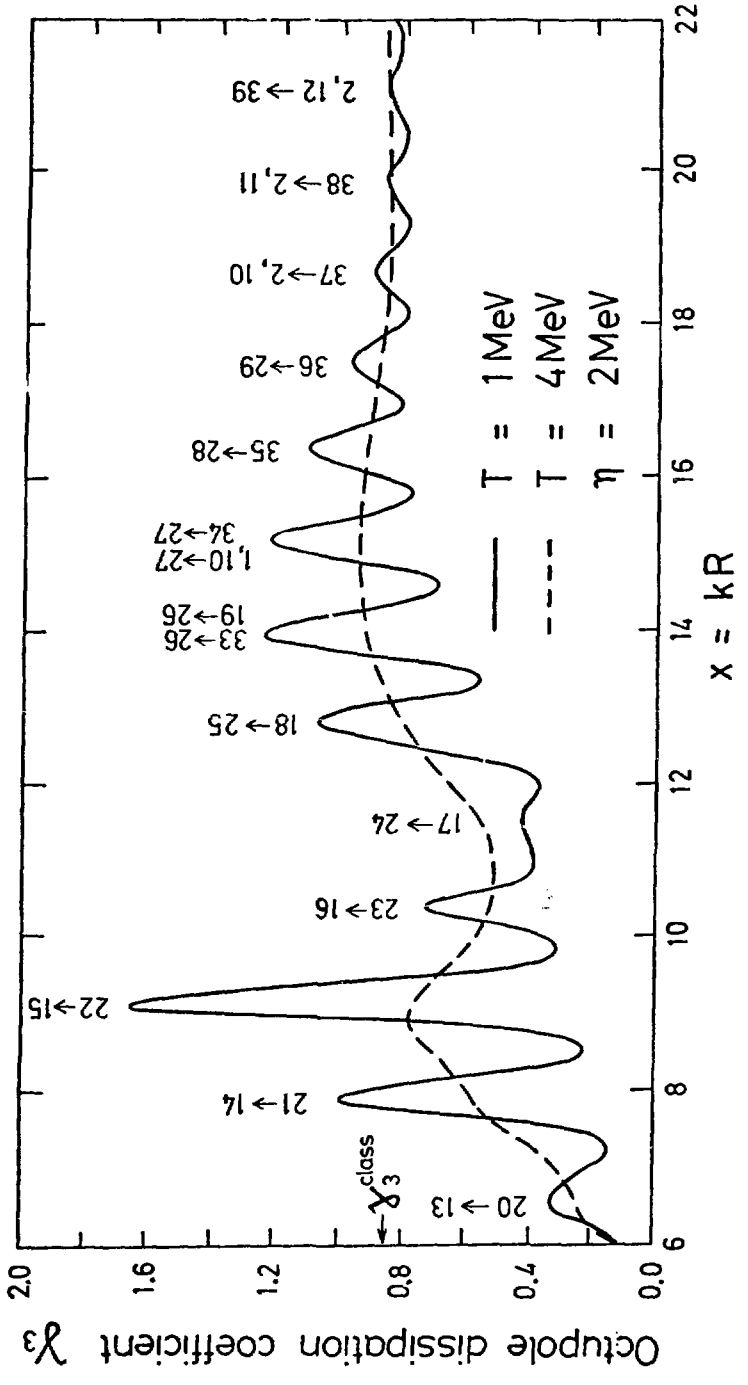
Octupole dissipation coefficient γ_3
γ_3^{class}
x = kR
T = 1 MeV
T = 4 MeV
η = 2 MeV
20 ← 13
21 ← 14
22 ← 15
23 ← 16
17 ← 24
18 ← 25
33 ← 26
19 ← 26
1, 10 ← 27
34 ← 27
35 ← 28
36 ← 29
37 ← 2, 10
38 ← 2, 11
2, 12 ← 39

Fig. 11

DISSIPATION AND FLUCTUATIONS WITHIN A MACROSCOPIC TREATMENT FOR HEAVY ION COLLISIONS[+]

Helmut HOFMANN[*] and Christian NGO

Institut de Physique Nucléaire, BP n°1, 91406 Orsay (France)

Abstract

We review the quasi static approach to deep inelastic reactions, its basic assumptions as well as its fundamental formulas. The typical experimental features are briefly discussed. An application using phenomenological forces is described and compared with the experimental results.

[+]Supported in part by the Bundesministerium für Forschung und Technologie.

[*]Permanent address : Physik Department der TUM, James Franck straße 8046 Garching, FRG

Introduction

In this review we would like to concentrate on deep inelastic reactions. They are found in experiments where the kinetic energy of relative motion is between one and a few time the interaction barrier[1]. These deep inelastic collisions show features which one did not encounter in nuclear physics before. During the reaction a large amount of kinetic energy in the relative motion is lost during the process. This can amount to more than 100 MeV. It is hard to believe such processes to be possible without sharing the energy among many excitations of the intrinsic system and exciting some collective modes. Whereas this feature might indicate a compound like reaction, the angular distribution of the final products tells us that the exit channel remembers somehow the initial configuration. This may also be concluded from the fact that for the most probable events, the masses of the products are close to the masses of the projectile and of the target.

The simplest way to describe these characteristics is in terms of equations of motion for macroscopic degrees. We may define them as those degrees which determine directly the quantities measured in experiments like angle, kinetic energy of the fragments as well as their mass asymmetry, spins etc... As mentioned before, these degrees will not reach thermal equilibrium but they keep the memory of the entrance channel. We shall refer to them as the slow degrees of the system. Since they always describe a motion of many nucleons they are similar in nature to the collective degrees in the nuclear collective model[2]. We will consider the words macroscopic and collective as synonymous henceforth.

To guess the form of the equations of motion one has borrowed from pictures which have been very successful in many fields of physics where statistical phenomena take place. The energy loss is described as a dissipative or frictional process[3]. The friction force taken to be proportional to the velocity is inserted into classical Newton equations[4-10]. The classical limit being justified because the De Broglie wavelength is much smaller than the typical dimensions of the system. The exchange of nucleons, on the other hand, is sometimes described as a diffusion process[11]. The equations of motion are then of Fokker-Planck (or master) type[11-14].

In trajectory calculations (which are based on the Newton equations) one gets informations for the mean values of the macroscopic degrees. Such calculations reproduce qualitatively the observed energy loss if the two ions remain spherical during the whole process[4,5,7]. The agreement becomes better when deformations in the exit channel are included either explicitely[6,8] or implicitely[9,10]. With such calculations one also obtains an idea of the angular distribution $d\sigma/d\theta$, except in the vicinity of the rainbow angles where the classical cross section becomes infinite.

With a Fokker Planck equation, it is possible to describe the time evolution of fluctuations. By working with some simple approximation, one

has been able to understand qualitatively the increase in time of the widths of mass (or atomic number) and energy distributions as well as the variation of the position of their maximum[11-14]). In some favoured cases a correlation between these quantities and the detection angle is also obtained[11,12]).

One would guess, however, that the coupling of relative motion to such "diffusion" processes should be treated more carefully. This amounts to say that a connection should be established between dissipation which is accounted for in trajectory calculations, and "diffusion" phenomena. Indeed, if these statistical processes are of the same nature as those found in real macroscopic bodies (like gases, liquids or solids), one would expect a strong relationship between dissipation and fluctuations. This fact is even established in a theorem, the so called fluctuation dissipation theorem. The question then arises whether and how these pictures can be applied to nuclear physics.

This problem was attacked in ref.15,16) in trying to extend the nuclear collective model to include dissipative phenomena. The tool for it was linear response theory. In this way the question of "how" was solved, for the other part, one has only hints so far without a definite answer.

In the following we shall concentrate on this approach. We want however to draw attention on the work of Agasi, Ko and Weidenmüller[17]) who attacked the problem in a different way using a random matrix model and refer to the review given by Pr. Weidenmüller at this conference[18]).

I) Application of linear response theory to deep inelastic collisions (ref.15,16,19).

For an understanding of such complex situations we are faced with in deep inelastic reactions, it is desirable to have a description in terms of single physical ideas. We certainly have to base heavily on simplifying assumptions. To find the right ones, we have to look at the goal we are aiming at and, more important, at the given physical situation.

We want to get equations of motion for the macroscopic degrees. Therefore, it is not only convenient, but almost necessary to start with a model hamiltonian which contains these degrees explicitely from the very beginning. The hamiltonian is assumed to have the following form :

$$\hat{\mathcal{H}} = \hat{H}(\hat{x}_i,\hat{p}_i) + \hat{V}(\hat{x}_i,\hat{Q}) + \hat{h}(\hat{Q},\hat{P}) \qquad (1)$$

Here and in the following, we restrict the discussion to the case of one collective degree Q (its conjugate momentum is called P). The intrinsic degrees and their momenta are respectively denoted by x_i and p_i. The operators $\hat{h}$ and $\hat{H}$ represent the hamiltonians for the bare collective and intrinsic motion. The coupling between both is given by $\hat{V}$.

Everybody will agree on this procedure if we introduce the vector of relative motion as the only macroscopic coordinates. But the assumption is less obvious for other degrees, like mass asymmetry for instance.

As for the physical situation we should have in mind two things. Firstly the excitation becomes so big that most likely statistical assumptions can be made. Secondly the kinetic energy of the macroscopic degrees counted per nucleon, E_{kin}/A, is small compared to the Fermi energy. Here, an upper limit is certainly given by the example of relative motion. As already mentioned, for this case E_{kin}/A is at most a few MeV in the neighborhood of the barrier. This is certainly small compared to the magnitude of the Fermi energy ($\simeq$ 37 MeV).

From the latter observation, two inferences can be drawn :

1) It is likely that the coupling of the intrinsic motion to the macroscopic degrees is mainly governed by single particle fields. That is to say $V(x_i,Q)$ can be assumed to be a deformed single particle potential. It could for instance represent a two center shell model potential. Another possibility would be to say that H represents the two unperturbed ions and V is constructed from the fact that the density of one nucleus feels the potential of the other. It should however be noted, in passing, that the formal theory also applies if H and $V(x_i,Q)$ contain residual two body interactions.

2) The second inference is that indeed the time scale for the intrinsic degrees seems to be shorter than that for the macroscopic degrees.

These considerations have been used to formulate the assumptions of the theory. The most drastic one is to require that at any time the intrinsic system relaxes very fast to statistical equilibrium. This equilibrium is parametrized by a temperature T. During the reaction, this temperature increases in time, according to the increasing energy loss. The long time behaviour of the system is then described completely in terms of the time evolution of the temperature and that of the mean values of the collective degrees. A microscopic study of the intrinsic motion is only necessary for a period of the order of the relaxation time τ since the system cannot remember for a longer time. Such a microscopic study will be used to determine the induced forces, that is to say the complete equations for the collective degrees.

According to our assumption, τ will be much shorter than a typical time τ_{coll} for the collective or macroscopic motion.

$$\tau \ll \tau_{coll} \tag{2}$$

In other words we assume that the system can be divided in slow modes (macroscopic degrees) and fast ones (intrinsic degrees). This fact can be used to justify a perturbation approach for the microscopic motion. Suppose we want to study the system in the interval

$$t_o < t < t_o + \delta t \tag{3}$$

with $$\tau \lesssim \delta t \ll \tau_{coll} \tag{4}$$

For this let us rearrange some terms in the hamiltonian (1) :

$$\hat{\mathcal{H}} = \hat{H} + \hat{V}(\hat{x}_i, Q_o) + \delta\hat{V} + \hat{h} \tag{5}$$

with $$\delta\hat{V} = \hat{V}(\hat{x}_i, \hat{Q}) - \hat{V}(\hat{x}_i, Q_o) \tag{6}$$

Here we have introduced the mean value of the collective degree

$$Q(t) = \langle\hat{Q}\rangle_t \tag{7}$$

taken at time t_o : $Q_o = Q(t_o)$.

The hamiltonian for the intrinsic motion is now considered to be given by :

$$\hat{H}_{int}(\hat{x}_i, \hat{p}_i, Q_o) = \hat{H} + \hat{V}(\hat{x}_i, Q_o) \tag{8}$$

It depends on the mean value of $\hat{Q}(t)$. According to our assumption of a small relaxation time, the density operator for the intrinsic system will be supposed to have the canonical form :

$$\hat{\rho}_{int}(Q_o, T_o) = \frac{1}{Z} \exp\left\{\frac{-\hat{H}_{int}(\hat{x}_i, \hat{p}_i, Q_o)}{T_o}\right\} \tag{9}$$

with $$Z = Tr \exp\left(\frac{-\hat{H}_{int}}{T_o}\right)$$

It depends on Q_o but also on the temperature T of the intrinsic system at this time t_o. We assume here and in the following that T does not change during the interval δt as defined in (4). If we now again make use of the inequalities (2)-(4), we see that δV can be considered as a small perturbation on the intrinsic motion.

It is important to note that the use of perturbation theory is made possible only by redefining the hamiltonian as well as the density operator of the intrinsic system as described above. It is only in this sense that we can benefit from the so called weak coupling limit. To our opinion, this has to be considered before one wants to compare with other approaches as for instance with the one of ref.17,18) in which the definition of the intrinsic system and its hamiltonian remains unchanged during the whole reaction.

In treating δV to lowest order time dependent perturbation theory we have achieved the linearization of the problem. Before we however can benefit from the tools of linear response theory, δV has to be brought

in a separable form :

$$\delta\hat{V} = \sum_{\nu} A_{\nu}(\hat{Q})\ \hat{F}_{\nu}(\hat{x}_i) \tag{10}$$

In the following we will assume that this form is obtained from a Taylor expansion of δV around Q_o to first order :

$$\delta\hat{V} = (\hat{Q}-Q_o)\ \hat{F}(\hat{x}_i,Q_o) \tag{11}$$

(A more general case is discussed and used in ref.19).

For our problem the most interesting quantity to be computed using linear response theory is the expectation value of the operator $\hat{F}$ at time t_o. It is the property of the intrinsic system which first of all is excited by the collective motion. In addition $-\langle F\rangle_t$ is equal to the induced force exerted back on the collective degree.

In terms of the response function $\tilde{\chi}(t)$, $\langle\hat{F}\rangle_t$ can be written as :

$$\langle F\rangle_t = \langle\hat{F}\rangle_{eq} - \int_{-\infty}^{+\infty} \tilde{\chi}(s)\ (U(t-s)-Q_o)ds \tag{12}$$

The response function can be computed from the time dependent operator $\hat{F}^I(t)$ in the interaction representation.

$$\hat{F}^I(t) = e^{i\hat{H}t}\ \hat{F}\ e^{-i\hat{H}t} \tag{13}$$

for positive times $\tilde{\chi}(t)$ is given by :

$$\tilde{\chi}(t) = i\,\mathrm{Tr}\,\hat{\rho}_{int}(Q_o,T_o)\ [\hat{F}^I(t),\hat{F}] \tag{14}$$

It is seen that $\tilde{\chi}(t)$ only depends on properties of the intrinsic system as defined at Q_o but not on $\hat{Q}(t)$.

The second term on the right of eq.(12) determines to first order in δV the deviation of $\langle\hat{F}\rangle_t$ from the equilibrium value :

$$\langle\hat{F}\rangle_{eq} = \mathrm{Tr}\,\hat{\rho}_{int}(Q_o,T_o)\ \hat{F}(\hat{x}_i,Q_o) \tag{15}$$

It can be used to measure the relaxation of the intrinsic excitation to equilibrium. Indeed, assuming for a moment the excitation to be produced by a sharp knock : $Q(t) - Q_o = \delta(t)$, then $\delta\langle\hat{F}\rangle = \langle\hat{F}\rangle_t - \langle\hat{F}\rangle_{eq}$ is given by $\delta\langle\hat{F}\rangle = -\tilde{\chi}(t)$. (To satisfy causality the response function $\tilde{\chi}(t)$ is different from zero only for positive times (see below)). So the response function contains all the information needed to check whether the approach is consistent or not. By computing it, the relaxation time can be for instance obtained.

Such a computation relies on the model for $\hat{H}_{int}$. In terms of its eigenstates and energies, one obtains from (14) :

$$\tilde{\chi}(t) = 2 \sum_{n,m} \frac{e^{-\frac{E_m}{T}}}{Z} |\langle m|\hat{F}|n\rangle|^2 \sin(E_n - E_m)t \qquad (17)$$

Clearly the question whether and how fast $\tilde{\chi}(t)$ decays to negligibly small values depends on the spectrum E_m and on the coupling matrix elements.

Suppose for the latter we take the estimates of ref.17,18), then we find the response function to be proportional (strictly speaking this is only true for high excitations which is the case here) to $e^{-\Delta^2 t^2/2}$ and that thus the relaxation time τ is given by Δ^{-1}. Taking their value of $\Delta = 7$ MeV, we find $\tau = 10^{-22}$s . The fact that we indeed find a decaying behavior for $\tilde{\chi}(t)$ is easily understood if we remember that the level spectrum was assumed to be quasi continuous. This is certainly justified for high intrinsic excitation. For lower excitations (as given at the beginning of the heavy ion collision or in the fission process) the knowledge of the detailed intrinsic structure will be more important. Then we have to be more specific about the model choice of H_{int}. Such a procedure is desirable also for another reason : estimates like the one of ref.17,18) necessarily will be very rough especially as far as the dependence on the collective degree is concerned. This dependence on the other hand determines the form factors for the friction forces. Their knowledge is very important for an application of the theory. The authors of ref.19) therefore went a step further and approximated H by a single particle hamiltonian. Then H_{int} is indeed of exactly the same nature as the one used in the collective model to generate the equations of motion. However it is less clear that in this way a finite value for a friction coefficient can be found. Indeed, the computed response function showed irregular oscillations also for very long times. They were removed by a cut off procedure. For a heavy ion reaction the latter is justified since the total reaction time τ_R is finite (indeed, the cut off time necessary to make the procedure consistent was of the same order as τ_R : $\approx 10^{-21}$s). For short times, the computed $\tilde{\chi}(t)$ indeed showed a decaying behaviour. The relaxation time infered in this way was equal to 2.10^{-22}s (for a head on collision of ^{16}O on ^{238}U). We may thus conclude that as a preliminary value for τ we find $\approx 10^{-22}$s. More careful computations might change this result. For instance, inclusion of configurations more complicated than of p- h type are expected to decrease it.

If we estimate τ_{coll} by τ_R, we would then say that as a lower limit, the ratio τ/τ_{coll} is of the order of 1/10.

Let us now go back to eq.(12) in order to study the nature of the forces induced by the coupling δV. For the force to be made local in time, we have to use again that the memory of the intrinsic system is small compared to the time scale of collective motion (see eq.(2)). The integral can then be approximately computed by expanding $Q(t-s)$ around $s = 0$:

$$Q(t-s) = Q(t) - s\dot{Q}(t) + \frac{s^2}{2}\ddot{Q}(t) + \ldots \tag{18}$$

By inserting into eq.(12) and defining the coefficients :

$$C(Q_o,T_o) = \int_{-\infty}^{+\infty} \tilde{\chi}(s)ds = \int_{-\infty}^{+\infty} \tilde{\chi}'(s)ds \tag{19}$$

$$\gamma(Q_o,T_o) = \int_{-\infty}^{+\infty} \tilde{\chi}(s)sds = i\int_{-\infty}^{+\infty} \tilde{\chi}''(s)sds \tag{20}$$

$$m(Q_o,T_o) = -\frac{1}{2}\int_{-\infty}^{+\infty} \tilde{\chi}(s)s^2ds = -\frac{1}{2}\int_{-\infty}^{+\infty} \tilde{\chi}'(s)s^2ds \tag{21}$$

we obtain

$$\langle\hat{F}\rangle_t = \langle\hat{F}\rangle_{eq} - C(Q-Q_o) + \gamma\dot{Q}(t) + m\ddot{Q}(t) \tag{22}$$

By recalling that the induced force is given by $-\langle F\rangle_t$ we see that γ can be interpreted as a friction coefficient, C and m as a renormalisation of the stiffness and inertia already present in h(Q,P). In eqs.(18) to (21) we used an important property of linear response theory. Namely that the function $\tilde{\chi}(t)$ can be split in :

$$\tilde{\chi}(t) = \tilde{\chi}'(t) + i\tilde{\chi}''(t) \tag{23}$$

where $\tilde{\chi}'(t)$ determines a reactive process (as given by virtual excitations) and $\tilde{\chi}''(t)$ a dissipative process (as given by real excitations of the intrinsic system)[15]. Since $\tilde{\chi}'(t)$ is an even function and $\tilde{\chi}''(t)$ and odd one, we see that indeed the conservative forces (proportional to C and m) are determined by $\tilde{\chi}'(t)$ whereas γ is determined by $\tilde{\chi}''(t)$.

So far we have found all the forces which enter the Newton equations. As mentioned before, there must be forces which create statistical fluctuations of the collective degrees. Physically, the reason for this is obvious : we have assumed that the intrinsic excitation is of statistical nature. That means, for instance, that the quantity F will exhibit statistical fluctuations. But F is directly coupled to Q (see the definition of the coupling operator δV). Therefore, also Q must exhibit statistical fluctuations.

Formally this comes about in the following way. One may start with the von Neumann equation for the density operator $\hat{\rho}_{tot}$ of the total system. Then one can reduce this equation to one for the density operator $\hat{d}$ of the subsystem of the collective degrees by averaging with respect to the intrinsic degrees. In this way there appear terms which represent the forces discussed above. They are induced by the interaction

δV are determined by the response function. In addition there appear induced forces which are determined by moments of the following function :

$$\psi(t) = \frac{1}{2} \mathrm{Tr}\, \hat{\rho}_{int}(Q_o, T_o)\, [\hat{F}^I(t), \hat{F}]_+ \qquad (24)$$

It is a correlation function for the quantity $\hat{F}$. As we shall see below the terms in the equation for $\hat{d}$ which are determined by this function represent indeed the fluctuating forces for the collective degrees.

The strong connection between dissipation on one hand and fluctuations on the other is established in the so called fluctuation dissipation theorem. It relates the Fourrier transforms of $\tilde{\chi}''(t)$ (the dissipative par of $\tilde{\chi}(t)$) and $\psi(t)$:

$$\chi''(\omega) = \mathrm{tgh}\left(\frac{\omega}{2T}\right) S(\omega) \qquad (25)$$

This relation can now be use to connect the moments of $\tilde{\chi}(t)$ (which determine the forces introduced above) and those of $\psi(t)$. This connection becomes especially simple if the temperature is not too small. (Precisely, one has to compare the temperature with the locally defined frequency of the collective degrees. Roughly the following inequality must be fulfilled: $\omega_{coll} << 3.5T$). Such an assumption was made to obtain the final eq.(96) of ref.16) which was also used for practical applications in ref.20,21). Under this condition of high temperature, the neglection of moments of $\tilde{\chi}(t)$ higher than n implies that moments of $\psi(t)$ higher than (n-1) can be neglected too[16]). (Note that there is no counterpart for $C = \int \tilde{\chi}(t)dt$).

In the applications of the theory, we have neglected a renormalisation of the reduced mass μ (i.e we omitted the last term of eq.(22) proportional to m). So the only fluctuating force taken into account has the coefficient :

$$D = \frac{1}{2} \int_{-\infty}^{+\infty} dt\ \psi(t) \qquad (26)$$

According to the fluctuation dissipation theorem (25), it can be related to the friction coefficient as

$$D = \gamma T \qquad (27)$$

which is the famous Einstein relation.

It should be strengthened at this point that this assumption of high temperature has been made only for simplifying reasons. This assumption, of course, is certainly not fulfilled at the beginning of the reaction. We have checked,however, that the final result does not change very much if we assume a finite temperature from the very beginning.

The equation for the reduced density operator $\hat{d}$ contains quantal effects. Since they are not expected to be essential (see introduction),

the classical limit is performed. Then the equation becomes the following Fokker Planck equation :

$$\frac{\partial d(t)}{\partial t} = -\frac{P}{\mu}\frac{\partial d(t)}{\partial Q} + \left(-K_c(Q_c) + C(Q_c)(Q-Q_c)\right)\frac{\partial d(t)}{\partial P}$$

$$+ \gamma(Q_c)\frac{\partial}{\partial P}\left(\frac{P}{\mu} + T(Q_c)\frac{\partial}{\partial P}\right)d(t) \qquad (28)$$

It describes the time evolution of the density distribution $d(t) = d(Q,P,t)$ in the classical phase space of the collective degrees. The quantity Q_c is defined as the solution of the classical Newton equations. It is identical to the first moment of Q :

$$Q_c(t) = \int dQdP\ d(Q,P,t)Q \qquad (29)$$

It replaces the mean value of $\hat{Q}$ introduced in eq.(7).

The fact that Q_c as well as

$$P_c(t) = \int dQdP\ d(Q,P,t)P \qquad (30)$$

together follow classical trajectory reflects the assumption that the fluctuations around the mean value, namely :

$$\omega(t) = \frac{1}{2}\int dQdP\ (P-P_c(t))^2 d(Q,P,t) \qquad (31)$$

$$\psi(t) = \frac{1}{2}\int dQdP\ (P-P_c(t))(Q-Q_c(t))d(Q,P,t) \qquad (32)$$

$$\chi(t) = \frac{1}{2}\int dQdP\ (Q-Q_c(t))^2 d(Q,P,t) \qquad (33)$$

($\psi(t)$ and $\chi(t)$ should not be confused with the correlation and the response function used above) must be relatively small. Otherwise the definition of a trajectory is meaningless. Furthermore, the parametrisation of the intrinsic system by $Q_0 = Q_c(t_0)$ as done above without using also $\chi(t)$ would be impossible. Lastly the Fokker Planck equation would contain terms of higher order than the first in Q and P. The assumption of small fluctuations was tested numerically and found to be satisfied[20].

Equation (28) is easily solvable. It is a gaussian entirely determined by its first and second moments as defined in eqs.(29) to (33). The second moments fulfill a coupled set of linear first order differential equations. They can be solved numerically together with the Newton equations for Q_c and P_c. In addition one has to compute simultaneously the temperature $T(Q_c) = T(t)$ by using for instance the simple expression as given by the Fermi gas model.

As this stage we want to draw attention to an important point. The theory gives the solution for the fluctuations of a few collective degrees

which built a subsystem of the total system. For instance, we can compute directly the fluctuations of the kinetic energy of the relative motion, which of course is also observed directly experimentally. We do not intend to calculate fluctuations of the intrinsic system as is done in ref.17,18). This should not be confused with the use of the concept of a temperature. By doing so the intrinsic energy artificially is ascertained with a big fluctuation. The latter is unphysical and has nothing to do with the one we are computing. The use of a temperature is justified only in this sense that we only want to look explicitely at a subsystem. Then the use of a canonical or microcanonical ensemble give the same results[22]).

II) Experimental results

Before we apply the theory of section I to the computation of cross sections, we would like to briefly summarize the gross features of the experimental results concerning deep inelastic reactions. We feel that section necessary because of two reasons. The first one is that a model should reproduce simultaneously all the basic features experimentally encountered in deep inelastic collisions. Therefore it seems to us necessary to see clearly to which extend this situation is reached. The second reason is that further simplications will be made before the theory of section I is applied and the experimental situation will give us some clue for some of them.

As the deep inelastic process is binary (neglecting some possible light particles (nucleons,α) preemission), it is sufficient to focus attention on the experimental properties of the light fragment, the properties of which, for technical reasons, being more easily measured.

1) Correlation between kinetic energy and detection angle

The most striking feature of deep inelastic reactions is the large energy loss observed in the relative motion. As proposed in ref.23), it is very convenient to plot the differential cross section $d^3\sigma/d\theta dE dZ$ for a given atomic number, versus the kinetic energy E and the detection angle θ in the center of mass system. Such two dimensional plots are displayed in fig.1 for the 280 MeV $^{40}Ar+^{58}Ni$ system which has been studied by Galin et al.[24]). For the plot corresponding to Z=19 which only corresponds to one charge transfer (and consequently to a small mass transfer), a large amount of cross section is observed in the region corresponding to the grazing angle ($\approx$ 30°) and for an energy close to the initial energy. This region corresponds to quasi elastic reactions. Another area can be seen at low energy, extending over a wide angular range. It corresponds to completely energy relaxed products because for these, the memory of the initial energy has been completely lost. Between these two regions, there is no clear a separation but rather a continuous evolution between them due to incompletely energy relaxed products. Now the important point is that when the mass transfer increases, the quasi elastic area gradually disappears as well as the incompletely energy relaxed region (when more than four charges have been transferred, in this particular case) and there only remains the completely energy relaxed component.

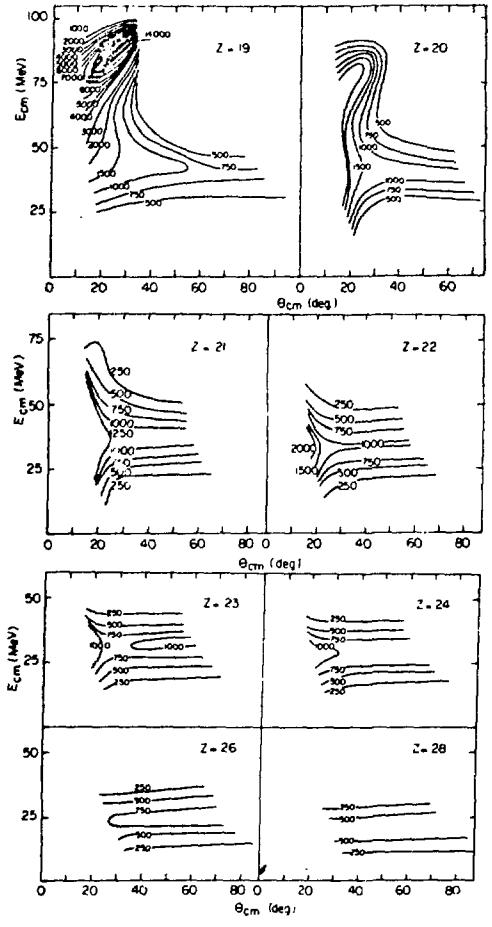

Fig. 1. Contour plot of the center of mass cross section $d^3\sigma/dEd\theta dZ$ (μb/MeV/rd/a.u) in the E,θ plane for different atomic numbers for the 280 MeV ^{40}Ar+^{58}Ni system. Results from Galin et al. [24].

From these pictures, we can very likely draw the inference that the energy transfer is a faster process than the transfer of nucleons (at least if we look at 80% of the total energy which can be dissipated[25])) because as soon as a small number of nucleons have been transferred, only the completely energy relaxed component can be observed. (For an extended discussion of this point, we refer the reader to the talk given by Moretto in Caen[1])).

2) Total kinetic energy of deep inelastic products

The total kinetic energy of completely energy relaxed deep inelastic products is smaller than the value of the interaction barrier in the entrance channel. For instance, it has been measured, in ref.26), for the ^{63}Cu+^{197}Au system at two different bombarding energies 365 MeV and 443 MeV a total kinetic energy of $\approx$ 205 MeV for the quasi fission products corresponding to almost no mass transfer. This value is much smaller than the interaction barrier in the entrance channel which is $\approx$ 250 MeV. This means that the end of the process corresponds to two deformed fragments in a scission configuration. Therefore deformations in the exit channel are important to be considered and they have to be treated either explicitely[6,8]) or simulated[9,10]) in a model which wants to quantitatively explain the energy loss.

3) Correlation between mass asymmetry and detection angle

Fig.2 corresponds to quasi fission products (completely energy relaxed deep inelastic events) detected in the 365 MeV Cu+Au reaction[13,26]. There, the differential cross section $d^2\sigma/d\theta dM$ has been plotted versus the mass M of the product and the detection angle θ. This system is interesting because the complete fusion cross section is vanishingly small compared to the quasi fission one, therefore the spectra presented here contains only, if any, a negligeable contribution from fission following complete fusion products.

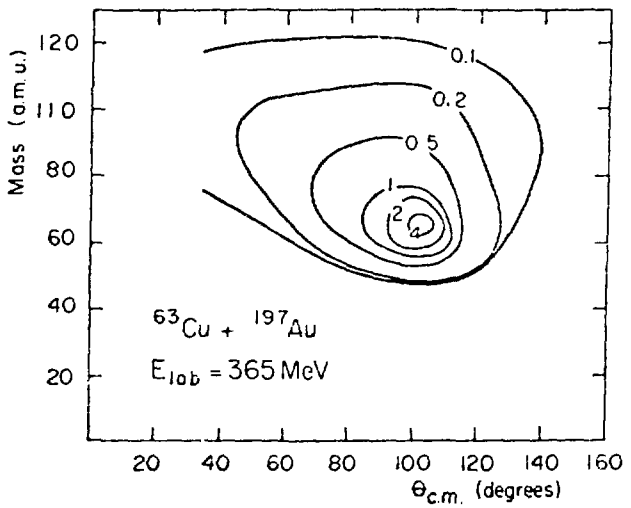

Fig.2. Contour plot of the center of mass cross section $d^2\sigma/d\theta dM$ (mb/a.m.u/rd) for quasi fission products of the 365 MeV $^{63}Cu+^{197}Au$ system. Results from ref.[13].

We observe that when the detection angle decreases from the grazing value (which is around 110°) toward small angles, the position of the maximum of the mass distribution is shifted toward larger masses and simultaneously the FWHM of the distribution increases. As these two quantities always evolve as a function of the detection angle without reaching any equilibrium value, this is very likely to indicate that the relaxation time τ_x associated to the mass asymmetry degree of freedom is much larger than the typical collision time τ_R. The shift of the position of the maximum which always occurs in the same direction is likely to be a hint that one has to deal with an overdamped motion along the mass asymmetry coordinate.

Backwards the grazing angle, still a large amount of cross section can be observed which is probably related to fluctuations.

If we now look at a given mass, we observe that as the mass transfer increases, the angular distribution becomes flatter and flatter which is an indication that the system lives longer and longer and therefore forget more and more about the entrance channel direction.

4) Neutron excess collective degree

Initially, for a given system, the ratio of the number of neutrons over the number of protons for the target and for the projectile are ge-

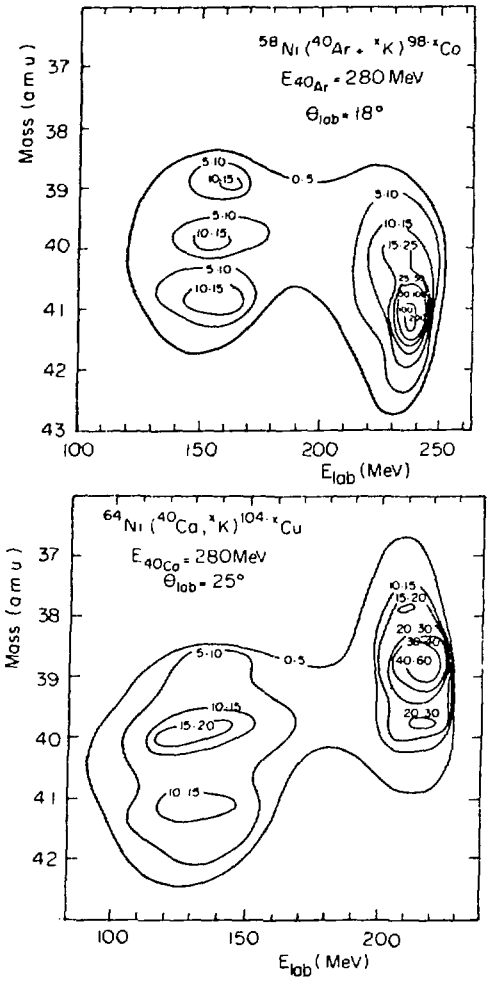

Fig.3. Contour plot of the K isotope yields in the mass-energy plane for the 280 MeV $^{40}Ar+^{58}Ni$ and $^{40}Ar+^{64}Ni$ systems. Results from Gatty et al.[27]).

nerally different. The neutron excess seems to be a very fast collective mode[27]). Indeed in fig.3 are shown contour plots where, for a given atomic number, the number of detected events is plotted versus their mass and their energy for angles close to the grazing. This is done for two systems corresponding to different neutron excess for the projectile, but leading to almost the same composite system. The results are taken from ref.27).

Two main area can be noticed in each case. The location of the first one with respect to the mass number depends on the entrance channel (quasi elastic events). *The second one,* corresponding to deep inelastic events, does not depend on the entrance channel indicating that the memory of the initial neutron excess is completely lost. This seems to indicate that the relaxation time $\tau_{N/Z}$ of the neutron excess is much smaller than the typical collision time τ_R. In addition, the equilibrium value of the neutron excess is reached before the energy loss has become important. This is likely to indicate that $\tau_{N/Z}$ is smaller than the relaxation time connected to the energy transfer τ_E. Galin[1]) gave $\tau_{N/Z} \sim 10^{-22}$s for $\tau_{N/Z}$ which is of the same order as the response time for the intrinsic degrees given in section I. Therefore it is expected for τ_E to be several time greater than this value and consequently it seems hopeful to treat energy transfer as a slow degree.

III) Macroscopic model for deep inelastic reactions

1) Basic features

In this section, we want to show how it is possible to easily apply the theory described in section I to the computation of experimental quantities corresponding to collective degrees which can be considered as slow compared to the intrinsic ones. The assumption of slow collective

degree is certainly valid for mass asymmetry but certainly not for the neutron excess which has to be treated by another method. As far as the energy loss is concerned we have seen in the previous section indications that it could be likely considered as a slow degree. Although the theory cannot be applied at the very beginning of the process, we hope nevertheless that this first stage of the reaction, where a statistical treatment cannot be applied, has only a small influence on the final results.

We are interested in the computation of experimental quantities. In order to do that, the distribution function $d(Q^\mu, P_\mu, t)$ of the collective degrees has to be known. We know from section I that it satisfies a Fokker Planck equation the solution of which is a gaussian entirely determined by the first and second moments of the collective variables. The first moments satisfy Newton equations in which enters the friction tensor $\gamma_{\mu\nu}$, the inertia tensor $m^{\mu\nu}$ and the stiffness tensor $C_{\mu\nu}$. Although these quantities can be microscopically calculated as proposed in ref.16), we did not perform such a calculation but rather proceeded as follows :

- As far as the relative motion is concerned, we can take for these tensors a phenomenological model as those of ref.4-10). Such models provide us with the mean values of the collective variables describing the relative motion which are the first moments needed. The second moments which describe statistical fluctuations of the collective variables satisfy a coupled set of linear differential equations in which no new parameters enter except for the temperature which has to be calculated from the intrinsic excitation energy.

- We have seen in section II that the mass asymmetry degree of freedom plays an important role in deep inelastic collisions. As its motion seems to be overdamped, it can be treated in a very simple way. Indeed, Kramers[28]) showed that in this case, the Fokker Planck equation (28) reduces to a Smoluchowski equation. This equation has already be used alone in ref.11-14) to describe the diffusion process along the mass asymmetry coordinate. This is equivalent to the neglect of the acceleration terms entering the differential equation for the first moment. In our approach, this motion along the mass asymmetry coordinate is coupled to the relative motion and this lead to interesting features.

2) Computation of cross sections

From the distribution function $d(Q^\mu, P_\mu, t)$ for $t \to \infty$, it is possible to compute cross sections for any physically observable quantity which can be expressed as function of the collective degrees Q^μ taken into account and of their conjugate momenta P_μ. In order to do this we have to integrate over the remaining degrees and the impact parameter. Simple forms can then be obtained and we shall give a typical example which will be used in the next paragraph.

The differential cross section $d^2\sigma/d\theta dx$, where θ is the scattering angle and x the mass asymmetry is given by[21]):

$$\frac{d^2\sigma}{d\theta dx} = \int 2\pi\, db\, d \lim_{t\to\infty} \frac{1}{4\pi\sqrt{\Delta}} \exp\left\{ -\frac{1}{4\Delta}\left[(\theta-\theta_c)^2\ \chi^{\theta\theta} - 2(\theta-\theta_c)(x-x_c)\ \chi^{\theta x} + (x-x_c)^2 \chi^{\theta\theta}\right]\right\} \tag{34}$$

with
$$\Delta(t,b) = \chi^{xx}(t,b)\chi^{\theta\theta}(t,b) - \left(\chi^{\theta x}(t,b)\right)^2 \tag{35}$$

variables with subscript c correspond to their classical values (first moments). $\chi^{\mu\nu}$ are the second moments as defined by :

$$\chi^{\mu\nu}(t,b) = \frac{1}{2} \left\langle \left(Q^\mu - Q_c^\mu(t,b)\right)\left(Q^\nu - Q_c^\nu(t,b)\right)\right\rangle \tag{36}$$

The first and second moments depend on the time t as well as on the impact parameter b.

If we are only interested in the angular distribution $d\sigma/d\theta$ we have to integrate expression (34) over x which gives[20] :

$$\frac{d\sigma}{d\theta} = \int 2\pi db\, d \lim_{t\to\infty} \frac{1}{\sqrt{4\pi\chi^{\theta\theta}}} \exp\left\{ -\frac{(\theta-\theta_c)^2}{4\chi^{\theta\theta}}\right\} \tag{37}$$

When the fluctuations vanish, we can easily check that the preceeding expression goes to the classical limit :

$$\frac{d\sigma}{d\theta} = \sum_n 2\pi b_n \left| \frac{1}{\frac{d\theta_c}{db_n}} \right| \tag{38}$$

However formula (37) gives a finite contribution to the differential cross section $d\sigma/d\theta$ at rainbow angles at variance to the classical formula (38) which becomes infinite.

3) Practical application of the model

As a first numerical application we choosed for the phenomenological classical model describing the relative motion the one of ref.4). There only two degrees of freedom are considered : the relative distance between the two ions r and the polar angle θ. The two colliding ions are assumed to remain spherical during the whole collision, therefore, with such a model it is not possible to quantitatively reproduce the experimental energy loss. We shall therefore not compute cross sections where the energy is involved as for instance $d^3\sigma/d\theta dE dx$. Calculations were deformations are simulated in the exit channel in the way proposed in ref. 9) are in progress[29]).

In the model of ref.4), the friction tensor is diagonal in the system of polar coordinates ($\gamma_{rr} = C_r f(r)$ and $\gamma_{\theta\theta} = C_\theta r^2 f(r)$). The radial and tangential friction constants C_r and C_t, as well as the form factor f(r) have been taken to be those of ref.4) ($C_r = .0025$, $C_t = 10^{-5}$ and $f(r) = (\partial U_N/\partial_r)^4$, where U_N is the nuclear part of the interaction potential). For the nuclear part of the interaction potential we used the simple approximate analytical form of the energy density potential of ref.30).

For the mass asymmetry degree of freedom x which is added to the preceeding variables, we also only consider the diagonal term γ_{xx} of the friction tensor. The further assumption we made is to consider relative motion and mass exchange as statistically uncorrelated ($\chi^{\theta x}=0$). This means, we assume the total Fokker Planck equation to be separable, i.e. the total solution to be given by :

$$d(r,\theta,x,P_r,P_\theta,t) = d_r(r,\theta,P_r,P_\theta,t)\,d_x(x,t) \qquad (39)$$

However we do not neglect the coupling between mass exchange and relative motion for the first moments. Consequently we treat explicitely the effect of mass exchange on relative motion and vice versa as far as the mean values are concerned. Since we have seen in section 2 that generally $\tau_x >> \tau_E$, we expect this decoupling to be a fair approximation.

In order to compute the fluctuations, the temperature of the intrinsic system is needed. We simply took the usual relation

$$aT^2(t) = E_{int}(t) \qquad \text{with} \quad a = \frac{A_1+A_2}{10} \qquad (40)$$

which relates the temperature T(t) to the intrinsic excitation energy $E_{int}(t)$. One has to note that these quantities depend on the time.

We finally need a connection between the mass and atomic number of the fragments. We use the fact that in deep inelastic reactions the neutron excess collective degree is very fast[27] (see section II). Consequently we assumed this degree to be equilibrated just before the mass transfer starts and treat it after like an intrinsic degree.

4) Results

We performed a numerical calculation along the lines described above for the 365 MeV Cu+Au system. In fig.4 is displayed the differential cross section $d^2\sigma/d\theta dx$ versus the detection angle and the mass asymmetry. Different from ref.21), this calculation has been performed using for mass asymmetry the same form factor as the one in the radial motion f(r) instead of using a step function (now $\gamma_{xx} = 15000$ MeV.10^{-23}s). In addition the radius parameter $\bar{r}$ of the nuclear potential has been decreased by 2.5% in order to get a better agreement for the complete fusion cross section.

Before we compare fig.4 to fig.3, we must have the following things in mind which tell us to what extend the comparison can be made :

- The calculation presented in fig.4 corresponds to all deep ine-

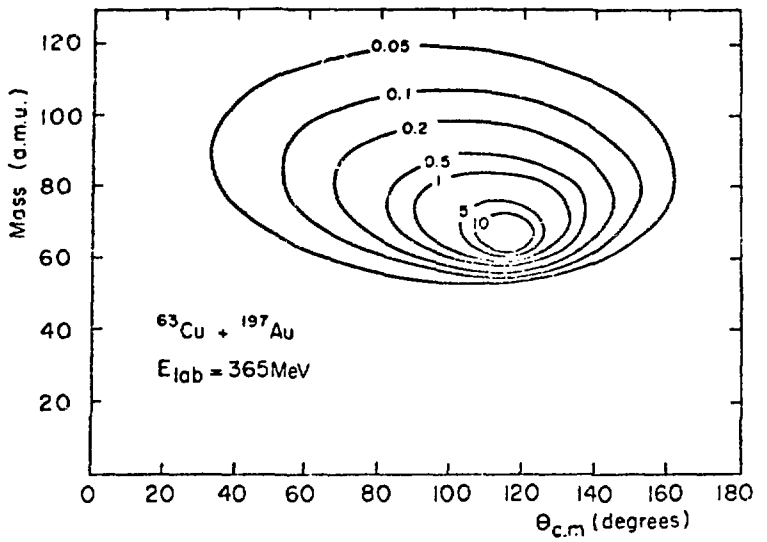

Fig.4. Calculated contour plot of the center of mass cross section $d^2\sigma/d\theta dM$ (mb/a.m.u/rd) for deep inelastic products of the 365 MeV $^{63}Cu+^{197}Au$ system.

lastic products including those which are associated to a small energy loss. In fig.4, the latter are concentrated at the top of the hill which is located in the vicinity of the grazing angle ($\sim$ 110°) and around the mass of the projectile. Have we selected deep inelastic events corresponding to some given energy loss, then the top of the hill will be displaced toward smaller angle (it can be displaced by about 10° if we only consider deep inelastic products corresponding to a large energy loss).

- Fig.3 corresponds to quasi fission products (completely energy relaxed products) extracted according to ref.26)). It is not possible in the calculation to select the same kind of events because the energy loss is not quantitatively reproduced. But, as indicated above, there should only be a difference for small mass transfer in the grazing region. This difference can clearly be seen by comparing the figures because the top of the hill is not located at the same place.

- Fig.3 corresponds to quasi fission products detected after de-excitation. A large part of the de-excitation is done by neutron evaporation for the primary quasi fission products. Therefore at a given angle, an additional broadening of the mass distributions is obtained which is not taken into account in the calculation.

Having these things in mind, if we now compare the two figures (the typical experimental error is about 30% in fig.3) we see that the pattern is very similar and that the experimental features described in section II are qualitatively and to some extend quantitatively reproduced although no fit has been searched. In particular the calculation clearly

shows that deep inelastic events are to be observed backward the grazing angle which is indeed observed experimentally. Such a feature could not be explained using a classical model and it is due to statistical fluctuations.

One of us (HH) wants to thank the Institut de Physique Nucléaire for kind hospitality and financial support.

References

1) We refer the reader to the following review papers where references to the experimental works can be found :

J.Galin, European Conference on Nuclear Physics with Heavy Ions,Caen (1976), J. Phys. C5 37 (1976) 83.
M. Lefort, Rep. Prog. Phys. (1976) 39 129-173.
L.G.Moretto and R.Schmitt, European Conference on Nuclear Physics with Heavy Ions, Caen (1976), J. Phys. C5 37 (1976) 109.

2) A.Bohr and B.R.Mottelson, Nuclear Structure vol.II W.A.Benjamin, INC (1975).

3) W.J.Swiatecki, J. de Phys. 33 (1972) 45.
W.J.Swiatecki and S.Bjornholm, Phys. Lett. Rep. 4C (1972) 326.
P.J.Siemens, Triestre publications STI/PUB/386 paper IAEA-SMR-14/8 vol.I.

4) D.H.E.Gross and H.Kalinowski, Phys. Lett. 48B (1974) 302.
D.H.E.Gross, H.Kalinowski and J.N.De, Proc. Heidelberg Symposium on Heavy Ion Reactions (1974), lecture notes in physics 33 (1975) 194.
H.Kalinowski, Thesis (1975).
J.N.De, D.H.E.Gross and H.Kalinowski, preprint (1976).

5) J.P.Bondorf, M.I.Sobel and D.Sperber, Phys. Lett. Rep. 15C (1975) 83.
J.P.Bondorf, J.R.Huizenga, M.I.Sobel and D.Sperber, Phys. Rev. C11 (1975) 1265.

6) A.J.Sierk and J.R.Nix, Proc. of the 3rd IAEA Symposium on the Physics and Chemistry of Fission, Rochester vol.II (1973) 273 (IAEA Vienna).
J.R.Nix and A.J.Sierk, Phys. Script., 10A (1974) 401.

7) C.F.Tsang, Phys. Script. 10A (1974) 90.
F.Beck, Phys. Lett. 62B (1976) 385.

8) H.H.Deubler and K.Dietrich, Phys. Lett. 56B (1975) 241.
H.H.Deubler and K.Dietrich, Nucl. Phys. on press.
H.H.Deubler and K.Dietrich, Preprint 1977.

9) K.Siwek-Wilczynska and J.Wilczynski, Nucl. Phys. A264 (1976) 115.

10) J.N.De, Phys. Lett. 66B (1977) 315.

11) W.Nörenberg, Phys. Lett. 53B (1974) 289.
W.Nörenberg, Z. Phys. A274 (1975) 241 and A276 (1976) 84.
S.Ayik, B.Schürmann and W.Nörenberg, Z.Phys. A277 (1976) 299 and Z. Phys. A279 (1976) 145.
W.Nörenberg, European Conference on Nuclear Physics with Heavy Ions, Caen (1976).

12) L.G.Moretto and J.S.Sventek, Phys. Lett. 58B (1975) 26.
J.S.Sventek and L.G.Moretto, Lawrence Berkeley Report LBL-5012 (1976).

13) C.Ngô, J.Péter, B.Tamain, M.Berlanger and F.Hanappe, Nucl. Phys. A267 (1976) and Proceeding of the International Workshop Hirschegg AED-Conf-76-015-000 p.122.

14) K.L.Wolf, C.T.Roche, R.L.Boudrie, J.R.Huizenga, J.R.Birkelund, W.U.Schröder and V.E.Viola, Proceeding Conf. Eur. Phys. Nucl. Caen (1976) p.176.
J.R.Huizenga, J.R.Birkelund, W.V.Schröder, K.C.Wolf and V.E.Viola, Proceeding Conf. Eur. Phys. Nucl. Caen (1976) p.177.

15) H.Hofmann and P.J.Siemens, Nucl. Phys. A257 (1976) 165.
see also : H.Hofmann, Phys. Lett. 61B (1976) 243.
H.Hofmann and P.J.Siemens, Phys. Lett. 58B (1975) 417.
H.Hofmann, XIIIth Int. Winter Meeting on Nucl. Phys., Bormio (Italy) 1975.

16) H.Hofmann and P.J.Siemens, Nucl. Phys. A275 (1977) 464.

17) D.Agassi, C.M.Ko and H.A.Weidenmüller, preprint MPI-H (1976) -V25.
C.M.Ko, D.Agassi and H.A.Weidenmüller, preprint MPI-H (1977) -V5.
see also : C.M.Ko, J.J.Pirner and H.A.Weidenmüller, Phys. Lett. 62B (1976) 248.

18) H.A.Weidenmüller, This conference.

19) P.J.Johansen, P.J.Siemens, A.S.Jensen and H.Hofmann, (preprint 1976).

20) H.Hofmann and C.Ngô, Phys. Lett. 65B (1976) 97.

21) C.Ngô and H.Hofmann, Z. Phys. A282 (1977) 83-92.

22) L.D.Landau and E.M.Lifschitz, Statistical Mechanics, Pergamon press, London, 1958.

23) J.Wilczynski, Phys. Lett. 47B (1973) 484.

24) J.Galin, B.Gatty, D.Guerreau, M.Lefort, X.Tarrago, R.Babinet, B.Cauvin, J.Girard and H.Nifenecker, Z. Phys. A278 (1976) 347.

25) J.R.Birkelund, W.V.Schröder, J.R.Huizenga, K.L.Wolf, J.P.Unik and V.E.Viola, preprint (1976).

26) J.Péter, C.Ngô and B.Tamain, J. Phys. Lett. 36 (1975) L23.
J.Péter, C.Ngô, F.Plasil, B.Tamain, M.Berlanger and F.Hanappe, Nucl. Phys. A279 (1977) 110.

27) B.Gatty, D.Guerreau, M.Lefort, J.Pouthas, X.Tarrago, J.Galin, B.Cauvin, J.Girard and H.Nifenecker, Z.Phys. A273 (1975) 65 and Nucl. Phys. A253 (1975) 511.

28) H.A.Kramers, Physica VII (1940) 284.

29) P.Grangé, J.Richert, M.Berlanger, H.Hofmann and C.Ngô, Contribution to this conference.

30) C.Ngô, B.Tamain, M.Beiner, R.J.Lombard, D.Mas and H.H.Deubler, Nucl. Phys. A252 (1975) 237, see also :
C.Ngô, B.Tamain, J.Galin, M.Beiner and R.J.Lombard, Nucl. Phys. A240 (1975) 353.

DEEP INELASTIC COLLISIONS BETWEEN VERY HEAVY NUCLEI

H. Sann, A. Olmi, Y. Civelekoglu, MPI für Kernphysik Heidelberg

D. Pelte, Universität Heidelberg

U. Lynen, H. Stelzer, A. Gobbi, Y. Eyal[+], W. Kohl, R. Renfordt, I. Rode, G. Rudolf[*], D. Schwalm, R. Bock, GSI Darmstadt

Introduction

One and a half years ago the UNILAC accelerator started to deliver heavy ion beams of 5.9 MeV/amu, which is a sufficient energy to overcome the Coulomb barrier and so to study nuclear interactions. Today, bombarding energies up to 8.5 MeV/amu are commonly available for a variety of beams including the very heavy projectiles like uranium and lead. This unique facility has opened up at GSI during the past year a broad spectrum of activities including the search for superheavy nuclei, for the spontaneous emission of positrons in the overcritical electric field, for yrast traps, etc.

What we shall report here will be on the shadow side of these real highlights, but if one thinks of the moon, the back side is as interesting as the enlighted one. The present talk will concentrate on a survey study of deep inelastic collisions and will not at all reflect the general spectrum of activities at GSI (GSI 76). The reactions investigated are summarized with a number of characteristic quantities in table. 1. It is a survey study performed for a wide span of targets and projectiles so as to recogrize the general features of the collision and their trends, while moving from the already known lighter systems to the heaviest possible target projectile combination U on U.

Several symmetric ingoing channels (Xe-Sn, Pb-Pb and U-U) were chosen as well as a number of asymmetric systems (Kr-Sn, Kr-Er, Xe-Au, Xe-U, U-Pb). The original 5.9 MeV/amu were not sufficient to reach the Coulomb barrier for the heaviest combinations and it was only at the end of 1976 that we were able to move on into the new region. Taking advantage of what we learned from this general survey we have recently started to investigate some more specific questions by observing the γ-multiplicity and the bombarding energy dependence of the deep inelastic process (Kr-Sn, Kr-Er).

Table 1 shows that the Coulomb barrier is typically exceeded by a factor of 1.3; in the energy dependent study we scan a region between

[+]) On leave from Weizmann Institute, Rehovot, Israel

[*]) Humboldt fellow, on leave from CRN Strasbourg, France

Table 1: List of the reactions investigated

Proj	Target	E_{Lab} (MeV/amu)	E_{CM} (MeV)	E^* (MeV)	E_{CM}/E_{Coul}	l_{max} (h)	η' +)
^{86}Kr	^{120}Sn	4.9	250	50	1.24	140	375
		5.99	300	99	1.50	199	265
		7.2	360	160	1.80	252	208
		8.2	411	210	2.04	289	182
^{86}Kr	^{166}Er	7.9	283	25	1.10	112	711
		5.99	339	81	1.32	203	397
		7.2	407	150	1.58	276	293
		8.2	464	206	1.80	323	249
^{132}Xe	^{120}Sn	5.9	370	90	1.32	227	516
	^{197}Au	7.55	596	184	1.47	402	571
	^{208}Pb	7.55	610	190	1.46	412	583
	^{238}U	7.55	641	118	1.40	423	831
^{208}Pb	^{208}Pb	7.5	780	188	1.32	499	702
	^{238}U	7.5	832	183	1.29	521	798
^{238}U	^{238}U	7.5	892	180	1.26	546	956

1.1 and 2. The corresponding kinetic energy above the Coulomb barrier, after the nuclei have already been slowed down in the Coulomb field is typically between 100 and 200 MeV: this is roughly the total kinetic energy available for the internal excitation of the interacting nuclei. The maximum angular momentum in the relative motion for grazing partial waves, is of the order of 200 to 500, and even if only a certain fraction ($\sim$2/7) can be absorbed, a large amount of angular momentum is also available to the internal degrees of freedom of the nuclei.

The variety of kinetic energies and target projectile combinations available make of these reactions a powerful tool to study many average properties of nuclear matter, while the interacting nuclei are strongly overlapping. From this point of view we are pursuing to the heavier systems the interesting investigations of the deep inelastic reaction and of the diffusion mechanism previously studied at Orsay (Le76, Ga76, Ng77), Berkeley (Hu77, Mo76) and Dubna (Ar 73). Typical to these reactions is, among other aspects, the increasing classical behaviour reflected by the Sommerfeld parameter η' and the vanishing fusion cross section, so that the whole total cross section undergoes the deep inelastic process. Also characteristic of the heavier systems is the presence of fission as a possible

+) η' is evaluated using the relative velocity at the Coulomb barrier.

decay mode of the excited primary products after the collision: this is usually called the sequential fission.

Summarizing, the general interest of this study lies in the reaction mechanism and the mass diffusion process, without forgetting possible nuclear structure effects. Expecially interesting is to investigate the mass transfer process for the heaviest systems (U on U), into the transuranic region, to determine the primary population probability as well as the decay properties of these nuclei.

The content of the report will be subdivided as following:

1. Experimental device.
2. A systematic study of the deflection function: a direct test of nuclear forces.
3. The nuclear diffusion process between heavy nuclei.
4. Results of the γ-multiplicity measurements.

1. The experimental device

The kinematic coincidence apparatus is schematically illustrated on fig. 1. A position sensitive ionisation chamber (Sa 75) is centered at the grazing angle of the reaction and is used as a trigger counter. For each particle the chamber measures scattering angle (x, y-read-out), total energy, energy loss and time of arrival. The distance from the target is 1 m, the substended solid angle ~3 msr.

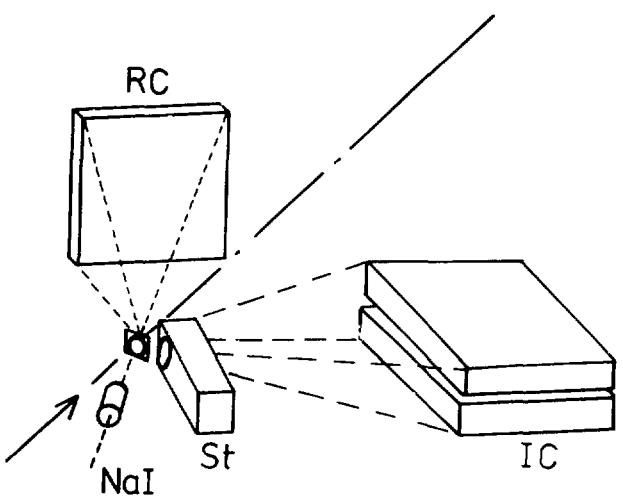

Fig. 1: Experimental apparatus. IC ionisation chamber RC recoil counter, St start detector, NaI 3"x3" sodium idide crystal.

The start signal is delivered by the secondary electrons ejected from a thin carbon foil placed 7 cm from the target: the electrons are amplified in a channel plate after deflection in a magnetic field (Re 77).

On the opposite side of the ionisation chamber a 250 msr detector (St 77) observes the particles emitted in the direction of the recoiling nuclei: it consists of a multiwire proportional counter which measures scattering angles (x-y-coordinates) and energy loss. It is followed by parallel plate detectors which deliver a stop signal.

Up to 3 NaI crystals were used to determine the γ-multiplicity in coincidence with the trigger counter information.

The data obtained up to now were collected during a total running time of 7 days. Most of the information, extracted from the data was gained from the ionisation chamber. The determination of scattering angle and

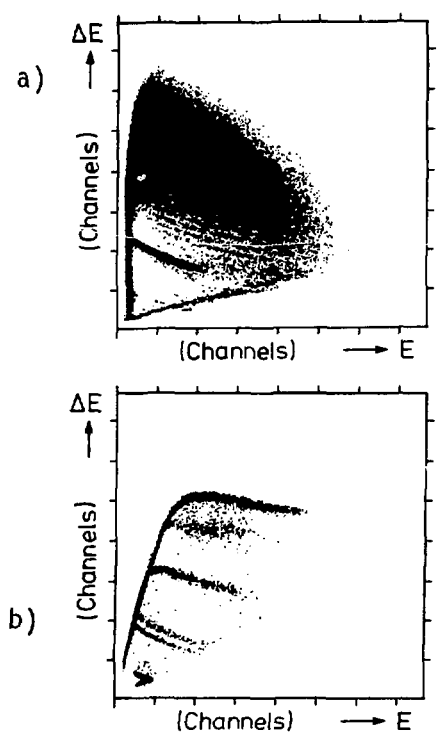

Fig. 2:

Two dimensional plots of energy loss versus total energy. In part a) are displayed light elements below Z ≃4o, while in part b) from the top to the bottom the elements Pb, Ho, Sn Cu, Fe and Al can be recognized.

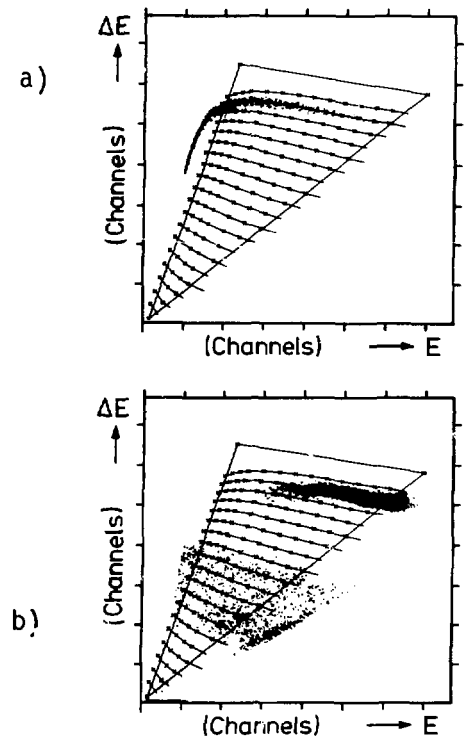

Fig. 3:

Proton number identification. Only the events inside the triangle are identified. On the outside, to the right, are seen the particles which are not fully stopped in the ionisation chamber.

total energy is quite straightforward, while the Z identification is more elaborated; it follows in the usual way from the relation between energy loss and total energy deposited in the counter. Fig. 2 shows two energy loss vs energy plots. The single charges can be resolved up to about Z=35 (fig. 2a), which is a good resolution considering the large aperture of 40 x 6 cm^2 of the counter. For the heavier systems, where the single charges are no more distinguishable, we found very useful to take, as calibration lines, the recoiling products emerging from thick wires of different elements hit by the beam (fig. 2b). In figure 3a is shown how we first matched a grid to the measured calibration line. The grid is calculated on the basis of a semiempirical dE/dx formula and then used to interpolate the data and extract the Z values for each event (fig. 3b). At present the shape of the dE/dx curve for a given Z is well reproduced by the formula, however, the spacing between adjacent Z for Z > 75 is found to deviate from the extrapolation based on the light elements: additional calibration work is in progress. The data of figure 3b are obtained from the U-U collision. Such a Z identification is essential in order to determine small deviations from the proton number of the projectile, while investigating the nucleons diffusion process.

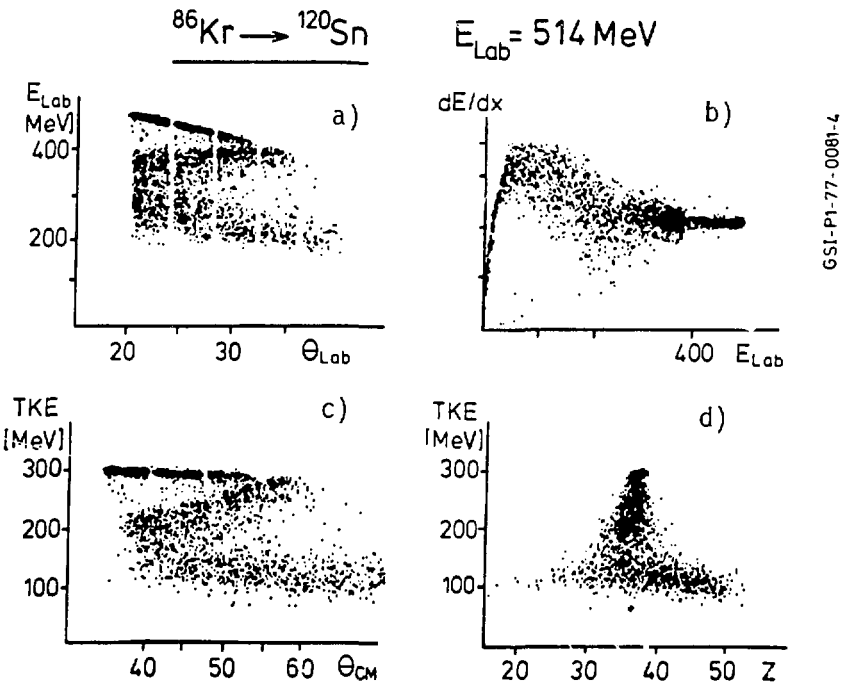

Fig. 4: On-line results from the storage display.

The plots of fig. 4 will demonstrate the advantages of the experimental device when applied to the deep inelastic reactions. The results of the Kr on Sn reactions are shown as they appear, on the storage display, during the data acquisition after 5 minutes of accumulation. The same event is plotted twice: in an energy loss vs total energy (fig. 4a) and in a total energy vs laboratory angle plot (fig. 4b). Through the density of the accumulated points it is easy to recognize the correlations between the 3 measured quantities. At small scattering angles emerges a strong elastic scattering: the energy decreases toward larger angles because of the kinematic dependence in the laboratory system for the elastic process. The empty spaces originate from the window support of the gas counter. At the grazing angle, where the nuclear interaction starts, the elastic scattering drops drastically in intensity. Just before the grazing angle, the increasing attractive nuclear forces constrain the scattered particles on a trajectory toward smaller angles (fig. 5). At the same time, due to the nuclear interaction, the nuclei are excited. This takes energy from the relative motion, the observed kinetic energy drops continuously as the excitation energy increases. This is how the deep inelastic process develops, coming from the elastic, partly damped going to the deep inelastic component. The events, which have a laboratory energy smaller than 300 MeV can be attributed to the fully relaxed component. It is not possible to tell directly from these data what is the deflection angle of the fully relaxed or so called orbiting component: if it has been scattered from the same side of the nucleus as the partly damped component, if it comes from a negative angle trajectory, or if the composite system has already made many turns as in the fusion fission process. As we shall see later, such a question cannot be answered in general for all systems and, even for a given system different contributions may be present at once.

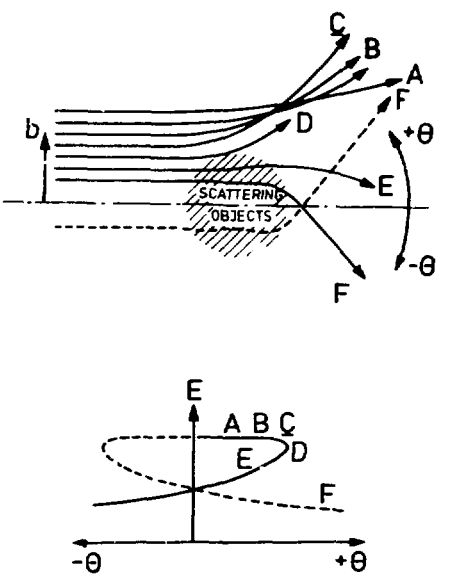

Fig. 5: The different trajectories of a Wilczynski diagram (Wi 73).

A complementary information on the mass diffusion is obtained from the ΔE vs E diagram of figure 4b. For decreasing energy we observe a spreading and a shift on the ΔE scale, which correspond to an increased mass diffusion as the nuclei are excited, with a tendency to populate a symmetric fragmentation of two roughly equal nuclei.

This is not only a quite efficient way to accumulate data, but it also makes possible to follow continuously the evolution of the distributions and, in a few minutes, to recognize the main features of the collision process for a given target projectile combination at a given bombarding energy. This type of representation underlines the continuity of the whole process from the grazing collisions to the compound nucleus formation: this is certainly a challenge for a general scattering theory.

The three measured quantities Θ, E, Z are sufficient to transform the two body kinematic quantities from the laboratory into the CM system. The mass is deduced from Z over a 1 to 1 correspondence, which follows the β-stability valley. The light particles evaporation is neglected in the transformation.

The results of the event by event transformation are shown on part d) and c) of figure 4. The new calculated quantities are the total kinetic energy TKE and the center of mass scattering angle Θ_{CM}. The so called Wilczynski diagram (Wi 73) is obtained by plotting TKE vs Θ_{CM}. From such a representation it is easy to read out the energy of the relaxed component, which corresponds roughly to the repulsion energy of the Coulomb barrier. The TKE vs Z diagram illustrate again the charge diffusion with a tendency toward symmetry. While considering the data in the CM system, it should be remembered that the limited range of observation in the laboratory introduces diffuse cuts on the distributions. The recoiling nuclei are usually not detected because their grazing angle in the laboratory system is out of the observation range of the detector and even if they hit the detector their kinetic energy is so low, that it is very hard to identify them.

In the following we shall study the evolution of the deflection function from the elastic to the fully relaxed component for six different systems. This will clarify the relative motion of the colliding heavy particles. Afterwards we shall consider, for the same systems, the evolution of the proton number as a function of the total kinetic energy loss (TKEL) and this will illustrate the mass diffusion process overimposed on the motion of the colliding objects.

2. A systematic study of the deflection function

Figure 6 shows three asymmetric Kr-Er, Xe-Au, U-Pb and three symmetric systems Xe-Sn, Pb-Pb and U-U. They are ordered for increasing strength of the Coulomb repulsion. The Coulomb barrier is exceeded by a factor of 1.25 to 1.4 which is a lower value as the 1.5 of the Kr on Sn system of figure 4. This explains the absence of an orbiting component (MO 76).

With Kr on Er and Xe on Sn we compare an asymmetric (fig. 6b) with a symmetric ingoing channel (fig. 6a) at the same total energy of the composite nucleus. They both display a quite similar trend: the nuclear attraction takes the upper hand against Coulomb repulsion; the particles are constrained to smaller scattering angles, while the overlap increases.

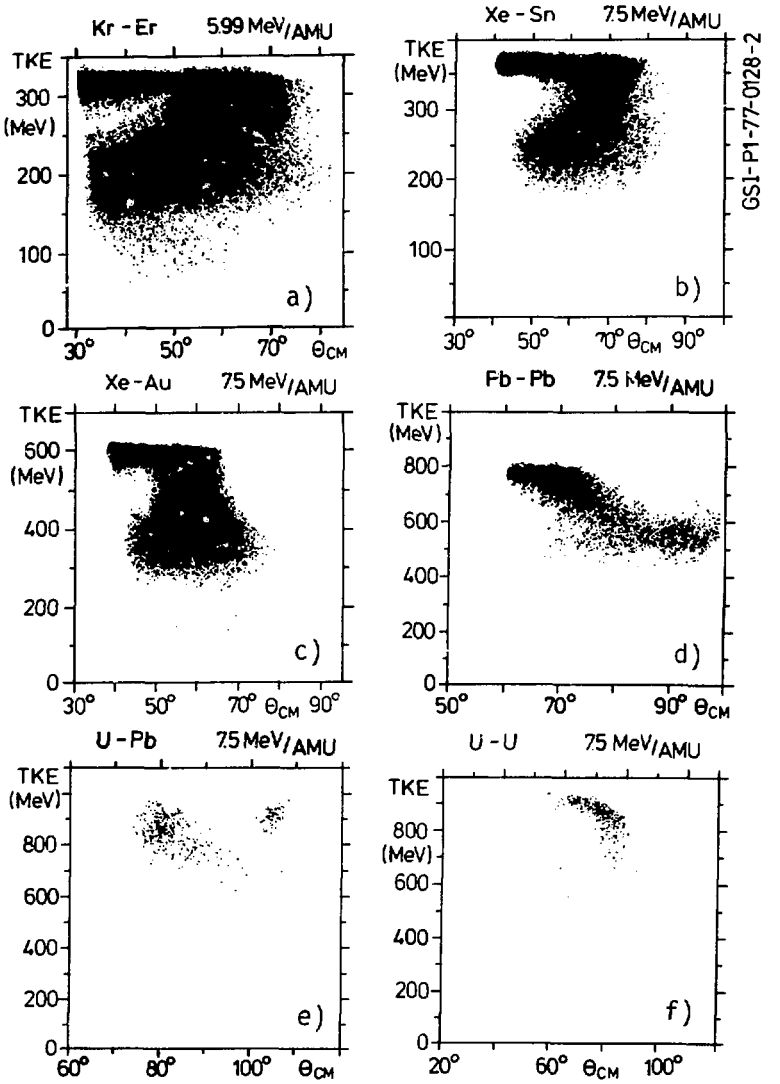

Fig. 6: Wilczynski diagrams of 6 different reactions.

Moving on toward stronger Coulomb fields the Xe on Au scattering (fig. 6c) shows a particular balance between repulsive and attractive forces: the particles are scattered around a fix mean angle value. This is usually called the focusing effect (Hu 76). In the next heavier system Pb on Pb (fig. 6b) we observe a monotonic increase of the scattering angle for increasing TKEL. Because of the identity of the ingoing particles, we observe two distributions symmetric about 90° (CM), which cross at 90°. The same behaviour is also present in the U-Pb system (fig. 6d). From the left to the right we observe how the Pb component develops; in the right upper corner we see the uranium

component which should, in principle, be mirror symmetric about 90° to the lead component. Because of the sequential fission, the highly excited uranium-like nuclei, which have low kinetic energies, are missing in the diagram. Therefore, in the asymmetrich U-Pb system, it is possible to distinguish the projectile-like from the recoil-like-nuclei and the trends are more readily recognized.

In the U-U-scattering we observed, as it will be shown in same details later, a dominance of the sequential fission: this can already be anticipated form the Pb-U interaction. The Wilczynski plot is shown in fig. 5e for selected ternary processes, by requiring a coincident fission fragment in the recoil counter. In this way it is possible to drastically reduce the elastic events, which otherwise would overwhelm the plot. It seems that the general trend of the deflection function towards larger scattering angles is still present in the U-U-scattering, although very few events survive the sequential fission at high excitation energies.

From the observation of figure 6 we deduce that a gradual trend exist, where between the lighter systems (Kr-Sn) and the heavy systems (Pb-Pb) the deflection function, after the first rainbow but before the grazing angle, possibly describes a second rainbow angle (De 75): this second rainbow angle moves toward larger angles for the heavier masses. In addition the relation between impact parameter and scattering angle seems to be washed out in the fully relaxed component.

The general interest of these deflection function studies can be summarized in two main points:

1. Test of nuclear forces: Through the delicate balance between Coulomb, centrifugal and nuclear forces of the rotating dinuclear molecular system (fig. 7) it should be possible to deduce form the known Coulomb and centrifugal forces the nuclear attraction as a function of the strength of the overlap integral. The important degrees of freedom to be considered are besides the dependence from the impact parameter, the time dependent changes of the overlap integral because of deformations, and the change of the centrifugal forces because of tangential frictional forces during the slowing down process. This dynamical situation of the dinuclear molecular system is also essential to understand the limits onto the compound nucleus formation.

   One interesting aspect of this inverse scattering problem for the reconstruction of the interacting potential, is the fact that there is no missing cross section over a large range of observation; so there is no absorption, we are observing all elements of the scattering matrix. In this sense we have a situation very different from an elastic scattering study of the interaction potential where only one single channel is investigated and where the absorption

prevents the analysis of the interior. The price to be paid comes from the superposition of the mass diffusion process on top of the relative motion process, so that both are intimately correlated and cannot be easily unfolded. The mass diffusion will be treated in same details in the next chapter.

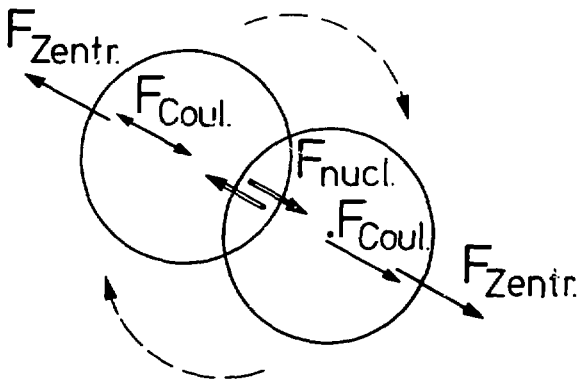

Fig. 7: The rotating dinclear molecular system.

2. Determination of the time scale of the interaction: The interaction time can be obtained from the scattering angle thorugh an integration along the trajectory of the relation

$$l_{rel} = I \cdot \Delta\Theta / \Delta t$$

which describes the angular velocity of the dinuclear molecule (Hu 77, Nö 76). The moment of inertia I(t) depends on the shapes the system assumes. The relative angular momentum $l_{rel}(t)$ depends on the internal spin absorbed by the fragments. The trajectories of the U-U collision are illustrated in figure 8. Part a) considers a grazing situation, while part b) shows a fully damped collision at small impact parameters. The scattering angle is roughly the same in both cases but the nuclei are mostly deflected in the Coulomb field for a peripheral collision and in the overlapping nuclear field for the central collision. We expect from this consideration the U-U interaction time to be similar to the one of the Xe-Bi reaction analyzed in some details by Huizenga (Hu 77), which is of the order of 10^{-22} to 10^{-21} sec. The knowledge of such a time scale is important for the prediction, through the diffusion model, of the strength of the mass transfer in the transuranic region.

The derivation of a time scale can be of considerable help not only in understanding the diffusion process but also the relaxation phenomena of the various degrees of freedom.

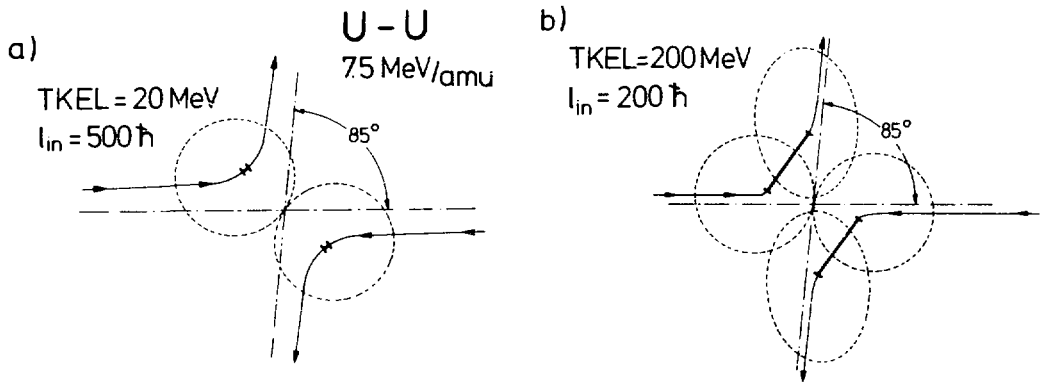

Fig. 8: The trajectories in the U-U collisions.

3. The diffusion of nucleons between heavy nuclei.

Figure 9 illustrates the evolution of the nucleons diffusion as a function of the loss on total kinetic energy. The same symmetric and asymmetric systems of figure 6 are reconsidered. The Xe on Sn reaction shows a nice symmetric distribution, which monotonically widens as the kinetic energy decreases. The corresponding asymmetric ingoing channel shows a preferential population of the heavier masses: this is usually called a driving force toward symmetry. The Xe on Au combination behaves very similarly to Kr on Er. A weak component of the sequential fission of Au is seen at low kinetic energies. If the Pb-Pb distributions are compared to the Xe on Sn case, one observes a shift to the lower proton numbers. The same trend is present on the U-U case, although few events are observed at the high excitation energies. The same is also true in the U-Pb scattering,which directly illustrates the drastic change taking place for the heavy masses above lead. From potential energy surface we would expect that the primary masses produced in the Pb-Pb, and U-U interaction would be similar to the Xe-Sn interaction. The question to be discussed later will be if the sequential fission can explain the missing part of the Z distribution for the heavier elements. Before investigating these questions let us understand better the lighter systems where the decay of the primary excited masses is limited to the neutron evaporation, so it doesn't alter the Z distribution.

Until now we have been rather qualitative in the description of the data, the following figures shall give a quantitative representation of the results after normalization to the Rutherford cross section. Instead of the usual $d\sigma/d\Omega$ we have chosen a $d\sigma/d\theta$ representation, because the later is proportional to the total reaction cross section when the whole angular range is observed. Figure 10 displays the

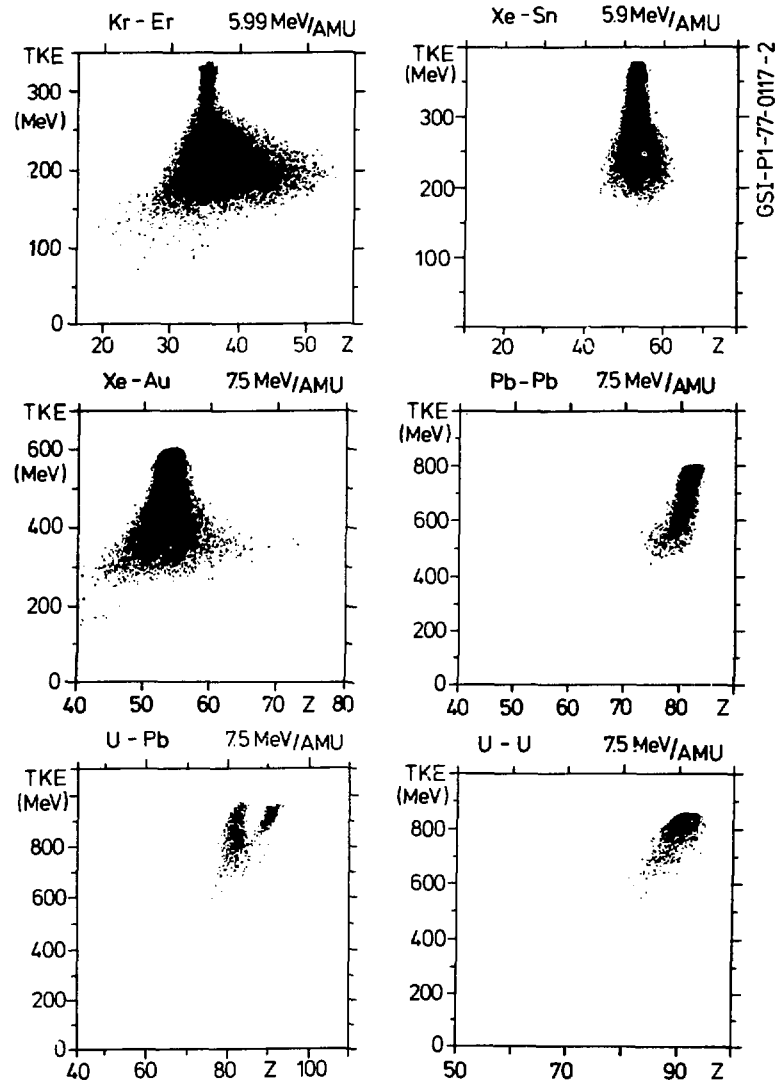

Fig. 9: The nucleons diffusion as a function of the TKEL. The distributions are measured for a given setting of the position sensitive ionisation chamber, which is centered around the grazing angle of the reaction and observes the projectile-like fragments. The recoil-like fragments are observed partially in the U-Pb reaction.

absolute cross sections for the Kr on Er reaction. The proton number- and angular-distributions are shown on a logarithmic scale for several cuts as a function of the total kinetic energy loss (TKEL). For lower excitation energies the Z-distribution is narrow as well as the angular distribution. As we move up in energy, we observe a broadening and an increasing slope on the heavy element side above the

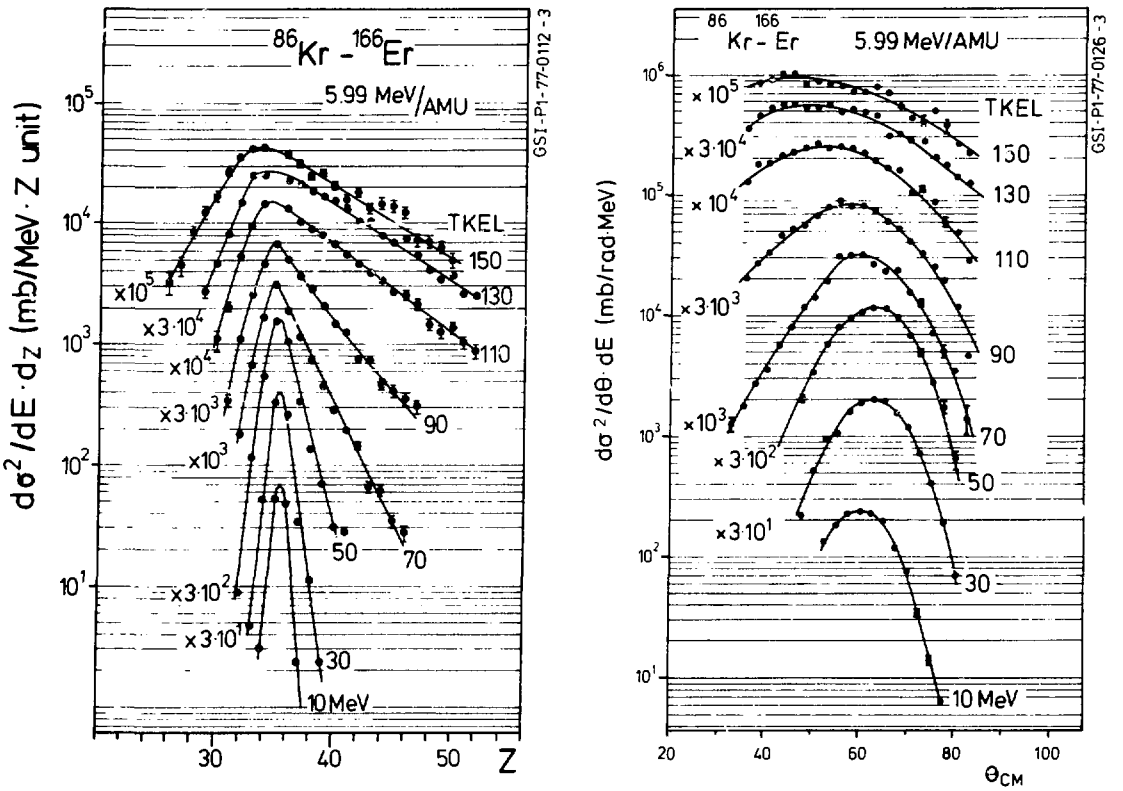

Fig.1o: Absolute differential cross sections of the Kr-Er collision. The number to the right of each Z-distribution indicates the average total kinetic energy loss of the considered events. The number displayed to the left is the scaling factor. If all reaction products would be observed and identified, symmetric Z-distributions (about Z=52) would also be observed, centered at the Z of the recoil products (Z=68).

Z-value of the projectile; we observe a shift and a broadening for the angular distribution. These are the same general features considered before on the two dime ional plots of the Wilczynski- and of the diffusion-diagrams (fig. 6 resp. 9).

What we want to learn now on a quantitative scale is how the width of the distributions, the σ_Z^2 value, changes as a function of the TKEL, as suggested by Huizenga in his systematic work (Hu 76) for a number of similar systems. We want to investigate if there is a general relation followed by the mass diffusion process.

It is rather instructive to compare the symmetric Xe-Sn system to the asymmetric Kr-Er system (figure 11). The Xe on Sn distributions remain Gaussian in shape, fully symmetric independently from the TKEL: the system is symmetric from the beginning and there is no driving force

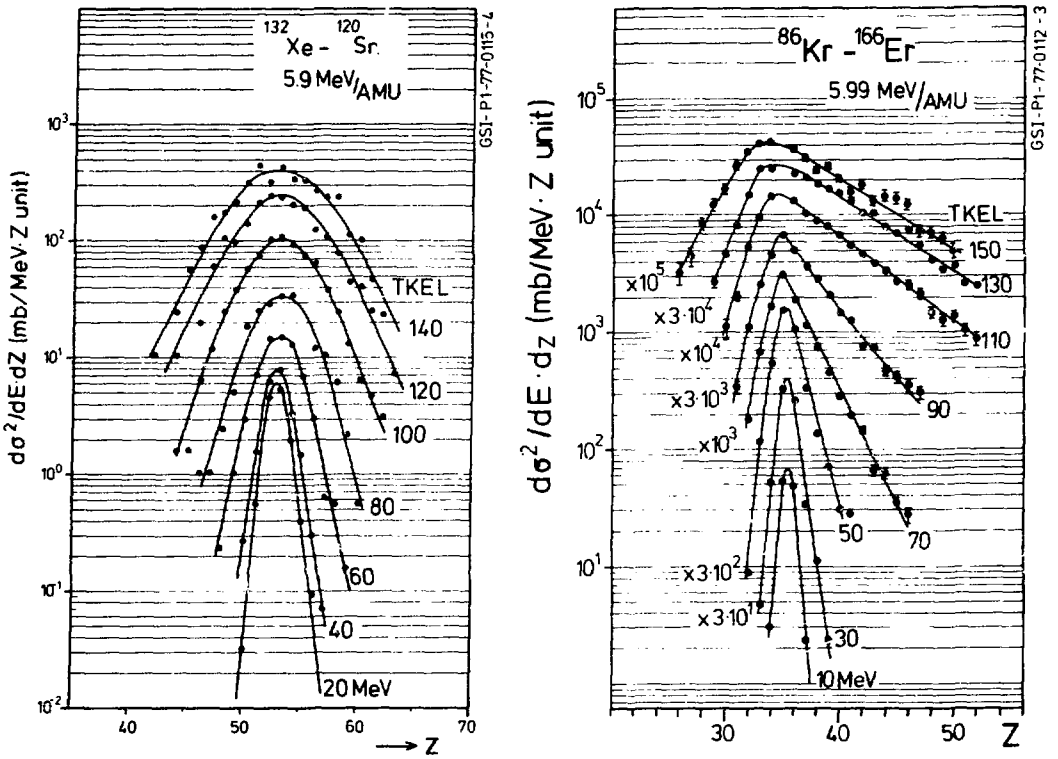

Fig.11: Comparison of the protons diffusion in a symmetric and asymmetric system. For the Xe-Sn reaction the scaling factor is always a multiple of $\sqrt{10}$.

expected from a potential energy surface; the centrifugal barrier tends to conserve the symmetry. There are good reasons to study symmetric, as well as asymmetric ingoing systems. The symmetric case dispalys a number of simplifying features. Let us compare these experimental results to the most simple form of a diffusion theory. We assume a frozen geometry between two overlapping nuclei and we apply the transport theory with the Fokker Planck equation as suggested by Nörenberg (Nö 76). It gives the proton number occupation probability as a function of time

$$P(Z,t) = (4\pi \cdot D_Z \cdot t)^{-1/2} \exp\left[-(Z-Z_0-v_Z \cdot t)^2 / 4 \cdot D_Z \cdot t\right]$$

where v_Z is the charge drift coefficient and D_Z the diffusion coefficient. The measured variance σ_Z^2 of the proton number distribution is related to the drift coefficient by

$$\sigma_Z^2 = 2 \cdot D_Z \cdot t$$

In this picture, for the Xe on Sn reaction, v_Z is approximately zero and we test the diffusion coefficient D_Z alone. In the framework of this model it seems difficult to explain why, in the Kr on Er

reaction we observe only a change in the skewness of the Z distribution without a drift of the centroid value: we observe that the cuts on TKEL do not sample only a given time intervall, overlap strength and impact parameter, but that these Z distributions may possibly come from a superposition of the different components of figure 12, with changing weighting factors. The unfolding of a time scale and the association of given impact parameters to well defined TKEL appear to be quite difficult in these cases.

The Xe on Au results of figure 13 represent also, for different reasons, an interesting piece of information. Like in the Kr-Er system, we observe a broadening and a decreasing slope as the TKEL increases, but in addition notice the puzzling shift of the maximum in a direction opposite to the one expected from a driving force toward symmetry which is predicted from simple liquid drop model consideration. We believe that this is due to a shell structure effect where both Xe and Au feel a coherent driving force toward close shells: Xe toward Z=50 and Au toward Z=82. These observations are

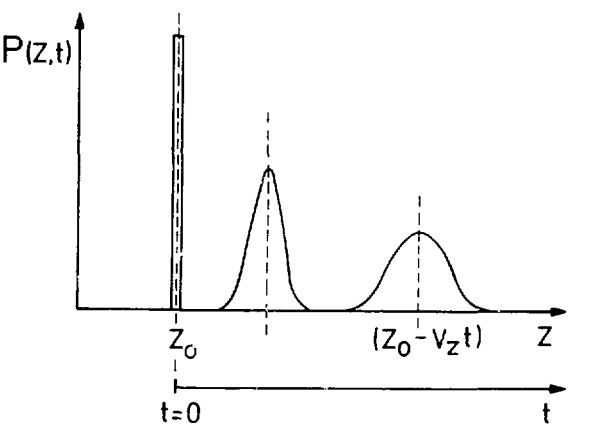

F.g.12: Predictions of a simple diffusion model.

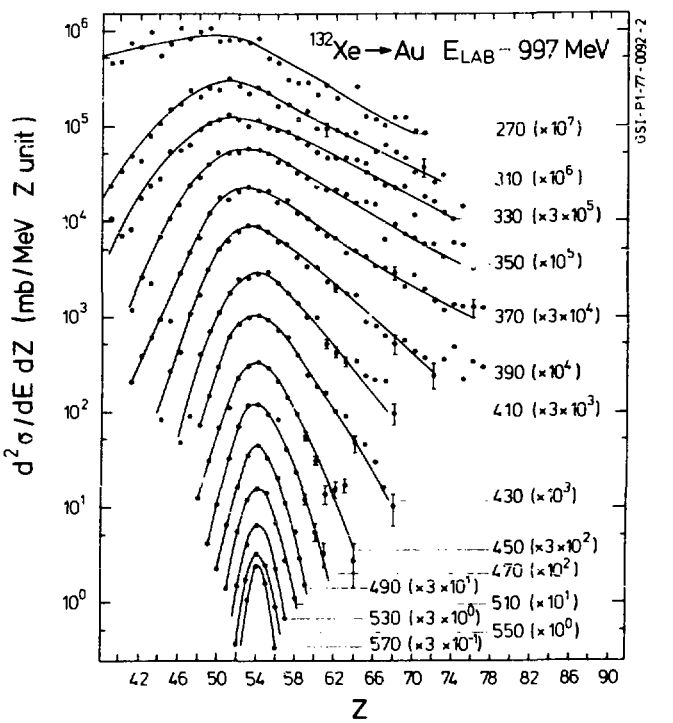

Fig.13: Center of mass data ($d\sigma/d\theta$) of the Xe-Au interaction. The TKEL value is indicated on the right of each distribution: the number in parenthesis is the scaling factor. For large energy dumping the calculated TKEL could be affected by the γ-evaporation of the excited fragments.

consistent with recent radiochemical measurements of Kratz et al. (Kr 77) where both light and heavy fragment were observed. It can nevertheless not be completely ruled out, at this point, that a light charged particles evaporation also contributes to the observed shift. However, these results are certainly of considerable interest and should stimulate additional experimental and theoretical work because the Xe on Au systems display optimum conditions for the observation of shell structure effects.

The next question to be considered is how the Xe-Sn, Kr-Er and Xe-Au results do fit into the present general understanding of the mass diffusion as investigated by Huizenga (Hu 77). The next figure (14) gives the relation between the variance σ_z^2 of the proton number distribution and the TKEL.

The results of the original Berkeley measurements are summarized by the full line. It should be pointed out that for the Berkeley data the Coulomb barrier is exceeded by 200 to 270 MeV, while for Kr on Er the total available kinetic energy was 85 MeV, for Xe on Sn 95 MeV and for Xe on Au 190 MeV. The comparison shows that all measurements roughly match on the TKEL scale as long as the energy dumping has not reached the fully relaxed component. It is also interesting to compare these same results in terms of a simple friction model (one body dissipation model) along the same line followed by Huizenga, where the rate of energy dissipation per unit of time is proportional at each instant to the remaining available energy.

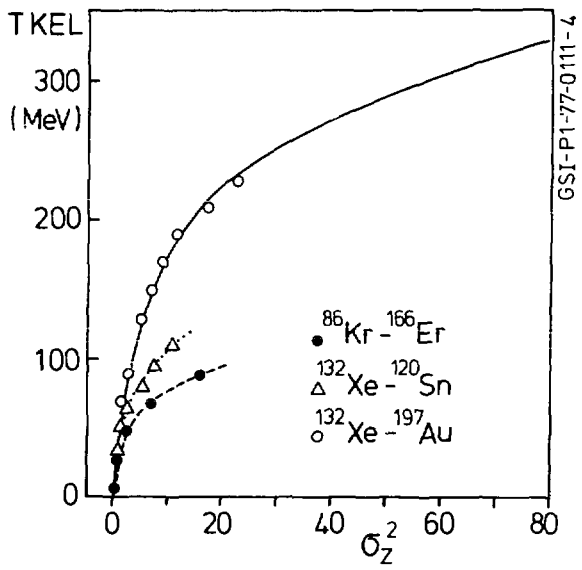

Fig.14: General relation between total kinetic energy loss and mass diffusion. The full line curve summarizes the results of Huizenga et al. (Hu 77) for the reactions Xe-Bi, Xe-Ho, Kr-Bi and Kr-Ho.

This leads to the diagram of figure 15 where σ_z^2 is plotted versus $\ln(E_0/E)$. The quantity E_0 is the total available energy and E the available energy at each moment; σ_z^2 is assumed to be a measure of the time scale. These results show that the slope depends on the total available energy, this means that the friction force (the slope gives the frictional coefficient) is not velocity dependent. At low bombarding energies the friction coefficient is larger as compared to higher energies.

An energy dependent study done for different bombarding energies, as it has been performed for Kr on Sn and Kr on Er, should be of considerable help in order to clarify the nature of the energy dissipation mechanism. The accumulated data re not yet fully analyzed, but we have learned from the presented data that the simple frictional model is not valid, that the amount of energy dissipated per exchange is too large to be accounted for by a simple frictional force. The microscopic nature of the energy dissipation remains quite an open question: is it due to particle hole excitation with the promotion of nucleons to higher shells (Wei 77), due to collective excitation including the giant mode (Wi 77), or is it just based on Q-window matching and phase space considerations?

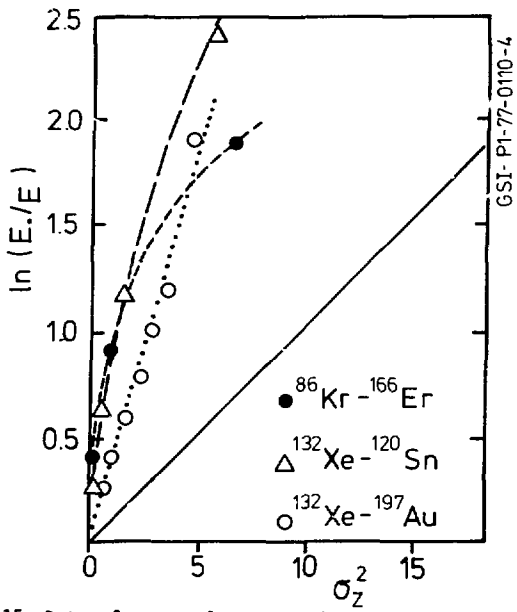

Fig.15: Rate of energy loss as a function of the number of proton exchanges. The quantity E_0 is the total available energy above the barrier, while E is the available energy for each energy loss. The straight line corresponds to the observed behaviour of the reaction Xe-Bi and Xe-Ho (Hu 76).

Additional information on the energy dissipation will be presented with the results of the γ-multiplicity measurements in the last chapter. We shall now first move on to the question of the mass diffusion for the heavier systems with the Pb-Pb, Pb-U and U-U interaction.

Until now we were considering primary products in the mass region between 80 and 200 amu, which are known from compound nucleus studies to decay predominantly by neutron emission: the measured Z-distributions were therefore fully representative of the primary Z-distributions. For nuclei with masses A >200 it is known both from compound nucleus decay studies and from the liquid drop calculations of Cohen, Plasil and Swiatecki (fig.16) that the excited fragments can easily decay by sequential fission. The aim of the present investigations is therefore on one side to delucidate if the heaviest systems follow the general trend displayed in fig. 14, to determine the primary population as a function of excitation energy in the transuranic region, and on the other side to investigate which new phenomena will occur. It is for example unknown, whether during the collision of very heavy nuclei fission will occur on a much faster time scale comparable to the interaction time, or whether the strongly deformed nuclei might favor the emission of charged particles during the collision.

The results of the three reactions U-U, U-Pb and Pb-Pb are shown in fig. 17 on a logarithmic scale for comparable observation angles and

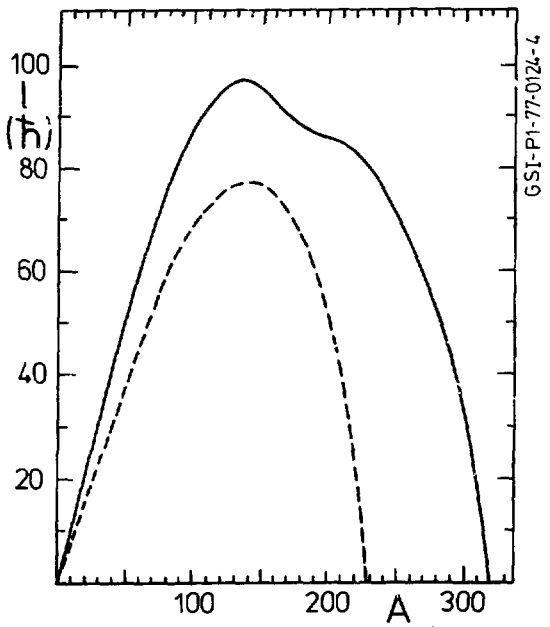

Fig.16: Liquid drop model predictions (Co 74) of the fission barrier for Q = 0 (full line) and Q =-8 MeV. The dashed line shows where the fission-starts to compete with the neutron decay mode.

bombarding energies. In each spectrum we see after elimination of the elastically scattered events two peaks: one, close to the Z of the projectile, is narrower and asymmetric and corresponds to the normal deep inelastic scattering, whereas the second, broader, is roughly centered at half the proton number of the heavy fragments and can be associated with the sequential fission of the excited primary products (Kr 74).

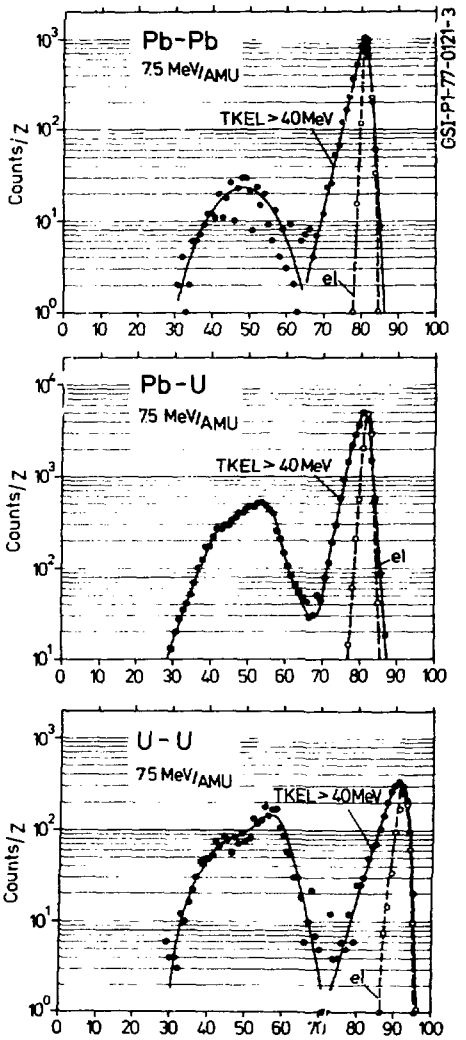

Fig.17: Overall results of the Pb-Pb, Pb-U and U-U reactions. The broad bump is originated by the sequential fission but his shape is not fully representative because the fast fission fragments are not completely stopped in the detector.

Comparing the three systems it is clear that the part of the reaction cross section which undergoes sequential fission increases with increasing mass.

The deep inelastic component has in all three cases a steep slope towards heavier elements, and a much flatter one towards lighter elements, the latter falling off much slower for U-U than for the two other reactions. The dashed lines in fig. 17 indicate the experimental resolution determined from the elastic scattering.

For comparison the Z-distribution of deep inelastic collision of Xe on Sn, where no sequential fission is observed, is shown in fig. 18.

This distribution is fully symmetric.

In fig. 19 the Z-distributions for Xe-Sn and Pb-Pb are plotted for different values of TKEL. With increasing energy dissipation for Pb-Pb the distributions become more and more asymmetric, which can be explained by the fission barrier shifting to lighter nuclei. The fission probability as a function of Z can be determined from the large area recoil detector if the corresponding light reaction fragments are seen in the ionisation chamber. The results are shown in fig. 20. For the reaction Pb-Pb the fission probability rises steeply from 5 % for Z=83 to 75 % for Z=87.

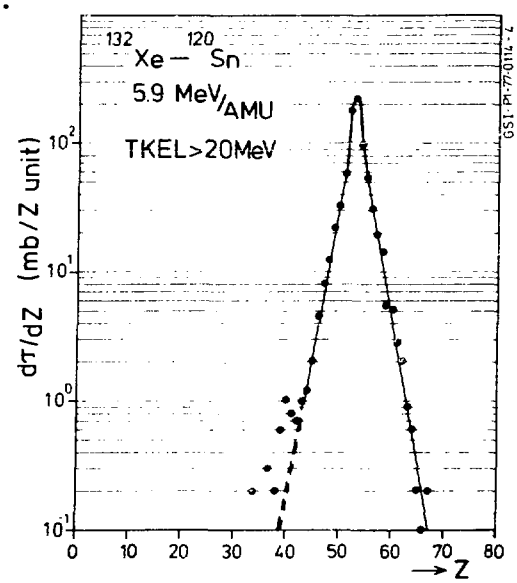

Fig.18: Same data as in figure 11a, but integrated over all non elastic events.

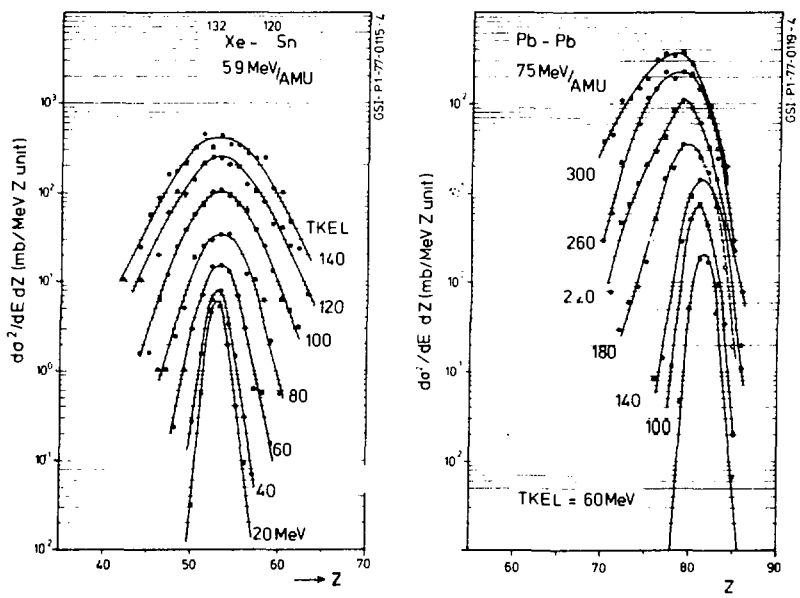

Fig.19: Proton number distributions for bins of total kinetic energy losses. The scaling factor increases from the bottom by a multiple of $\sqrt{10}$.

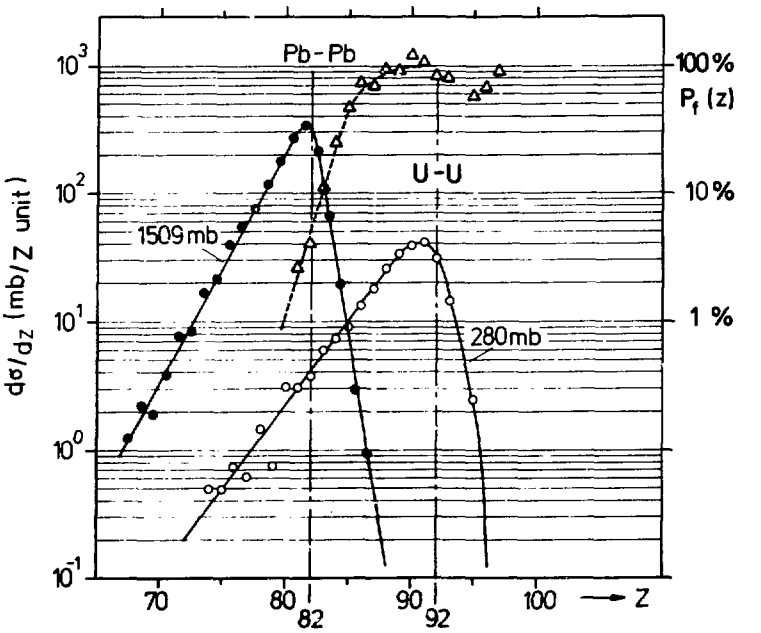

Fig.2o: The same distributions of figure 18a) and c) are compared on an enlarged Z-scale. The measured fission probability of the heavy recoil nuclei in the Pb-Pb reaction is shown by the triangles: the corresponding scale is indicated on the right side of the figure.

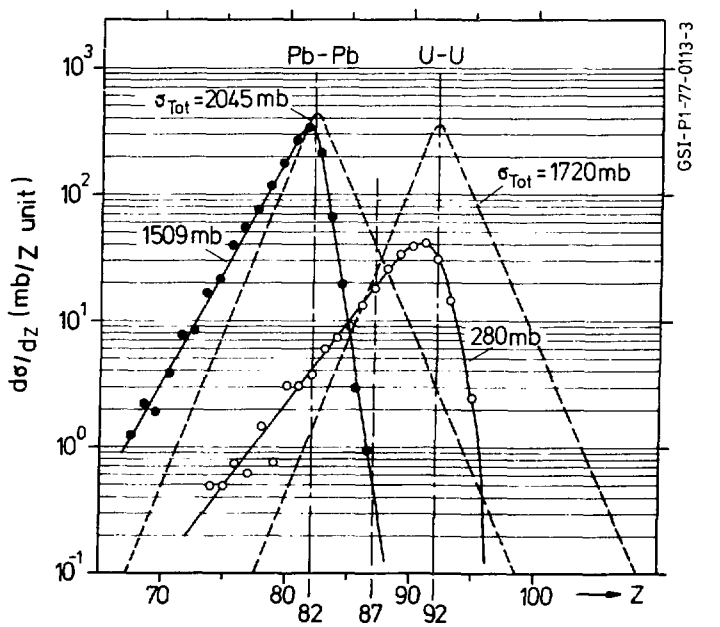

Fig.21: Primary and final distributions of the Pb-Pb and U-U reactions. The primary Z-distributions are guessed by assuming the same shape as in the Xe-Sn data of figure 19: The integral of the distribution is normalized to the total reaction cross section as determined by the grazing angle (quarter-point procedure).

In figure 21 a) the Z-distributions of the deep inelastic fragments are compared more closely for U-u and Pb-Pb. From studies performed with lighter systems, from potential energy surface arguments and especially from the fact that the two systems are symmetric, there is no reason to believe that the primary Z-distributions should not be symmetric (fig. 21). We therefore would expect similar if not identical primary yields for element Z = 87, which is in the middle between Pb and U. This intensity ratio should also not be changed by sequential fission as long as the general relation between nuclear excitation and width of the Z-distribution (fig. 14)is the same in both reactions. From fig. 21 it can however be seen that the yield of element Z = 87 is about 40 times larger in U-U than in Pb-Pb. One possible explanation would be the emission of light charged particles during or after the primary fragmentation. An alternative explanation would be that in the reaction U-U the mass transfer already occurs at lower excitation energies than in Pb-Pb. This would be of considerable importance for the production of transuranic elements and might be due to nuclear structure: Pb being doubly magic and U being deformed. Additional experiments will be performed to clarify these questions.

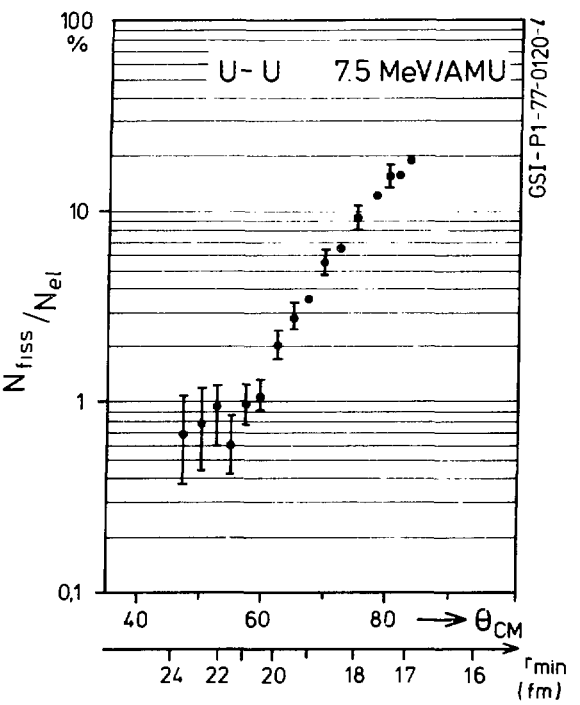

Fig.22: *Coulomb fission measurement. The distance* **of closest approach** r_{max} is evaluated for **pure classical Coulomb trajectories.**

The strongest possible Coulomb forces exist between two Uranium nuclei, so that this reaction is best suited for the investigation of Coulomb fission. The present measurement has been performed at a bombarding energy well above the Coulomb barrier ($E_{CM} = 1.26\ E_{Coul}$), however by selecting "elastic" scattered events at sufficiently small scattering angles (fig. 6f) it is possible to select collisions with large impact parameters for which the overlap of nuclear matter is vanishing.

The energy and angle of these "quasielastic" events have been determined with the ionisation chamber and the recoil detector (RC in fig. 1) was used to determine the fission probability of the recoiling nuclei. The measured fission probability is displayed in fig. 22.

We observe an important fission cross section even at large impact parameters. It is not possible, at present, to exclude experimentally a contribution, to the measured cross section of the subcoulomb neutron transfer induced fission. However, in our case, the contribution of such a transfer is less important on a relative scale, than the one observed in recent subcoulomb fission measurements with lighter projectiles (Co 76, Sp 77, Kr 77). Theoretical calculations (Gr 73, Wi 75, Ob 77) should be extended to this heavy system.

4. Results of the γ-multiplicity measurements

The γ-multiplicity can be considered as a measure of the total spin of the fragments after the collision, although the reconstruction of the absolute spin values from a γ-multiplicity is rather complex (Ha 75, Al 75, Ba 76, Gl 77, Pe 77, Is 76). The total spin depends on the initial angular momentum, on the slow down process and on the time scale of the interaction, which are important hidden quantities, not directly measurable: So it could turn out that the γ-multiplicty studies bring new insight into these processes and allow to distinguish between models.

We present here the results for the Kr-Sn and Kr-Er systems: they are summarized on figure 22, 23. The dependence of $\langle M_\gamma \rangle$ on angle is shown (22c) for the three branches of figure 22a: the elastic, the partly dumped and the fully relaxed. Due to tangential friction, there is a steep increase along the partly dumped component. Sticking, if any, is only achieved in the completely relaxed component. This can also be seen on figure 22d, where $\langle M_\gamma \rangle$ is plotted as a function of the TKEL. The differences in $\langle M_\gamma \rangle$ at low TKEL between Kr on Er and Kr on Sn, which have nearly equal l_{max} values indicate the presence of nuclear structure effects: the deformed Er nucleus can be easily excited in the Coulomb field, while the spherical Sn nucleus remains unexcited at large impact parameters (fig. 21c). The relation between σ_z^2 and the TKEL of figure 14 is again displayed on figure 22b. This shows how the energy and the angular momentum are simultaneously introduced into the internal degrees of freedom of the system. The fact that for small energy loss the dissipated energy per exchange is in-

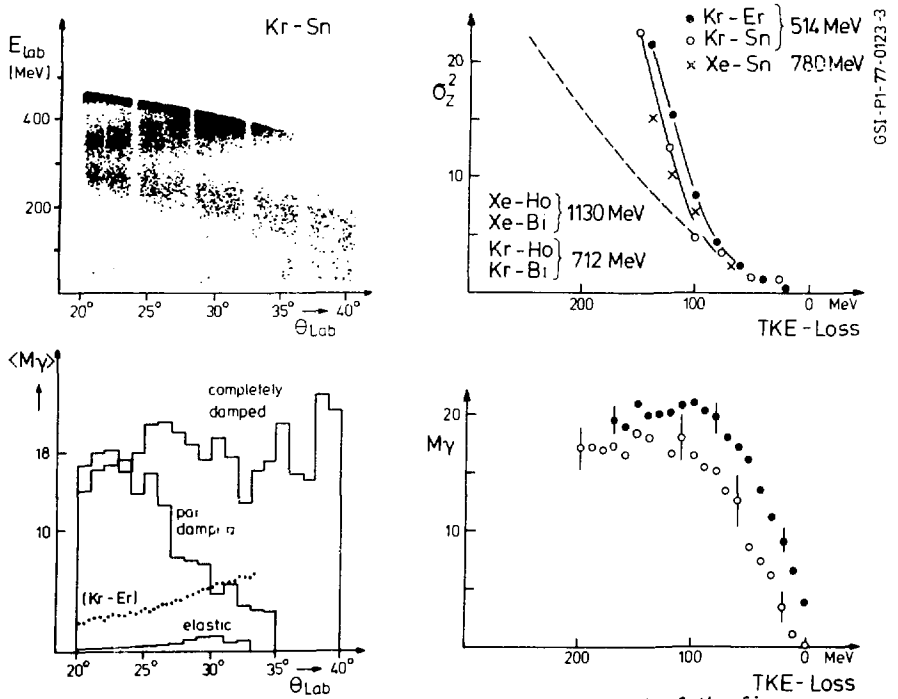

Fig.23: Results of the γ-multiplicity measurement. Part c) of the figure shows how the average γ-multiplicity of the reaction Kr-Sn increases as a function of the laboratory scattering angle for the three branches illustrated in part a): the elastic, the partly damped and the fully relaxed component. The elastic component for the reaction Kr-Er is also shown in part c) of the figure.

dependent from the bombarding energy indicates that not only velocity dependent friction forces have to be considered. This shows already a limitation of the simple classical model.

The same γ-multiplicity data of the Kr on Er reaction can also be analyzed as a function of the proton transfer. This is displayed in figure 24 for different bins of the TKEL. A dependence on the number of transferred protons is only present in the partly damped component where the system is not equilibrated. In the fully relaxed component the value of $<M\gamma>$ is independent from Z over the observed range: this is not expected in a simple sticking model picture, which predicts an increase toward asymmetric fragmentation (Bo 76).

It is of particular importance for a γ-multiplicity measurement to investigate the dependence from the impact parameter (ingoing angular momentum). Although it is difficult to associate the observed events to the ingoing angular momentum (l_{in}), a possible approach consists to integrate the observed total cross section, as a function of the TKEL, after normalization to the Rutherford scattering (Hu 77). The results of such a derivation are drawn as a full line on figure 26a. This shows that the partly damped events cover a main fraction of the total reaction cross section. If a sharp correspondence exists between l_{in} and TKEL, then the fully relaxed component has to be

associated to angular momenta smaller than 95, with an average value of 6o. The corresponding internal spin would be, in the sticking model, of about 22. This is a value much too small to explain the observed multiplicity value of 2o. It leads to two possible consequences: the nuclei are able to accomodate in the internal degree of freedom more angular momentum than the sticking model predicts or the correspondence between l_{in} and TKEL is quite broad and large impact parameters can lead to fully relaxed events. This last explanation seems to be more likely, however, the limitations of the simple classical model are disclosed here again. A number of explanations for the observed behaviour can be found in the framework of the fluctuation theory (Ngo 77) or in a microscopic quantum mechanical treatment (Wei 77, Nö 77).

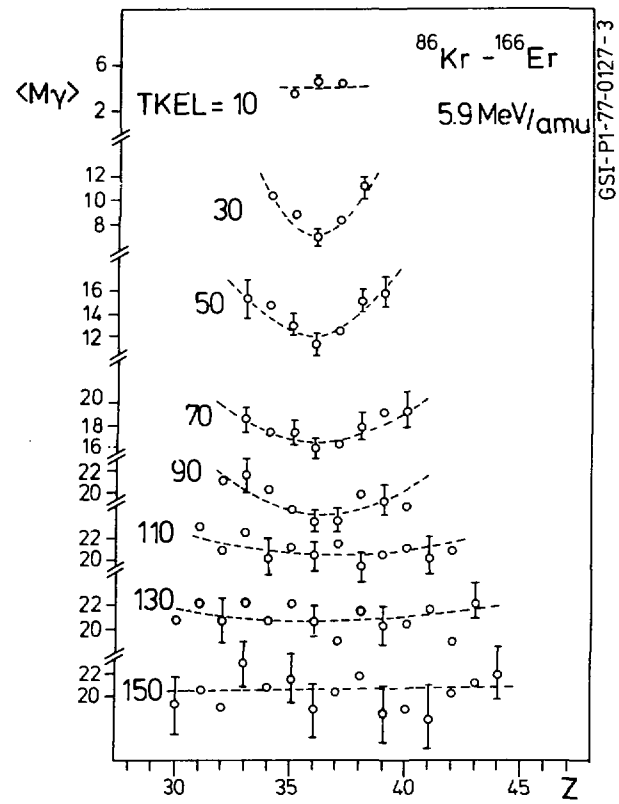

Fig.24: Dependence of the average γ-multiplicity on the total number of transferred protons.

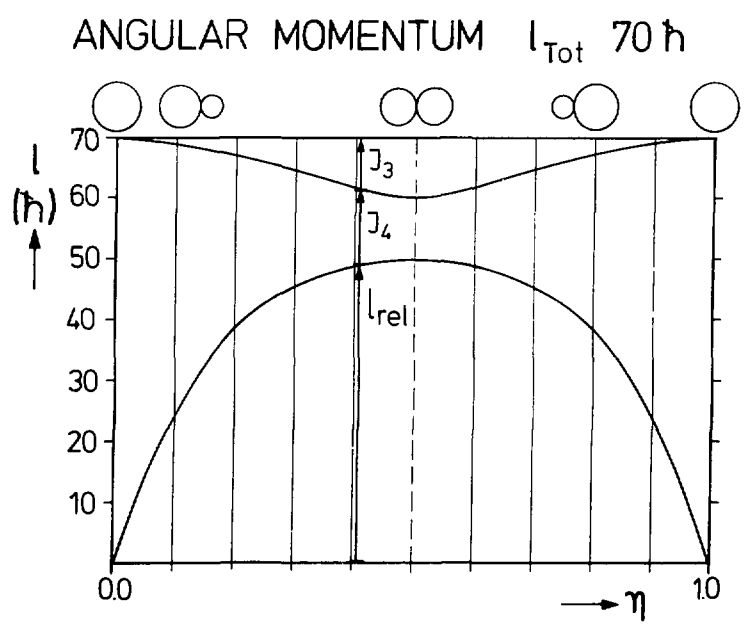

Fig.25:

Prediction of a sticking model ot two touching spheres describing the sharing of the angular momentum between internal and relative motion as a function of the asymmetry parameter $\eta = m_1/(m_1+m_2)$ for a constant total mass.

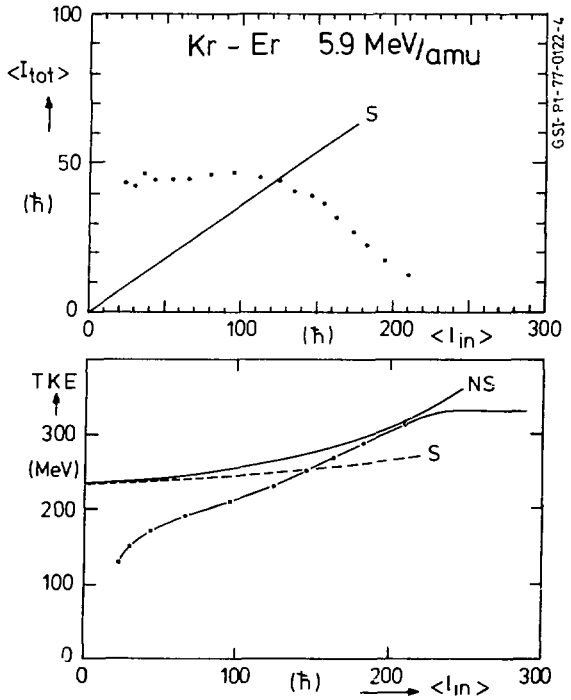

Fig.26: Comparison of the sticking model to the results of the Kr on Er reaction. Sticking is labelled by (S) non sticking by (NS). The dots of part a) were calculated from the measured γ-multiplicity by the relation $\langle l_{in} \rangle = 4 + 2 \cdot \langle M_\gamma \rangle$. The ingoing angular momentum value l_{in} was obtained from the integration of the cross section in bins of the TKEL.

Another interesting information, which can be derived from the data consists in associating the observed low kinetic energies to the deformation at the scission point. In figure 25a are indicated the barrier heights for two touching spheres ($R = 1.50 \{A_1^{1/3} + A_2^{1/3}\}$) in a non sticking (NS) and in a sticking configuration (S). The observed TKE is small, which suggests that deformation effects can be of importance, not only in the fully relaxed component but even at an earlier stage in the partially damped component. This can be interpreted in terms of collective excitation modes (Wi 77) or in terms of a neck formation between elongated fragments (Bo 77).

Conclusions

A systematic survey of deep inelastic reactions was performed for colliding nuclei of masses between 8o and 24o amu.

The application of large surface detectors and, particularly, of a position sensitive ionisation chamber, has proved to be very effective and appropriate for this type of investigations.

The Wilczynski diagrams describing the relative motion between the colliding objects shows a gradual trend as a function of growing masses of target and projectile where the trajectories lead the particles not toward negative scattering angles but increasingly into the direction around and above the grazing angle. We attribute this behaviour to a delicate balance between Coulomb and nuclear forces.

The energy dumping as a function of the mass transfer strength matches a general law between total kinetic energy loss and the variance of the proton number distribution. For the partly damped component this relation seems to hold independently from the choice of ingoing channel and bombarding energy. The dissipation of the kinetic energy does not depend only on the relative velocity of the impinging nuclei, and the simple friction model is not appropriate to describe these processes.

The γ-multiplicity measurement displays a rapid increase as a function of scattering angle and total kinetic energy loss, which give new insights to the process and indicate the necessity of microscopic quantum mechanical calculations of the interaction.

In the U-U collision large mass transfers are present which possibly populate with relatively large cross sections the transuranic elements. In the Pb-Pb reaction the mass transfer is more restricted. The decay probability by fission of the primary masses increases strongly for growing masses and excitation energies. The presented investigations are by no means completed and hold promise of additional surprises and excitements.

Acknowledgements

The authors would like to thank the staff of the UNILAC accelerator for providing unique ion beams and D. Maier, M. Ludwig,and H.J. Beeskov for their technical support and H. Folger for the preparation of a variety of excellent targets. The assistance of P. Rother and collaborators for the off-line data reduction is gratefully acknowledged. It is a pleasure to thank Dr. Sven Björnholm for many fruitful discussions.

References

Al 75 R. Albrecht, W. Dünnweber, G. Graw, H. Ho, S.G. Steadman, and J.P. Wurm, Phys. Rev. Lett. 34, 1400 (1975)

Ar 73 A.G. Artukh, G.F. Gridnev, V.L.Mikheev, V.V. Volkov, and J. Wilczynski, Nucl. Phys. A215, 91 (1973)

Be 69 K. Beyer and A. Winther, Phys. Lett. B 30, 296 (1969)

Bo 77 R. Bock, B. Fischer, A. Gobbi, K. Hildenbrand, W. Kohl, U. Lynen, I. Rode, H. Stelzer, G. Auger, J. Galin, J.M. Lagrange, R. Albrecht, B.B. Back, IX Masurian School in Nuclear Physics, published in Nucteonica (1977)

Br 76 R.A. Broglia, C.H. Dasso and Aa. Winther, Phys. Lett. 61B, 113 (1976)

Co 74 S. Cohen, F. Plasil, W.J. Swiatecki, Annals of Physics, 82, 557 (1974)

Co 76 P. Colombani, P.A. Butler, I.Y. Lee, D. Cline, R.M. Diamond, F.S. Stephens and D. Ward, Phys. Lett. B 65, 39 (1976)

De 75 H.H. Deubler, K. Dietrich, Phys. Lett 56B, 241 (1975)

Fr 77 G. Franz, H. Ahrens, W. Brüchle, H. Folger, J.-V. Kratz, M. Schädel, I. Warnecke, G. Wirth, GSI Annual Report 1976

Ga 76 G. Galin, European Conference on Physics with Heavy Ions. CAEN J. Physique (1976)

GSI 76 GSI, Annual Report 1976

Ha 75 G.B. Hagemann, R. Broda, B. Herskind, M. Ishihava, S. OGaza, H. Ryde, Nucl. Phys. A245, 166 (1975)

Ha 77 D. Habs, V. Metag, J. Schukraft, H.J. Specht, C.O. Wene, K.D. Hildenbrand, submitted for publication in Zeitschrift für Physik (1977)

Ho 72 H. Holm and W. Greiner, Nucl. Phys. A 195, 333 (1972)

Hu 76 J.R. Huizenga, J.R. Birkelund, W.U. Schroeder, K.L. Wolf, V.E. Viola, Phys. Rev. Lett. 37, 885 (1976) and J.R. Huizenga Erda Report Coo3496-56

Hu 77 J.R. Huizenga, W.U. Schröder, Ann. Rev. Nucl. Sci. 27 (1977)

Is 76 M. Ishihara, T. Numao, T. Fukuda, K. Tanaka, and I. Inamura, in Proceedings of the Symposium on Macroscopic Features of Heavy-Ion Collisions, Argonne, Illinois, 1976, edited by D.G. Kovar, ANL Report No. ANL/PHY 76-2, p. 617

Kr 74 J.V. Kratz, A.E. Norris, and G.T. Seaborg, Phys. Rev. Lett. 33, 5o2 (1974)

Kr 77 J.V. Kratz et al., GSI, Annual Report 1976

Le 76 M. Lefort, Symposium on New Avenues in Nuclear Physics, Rehovot (Israel) Nov. 7-9, 1976

Mo 76 L.G. Moretto, LBL 5o57 European Conference on Physics with Heavy Ions CAEN (1976)

L.G. Moretto, B. Cauvin, P. Classel, R. Jared, P. Russo, J. Sventck, G. Wozniak, Phys. Rev. Lett. 36, 1o69 (1976)

Ng 77 C. Ngô, H. Hofmann, this Conference

Nö 76 W. Nörenberg, European Conference on Physics with Heavy Ions, Caen, 1976

Ob 77 V. Oberacker, G. Soff and W. Greiner, preprint

Pe 77 N. Perrin, J. Peter, Institut de Physique Nucléaire, Orsay, preprint

Re 77 R. Renfordt, GSI Annual Report, 1976.

Sa 75 H. Sann, Nucl. Instr. al.Meth 124, 5o9 (1975)

St 76 H. Stelzer, GSI Annual Report, 1976.
H. Stelzer, Nucl. Instr. al.Meth. 138, 4o9 (1976)

Wei 77 H. Weidenmüller, this Conference

Wi 77 J. Wilczynski, Phys. Lett. 47A, 484 (1973).

CONF-770602-4

Microscopic Descriptions of High-Energy Heavy-Ion Collisions

A. R. Bodmer

Argonne National Laboratory, Argonne, Illinois 60439*

and

University of Illinois at Chicago Circle, Chicago, Illinois 60680

*Work supported by the U.S. Energy Research and Development Administration, Division of Physical Research.

Introduction

In part I we give a brief account of the essentials of the equation-of-motion (EOM) approach and of some of its significant and interesting results. In part II we attempt to provide a framework for the theoretical description of high-energy heavy-ion (HE-HI) collisions; in particular we give a critical assessment of various approaches: EOM calculations, Boltzmann equations/ cascade calculations, and hydrodynamics - their relationships and their respective domains of applicability--if any--to HE-HI collisions.

I. EQUATIONS-OF-MOTION (EOM) CALCULATIONS

The EOM approach (refs. 1—5) is essentially an application to HE-HI collisions of the method of molecular dynamics, used to study classical liquids. The justification for this application depends on 1. the probable need for a microscopic description (mean free path $\Lambda \gtrsim 2$fm and shock thickness $\gtrsim \Lambda$ of the order of nuclear dimensions, i.e. large transparency), 2. the denseness of nuclear matter especially as produced in central collisions, and 3. the possibility of an approximately valid classical description at high energies (laboratory energies $E_L \gtrsim 200$ MeV). Critical discussion of these points is given in part II.

Pion production has been neglected and relativistic effects when included (ref. 5) are considered only to order v^2/c^2. We have then restricted ourselves to laboratory energies $E_L \lesssim 500$ MeV/nucleon (for equal mass target and projectile, $A_p = A_T$),--i.e. to "fast" collisions in Hüfner's terminology. Such energies are sufficiently high that hot dense nuclear matter is expected to be produced in central collisions. On the other hand the energies are still sufficiently low that potential energy and correlation effects are expected to be quite large and that one can thus expect to obtain significant information related to interaction effects for the equation of state. Furthermore, the energies

are sufficiently low that a theoretical understanding in terms of more or less conventional nuclear forces may still be possible.

The essence of the EOM approach is the calculation of the $A = A_p + A_T$ trajectories by integration of the classical equations of motion with 2-body forces between all pairs of nucleons. This is computationally feasible for quite large A ($\lesssim$ 500 for Newton's equations). We will almost entirely consider the equal mass case, $A_p = A_T$. The c.m. energy/nucleon is then $E_L/4$ (nonrelativistic) or $1/4\ E_L(1 - \frac{E_L}{8mc^2})$ (relativistic to order v^2/c^2, m = nucleon mass). The following discussion is mainly based on the EOM calculations as described in ref. 4 and on recent developments of these calculations.

An ensemble of N initial nucleon distributions is prepared appropriate to the initial projectile and target nuclei. The spatial distributions for the initial nuclei have a radius $R = r_o A^{1/3}$ ($r_o \approx 1.1$ fm), a uniform (Fermi) momentum distribution with an average kinetic energy/nucleon $\approx$ 25 MeV and 2-body potentials (see below) such that the binding energy/nucleon $\approx$ 8 MeV. These classical nuclei are not at zero temperature because of the kinetic energy and also because the potentials give saturation at a density $\rho > \rho_o = (3/4\pi r_o^3) \approx 0.18\ \text{fm}^{-3}$. However, the 2-body correlations have been relaxed as much as possible and the nuclei are as cold as possible consistent with the above requirements. These nuclei therefore condense and evaporate. These effects are small during the nucleus-nucleus collision time for $A_p = A_T =$ 20, 50 and have been carefully monitored. In particular, calculations are made for the "no-mutual-interaction" case, i.e. when the two nuclei are allowed to interpenetrate each other without any interactions between target and projectile nucleons. (This is the case of extreme transparency when the only changes--for classical nuclei--are those due to evaporation and condensation in each nucleus). For a given impact parameter b the projectile and target nuclei are

initially almost touching in order to minimize the effects of evaporation and condensation. As discussed in II, the correct saturation properties for the initial nuclei are not particularly relevant for HE-HI collisions.

The nucleon-nucleon potentials are chosen:

1. To have physically reasonable attractive and repulsive parts (based on potentials of Bethe and Johnson).
2. To give a binding energy/nucleon $\gtrsim$ 8 MeV.
3. To fit the empirical $\sin^2\theta$ weighted cross section $\sigma^{(2)}$ (isospin averaged over pp and np cross sections) for $50 \lesssim E_L \lesssim 500$ MeV by use of 2-body classical trajectory calculations. $\sigma^{(n)} = \int (1-\cos^n\theta)bdb$ where $\theta(b)$ is the c.m. deflection function, b the impact parameter. $\sigma^{(2)}$ is chosen because it determines the viscosity and thermal conductivity (for dilute systems) which in particular determine shock structure in hydrodynamics (see Part II).

Results for $\sigma^{(2)}$ are shown in fig. 1 for a static potential V_{st} and for a potential V_{ret} which includes (momentum-dependent) retarded terms. For the latter the calculations are relativistic to order v^2/c^2. Both potentials depend on four parameters. The static potentials are of the form

$$V_{st}(r) = V_o(r) = V_V(r) + V_S(r) = V_R \frac{e^{-\mu_R r}}{r} - V_A \frac{e^{-\mu_A r}}{r} .$$

There is no unique way to obtain the relativistic (retarded) corrections to order v^2/c^2 for a given static potential. However, if an underlying field-theory is assumed such that the repulsive and attractive parts in V_o (i.e. V_V and V_S) are attributed to vector and scalar fields, respectively, then the retarded correction is uniquely determined (ref. 6). Then

$$V_{ret} = V_o + V_2 ,$$

$$V_2(r,\vec{p}_1,\vec{p}_2) = \frac{1}{4m^2c^2}\left\{\left[(\vec{p}_1\cdot\vec{p}_2)\ V_V(r) - \frac{(\vec{p}_1\cdot\vec{r})(\vec{p}_2\cdot\vec{r})}{r}\ \frac{dV_V}{dr}\right]\right.$$

$$\left. + \left[-(\vec{p}_1-\vec{p}_2)^2 + \vec{p}_1\cdot\vec{p}_2)\ V_S(r) - \frac{(\vec{p}_1\cdot\vec{r})(\vec{p}_2\cdot\vec{r})}{r}\ \frac{dV_S}{dr}\right]\right\} .$$

[The relativistic character of V_{ret} appears through the fact that V_{ret} is not invariant to Galilean boosts (thus it depends on the momenta not only through $\vec{p}_1 - \vec{p}_2$) but is invariant, to $O(v^2/c^2)$, to Lorentz boosts.]

V_2 does not introduce additional parameters, but the parameters V_A, μ_R, V_A, μ_A must be readjusted so that V_{ret} fits the empirical values of $\sigma^{(2)}$. It is interesting, although probably not significant, that a better fit to $\sigma^{(2)}$ is obtained with V_{ret}; in particular this can give a more nearly constant $\sigma^{(2)}$, in agreement with the empirical value, than can V_{st}. The retarded terms V_2, generally give a net repulsive contribution. However, we already note here that the longitudinal momentum-loss cross section $\sigma^{(1)}$ (ref. 7) may be more appropriate for conditions of large transparency (e.g. the initial stage in central collisions--see below). The value of $\sigma^{(1)}$ for V_{st} and V_{ret} is then less than the empirical value, i.e. these potentials will give somewhat too much transparency. Also, $\sigma^{(1)}$ is somewhat less for V_{st} than for V_{ret}, indicating that the latter gives relatively more transverse scattering.

We remark that Wilets et al. (ref. 3) have made a very ingenious proposal for obtaining a momentum-dependent 2-body "Pauli" potential which allows them to obtain cold nuclei with approximately the empirical saturation properties. (Thus for the state of minimum energy the momenta are not zero even though the velocities are.) These nuclei in their state of lowest energy are then frozen and do not condense or evaporate when left on their own.

Further critical discussion of the choice of potentials in the EOM approach is given in part II.

Trajectory calculations are made by solving either Newton's equations (nonrelativistic, static potentials) or Hamilton's equations (relativistic or momentum-dependent potentials). The relativistic calculations are to order v^2/c^2. Thus the relativistic kinetic energy and Lorentz transformations to this order are used (the latter is needed e.g. when transforming between the lab. and c.m. systems), and the potential for consistency should be V_{ret}. Thus

$$H = \sum_{i=1}^{A} \left(\frac{p_i^2}{2m} + \frac{p_i^4}{8m^3c^2} \right) + \frac{1}{2} \sum_{i,j(i\neq j)}^{A} V_{ret}(r_{ij}, \vec{p}_i, \vec{p}_j) \qquad (a)$$

$$\dot{\vec{x}}_i = \nabla_{\vec{p}_i} H \ , \quad \dot{\vec{p}}_i = - \nabla_{\vec{x}_i} H \quad (i = 1,\ldots A) \ . \qquad (b)$$

However "relativistic" calculations can also be made for V_{st}. These are then very close to the corresponding nonrelativistic calculations since only kinematic and kinetic-energy effects to $O(v^2/c^2)$ are included.

The 10 conserved quantities H, $\vec{P} = \Sigma\vec{p}_i$, $\vec{L} = \Sigma(\vec{x}_i \times \vec{p}_i)$, $\vec{K} = M\vec{R} - t\vec{P}$ are monitored. $\vec{K}$ corresponds to conservation of the c.m. velocity (M is the total mass including relativistic and interaction contributions to lowest order and $\vec{R}$ is the c.m. position. Thus $M\vec{R} = \Sigma m_i^* \vec{x}_i$ with $m_i^* = m(1 + \frac{p_i^2}{2m^2c^2}) + \frac{1}{2c^2} \sum_{j(\neq i)} V_o(r_{ij})$, and $\dot{\vec{K}} = 0$ together with $\dot{M} \approx \dot{H} = 0$ and $\dot{\vec{P}} = 0$ then gives $\dot{\vec{R}} = \vec{P}/M$ = constant.

Note, if Hamilton's equations (b) are solved exactly for the approximately relativistic H of eq. (a), then H, $\vec{P}$, $\vec{L}$ will be conserved exactly, but $\vec{K}$ only approximately to order v^2/c^2). $\vec{P}$ and $\vec{L}$ are in fact conserved very accurately; conservation of H to within about 1 % is achieved by suitable choice of step length in the integration algorithm (5th order predictor-corrector Nordsieck method).

Another check of the accuracy of the integration procedures used is to reverse the motion at some time T and check how accurately the initial conditions at t = 0 are recovered by the time-reversed motion. This is in fact recovered very accurately (for $A_p = A_T = 20$) even for central collisions (for both static and retarded potentials) and for times (T = 25 and 50 fm/c) long after the collision is over. It is amusing to change the conditions at T slightly from those attained in the forward motion and see to what extent the time reversed motion now "misses" the original conditions at t = 0. Thus if (for $A_p = A_T = 20$, E_L = 500 MeV/nucleon, b = 0) the positions at T = 25 fm/c are randomized by an amount within ±0.1 fm for each nucleon, then the original initial conditions at t = 0 are missed by a sizable amount, although for some time the reversed motion (especially the density) resembles the original one. Because of the strong interactions between the nucleons, one must "aim" very accurately if one is to recover the conditions at t = 0. This is an example of the instability of the dynamics of many-particle systems with respect to the precise initial conditions and is related (for a closed system) to the property of "mixing" in phase space. This also indicates that, for reasonably large A, there is effectively considerable averaging even for a particular initial distribution.

Analysis and Averaging. The A trajectories obtained for any given initial distribution are analyzed to give energies, populations, hydrodynamic-type

averages such as densities, average velocities, etc., all as a function of t. These results are then averaged over the N members of the initial ensemble. For our (nonrelativistic) calculations for $A_p = A_T = 50$ we used N = 10 and the impact parameter was varied from b = 0 to b = 2R in steps of 0.25 R. Nonrelativistic calculations in progress for $A_p = 20$, $A_T = 238$, $E_L =$ 250 MeV/nucleon use N = 12. Relativistic calculations to date have been made only for individual distributions for $A_p = A_T = 20$, b = 0, R and mostly for $E_L = 500$ MeV/nucleon. Angular distributions and other quantities for given A_p, A_T, E_L are obtained by integration of the results over b (with weighting b).

There are --unanswered-- questions about the size, choice and sampling of the initial ensemble. Hopefully, any related inadequacies are alleviated by the mixing property discussed above.

Results of EOM Calculations.

We give some examples to illustrate the results obtained with the EOM approach. The most comprehensive results are nonrelativistic calculations for $A_p = A_T = 50$ and $E_L = 117$ and 300 MeV/nucleon (relative velocity v/c = 0.5 and 0.8, respectively), reported in ref. 4. We also present some relativistic (unpublished) results (ref. 5) for $A_p = A_T = 20$ (i.e., $^{20}Ne + {}^{20}Ne$) for both V_{st} and V_{ret}. For both sets of results, evaporation and consensation are minor problems.

Central ($b \lesssim 0.5R$) or near central collisions ($b \lesssim R$). There is an initial stage when the relative displacement of the nuclei is $\Delta z \lesssim 2\lambda \approx 4$ fm. The nuclei effectively pass through each other without much change (especially figs. 2,4). This stage is characterized by large transparency.

Subsequently there is a stage of large overlap, characterized by strong dissipation (the translational energy T is rapidly dissipated, the distributions rapidly become near isotropic as indicated by the change in the velocity asymmetry ω). The densities become quite large, $\rho \gtrsim \rho_0$ (figs. 2,5) with associated large internal kinetic energies; the projectile and target nucleons become intermingled (e.g. fig. 2) and there appears to be approximate thermalization.

Finally there is an "explosive" adiabatic expansion (fig. 2). This stage seems to retain little memory of the initial stage, indicating again that an appreciable degree of thermal equilibrium occurred during the previous stage.

Noteworthy is the large repulsive contribution due to retardation (fig. 3) during the stage of large overlap. This presumably makes the equation of state relatively "hard" as compared for a static potential. An interesting related feature (not yet conclusively established) with possible important observational consequences is the pronounced sideways peaking of the c.m. angular distribution for V_{rot} (fig. 4). This is also indicated by the final velocity "asymmetry" $\omega_f = \langle v_z^2 / v_\perp^2 \rangle^{1/2} \sim 0.8$. This sideways peaking is reminescent of some hydrodynamic predictions (ref.8) and of the sideways splashing of two colliding incompressible drops. For comparison the static potential gives an essentially isotropic angular distribution, (fig. 4) and correspondingly $\omega_f \gtrsim 1$. We consider this difference in angular distribution,

which we conjecture is related to a difference in equation of state, to be significant. However, for a more precise test of such potential dependent effects it is necessary to compare results for potentials which give the same scattering, i.e. the same deflection function.

It seems also of interest that even for quite light nuclei ($A_p = A_T = 20$) the central collisions are explosive and not dominated by transparency effects (for $E_L \lesssim 500$ MeV).

Another possibly significant feature are the large final fused residues with $A \gtrsim 60$ found for $A_p = A_T = 50$ at $E_L = 117$ MeV/nucleon and for near central collisions, $b \lesssim 0.25R$ (figs. 5 and 8). These are described in ref. 4 and indicate that at the stage of maximum compression there is the possibility of rapid transfer (by thermal conduction) of the large thermal energy of the nucleons in the interior region to those on the outside which are explosively blown off.

Noncentral ($b \gtrsim R$ and peripheral ($b \gtrsim 1.5R$) collisions. As b is increased transparency effects rapidly increase and become dominant for $b \gtrsim R$. In fact transparency effects are already evident for quite small b. Thus (fig. 9), the c.m. angular distributions vs. b become rapidly forward-backward peaked with increasing b. For larger b the nuclei retain much of their identity after the collision (figs. 6-8) especially for $b \gtrsim 1.5R$. Correspondingly, much less of the initial translational energy is dissipated (fig. 8). Nevertheless for $b \gtrsim R$ there are still an appreciable number of fast (explosive-type) nucleons. The general resumblance (for large $b \gtrsim 1.5R$) to the experimentally observed fragmentation collisions (ref. 9) is evident. The overall c.m. angular distributions are dominated by the distributions for large b and hence are strongly forward-backward peaked.

General Conclusions. Clearly, for EOM calculations based on the free N.N. interaction, transparency and nonequilibrium effects are important or even dominant for most impact parameters (at least for the collision of equal mass medium nuclei). At least for $A_p = A_T \lesssim 50$, there seem on average to be only relatively few collisions/nucleon even for b = 0. A microscopic description, such as the EOM approach, is therefore required for a unified description. Furthermore, hydrodynamic conditions, corresponding to local, or approximately local, thermodynamic equilibrium (see Part II) are probably never fully attained although the kinetic energy may be approximately thermalized. Thus even for quite small b there is probably a complicated interplay of equilibrium and transparency effects corresponding to important nonequilibrium features. It will be important to elucidate these and extract information about them from the experimental data. This may, in particular, allow determination of transport effects and a determination of the effective mean free path λ. It will clearly be of great interest to establish potential dependent effects. These are expected to show up most strongly in central collisions and are further discussed in part II.

II. MICROSCOPIC AND HYDRODYNAMIC DESCRIPTIONS OF HIGH-ENERGY HEAVY-ION COLLISIONS

In this part we attempt to provide a framework for the theoretical description of HE-HI collisions. In particular this will involve a critique of the various approaches mentioned in the introduction, their relation to each other and their respective domains of applicability, and also a search for justified simplifications at high energies ($\lesssim$ 500 MeV/nucleon). Our understanding of HE-HI collisions will be greatly helped by one or more such simplifications.

At low energies (a few MeV/nucleon) the mean free path Λ is large ($\gtrsim$ 10 fm), the effective nuclear forces being weak. The approximate validity of single-particle motion may then provide a great simplification of nuclear dynamics. A meaningful separation between single particle and collective motions is possible. Useful and valid descriptions, discussed extensively at this conference, may be a time-dependent Hartree-Fock description (with dissipative effects perhaps dominated by one-body viscosity) or stochastic descriptions involving only a few collective degrees of freedom, with partial equilibration and dissipation as a result of the particle degrees of freedom not explicitly included.

At higher energies, comparable to or greater than the Fermi energy E_F, most or all particle degrees of freedom must be treated on an equal footing, $\Lambda \lesssim 2$ fm (for not too high energies) and one essentially has the strong interaction picture of Niels Bohr.

One may then ask whether at higher energies ($\gtrsim$ few hundred MeV/nucleon) there are one or more justified simplifications of the assumed underlying A-body quantum mechanical description (A-body Schrödinger or density-matrix equations, non relativistic or approximately relativistic, with more-or-less conventional forces.) If this is not the case then an adequate understanding of HE-HI collisions may prove very difficult.

Possible simplifications are associated with the smallness of various non-dimensional quantities. Thus one has, broadly, the following three physical simplifications and associated non-dimensional quantities.

1. Classical microscopic descriptions, especially EOM method ("$h \to 0$"): $n\lambda_T^3$, E_L/E_F, λ/r_0, $\theta_{diff}/\theta_{class} \ll 1$ (n is the particle density, λ_T is the thermal de Broglie wavelength; θ_{diff}, θ_{class} are typical diffraction and classical scattering angles. More detailed definitions are given below).

2. Dilute systems (impulse approximation effectively valid), especially Boltzmann and Uehling-Uhlenbeck (U^2) equations and corresponding cascade calculations: $nd^3 \ll 1$ (d = range of nuclear forces).

3. "Small" density, velocity or thermal gradients, i.e., local, or approximately local, thermodynamic equilibrium; hydrodynamics: $\Lambda/L \ll 1$ (L = length of nuclear dimension).

Note that the various nondimensional quantities may involve not only lengths or times but, e.g., also energies. Thus, e.g., $\theta_{class} = C(|V|/E_L)$, where V is a typical NN interaction strength; also the effective force range d will depend on energy through V/E_L.

We first consider 2. and 3. and defer consideration of quantum-mechanical effects till later.

Length and time scales and associated nondimensional quantities (for $h = 0$).

Length scales for HE-HI collisions are: d = force range. This depends on energy but typically is about 1 fm for $E_L \gtrsim 200$---500 Mev/nucleon. d may become quite small for large E_L.

Λ = mean free path ($\approx 1/n\pi d^2$). Λ characterizes the relaxation or dissipative effects. Again for $E_L \gtrsim 200$--500 MeV/nucleon, $\Lambda \gtrsim 2$ fm.

L = "macroscopic" length characteristic of nucleus-nucleus collisions.

L $\approx$ 2-4 fm for noncentral or peripheral collisions.

$\approx$ 4-6 fm for central or near-central collisions.

Time scales are obtained by use of a typical velocity, v $\approx$ 0.5 c. Thus

$\tau \approx d/v$ is the NN collision time,

$T \approx \Lambda/v$ is the mean free or relaxation time,

$T \approx L/v$ is the macroscopic, nucleus-nucleus collision time.

The pertinent nondimensional quantities (for $\hbar = 0$) are the following: The Knudsen number, $Kn = \tau/T = \Lambda/L \approx 1/nd^2L$. This is a measure of the relative variation (over a distance $\approx \Lambda$) of thermal, density or velocity gradients. If $Kn \ll 1$ one has local, or approximately local, thermodynamic equilibrium as a consequence of the smallness of the relaxation time. Correspondingly, one has a hydrodynamic description, i.e., a contracted description involving only n, the average flow velocity $\vec{u} = \langle \vec{v} \rangle$ and the internal energy e all as functions of $\vec{x}$, t, and determined by hydrodynamic equations.

The diluteness or (covolume), $\omega = \frac{2\pi}{3} d^3/2r_0^2 \approx \tau/T \approx d/\Lambda$. $\omega \ll 1$ corresponds to dilute systems for which the collision time τ is short compared to the time T between collisions. Potential energy and correlation effects are then negligible, corresponding effectively to the validity of the impulse approximation. Classically, a Boltzmann-equation or cascade-calculation description is then valid.

The table shows length and time scales and Kn, ω for classical fluids and for HE-HI collisions. For macroscopic volumes of classical fluids there is always a hydrodynamic regime, $L \gg \Lambda$. In contrast, for HE-HI collisions it is striking that there is no clear differentiation of time and length scales. One has a coalescence of time and length scales such that for not too high energies

both Kn, $\omega \simeq O(1)$. Thus neither hydrodynamics (Kn $\ll$ 1) nor a description (such as the Boltzmann equation) appropriate for a dilute system ($\omega \ll 1$) is expected to be adequate for HE-HI collisions. Note that since the velocity corresponding to the Fermi momentum is $v_F \simeq 0.3c$, the corresponding time L/v_F is also comparable to T.

Time and length scales and related nondimensional quantities

	Lengths			Kn	ω
units	d	λ	L	$\simeq\lambda/L$	$\simeq d/\lambda$
air (10^{-8} cm)	1	10^5	10^8	10^{-3}	10^{-3}
liquid (10^{-8} cm)	1	2-10	10^8	10^{-7}	0.5
nuclei (fm)	1	2	2-5	1-0.4	0.5

		Times		
	v	t	τ	T
air (s)	300 m/s	10^{-12}	10^{-7}	10^{-4}
liquid (s)	300 m/s	10^{-12}	10^{-11}	10^{-4}
nuclei (fm/c)	0.5 c	2	4	4-10

Kinetic Equations and Hydrodynamics

For a more precise and quantitative understanding we consider kinetic equations and the associated derived hydrodynamic equations. The problem of the derivation of kinetic equations (e.g., from the A-body density-matrix or Liouville equations) is a difficult one, even for classical fluids in the thermodynamic limit, which we will not consider (see, e.g. refs. 10, 11). However, kinetic equations may be considered as very useful quantitative models of physical effects more qualitatively characterized by the nondimensional

quantities discussed above. This is especially so because of the close correspondence between kinetic equations and the related cascade calculations. A kinetic equation may thus be considered as the representative of the related cascade calculation.

Kinetic equations are equations for the one-particle distribution function $f(\vec{x},\vec{v},t)$ (or quantum mechanically for the Wigner function). Thus $f(\vec{x},\vec{v},t)\ d^3x\ d^3v$ is the number of particles with position in range d^3x about $\vec{x}$ and velocity in range d^3v about $\vec{v}$ ($= \vec{p}/m$) at time t. (The Wigner function only has a probability interpretation if integrated over $\vec{x}$ or $\vec{p}$.) Kinetic equations imply the validity of a contracted description involving just f, implying that the system is in the so-called kinetic stage ($t \ll T$) where it is independent of the initial correlations. Formally, one requires the Bogoliubov functional assumption that the time dependence of the two- and more-particle distribution functions occurs only through their functional dependence on the one-body distribution function f. It is not at all obvious that a kinetic-equation description can be rigorously justified for HE-HI collisions in view of the shortness of the kinetic stage and the fact that one is dealing with finite systems of a few particles for which one is far from the thermodynamic limit (i.e., $A \to \infty$, volume $\to \infty$, but $n = A/\text{volume} = \text{constant}$).

Quite generally one has

$$\frac{Df}{Dt} \equiv \frac{\partial f}{\partial t} + \vec{v} \cdot \nabla_x f = \left(\frac{\partial f}{\partial t}\right)_{coll} . \qquad (1)$$

D/Dt is the free streaming operator (external forces assumed absent) and Df/Dt = 0 represents free streaming (straight-line trajectories) appropriate for conditions of extreme transparency. $(\partial f/\partial t)_{coll}$ gives the change in f due to collisions.

For dilute systems ($nd^3 << 1$) only binary collisions are important and one has the Boltzmann equation for which

$$\left(\frac{\partial f}{\partial t}\right)_{coll} = J(ff) = J^+ - J^- = \int\int (f'f_1' - ff_1)|v| b db d\phi d^3v_1 \qquad (2a)$$

$$= \int\int (f'f_1' - ff_1)|v| \sigma(\theta) d^2\Omega d^3f_1. \qquad (2b)$$

J^+ is the gain term due to (restitution) collisions between particles with velocities $\vec{v}'$ and $\vec{v}_1'$, impact parameter b and aximuth ϕ, which populate the number of particles about $\vec{x}$ and $\vec{v}$; J^- is the loss term due to the (direct) collisions between particles with $\vec{v}$ and $\vec{v}_1'$, etc., which decrease the number..... . $|v|$ is the relative velocity (equal before and after elastic collisions which are the only ones we consider). The form (2b) uses the (c.m.) differential cross section directly and is equivalent to (2a) if the trajectories are described classically.

The Boltzmann equation is valid for dilute systems when only binary collisions are important, i.e., when $nd^3 << 1$. The interactions enter only indirectly, namely through $\sigma(\theta)$ in giving rise to $(\partial f/\partial t)_{coll}$. Thus potential energy and correlation effects are neglected, and the equation of state is that of an ideal gas. One has straight-line trajectories between collisions, with the collision time $\tau << T$ the time between collisions. These are just the ingredients which enter into cascade calculations (neglecting exclusion-principle effects) and there is clearly a close correspondence, if not precise equivalence, between cascade calculations and the Boltzmann equation. We shall regard them as effectively equivalent for the purposes of our discussion. The validity of the Boltzmann equation/cascade calculations is also closely related (and effectively

physically equivalent to that of the impulse approximation ($\tau \ll T$), binding effects neglected, use of on-shell amplitudes - c.f. use of $\sigma(0)$ in J(ff)); however some off-shell and binding effects can be included as in ref. 14.

For very high energies (relativistic collisions) the range d may effectively become quite small and $nd^3 \ll 1$ (impulse approximation valid, potential energy effects small) and a Boltzmann equation/cascade description may become adequate.

For dense systems, $\omega \sim nd^3 \doteq O(1)$, the effects of multiple collisions must be included and potential energy and correlation effects become important. Thus

$$\left(\frac{\partial f}{\partial t}\right)_{coll} = J(ff) + K(fff) + \ldots \tag{3}$$

where K(fff) is due to triple collisions, etc. (The derivation of such an expansion in collision orders is related to a cluster-type expansion in powers of $\omega \sim nd^3$, see e.g. refs. 10, 11). The best known and studied example of a kinetic equation for dense systems is the Enskog equation for rigid spheres (of diameter d). Very little is known about kinetic equations for potentials with an attractive component and in practice one must use Monte-Carlo methods (for equilibrium conditions) or molecular dynamics methods (for equilibrium and nonequilibrium conditions).

Hydrodynamics

Quite generally one obtains, from a kinetic equation, the following conservation equations

$$\frac{1}{\rho}\frac{d\rho}{dt} = -\nabla\cdot\vec{u} \qquad \text{(mass)}$$

$$\rho\frac{d\vec{u}}{dt} = -\nabla\cdot\overleftrightarrow{P} \qquad \text{(momentum)} \qquad (4)$$

$$\frac{de}{dt} = -(\nabla\cdot\vec{q} + \overleftrightarrow{P} : \nabla\vec{u}) \qquad \text{(energy)} .$$

($\rho = mn$ = mass density, $\vec{u} = \langle\vec{v}\rangle$ = flow velocity, e = internal energy; these are all velocity averages over $f(\vec{x}, \vec{v}, t)$ and thus functions of $\vec{x}$,t). $\overleftrightarrow{P} = \overleftrightarrow{P}_K + \overleftrightarrow{P}_V$ is the pressure tensor, $\vec{q} = \vec{q}_K + \vec{q}_V$ the heat flow vector, both given by velocity averages over the one and two-particle distribution functions (the latter in turn a function of f). $\overleftrightarrow{P}_K, \vec{q}_K$ are the kinetic, i.e. translational, contributions and $\overleftrightarrow{P}_V$, $\vec{q}_V$ are the potential contributions. For the Boltzmann equation (and also for cascade calculations) only the kinetic contributions enter and transfer of momentum and energy can only occur via translation.

The conservation equations (4) are quite general, but purely formal since $\overleftrightarrow{P}$, $\vec{q}$ depend on the one and two-particle distribution functions. One obtains hydrodynamic equations, i.e. a contracted description involving only ρ, $\vec{u}$, e (or the temperature T), only if $\overleftrightarrow{P}$, $\vec{q}$ can be expressed in terms of ρ, $\vec{u}$, e.

For $\Lambda/L \ll 1$, the Chapman-Enskog method, which is an expansion in powers of the relative gradients of ρ, $\vec{u}$, T, i.e. essentially an expansion in powers of Λ/L, allows one to derive hydrodynamic equations from kinetic equations. Corresponding to increasing powers of Λ/L one obtains hydrodynamic equations which involve increasingly higher spatial derivatives. We do not give details (see e.g., refs. 10--13 for these) but only give some pertinent

results for the Boltzmann equation ($\omega << 1$) and, in order to illustrate the dependence on ω, also for the Enskog equation ($\omega = O(1)$). Quantum mechanical effects will be discussed later but it must be emphasized that the Chapman-Enskog method can be applied to kinetic equations which include quantum mechanical effects and that hydrodynamics, as is well known, can thus include such effects. Quite generally, phenomenological hydrodynamic equations may be obtained by the use of phenomenological equations relating $\overleftrightarrow{P}, \vec{q}$ to n, $\vec{u}$ and e or T (equation of state and constitutive relations). However, in our discussion we emphasize the derivation of hydrodynamic from the corresponding kinetic equations in order to make clear the relation between microscopic and hydrodynamic approaches. For further discussion of hydrodynamics, especially in its phenomenological aspects, see the talk by Maruhn (ref. 15) and also refs. 8 and 16.

$(\Lambda/L)^0$ - Euler equations of inviscid compressible hydrodynamics

Boltzmann equation ($\omega << 1$) Enskog equation ($\omega = O(1)$)

Local thermodynamic equilibrium

$f = f^{(0)} = n(m/2\pi kT)^{3/2} \exp(-m(\vec{v}-\vec{u})^2/2kT)$ = local equilibrium distribution

n, $\vec{u}$, T functions of $\vec{x}$, t

$\overleftrightarrow{P}^{(0)} = p\overleftrightarrow{I}$, $\vec{q} = 0$ ($\overleftrightarrow{I}$ = unit tensor)

no viscosity or heat conductivity

$$p = nkT - \frac{1}{6} n^2 \int \frac{dV}{dr} r\, g(r)\, d^3r \quad \text{(eq. of state)}$$

$$e = \frac{3}{2} k T + \frac{1}{2} n \int V(r)\, g(r)\, d^3r \quad \text{(internal energy)}$$

(g(r) = 2-body correlation function, i.e. $n(\vec{x}_1, \vec{x}_2) = n^2 g(r)$, where $n(\vec{x}_1, \vec{x}_2)$ is 2-particle position distribution function)

Euler equations of inviscid compressible hydrodynamics:

conservation equations (4) with $\overleftrightarrow{P} = p\overleftrightarrow{1}$, $\vec{q} = 0$.

$\rho(\vec{x},t)$, $\vec{u}(\vec{x},t)$, $e(\vec{x},t)$ determined by Euler equations and equation of state.

Euler eqs. for ideal gas		Euler eqs. for dense fluid
$p = nkT$	ideal gas equations	$p = nkT\,(1 + O(\omega))$
		$\approx 1.7\ nkT$ for $\omega \gtrsim 0.5$
$e = \frac{3}{2}\,kT$		$e = \frac{3}{2}\,kT\,(1 + O(\omega))$

The characteristic nondimensional quantity of inviscid compressible hydrodynamics is the Mach number, $M = v/c_s$, c_s = sound velocity $= (dp/d\rho)_S$ (adiabatic compressibility). For $M > 1$ one can have discontinuous shocks whose properties are determined by the Rankine-Hugoniot relations (conservation relations across shock) together with the equation of state. There is thus a rather direct connection of the flow (and resultant angular distributions for HE-HI collisions) with the equation of state (refs. 8, 15, 16). Dissipation occurs only through shocks (otherwise, entropy S is constant along stream lines).

$(\Lambda/L)^1$ - Navier-Stokes equations of viscous hydrodynamics

Approximate local thermodynamic equilibrium

$$f = f^{(0)}(1 + \phi_1),\quad \phi_1 = -\frac{1}{n}\vec{A}\cdot\nabla \log kT - \frac{1}{n}\overleftrightarrow{B}:\nabla\vec{u} - \frac{1}{n}\nabla\cdot\vec{u}$$

Thus f now has corrections depending on the gradients of T and $\vec{u}$.

($\vec{A}, \overleftrightarrow{B}$, Γ are determined from a linearized Boltzmann equation and determine the transport coefficients η, κ, λ)

$$\overleftrightarrow{P} = p\,\overleftrightarrow{I} - 2\eta\,\overleftrightarrow{S} + \kappa(\nabla.\vec{u})\,\overleftrightarrow{I}\,,\quad \vec{q} = -\lambda\nabla T$$

$$\left(\overleftrightarrow{S}_{\alpha\beta} = \frac{1}{2}\frac{\partial u_\beta}{\partial x_\alpha} + \frac{\partial u_\alpha}{\partial x_\beta} - \frac{1}{3}(\nabla.\vec{u})\,\delta_{\alpha\beta} = \text{rate of shear tensor}\right)$$

η = coefficient of shear viscosity

λ = coefficient of thermal conductivity

κ = coefficient of bulk viscosity

Navier-Stokes equations of viscous compressible hydrodynamics: These are obtained from the conservation equations with $\overleftrightarrow{P}$ and $\vec{q}$ as above and with the equation of state as for the Euler equations. Quite generally there is now dissipation; shocks have a finite thickness ($O(\Lambda)$) and are (qualitatively) described by the Navier-Stokes equations. Thus the rate of entropy production/unit volume is (for $\kappa = 0$)

$$\frac{\partial s}{\partial t} = \lambda\left|\nabla \log T\right|^2 + (2\eta/T)\,\overleftrightarrow{S}:\overleftrightarrow{S}$$

The transport coefficients are as follows:

Boltzmann equation	Enskog equation ($\omega \approx 0.5$)
$\eta = \eta^{(0)} = \frac{5}{16}\frac{(\pi m k T)^{1/2}}{\pi d^2}\frac{1}{\Omega^{(2,2)*}}$	$\eta/\eta^{(0)} = 1 + O(\omega) \approx 1.4$
$\lambda = \lambda^{(0)} = \frac{15k}{4m}\,\eta^{(0)}$	$\lambda/\lambda^{(0)} = 1 + O(\omega) \approx 1.6$
$\kappa = 0$	$\kappa/\eta^{(0)} = O(\omega^2) \approx 0.35$

Here $\Omega^{(2,2)*}$ is nondimensional and is determined by $\sigma^{(2)} = 2\pi\int \sin^2\theta\ \sigma(\theta)\ d(\cos\theta)$; $\Omega^{(2,2)*} = 1$ for rigid spheres of diameter d. Thus we have some justification for procedure used to fit potentials in the EOM approach - at least for dilute conditions not too far from equilibrium. Note the well known (Maxwell) independence of $\eta^{(0)}$, $\lambda^{(0)}$ of ρ (e.g., $\eta^{(0)} \sim (mT)^{\frac{1}{2}}\ n\ \Lambda$, $\Lambda \sim 1/nd^2$).

With the above expressions for the transport coefficients one may estimate typical dissipations during a HE-HI collision. For $A_p = A_T \gtrsim 50$, $E_L \gtrsim 300$ MeV/nucleon, b = 0, d $\approx$ 1 fm one has $\eta \gtrsim 50\,\mathrm{fm}^{-2}$ MeV c^{-1} (or equivalently $\approx 0.25\ h\ \mathrm{fm}^{-3}$), $\lambda/k \gtrsim 0.24\ c^2\mathrm{fm}^{-2}$, $\kappa \gtrsim 12\ \mathrm{fm}^{-2}\mathrm{MeV}c^{-1}$ ($\approx 0.06\ h\ \mathrm{fm}^{-3}$); then

shear viscous work/nucleon	$\gtrsim$ 15 MeV
heat transfer/nucleon	$\approx$ 10 MeV
dilatation viscous work/nucleon	$\gtrsim$ 3 MeV
Total dissipation/nucleon	$\approx$ 28 MeV (c.f., $E_L/4 \gtrsim 75$ MeV).

Thus dissipation cannot be neglected in central or near central HE-HI collisions. Hot nuclear matter is a viscous and thermally conductive fluid, and for hydrodynamics (with transport coefficients based on the free NN interaction) one should use the Navier-Stokes equations. The large dissipative effects are a consequence of $\Lambda/L = O(1)$, i.e. of large thermal, velocity and density gradients.

An important nondimensional quantity associated with viscous hydrodynamics is the Reynolds number:

$$\mathrm{Re} = vL\rho/\eta \approx \text{inertial forces/viscous forces}$$

$$\approx M/(\Lambda/L)$$

$$\gtrsim 5 - 10 \quad (M \gtrsim 2, \Lambda/L \gtrsim 0.5).$$

These small Reynolds numbers reflect large viscous effects and are again a consequence of $\Lambda/L = O(1)$. For comparison, the critical Reynolds numbers above which a flow becomes turbulent are in the range 100-1000. Thus one expects laminar flows for HE-HI collisions because of the stabilizing effects of the large viscous forces.

The Navier-Stokes equations give a good description of shocks for M not too large; for larger M they give a qualitatively reasonable description.

To order $(\Lambda/L)^2$, $(\Lambda/L)^3$ one obtains the Burnett and super-Burnett equations, respectively, which involve higher spatial derivatives. The boundary and initial value problems, especially for the super-Burnett equations are not well understood and it is not clear that these higher-order equations give any significant improvement over the Navier-Stokes equations.

Of course, transparency effects, which are large for the initial stage and for noncentral collisions, cannot be represented by any (one fluid) hydrodynamic equations even if these include dissipative effects as the Navier-Stokes equations do.

Thus because $Kn = \Lambda/L = O(1)$ one needs a microscopic description to provide a unified description of all collision stages. The appropriate microscopic description then depends on the diluteness, i.e. on whether $\omega \sim nd^3 \ll 1$ or $O(1)$.

For $\omega \ll 1$ one has the Boltzmann equation/cascade calculations. (If quantum-mechanical effects are important the corresponding equation is the Uehling-Uhlenbeck equation as discussed below). In the hydrodynamic limit the Boltzmann equation/cascade calculations can only give results corresponding to the Euler equations for an ideal gas (ideal gas equation of state and density independent transport coefficients). The Boltzmann equation and thus also

cascade calculations can give shocks, but the shock relations, in particular the compressions across a shock, can only be those appropriate to an ideal gas. (Nonrelativistically, the maximum compression for an ideal monatomic gas is 4). Also note that the full nonlinear collision term is required for the description of shocks.

For $\omega = O(1)$ potential energy and correlation effects are important and one must use either kinetic equations for dense systems (in practice only the Enskog equation for rigid spheres) or the EOM approach, the only one available for realistic potentials.

Hydrodynamics is to be understood as a "macroscopic" contracted description valid for conditions of local, or approximately local, thermal equilibrium. Because $\Lambda/L = O(1)$ (unless there are large modifications of the free NN interaction as considered in ref. 18), dissipative effects will be large and the Navier-Stokes equations should be used for hydrodynamic calculations of HE-HI collisions. Hydrodynamics can include quantum mechanical effects through the equation of state and transport coefficients (see also below) and has the great merit that one can investigate the effect of model equations of state.

Denseness of Nuclear Matter in HE-HI Collisions

The nondimensionless measure of this (as, e.g. used for the Enskog equation) is $\omega = \frac{2\pi}{3} d^3 / \frac{4\pi r_o^3}{3} = d^3/2r_o^3$. For realistic potentials the range d will depend on energy. Thus for sufficiently high E_L, d may effectively become quite small.

For $E_L \lesssim 500$ MeV some estimate of the magnitude of d and ω may be obtained from the following two considerations.

1. Equation of state and internal energy e as obtained from EOM calculations. In particular, we have results pertinent for e, namely average potential (P.E.) and kinetic (K.E.) energies/nucleon for the stage of large overlap in central collisions (for which $\rho \gtrsim 0.3$ fm^{-3}). (Recall that for equilibrium $e = \frac{3}{2} T + \frac{1}{2} n \int V(r)g(r)d^3r$ = kinetic + potential contributions).

E_L/A (MeV)	K.E./A (MeV)	| P.E.| /A (MeV)	| P.E.| /K.E.	
100	50	40	0.8	Ret.
		55	1.1	St.
300	90	35	0.4	Ret.
		60	0.7	St.
500	140	30	0.2	Ret.
		60	0.4	St.

Thus even at E_L = 500 MeV/nucleon there are large potential energy contributions and correspondingly one has to deal with a dense fluid.

2. Empirical values of $\sigma^{(n)} = 2\pi \int (1-\cos^n\theta)\sigma(\theta)d(\cos\theta)$ for n = 1,2. It is convenient to use reduced nondimensional cross sections:

$$\sigma^{(1)*} = \sigma^{(1)}/\pi d^2 \quad , \quad \sigma^{(2)*} = \sigma^{(2)}/\frac{3\pi}{2}d^2 \quad .$$

For rigid spheres of diameter d, $\sigma^{(n)*} = 1$. The empirical values are shown in fig. 10 for d = 1 fm. It is seen that d $\gtrsim$ 1 fm; in particular d $\approx$ 1.1 fm for 300 $\lesssim E_L \lesssim$ 500 MeV and thus $\omega \approx 0.5$ for r_0 = 1 fm, and correspondingly larger for smaller r_0: for $\rho \approx 3\rho_0$ ($r_0 \approx 0.76$) one has $\omega \approx 0.85$!

Thus (for $E_L \lesssim$ 500 MeV) one has $\omega = O(1)$; and conditions correspond to a dense nuclear fluid and one must use an appropriate microscopic description. In particular, approaches which use the Boltzmann (U^2 equation if quantum mechanical effects are included) or equivalent cascade calculations are inadequate especially for central collisions for which large densities are expected to occur. There are then two general possibilities:

1. Kinetic equations for a dense fluid (or the equivalent cascade calculations). In practice this means a kinetic equation for rigid spheres which includes the effects of triple collisions. The Enskog equation is then a good approximation (for not too large ω) and is well studied with a known equation of state and transport coefficient (refs. 10-13). The corresponding cascade calculations are those of Halbert et al. (ref. 1) for the case of rigid spheres. There is of course no binding, the forces are impulsive, and the trajectories are straight lines between collisions; also $\sigma^{(1)*}$, $\sigma^{(2)*}$ are constant instead of decreasing with energy as do the empirical values.

As already mentioned, there is the general question about the validity of any kinetic equation for HE-HI collisions. (Kinetic stage too

short for memory of initial correlations to have been lost, i.e. no justification for Bogoliubov functional assumption, a finite system of few particles and no thermodynamic limit).

2. The classical EOM approach. This is essentially the molecular dynamics approach used to study classical liquids. It is the only one available for realistic potentials with attraction. Note that for a given potential the equation of state and the transport coefficients are not known a priori and should be obtained.

For dense conditions qualitatively new effects arise because of the possibility of transport via the potential (viz. the terms $\overleftrightarrow{P}_V$, $\vec{q}_V$ which are zero for dilute conditions and which give the ρ dependence of η, λ for the Enskog equation). For dilute conditions (Boltzmann and U^2 equation) transport properties are entirely determined by the free cross section $\sigma(\theta)$. For dense conditions transport will depend on (finite range) properties of the potential which are not uniquely determined by $\sigma(\theta)$. Thus for HE-HI collisions one may expect differences in angular distributions for different potentials which give the same free 2-body $\sigma(\theta)$. (See the remarks in I about the differences in results for V_{st} and V_{ret}.) To more precisely investigate this dependence on potential one needs potentials which give the same scattering. Classically this means potentials which give the same deflection function $\theta(b;E_L)$ at all energies. Such families of classically "elastically-equivalent" (momentum-dependent) potentials can be obtained by means of canonical point transformations which distort the radial scale within a finite range (ref. 17).

A (probably difficult) goal for the EOM calculations is to investigate potentials which give an adequate representation of the free NN scattering and at the same time give some desired equation of state (e.g. one with a second minimum for $\rho > \rho_0$, corresponding to a density isomer).

Ability of Classical 2-body Trajectory Calculations to represent NN Scattering.

If classical 2-body calculations could reproduce the empirical NN scattering, in particular $\sigma(\theta)$, then for dilute conditions ($nd^3 \ll 1$) the EOM calculations would be equivalent (and at least as good) as Boltzmann equation/cascade calculations which use the empirical $\sigma(\theta)$ directly. For such dilute conditions quantum-mechanical "diffraction" effects for $\sigma(\theta)$ (discussed below) would then not be relevant since the classical calculations would reproduce the empirical $\sigma(\theta)$.

The approach, so far, in the EOM calculations has been to consider adequate fits to $\sigma^{(2)}$ as the criterion for the ability of a potential, when used in trajectory calculations, to reproduce the empirical scattering. One may, more stringently, require that a potential reproduce the empirical values of both $\sigma^{(1)}$ and $\sigma^{(2)}$. Thus, assuming that $\sigma^{(2)}$ is adequately fitted, the relevant measure is then the ratio $r = \sigma^{(2)*}/\sigma^{(1)*}$. The empirical value (isospin average as well as the individual np and pp values) is $r \approx 0.95$ and varies little for $50 \lesssim E_L \lesssim 500$ MeV. For $50 \lesssim E_L \lesssim 200$ MeV, r varies from ≈ 1.8 to 1.5 for both the static and retarded potentials discussed in I, whereas for $200 \lesssim E_L \lesssim 500$, one has $1.55 \lesssim r \lesssim 1.9$ for V_{ret} and $r \approx 1.45$ (almost constant) for V_{st}. (Thus as mentioned in I, V_{ret} gives somewhat more transverse scattering than V_{st} at the higher energies.)

The rather slight variations of r with E_L indicate that the difference between the empirical and calculated ratios is unlikely to be due to diffraction effects which vary quite rapidly with E_L (see below). In fact the pp and np angular distributions imply exchange and momentum dependent forces. Hopefully, it may prove possible to simulate such effects classically by the use of momentum dependent potentials. In particular one may hope to obtain potentials which fit the empirical values of both $\sigma^{(1)}$ and $\sigma^{(2)}$. Such

potentials would then be more adequate also for transparent collision conditions. For such conditions, $\sigma^{(1)}$, i.e. the longitudinal-momentum loss cross section (ref. 7), may be more appropriate than $\sigma^{(2)}$ which is appropriate for conditions of approximate thermalization.

Since our potentials were fitted to $\sigma^{(2)}$, comparison of the calculated and empirical values of r shows that the calculated values of $\sigma^{(1)}$ are too small. Thus transparency effects may be somewhat overestimated in our present EOM calculations. (However, this may partially simulate the increased transparency due to the exclusion principle.)

Very high energies. It is of interest to briefly discuss very high energies ($\gtrsim$ 1 GeV). Recall that $Kn \sim \Lambda/L \sim 1/nd^2L \sim r_0^3/d^2L$ and $\omega \sim d^3/r_0^3$. Thus if $d \ll 1$ fm at high energies (impulse approximation valid) then $Kn \gg 1$, i.e. large transparency (linearized kinetic equation applicable-see below) and also $\omega \ll 1$, i.e., also a dilute system (Boltzmann or U^2 equation/cascade calculations applicable). Thus if d should effectively become small at very high energies (as suggested by the behavior of the cross section $\sigma^{(1)}$ and discussed in ref. 7) one has great simplifications but correspondingly little significant physics! Note that pion and other particle production and/or collective effects such as pion condensation (ref. 18) could change this conclusion.

Quantum-mechanical Effects, Equation of State, etc.

Different aspects of $h \neq 0$ are associated with the following nondimensional quantities: $\chi = n\lambda_T^3/4 \sim \lambda_T^3/r_0^3$, λ_T/r_0 (degeneracy, validity of Boltzmann statistics), E_F/E_L (exclusion principle effects for transparent conditions), λ/r_0, $\theta_{diff}/\theta_{class}$ (diffraction effects for NN scattering). Here χ is the Sommerfeld degeneracy parameter, i.e. the average occupation in a volume h^3 in phase space; $\lambda_T = (2\pi\hbar^2/nkT)^{1/2}$ is the thermal de Broglie wavelength; θ_{diff}, θ_{class} are typical diffraction and classical scattering angles. The factor 4 for χ is the degeneracy (n,p, spin up, spin down).

For dilute systems ($nd^3 \ll 1$) the appropriate kinetic equation is the Uehling-Uhlenbeck (U^2) equation for fermions (refs. 13,19):

$$\frac{Df}{Dt} = \left(\frac{\partial f}{\partial t}\right)_{coll} = J(ff) + S_{FD}(fff)$$

$$= \int\int [f'(1-f)f_1'(1-f_1) - f(1-f')f_1(1-f_1')] \quad |v|\sigma(\theta)\, d^2\Omega d^3 \vec{v}_1 .$$

(The quartic terms cancel.) The U^2 equation is thus obtained by making the following replacements in the Boltzmann collision term J(ff).

1. Statistics: $f \to f(1-f')$. This allows for the occupation of final states (blocking) on the collision rate. These effects ($\sim fff$) imply statistical correlations important at densities such that $n\lambda_T^3 = O(1)$.

2. "Diffraction" effects for (free) 2-body scattering: $b\, db \to \sigma(\theta)d(\cos\theta)$, i.e., use of the quantum mechanically calculated $\sigma(\theta)$.

If only the second replacement is made then one has just the Boltzmann equation but with $\sigma(\theta)$ calculated quantum mechanically instead of classically; in particular one still has the ideal gas equation of state and density independent transport coefficients. However, the latter are now calculated using the quantum mechanical values for $\sigma^{(2)}$ (refs. 11-13). This is then equivalent to cascade calculations at high energies which use $\sigma(\theta)$ directly and which ignore the exclusion principle.

Statistics for conditions of approximate thermal equilibrium.

Such conditions may be attained in the large overlap regime in central or near-central collisions. One may then apply the Chapman-Enskog expansion to the U^2 equation (valid for $nd^3 \ll 1$). Local thermal equilibrium $[(\Lambda/L)^0, (\partial f/\partial t)_{coll} = 0]$ now corresponds to a local Fermi-Dirac distribution: $f^{(0)} = f_{FD} \sim [1 + \exp(E - E_F)/kT]^{-1}$. The equation of state is that of a (noninteracting) Fermi gas: $p = nkTF(n\lambda_T^3) = nkT(1 + n\lambda_T^3/2^{5/2} + \ldots)$. The (isospin averaged) correlation function (for $\chi \ll 1$) is $g(r) = [1 - \frac{1}{4}\exp(-2\pi r^2/\lambda_T^2)]$. These expressions illustrate the effects of statistical correlations on the equilibrium properties of a (slightly degenerate) Fermi gas.

To order $(\Lambda/L)^1$ one again obtains the Navier-Stokes equations with the above Fermi-gas equation of state but with transport coefficients which now depend on n: $\eta/\eta^{(0)}$, $\lambda/\lambda^{(0)} = 1 + 0(n\lambda_T^3)$. The leading corrections, to order $n\lambda_T^3$, are again determined by $\sigma^{(2)}$ (refs. 13, 19).

Boltzmann statistics and the ideal gas values are a reasonable approximation if $\chi \lesssim 1$. The table shows values appropriate for the stage of large overlap for $A_p \approx A_T$ ($\frac{3}{2}kT = E_L/4$, $\lambda_T(\text{fm}) = 16.15\ T^{-1/2}$ with T in MeV). It is seen that Boltzmann statistics is expected to be a fair approximation for $E_L \gtrsim 250$ MeV for $r_0 \gtrsim 1$ fm ($\rho \gtrsim \rho_0$) but possibly only for $E_L \gtrsim 500$ MeV for $\rho \gtrsim {}^3\rho_0$. It should be noted that for dense systems the energies at which Boltzmann statistics become reasonable may be significantly different from those for an ideal gas.

E_L(MeV)	T(MeV)	λ_T(fm)	$\chi(r_0=1fm)$	$\exp(-2\pi/\lambda_T^2)$
100	17	3.92	3.51	0.66
300	50	2.28	0.71	0.30
500	85	1.75	0.32	0.13

Effects of exclusion principle for large transparency. For dilute conditions ($nd^3 << 1$) such effects are described by the U^2 equation or equivalent cascade calculations. One can distinguish two effects:

1. If $p_{cm} = (m E_L/2)^{1/2} > p_F \approx$ 270 MeV/c, i.e. for $E_L \gtrsim$ 150 MeV, then there is no overlap between the Fermi spheres of the initial projectile and target nuclei and there is no consistency problem for the initial overall momentum distribution of all A nucleons.

2. Blocking of nucleon states as a result of the initial collisions between projectile and target nucleons. The relative importance (from estimates of the reduction in the effective cross section due to the excluded plase space) is expected to be $\sim (3\text{-}4)E_F/E_L$ for central collisions, i.e. possibly as much as 30% even for E_L = 500 MeV (although an average over all impact parameters may reduce this). Such blocking effects can give rise to:

   a. An initial increase in Λ, i.e. in transparency which could be of significance for details of central collisions.

   b. Depletion of forward-backward scattered nucleons (in the c.m.) for angles $\theta \lesssim \theta_{crit} \approx p_F/p_{cm}\langle\sin\theta\rangle$. For E_L = 500 MeV one has $\theta_{crit} \approx 30^o$ (based on $\langle\sin\theta\rangle \approx 0.8$ as obtained from EOM calculations). Again,

averaging over b may reduce this. This estimate seems consistent with a recent calculation by Koonin (ref. 20) which is effectively equivalent to the use of the U^2 equation for the initial knock-out nucleus.

c. Two-nucleon correlations characteristic of quasifree knockout nucleons, as pointed out by Koonin (ref. 20).

To obtain estimates for the above effects it will be of interest to compare results for the Boltzmann and U^2 equations (or equivalently, cascade calculations with and without the exclusion principle).

Linearized kinetic equations. For conditions of large transparency a linearized kinetic equation may be a good approximation. Thus, if the colliding nuclei are not much changed by the collision (slight depletion, $\lesssim 1$ collision/nucleon between projectile and target nucleons) then $f = f^{(0)}\ (1 + \phi)$, where ϕ is small and $f^{(0)}$ is a solution of the collisionless kinetic equation: $Df^{(0)}/Dt = 0$. (Thus, $f^{(0)}(\vec{x},\vec{v},t)$ corresponds to the no-mutual-interaction case for the EOM calculations). To lowest order one then obtains a linearized integro-differential equation for ϕ: $D\phi/Dt = I(f^{(0)},\phi)$. Such a description is expected to be useful for collision regimes corresponding roughly to less than about one collision, on average, between the projectile and target nucleons, i.e. for the initial stage of central collisions or for noncentral collisions. A (relativistic) linearized Boltzmann equation seems to be closely equivalent to a Glauber-model approximation as used by Hüfner et al. (ref. 21).

Role of equation of state. The equation of state is clearly not very relevant for transparent conditions dominated on average by not more than about one collision between projectile and target nucleons. Conditions are then far from equilibrium and a linearized kinetic equation, as discussed above, may provide a suitable description. Thus there is not too much physical significance in having the correct T = 0 equation of state for the initial nuclei (i.e. the correct saturation properties) for microscopic calculations. In particular for the EOM calculation the correct saturation properties for the initial nuclei are not particularly relevant, although it is important to have realistic initial position and momentum distributions.

For the stage of strong overlap in central collisions one has large densities and perhaps approximate thermalization of the kinetic energy, but probably not complete thermal equilibrium. Features of the interaction important for the equation of state (complete thermal equilibrium) are then expected to be more relevant. However, even then the connection with the equation of state cannot be assumed to be as direct as for hydrodynamics since nonequilibrium features are not expected to be negligible. This may be so especially if potential and correlation contributions are important as is in fact expected. Thus although the momentum distribution may then be approximately thermally relaxed, this may be much less true for the correlations.

Exclusion principle and effective (Pauli) 2-body forces. It is clear from the above discussion (e.g., from the above equilibrium expression for g(r) for $\chi << 1$, or from the well-known expression for g(r) for T = 0) that the exclusion principle is a many-body effect. In particular, the blocking of final states depends on the occupation of these states by particles other than the two which are scattered (e.g., the collision term in the U^2 equation). It is not clear to what extent effective momentum-dependent 2-body "Pauli" forces (ref. 3) can represent such blocking effects; at best this can only be true in some average sense.

"Diffraction" effects for NN scattering. For dilute conditions, "diffraction" effects for the collision term of the Boltzmann or U^2 equation are allowed for by use of the quantum mechanical $\sigma(\theta)$ (instead of the classically calculated value $b/\frac{d\theta}{db}\sin\theta$, where $\theta(b)$ is the deflection function).

Diffraction scattering is predominantly forward at high energies ($\theta_{diff} \sim \lambda/d$). A typical angle for classical scattering is the rainbow angle θ_R. Our classical 2-body trajectory calculations for our fitted potentials give $\theta_R \gtrsim -50/E_L(\text{MeV})$ ($\gtrsim |V|/E_L$). Thus $\theta_{diff}/|\theta_R| \gtrsim 0.2\, E_L^{1/2}$. For $E_L \gtrsim 100$ MeV this is always greater than one and increases with E_L. Thus diffraction effects are never small, essentially because the NN potential is rather weak (the phase shifts δ_L are mostly small and the--nonclassical--Born approximation is fairly good for most δ_L). Thus although λ is quite small, it is not clear that there is any energy range for which classical trajectory calculations are justified. However, the situation is in fact more favorable for these calculations because transverse momentum transfers are emphasized and the forward diffraction scattering is deemphasized. Thus for a dilute gas, for conditions of approximate local thermal equilibrium, the transport coefficients η, λ are determined by $\sigma^{(2)}$, whereas for transparent conditions the longitudinal momentum-loss cross section $\sigma^{(1)}$ may be more appropriate. The adequacy of a classical calculation is then indicated by the ratios $q^{(n)} = \sigma^{(n)}(\text{class.})/\sigma^{(n)}(\text{q.mech.})$. Figure 31 shows $q^{(1)}$, $q^{(2)}$ for the static potential V_{st} described in I. For $E_L \gtrsim 300$ MeV one has $q^{(n)} \gtrsim 0.8$, and a classical description of the free NN scattering is then not unreasonable. As already discussed, if one could find potentials which classically reproduce the empirical $\sigma(\theta)$ then for dilute conditions diffraction effects would not be relevant and the EOM calculations would be as good as Boltzmann equation/cascade calculations.

Quantum-mechanical effects for dense systems. Above we have only considered the adequacy of trajectory calculations for representing the free NN cross section appropriate for dilute systems. For dense conditions multiple collisions will be important and several nucleons may interact simultaneously; in particular a nucleon scattering successively with several other nucleons may not be out of the range of interaction of the first nucleon before it starts scattering (interacting) with another nucleon. Thus, off-energy shell effects may be significant for dense systems. Even though quantum-mechanical effects are relatively unimportant for $\sigma^{(1)}$, $\sigma^{(2)}$ for $E_L \gtrsim 300$ MeV, there is no guarantee that a similar result will be true for the multiple scattering effects important for dense systems.

Relativistic Effects

Apart from quantum field theory ("Nirvana"), there are the following possibilities. Relativistic hydrodynamic calculations can and have been made (refs. 8, 16).

For dilute systems one has microscopic approaches which use the Boltzmann or U^2 equations (ref. 10) or relativistic cascade calculations. The former involve the use of relativistic kinematics and invariant cross sections in the collision term. Relativistic cascade calculations (ref. 14) can readily include particle production.

For dense systems (classical) kinetic equations which include potential effects (e.g., a relativistic generalization of the Enskog equation) seem not to be known. The problem is one of obtaining a relativistic description involving (finite range) interactions between particles.

Such (retarded) interactions between particles can be obtained to order v^2/c^2 as described in part I. Since a classical (EOM) description with explicit inclusion of fields (in addition to particles) seems exceedingly difficult computationally, the only feasible relativistic microscopic description for dense systems therefore seems to be an EOM approach which uses retarded potentials and which is valid to $O(v^2/c^2)$.

Conclusions

Theoretical descriptions of HE-HI collisions based on the free NN interaction imply a coalescence of length and time scales such that neither λ/L nor $nd^3 \sim d^3/r_0^3$ are small compared to unity. Thus neither the simplifications of hydrodynamics ($\lambda/L \ll 1$; local, or approximately local, thermal equilibrium) nor that of microscopic descriptions appropriate for dilute systems ($nd^3 \ll 1$) - i.e. use of Boltzmann or Uehling-Uhlenbeck equations or of cascade calculations- are adequate. Hydrodynamics if used should include dissipation, and at least the Navier-Stokes equations should be used. For dense systems, corresponding to the case of HE-HI collisions at not too high energies, the only available microscopic approach for realistic potentials with attraction is the EOM approach which assumes the simplification "h = 0". Quantum mechanical effects although perhaps not of dominant importance at higher energies ($\gtrsim$300 MeV/nucleon) are probably not negligible. It is thus not clear that there are any fully justified simplifications of a general quantum mechanical A-body description of HE-HI collisions at not too high energies.

To distinguish between features appropriate to different descriptions one may have to look at more detail than just the single

proton inclusive data (ref. 22) since this may not in fact provide a very sensitive test (ref. 23). Thus cross sections for the production of light nuclei with $A \geq 2$ (ref. 22) or two-nucleon correlations (ref. 20) may be much more informative. The latter, may for example, be quite sensitive to finite-range potential effects. The determination of transport coefficients and hence of the effective mean free path, or the determination of the dependence of transparency effects on impact parameter, is expected to shed light on the basic question of whether descriptions based on the free NN interaction are justified, or whether there are important collective effects, such as pion condensation (ref. 18), which could significantly reduce Λ and hence give conditions more favorable for hydrodynamics.

REFERENCES

1. J. P. Bondorf, H. T. Feldmeier, S. Garpman, and E. C. Halbert, Phys. Letters 65B, 217 (1976); J. P. Bondorf, S. Garpman, E. C. Halbert, and P. J. Siemens, Z. Phys. 279, 385 (1976).

2. A. D. MacKellar, L. Wilets and G. A. Rinker, Proceedings of the Symposium on Macroscopic Features of Heavy-Ion Collisions (Argonne National Laboratory, Report No. ANL-PHY-76-2, May 1976) p. 663.

3. L. Wilets, E. M. Henley, M. Kraft and A. D. MacKellar, Nucl. Phys. A 282, 341 (1977).

4. A. R. Bodmer and C. N. Panos, Proceedings of the Symposium on Macroscopic Features (ref. 2) p. 463; Phys. Rev. C 15, 1342 (1977).

5. A. R. Bodmer, A. D. MacKellar and C. N. Panos, Relativistic Corrections to Classical Microscopic Equations-of-Motion Calculations of High-Energy Heavy-Ion Collisions, Bull. Am. Phys. Soc. 22, 104 (1977), and contributed paper to this conference.

6. J. Stachel and P. Havas, Phys. Rev. D 13, 1598 (1976), and references cited there.

7. M. I. Sobel, P. J. Siemens, J. P. Bondorf and H. A. Bethe, Nucl. Phys. A251, 502 (1975).

8. W. Scheid, H. Müller and W. Greiner, Phys. Rev. Lett. 32, 741 (1974); H. G. Baumgardt, J. U. Schott, Y. Sakamoto, E. Schopper, H. Stöcker, J. Hofmann, W. Scheid, and W. Greiner, Z. Phys. A 273, 359 (1975); J. Hofmann, H. Stöcker, U. Heinz, W. Scheid, and W. Greiner, Phys. Rev. Lett. 36, 88 (1976); W. Greiner, proceedings of this conference.

9. D. E. Greiner, P. J. Lindstrom, H. H. Heckman, B. Cork, and F. S. Bieser, Phys. Rev. Lett. 35, 152 (1975); P. J. Lindstrom, D. E. Greiner, H. H. Heckman, B. Cork, and F. S. Bieser, LBL Report 3650 (1975).

10. "The Boltzmann Equation", eds. E. G. D. Cohen and W. Thirring (Springer Verlag, 1973);
"Transport Phenomena", eds. G. Kirczenow and J. Marrow (Lecture Notes in Physics, Vol. 31, Springer Verlag, 1974).

11. J. H. Ferziger and H. G. Kaper, "Mathematical Theory of Transport Processes in Gases" (North-Holland Publishing Co., 1972).

12. S. Chapman and T. G. Cowling, "The Mathematical Theory of Non-Uniform Gases (Cambridge, U. P., 1970).

13. J. O. Hirschfelder, C. F. Curtiss, and R. B. Bird, "Molecular Theory of Gases and Liquids" (Wiley, New York, 1954).

14. R. K. Smith, "An Intranuclear Cascade Description of Relativistic Heavy-Ion Collisions", Proceedings of this conference; R. K. Smith and M. Danos, to be published.

15. J. A. Maruhn, "Fluid Dynamic Model for Heavy-Ion Collisions in Three Dimensions", proceedings of this conference.

16. A. A. Amsden, G. F. Bertsch, F. H. Harlow, and J. R. Nix, Phys. Rev. Lett. 35, 905 (1975); A. A. Amsden, F. H. Harlow, and J. R. Nix, "Relativistic Nuclear Fluid Dynamics" LASL preprint (1977).

17. J. E. Monahan, C. M. Shakin and R. M. Thaler, "Elastic Equivalence of Two-body Interactions in Classical and Quantum Mechanics", preprint (Argonne National Laboratory, 1973).

18. V. Ruck, M. Gyulassy, and W. Greiner, Z. Phys. A 277, 391 (1976); and to be published; also talks by M. Gyulassy and W. Greiner in the proceedings of this conference.

19. E. A. Uehling and G. E. Uhlenbeck, Phys. Rev. 43, 552 (1933); E. A. Uehling, Phys. Rev. 46, 917 (1934).

20. S. E. Koonin, "Knock-out Nucleons from Relativistic Nuclear Collisions", preprint (The Niels Bohr Institute, 1977).

21. J. Hüfner, K. Schäfer, and B. Schürmann, Phys. Rev. C 12, 1888 (1975); A. Abul-Magd, J. Hüfner, and B. Schürmann, Phys. Lett. 60B, 327 (1976); J. Hüfner and J. Knoll, "Rows on Rows - a Theory for Collisions between Heavy Ions at High Energy", preprint (Univ. of Heidelberg, 1977).

22. J. Gosset, H. H. Gutbrod, W. G. Meyer, A. M. Poskanzer, A. Sandoval, R. Stock, and G. D. Westfall, "Central Collisions of Relativistic Heavy Ions", LBL preprint 5820 (1977).

23. A. A. Amsden, J. N. Ginocchio, F. H. Harlow, J. R. Nix, M. Danos, E. C. Halbert and R. K. Smith, Phys. Rev. Lett. 38, 1055 (1977).

Figure Captions

Figure 1. Empirical and calculated cross sections $\sigma^{(2)}$. The parameters for V_{st} are $\mu_A = 2.469$, $V_A = 2569.6$, $\mu_R = 3.358$, $V_R = 6569.5$; for V_{ret}: $\mu_A = 2.401$ with the other values the same as for V_{st} (μ in fm^{-1}, V in MeV).

Figure 2. C.M. quantities vs. time for relativistic calculations for $A_p = A_T = 20$, $E_L = 500$ MeV/nucleon, b = 0 and for V_{ret}. $\rho^{(2)}$ is the average density inside a radius 2 fm with c.m. as origin; $R = \left(\frac{5}{3}\sum_{i=1}^{A} r_i^2/A\right)^{1/2}$ is the radius of the equivalent uniform distribution of all nucleons; $R_{P,T}$ that of the target or projectile nucleons; $\omega = \langle v_z^2\rangle^{1/2}/\langle v_\perp^2\rangle^{1/2}$ is the velocity asymmetry. Note the constancy of $R_{P,T}$ and the corresponding decrease of R during the initial transparent state ($t \lesssim 5$ fm/c), and the rapid increase of R, corresponding to the final explosive stage, which follows the stage of maximum compression for which $\rho^{(2)} \approx 3\rho_0$.

Figure 3. Energies in the c.m. vs. t for the same conditions as for Fig. 2. $T = \frac{1}{2} m[\sum_{i=1}^{Ap} \vec{v}_i/A_p]^2$ is the collisional translational energy/nucleon of the projectile (and also the target) nucleons; W_{ret} is the magnitude of the average potential energy/nucleon; W_0 that due to only the static part V_0 of V_{ret}.

Fig. 4. C.M. angular distributions for relativistic calculations for $A_p = A_T = 20$, $E_L = 500$ MeV/nucleon and b = 0. The values are averages over the corresponding forward and backward intervals. Fig. 4a is for V_{st}, Fig. 4b for V_{ret}. Note the transverse peaking for the latter.

Figure 5. Time-dependent c.m. results for E_L = 117 MeV/nucleon (v/c = 0.5) and b = 0. The results of Figs. 5-9 are all for the nonrelativistic calculations for $A_p = A_T = 50$, described in Ref. 4. $\rho^{(3)}$ is the average density inside a radius 3 fm with c.m. as origin; $\rho_{NI}^{(3)}$ is the value in the absence of mutual interaction between projectile and target nucleons. T is the collisional translational energy/nucleon (see caption for Fig. 3) and W is the magnitude of the average potential energy/nucleon. The large persistent values of W and $\rho^{(3)}$ for $t \gtrsim 40$ fm/c are a reflection of large fused residues.

Figure 6. The density $\rho^{(3)}$ in the c.m. system vs. t for v/c = 0.5 and for b = R and 1.5 R. Here and in subsequent figures R denotes the initial radius of the projectile or target nuclei.

Figure 7. The final velocity asymmetry ω_f (see caption for Fig. 2) in the c.m. system vs. b/R. The velocities are in units of c (v/c = 0.8 corresponds, nonrelativistically, to E_L = 300 MeV/nucleon). Note that ω_f is close to unity for small b, indicating near isotropy for central collisions. The values labelled "no mutual interaction" are also the initial values. Note that ω_f approaches this value more rapidly, as a function of b/R, for v/c = 0.8 than for 0.5, indicating greater transparency for v/c = 0.8.

Figure 8. The inelasticity I_f and the ratio W_f/W_i vs b/R. The subscripts i, f denote initial and final values, respectively. Note that for small b almost all the initial collisional translational energy is dissipated; also that I_f decreases more rapidly with b for v/c = 0.8 than for v/c = 0.5, again indicating greater transparency for the former. The large values of W_f/W_i for v/c = 0.5 and for small b are again a reflection of large fused residues; for v/c = 0.8 there are only some small final fragments. The large values of W_f/W_i for large b reflect the correspondingly large transparency and that the nuclei are relatively unaffected by the collision if this is peripheral.

Figure 9. C.M. angular distributions for v/c = 0.5 for nucleons of all final energies vs. b/R. The labels 1, ...5 denote the following intervals of cosθ: 1-0.8(1), 0.8-0.6 (2), 0.6-0.4 (3), 0.4-0.2 (4), 0.2-0 (5). N denotes the number of nucleons, the normalization being such that the total number of nucleons for $0 \leq \cos\theta \leq 1$ is 50 for each value of b/R. The values are averages over the corresponding forward and backward intervals, the angular distributions being symmetrical about 90^o to within the expected small fluctuations. Note the rapidly increasing forward peaking with b, indicative of large transparency effects.

Fig. 10. The empirical reduced (nondimensional) cross sections $\sigma^{(1)*}$, $\sigma^{(2)*}$ vs. E_L. $\sigma^{(n)*}$ are the values of $\sigma^{(n)}$ relative to those for rigid spheres of diameter d = 1 fm (see text).

Fig. 11. The ratios $q^{(n)} = \sigma^{(n)}(\text{classical})/\sigma^{(n)}$ (quantum mechanical) vs. E_L for the static potential V_{st} described in part 1.

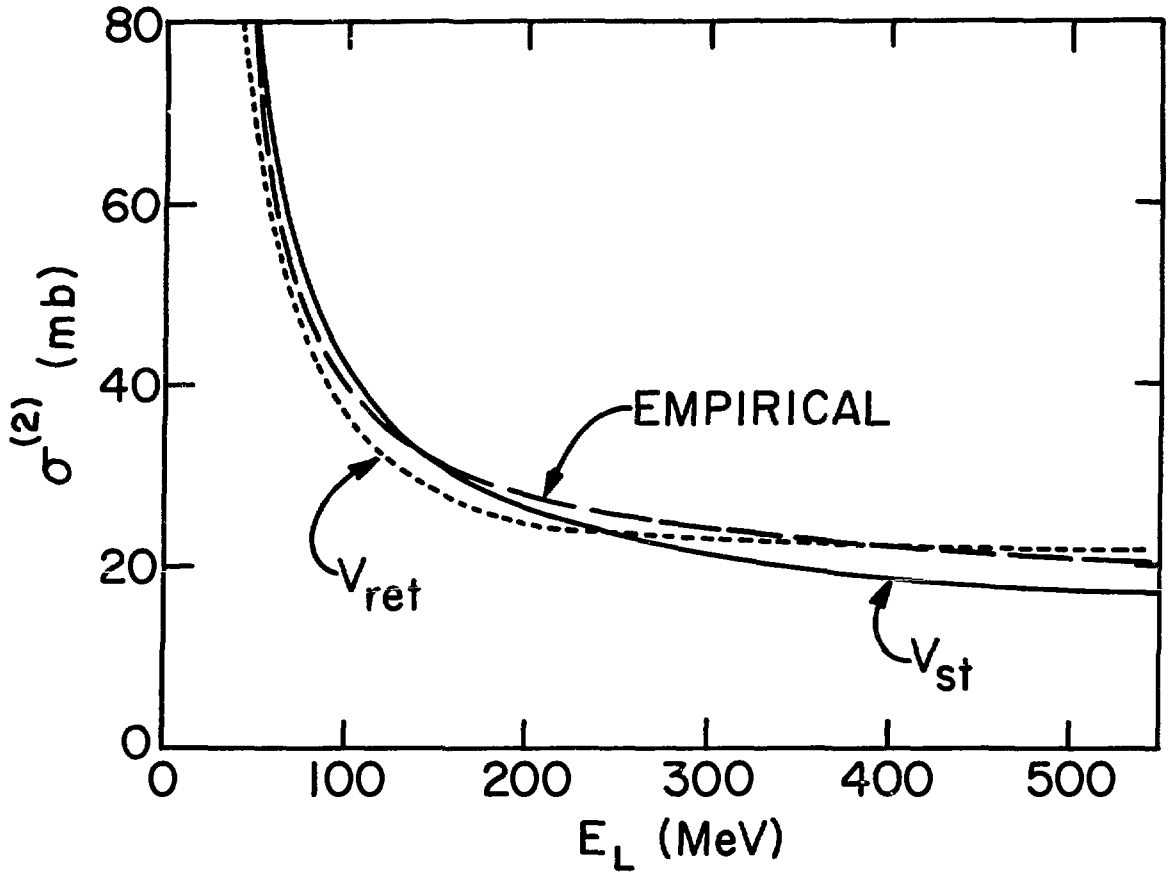
80
60
40
20
0
$\sigma^{(2)}$ (mb)
EMPIRICAL
V_{ret}
V_{st}
0
100
200
300
400
500
E_L (MeV)

Figure 1

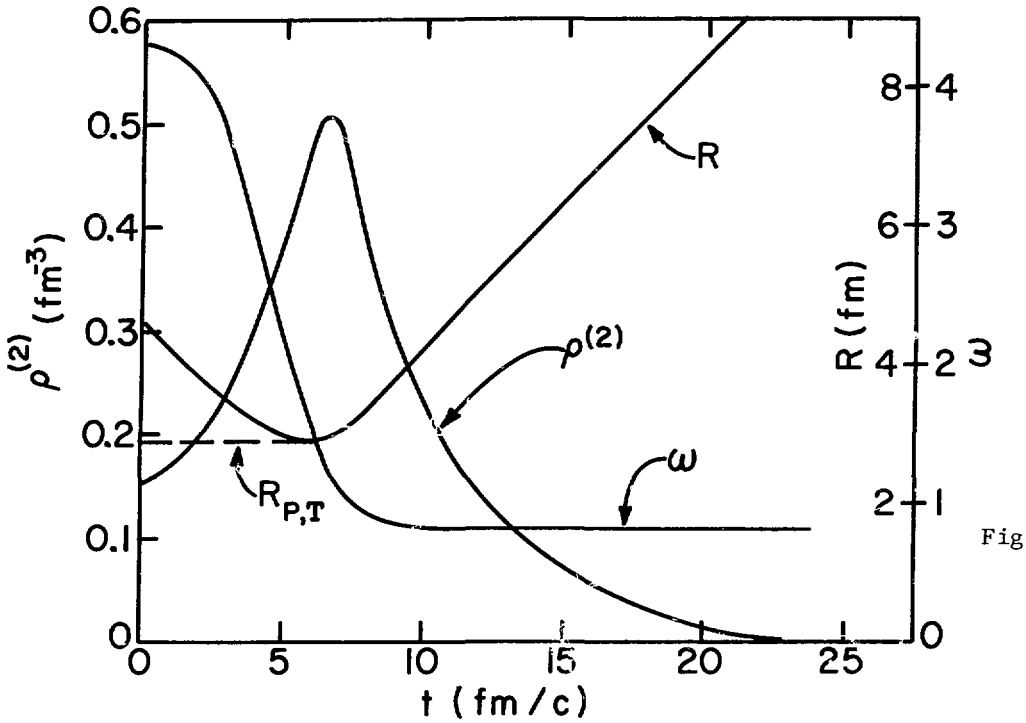

Figure 2

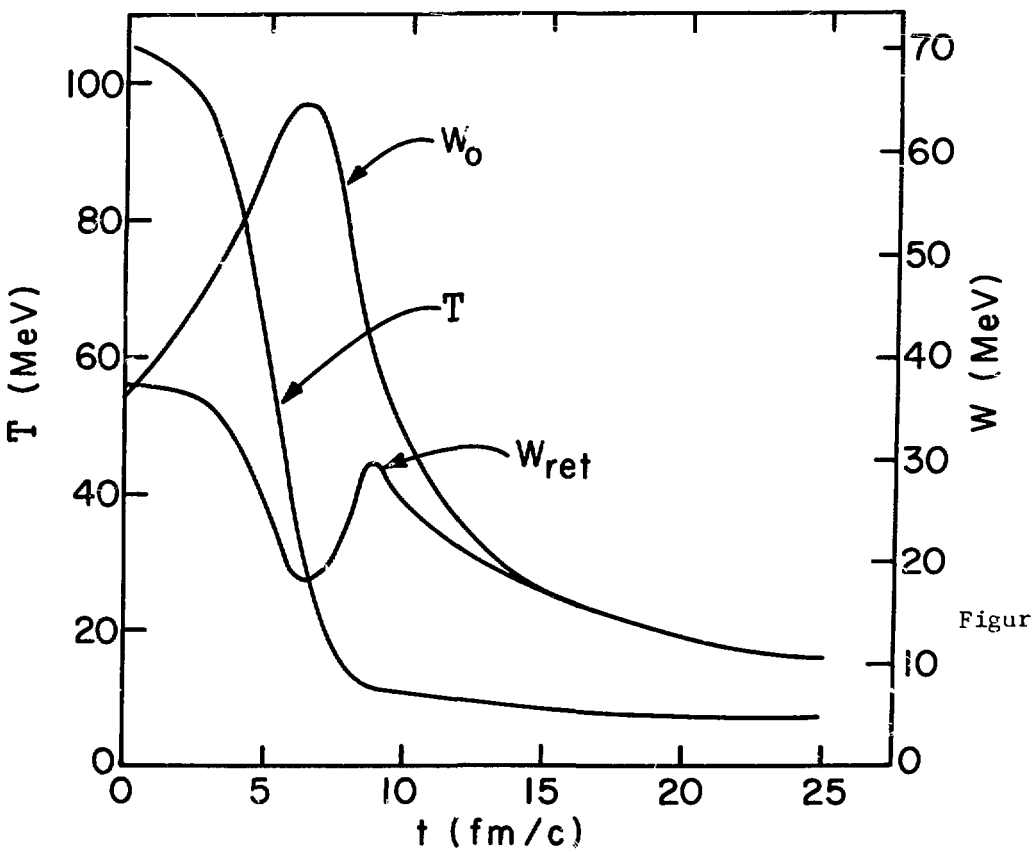

Figure 3

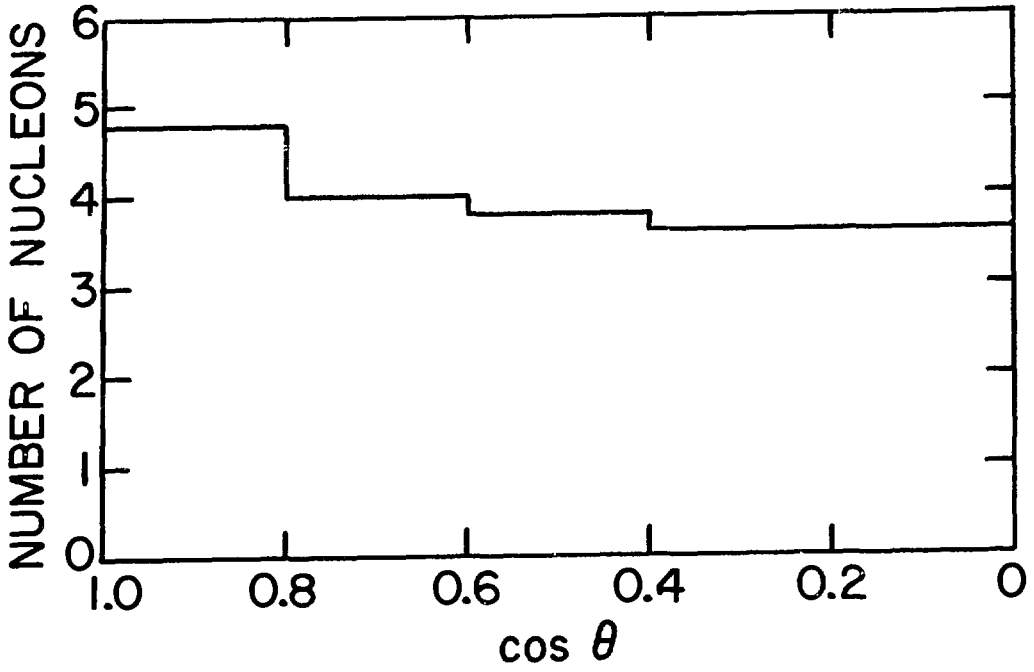

Figure 4a

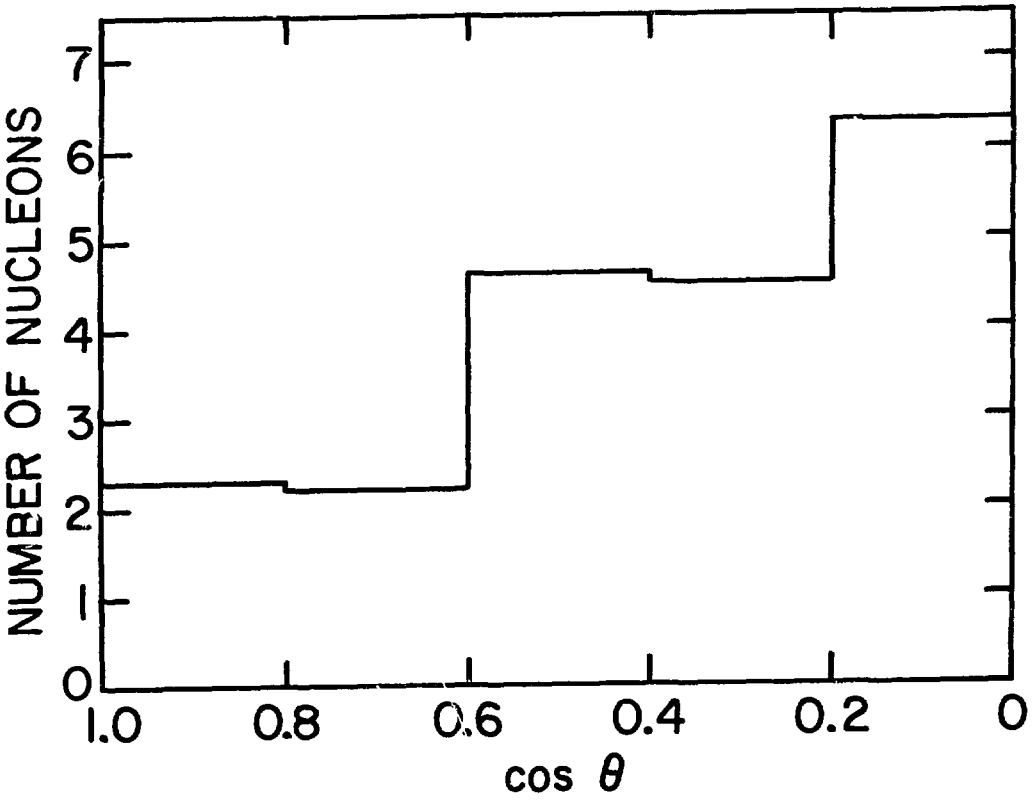

Figure 4b

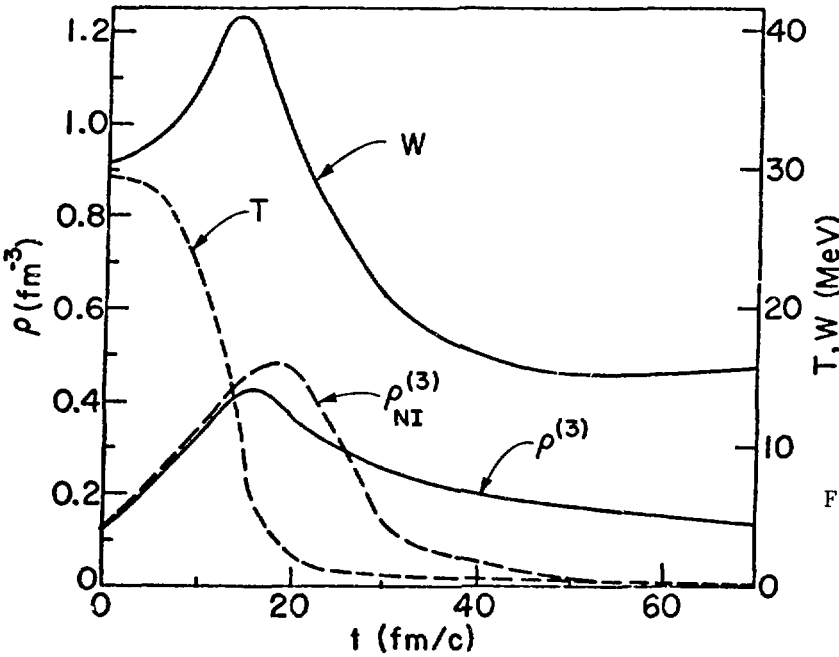

Figure 5

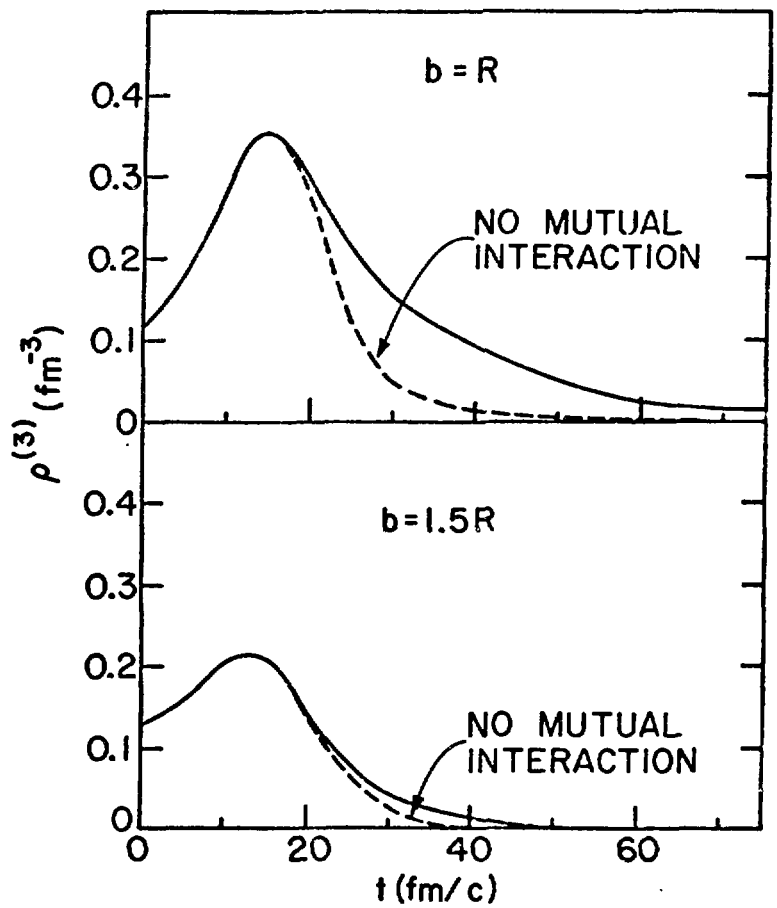

Figure 6

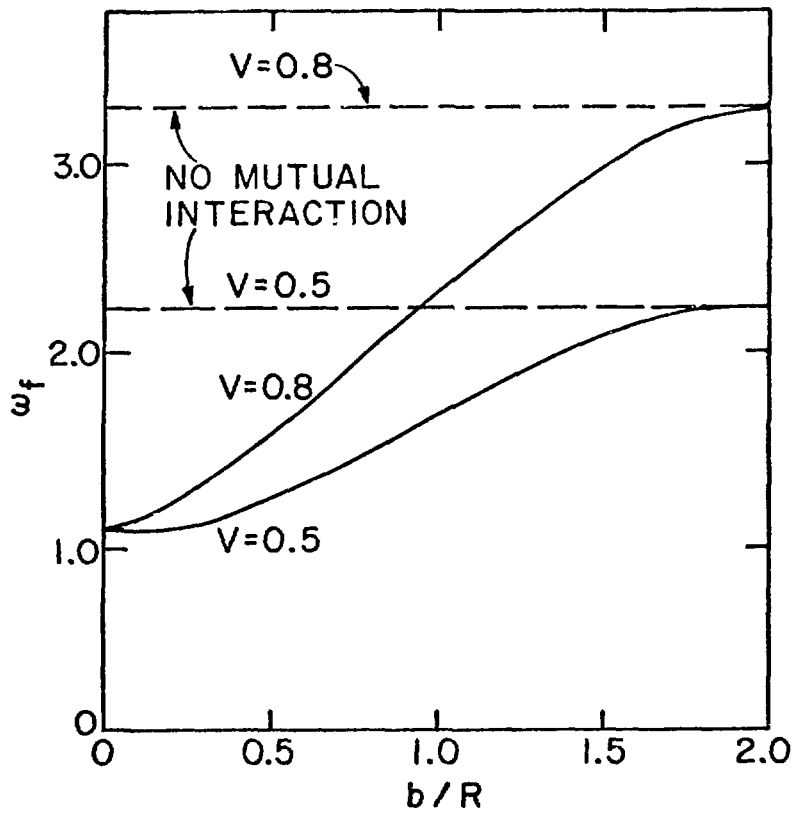

Figure 7

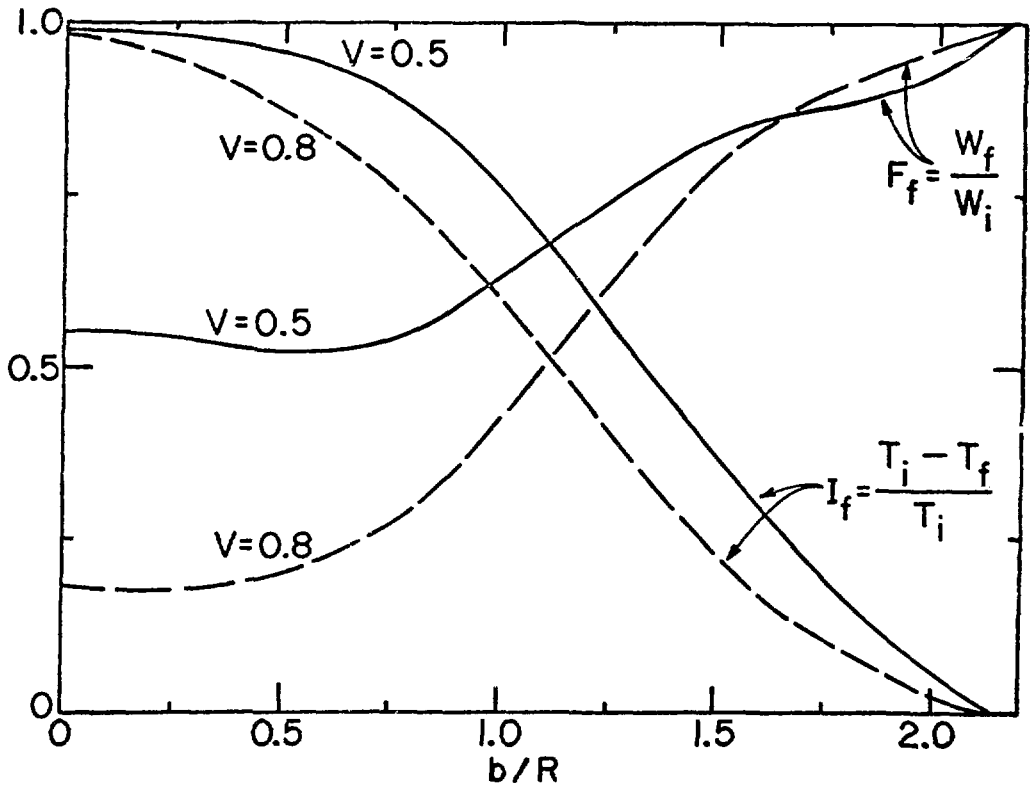

Figure 8

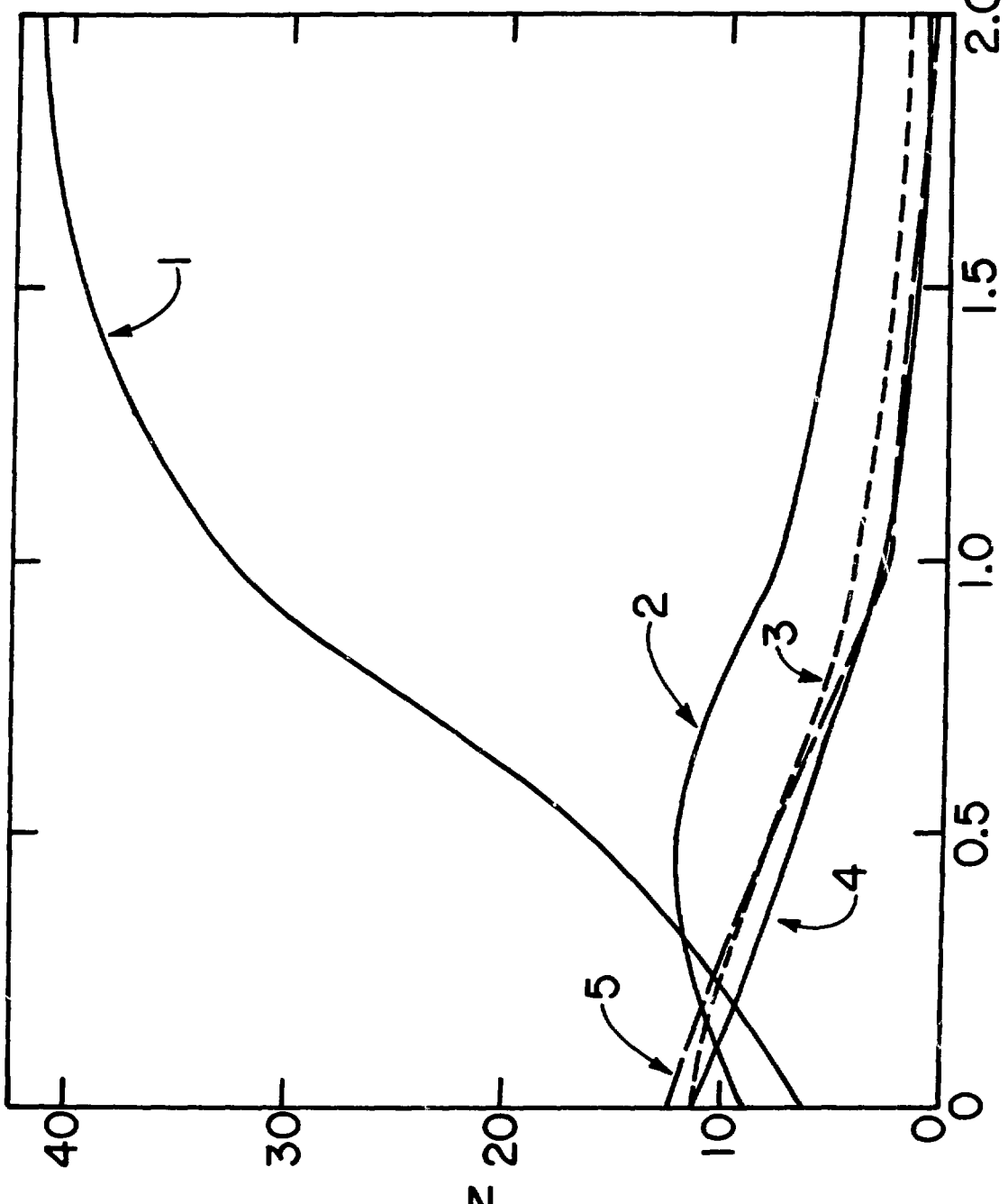

Figure 9

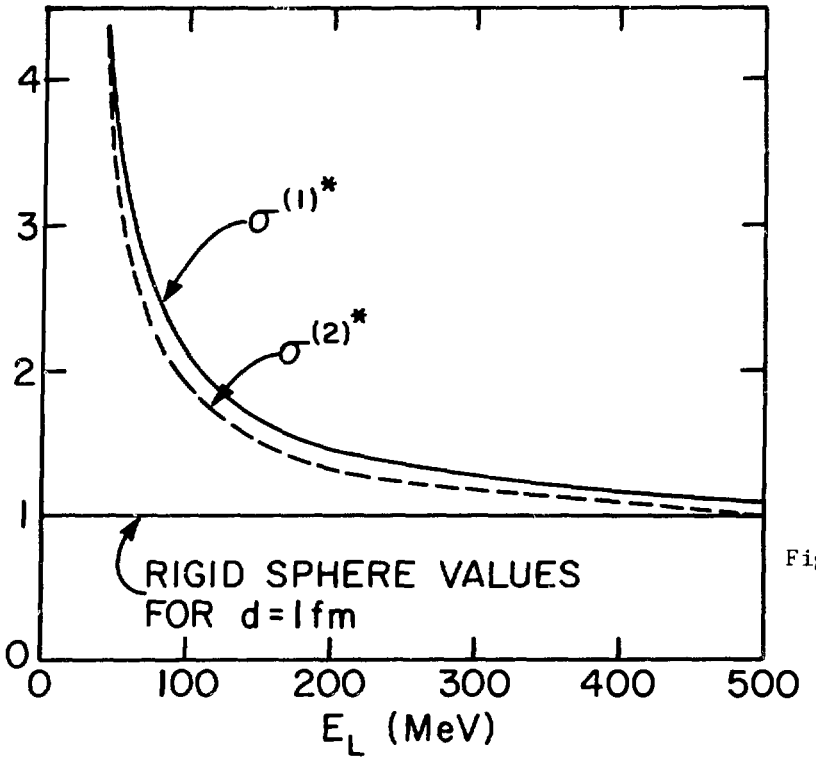

Figure 10

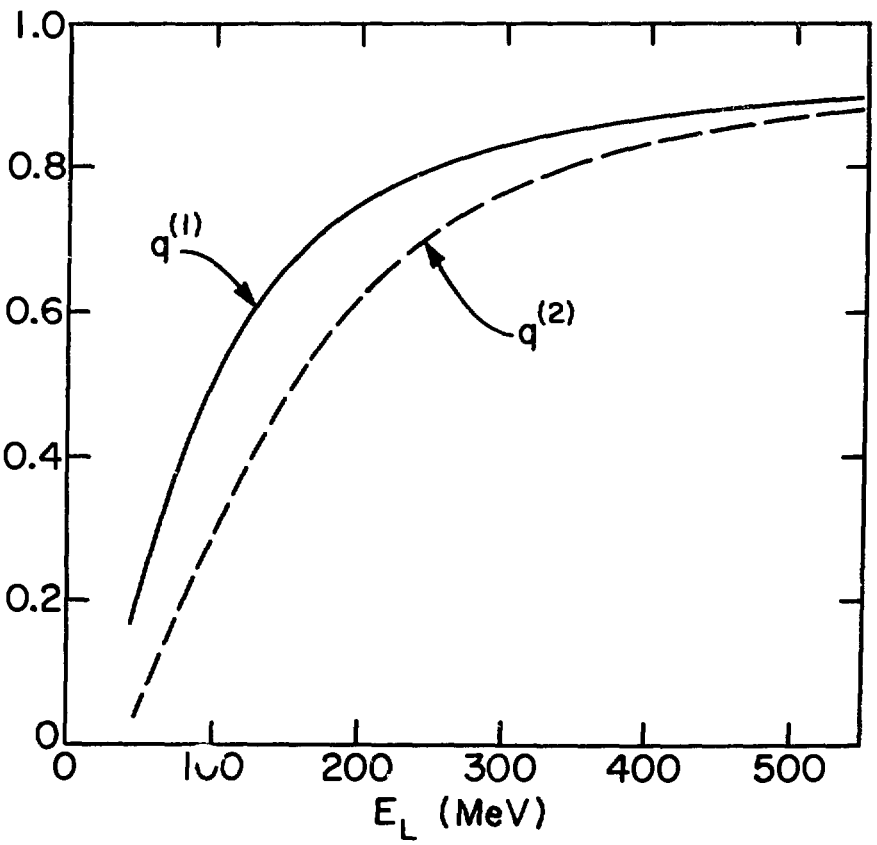

Figure 11

AN INTRANUCLEAR CASCADE DESCRIPTION OF RELATIVISTIC HEAVY-ION COLLISIONS

R. K. Smith, Duke University, Durham, North Carolina 27706
and M. Danos, National Bureau of Standards, Washington, D.C. 20234

The possibility of compressing nuclear matter during heavy ion collisions has stimulated considerable theoretical[1] and experimental[2-3] interest in relativistic heavy ion collisions. We have constructed a microscopic theory of such collisions,[4] based upon the intranuclear cascade model[5]. The underlying structure of our model approaches an effective Lagrangian field theory[6].

For relativistic heavy ion collisions, it is essential that both composite ions be treated on the same footing. For this purpose, a particle in a cell technique is used. Integrating the local density over the cell gives the probability of finding a nucleon within each cell. As the collision proceeds in time, the projectile and target cells overlap. From the nucleon probabilities and the total cross-section, the probability that a collision occurs within a cell is constructed. The final outcome is determined by a Monte Carlo technique. While energy and momentum are conserved for each collision, assumed to be pointlike in space and time, the angular distribution of the final particles are determined from the free differential cross-sections. The final momentum distribution is required to be consistent with the Pauli exclusion principle. To insure baryon conservation, the continuous nuclear density distributions, which are difuse, are depleted using a Gaussian weighting factor centered about every collision site. The range of this distribution is determined self-consistently from the local nucleon density. Pion production occurs through the production and subsequent decay of nuclear isobars, primarily the Δ_{33} resonance. Pion absorption proceeds through the inverse process.

The initial momentum of both projectile and target nucleons is selected from a zero temperature Fermi distribution. To encorporate single particle binding energy and evaporation effects, all nucleons are placed off their mass shell. In the first collision between a projectile nucleon and a target nucleon, an initial "off mass" is selected from a Gaussian distribution, centered below the physical nucleon mass, to reproduce the average binding

energy. Since the final collision partners are permitted to interact with all other particles in the system, the final off mass distribution is centered about the physical nucleon mass to avoid double counting. Such a treatment of binding effects is consistent with a propogator approach to scattering theory[6]. Since the ground state of the nuclear system is assumed to contain no mesons, the meson off mass distribution is centered about the physical pion mass.

We have studied $^{20}Ne + ^{238}U$ collisions both as a function of impact parameter and bombarding energies for projectile energies between 100-900 MeV/nucleon. The proton inclusive double differential cross-section for 250 and 400 MeV/nucleon is compared with the experimental spectrum[3] in Fig. 1. The theoretical histograms are absolute cross-sections with no applied normalization. Except for the low energy spectrum at forward angles for 250 MeV/nucleon, the theory quantatively reproduces the experimental spectrum. Within this low energy region, the theory lies above the experimental data by at most a factor of 2.

In order to understand the collision process the results of a single collision are shown in Fig. 2. The total number of nucleons, N, that have interacted at least once is plotted as a function of time. This number is decomposed into the nucleons originating from the projectile, N_P, and those originating from the target, N_T. In addition, we also consider the number of pions, N_π, the number of bound particles, N_B, and the number of free particles, N_F. The collision process can be divided into roughly three regions. The first few collisions are due to the diffuse surface. Here we find only one or two collisions. Once the nuclear densities overlap, projectile-target interactions dominate. Since the projectile energy is large, these collisions are characterized by direct excitation into the continuum, i.e., all particles are placed on their mass shell. The Pauli principle has little effect due to the large available phase space. This process continues until all particles from the projectile have interacted at least once. Due to a finite mean free path, the nuclear density gradually increases to a maximum of $\rho/\rho_0 \approx 3\text{-}5$. Since the average number of collisions per particle is $\lesssim 2$, a highly compressed, non-equilibrated nuclear matter distribution enters the second region.

Due to the large internal velocities, the compressed nuclear matter begins to expand. As the nucleons transverse the target, this distribution tends to thermalize due to collisions with target nucleons. Unlike the first region, the spatial location of these collisions is not concentrated about the projectile but instead distributed throughout the entire target. Thus the number of target nucleons that have interacted continues to increase. Again, there is sufficient energy to excite these nucleons into the continuum. However, since the available phase space is reduced, the Pauli principle prevents some collisions from occurring. During this thermalization process, nucleons are ejected from the target. During the last stage of the collision, free particle production essentially ends. The continually increasing number of interacting particles is primarily due to bound state collisions. The slight increase in N_F is due to target evaporation.

The results of collisions at different impact parameters is shown in Fig. 3. At an intermediate impact parameter, b = 5 fm, the results are similar to central collisions. After about 10 fm/C, the projectile is depleted and a state of highly compressed nuclear matter exists. This occurs after the projectile has traversed approximately the same distance as for central collisions. However, the finite geometry of both the projectile and the target reduces the nuclear environment and, therefore, the thermalization of this distribution. First of all, the distance traversed by the projectile is reduced resulting in fewer collisions with the target. Secondly, particles moving away from the target are immediately ejected whereas particles moving toward the target will experience many more collisions before escaping. Thus the degree of thermalization of the system is substantially reduced.

For a peripheral collision, b = 9 fm, most nucleons are ejected after only one collision. In addition, nucleons may be transferred from the projectile to the target resulting in both target and projectile fragmentation.

The beam energy dependence for central collisions is shown in Fig. 4. As the beam energy increases, the total multiplicity increases which is a reflection of the changing nucleon-nucleon mean free path. As the beam energy increases, so does the available phase space resulting in a surpression of the Pauli exclusion principle. Thus while the free nucleon-nucleon cross-section has a minimum

at ≈ 250 MeV the effective mean free path decreases monotonically with beam energy. The degree of thermalization then increases with beam energy.

For the larger ion energies, inelastic channels (pion production) become important. Even for beam energies below the pion threshold, pion production is possible due to the internal momentum distributions of the collision partners. The effect of pi production is illustrated by considering the 870 MeV/nucleon collision. Pion production is most prevalent during the first collision between a projectile nucleon and a target nucleon. Thus in every collision there is a 50% chance of producing a pion with an average total energy of 200-300 MeV. This results in a removal of 10-15% of the projectile energy per nucleon. However, since the mean free path for a pion is smaller than for a nucleon, more target nucleons participate in collisions with pions. Thus there is not a substantial increase in the average number of collisions per particle but instead an increase in the nucleon multiplicity. Pion and nucleon multiplicities are given in Table I.

The effects of these phenomenon upon the experimental spectrum may be illustrated by considering the transverse momentum and rapidity spectrum. A convenient representation for this spectrum is to consider a Lorentz invariant cross-section

$$\frac{1}{\pi m^2} \frac{d^2\sigma}{d\nu_\perp^2 dy}$$

as a function of rapidity $y \equiv \tanh^{-1}(\beta_z)$ and $\nu_\perp = P_\perp/m$ where β_z is the longitudinal velocity and $P_\perp$ is the transverse momentum. The advantage of such a representation may be illustrated by considering the nonrelativistic reduction of these variables.

$$y \to v_z$$

$$\nu_\perp \to v_\perp$$

Thus a Galilean transformation results in just a change of origin. Furthermore, contours of constant energy are semicircles centered about the emitting source. The advantage of rapidity is that a Lorentz transformation along the beam axis simply changes the origin of the distribution. For example, suppose the projectile moving at relativistic

energies is simply excited. For nonrelativistic energies in the projectile frame, a Boltzman distribution becomes

$$\frac{1}{\pi m^2}\frac{d^2\sigma}{d\nu_\perp^2 dy} = \frac{\sigma_{tot}}{m^2(2\pi\tau/m)^{3/2}} e^{-\frac{1}{2}m[(y-y_p)^2+\nu_\perp^2]/\tau}$$

where τ is the temperature. Any isotropic distribution centered along the beam axis will have the same distribution except centered about a different rapidity.

Since the above Boltzman distribution factors, we consider the $\nu_\perp$ and y spectrums separately. The impact parameter dependence of these distributions is shown in Fig. 5. By matching the area, i.e., the total cross-section, and the first two moments, Boltzman distributions are constructed for each distribution. While such a distribution (solid lines) reproduces the gross structure of the spectrum, noticeable deviations exist for low transverse momentum and low rapidity. This may reflect the non-equilibration of the system. Since the transverse and longitudinal directions are treated separately, a single temperature distribution is characterized by a temperature $\tau = \tau_\perp = \tau_{11}$. While a single temperature seems adequate for central collisions, the longitudinal temperatures are almost a factor of two larger for peripheral collisions. In addition, the transverse temperature is initially increased by 20% for an intermediate impact parameter and then remains relatively independent of impact parameter. Such a dependence is contrary to the predictions of the fireball model. While the distributions for the total spectrum (integrated over impact parameter) resemble the intermediate impact parameter, the longitudinal temperature is significantly larger. These features are a result of a larger degree of thermalization of the nucleon spectrum for central collisions.

The spectrum as a function of $\nu_\perp$ and y is shown in Fig. 6 and Fig. 7 for central and peripheral collisions. No preferential enhancement in the $\nu_\perp$-y plane is observed for central collisions. However, the low velocity enhancement is clearly indicated. For b = 9 fm, a three peaked distribution is observed for low transverse velocities. For larger transverse velocities onlythe central peak survives. This distribution reflects a low temperature projectile and target evaporation as well as a direct

excitation distribution. Statistics prevent a quantitative examination of these three distributions.

The differential cross-section for these impact parameters is shown in Fig. 8. The distribution for nucleon energies less than 40 MeV is characterized by a very broad peak near 55° with a width of ≈ 100°. On the other hand, the total spectrum is peaked at a forward angle at 45° with approximately the same width. As a function of impact parameters, the peaks move more toward forward angles, and become much narrower.

The differential cross-sections for central collisions as a function of ion energy is shown in Fig. 9. The solid lines are calculated from a single temperature Boltzman distribution moving along the beam axis. As the ion energy increases the degree of thermalization increases due to the decreasing mean free path. The best single temperature representation of the data occurs for 400 MeV/nucleon. However, this agreement deteriorates as pion production becomes more important. While all the spectra appear very similar, there is a slight shift of the peak toward the backward angles as the ion energy increases.

These results indicate that for central collisions, nuclear matter is initially highly compressed but in a non-equilibrium state. As this distribution expands, due to collisions with the surrounding nuclear environment, the system tends to thermalize. Due to the decreasing mean free path, as the ion energy increases, better thermalization is achieved until pion production becomes important. However, there are indications that such an equilibration is not complete, even for central collisions. At intermediate impact parameters, this thermalization is suppressed due to the finite geometry of both the projectile and the target. Such an interpretation suggests that the spectrum when integrated over impact parameters may be a more sensitive probe of highly dense nuclear matter than central collisions.

References

1. A.R. Bodmer and C.N. Panos, "Classical Microscopic Calculations of High Energy Collisions of Heavy Ions", (Preprint, Argonne National Laboratory, 1976); A.D. MacKeller, L. Willets and G.A. Rinker, Bull. Am. Phys. Soc. 21, 13 (1976); J.P. Bondorf, H. Feldmeier, S. Garpman and E.C. Halbert, Phys. Lett. 65B, 217 (1976); W. Scheid, H. Müller, and W. Greiner, Phys. Rev. Lett. 32 (1974) 741;

J.P. Bondorf, P.J. Siemens, S. Garpman and E.C. Halbert Z. Phys. 279, 385 (1976); M.I. Sobel, P.J. Siemens, J.P. Bondorf and H.A. Bethe, Nucl. Phys. A251, 502 (1975); Y. Kitazoe, K. Matsuoka and M. Sano, "Formation and Disintegration of High-Density Nuclear Matter in Heavy-Ion Collisions", (Preprint, Osaka University, Osaka, Japan, 1976); J.A. Maruhn, T.A. Welton and C.Y. Wong, (Private Communication); A.A. Amsden, G.F. Bertsch, F.H. Harlow and J.R. Nix, Phys. Rev. Lett. 35, 905 (1975).

2. H.G. Baumgardt, J.U. Scott, Y. Sakamoto, E. Schopper, H. Stöcker, J. Hofman, W. Scheid and W. Greiner, Z. Physik A273, 359 (1975).
3. G.D. Westfall, J. Gosset, P.J. Johansen, A.M. Poskanzer, W.G. Mayer, H.H. Gutbrod, A. Sandoval and R. Stock, Phys. Rev. Lett. 37, 1202 (1976).
4. R.K. Smith and M. Danos, to be published.
5. M.L. Goldberger, Phys. Rev. 74, 1269 (1948); N. Metropolis, R. Bivins, M. Storm, A. Turkevich, J.M. Miller and G. Friedlander, Phys. Rev. 110, 185 (1958); N. Metropolis, ibid., page 204; G.D. Harp, Phys. Rev. C10, 2387 (1974); G.D. Harp, K. Chen, G. Friedlander, Z Frankel and J.M. Miller, Phys. Rev. C8, 581 (1973).
6. R.P. Feynman, Phys. Rev. 76, 769 (1949).

Figure Captions

1. Double differential proton inclusive energy spectra. Experimental points are taken from Ref. 3. The error bars are statistical.

2. Number of particles, N, that have interacted at least once as a function of time. This is decomposed into those particles originating from the target, N_T, and the projectile, N_P, as well as those particles that are free, N_F, and bound, N_B. The diagram gives the location of the projectile if there were no interactions.

3. Same as 2 for different impact parameters.

4. Same as 2 for different projectile energies.

5. Transverseand longitudinal distributions for different impact parameters and the total spectrum. The solid curves are Boltzman distributions constructed from the data.

6. Distributions in the $v_\perp$-y plane for central collisions.

7. Distributions in the $v_\perp$-y plane for peripheral collisions.

8. Angular distributions for three different impact parameters.

9. Angular distributions for central collisions as a function of projectile energy.

E_{ion}/Nucleon	110	250	400	870
nucleon multiplicity	70	103	118	138
pion multiplicity	0.02	0.12	1.46	12.34
β_{11}	0.10	0.11	0.13	0.18
τ_{11} (MeV)	31.6	33.0	38.7	63.3
$\tau_{\perp}$ (MeV)	29.3	31.9	38.0	52.9
Collisions prevent by Pauli Principle	34%	19%	15%	7%

Table I. Characteristics for central collisions as a function of projectile energy.

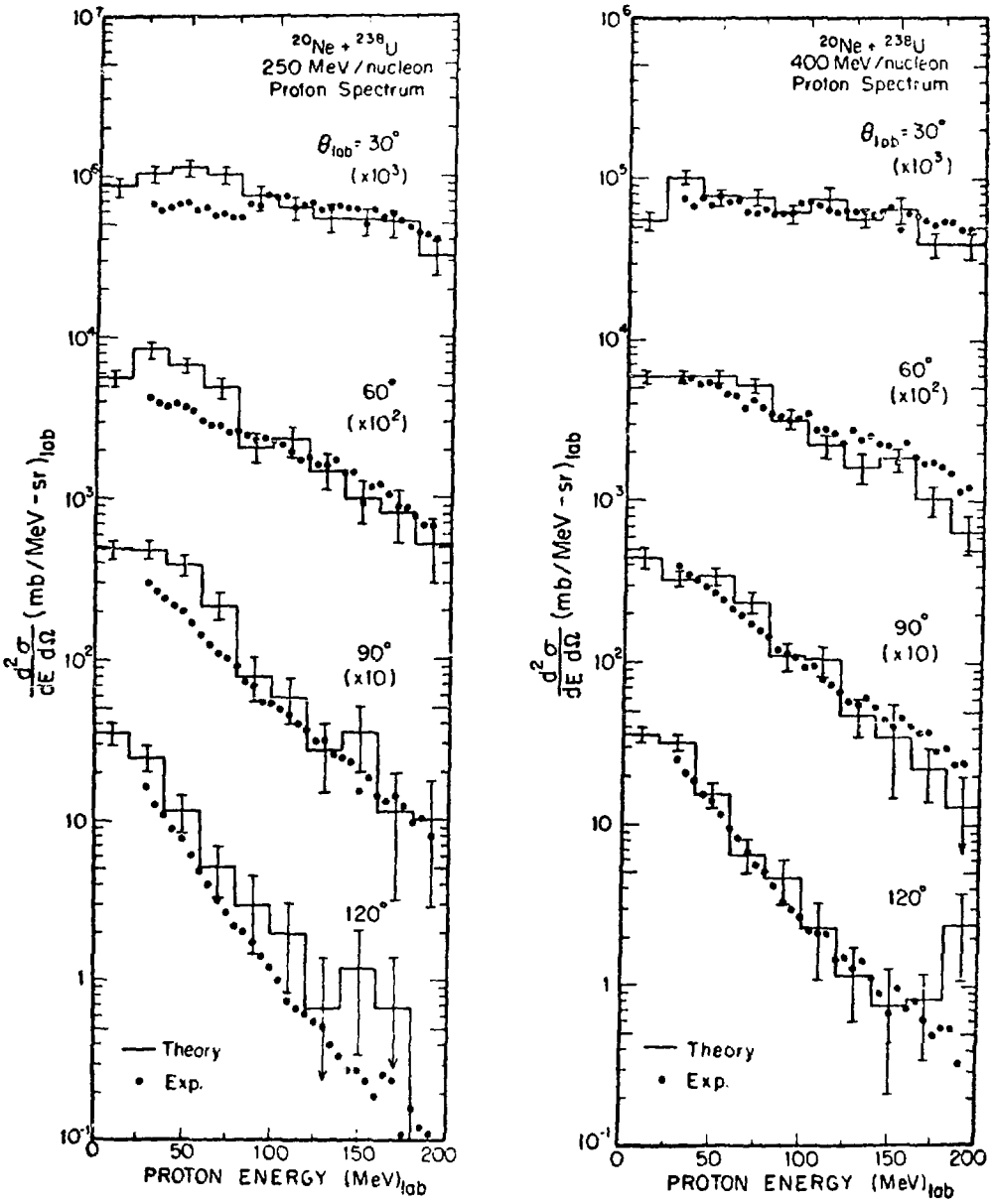
$^{20}Ne + ^{238}U$
250 MeV/nucleon
Proton Spectrum
$\theta_{lab} = 30°$
(x10³)
60°
(x10²)
90°
(x10)
120°
Theory
Exp.
$\frac{d^2\sigma}{dE\,d\Omega}$ (mb/MeV - sr)$_{lab}$
PROTON ENERGY (MeV)$_{lab}$
$^{20}Ne + ^{238}U$
400 MeV/nucleon
Proton Spectrum
$\theta_{lab} = 30°$
(x10³)
60°
(x10²)
90°
(x10)
120°
Theory
Exp.
$\frac{d^2\sigma}{dE\,d\Omega}$ (mb/MeV - sr)$_{lab}$
PROTON ENERGY (MeV)$_{lab}$

Figure 1

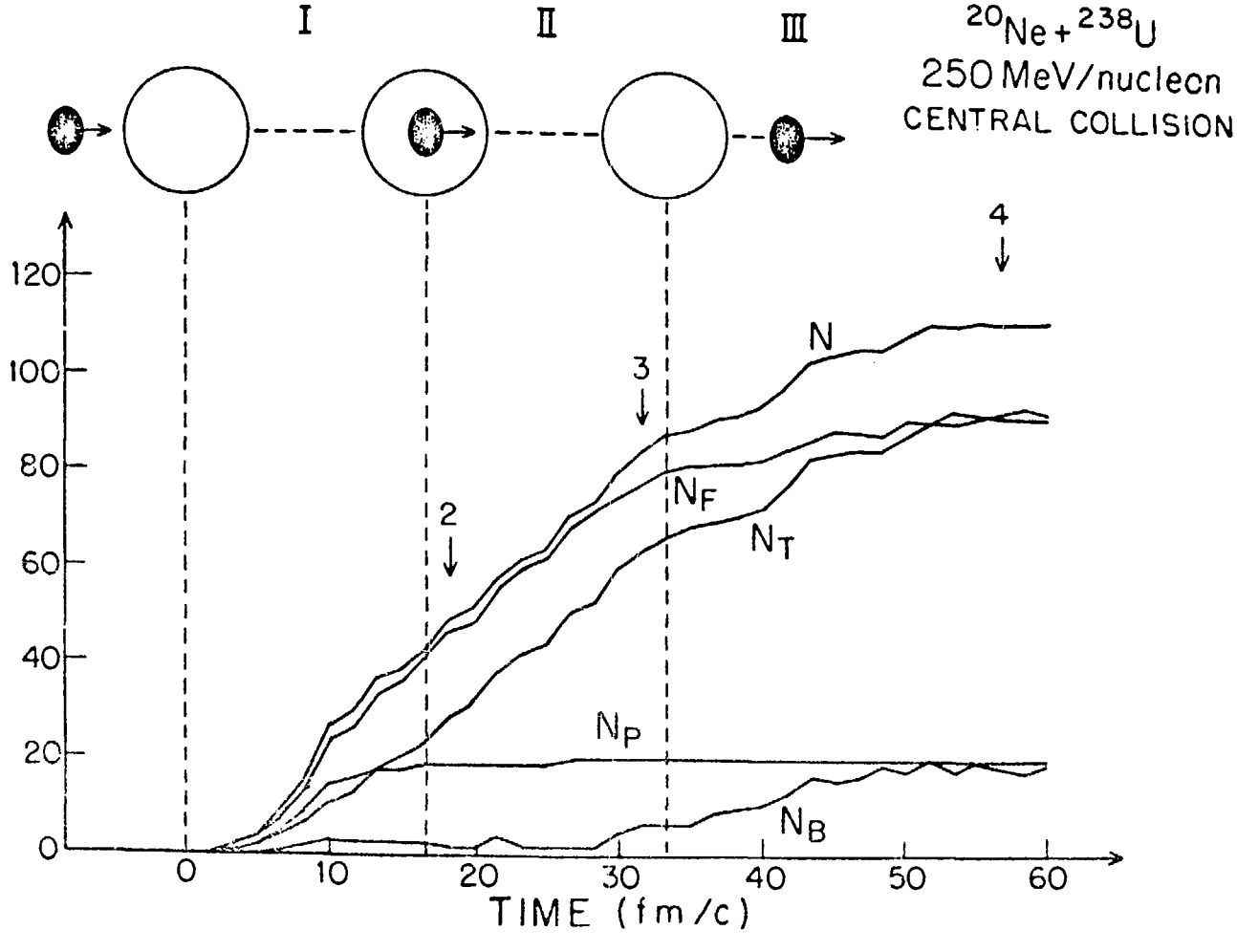
I
II
III
$^{20}Ne + ^{238}U$
250 MeV/nucleon
CENTRAL COLLISION
4
3
2
N
N_F
N_T
N_P
N_B
120
100
80
60
40
20
0
0
10
20
30
40
50
60
TIME (fm/c)

Figure 2

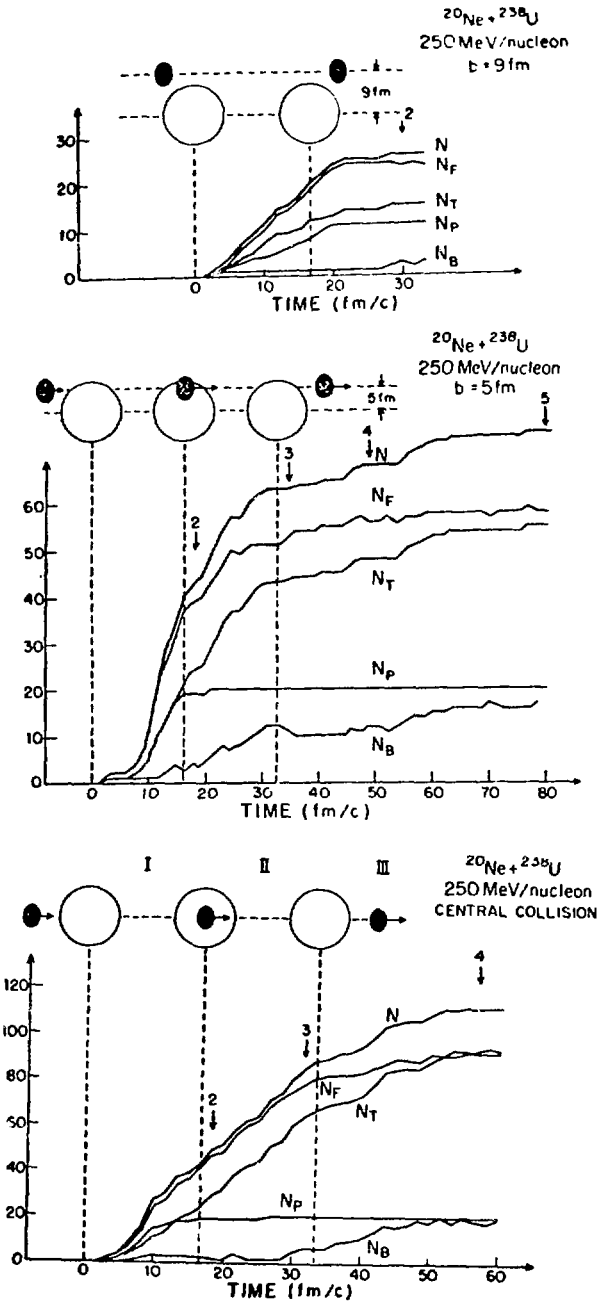
$^{20}Ne + ^{238}U$
250 MeV/nucleon
b = 9fm
9fm
N
N_F
N_T
N_P
N_B
TIME (fm/c)
$^{20}Ne + ^{238}U$
250 MeV/nucleon
b = 5fm
5fm
TIME (fm/c)
I
II
III
$^{20}Ne + ^{238}U$
250 MeV/nucleon
CENTRAL COLLISION
TIME (fm/c)

Figure 3

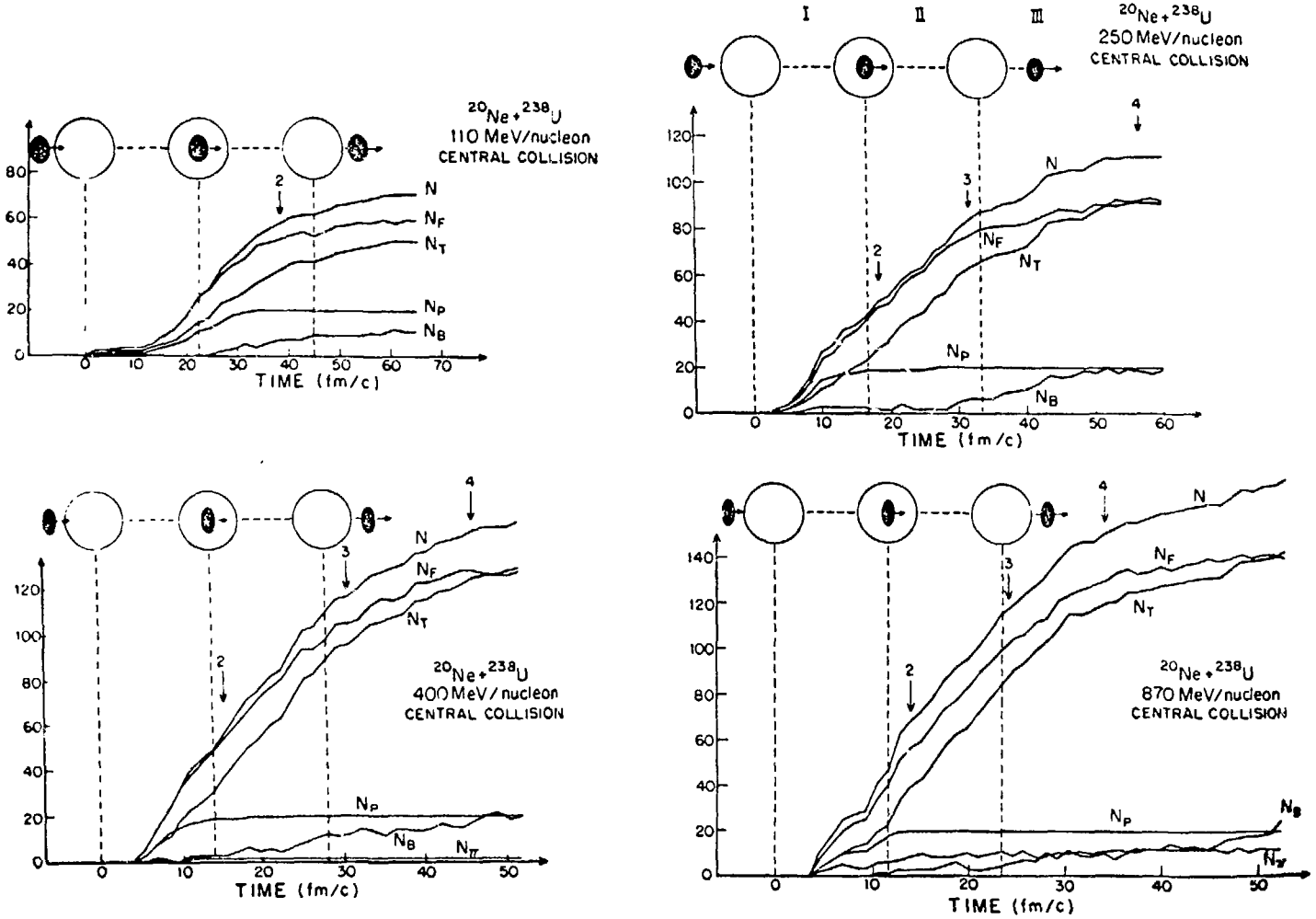
$^{20}Ne + ^{238}U$
110 MeV/nucleon
CENTRAL COLLISION
N
N_F
N_T
N_P
N_B
TIME (fm/c)
I
II
III
$^{20}Ne + ^{238}U$
250 MeV/nucleon
CENTRAL COLLISION
$^{20}Ne + ^{238}U$
400 MeV/nucleon
CENTRAL COLLISION
N_π
$^{20}Ne + ^{238}U$
870 MeV/nucleon
CENTRAL COLLISION

Figure 4

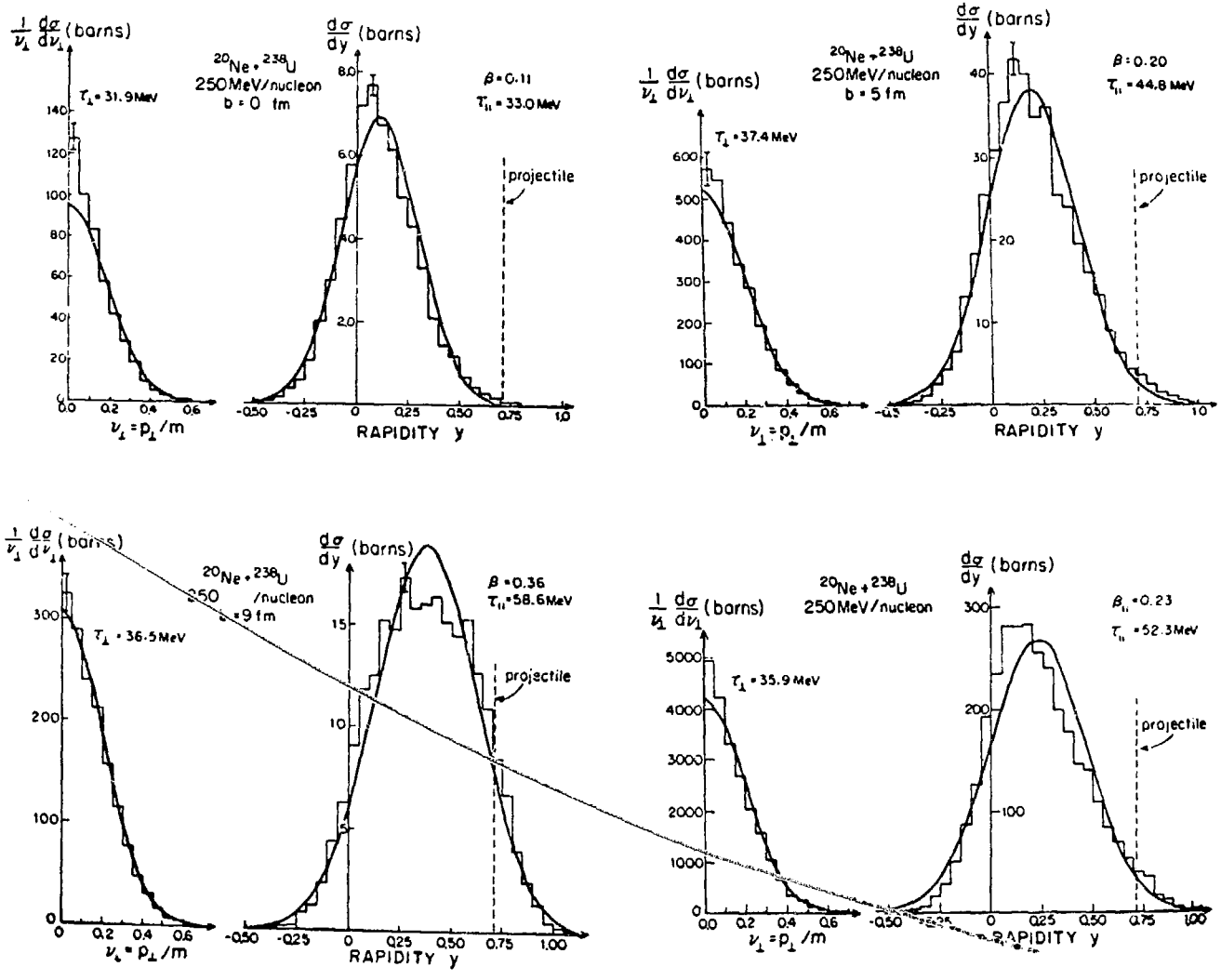
$\frac{1}{\nu_\perp}\frac{d\sigma}{d\nu_\perp}$ (barns)
$^{20}Ne + ^{238}U$
250MeV/nucleon
b = 0 fm
$\tau_\perp$ = 31.9MeV
$\nu_\perp = p_\perp/m$
$\frac{d\sigma}{dy}$ (barns)
β = 0.11
$\tau_{||}$ = 33.0MeV
projectile
RAPIDITY y
$\tau_\perp$ = 37.4MeV
b = 5 fm
β = 0.20
$\tau_{||}$ = 44.8 MeV
$\tau_\perp$ = 36.5MeV
b = 9 fm
β = 0.36
$\tau_{||}$ = 58.6MeV
$\tau_\perp$ = 35.9 MeV
$\beta_{||}$ = 0.23
$\tau_{||}$ = 52.3MeV

Figure 5

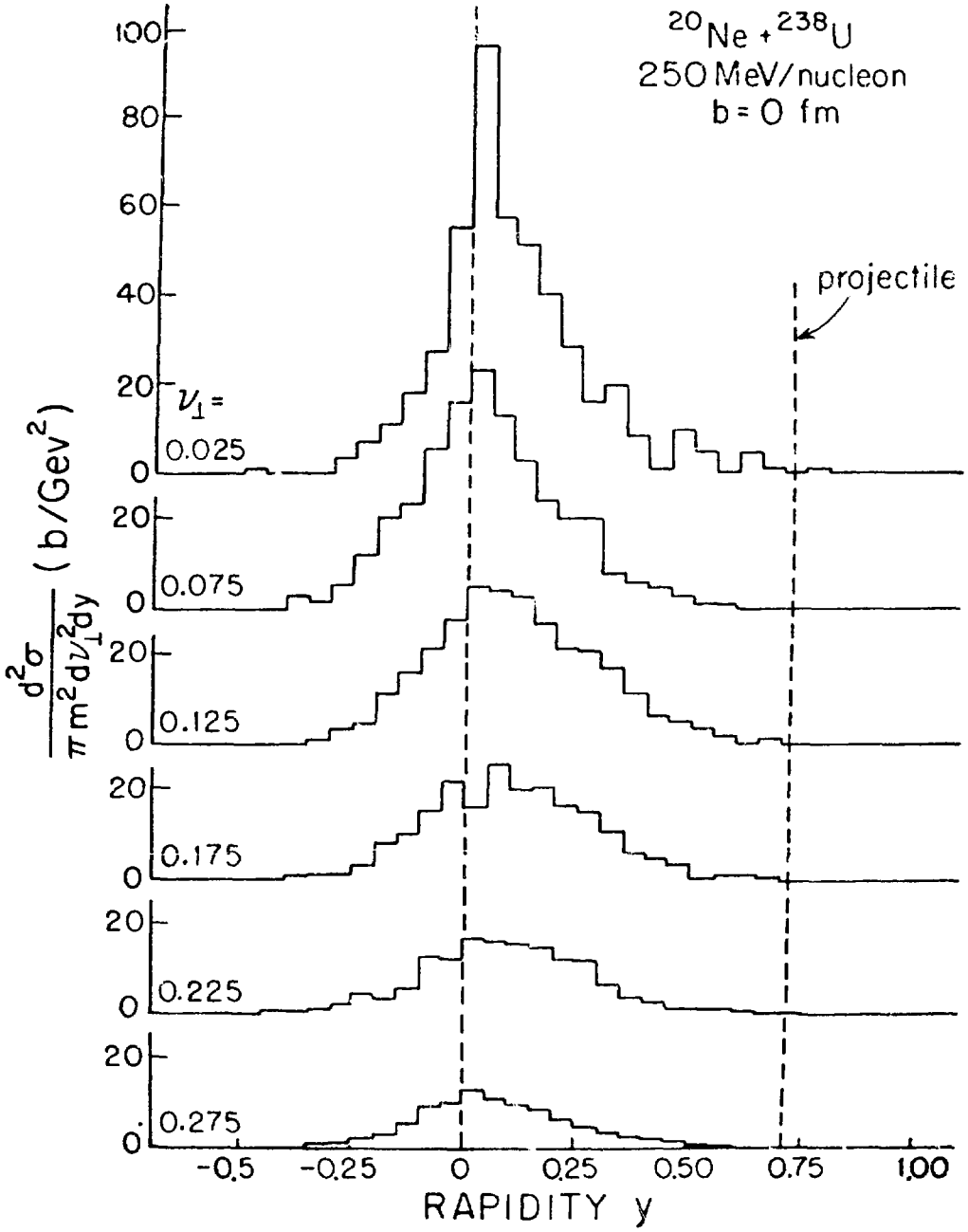
$^{20}Ne + ^{238}U$
250 MeV/nucleon
b = 0 fm
projectile
ν_1 =
0.025
0.075
0.125
0.175
0.225
0.275
$\frac{d^2\sigma}{\pi m^2 d\nu_1^2 dy}$ (b/Gev^2)
RAPIDITY y
-0.5
-0.25
0
0.25
0.50
0.75
1.00

Figure 6

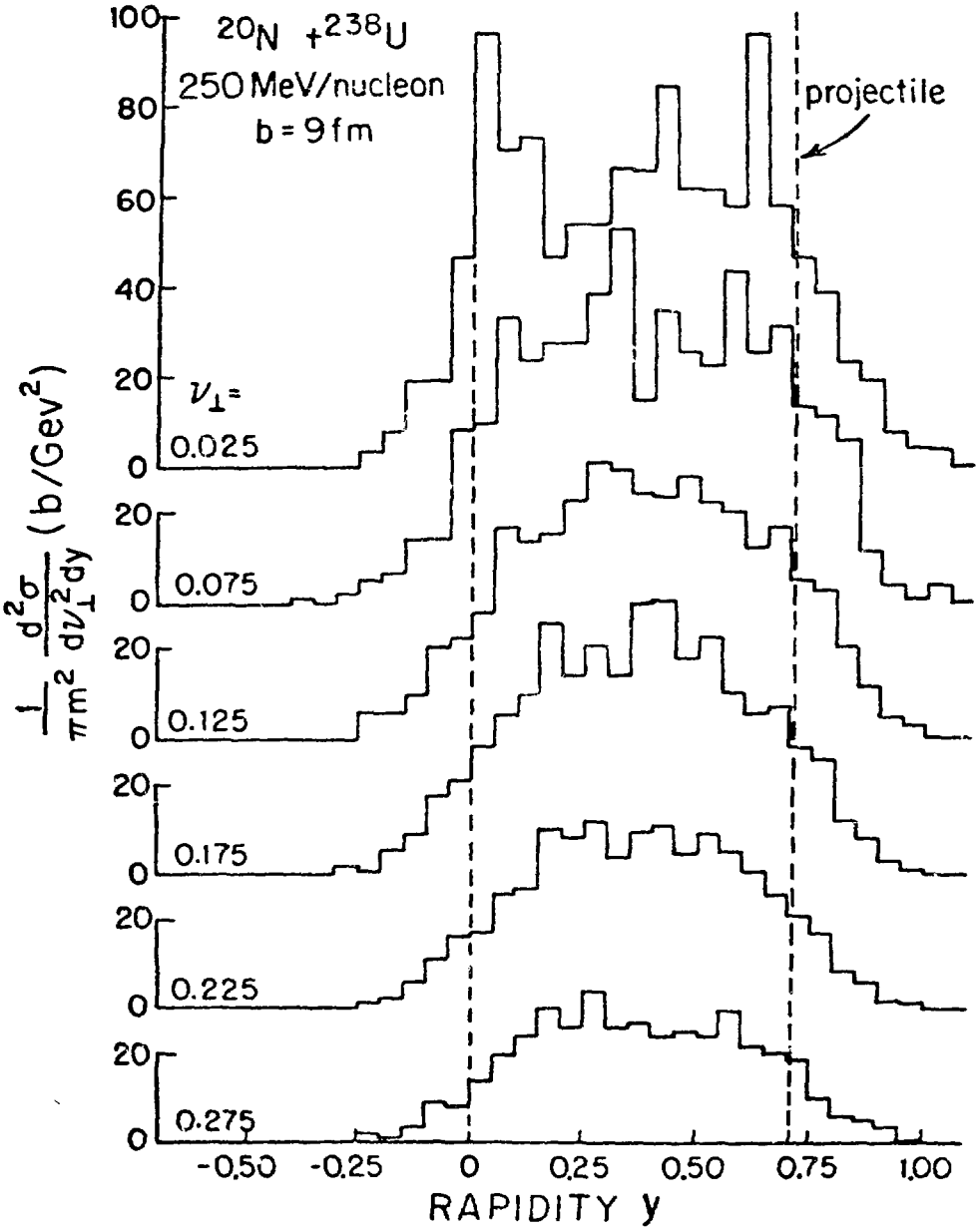
$^{20}N + ^{238}U$
250 MeV/nucleon
b = 9 fm
projectile
$\nu_\perp$ =
0.025
0.075
0.125
0.175
0.225
0.275
$\frac{1}{\pi m^2} \frac{d^2\sigma}{d\nu_\perp^2 dy}$ (b/Gev^2)
100
80
60
40
20
0
-0.50
-0.25
0
0.25
0.50
0.75
1.00
RAPIDITY y

Figure 7

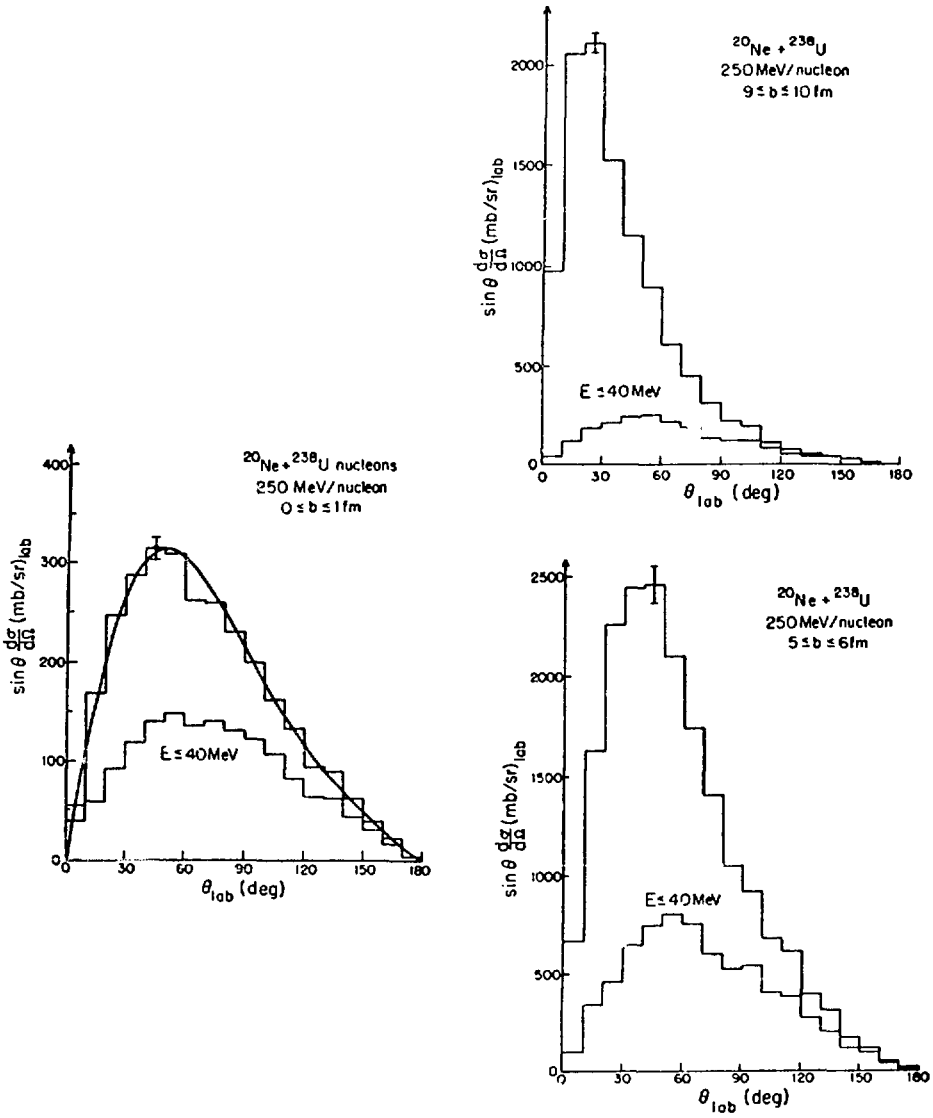
$^{20}Ne + ^{238}U$
250 MeV/nucleon
9 ≤ b ≤ 10 fm
E ≤ 40 MeV
$\sin\theta \frac{d\sigma}{d\Omega}$ (mb/sr)$_{lab}$
θ_{lab} (deg)
$^{20}Ne + ^{238}U$ nucleons
250 MeV/nucleon
0 ≤ b ≤ 1 fm
E ≤ 40 MeV
$\sin\theta \frac{d\sigma}{d\Omega}$ (mb/sr)$_{lab}$
θ_{lab} (deg)
$^{20}Ne + ^{238}U$
250 MeV/nucleon
5 ≤ b ≤ 6 fm
E ≤ 40 MeV
$\sin\theta \frac{d\sigma}{d\Omega}$ (mb/sr)$_{lab}$
θ_{lab} (deg)

Figure 8

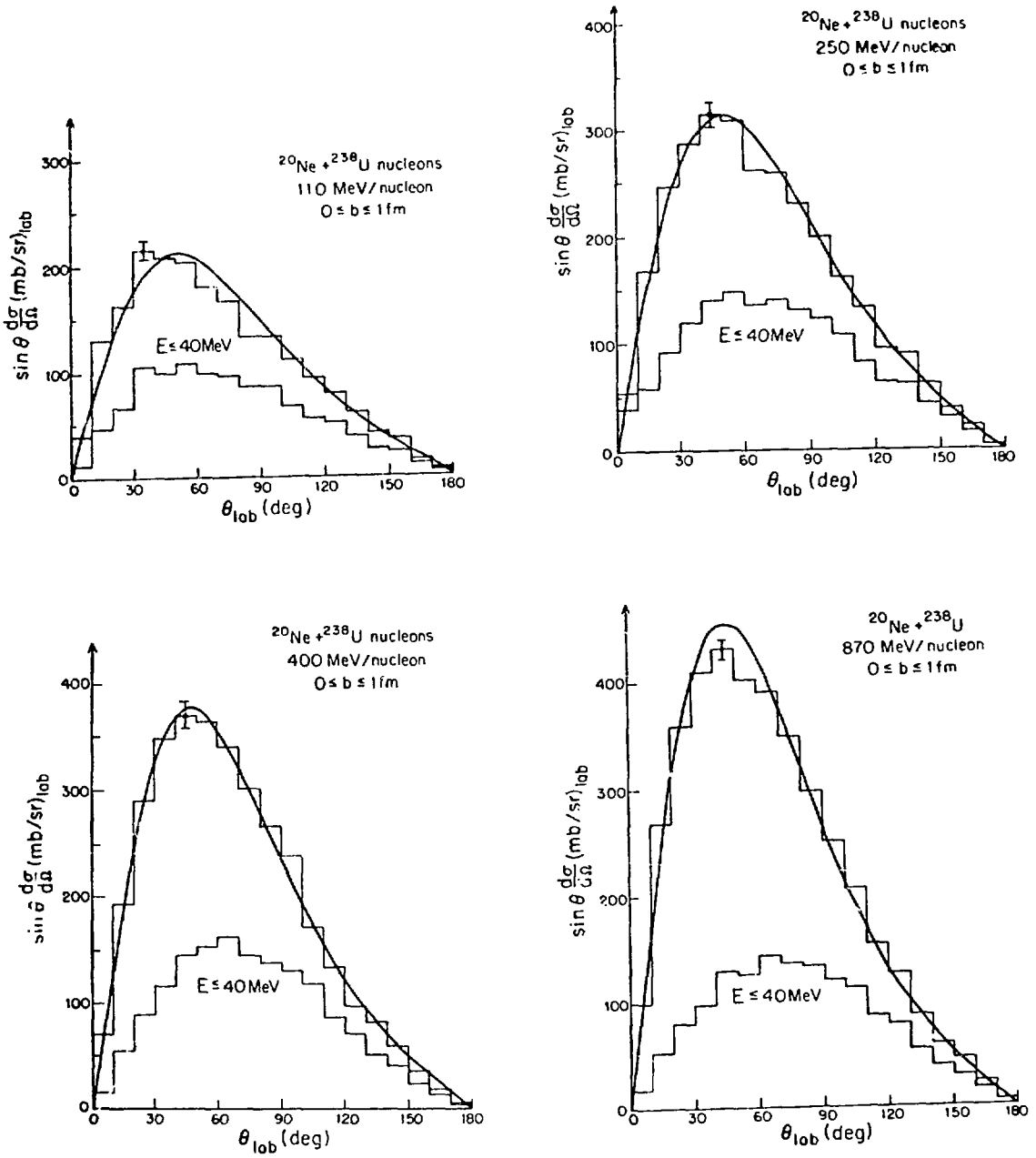
$^{20}Ne + ^{238}U$ nucleons
110 MeV/nucleon
$0 \le b \le 1$ fm
$^{20}Ne + ^{238}U$ nucleons
250 MeV/nucleon
$0 \le b \le 1$ fm
$^{20}Ne + ^{238}U$ nucleons
400 MeV/nucleon
$0 \le b \le 1$ fm
$^{20}Ne + ^{238}U$
870 MeV/nucleon
$0 \le b \le 1$ fm
$E \le 40$MeV
$\sin\theta \frac{d\sigma}{d\Omega}$ (mb/sr)$_{lab}$
θ_{lab} (deg)

Figure 9

CONF-770602--6

MULTIPLICITY AND CHARGED PARTICLE EMISSION IN RELATIVISTIC HEAVY ION COLLISIONS[1)]

H. H. Gutbrod, J. Gosset, W. G. Meyer, A. M. Poskanzer
A. Sandoval, R. Stock and G. D. Westfall

Lawrence Berkeley Laboratory, Berkeley, CA 94720
Gesellschaft für Schwerionenforschung, Darmstadt, Germany
Fachbereich Physik, Universitat Marburg, Marburg, Germany

The π^- data were taken by S. Nagamiya, et al.[2)] and we are grateful to the authors to allow us to present them here.

I. Introduction

After nearly three years of Bevalac research, the interest has shifted from the peripheral reactions -- studied intensively by the Heckman/Greiner group and described successfully by the abrasion-ablation model[7)] -- to near-central collisions[1)]. Whereas peripheral reactions proceed with relatively small transfer of momentum and energy, the near-central collision is characterized at high incident energies with an almost complete dissociation of both target and projectile, as made visible in some streamer chamber pictures[3)].

It has been generally accepted that a high multiplicity of fragments and pions at large angles and intermediate energies may be used as a distinctive feature that allows one to select near-central collisions of relativistic nuclei. Since many motivations for the relativistic heavy ion physics have and will be given by the theorists present at this conference, we can cut this introduction short and focus immediately onto experimental facts and observations available now after about two years of central collision studies at the Bevalac. We will have to leave the beautiful "star-observations" to the next two speakers and will concentrate onto single particle inclusive cross sections of precisely identified fragments (as to their charge, mass, energy, and emission angle) together with associated multiplicities of fast charged particles.

We will see that all the observed fragment spectra are structureless and more or less exponentially decaying throughout the range of studied fragment masses. We will give a catalogue of experimentally found qualitative features and will look then into the applicability of simple statistical thermodynamic models by tracing down in the spectra kinematical effects in the framework of a source of a temperature τ

and a velocity β. This leads directly to the "nuclear fireball-model"[4]) we presented nearly a year ago.

The production of complex particles will be discussed next. A simple mass dependence in the cross section of the fragments is observed[5]) and leads us to the question if a stuck projectile and the explosion of a "compound nucleus" would make any sense.

II. Experimental Techniques

The basic layout of the experimental setup consisted of a particle telescope mounted on a movable arm inside a scattering chamber, a monitor telescope fixed at 90°, used to obtain the relative normalization, and an array of fifteen plastic scintillator paddles (tag counters) placed outside the scattering chamber, subtending the angles between 15° and 60° with respect to the beam direction, and about one-third of the azimuth. This array was used to determine the multiplicity of charged particles, with energies above ~50 MeV/nucleon, associated with each event measured in the telescope.

Several different telescopes have been used to measure the large spectrum of masses and energies in this experiment. Evaporation-like fragments were detected in thin ΔE-E silicon detector telescopes with thicknesses of 22 μm, 205 μm, and 177 μm and 1500 μm. The high energy components of helium and hydrogen isotopes were measured with a ΔE-E telescope consisting of a 2 mm ΔE-silicon detector and a 10 cm, conically shaped scintillator coupled to a 2.5 cm phototube as an E detector.

The yields of the elements between lithium and oxygen above an energy of about 100 MeV were measured with a three element telescope, Fig. 1, consisting of a large area of thin Si ΔE detectors (180 μm) followed by the same area of 3 mm thick intrinsic germanium which was followed by the 3rd element an 8 mm intrinsic germanium detector. This ΔE_1-ΔE_2-E telescope was in the Si elements subgrouped into six angular bins so that six angular steps could be measured simultaneously. Particle identifier spectra of these telescopes are shown in Fig. 2. As a result of the quality of these detectors, we can give the precise mass, charge, and

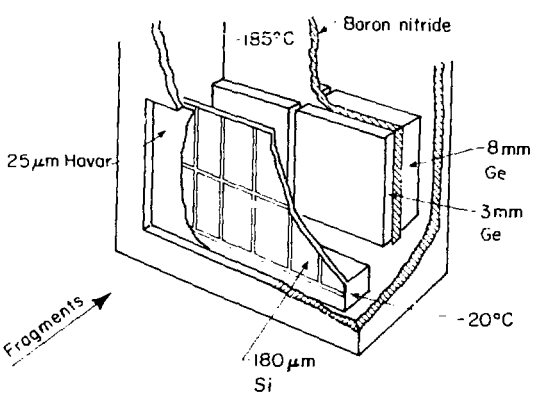

Fig. 1 XBL 773-545

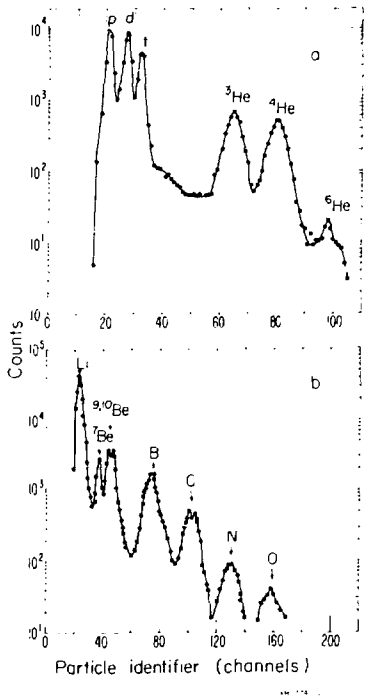

Fig. 2

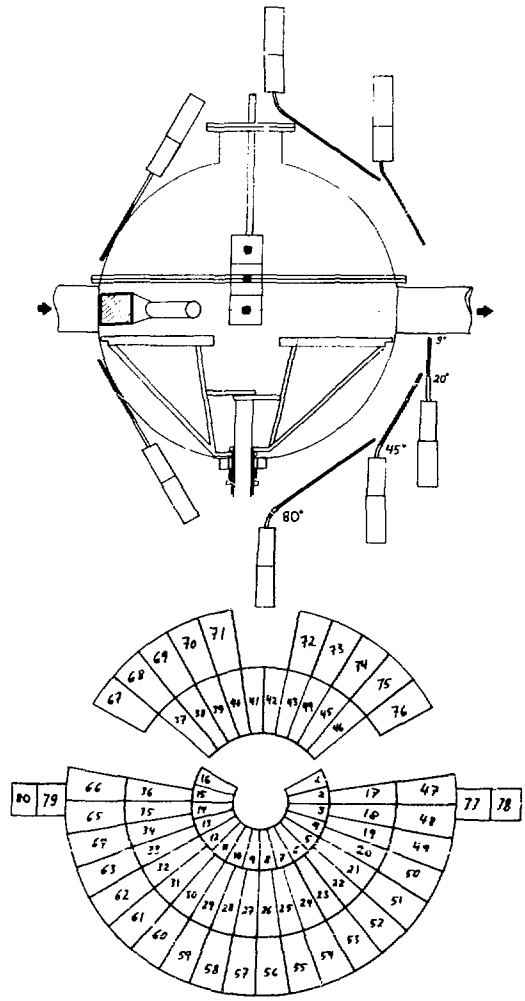

Fig. 3

energy as well as the reaction angle of the detected particles up to ^{4}He. From Li on we have isotope resolution only where indicated in the figures.

We have recently improved our setup by placing 80 photomultipliers with scintillators around a thin spherical scattering chamber, Fig. 3, which allows us to recognize much better the pattern of the star-event. The lower part of the figure shows the multiplicity-ring pattern looking in beam direction. Also in this new setup, we do exclude from the measured multiplicity all particles below an energy of 25 MeV/n. Thus we are sure not to measure low evaporation like fragments in the associated multiplicity. Furthermore we built a new telescope capable of detecting π^+ from 17 to 100 MeV and protons from 5 to 200 MeV etc. Some of the data I show are already from this vintage. The π^- distributions are taken from ref. [2]) and were measured in a magnetic spectrometer.

III. Experimental Results

Let us have first a look at the low-energy or evaporation like fragments. Figure 4 shows the 90° energy spectra of He to Be isotopes in the low energy region for ^{20}Ne bombardment of U at 2.1 GeV/nucleon. These energy spectra show a Maxwellian shape with the peak position shifting towards higher energies as the atomic number of the fragment increases. For a given element, the most neutron deficient isotope displays a more prominent high energy component. This trend is most obvious in Fig. 4 for ^{6}Li and ^{7}Be. It is also observed for the He isotopes as will be indicated below.

The cross section for the evaporation like α-particle is so high that--from an estimate of the integrated low energy α-particle yield--on the average about 7 α-particles are emitted per interaction. These low energy particles are not included in the later discussed associated multiplicities.

At high fragment energies the double differential cross sections for ^{20}Ne on U at 400 MeV/nucleon as an example presented in Fig. 5 are smooth and exponentially decaying with increasing energy, being flattest for the protons and becoming steeper as the mass of the fragment increases. For a given fragment the slope of the energy spectra rapidly increases with increasing angle, and the yield of each fragment decreases as the mass or charge of the fragment increases. A deviation from this general trend is

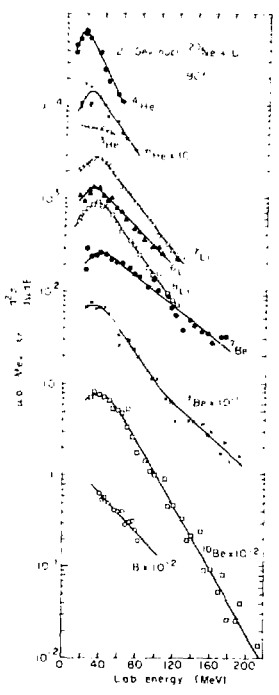

Fig. 4

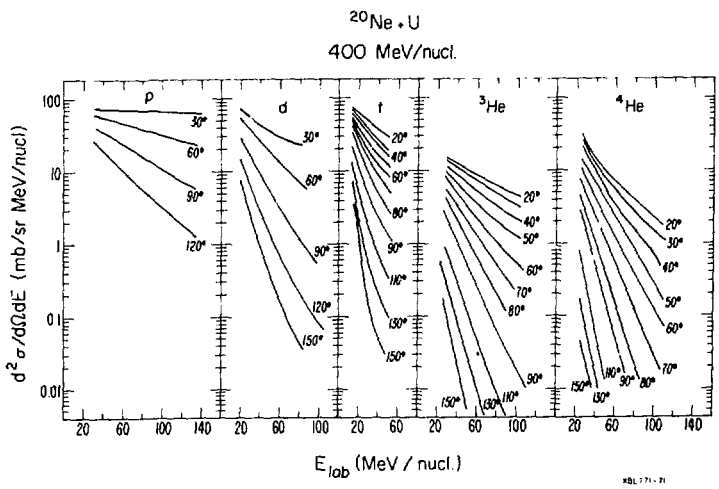

Fig. 5

observed in the vicinity of the evaporation region where the yield is higher for ^{4}He than for ^{3}He. In turn, ^{3}He exhibits a relatively more prominent high energy cross section. In this respect, the He isotope cross sections follow the trend of neutron deficient isotope cross sections, as described earlier.

The proton energy spectra from ^{20}Ne on U at forward angles are extremely flat in the measured energy range. It is surprising to find that the usual kinematical argument that would predict more forward peaked angular distributions the higher the combarding energy does not apply. In fact the trend is opposite for all the fragments as shown in Fig. 6 in the angular distributions labeled a, b, c, which are ^{3}He fragments integrated in the indicated energy windows from Ne on U at 2100, 400, 250 MeV/nucleon respectively. At the highest bombarding energy the cross section changes by less than an order of magnitude from 20 to 130 degrees, while for the 250 MeV/nucleon bombarding energy it changes by more than two orders of magnitude. Similar ^{3}He angular distributions are observed in the energy window from 50 to 100 MeV/nucleon. The overall features are the same but all slopes are steeper. A comparison at 2100 MeV/nucleon between (a) uranium and (b) Al as target shows that for light targets the backward hemisphere is depleted. At 400 MeV/nucleon incident (e) ^{4}He and (b) ^{20}Ne on uranium there is no significant difference in the shape of the angular distributions. Note that curves (d) and (e) are raised in absolute value by a factor of 10 for better graphical representation.

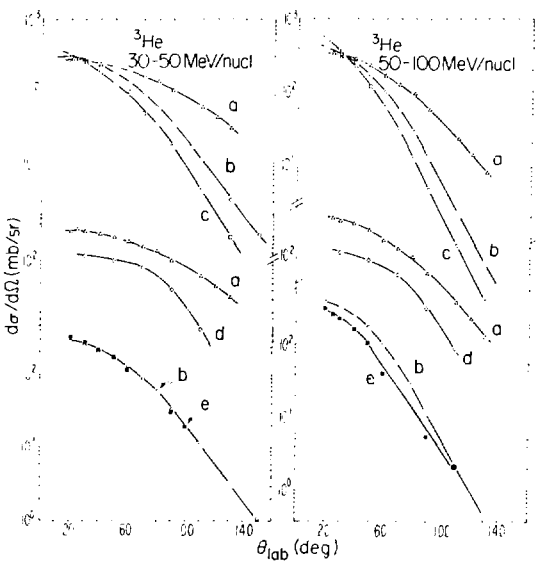

Fig. 6

In general for fixed target, projectile, and incident energy, the angular distributions of all fragments become more forward peaked the higher the energy window considered. Therefore, the value of angular distributions of integrated spectra in these experiments is small and the presentation of double differential cross sections should be preferred.

Looking now at the heavier fragments at intermediate energies in Fig. 7, the slopes of the spectra also get steeper with increase in reaction angle

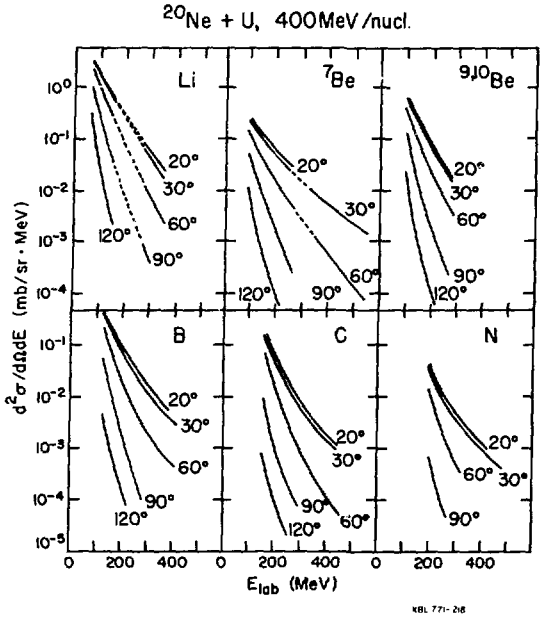

Fig. 7

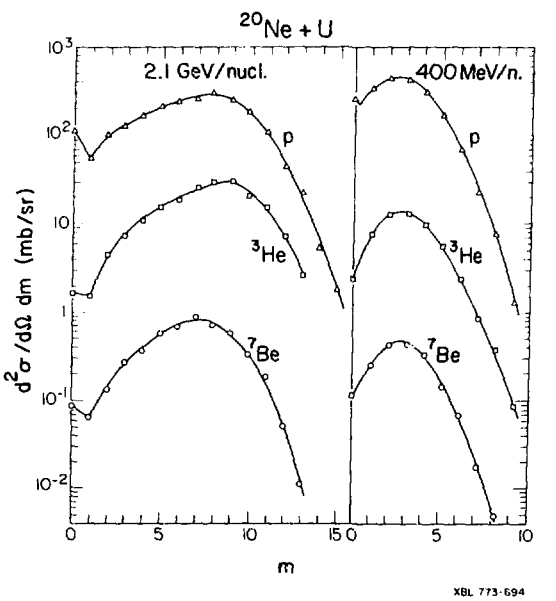

Fig. 8

for a fixed fragment. The changes of the slopes with fragment mass at a given angle are less pronounced than before, but note that here the spectra are plotted in MeV instead of MeV/nucleon as in the case of hydrogen and helium isotopes previously shown.

The associated multiplicities should give us a hint whether we are indeed observing near central collisions. Figure 8 shows from the 15 tag counter array m-fold coincidence cross sections associated with three different fragments detected in the telescope at 90°. For all fragments the average multiplicity is large reflecting quite a large transverse momentum transfer since the tag array is sensitive to particles like protons above 50 MeV. In the new experimental set-up the selection of various multiplicity patterns is possible.

In Fig. 9(a) the paddle histogram is shown on the top associated with Si-Ge telescope events on the bottom associated with the monitor telescope. Monitor telescope and Si-Ge telescope are placed opposite of each other at 90°. We observe clearly in ring A and B a large angle--two particle--correlation between fragments in the telescope and fragments in the paddles enhancing the yield in the forward angles opposite to

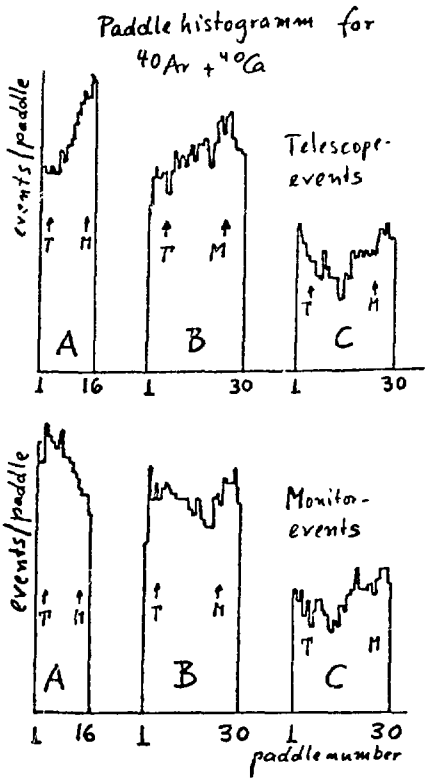

Fig. 9 (a)

the detected fragment. Note that we are looking here at star events with average total multiplicities of at least 12 high energy particles in the 9°-80° forward hemisphere. We are presently studying this correlation as a function of angle θ of the telescope and fragment energy. Figure 9(b) shows the difference in the paddle histogram for ^{40}Ar on Ca and U. For ^{40}Ar on Ca the prongs are much more forward peaked than for U.

In order to ease the discussion the main characteristic features of the data may be summarized in the following way:

Summary of Qualitative Features of the Data

1) All light fragment energy spectra are smooth except for an "evaporation peak" at very low energies.
2) The most neutron deficient isotopes exhibit spectra with

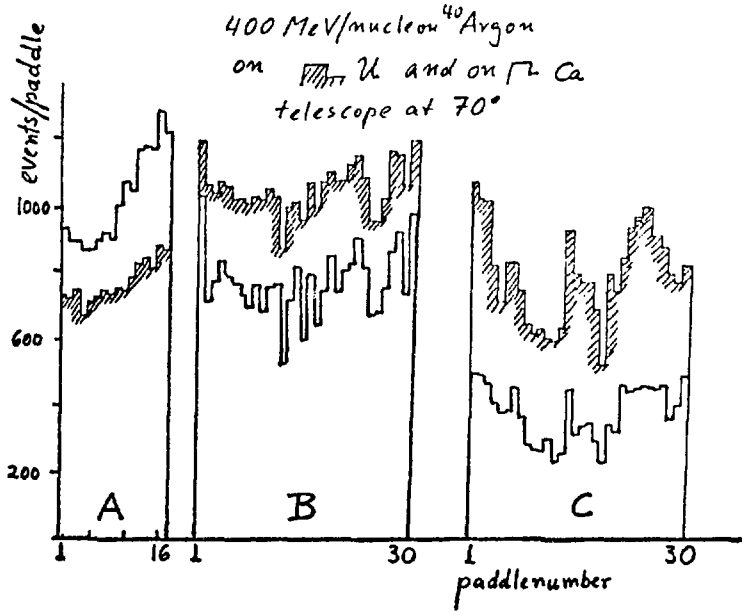

Fig. 9 (b)

a relatively higher cross section in the high energy tail.
3) The slope of the fragment spectra in the intermediate energy range gets steeper with increasing detection angle. Angular distributions are forward peaked.
4) The double differential cross sections for Ne on U at 30° are approximately independent of the incident energy for a given fragment. At larger angles the yield increases and the slope decreases with increasing bombarding energy.
5) The slope of the fragment spectra in energy/nucleon at a given angle gets steeper with increase in fragment mass.
6) The total yields of light fragments fall off with increase in mass. At energies of 30-50 MeV/nucleon cluster emission comprises a significant fraction (about 50%) of the total baryonic cross section. Towards higher energies protons become predominant.
7) Increasing the projectile mass at a fixed incident energy per nucleon leads to a small increase in the cross section for low energy fragments but to a larger increase at high fragment energies, especially for the heavier clusters.
8) In Ne and Ar bombardment of U, Ca, and Al targets besides the difference in overall absolute cross section, one finds for Ca and Al a depletion of cross section at back angles.
9) For all particles detected at angles between 20° and 160° the mean associated multiplicity is high and not changing remarkably with fragment mass or energy.
10) The mean associated multiplicity increases with the projectile mass and with the target mass.
11) Large angle emission of energetic fragments is enhanced in high multiplicity events.

IV. Discussion of the Data

In the peripheral reactions it is rather easy to determine where the particles originated by just looking at around 0° and at a fragment velocity equivalent to that of the projectile. Here, however, we cover a large spectrum of longitudinal velocities and need therefore an appropriate representation of the longitudinal and transverse momenta of the fragments.

In Figs. 10 and 11 contours of constant invariant cross sections $\frac{1}{p}\frac{d^2\sigma}{dEd\Omega}$ are given in a $(y,p_\perp)$ plane for different fragments from ^{20}Ne on U at 400 MeV/nucleon and for ^{3}He fragments from ^{20}Ne on U at different bombarding energies. y is the rapidity of the fragment defined as

$$y = \frac{1}{2}\,\ell n[(E+p_\parallel)/(E-p_\parallel)].$$

This variable is simply shifted by a constant value if

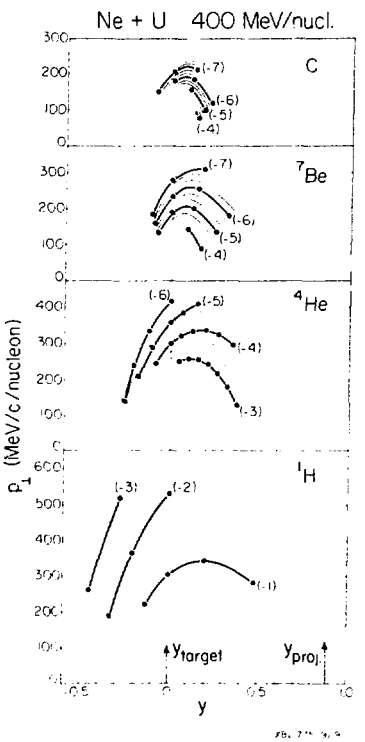

Fig. 10

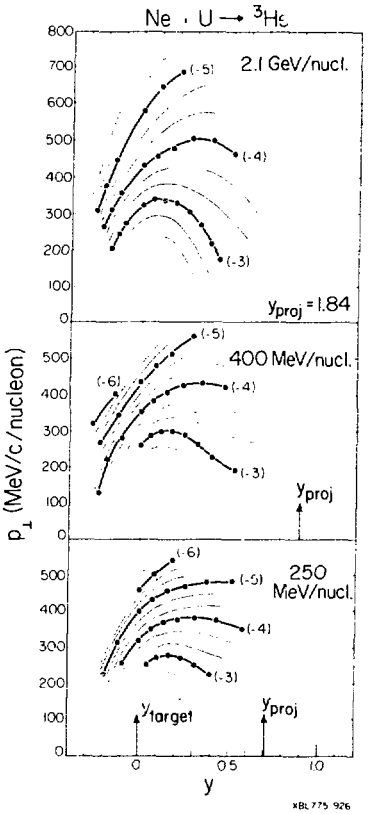

Fig. 11

expressed in a moving frame. y is approximately equal to β for small velocities. $p_\perp$ is the transverse momentum per nucleon of a fragment. In the contours the spacing between the lines corresponds to a constant factor in cross section. The thick lines are labelled by the common logarithm of the invariant cross sections. Such contour plots are invariant with respect to Lorentz transformations, except for a shift of the rapidity axis.

In these contour plots the maximum $p_\perp$ on a given contour line lies at a value of y which can be attributed to the velocity of an apparent source. In Fig. 10 it is clear that at low $p_\perp$ values the apparent source velocities are close to zero but that as we go up in $p_\perp$ the associated y goes up too. (Note that we plot here $p_\perp$/nucleon.) Thus it is clear that these fragments are not emitted isotropically from one unique moving source, which would give contour lines all centered around the rapidity of that source. In a peripheral collision the fragments from target and projectile would be

represented by two steep "mountains" symmetric about the target and projectile rapidities. It is obvious that the present data do not cover the region of projectile fragmentation. Target fragmentation products may be part of the cross section only for the lowest values of $p_\perp$ and y. Most of our data thus represent fragments from non-peripheral collisions.

The maximum of the invariant cross section at a given level of $p_\perp$ occurs at increasing values of the rapidity for increasing $p_\perp$. Due to the shift of the contour lines towards intermediate rapidities with wider spacing, there is clear indication for at least two qualitatively different sources

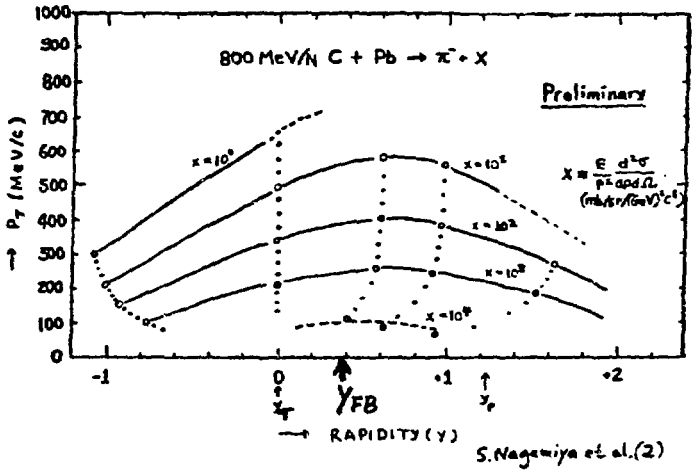

Fig. 12

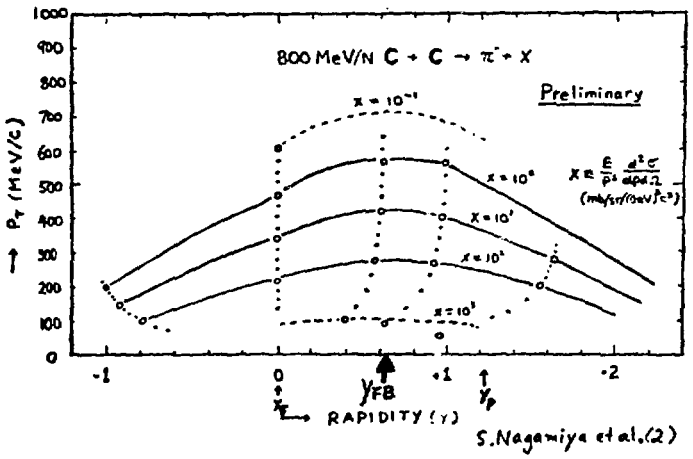

participating in the fragment emission. One source is moving slowly in the lab with a rapidity smaller than about 0.1. It accounts for the emission both of protons and clusters at small transverse momenta, $p_\perp$/nucleon $\lesssim$250 MeV/c (explosion of the total target and projectile system and/or target spectator decay). The other source moves with a rapidity intermediate between those of the target and projectile, and its decay products extend towards higher transverse momenta, corresponding to the highest energy and momentum transfer between the target and the projectile.

Before we go to the fireball model which tries to reproduce these findings, I show you again a $(y,p_\perp)$ contour plot, Fig. 12, this time for π^- emitted from 800 MeV/nucleon C on C and U, measured by S. Nagamiya, et al. The picture here is totally different from that just seen. There is no difference between C and C--which is in a kinematical point of view a nucleon-nucleon system--and C on Pb. Therefore one is led to conclude that the source of pions at these transverse momenta is purely of nucleon-nucleon nature and does not reflect any collective effects, in contrast to that of the charged particle distributions which cannot be described with one single longitudinal source velocity.

V. Fireball and Coalescence

The change in slope of the spectra as a function of angle gave a clear hint to try a thermodynamic model based on a moving source with velocity β and temperature τ. Since the observed rapidities were much higher than that of the center of mass of projectile and target, subsystems had to be found with higher apparent velocity. This led directly to the nuclear fireball model presented nearly a year ago[4]), which will be outlined shortly in the following:

When a relativistic heavy ion projectile collides with a target nucleus there should be during a primary fast stage a localization of the interaction to the overlapping domain of target and projectile densities while the rest of the two nuclei remain relatively undisturbed. On a secondary time scale, dissipation of compressional and surface energy, as well as reabsorption of pions and nucleons emitted from the primary interaction region will excite these remnants, resulting in their subsequent decay that should be characterized by moderately low energies. This idea leads to the separation of the nucleons in the system into participants and spectators with respect to the time scale of the fast interaction stage. The nuclear fireball model deals only with the participant nucleons, i.e., it refers to a sub-set of the emitted particles. The model assumes that the two nuclei sweep out cylindrical cuts through each other, Fig. 13.

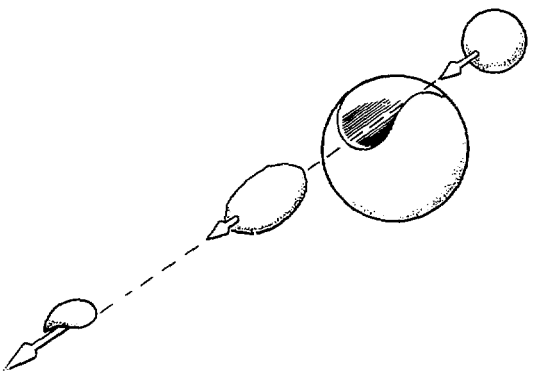

Fig. 13

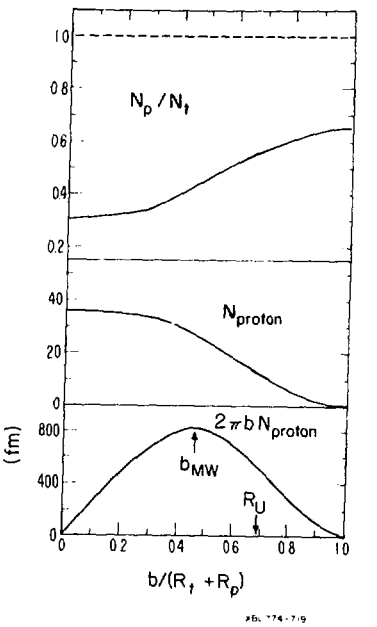

Fig. 14

The projectile participants are assumed to transfer all of their momentum to the effective center of mass system of all the participant nucleons forming a fireball which moves forward in the lab at a velocity intermediate between those of target and projectile. Its average internal kinetic energy per nucleon is much higher than the binding energy per nucleon. The participant nucleon fireball is then treated as an equilibrated non-rotating ideal gas characterized by a temperature, which expands isotropically in the center of mass of the fireball with a Maxwellian distribution in energy. The number of participants is calculated for each impact parameter. For nonsymmetric systems the effective center of mass of the participants is impact parameter dependent as is the fireball temperature. Only for symmetric systems like ^{40}Ar on ^{40}Ca exists a unique $\beta_{fireball}$ and $T_{fireball}$. Figure 14 shows the geometrical quantities as a function of impact parameter. N_p/N_t is the ratio of projectile to target participant nucleons, N_{proton} is the number of participant protons, and $2\pi bN_{proton}$ is the weight given to each impact parameter. The solid lines represent the case of Ne on U and the dashed line an equal mass projectile-target combination. The arrow on the abscissa indicates the radius of uranium and the arrow labeled b_{mw} indicates the impact parameter with the maximum weight.

Figure 15 shows kinematical quantities as a function of impact parameter calculated in the fireball model. The velocity of the fireball in the lab is β and ε is the available kinetic energy per nucleon in the fireball. The comparison of the data with that model, integrated over all

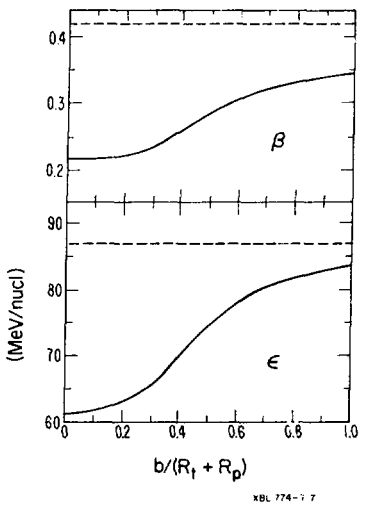

← Fig. 15

Fig. 16 →

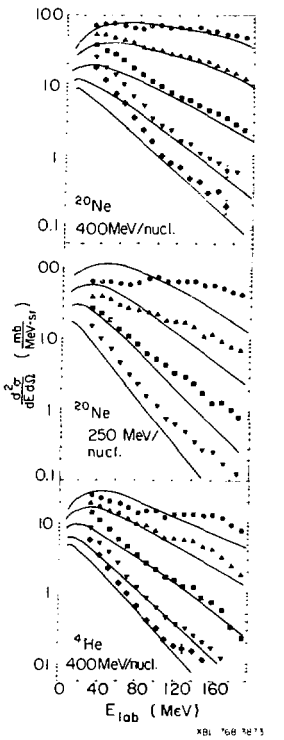

impact parameters, is shown in Fig. 16 for ^{20}Ne+U at 400 MeV/nucleon, 250 MeV/nucleon and for ^{4}He+U at 400 MeV/nucleon.

Going back to Figs. 10 and 11 for 400 MeV/nucleon ^{20}Ne+U, the fireball rapidity is 0.28 for the most probable weight and fits well with simply extracted values of y for high $p_\perp$ values. For the π^- data in Fig. 12 we see that the fireball rapidity for C+Pb is totally off from the extracted value of 0.6, equivalent to that in C+C.

Contemplating over such a simple model one often questions first the assumption of clear cylindrical cuts. Shooting holes into nuclei does not sound reasonable in the face of nucleon mean-free-path arguments. Yet, a single molecule hitting a thick wooden plate with a velocity of 1 km/sec has no chance to go through, but if this molecule travels as part of a bullet it easily can make it to the other side. From this viewpoint the nuclear fireball model should be more successful the heavier the projectile mass is. Surprisingly, however, the model can even describe double differential spectra of protons from p on Bi at 450 MeV.

The presented fireball model has been extended to include complex particle production[6,7]. This will raise the temperature in the fireball, since in the chemical equilibrium fewer degrees of freedom are available if clusters do exist. Our data do indicate (see Figs. 10 and 11) that the low $p_\perp$ fragments do come from slow moving sources with velocities from

that of the target-projectile center-of-mass down to zero. If one looks at boron (Fig. 17) then a two parameter fit of a moving source with a velocity $\beta = 0.6$ and a temperature $\tau = 27$ MeV yields fair agreement with the data. This velocity and temperature combination, however, is close to that of a formed compound system, i.e., the projectile gets stuck in the target nucleus and randomizes totally its energy. If such a picture would be true the tremendous angular momenta in that system (nearly 500$\hbar$ for Ne+U at 400 MeV/nucleon) would change the decay pattern of the fragments and lower the temperature due to the rotational energy.

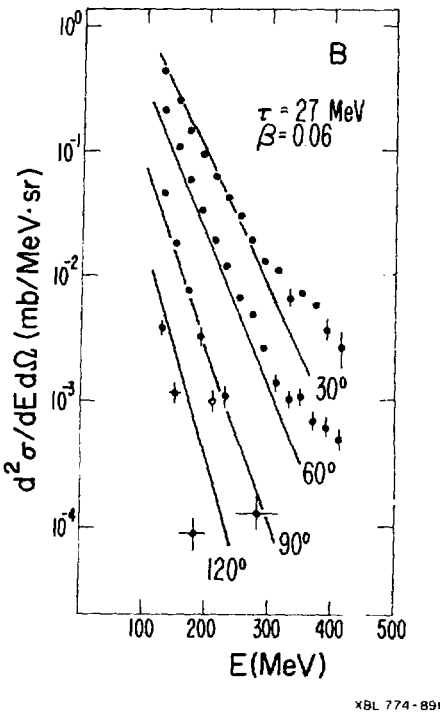

Fig. 17

If one assumes that protons at a given momentum are produced by the same mechanism as the heavier fragments at the same momentum/nucleon then one can, as we did[5]), try to express the complex particles in terms of nucleon double differential cross sections.

Our first attempt to explain the emission of high energy light nuclei in relativistic heavy ion collisions was by final state interactions, or coalescence of emitted nucleons. In this model, if any number of protons and neutrons corresponding to a bound nucleus are emitted in a reaction with momenta differing by less than a coalescence radius p_o, these nucleons are assumed to coalesce and form a nucleus. The cross sections for the emission of light nuclei are then simply related to the cross sections for the emission of nucleons at the same momentum per nucleon, namely,

$$\frac{d^2\sigma_A}{p^2 dp d\Omega} = \frac{1}{A!}\left(\frac{4\pi\, p_o^3\, \gamma}{3\sigma_o}\right)^{A-1}\left(\frac{d^2\sigma_1}{p^2 dp d\Omega}\right)^A \quad .$$

Both cross sections σ_A, for emission of a light nucleus formed with A nucleons, and σ_1, for emission of a single nucleon, are evaluated at the same momentum per nucleon p with Lorentz

factor γ, and σ_o is the total reaction cross section. Our proton data have been used to calculate the light fragment cross sections from this euqation; the results have been compared with our experimental data, the only adjustable parameter being p_o. In Fig. 18 such a comparison is shown for d, t, ^{3}He, and ^{4}He from the reactions of Ne on U at 250 and 400 MeV/nucleon. The agreement between this simple calculation and our data is rather impressive, the largest discrepancy being for ^{3}He fragments at the lowest energies and at forward angles. The values of the parameter p_o are remarkably uniform and of reasonable magnitude, between 126 and 147 MeV/c, since they are smaller than the Fermi momenta of the clusters. It should be noticed that this simple phase space calculation does not explicitly include many factors, like spin and isospin couplings, integration over configuration space (not only momentum space) and time. All these factors are hidden in the p_o value. In Fig. 19 it is shown that a similar calculation leads to a similar agreement with our data for heavier fragments, namely the lithium isotopes (our data include all isotopes, but the calculation has been done assuming mass 6) and ^{7}Be, with a p_o of the same order of magnitude as that found from the light fragments. For the heaviest fragments, ^{9,10}Be to O, the overlap between the energy per nucleon

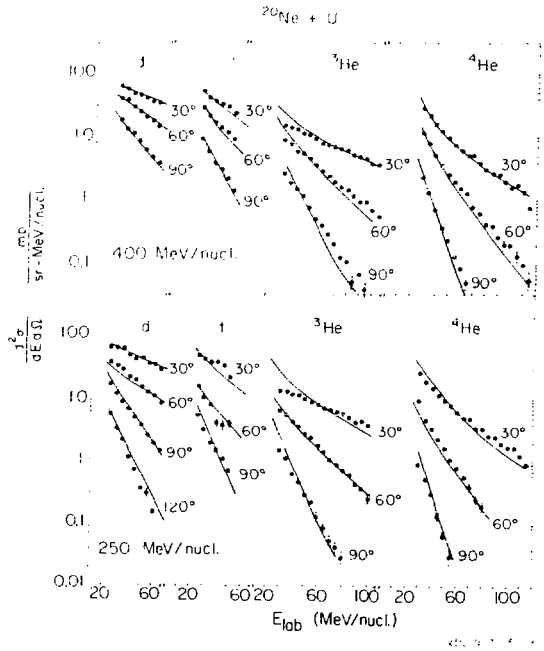

Fig. 18

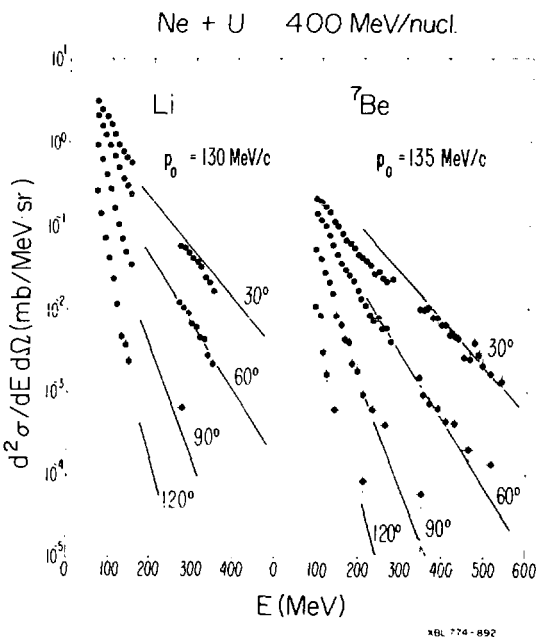

Fig. 19

range of these data and the range of our proton data is too small to make useful comparisons.

The success of the coalescence model, however, has to be looked at as a first glance into the mass dependence of the fragment distribution. The correct treatment of a final state interaction model has to start with a primary nucleon distribution which is different from our procedure. In fact if one guesses such a primary proton distribution one gets smaller values of p_o and destroys the simple dependence of light nuclei cross sections on nucleon cross sections.

It is very interesting to note that the observed power-law between proton- and cluster cross sections is valid in a thermodynamical picture like that of the fireball. There, the double differential cross section in momentum space for emitting any cluster consisting of A nucleons decreases exponentially with the total kinetic energy E of the cluster like $\exp(-E/\tau)$ where τ is the temperature. Hence with respect to the kinetic energy per nucleon E/A it behaves like $(\exp - \frac{E/A}{\tau})^A$ which is proportional to the A^{th} power of the cross section for emitting a single nucleon at this energy per nucleon E/A, in contrast to the coalescence model. In the thermodynamical model we do not have to guess a primary nucleon distribution in momentum space. There is interesting physical information in the thermodynamic model, since the yeilds of different nuclear species measured in relativistic heavy ion collisions can be used to obtain the freeze-out density[6]) of their emitting systems, namely the density below which the hot matter expands freely.

In summary, fragments from near central collisions of relativistic heavy ions may originate from several qualitatively different sybsystems of the overall decaying nuclear system, such as the fireball, the target spectators, or alternatively, an explosion of the fused target-projectile system. There is strong support of the validity of thermodynamical models in the production of all fragments observed and the large amount of theorists in this field is promising exciting insights in the near future. The charged particles seem to have clear fingerprints of a collective reaction mechanism whereas the π^- data observed at high pion energies seems not to be different from nucleon-nucleon collisions.

References

1) J. Gosset, H. H. Gutbrod, W. G. Meyer, A. M. Poskanzer, A. Sandoval, R. Stock, and G. D. Westfall, LBL-5820, 1977, and submitted to Phys. Rev. C.

2) S. Nagamiya, I. Tanihata, S. R. Schnetzer, W. Brückner, L. Anderson, G. Shapiro, H. Steiner, and O. Chamberlain, private communication.

3) R. Poe, S. Fung, B. Gorn, A. Kernan, G. Kiernan, J. Lee, J. Ozawa, B. Shen, G. Van Dalin, L. Schroeder, and H. Steiner, to be published.

4) G. D. Westfall, J. Gosset, P. J. Johansen, A. M. Poskanzer, W. G. Meyer, H. H. Gutbrod, A. Sandoval, and R. Stock, Phys. Rev. Letters 37 (1976) 1202.

5) H. H. Gutbrod, A. Sandoval, P. J. Johansen, A. M. Poskanzer, J. Gosset, W. G. Meyer, G. D. Westfall, and R. Stock, Phys. Rev. Letters 37 (1976) 667; and H. H. Gutbrod, Journal de Physique Colloque C-5 (1976) 209.

6) A. Mekjian, Phys. Rev. Letters 38 (1977) 640; and S. Garpman, J. Bond, and P. J. Johansen, to be published.

7) J. D. Bowman, W. J. Swiatecki, and C. F. Tsang, LBL-2908, unpublished report (1973).

EXPERIMENTAL SEARCH FOR COMPRESSION PHENOMENA IN FAST NUCLEUS-NUCLEUS COLLISIONS

E. Schopper[x], H.G. Baumgardt, E. Obst
Institut für Kernphysik
der J.W. Goethe-Universität, Frankfurt/Main

Soon after the discovery of heavy nuclei in cosmic radiation in 1948, investigations of high energetic nucleus-nucleus interactions have been undertaken, mainly with nuclear emulsion as detector and target. A remarkable amount of data exists. They are, however, suffering from being averaged in general over a more or less broad range of energies and charges of the projectile, and of the nuclides of the emulsion.

The situation changed when heavy projectiles of definite energies in the GeV/N region became available from accelerators, which made accessible such investigations also to multiparametric electronic devices. One of the very actual questions arising was the occurence of compression phenomena and shock waves, connected with the increase of the density of the nuclear matter during the interpenetration of two fast nuclei.

This paper was provided to review current experiments dealing with this problem. Since two big experimental groups from Berkeley are presenting results by their own (H.H. Gutbrod, H. Heckman), these need not to be covered in detail by this paper; it will be restricted to experiments with particle track-detectors (nuclear emulsions, and the silver-chloride detectors of the Frankfurt group).

Before considering the mechanism of the interpenetration of two fast nuclei, which is obviously rather complex, it may be useful to throw a glance on more simple situations, i.e. proton-proton interactions, then to envelop them with nuclear matter, considering proton-nucleus interactions. We only shall describe very general features, which may give us suggestions for the understanding of the nucleus-nucleus impact.

1. Proton-proton and proton-nucleus collisions

The shower particles in the jet generated in a p-p impact (fig. 1), consisting mainly of π-mesons, are characterized by velocities $\beta > 0.7$; they have been in-

---

x) invited speaker

vestigated over a wide range of energies of the projectile-nucleon. They exhibit the following features:

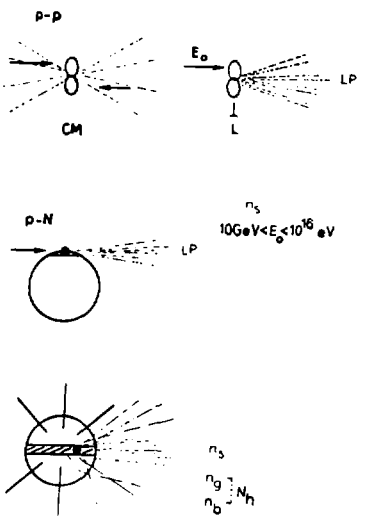

Fig. 1 : pp and pN interactions schematically

a. The multiplicity, i.e. the number n_s of shower particles depends on the projectile energy E_o (in the L-system) as

$$n_s \gtrsim E_o^{1/4}. \qquad (1)$$

The jet always contains a so-called leading nucleon (proton; LP in fig. 1).

b. The constancy of the transverse momenta $p \sim 300$ MeV/$_c$ of the shower particles, and the constant ratio of π/K mesons valid in the range of 10 GeV $< E_o < 10^6$ GeV of the projectile energy, suggested the model of the fireball:

In the pp impact a hadronic state is generated which decays into the shower particles of the jet and the leading particle.

A peripheral p-N interaction which leads to a star without heavy secondaries N_h ($\beta < 0.7$) - a so-called clean event - represents an analogue to the pp-interaction.

What is the situation with nonperipheral p-N interactions at small impact parameters, in particular with central collisions? Accelerator experiments with nuclear emulsions up to energies of 400 GeV by several collaboration groups[1,2,3] have yielded valuable data. For instance, the multiplicity $n_{s,A}$ of shower particles emitted from pN collisions with a nucleus of A nucleons, compared to $n_{s,p}$ from pp-interactions at the same energy:
$R = \frac{n_{s,A}}{n_{s,p}}$ is surprisingly low, ~ 1.7 at 200 and 300 GeV, and depends only weakly on A: $n_{s,A} \sim A^{0,2}$; this contradicts the development of a large intranuclear cascade.

The shower multiplicity can be partitioned, as proposed by Andersson and Otterlund[4], into the components

$$n_{s,A} = n_{s,p} \; (1 + y \cdot (\bar{\nu} - 1))$$

with $y \sim 0.3$

$\bar{\nu} = 0.7 \cdot A^{0.28}$ = mean number of collisions of the projectile

the first term being attributed to a fixed leading particle contribution like in pp-collisions, the second one to "repeated collisions" of the projectile. In other words, the hadronic fireball-state seems to consist of a persisting component and a dropping out - part generating the $n_{s,A}$ - excess, according to the Gottfried-model[5]. This behaviour shows up too, in the relation between $n_{s,A}$ and the mean number of heavy secondaries N_h (fig. 2):

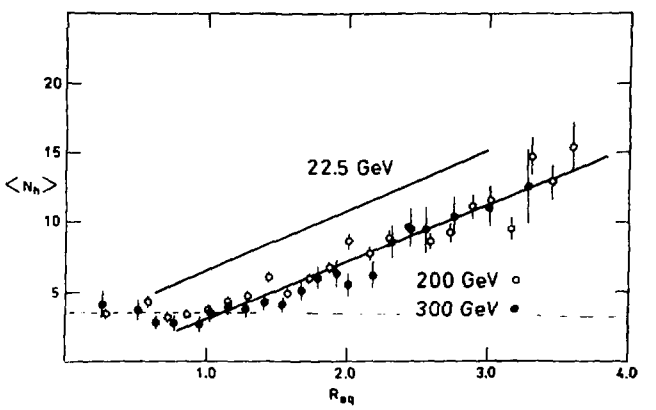

Fig. 2 :
mean number $\bar{N}_h$ of secondaries versus shower multiplicity $R = \frac{n_{s,A}}{n_{s,p}}$ in pN-collisions (Andersson et al.[4])

The mechanism generating the $n_{s,A}$-excess, seems not to start before the number of shower particles, corresponding to pp-collisions at the same energy, has developed ($R = 1$ in fig. 2).

Central collisions with very small impact parameters lead to a complete disintegration of the target nucleus with high transverse momenta of the disintegration fragments (fig. 3).

The probability of such central collisions with complete decay has been determined by Badaway et al.[6]. For p-N interactions concerning Ag and Br nuclei it is, independent of the projectile energy, 2.5 % between 6.2 GeV and 200 GeV; for α-N collisions at 3.85 GeV/N 7.2 % of all events.

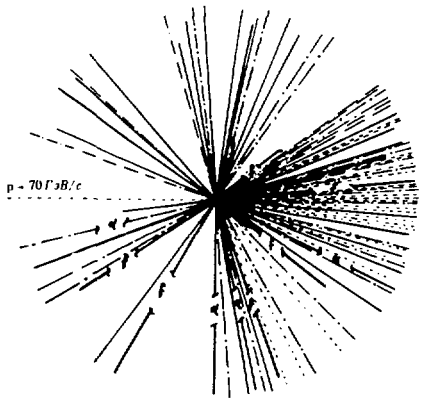

Рис. 6. Звезда с N_h - 66, N_s = 22.

Fig. 3 :

Complete disintegration of a Pb-nucleus in a central collision with a proton of momentum P = 70 GeV/c. Emulsion soaked with Pb-salt. (courtesy of Prof. K.D. Tolstov, Dubna)

2. Nucleus-nucleus collisions

The energy range considered in the case of p-N interactions is admittedly higher than that of the NN-collisions which we are now discussing. It is the high energy end of a region which, between 0.1 GeV/N and 5 GeV/N, could be regarded as a transition region, with respect to pionic contributions for example. On the other hand the relativistically contracted A nucleons of the projectile will behave in a way different from free particles, at least after the first collision, and generate high energy density and baryonic states in the reaction zone, comparable to the fireball state of the proton-projectile.

In our search for compression phenomena amongst the achievable mechanisms involved in a nucleus-nucleus collision, we used as a guide-line the model depicted in fig. 4.

We are excluding peripheral collisions, which are leading either to pure fragmentation of the projectile with only one or two heavy recoils, or to a mixed event from the overlap-area. We are investigating non-peripheral collisions, defined as collisions with full overlap of target and projectile area. They are selected by a required minimum number of prongs of recoil secondaries N_h, as described below.

The final stage of all these collisions is characterized by the deexcitation or decay of the target or the residual nucleus, respectively. Except perhaps the very central collisions which result in a complete decay of the target, this final stage is characterized by the emission of low energetic particles, evaporating with a "temperature spectrum" corresponding to T ~ 4 - 8 MeV,

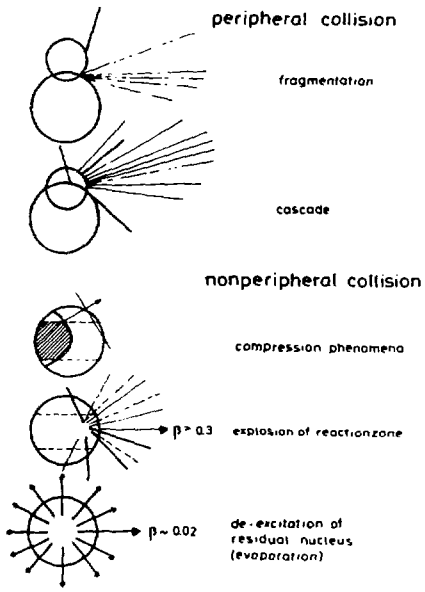

Fig. 4 :
N-N collisions schematic

and very low forward momenta of the particles; this corresponds to a forward velocity β_{res} of the residual nucleus $\beta \sim 0.02$ (fig. 5a,b) in the energy range from 100 MeV/N to 15 GeV/N

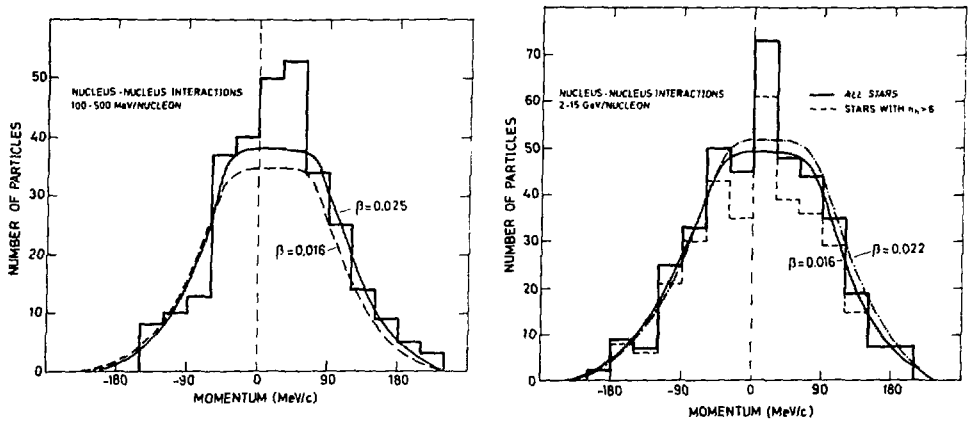

Fig. 5 : $p_{\parallel}$-momentum distribution of evaporation particles in N-N collisions: C,N,O projectiles on Ag, Br - nuclei in the energy range [14]
a) 100 - 500 MeV/N, b) 2 - 15 GeV/N

As a foregoing stage in the N-N collision, we have to consider the reaction-zone of the projectile which - whatever its state may be - is expected to consist of hot baryonic matter and composite particles. It may be a particular state, as postulated by the Frankfurt group of W. Greiner[10], combined with a quickly equilibrizing pion condensate[11] or a fireball-like system proposed by the Berkeley group[12].

The question is, what are and how can we find signatures for compression phenomena? We can expect to draw information either from the investigation of the particles from the fast projectile-system (the "actor" particles) or from the nuclear matter of the surrounding target system. If we assume that the high compression caused by the interpenetration of the nuclei propagate as a Mach-shock wave, it will lead to a preferential angular distribution of secondaries [13]. Following theoretical considerations, the propagation velocity of the compression wave will be $v_M < 0.6$ c in the considered range of projectile energies between 0.2 GeV/N and 4.2 GeV/N. We have therefore to look for the N_h-particle group of medium energy amongst the secondaries.

The energy distribution of the N_h-group[14], schematically depicted in fig. 6, shows in the low energy part the typical evaporation spectrum (a and c) for H and He particles, with a tail (b and c) towards higher energies, not belonging to the evaporation spectrum.

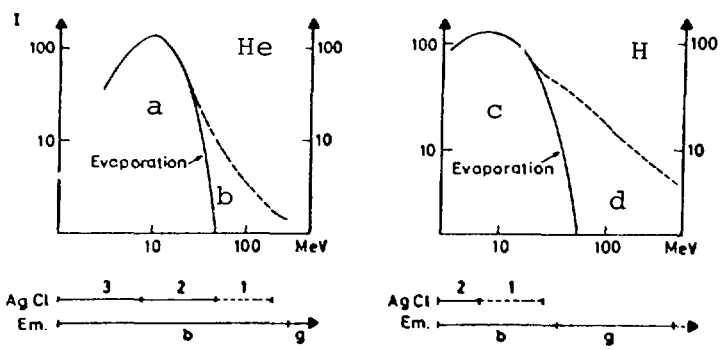

Fig. 6 :
Energy spectra of N_h-particles
left: He
right: H
(schematic)

It is much broader for the proton group than for the He-group; may be on account of the higher "temperature" of the protons or on account of an admixture of protons from the projectile system.

The tail of the He-group is predominantly connected with large stars with a large number of N_h-particles[14], which are due to collisions with the heavy nuclei Ag (or Br in emulsion) at small impact parameters. In such

stars the proton group exhibits a broad distribution of high transverse momenta, and a rather flat angular distribution, compared to the much steeper one of the He-group (see fig. 11c).

Hence we regarded this He-group as candidate for signatures of compression phenomena.

3. Experimental results

Sheets of silverchloride detectors on quartz glass and stacks of nuclear emulsion (for comparison) were exposed to the heavy-ion beam parallel to the surface of the sheets with a total flux of about 10^5 particle/cm^2.

Stars occurring at the nuclides of the detector are observed in 4π-geometry event by event. The disadvantage of the time-consuming scanning of the events in these detectors has been strongly reduced by our video-electronic analyzing system, developed for the special purpose of track measurements[15].

In nuclear emulsion technique tracks are classified following the energy loss of the particles by ionization and the corresponding density of the track in white (s), grey (g) and black (b) tracks which belong to certain energy ranges of the particle; s-tracks correspond to shower particles, g and b tracks to the secondaries $N_h = n_g + n_b$. In fig. 6 we have inserted the corresponding energy ranges of g and b-tracks for α-particles and protons in K5 emulsion, in comparison to the less sensitive AgCl-detectors with the track-classification 1,2,3. On account of their sensitivity threshold, the AgCl-detectors are recording protons only from the evaporation group. We are recording neither the proton tail d, nor fast protons from the projectile above E = 30 MeV, in other words, we are recording the evaporation groups a and c and the α-tail b, suppressing the proton tail d.

In order to find the angular distribution of the α-group, we have to subtract the evaporation components. Measuring only particles of class 1 and 2, we are increasing the relative contribution of the α-tail (energy window).

In order to select central collisions on Ag-nuclei, and to eliminate Cl-collisions and peripherical collisions, we require the prong number of a star $N_h \geq 12$ (prong window); this corresponds to a star with $\bar{N}_h \geq 28$ prongs in nuclear emulsion: The mean number of prongs of this star, falling into the groups a,b,c,d would be $\bar{n}_a = 3.5$, $\bar{n}_b = 1.5$, $\bar{n}_c = 7$, $\bar{n}_d = 17$; this means in stars in AgCl with m = 12 prongs we find an average number of 1.5 particles of the α-tail.

The simplicity of the experiment allowed us, with the kind help of our colleagues in Berkeley[x)] and in Dubna[xx)] to expose, in favor of systematics, detectors over a wide range of energies, from 0.2 GeV/N up to 4.2 GeV/N, between 1.1 GeV/N and 2.6 GeV/N in 300 MeV/N steps, mainly with He, C and O projectiles.

Figure 7 contains as idiograms angular distributions $d\sigma/d\Theta$, measured in AgCl-detectors, with C, O projectiles and He-projectiles at different energies. The curves inserted are belonging to fitted evaporation components, adjusted by X^2-fits with parameters following the Le Couteur-theory, by Baumgardt[16)]. The remaining component belongs to the α-tail of the energy spectrum (fig. 5) and shows a shift toward 75^o at 2.1 GeV/N and a return to 60^o at 4.0 GeV/N. These results have been confirmed by new exposures evaluated by our analyzir device, shown in figs. 9 and 10.

Figure 8 shows measurements in nuclear emulsion, by Otterlund[16)] et al.: the angular distribution $dN/d\Theta$ of the black prongs reflects the shift to larger angles with increasing energy of the projectile.

In order to elucidate the peak of the angular distribution originating from the α-tail, we have depicted it in fig. 11a as difference between the histogram and the evaporation component (x). It can be reproduced (o) from a theoretical distribution, calculated on the basis of a microscopic theory by Smith [18)], which represents the angular distribution of nucleons (disregarding composite particles) from a Ne-N-collision at 0.87 GeV/N. Assuming that this distribution contains our α-particles, we can deduce their intensity and angular distribution, using the absolute cross sections measured by Gutbrod, Poskanzer et al. [19)] of fig. 11c. The peak is due to the much steeper angular distribution of the He-component towards backward angles compared to protons. We would not have "seen" it, if we had not excluded the proton-component.

The steep angular distribution of the He-group, which contains a surprisingly high amount of ^{3}He-particles (fig. 11c) is interesting. We may conclude that it reflects lower temperature of composite particles of larger masses in hot nuclear matter. In the picture of a compression wave, it means that α-particles have a better alignment to the direction of its propagation. In addition, in nuclear matter of high temperature, α-particles can hardly be scattered morefold without dissociating. Hence if α-particles are emitted, they either stem from the surface region of the nucleus or, if coming from inner zones, they have escaped unscattered. In both cases they have the better "remember" of their direction. We therefore conclude

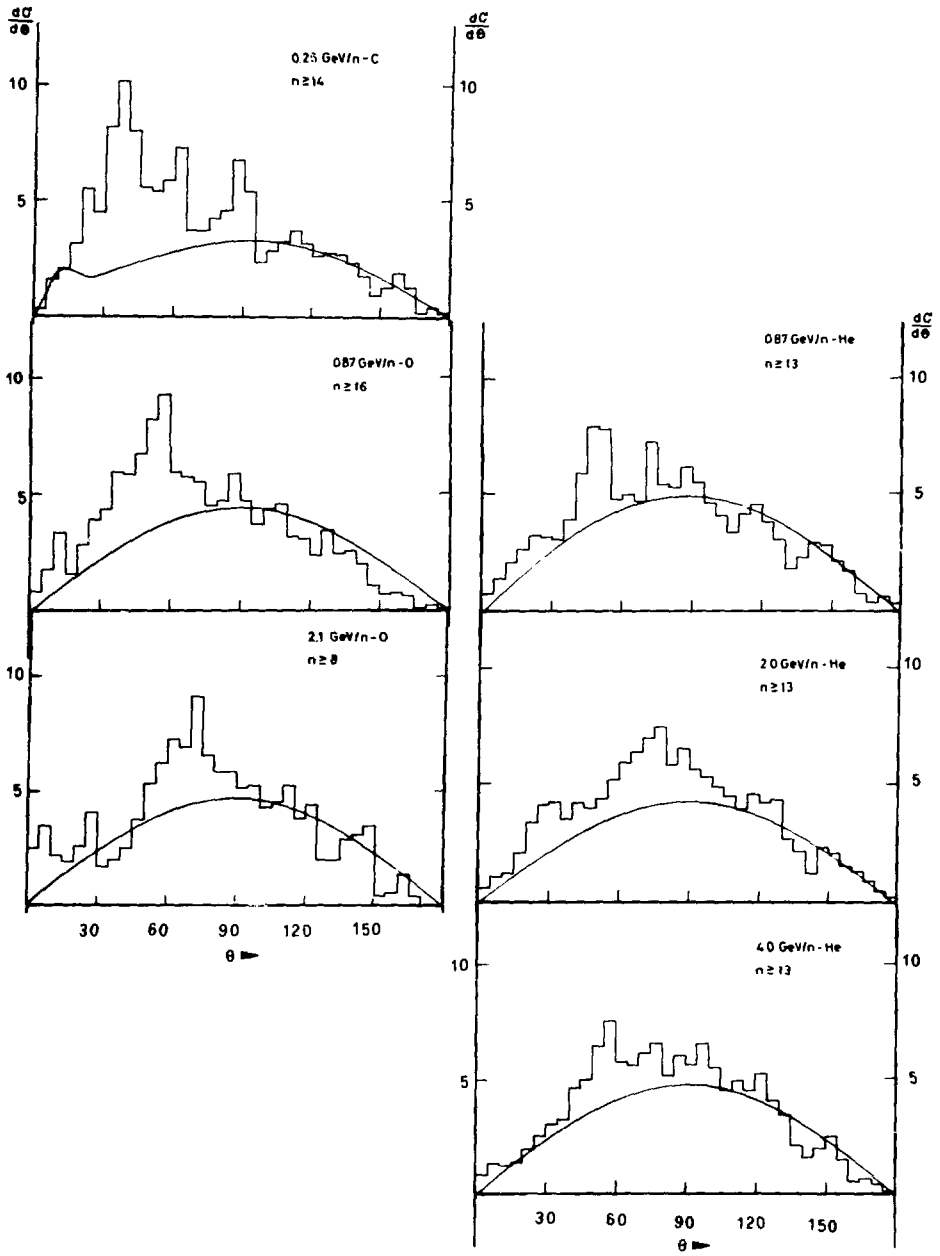

Fig. 7 : Angular distributions $d\sigma/d\Theta$ and fitted evaporation component[16)]

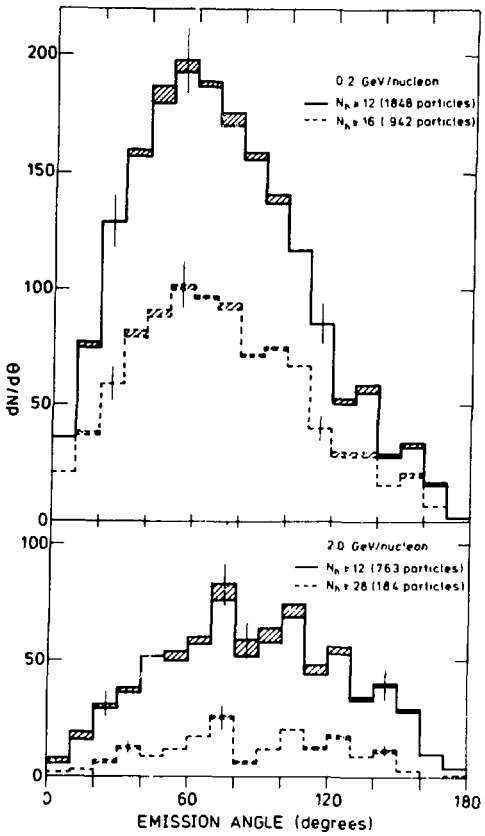

Fig. 8 :

Angular distribution $dN/d\Theta$ of black prongs in nuclear emulsion (Otterlund et al.[17])

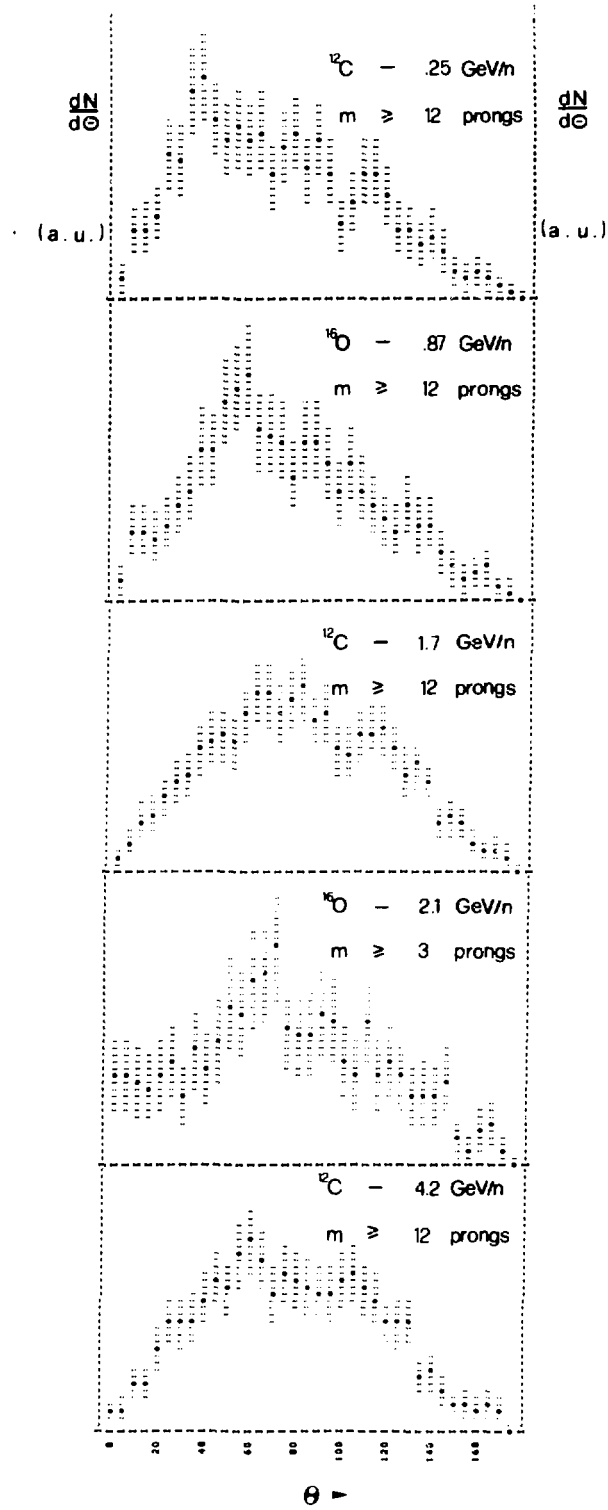

Fig. 9 : Angular distributions at different energies of C and O projectiles in AgCl-detectors

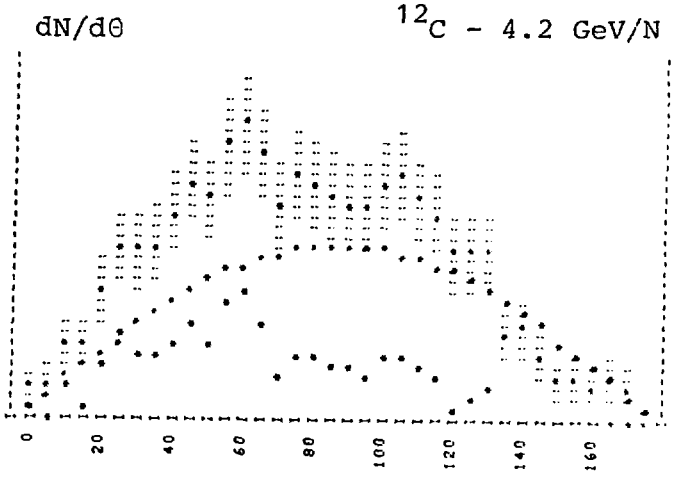

Fig. 10 :

Angular distribution dN/dθ, fitted evaporation component, and residual peak.

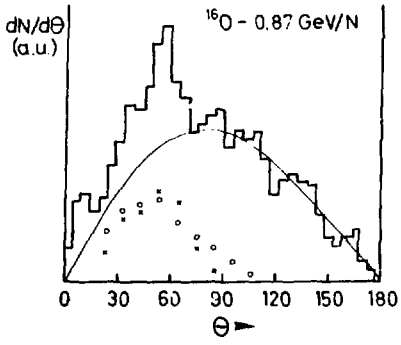

a

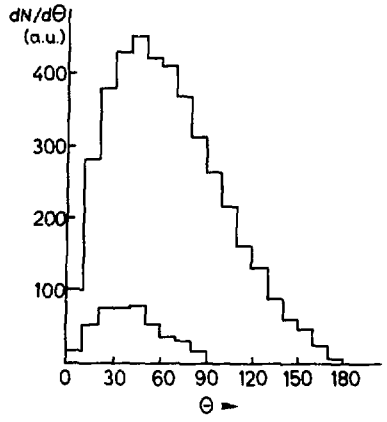

b

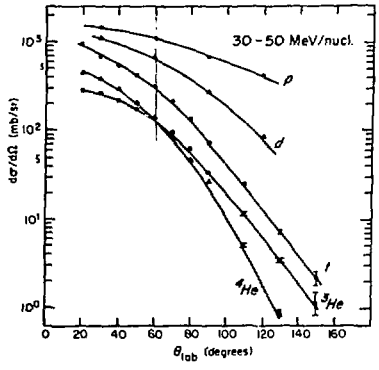

c

Fig. 11 : (s. text)

that their angular distribution and its shift reveal information about compression effects. They will be discussed in the paper given by W. Greiner.

Acknowledgments:

This work was supported by the Bundesministerium für Forschung und Technologie (BMFT) and the Gesellschaft für Schwerionenforschung (GSI).

x) We are highly indebted to our colleagues in Berkeley, Dr. F. Grunder, Dr. H. Heckman and Prof. E. Benton for their permanent friendly help with exposures at the Bevalac.

xx) We are sincerely grateful to Prof. Bogoljubov and Prof. Baldin, JINR, for arranging the Dubna-Frankfurt cooperation, which gave us the opportunity to cooperate with Prof. Tolstov at Dubna, and to expose detectors at the Synchropasotron-accelerator.

References:

1) Barcelona-Batavia-Belgrade-Bucharest-Lund-Lyons-Montreal-Nancy-Ottawa-Paris-Rome-Strasbourg-Valencia Collaboration
Proceed. 14th Int. Cosmic Ray Conf. Vol. 7 (1975) 2248
Physics Report LKIP - CR75 - 07 (1975)
University of Lund (Sweden)

2) Alma Ata-Leningrad-Moscow-Taschkent Collaboration
Preprint No 9, Moscow 1974

3) K.M. Abdo, N. Dalkhazhav, R.A. Khoshmukhamedov, G.S. Shabratowa, K.D. Tolstov, JINR-Dubna E1-7548 (1973) and E1 8021 (1974)

4) B. Andersson, I. Otterlund
1. Nuclear Physics B99 (1975) 425
2. Proceed. 14th Int. Cosmic Ray Conf. 7 (1975) 2280

5) K. Gottfried, Proc. 5th Int. Conf. on High Energy Physics and Nuclear Structure Uppsala (1973); Phys. Rev. Letters 32 (1974) 957

6) O.E. Badaway, A.M. Hussien, N. Mettwalli, Z. Physik A279 (1976) 407

7) K.D. Tolstov, JINR, R1, 2016, Dubna (1965)
K.D. Tolstov, R.A. Hoshmuhamedov, JINR, R1, 6897, Dubna (1973)

8) Yu.F. Gagarin, N.S. Ivanova, V.N. Kulikov, Sovjet J. Nucl. Phys. 11 (1970) 1255

9) R. Resman, I. Otterlund, Physica Scripta 4 (1971)

10) W. Greiner, these proceedings, and
J. Hofmann, W. Scheid, W. Greiner, Nuovo Cimento 33A (1976) 343

11) M. Gyulassi, these proceedings, and
V. Ruck, M. Gyulassi and W. Greiner, Z. Physik A277 (1976) 391

12) G.D. Westfall, J. Gosset, P.J. Johannsen, A.M. Poskanzer, W.G. Meyer, H.H. Gutbrod, A. Sandoval, R. Stock, LBL-Report 5072 (1976)

13) 1. H.G. Baumgardt, J.U. Schott, Y. Sakamoto, E. Schopper, H. Stöcker, J. Hofmann, W. Scheid, W. Greiner, Z. Physik A279 (1975) 273
2. H.G. Baumgardt, E. Schopper, J.U. Schott, N.P. Kocherov, A.V. Voronov, I.D. Issinsky, L.G. Makarov, Proceed. Int. Workshop IV, Hirschegg (Austria), AED-Conf. 76 - 056 000
3. J. Hofmann, H. Stöcker, M. Gyulassi, W. Scheid, W. Greiner, H.G. Baumgardt, J.U. Schott, E. Schopper, Proc. Int. Conf. on Selected Topics in Nucl. Structure, Dubna 1976

14) R. Kullberg, I. Otterlund, Z. Physik 259 (1973) 245

15) J.U. Schott, E. Schopper, R. Staudte,
Proceed. 9th Int. Conf. on Solid State Nuclear Track Detectors, Munich 1976, under press
Nucl. Inst. and Meth., under press

16) H.G. Baumgardt, Diploma Thesis, Frankfurt 1976

17) B. Jakobsson, R. Kullberg, I. Otterlund, LUIP - CR - 76 - 04 Lund (1976)

18) R.K. Smith, these proceedings

19) J. Gosset, H.H. Gutbrod, W.G. Meyer, A.M. Poskanzer, A. Sandoval, R. Stock and G.D. Westfall, LBL-Report 5820 (1976)

CONF-770602--5

NON-PERIPHERAL COLLISIONS OF HEAVY IONS IN NUCLEAR EMULSION

H.H. Heckman, H.J. Crawford, D.E. Greiner, P.J. Lindstrom, and L.W. Wilson
Lawrence Berkeley Laboratory and Space Sciences Laboratory
University of California, Berkeley, California 94720 U.S.A.

Introduction: Because of the large range of ionization and multiplicities of fragments that are produced in collisions between heavy ions, electron-sensitive nuclear track emulsions are particularly suited for studies of heavy ion interactions owing to their high spatial resolution and unrestricted sensitivity to rates of energy loss. We are presently carrying out an experimental study using the emulsion technique to examine the angular and momentum distributions of fragments emitted from non-peripheral collisions between emulsion nuclei (AgBr) and heavy-ion projectiles ^{4}He, ^{16}O, and ^{40}Ar in the range of energies 0.2 to 2.1 GeV/A. The beams and their specific energies used for the experiment are:

Beam	Energy(GeV/A)
^{4}He	2.1, 1.05
^{16}O	2.1, 0.20
^{40}Ar	1.8

Selection Criteria: The selection criterion we have adopted for a non-peripheral collision is that the interaction exhibits an absence of projectile fragmentation, i.e., an interaction where no beam-velocity fragments ($Z_F \geq 1$ from ^{4}He interactions, $Z_F \geq 2$ from ^{16}O and ^{40}Ar interactions) are produced within 5° (when E_{beam} = 1.05 and 2.1 GeV/A) or 10° (when E_{beam} = 0.20 GeV/A) of the incident beam direction. Interactions selected under this criterion are

deemed to be "central" collisions between the projectile and target nuclei, qualitatively characterized by impact parameters that are in the range $0 \leqslant b \lesssim |R_T - R_p|$.

Scanning and Measuring: Both along-the-track and volume scanning techniques were used to locate events. All track-coordinate measurements were made under oil-immersion objectives, 1000x total magnification, using three-coordinate digitally-encoded microscopes.

Measurements: For those heavy-ion interactions that satisfied the selection criterion, the following measurements of angle and track range were carried out for each beam nucleus:

1) The production angles were measured for all secondary fragments having a restricted grain density $g \geqslant 2\ g_{min}$, after correcting for the dip angle. (A Z=1 particle with $g \geqslant 2\ g_{min}$ has an energy $E \leqslant 250$ MeV/A.)
2) Track ranges and angles were measured for a subset of fragments with ranges $\leqslant 4$ mm, with no minimum range cutoff except that due to obscuration of short tracks at the point of interaction. (A 4 mm range in emulsion corresponds to proton and ^{4}He energies equal to 31 MeV/A.)
3) Each fragment measured under (1) was classified as to whether its potential range was less or greater than 4 mm. This visual estimate of potential range was made by the scanner-measurer by observing the grain density ($g \geqslant 10\ g_{min}$ for protons) and multiple scattering of the track in the pellicle containing the event.

In order to identify data measured under the above procedures, we shall use the notation "$E_p <$" to signify data whose energy limits are made either by measurements of grain density (1), or by estimated range (3). Data identified by $R \leqslant 4$ mm (2), for which $\in$ = E/A = 31 MeV/A for protons and ^{4}He, will signify that the data are based on actual range measurements.

Analytic Procedure: Owing to the high excitation energies and the large average number of particles that partake in non-peripheral (central) collisions of the type selected for this investigation, we make the practical assumption that the system we are considering is large enough and the mutual interactions are strong enough so that it can be described statistically, based on the hypothesis of equal *a priori* probabilites in phase space. Such a statistical distribution is the Maxwell-Boltzmann distribution. This distribution, expressed in a covariant, non-relativistic form, in terms of the velocity β of the emitted fragments appropriate for the range of velocities we consider in this experiment is as follows:

$$d^2N/d\beta d\mu \propto \beta^2 \, e^{-(\beta^2 - 2\beta\bar{\beta}_{\|}\mu)/\bar{\beta}_o^2}, \qquad (1)$$

where $\bar{\beta}_{\|}$ is the longitudinal velocity of the particle-emitting system, $\mu = \cos\theta$, where θ is the laboratory angle between the momenta of the fragment of mass M and the incident projectile, and $\bar{\beta}_o = \sqrt{2\tau/M_n}$ is the characteristic spectral velocity of Maxwell-Boltzmann distribution. The effective "temperature" of the system is τ(MeV/A), for a fragment of mass $M = AM_n$.

We now express Eq. 1 in terms of range R and μ, the two quantities measured in this experiment. In general, the velocity $\beta(\approx P/M)$ of a particle

with mass M and charge z, having a residual range R is given by the relation

$$\beta = f(Rz^2/M). \tag{2}$$

To good approximation, the R-β relation for nuclear emulsion is given by the power-law expression

$$\beta = k(Rz^2/m)^n \tag{3}$$

where k = 0.174, n = 0.29, R is in mm, and z and m are the atomic mass number and mass of the fragment, respectively, the latter being in units of the proton mass, i.e., $m = M/M_p$. In terms of range R and $\mu = \cos\theta$, the Maxwell-Boltzmann distribution (Eq. 1) becomes

$$d^2N/dRd\mu \propto (z^2/m)^{3n} R^{3n-1} e^{-(k^2R^{2n}-2kR^n\beta_{||}\mu)/\beta_o^2} \tag{4}$$

where

$$\beta_{||} = \bar{\beta}_{||}(m/z^2)^n \text{ and } \beta_o = \bar{\beta}_o(m/z^2)^n. \tag{5a}$$

It follows that the parameter we shall denote as

$$\chi_o = \beta_{||}/\beta_o = \bar{\beta}_{||}/\bar{\beta}_o, \tag{5b}$$

which is the ratio of the longitudinal velocity of the center of mass $\beta_{||}$ to the characteristic spectral velocity β_o of the fragmenting system, is common to both the velocity and range spectra, and is independent of (m,z).

Thus, the longitudinal velocity $\beta_{||}$ and spectral velocity β_o that characterize the range spectrum of unidentified fragments (Eq. 4) are related to the corresponding quantities for the velocity spectrum (Eq. 1) for any fragment (m,z) by the quantity $(m/z^2)^n$, where n is the range-velocity index. In this experiment, the parameters $\beta_{||}$ and β_o are determined from the range and angle data using Eq. 4, assuming $m/z^2 = 1$, for which $\bar{\beta}_o = \beta_o$ and $\bar{\beta}_{||} = \beta_{||}$. By fitting the measured range and angle data to evaluate $\beta_{||}$ and β_o we are effectively testing how well such data can be described given the following assumptions:

i) the observed range and angle distributions are interpretable in terms of a single Maxwellian-range (velocity) distribution,

ii) the isotopic distribution of fragments is dominated by one species, i.e., protons, thereby minimizing any significant difficulties in defining β_c in the Maxwell distribution (Eq. 1), and

iii) to the extent that (ii) is satisfied, the $\beta_{||}$ and β_o parameters that characterize the range and angular distributions are the same as those that describe the velocity distribution for nucleons.

Experimental Results:

A. *Prong number distributions.* Figure 1 presents the distributions of prong number per event, N_p, for the interactions of each heavy ion beam (^{4}He and ^{16}O at 2.1 GeV/A, ^{40}Ar at 1.8 GeV/A) selected under the criteria previously described. The prong distributions for the lower energy ^{4}He and ^{16}O beams are similar to those shown. The distributions pertain to charged prongs having restricted grain densities $g \geqslant 2\ g_{min}$, i.e., equivalent to proton energies $\leqslant 250$ MeV, emitted from events selected only when the projectile was fully occulted by the target nucleus. If we first consider the multiplicity

distributions of prongs arising from ^{40}Ar and ^{16}O collisions, we note that each distribution shows a single maximum and is approximately symmetric about its mean-prong number. In contrast, the N_p-distribution for ^4He projectiles shows two maxima, one in the region of $N_p = 6$ to 8, and the other at $N_p \approx 19$. We attribute the low-prong-number peak to collisions between the ^4He projectile and CNO (light) nuclei, and the high-prong-number peak to collisions with AgBr (heavy) nuclei because ^4He can be occulted in CNO as well as in AgBr collisions. The absence of a CNO peak in the ^{16}O and ^{40}Ar prong distributions indicates that the non-occultation of these projectiles by the light CNO target nuclei invariably shows visual evidence for projectile fragmentation. Thus, by eliminating prong numbers $N_p \leqslant 9$ from the ^4He data, we limit the interactions of high energy ^4He, ^{16}O, and ^{40}Ar nuclei to near-central collisions with Ag and Br with little, if any, contribution to the data from collisions with lighter emulsion nuclei.

B. *Range and angular distributions: $R \leqslant 4$ mm.* Measurements of the ranges and angular distribution of the fragments with $R \leqslant 4$ mm permit us to determine the velocity-parameters $\beta_{||}$ and β_o, and therefore χ_o, by least-squares fits of these data to Eq. 4. These parameters are tabulated in Table I. One of the features of these data is the near independence of the range and angular distributions for fragments with $R \leqslant 4$ mm, with respect to the mass of the projectile at beam energy 2.1 (1.8) GeV/A, as indicated by the approximate constancy of each of the fitted parameters. The longitudinal velocities of the particle-emitting systems, $\beta_{||}$, increase with decreasing beam energy, whereas the spectral velocities appear to be equal to within 10%, irrespective of the mass and energy of the projectile. The values of $\beta_{||}$ are in close agreement

with those measured for low-energy fragment-emitting systems produced in a variety of nucleus-nucleus and proton-nucleus collisions over a broad range of energies.[1,2] The temperature τ implied by the velocities $\beta_o = \sqrt{2\tau/M_n}$ are typically 6-7 MeV/A, characteristic of the binding energies of nuclei, and also compatible with the temperatures associated with projectile fragmentation.[3,4]

In Fig. 2 we present an example of the range-angle data obtained at beam energies 2.1 (1.8) GeV/A in terms of the rapidity variable $y \approx \beta_L$ ($y = \tanh^{-1}\beta_L$), where β_L is the longitudinal component of the quantity $\vec{\beta} = k(Rz^2/m)^n$, assuming $z^2/m = 1$. The mean value $\langle y \rangle = \beta_{||}$ is indicated for each distribution, as is the standard deviation $\sigma = \beta_o/\sqrt{2} = \sqrt{\tau/M_n}$. The average standard deviation of the three rapidity distributions is $\langle \sigma \rangle = 0.082 \pm 0.001$, which corresponds to a longitudinal momentum $P_L = 77$ MeV/c per nucleon.

C. *Angular distributions.* Examples of the angular distributions observed for fragments with energies $E_p < 31$ MeV and $E_p < 250$ MeV obtained with 2.1 (1.8)-GeV/A beam projectiles are shown in Figs. 3 and 4, respectively. The distributions are presented as functions of both θ and $\cos\theta$. Drawn through the data are curves derived from the fitted Maxwell-Boltzmann distributions. Because the angular distributions of the low energy fragments $E_p \leq 31$ MeV (Fig. 3) were taken without knowledge of particle ranges, subject only to the condition that $E_p < 31$ MeV, we found that the minimum χ^2-fits did not yield unique values for $\beta_{||}$ and β_o, but rather gave values of $\beta_{||}$ and β_o that were linearly coupled. Thus, we chose to fix β_o at the value determined previously from the range-angle data and evaluate $\beta_{||}$. The values thus obtained are indicated in Fig. 3 , along with the appropriate β_o's taken from Table I.

When the angular distribution of fragments is measured without regard to fragment velocity, $dN/d\mu$ (Eq. 1) becomes a function of $\chi_o \equiv \beta_{||}/\beta_o$ only. We have fitted the measured angular distribution for fragments with $E_p < 250$ MeV to this asymptotic form of the angular distribution to obtain one-parameter fits to the data (Fig. 4).

Figs. 5 and 6 show the angular distributions $dN/d\cos\theta$ vs. $\cos\theta$ for $E_p <$ 31 MeV and $E_p < 250$ MeV, respectively, for the lowest beam energy, ^{16}O at 0.20 GeV/A. The notable difference between the ^{16}O-produced fragments at 2.1 and 0.2 GeV/A is the significant increase in the relative production of fragments $E_p < 31$ and $E_p < 250$ MeV, in the forward hemisphere as the beam energy decreases. The shift of the angular distribution of the low energy fragments $E_p < 31$ MeV to smaller forward angles is due to an increase in $\beta_{||}$, 0.017 to 0.039, while the spectral velocity (temperature), based on the results of the $R \leq 4$ mm data (Table I), remains essentially constant, i.e., 0.106-0.115 (5.3-6.2 MeV/A). For energies $E_p < 250$ MeV, the distribution of fragments produced by 0.20 GeV/A ^{16}O is increasingly peaked forward, indicated by the fact that $\chi_o \equiv \beta_{||}/\beta_o$ increases from 0.26 to 0.62 as the beam energy decreases from 2.1 to 0.20 GeV/A.

The beam-energy dependence of the angular distribution data for ^4He and ^{16}O projectiles are summarized in Tables II and III. Here we give the values of the parameter $\chi_o = \beta_{||}/\beta_o$ obtained by fitting the angular distributions in the backward, forward and combined hemispheres, for $E_p < 31$ and $E_p < 250$ MeV, respectively.

Salient features of the angular distributions are:

For $E_p < 31$ MeV,

1) The values of χ_o for the combined hemispheres, $-1 \leq \mu \leq 1$, increase with decreasing E_{beam}.

2) The change in $\chi_o(-1 \leq \mu \leq 1)$ is primarily due to the increase in χ_o for the forward hemisphere, i.e., the angular distribution becomes more anisotropic.

3) At 2.1 GeV/A beam energy, the fragments are consistent with isotropy in the laboratory, $\chi_o(0 \leq \mu \leq 1) \approx 0$. (This is illustrated in Fig. 3.)

4) The angular distribution in the backward hemisphere is essentially invariant with respect to beam and energy. Note the near equality of the values of $\chi_o(-1 \leq \mu \leq 0)$ for the pairs of ^4He and ^{16}C data, Table II.

For $E_p < 250$ MeV,

1) The angular distributions are more anisotropic than those at $E_p < 31$ MeV.

2) The shape of the angular distributions in backward hemisphere remains invariant with respect to beam and energy. The values $\chi_o(-1 \leq \mu \leq 0)$ for ^4He and ^{16}O are, pairwise, the same.

3) The values of $\chi_o(0 \leq \mu \leq 1)$ increase with decreasing beam energy. At 2.1 GeV/A, fragment production continues to be more isotropic in the forward, relative to the backward, hemisphere (Fig. 4).

Some general conclusions of the experiment are (not all of which are obvious from this preview of the data):

1) There is no unique particle-emitting system, characterized by a center-of-mass velocity $\beta_{\|}$ and spectral velocity $\beta_o = \sqrt{2\tau/M_n}$, that accounts for the spectra of fragment ranges (momenta) and angles.

2) The $dN/d\theta$ distributions are broad, Maxwellian-like, with maxima that

shift toward smaller angles as the fragment energy increases, and as beam energy decreases.

3) No statistically significant structure, attributable to well-defined collective phenomena, is observed in the range or angular distributions.

4) By invoking the results of Ref. 5, there is no evidence that the angular distribution for low-energy fragments depends on the impact parameters of the collision between heavy ions at E_{beam} = 2.1 GeV/A.

5) At beam energy 2.1 (1.8) GeV/A, the number of fragments per event that are emitted in the backward hemisphere is insensitive to the projectile mass, e.g. 6.8, 6.7, and 7.1 for ^{4}He, ^{16}O, and ^{40}Ar, respectively.

Acknowledgements. We thank Margret Banks, Hester Yee, and Robert Turner for their assistance in scanning the nuclear emulsions. We also appreciate the guidance and advice given us by Dr. T.F. Hoang in the analysis and interpretation of the data. This work was carried out under the auspices of U.S. Energy Research and Development Administration, Contract W-7405-ENG-48 and the National Aeronautics and Space Administration, Grant NGR 05-003-513.

REFERENCES

1. E.K. Hyde, G.W. Butler, and A.M. Poskanzer, Phys. Rev. C 4, 1759 (1971).

2. H.H. Heckman, LBL Report 6561 (to be published).

3. D.E. Greiner, P.J. Lindstrom, H.H. Heckman, Bruce Cork, and F.S. Bieser, Phys. Rev. Lett. 35, 152 (1975).

4. A.S. Goldhaber, Phys. Lett. 53B, 306 (1974).

5. G.M. Chernov, K.G. Gulamov, U.G. Gulyamov, S.K. Nasyrov, and L.N. Svechnikova, Nucl. Phys. A280, 478 (1977).

TABLE I. Fitted parameters $\beta_{||}$, β_o, and $\chi_o \equiv \beta_{||}/\beta_o$ obtained from the range and angular distributions of fragments, $R \leq 4$ mm ($\in$ = 31 MeV/A).

E_{beam} (GeV/A)		^{4}He	^{16}O	^{40}Ar
2.1 (1.8)	$\beta_{||}$	0.016 ± 0.004	0.015 ± 0.002	0.012 ± 0.002
	β_o	0.117 ± 0.002	0.115 ± 0.002	0.117 ± 0.002
	χ_o	0.14 ± 0.04	0.13 ± 0.02	0.10 ± 0.02
1.05	$\beta_{||}$	0.021 ± 0.001		
	β_o	0.116 ± 0.002		
	χ_o	0.18 ± 0.01		
0.20	$\beta_{||}$		0.38 ± 0.003	
	β_o		0.106 ± 0.002	
	χ_o		0.36 ± 0.03	

TABLE II. Parameter $\chi_o \equiv \beta_{\parallel}/\beta_o$ for the Maxwellian distribution (Eq. 1) fitted to the angular distributions of fragments with $E_p \lesssim 31$ MeV. The values of β_o are given for the backward, forward, and combined hemispheres.

E_{beam}	Beam	$-1 \leqslant \mu \leqslant 0$	$0 \leqslant \mu \leqslant 1$	$-1 \leqslant \mu \leqslant 1$
0.20	^{16}O	0.33 ± 0.10	0.35 ± 0.05	0.37 ± 0.02
1.05	^{4}He	0.22 ± 0.07	0.20 ± 0.05	0.22 ± 0.06
2.1	^{16}O	0.31 ± 0.10	0.07 ± 0.07	0.15 ± 0.04
2.1	^{4}He	0.25 ± 0.07	0.05 ± 0.10	0.16 ± 0.02

TABLE III. Parameter χ_o for the Maxwellian distribution fitted to the observed angular distribution of fragments with $g > 2\ g_{min}$ ($E_p > 250$ MeV). The values of χ_o are given for the backward, forward, and combined hemispheres.

E_{beam}	Beam	$-1 \leqslant \mu \leqslant 0$	$0 \leqslant \mu \leqslant 1$	$-1 \leqslant \mu \leqslant 1$
0.20	^{16}O	0.41 ± 0.08	0.70 ± 0.04	0.62 ± 0.02
1.05	^{4}He	0.31 ± 0.09	0.34 ± 0.04	0.34 ± 0.02
2.1	^{16}O	0.37 ± 0.09	0.18 ± 0.03	0.26 ± 0.02
2.1	^{4}He	0.31 ± 0.08	0.24 ± 0.04	0.28 ± 0.03

FIGURE CAPTIONS

Fig. 1 Distribution of number of prongs (fragments) per event emitted from non-peripheral collisions with restricted grain densities $g > 2\ g_{min}$, corresponding to proton energies $E_p < 250$ MeV. Beam energies are 2.1 GeV/A for ^{4}He and ^{16}O, and 1.8 GeV/A for ^{40}Ar. The mean number of prongs/event, $\langle n \rangle$, are indicated. The CNO peak ($N_f \sim 6$-8) is not included in the value of $\langle n \rangle$ for ^{4}He.

Fig. 2 Rapidity distributions $y = \beta_L$ of fragments with ranges $R \leq 4$ mm, assuming $m/z^2 = 1$. Cut-off values of $\beta_L = 0.26$ are indicated by the arrows on the abscissa. Values of $\beta_{\|}$ and $\beta_o = \sqrt{2}\sigma$ are given in Table I, $E_{beams} = 2.1$ (1.8) GeV/A.

Fig. 3 Angular distributions for fragments, $E_p < 31$ MeV. Solid curves are fits of the data to Eq. 1, $-1 \leq \cos\theta \leq 1$, using the parameters indicated. The dashed and dotted curves are fits to the data, for the backward and forward hemispheres, respectively.

Fig. 4 Angular distributions for fragments with $g < 2\ g_{min}$, $E_p < 250$ MeV. See caption Fig. 3 for identification of the plotted curves.

Fig. 5 Angular distribution $dN/d\cos\theta$ vs. $\cos\theta$ for fragments, $E_p < 31$ MeV. Projectile nucleus is ^{16}O at 0.2 GeV/A. The parameters of the fitted curve are $\beta_{\|} = 0.039$ and $\beta_o = 0.106$.

Fig. 6 Angular distribution $dN/d\cos\theta$ vs. $\cos\theta$ for fragments with $g \geq 2\ g_{min}$

($E_p \lesssim 250$ MeV). Projectile nucleus is ^{16}O at 0.2 GeV/A. The parameter for the fitted curve is $\chi_o = 0.62$. The data point at $\cos\theta = 0.9$ was not included in the fit, owing to a background of Z=1 fragments of the projectile not excluded by our selection criteria.

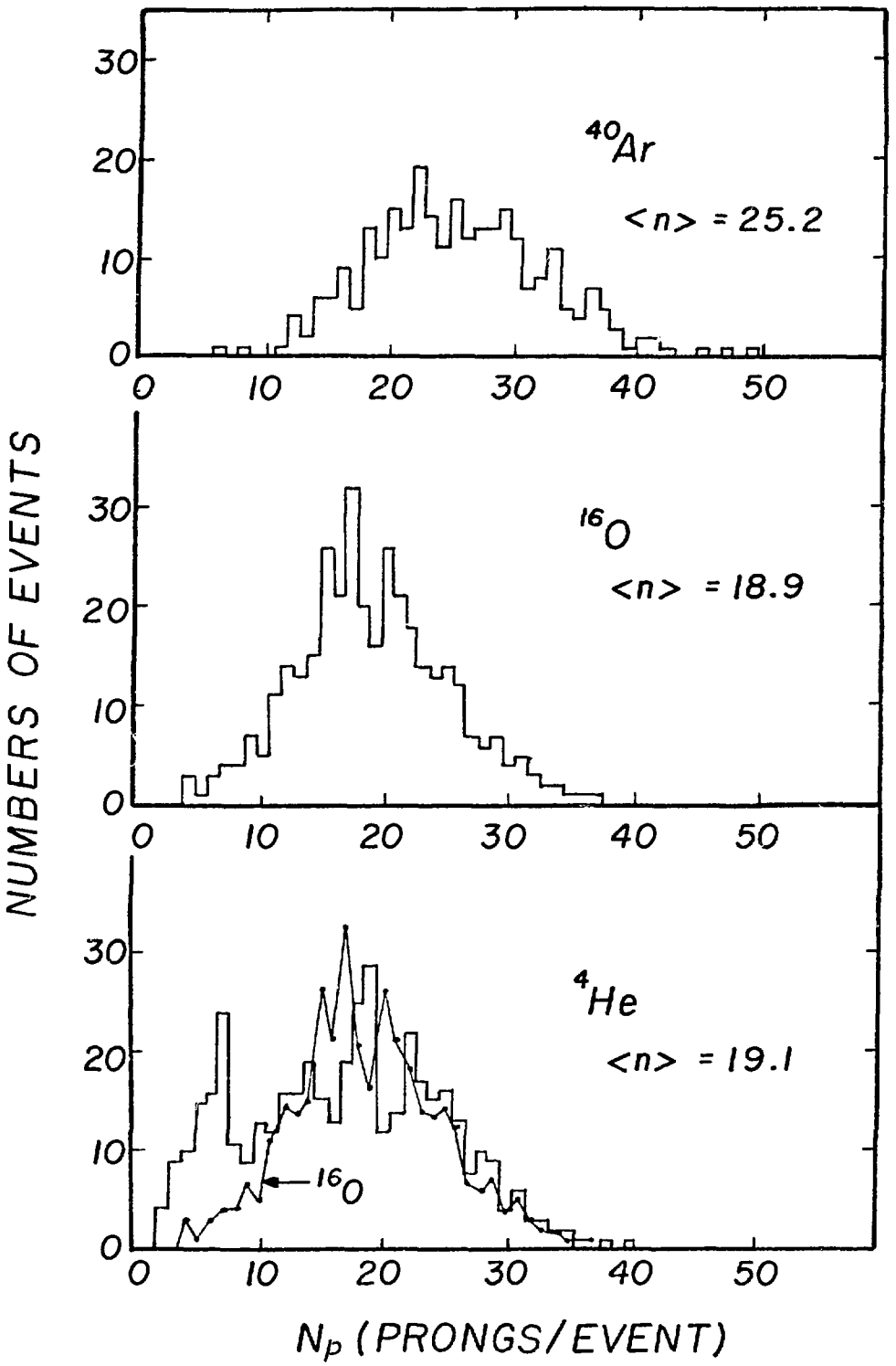
NUMBERS OF EVENTS
30
20
10
0
0
10
20
30
40
50
^{40}Ar
<n> = 25.2
^{16}O
<n> = 18.9
^{4}He
<n> = 19.1
^{16}O
N_p (PRONGS/EVENT)

FIGURE 1

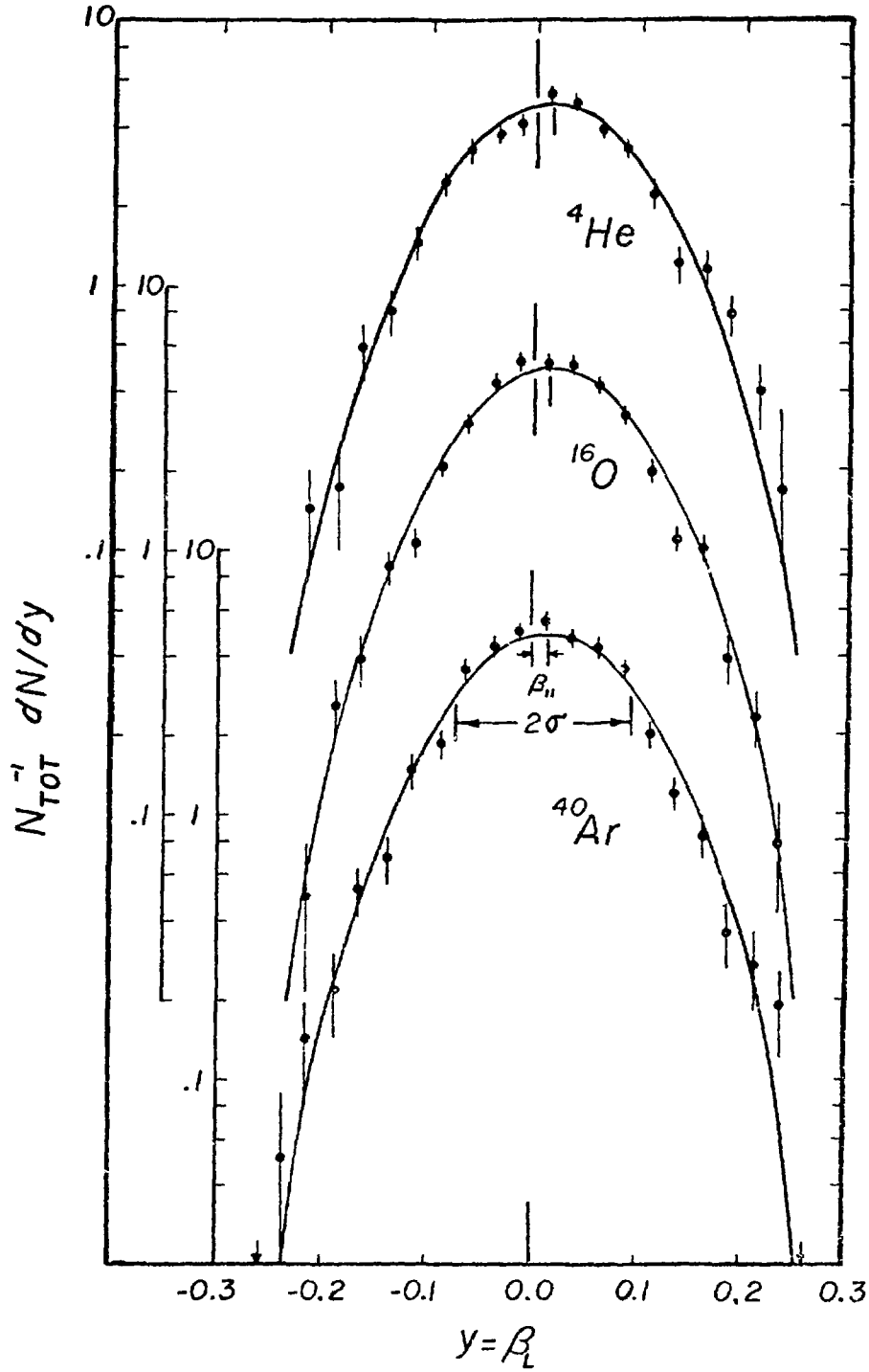
10
1
.1
10
1
.1
10
1
.1
^{4}He
^{16}O
^{40}Ar
$\beta_{\parallel}$
2σ
$N_{TOT}^{-1}\ dN/dy$
-0.3
-0.2
-0.1
0.0
0.1
0.2
0.3
$y=\beta_L$

FIGURE 2

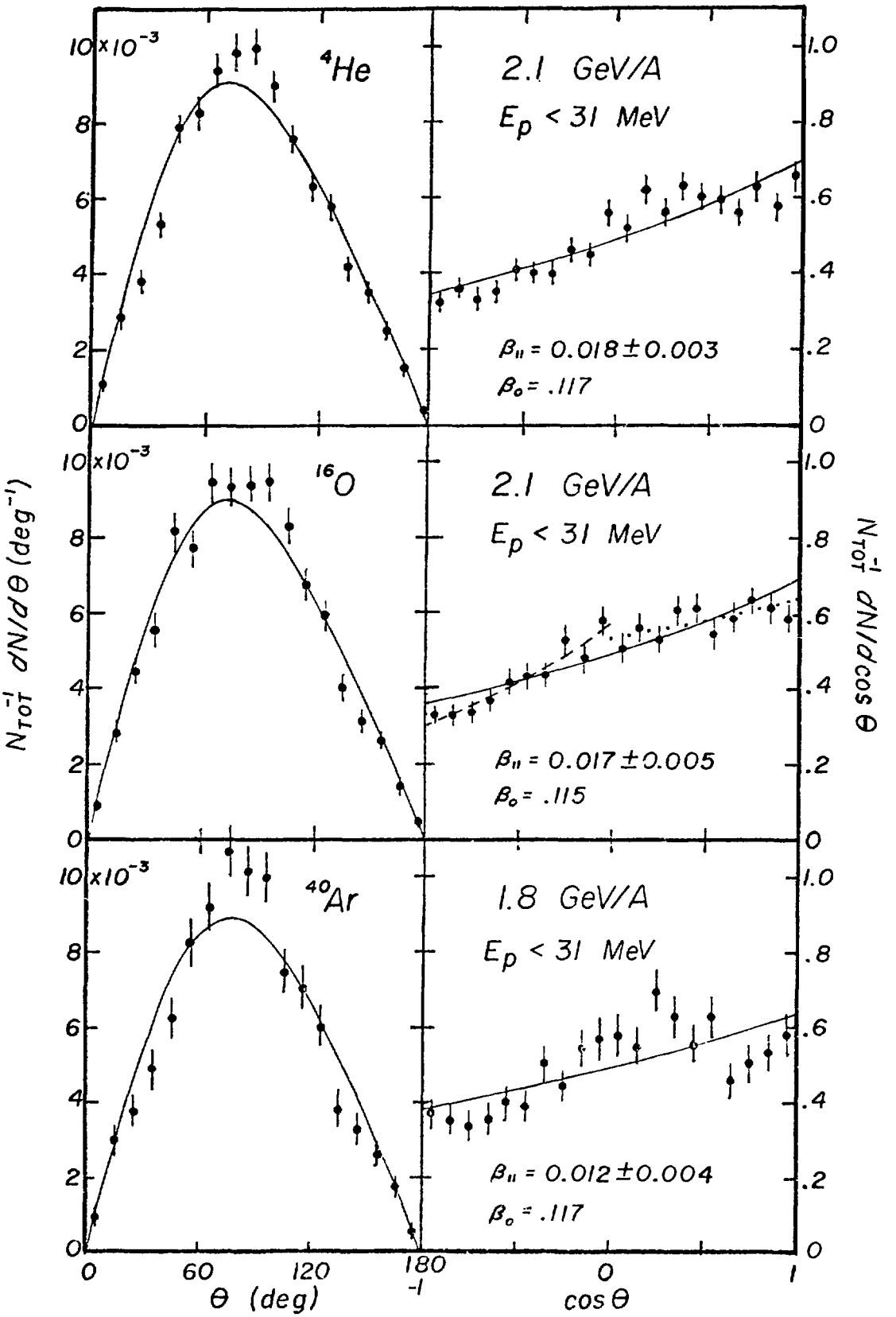
^{4}He
2.1 GeV/A
E_p < 31 MeV
β_{II} = 0.018 ± 0.003
β_o = .117
^{16}O
2.1 GeV/A
E_p < 31 MeV
β_{II} = 0.017 ± 0.005
β_o = .115
^{40}Ar
1.8 GeV/A
E_p < 31 MeV
β_{II} = 0.012 ± 0.004
β_o = .117
N_{TOT}^{-1} dN/dθ (deg^{-1})
θ (deg)
N_{TOT}^{-1} dN/d cos θ
cos θ

FIGURE 3

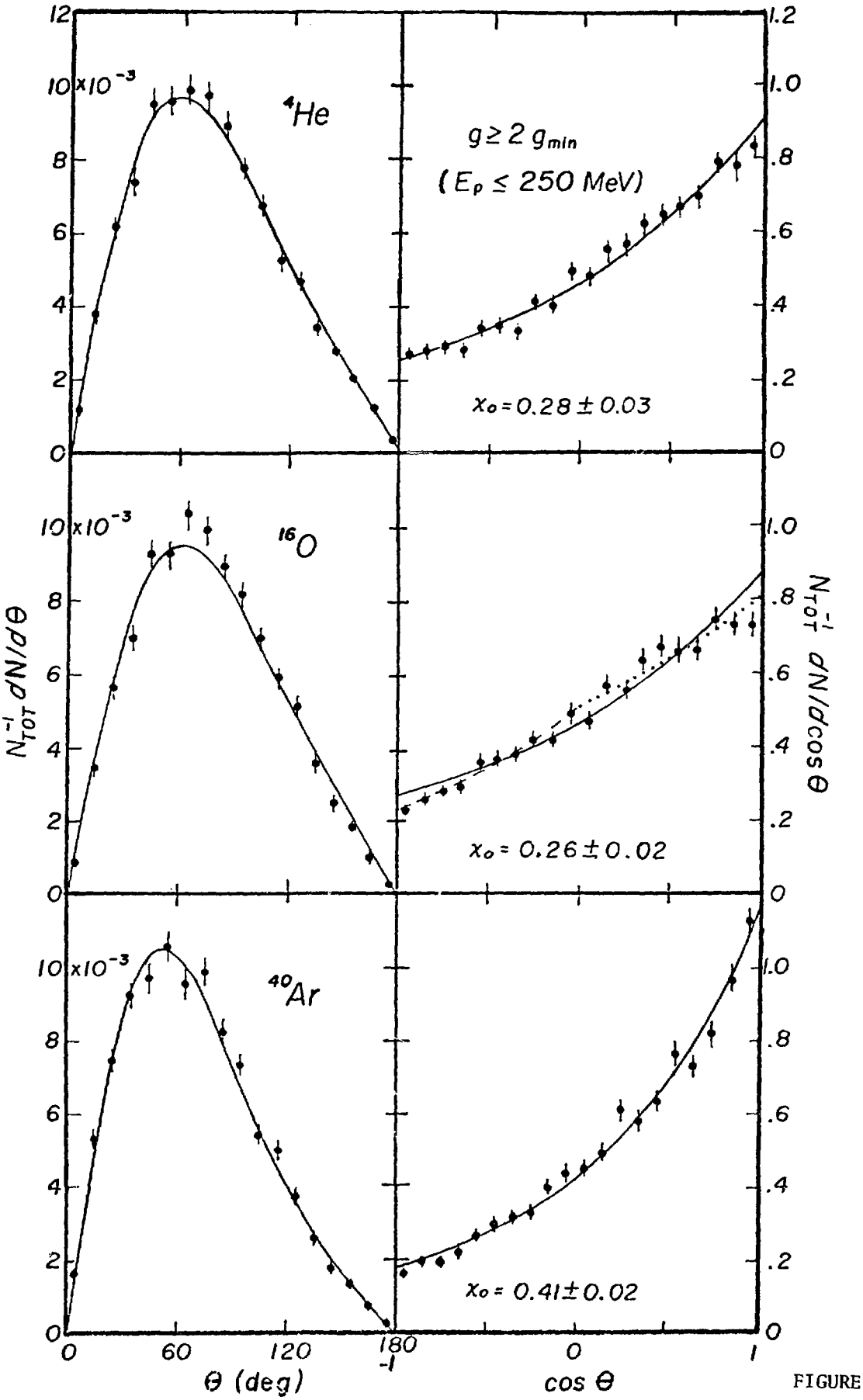
^4He
$g \geq 2\, g_{min}$
$(E_p \leq 250\ MeV)$
$x_o = 0.28 \pm 0.03$
^{16}O
$x_o = 0.26 \pm 0.02$
^{40}Ar
$x_o = 0.41 \pm 0.02$
10×10^{-3}
$N_{TOT}^{-1}\, dN/d\theta$
$N_{TOT}^{-1}\, dN/d\cos\theta$
θ (deg)
$\cos\theta$
0
60
120
180
-1
1

FIGURE 4

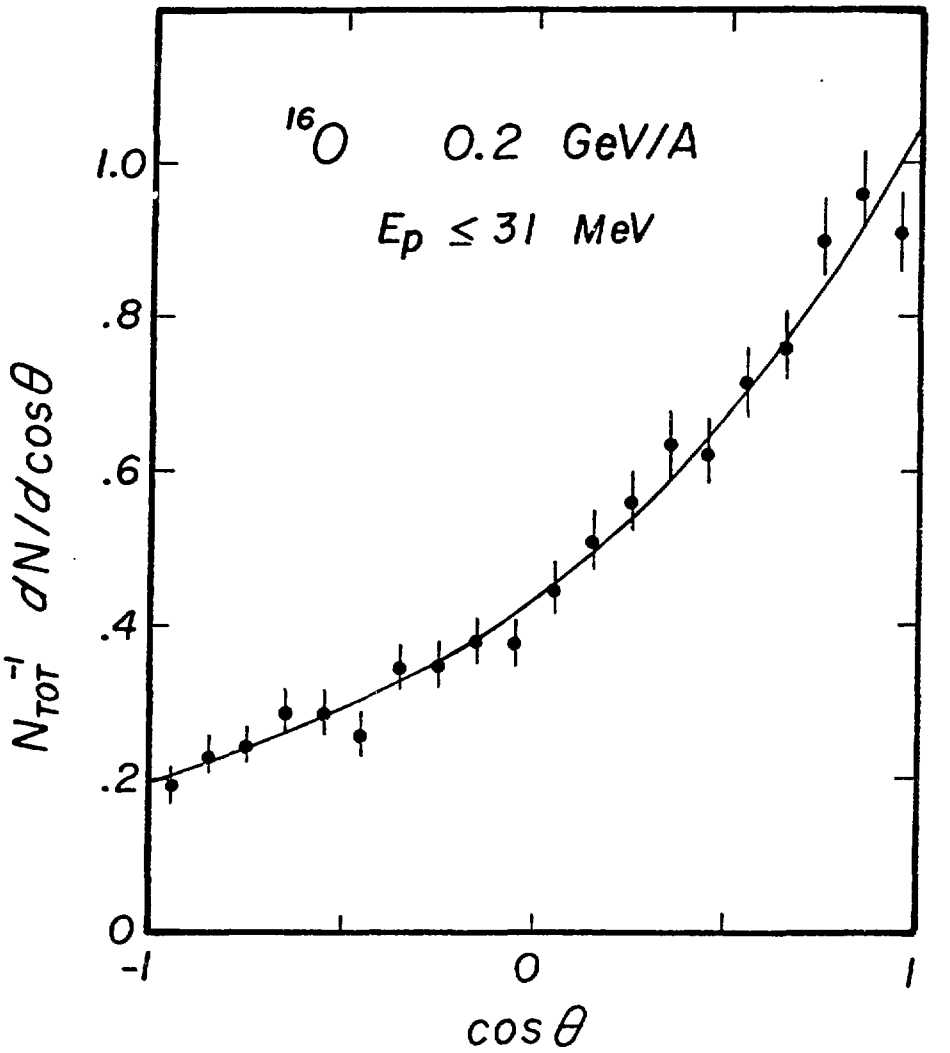
^{16}O 0.2 GeV/A
$E_p \leq 31$ MeV
1.0
.8
.6
.4
.2
0
-1
0
1
$N_{TOT}^{-1}\ dN/d\cos\theta$
$\cos\theta$

FIGURE 5

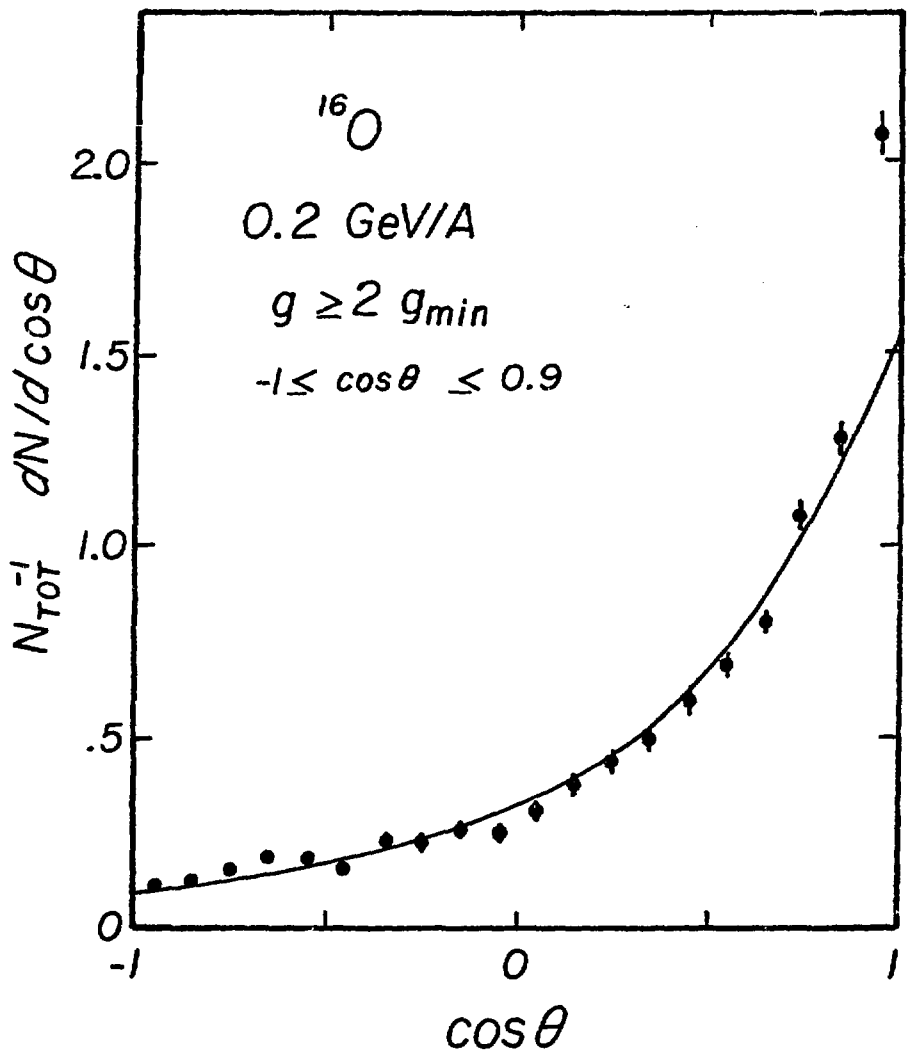
^{16}O
0.2 GeV/A
$g \geq 2\, g_{min}$
$-1 \leq \cos\theta \leq 0.9$
$N_{TOT}^{-1}\ dN/d\cos\theta$
2.0
1.5
1.0
.5
0
-1
0
1
$\cos\theta$

FIGURE 6

PHYSICS OF HIGHLY DENSE NUCLEAR MATTER FORMED IN RELATIVISTIC NUCLEUS NUCLEUS COLLISIONS*

Horst Stöcker, Werner Scheid**, and Walter Greiner***

Institut für Theoretische Physik
der Johann Wolfgang Goethe Universität
Frankfurt am Main, Germany

Abstract: High Density Nuclear Mach Shock Waves (HDNMSW) occuring in central heavy ion collisions of high energy are up to now the only tool to produce and investigate bulks of highly excited and strongly compressed nuclear matter. Due to strong meson (π^-, σ^-) condensates phase transitions of dense nuclear matter into density isomeric states (superdense nuclei) can be expected. We discuss the occurence of pion condensation in - and the influence of phase transitions on - relativistic nucleus nucleus collisions. We calculate the propagation of HDNMSW in a relativistic dynamical model. The comparison of the calculated angular - and energy distributions for the emission of matter with recent experimental data seems to indicate a phase transition in nuclear matter at densities of about $3\rho_0$.

1. Introduction:

Early speculations on the existence of abnormal superdense nuclei[1,2,3,4] ("Density Isomers") have recently been explored and founded by field theoretical model calculations,[5-16] which show that compressed nuclear matter ($\rho/\rho_0 \gtrsim 2$) due to meson (π^-, σ^-) condensation may become unstable. Then it may undergo a phase transition into a new form of matter with densities, binding energies and (Z/m)-ratios several times the nuclear groundstate values[1-4,7-16] (see Fig. 1a). At even higher densities ($\rho/\rho_0 \approx$ 8-15) phase transitions from baryon to quark matter can be discussed.[17]

Although the stability of superdense nuclei is questionable because of their high surface energies[18] there may exist at least metastable superdense nuclear states.[14] Up to now the only feasible way to produce bulks of strongly compressed nuclear matter consists in the creation of nuclear shock waves[14,19-31] which occur in head-on collisions of two nuclei, when their relative velocity exceeds the nuclear sound velocity ($c_s/c \approx 0.2$). The nucleon Pauli principle then forces their wavefunctions apart,[19] which can be interpreted phenomenologically as

compression energy. At higher energies the hard core of the nucleon nucleon potential, which may stem from the Pauli principle for quark matter, gives strong repulsion.

Contrary to sound waves in nuclear matter[32] nuclear shock waves are connected with strong, density dependent matter flows with flow velocity $v_F(\rho)$. The shock front propagates with shock velocity $v_S(\rho)$, also strongly dependent on the compression amplitude. Hence very non-linear phenomena appear for very large amplitudes, both $v_S(\rho)$ and $v_F(\rho)$ tend to the velocity of light c, while for small perturbations they approach the linear limit for sound waves(see Fig. 1b)

$$c_s = v_S(\rho_o) \leq v_S(\rho > \rho_o) < c$$
$$0 = v_F(\rho_o) \leq v_F(\rho > \rho_o) < v_S(\rho > \rho_o) < c$$

The formation of nuclear shock waves calls for the validity of hydrodynamical concepts, which means that fast thermalization (short mean free path or more precisely: short longitudinal momentum decay length) during high energy heavy ion collisions must occur. High relative momenta between two nuclei, signifying no overlap in phase space, as well as long longitudinal momentum decay length calculated from the free n-n scattering cross sections were interpreted as disease for nuclear shock waves at bombarding energies above one GeV per nucleon.[27] However, in the "formation flight" of ensembles of nucleons collective phenomena become important: Pionic waves, produced in inelastic n-n collisions by the creation and decay of nuclear isobars (nucleon resonances) by processes of the type $N+N \rightarrow N+N^* \rightarrow N+\pi+N \rightarrow N^*+N \rightarrow \ldots$ may lead to rapid randomization of longitudinal momentum and energy and thus to short mean free path and to the generation of shock waves.[20-23,25,26,30]

2. Pion Condensation and the Nuclear Equation of State

Another important process for randomization is the critical scattering of nucleons in the vicinity of a phase transition point.[15,31,35] This is analogous to the critical opalescence, which is e.g. characterized by the great enhancement of the scattering cross section of light near a liquid-gas phase transition or the critical scattering of neutrons in ferromagnets near the Curie point or - as the last example - by the critical scattering appearing in two colliding plasma beams when the drift velocity of the two plasmas exceeds a critical value. Then unstable plasmon modes appear, resulting in the growth of strong electric fields, greatly reducing the penetration depth of the two plasma beams in comparison with estimat-

ed values from simple twobody collisions.

Thus the vicinity of a phase transition point, as the onset of pion condensation, is expected to be marked by the occurence of critical nucleon scattering, i.e. a large enhancement (a factor 2 - 4)[33] of the density dependent n-n-cross section and a sudden reduction of the longitudinal momentum decay length. Recently this has experimentally been confirmed[26,34-40] Theoretically the onset of pion condensation is often described as the decay of the Hartree-Fock groundstate into ordered zero frequency (null energy) particle-hole excitations carrying pionic quantum numbers. In the new phase at high density the groundstate nuclear matter consists of nucleons forming a spin-isospin lattice[11]. This can phenomenologically be interpreted as a phase transition from the nuclear liquid to a nuclear spin - isospin - crystal.

The occurrence of a pion condensate in high energy heavy ion collisions depends strongly on the question of temperature, finite size and time scale during such collisions:[15,31,33] The critical temperature $T_c(\rho)$ above which the thermal excitations destroy the ordered spin - isospin lattice lie substantially above those expected in shock waves (see Fig. 1c).

As the condensate occurs at finite momentum $k_c \approx 2 m_\pi$, the critical distance $R_c \sim k_c^{-1} \approx 1\,fm$. Thus a dense system of dimension $\approx 2\,fm$ could support a condensate.

The relaxation time of the pion condensate can be estimated from $\tau_{cond}^{-1} = \max |2 \operatorname{Im} \omega|$, where ω is the complex zero of the pion propagator Δ_π in nuclear matter. This gives $\tau_{cond} \approx \tau_0 \cdot \Delta\tilde{\rho}$ with $\tau_0 = 10^{-23}$ sec and $\Delta\tilde{\rho} = (\rho - \rho_c)/\rho_0$. As the collision time is of the order of $5\tau_0$ and $\tau_{cond} \approx \tau_0$ the time scale is not too good. More detailed calculations were needed. We refer to the paper by Gyulassy at this meeting.

In the following we use a phenomenological description of nuclear matter, where phase transitions of first order (density isomers) and second order can be described as secondary minima or bends respectively in the density - dependent binding energy per nucleon $E_c(\rho)$ (see Fig. 1a) We treat the colliding nuclei as drops of nuclear matter, neglecting quantum mechanical effects as pairing, shell corrections and surface - as well as Coulomb energies, which are of the order of a few MeV per nucleon, while we are dealing with bombarding energies in the 0.1 - 4.2 GeV/N range! Furthermore, as the de Broglie wave length at these energies is small compared to the nuclear dimensions, classical calculations are justified. Substantially below about 100 MeV/N, these approximations

will become worse. Taking care of the possibility of thermal excitation of nucleons into baryonic resonances[20,22,26,28,30], we write the energy per baryon as a function of density ρ and temperature T as

$$W(\rho,T) = M_o c^2 + E_c(\rho, T=0) + \sum_{i=0}^{N} (E_{T_i} + E_i) \cdot \lambda_i$$

where $M_o c^2$ = 939 MeV is the rest mass of a free nucleon, $E_c(\rho, T^o = 0)$ gives the binding energy per nucleon,

$$E_{T_i} = \frac{\beta_i}{2} \rho_i^{-2/3} T^2 \quad \text{with } \beta_i = \left(\frac{2}{3}\tau_i \pi\right)^{2/3} \cdot M_i c^2/(\hbar c)^2$$

is the thermal energy at the i-th phase, τ_i and $\lambda_i = \frac{\tau_i e^{-E_i/T}}{\sum_i \tau_i e^{-E_i/T}}$ are statistical factors respectively, while $E_i \equiv (M_i - M_o)c^2$ is the excitation energy of the i-th resonance. Here we used for E_{T_i} the first term of a nonrelativistic non-interacting Fermi gas expansion, which is in good approximation valid[37] for $T \lesssim 100$ MeV. Later we shall show results also for other temperature-dependent energy functionals, as e.g. a Boltzmann gas. It is assumed that T is the same for all different phases. This is true for equilibrium thermodynamics and should be good for non-equilibrium states as long as $M_i \approx M_o$. Furthermore it is assumed that the excitation probability of the i-th resonance is given by a Boltzmann distribution. This means that we accept equilibrium thermodynamics as a first approximation.

$E_c(\rho)$ is practically unknown: Only $E_c(0) = 0$ and $E_c(\rho_o) \approx -16$ MeV (groundstate nuclear matter) are fairly certain. (See Fig. 1a). At higher densities the binding energy will smoothly increase up to a possible critical point, where a phase transition occurs. (See Fig. 1a) This can be a phase transition of the first or second kind: The second order transitions can be described by a bend in $E_c(\rho)$, the pressure is positive during the transition ($p > 0$). Phase transitions of the first kind have a strong secondary minimum in $E_c(\rho)$, with a density region of negative pressure ($p < 0$). This has drastic consequences[14] on the propagation of shock waves, as will be discussed below. Also the coexistence of two phases with different energies at the same densities is in principle possible, which can lead to two different shock waves in the first and second phase. The curvature in the first minimum at ρ_o is connected with the nuclear compression constant

$$K = 9\rho^2 \partial^2 W/\partial\rho^2 \Big|_{\rho=\rho_o, T=0, \text{ const. entropy}} \approx 200 \pm 100 \text{ MeV}$$

which determines the sound velocity for groundstate nuclear matter

$$c_s/c = \left(\partial p/\partial e\right)^{1/2} \Big|_{\text{const. entropy}} = (K/9W_o)^{1/2} \approx 0.2$$

where $p = \rho^2 \partial W/\partial \rho \,|_{\text{const. entropy}} = p_c + p_T = \rho^2 \partial E_c/\partial \rho + \beta_0/3 \cdot T \rho^{1/3} \sum_{i=0}^{N} \{ \frac{\beta_i}{\beta_0} \int_0^T \lambda_i \, dT \}$ is the pressure, $e = W\rho$ is the energy density and $W_0 \equiv W(\rho_0, T = 0) \approx 923$ MeV is the nucleon's groundstate energy.

3. The Relativistic Shock Equations

The state variables at the two sides of a shock front have to fulfill the following requirements: Energy -, momentum -, and baryon - number - flux - density have to be conserved by passing through the shock front. This yields the following consistency condition for the state variables in the rest system of the "shocked" and undisturbed (groundstate) nuclear matter.

$$W(\rho,T)^2 - W_0^2 + p(\rho,T) \cdot \left(W(\rho,T)/\rho - W_0/\rho_0 \right) = 0$$

This equation is called the relativistic shock equation[25,26], which for $W - W_0 \gg W_0$ becomes $2(W - W_0) + p(1/\rho - 1/\rho_0) \approx 0$ i.e. the (non-relativistic) Rankine-Hugoniot equation[21,22]. The shock front velocity $v_S(\rho)$ and the velocity for matter flow $v_F(\rho)$ with respect to the undisturbed matter are then given by

$$v_S/c = \left(p \cdot W \cdot \rho / ((W\rho - W_0\rho_0)(W_0\rho_0 + p)) \right)^{1/2}$$

$$v_F/c = \left(p \cdot (\rho W - \rho_0 W_0) / (\rho W \cdot (p + \rho_0 W_0)) \right)^{1/2}$$

respectively. One recognizes that v_S and v_F are proportional to $p^{1/2}$ where the pressure $p \sim \frac{\partial W}{\partial \rho}$. So in the presence of a phase transition, where the pressure becomes negative during the collapse, the shock phenomena must vanish. This is of great importance for the possible detection of a density isomer.[14] For a nucleon gas, excluding resonances and their "cooling" effects[22,26,30], we can find an unique analytical relation between thermal energy and density in the compressed matter[26]

$$E_T = \{ -B + (B^2 - 4AC)^{1/2} \} / (2A)$$

where

$$A = 1 + \alpha \,, \quad B = (W_0 + E_c) \cdot (2 + \alpha) + p_c/\rho - \alpha W_0 \rho/\rho_0 \,,$$

$$C = (W_0 + E_c)^2 - W_0^2 + W_0 p_c (1/\rho - 1/\rho_0) + E_c/\rho \cdot p_c$$

and $p = \alpha \rho E_T$, which with $\alpha = 2/3$ is valid for as well ideal- and Fermi-gases. Now we have a connection between all state variables behind the shock front and the velocities with the density ρ (see Fig. 1b).

4. Central High Energy Collision of Small Projectile and Heavy Target

Our model describes phenomenologically the geometry and dynamical variables during a central high energy collision of a smaller projectile and a heavy target as well as the angular- and energy distribution of the reaction fragments. We carried out the calculations in the lab-frame (target at rest). There are mainly three different phases of evolution during such a collision[14,26] (see Fig. 2).

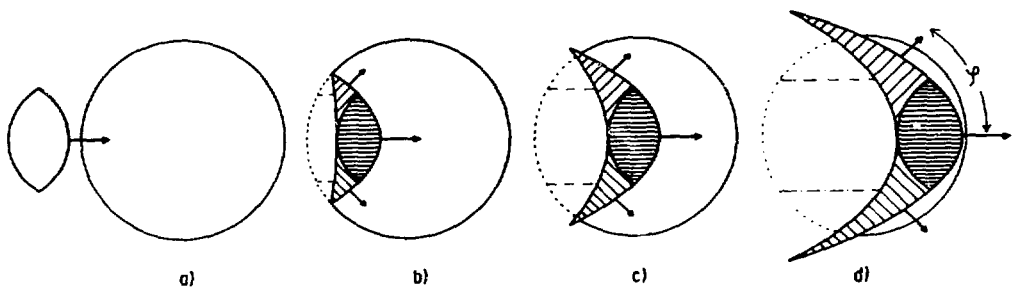

Fig. 2 shows the various stages of a head-on collision of a 870 MeV/N ^{16}O-nucleus with a ^{107}Ag-nucleus (which is at rest in the laboratory frame), calculated within our relativistic dynamical model.

b) the diving phase: The kinematically contracted projectile enters the target, becomes highly compressed a nd excited. In the diving process a splashing (backwards directed) tide wave should lead to emission of matter.
c) the penetrating stage: The projectile interpenetrates the target, pushing matter to the side; thus initiating the sidewards travelling strongly compressed Mach shock wave.
d) The evaporation phase: The projectile- and Mach shock matter leaves the residual target which now evaporates, while projectile and Mach shock explode because of their very high excitation energies which correspond to temperatures from 20 - 60 MeV.

The explosion of the head shock wave which contains at the end of the collision more than double the nucleons of the incoming projectile, can be identified with the explosion of the nuclear fireball, which has recently been used to

explain angular- and energy distributions in non-central high energy heavy ion collisions.[37]

It may also be possible, that the strongly compressed and highly excited projectile explodes inside the target during the interpenetrating stage. This will lead to superstars with enormous multiplicities. In this case the Mach angle will be washed out and can not be seen. This will be taken into account in a further calculation.

To restrict the number of degrees of freedom, we parametrize the compression zone by two paraboloids, $z = a_1 r^2 + z_1$, $z = a_2 r^2 + z_2$, which describe the shock front and the backside of the compression zone respectively. The undisturbed part of the target nucleus is described by the part of a spheroid of radius R up to the shock front (paraboloid 1), while the residual nucleus is described by a spheroid up to the backside of the compression zone (paraboloid 2) with a drilled hole of radius R_p in it. The residual nucleus has not yet been incorporated in our present calculations. The projectile (head shock wave) is divided from the Mach shock zone by a third paraboloid $z = -a_1 r^2 + z_2$ (see Fig. 2).

So the geometry of the system is determined by four variables: a_1 , a_2 , z_1 , z_2 .

The dynamical variables (energy density, momentum, pressure, temperature, density) are obtained by assuming homogeneous density-, velocity-, and temperature fields in each compression region. Thus for the sake of simplicity we concentrate on the mean values of the physical observables in the different regions as a function of time.

The shock equations yield an unique relation between energy, pressure, temperature, velocities, and the rest density ρ in the compression zone. Using these, we can describe the stage of our system by the four geometrical variables and the density in the Mach- and head shock region.

To describe the evolution of the system in time, we need six differential equations for these six variables:

The surface points on the paraboloids shall fulfil the shock equations. They move with the shock velocities:

$$\frac{dF}{dt} = \frac{\partial F}{\partial t} + \vec{\nabla} \cdot \vec{F} = 0 \quad \Rightarrow \quad \dot{z}_1 = v_S(\rho_1) \quad , \quad \dot{z}_2 = v_F(\rho_1)$$

$$\dot{a}_2 = \left(v_F(\rho_2) \cdot \left(1 + 4\, a_2^2\, r_{P_2}^2\right)^{1/2} - v_F(\rho_1) \right) / \, r_{P_2}^2$$

$$\dot{a}_1 = \left(v_S(\rho_2) \cdot \left(1 + 4\, a_1^2\, r_{P_1}^2\right)^{1/2} - v_S(\rho_1) \right) / \, r_{P_1}^2$$

where F is the surface.

The time derivatives of the Mach- and head shock densities are determined by use of the conservation of the total baryon number A_G and the total energy E_G

a) $A_G = A_T + A_p = \int_{V'} \rho'(x)\, d^3x$

b) $E_G = (A_T + A_p)\cdot W_0' + E_{LAB}\cdot A_p = \int_{V'} \rho'(x)\, W'(\rho'(x), T(\rho'(x)))\, d^3x$

$= \sum_j \rho_j' W_j' V_j'$

There j indicates the different density regions. The primes indicate the quantities in the lab frame. They are connected by Lorentz-transformations with the quantities in the respective rest frame:

$$E_G = \int_{V'} \rho(x)\cdot W(\rho(x), T(\rho(x)))\,/\,(1 - v_F^2(\rho(x)))\, d^3x$$

The indices 0, 1, 2 are connected with the rest target, head- and Mach shock respectively. The differentiation of a) and b) with respect to time yields:

a') $\frac{d}{dt}\rho_2' = -\left\{\left(\rho_0' \frac{dV_0'}{dt} + \frac{d\rho_1'}{dt} V_1' + \rho_1' \frac{dV_1'}{dt}\right)\cdot V_2' + \frac{dV_2'}{dt}\cdot\left(A_T + A_p - \rho_0' V_0' - \rho_1' V_1'\right)\right\} / V_2'^2$

b') $\frac{d}{dt}\rho_1' = -\left\{\sum_{j=0}^{2} \rho_j' \frac{d}{dt}(V_j')\cdot\left(W_j' - W_2' - \rho_2' \frac{\partial W_2'}{\partial \rho_2'}\right)\right\} : \left\{V_1\cdot\left(W_1' + \rho_1' \frac{\partial W_1'}{\partial \rho_1'} - \left(W_2' + \rho_2' \frac{\partial W_2'}{\partial \rho_2'}\right)\right)\right\}$

where $\frac{\partial W_j'}{\partial \rho_j'} = \left\{\frac{\partial W_j}{\partial \rho_j}\cdot\gamma_j + W_j \frac{\partial \gamma_j}{\partial \rho_j}\right\} : \left\{\gamma_j + \rho_j \frac{\partial \gamma_j}{\partial \rho_j}\right\}$

with $\gamma_j = (1 - v_F^2(\rho_j))^{-1/2}$

and $V_j' = \int_{z_j} r^2(z)\, dz$

The V_j' are calculated using the rotational symmetry around the z-axis. The time derivatives of V_j' depend on the geometrical parameters and their time derivatives only. The quantities ρ_j, W_j, v_{Fj} in the rest system are calculated by numerical iteration from the primed lab-quantities. Also the densities, velocities, and geometrical parameters are iteratively calculated in their starting points by requiring the correct total energy and baryon number.

The time evolution of the physical quantities is obtained by simultaneous numerical integration of the six differential equations in time-steps of $\Delta t = 0.1$ fm/c, whichis sufficiently exact to ensure energy- and baryon - number conservation better than one per cent.

5. The Results of the Calculations

The head- and the Mach shock densities ρ_1 and ρ_2 as a function of time are shown in Fig. 3 for various energies: In the beginning, the projectile is strongly compressed, but this compression is substantially decreased later on. The Mach shock density ρ_2 is about $2\rho_0$ below ρ_1 respectively.

The mean compression in the head- and Mach shock (each at t = 5 fm/c) is shown in Fig. 4a as function of the bombarding energy. The mean kinetic energy $E_{kin} = ((1 - v_F^2)^{-1/2} - 1) \cdot W_0$ of the emitted particles (Fig. 4b) after the collision is smaller than 200 MeV/N for Mach shock particles up to bombarding energies of 5 GeV/N, while it is larger than this experimentally important threshold for the projectile (head shock) at higher energies. The temperature in head- and Mach shock just after the collision is shown in Fig. 4c. It has been corrected within a one-dimensional model[26] by the cooling influence of nuclear isobars which were not yet included in our present calculations.

As the mean head shock densities are approximately equal to those calculated within the one-dimensional model[26], we make use of the later model to yield the pion production rate from the decay of nuclear isobars (see Fig. 5).

The Mach shock angle φ is depicted as a function of lab - energy in Fig. 7a. It smoothly decreases from about 60 degrees at 0.1 GeV/N to 35 degrees at 4 GeV/N. It is smeared out very much because of the temperature in the Mach shock and because of the curvature of the Mach-"cone".[26] The explosion of the highly excited head shock causes strong emission of fast particles into forward directions, which may hinder the visibility of the Mach shock peak at small bombarding energies. The energy spectra of the exploding projectiles (head shock) drawn in Fig. 6 were calculated by relativistic addition of the flow velocity and the

thermal velocity in the head shock after the collision, taking into account the isotropic decay cross section in the rest system of the projectile.

6. The Influence of a Density Isomer on the Reactions

If we assume a density isomer at $\rho/\rho_0 \approx 3$, the above picture applies only below $E_{LAB} \approx 0.2$ GeV/N, as then the projectile density reaches the phase transition region, i.e. the region of negative pressure $p \sim \partial W/\partial \rho < 0$ (see Figs. 1a and 4a). The projectile collapses into the density isomeric state. Thus the quasi-stable nuclear crystal can move with rather small dispersion through the surrounding normal nuclear fluid. One may think on a piece of ice which moves through water - this is important for the appearance of the Mach shock wave, since a water droplet dumping into water would produce too high friction and therefore soon damp out the collective motion. This, in fact, can to some extent be seen in the hydrodynamic calculations of Nix et al.[29].

As during the phase transition the head shock velocity becomes small, the Mach shock angle φ substantially decreases in this energy region, since the Mach shock moves faster than the collapsing head shock during this time period. The crystallization of the projectile causes a much more pronounced Mach shock peak at higher energy, because the projectile moves with much less friction through the target.

At bombarding energies between 1-2 GeV/N the Mach shock density approaches the phase transition region.[14] Now the Mach shock matter collapses into the isomeric state: the pressure is negative and the shock phenomena vanish. Then no Mach shock peak is observable.

At even higher energies, the Mach shock density again increases. As soon as the Mach shock density is above the secondary minimum, the shock phenomena reappear again. The Mach angle here sets in at large angles (around 90^0), as $v_S(\rho)$ and $v_F(\rho)$ are very small in this region. This means small kinetic energies of the emitted fragments. At even higher energies the Mach shock angle shall decrease again, as both $v_S(\rho)$ and $v_F(\rho)$ increase up to the light velocity c at very high densities, so that $\varphi \to 0$ for very high energies. Also one may think that higher phase transitions do occur, which may again produce a characteristic dependence of the Mach angle φ on the bombarding energy.

7. Comparison of Our Calculations with the Experimental Observations

HDNMSW should be observable in central collisions of high energy collisions of light projectiles with heavy targets:

1) In azimuthally symmetric central collisions, which can be identified e.g. by many prong stars in AgCl - detectors, a preferential emission angle must be observed[26].

2) The kinetic energy of these particles will be smaller than 200 MeV/N. It will be decreased to even lower values, if the Mach shock density is in the secondary minimum.

3) The Mach shock peak and the decay of the head shock should predominantly be seen in the α-particle channel for three reasons:
   a) A pion condensate with a structure of a spin-isospin lattice preferentially decays into α-particles as smallest lattice cells.
   b) When the Mach shock wave approaches the nuclear surface, it kicks out the α-particles contained enhanced in the nuclear surface.
   c) During the individual collisions of the constituent particles in the high temperature zone of the Mach shock, only those α-particles (and heavier clusters) survive, which have not undergone a scattering. Thus the Mach angle is conserved by those clusters, while scattered and unscattered nucleons cannot be distin guished.

4) One should find fast pions emitted by highly excited nuclear isobars. The occurence of pion condensation should also lead to a large enhancement of the pion production cross section.

In the presence of a pion condensate the Mach shock peak should be more clearly pronounced and also should have the above predicted dependence on energy. Recent experimental data,[26,36,38-40] which fulfil the above criteria on centrality, energy- and α-particle windows. show a peak in the angular distributions of the reaction fragments. The systematic shift of this preferential angle with energy can be interpreted in comparison with our calculations as indication for a phase transition in dense nuclear matter at $\rho/\rho_0 \simeq 3$ (see Fig. 7a and 7b, and figure caption).

8. Summary and Conclusions

HDNMSW can be used as a tool to study bulks of highly excited and strongly compressed nuclear matter, which means the investigation of the nuclear equation of state under extreme conditions. We have shown, that HDNMSW show specific effects, when phase transitions of nuclear matter into the pion condensate or density isomer occur at high densities. We can study the properties of the so-formed highly excited isobaric gas (eventually quark gas), and we can look for a possible limiting temperature $T_{Max} \approx 120$ MeV, first mentioned by Hagedorn and recently discussed in the context of shock waves.

Besides that, information on the compressibility constant K and sound velocity c_s in ground state nuclear matter can be gained. It thus seems that high energy heavy ion physics can furnish fundamental information about nuclear matter. This may lead to an exciting future.

References

* This work has been supported by the Bundesministerium für Forschung und Technologie (BMFT) and by the Gesellschaft für Schwerionenforschung (GSI).

** Permanent address: Institut für theoretische Physik, Justus Liebig Universität, Giessen, Germany.

*** Invited speaker at the FALL CREEK FALLS MEETING ON HEAVY-ION COLLISIONS, June 13-17, 1977.

1) E. Feenberg and H. Primakoff, Phys. Rev. 70 (1946) 980

2) A. R. Bodmer, Phys. Rev. D 4 (1971) 1601

3) *A. R. Bodmer,* in Proceedings of the International Symposium on *Present Status and Novel Developments* in the Nuclear Many-Body Problem, Rome, Italy, 1972, edited by F. Calogero and C. Ciofi Degli Atti (*Editrice Compositori, Bologna, 1973*), Vol. 2, p. 505

4) Y. Ne'eman, in Proceedings of the International Astronomical Union Symposium No. 53 on Physics of Dense Matter, Boulder, Colorado, 1972, edited by C. J. Hansen (Reidel, Dordrecht/Boston, 1974), p. 111

5) A. B. Migdal, Zh. Eksp. Teor. Fiz. 61 (1971) 2209

6) R. F. Sawyer and D. J. Scalapino, Phys. Rev. D 7 (1973) 953;
W. Weise and G. E. Brown, Phys. Lett. 48B (1974) 297;
G. Baym and E. Flowers, Nucl. Phys. A222 (1974) 29

7) T. D. Lee and G. C. Wick, Phys. Rev. D 9 (1974) 2291

8) T. D. Lee, Rev. Mod. Phys. 47 (1975) 267

9) A. K. Kerman and L. D. Miller, in Proceedings of the 2nd High Energy Heavy Ion Summer Study, Berkeley, California, 1974, edited by L. S. Schroeder [Lawrence Berkeley Laboratory Report No. LBL-3675, 1975 (unpublished)], p. 73

10) E. M. Nyman and M. Rho, Nucl. Phys. A268 (1976) 408

11) J. M. Irvine, Rep. Prog. Phys. 38 (1975) 1385

12) D. K. Campbell, R. F. Dashen, and J. T. Manassah, Phys. Rev. D 12 (1975) 979

13) D. K. Campbell, R. F. Dashen, and J. T. Manassah, Phys. Rev. D 12 (1975) 1010

14) J. Hofmann, H. Stöcker, U. Heinz, W. Scheid, and W. Greiner, Phys. Rev. Lett. 36 (1976) 88

15) V. Ruck, M. Gyulassy, and W. Greiner, Z. Phys. A277 (1976) 391

16) A. B. Migdal, G. A. Sorokin, O. A. Markin, and I. N. Mishustin, Phys. Lett. 65B (1976) 423

17) G. Chapline and M. Nauenberg, preprint, Lawrence Livermore Lab. (1976)

18) U. Heinz, H. Stock, W. Scheid, and W. Greiner, J. Phys. G (Nucl. Phys.) 3 (1977) 21

19) W. Scheid, R. Ligensa, and W. Greiner, Phys. Rev. Lett. 21 (1968) 1479

20) G. F. Chapline, M. H. Johnson, E. Teller, and M. S. Weiss, Phys. Rev. D 8 (1973) 4302

21) W. Scheid, H. Müller, and W. Greiner, Phys. Rev. Lett. 32 (1974) 741

22) W. Scheid, J. Hofmann, and W. Greiner, in Proceedings of the 2nd High Energy Heavy Ion Summer Study, Berkeley, California, 1974, edited by L. S. Schroeder [Lawrence Berkeley Laboratory Report No. LBL-3675, 1975 (unpublished)], p. 1

23) G. F. Chapline, in Proceedings of the 2nd High Energy Heavy Ion Summer Study, Berkeley, California, 1974, edited by L. S. Schroeder [Lawrence Berkeley Laboratory Report No. LBL-3675, 1975 (unpublished)], p. 51

24) C. Y. Wong and T. A. Welton, Phys. Lett. 49B (1974) 243

25) J. Hofmann, H. Stöcker, W. Scheid, and W. Greiner, in Proceedings of the Bear Mountain Symposium on Relativistic Heavy Ions (1974);

26) H. G. Baumgardt, J. U. Schott, Y. Sakamoto, E. Schopper, H. Stöcker, J. Hofmann, W. Scheid, and W. Greiner, Z. Phys. A273 (1975) 359
H. Stöcker, Diploma Thesis, Frankfurt 1975 (unpublished)

27) M. I. Sobel, P. J. Siemens, J. P. Bondorf, and H. A. Bethe, Nucl. Phys. A251 (1975) 502

28) Y. Kitazoe, M. Sano, and H. Toki, Nuovo Cimento Lett. 13 (1975) 139

29) A. A. Amsden, G. F. Bertsch, F. H. Harlow, and J. R. Nix, Phys. Rev. Lett. 35 (1975) 905

30) J. Hofmann, W. Scheid, and W. Greiner, Nuov. Cim. 33A (1976) 343

31) J. Hofmann, H. Stöcker, M. Gyulassy, W. Scheid, and W. Greiner, Proceedings of the International Conference on Selected Topics in Nuclear Structure

32) A. E. Glassgold, W. Heckrotte, and K. M. Watson, Ann. Phys. (N.Y.) 6 (1959) 1

33) M. Gyulassy and W. Greiner, to be published in Ann. Phys.

34) B. Jakobsson, R. Kullberg, and I. Otterlund, Z. Phys. A272 (1975) 159

35) A. M. Poskanzer, R. G. Sextro, A. M. Zebelman, H. H. Gutbrod, A. Sandoval, and R. Stock, Phys. Rev. Lett. 35 (1975) 1701

36) H. G. Baumgardt, E. Schopper, J. U. Schott, N. P. Kocherov, A. V. Voronow, I. D. Issinsky, and L. G. Makarov, in Proceedings of the International Workshop IV on Gross Properties of Nuclei and Nuclear Excitations, Hirschegg, Kleinwalsertal, Austria, 1976 [Technische Hochschule Darmstadt Report No. AED-Conf.76-015-000, 1976 (unpublished), p. 105

37) G. D. Westfall, J. Gosset, P. J. Johansen, A. M. Poskanzer, W. G. Meyer, H. H. Gutbrod, A. Sandoval, and R. Stock, Phys. Rev. Lett. 37 (1976) 1202

38) H. Heckman, private communication

39) I. Otterlund, private communication

40) E. Schopper, H. G. Baumgardt, J. U. Schott, to be published

Figure Captions

Fig. 1a: shows various possible forms of the binding energy E_c (ρ) per nucleon (as described in the text).

Fig. 1b: Here the influence of a density isomer on the propagation of nuclear shock waves is depicted (solid curves). The dashed curves show the shock velocity and the flow velocity as function of the compression, if no phase transitions occur.

Fig. 1c: Phase diagram of nuclear matter, which shows, that the critical temperature T_c (ρ) above which a possible pion condensate cannot be formed, is always much higher than the temperature occuring in nuclear shock waves. So pion condensates[15] can occur in high energy heavy ion collisions.

Fig. 2: shows the various stages of a head-on collision of a 870 MeV/N ^{16}O-nucleus with a ^{107}Ag-nucleus (which is at rest in the laboratory frame), calculated within our relativistic dynamical model.

Fig. 3a and b: show the head- and Mach shock densities as a function of time for various bombarding energies indicated by the number (in GeV/N) at each curve.

Fig. 4a: The mean density of the head- and the Mach shock (at t = 5 fm/c respectively) as function of the bombarding energy is depicted. An indicated phase transition at a given density will affect the headshock formation for relatively low energies, while the Mach shock will reach this phase transition region at much higher energies.

Fig. 4b: The kinetic energy E_{kin} per nucleon of the reaction fragments stemming from the head- and Mach shock respectively is drawn as a function of the bombarding energy.

Fig. 4c: The temperatures of the head- and Mach shock before their explosion is shown. The dashed lines are the temperatures taking into account the cooling influence of the production of nuclear isobars.

Fig. 5: The number of pions produced by the decay of resonances is depicted as function of the bombarding energy. This has been calculated by use of the corrected temperatures of Fig. 4c.

Fig. 6: The energy spectrum of the projectile, which explodes because of its high excitation energy when it leaves the target, is shown for E_{LAB}/N =0.25 and 4 GeV/N.

Fig. 7a: The solid line shows the energy dependent position of the Mach shock peak calculated without a density isomer in $E_C(\rho)$. The dashed line shows the influence of a phase transition point at $\rho/\rho_o = 3$: At 0.25 GeV/N the projectile dives into the density isomeric state (crystallization) which results in a smaller angle than expected without density isomer. At energies between 1 and 2 GeV, the Mach shock reaches the phase transition region: The shock phenomena break off and reappear again at angles around 90^o, tending to smaller angles for even higher energies. The dots represent the peak position in recent experiments of E. Schopper, H. Heckman (squares) and I. Otterlund (crosses) and their collaborators. They show just the behaviour which can be expected within our model. This seems to indicate the existence of a phase transition (density isomer) in nuclear matter around $3\,\rho/\rho_o$.

Fig. 7b: shows the Mach shock velocity calculated as a function of the bombarding energy in the presence of a density isomer; the points are deduced from the experimental data by use of projectile. It can be seen that in the phase

transition region the shock phenomena vanish and reappear again with small velocities at higher bombarding energies.

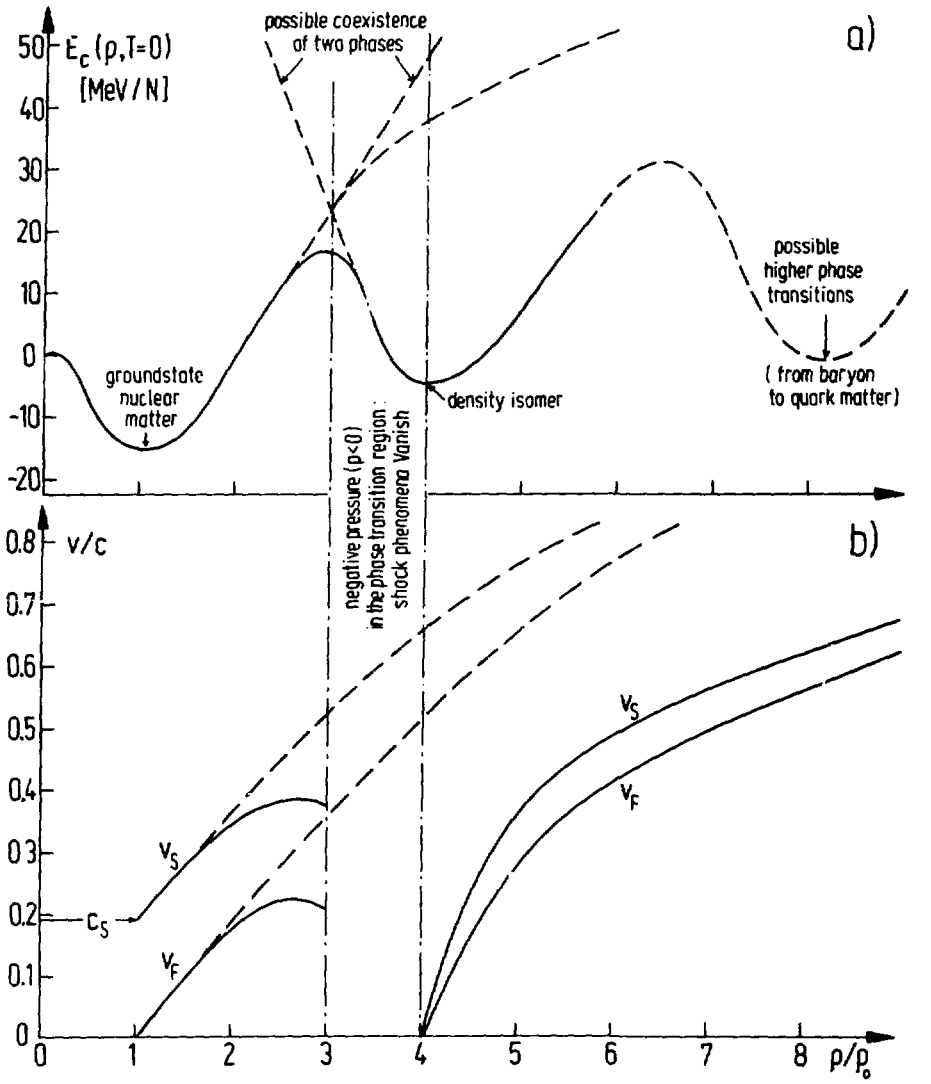
a)
$E_c(\rho,T=0)$ [MeV/N]
possible coexistence of two phases
groundstate nuclear matter
density isomer
possible higher phase transitions
(from baryon to quark matter)
negative pressure ($p<0$) in the phase transition region: shock phenomena Vanish
b)
v/c
v_S
v_F
c_S
ρ/ρ_0

Fig.1

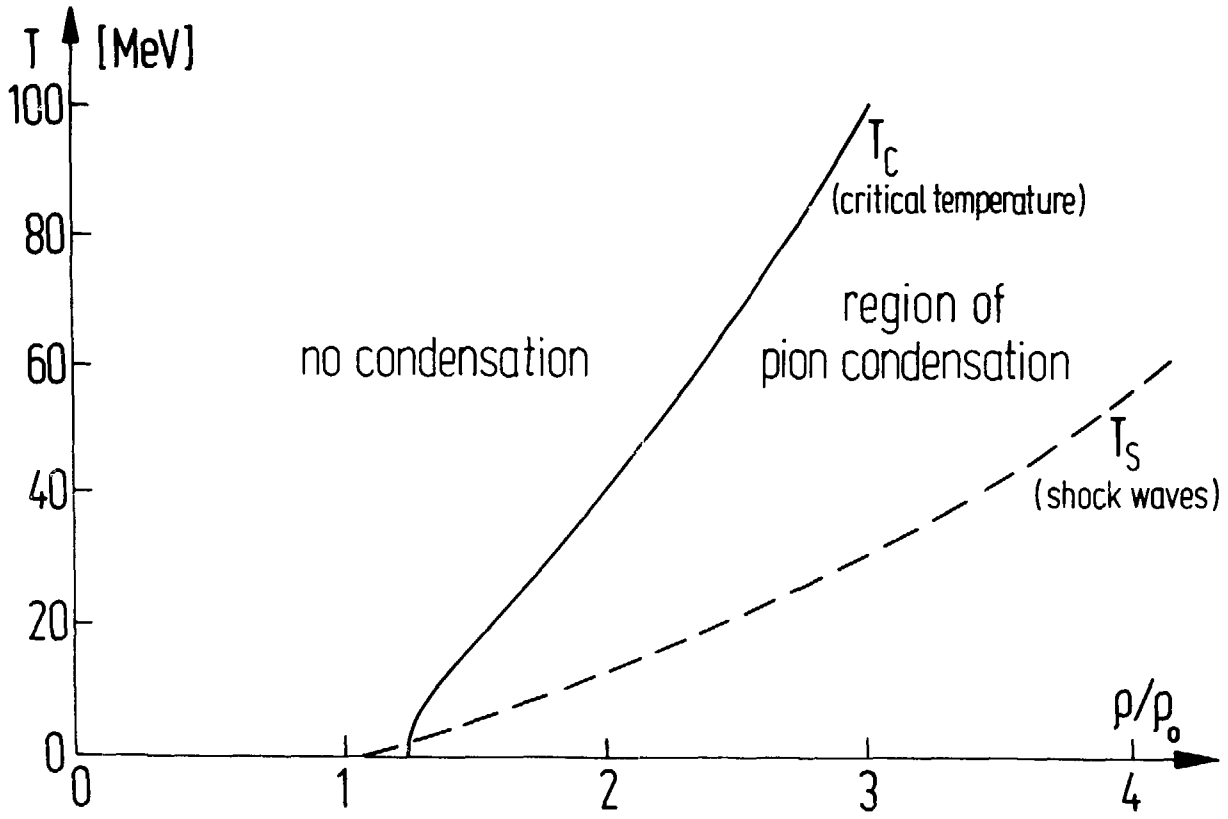
T [MeV]
100
80
60
40
20
0
0
1
2
3
4
T_C
(critical temperature)
region of
pion condensation
no condensation
T_S
(shock waves)
ρ/ρ_o

Fig.1c

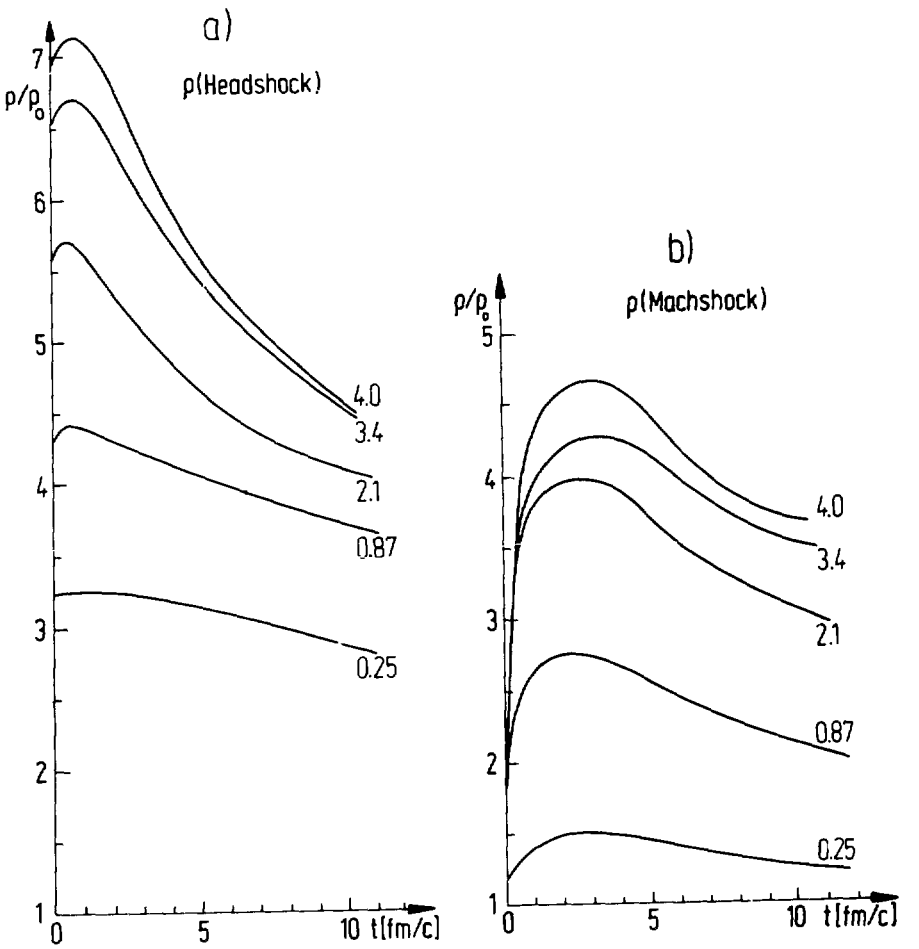
a)
ρ(Headshock)
ρ/ρ0
7
6
5
4
3
2
1
0
5
10 t[fm/c]
4.0
3.4
2.1
0.87
0.25
b)
ρ(Machshock)
ρ/ρ0
5
4
3
2
1
0
5
10 t[fm/c]
4.0
3.4
2.1
0.87
0.25

Fig.3

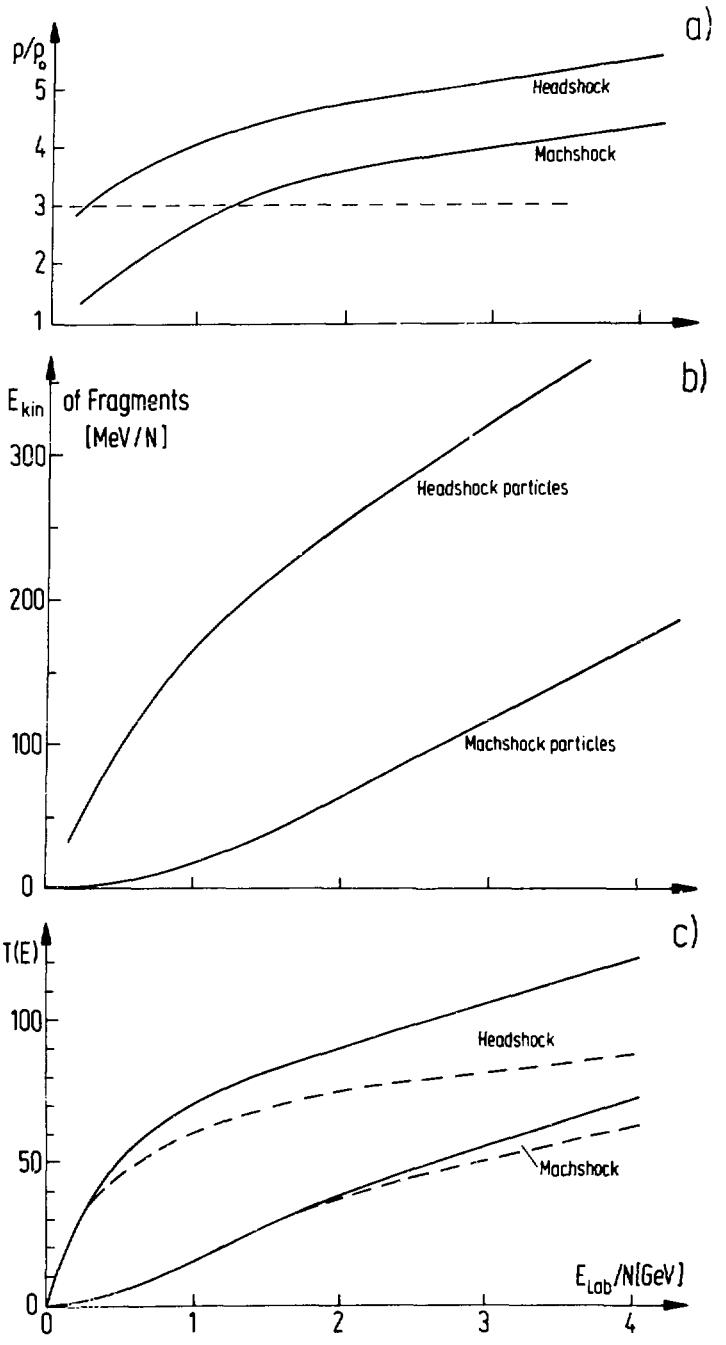
a)
p/p₀
5
4
3
2
1
Headshock
Machshock
b)
E_kin of Fragments
[MeV/N]
300
200
100
0
Headshock particles
Machshock particles
c)
T(E)
100
50
0
Headshock
Machshock
E_Lab/N[GeV]
0
1
2
3
4

Fig.4

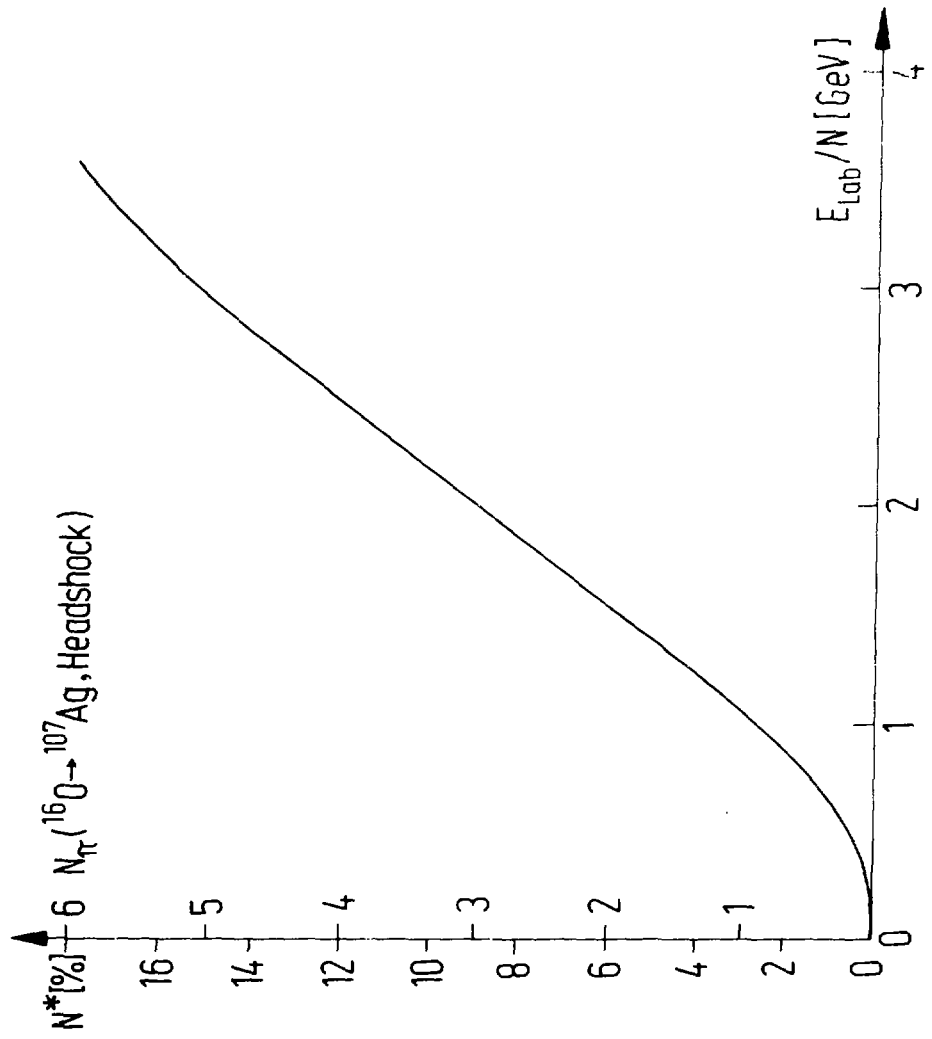
N*[%]
$N_\pi(^{16}O \rightarrow {}^{107}Ag, Headshock)$
0
2
4
6
8
10
12
14
16
1
2
3
4
5
6
E_{Lab}/N [GeV]

Fig.5

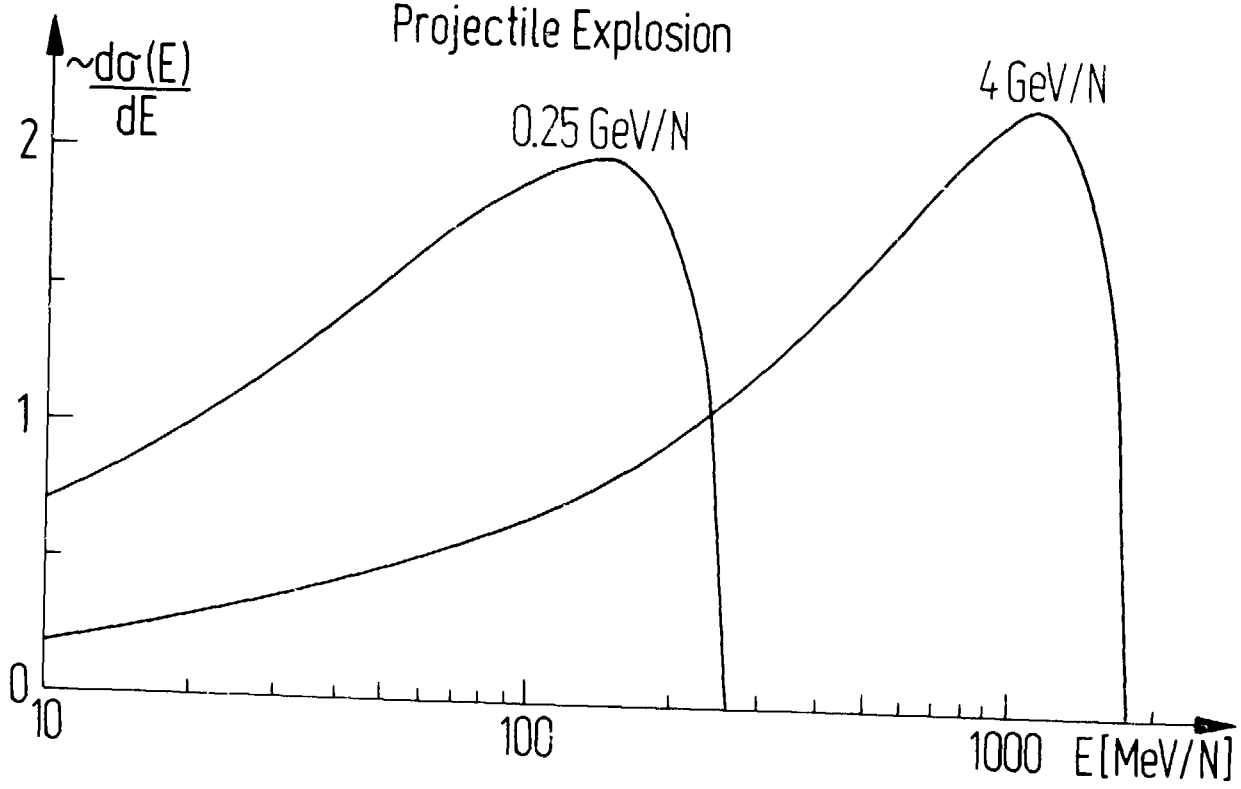
Projectile Explosion
~dσ(E)/dE
2
1
0
0.25 GeV/N
4 GeV/N
10
100
1000
E[MeV/N]

Fig.6

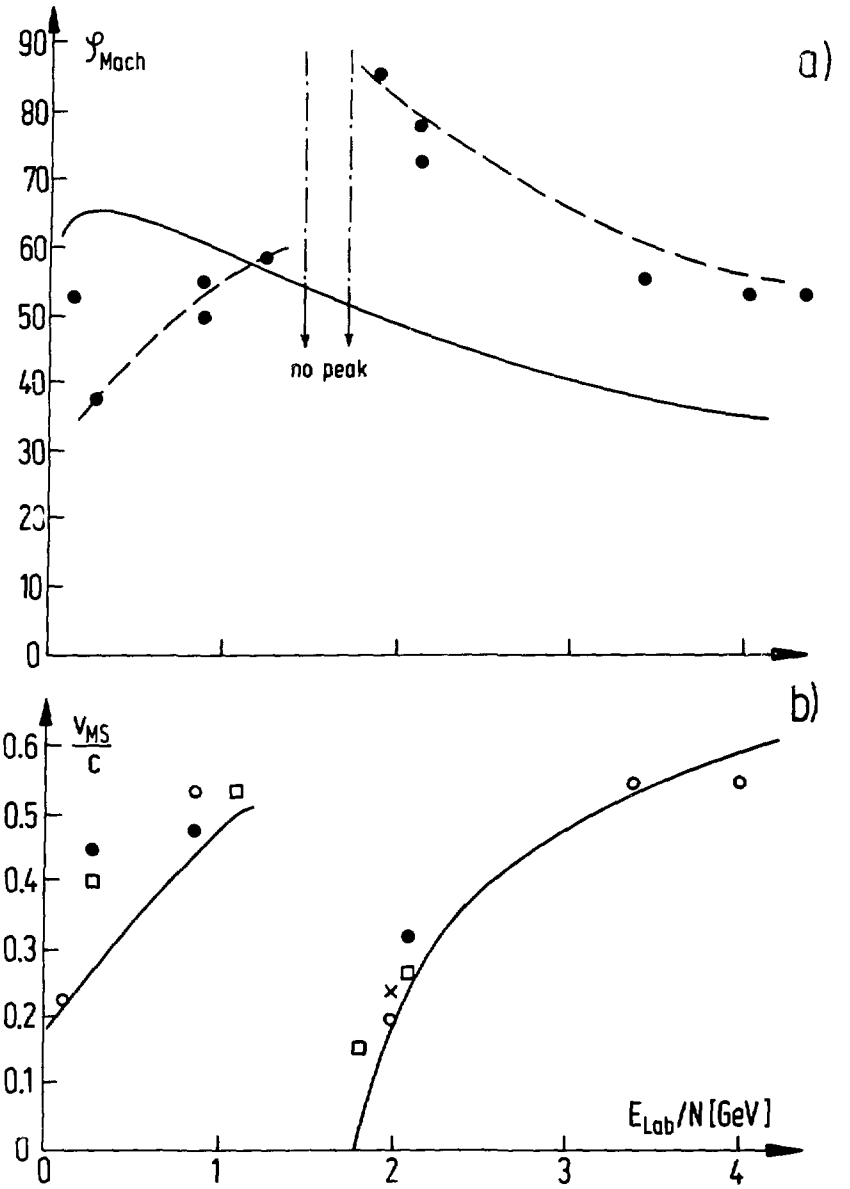
a)
φ_{Mach}
90
80
70
60
50
40
30
20
10
0
no peak
b)
$\frac{V_{MS}}{C}$
0.6
0.5
0.4
0.3
0.2
0.1
0
0
1
2
3
4
E_{Lab}/N [GeV]

Fig.7

CONF-770602--3

PIONIC INSTABILITIES IN HIGH-ENERGY HEAVY ION COLLISIONS*

Miklos Gyulassy
Nuclear Science Division, Lawrence Berkeley Lab,
University of California, Berkeley CA 94720

I. Introduction

Heavy ion scattering at energies 0.2 - 2.0 GeV/nucleon provides a unique opportunity to study properties of nuclear systems far outside the realm of conventional nuclear physics. In such collisions nuclear matter could be compressed to densities $\rho \sim (2\text{-}4)\rho_0$ where $\rho_0 \approx 0.17\ \text{fm}^{-3} \approx m_\pi^3/2$. At these densities collective phenomena may become important, leading to phase transitions in the nuclear system. Indeed, model calculations[1,2] for cold nuclear systems (T = 0) indicate that above some critical density $\rho_c \sim (1\text{-}2)\rho_0$, the pion field acquires a finite ground state expectation value. This phase transition, called pion condensation, would lead to a spin-isospin lattice, $\langle \psi^+(x)\sigma_i \tau_\alpha \psi(x)\rangle = \chi_{i\alpha} \exp(i\,\tilde{k}_c\tilde{x})$ with wavelength $2\pi/k_c \sim (3\text{-}5)\, m_\pi^{-1}$ in the nuclear system. While densities $\rho > \rho_c$ could easily be reached in heavy ion collisions, these high densities are produced only at the price of high excitation energies E^* as well. For these collisions, E^* is typically on the order of 50-100 MeV/nucleon.

One may expect that such high excitation energies would tend to inhibit, if not eliminate, any possible collective instabilities involving the coherent interaction of many nucleons. This is certainly the case if the system has come to thermal equilibrium. In that case E^* is converted into random motion of the nucleons, and as E^* increases, so does the disorder in the system. Long range correlations will then eventually be destroyed as E^* increases. However, in non-equilibrium systems E^* can be tied up in ordered motion, e.g. half of the nucleons have momentum $\approx \tilde{p}_{cm}$ while the other half have momentum $\approx -\tilde{p}_{cm}$. In this case, collective instabilities may actually be enhanced as E^* increases!

The most familiar example that illustrates this dependence on E^* is colliding plasma beams.[3] Below some critical velocity v_c all plasmon modes are stable. However, as the relative velocity v increases beyond v_c, certain plasmon modes become unstable. This instability leads then to the growth of strong, collective electric fields with a growth rate that increases as a function of $v - v_c$. The instability exists, however, only in the non-equilibrium stage of the collision. As the plasma beams thermalize through the interactions with these collective fields, the plasmon instabilities disappear.

In heavy ion collisions we look for analogous collective instabilities. The analogue of the electric field in nuclear systems is the pion field. The program then is

(1) to determine whether pionic instabilities can exist at the densities and excitation energies expected in heavy ion collisions,
(2) to calculate growth rates of unstable pion modes, and

(3) to determine the effect such instabilities would have on the dynamics in heavy ion collisions.

II. Unstable pion modes in excited nuclear matter

The existence of pionic instabilities in excited nuclear matter was first investigated for thermal equilibrated systems.[4] The critical temperature $T_{crit}(\rho)$ is shown in Fig. I. For a given density ρ, nuclear matter is unstable with respect to pion condensation for $T < T_{crit}(\rho)$. The details of the calculation of T_{crit} are given in Ref. (4). The paths AB and BC follow the hydrodynamic compression and decompression of nuclear matter in heavy ion collisions. Curve AB is taken from Ref. (5) and corresponds to the solution of the Rankine shock equation for compressibility K = 300 MeV including also Δ_{33} isobar production. Curve BC is a guess for the decompression path noting that as the system expands, the compression energy E_{comp} at point B is converted into thermal energy E_{therm} by point C. Estimates in Ref. (5) indicate $E_{comp}/E_{therm} \sim 1/10$. As the system expands it also cools down through evaporation of nucleons. Beyond point C the system becomes so diffuse that local thermal equilibration can no longer be assumed. The important point to note in Fig. I is that for the maximum densities, ρ_B, expected at these energies (see Fig. 14 of Ref. (5)), the temperature T_B is less than $T_{crit}(\rho_B)$. Therefore, pion condensation is likely to occur in spite of the relatively high temperatures in heavy ion collisions.

We turn now to the question of whether pionic instabilities can also occur during the non-equilibrium stage of the collision. We are then looking for the pion field analogue of the two beam instability in plasmas.[3] The following considerations motivate our study of non-equilibrium systems. First, the stopping distance λ_L of a nucleon in nuclear matter is estimated to be $\lambda_L \gtrsim 4$ fm for $E_{lab} \gtrsim 1$ GeV. The thermalization time τ_{th} is then roughly $\tau_{th} \sim 2\lambda_L/v_{rel} \sim 2 - 3 \times 10^{-23}$ sec. Therefore, a substantial fraction of the total interaction time $\tau_{int} \sim 2 R_{target}/v_{rel} \sim 3 - 6 \times 10^{-23}$ sec involves non-equilibrium dynamics. Second, the effects of collective instabilities on the dynamics may in fact be greatest during that non-equilibrium stage of the collision. Depending on the ratio of the growth rate Γ_{col} of collective fields to the two body scattering rate Γ_{scat}, the dynamics will be categorized[7] either by (1) wave-particle interactions as in collisionless plasmas or (2) particle-particle interactions as in hydrodynamics. We discuss this point further in section IV.

As a model of the initial, non-equilibrium momentum distribution of nucleons we take[7]

$$n(\tilde{p}) = n_o(\tilde{p} + \tilde{p}_{cm}) + n_o(\tilde{p} - \tilde{p}_{cm}) \qquad (1)$$

with $n_o(\tilde{p}) = \theta(p_F - |\tilde{p}|)$ as illustrated in Fig. II. To look for pionic instabilities, we search for complex poles of the pion propagator $\Delta(\omega,\tilde{k})$.

In nuclear matter, $\Delta(\omega,\tilde{k})$ differs from the free space propagator $\Delta_o(\omega,\tilde{k}) = (\omega^2 - k^2 - 1 + i\varepsilon)^{-1}$ because of the polarizability of the medium as shown in Fig. IIIa. In terms of the polarization operator[1,2] $\Pi(\omega,\tilde{k})$,

$$\Delta^{-1} = \Delta_o^{-1} - \Pi \quad . \tag{2}$$

The dominant interactions that must be included in Π are[1,2] (1) the P-wave πNN interaction, (2) the P-wave $\pi N\Delta$ resonance interaction, and (3) hard core NN, NΔ and $\Delta\Delta$ interactions that lead to nucleon and isolar correlations. In symmetric nuclear matter the S-wave πN interaction does not contribute in lowest order.

The πNN interaction leads to a contribution Π_{NN} to the polarization operator due to the excitation of nucleon particle-hole states. We consider here only spin-isospin saturated nuclear systems having reflection symmetric momentum distributions ($n(\tilde{p}) = n(-\tilde{p})$). In that case[1,2,7]

$$\Pi_{NN}(\omega,\tilde{k}) = -i\,4\,f^2k^2\,F_\pi^2(\omega,\tilde{k}) \int \frac{d^4p}{(2\pi)^4}\; S_N(p)\; S_N(p+k) \tag{3a}$$

$$= 4f^2k^2F_\pi^2(\omega,\tilde{k}) \int \frac{d^3p}{(2\pi)^3}\; n(\tilde{p})\;\; (1-n(\tilde{p}+\tilde{k}))$$

$$\times \left\{ \frac{1}{\omega-\omega_{pk}+i\varepsilon} \;-\; \frac{1}{\omega+\omega_{pk}-i\varepsilon} \right\} \tag{3b}$$

$$= \frac{1}{\pi}\int_{-\infty}^{\infty} d\omega'\;\; I_{NN}(\omega',\tilde{k}) \left\{ \frac{1}{\omega-\omega'+i\varepsilon} - \frac{1}{\omega+\omega'-i\varepsilon} \right\} \tag{3c}$$

The non-relativistic nucleon propagator S_N is

$$S_N(p_o,\tilde{p}) = \frac{n(\tilde{p})}{p_o-\varepsilon_N(\tilde{p})-i\varepsilon} + \frac{(1-n(\tilde{p}))}{p_o-\varepsilon_N(\tilde{p})+i\varepsilon} \quad , \tag{4}$$

with $\varepsilon_N(\tilde{p})$ being the single particle energies. In eq. (3b), $\omega_{pk} = \varepsilon_N(\tilde{p}+\tilde{k}) - \varepsilon_N(\tilde{p})$. The πNN coupling $f^2 \approx m_\pi^{-2}$ and the form factor $F_\pi(\omega,\tilde{k})$ is taken to be

$$F_\pi(\omega,k) = (\Lambda^2 - 1)/(\Lambda^2 - \omega^2 + k^2) \tag{5}$$

with $\Lambda \approx M_N/m_\pi = 6.7$. Dipole form factors[8] with $\Lambda \approx 8.3$ differ by $< 10\%$ for the ω,k considered here.

In the dispersion relation form, eq. (3c), I_{NN} measures the discontinuity of Π_{NN} across cuts in the upper and lower half ω plane. These cuts arise because a pion of momentum $\tilde{k}$ and energy $\omega = \omega_{pk}$ can decay into a one particle - one hole excitation conserving energy-momentum.

Through the resonant $\pi N\Delta$ interaction, a pion can excite not only nucleon particle-hole states via Π_{NN} but also Δ-particle-nucleon hole states via $\Pi_{N\Delta}$, where

$$\Pi_{N\Delta}(\omega,\tilde{k}) = -i\, f_\Delta^2\, k^2 F_\pi^2(\omega,\tilde{k}) \int \frac{d^4p}{(2\pi)^4} \Big\{ S_N(p)\, S_\Delta(p+k) + S_N(p)\, S_\Delta(p-k) \Big\} \quad . \tag{6}$$

In. eq. (6), the Δ intermediate state is included in both s and u channels (direct + cross graphs). The $\pi N\Delta$ coupling (including spin-isospin factors) is[1,7] $f_\Delta^2 \approx 8 m_\pi^{-2}$. The form factor is taken to be the same as the πNN form factor, eq. (5), as suggested by fits to $\nu p \to \mu^- \Delta^{++}$ data.[9] For the Δ propagator we take

$$S_\Delta(p_o,\tilde{p}) = (p_o - \varepsilon_\Delta(\tilde{p}) - i\,\mathrm{Im}\,\Sigma_\Delta(p_o,\tilde{p}) + i\varepsilon)^{-1} \quad , \tag{7}$$

where the Δ self energy Σ_Δ is included to account for the finite Δ width. The real part of Σ_Δ is absorbed into $\varepsilon_\Delta(\tilde{p})$, which we approximate by $\varepsilon_\Delta(\tilde{p}) = m_\Delta + p^2/2m_\Delta$, with $m_\Delta = 8.8\, m_\pi$. $\mathrm{Im}\,\Sigma_\Delta \neq 0$ when the Δ can decay to a free pion and nucleon, i.e., when $p_o^2 - p^2 \geq (m_N + m_\pi)^2$. We ignore the relatively small modification of Σ_Δ due to the presence of nuclear matter[10] and take the free space value of Σ_Δ. The effect of $\mathrm{Im}\,\Sigma_\Delta$ is to smear out the Δ mass. We therefore write

$$S_\Delta(p) = \int_0^\infty dm\, \rho_\Delta(m) S_\Delta(p;m) \quad , \tag{8}$$

where

$$S_\Delta(p,m) \equiv (p_o - m - \frac{\tilde{p}^2}{2m_\Delta} + i\varepsilon)^{-1} \quad . \tag{9}$$

Then computing $\mathrm{Im}\, S_\Delta$ from eqs. (7,8,9), the Δ spectral density is seen to be

$$\rho_\Delta(m) = -\frac{1}{\pi}\,\mathrm{Im}\, S_\Delta(p_o = m + p^2/2m_\Delta\,,\ \tilde{p}) = \frac{c_\Delta\, \gamma_\Delta(m)}{(m-m_\Delta)^2 + \gamma_\Delta^2(m)} \quad , \tag{10}$$

The $\tilde{p}$ dependence of ρ_Δ and γ_Δ in eqs. (8,10) can be neglected because of

the small Δ width $\Gamma_\Delta = 2\gamma_\Delta(m_\Delta) = 120$ MeV $\Rightarrow \gamma_\Delta/m_\Delta << 1$. Then $\gamma_\Delta(m) \approx$ - Im $\sum_\Delta(m^2)$. For the moment $c_\Delta = 1/\pi$. We note that canonical anti-commutation stations for the Δ field require that

$$\int_0^\infty \rho_\Delta(m)dm = 1 \tag{11}$$

As long as $(p_o,\tilde{p})$ in eq. (8) is not near threshold ($m = m_N + m_\pi$), a good approximation for $S_\Delta(p)$ is obtained by taking $\rho_\Delta(m)$ to be Lorenzian, i.e., setting

$$\gamma_\Delta(m) = \theta(m-m_N-m_\pi)\ \theta(2m_\Delta-m_N-m_\pi-m)\ \gamma_\Delta(m_\Delta) \quad . \tag{12}$$

The upper mass cut off is chosen to give a symmetric weight of masses in eq. (8) about m_Δ. Larger mass are estimated to contribute only $\sim$10% to the sum rule, eq. (11), as a result of the small Δ width, γ_Δ=.43 m_π. With eq. (12), c_Δ in eq. (10) is then determined so that eq. (11) is satisfied.

With eqs. (6,8) we then get for $\Pi_{N\Delta}$

$$\Pi_{N\Delta}(\omega,\tilde{k}) = f_\Delta^2 k^2 F_\pi^2(\omega,\tilde{k}) \int_0^\infty dm\ \rho_\Delta(m) \left[U_{N\Delta}(\omega,\tilde{k};m) + U_{N\Delta}(-\omega,-\tilde{k};m) \right] \tag{13}$$

where the NΔ Lindhard function is

$$U_{N\Delta}(\omega,\tilde{k};m) = \int \frac{d^3p}{(2\pi)^3} \frac{n(\tilde{p})}{\omega + (m_N-m) + \frac{p^2}{2m_N} - \frac{(\tilde{p}+\tilde{k})^2}{2m_\Delta} + i\epsilon} \quad . \tag{14}$$

Note, eq. (13) reduces to eq. (4.4) of Ref. (7) when $\rho_\Delta(m) = \delta(m - m_\Delta)$. The inclusion of the finite Δ width will be important when we estimate on-shell pion production rates in section III. As in eq. (3c), it is convenient to write

$$\Pi_{N\Delta}(\omega,\tilde{k}) = \frac{1}{\pi} \int_{-\infty}^{\infty} d\omega'\ I_{N\Delta}(\omega',\tilde{k}) \left\{ \frac{1}{\omega-\omega'+i\epsilon} - \frac{1}{\omega+\omega'-i\epsilon} \right\} \quad . \tag{15}$$

Expressions for scattering rates become more compact in terms of I_{NN} and $I_{N\Delta}$ in section III.

Note that $\Pi_{NN} + \Pi_{N\Delta}$ is the pion-nucleon forward scattering amplitude summed over all the nucleons in the medium; Π_{NN} is the Born term involving only a single nucleon intermediate state while $\Pi_{N\Delta}$ is a model for the contribution from πN continuum intermediate states. The strong distortion of the πN continuum near the Δ_{33} resonance is described by $\rho_\Delta(m)$ in eq. (10). The propagation of a pion in the medium via eq. (2) with $\Pi = \Pi_{NN} + \Pi_{N\Delta}$ then consists of a series of elastic πN scatterings. However, in this multiple scattering series only one pion exchange (OPE) is included between successive collisions. Clearly, multiple meson exchange must also be included, especially the exchange of vector mesons ρ,ω that give rise to the hard core repulsion between nucleons. These interactions tend to keep nucleons apart and lead to short range correlations in the medium.

Such correlations are included in Π via an effective interaction $G_c(\tilde{k})$ as illustrated in Fig. IIIb. The correlated polarization operator is then[2,7]

$$\Pi(\omega,\tilde{k}) = \frac{\Pi_{NN}(\omega,\tilde{k}) + \Pi_{N\Delta}(\omega,\tilde{k})}{1 - G_c(k)\,(\Pi_{NN}(\omega,\tilde{k}) + \Pi_{N\Delta}(\omega,\tilde{k}))} \quad . \qquad (16)$$

Detailed calculations[11] show that $G_c(k) \approx g/k^2$, where the correlation parameter $g = 0.5 \pm 0.1$. This form of G_c follows[7] when the πNN and $\pi N\Delta$ vertices are included in the definition of Π_{NN} and $\Pi_{N\Delta}$ as in eqs. (3,13). The parameter g measures the strength of the repulsive hard core NN, NΔ, and $\Delta\Delta$ interactions. A value of $g = 1/3$ would just remove the attractive $\delta(\tilde{x})$ part of the OPE potential.[2] A value of $g = 2/3$ would then reverse the sign of that $\delta(\tilde{x})$ part of OPE.

Evaluating eq. (16) for the system specified by eq. (1), the singularities of $\Delta(\omega,\tilde{k})$ in eq. (2) and hence the pion spectrum can be determined. These singularities are analyzed in detail in Ref. 7. To look for unstable pion modes, we search for complex roots $\omega = \mathrm{Re}\,\omega_c(\tilde{k}) + i\gamma(\tilde{k})$ of $\Delta^{-1}(\omega,\tilde{k}) = 0$. As discussed in Ref. (7), $\gamma(\tilde{k})$ can be interpreted as the rate for spontaneous $\pi^+\pi^-$ or $\pi^o\pi^o$ phonon pair creation where one phonon carries momentum $\tilde{k}$ while the other carries $-\tilde{k}$. The rates $\gamma(\tilde{k})$ computed for typical non-equilibrium configurations, eq. (1), encountered in heavy ion collisions are presented in Figs. IV-VI. The contour lines define surfaces $k_\alpha(\theta_\pi)$ in the pion phase space on which $\gamma(k_\alpha(\theta_\pi), \theta_\pi, \phi_\pi) = \alpha$, where α is a constant. In these figures, α is chosen to be multiples of $0.1\,m_\pi$. The angle θ_π refers to the angle between the pion wavevector $\tilde{k}$ and $\tilde{p}_{cm}$ in eq. (1). The symmetry of $n(\tilde{p})$ in eq. (1) implies that $\gamma(k,\theta,\phi)$ is independent of ϕ and $\gamma(k,\theta) = \gamma(k,\pi-\theta)$.

The regions of phase space where unstable pion modes exist are bounded by critical surfaces $k_c(\theta) = \lim k_\alpha(\theta)$ for $\alpha \to 0^+$. In Figs. IV-VI, we find up to three distinct regions for pionic instabilities. These regions are differentiated from one another by the real parts of the frequencies, $\mathrm{Re}\,\omega_c(\tilde{k})$, for those unstable modes. In region I, $\mathrm{Re}\,\omega_c = 0$;

in region II, Re $\omega_c \approx 0.5\ m_\pi$; in region III, Re $\omega_c \gtrsim m_\pi$. Only the zero frequency modes (I) were considered in Ref. (7). The finite frequency instabilities (II,III) are the analogues of the two beam plasma instabilities[3] that we sought for these non-equilibrium configurations. The phase space for these instabilities is seen to decrease with decreasing p_{cm} and vanishes once the system comes to thermal equilibrium. This is in contrast to the zero frequency instabilities (I) that survive in equilibrated system if $T < T_c(\rho)$ in Fig. I. Further discussion of the differences between instabilities in these regions will be given elsewhere.

The essential feature we want to note here is that the typical phonon pair creation rates $\gamma(\tilde{k})$ are in the range $(0.1 - 0.2)\ m_\pi$. The number of phonons created per unstable mode $\tilde{k}$ is then on the order of one per 1.5×10^{-23} sec. Therefore, there is enough time during the characteristic (thermalization) time $\tau_{th} \sim (2 - 3) \times 10^{-23}$ sec, that specifies the duration of the non-equilibrium phase of the collision, for such pionic instabilities to develop. However, the number of phonons created per mode during this time is small, $\sim 1 - 2$, and thus the term pion condensation is not really appropriate for such systems.

The total number of unstable pion modes is[7]

$$n^\pi_{crit} = \int \frac{3V d^3k}{(2\pi)^3}\, \theta(\gamma(\tilde{k})) \equiv V/V^\pi_{crit} \quad , \qquad (17)$$

where V is the volume of nuclear matter where eq. (1) applies. Typically, we estimate $V \approx A_p/\rho_o = 2A_p\ m_\pi^{-3}$ = volume of projectile nucleus. The critical volume V^π_{crit} defined by eq. (17) is calculated to be in the range $(0.5 - 1.0)\ m_\pi^{-3} \Rightarrow n^\pi_{crit} \approx (2 - 4)\ A_p$. The total number of $\pi^\pm, \pi^o$ phonons that are created in the non-equilibrium phase is then estimated to be $\langle\gamma\rangle\ n^\pi_{crit}\ \tau_{th} \sim 4A_p$.

It is important to note the sensitivity of these estimates to the value of the correlation parameter g in eq. (16). Except for Fig. Vb, all calculations were made with g = 0.5. In Fig. Vb, we took g = 0.6. Compared to Fig. Va, the phase space of instabilities is seen to decrease very much. In fact, the pair production rate per unit volume[7], $\Gamma_{col}/V = \langle\gamma\rangle/V_{crit}$, decreases from $0.18\ m_\pi^4$ to $0.025\ m_\pi^4$ when g is increased from 0.5 to 0.6. For $g \gtrsim 0.65$, no instabilities are found. Therefore, with 20% uncertainties in estimates[2,11] for g, the above calculations with g = 0.5 can be considered only as order of magnitude estimates for $\langle\gamma\rangle$ and V^π_{crit}.

Finally, we note in Figs. IV-VI that the wavenumbers k of unstable modes are typically $\sim(2 - 3)\ m_\pi$. This is of course due to the P-wave nature of the πN interaction in eqs. (3,13). The wavelengths $2\pi/k \sim (3 - 5)$ fm of such modes are then comparable or less than the dimensions of nuclear systems involved in heavy ion collisions.

Therefore, infinite nuclear matter calculations, eqs. (2,16), can be applied to heavy ion collisions only as a result of the large values of k for pionic instabilities.

III. Effects of Pionic Instabilities on the Dynamics

Collective instabilities effect the dynamics in two essential ways: (1) through the growth of collective fields via spontaneous phonon pair creation, and (2) through the modification of two body scattering rates via phonon rather than bare meson exchange. To evaluate the importance of each effect, we first seek a formalism that incorporates them both. A convenient formalism was found in Ref. (7) that involves the calculation of the complex correlation energy density, M_{RPA}, of the system in the Random Phase Approximation. In terms of M_{RPA}, the decay rate Γ of an excited many body state is given by[7]

$$\Gamma = -2V \, \mathrm{Im} \, M_{RPA} \quad . \tag{18}$$

Diagrammatically, M_{RPA} is the sum of connected ring diagrams as shown in Fig. VII. A general term in this sum consists of a product of n bubbles and n interactions, where each bubble represents $\Pi_{NN} + \Pi_{N\Delta}$ and each interaction represents $\Delta_o + G_c$. Evaluating M_{RPA}, the decay rate per unit volume is found to be[7]

$$\Gamma/V = \mathrm{Re} \int \frac{3d^4k}{(2\pi)^4} \log \varepsilon(\omega,\tilde{k}) \quad , \tag{19}$$

where

$$\varepsilon(\omega,\tilde{k}) = 1 - (\Delta_o + G_c)(\Pi_{NN} + \Pi_{N\Delta}) \tag{20}$$

is the generalized "dielectric" function for the nuclear system. In non-equilibrium systems, the singularities of $\varepsilon(\omega,\tilde{k})$ include overlapping cuts in the ω plane, as seen from eqs. (3c,15), and isolated zeros at $\omega = \mathrm{Re}\,\omega_c(\tilde{k}) + i\gamma(\tilde{k})$ as found in section II. Equation (19) is then most easily evaluated by first integrating over ω by parts giving[7]

$$\Gamma/V = \int \frac{3d^3k}{(2\pi)^3} \gamma(\tilde{k}) - \frac{1}{2} \int \frac{3d^4k}{(2\pi)^4} \log \left(1 - 4\, I(\omega) I(-\omega) |\Delta_c|^2\right)$$

$$\equiv \Gamma_{col}/V + \Gamma_{scat}/V \quad , \tag{21}$$

where

$$I(\omega,\tilde{k}) = I_{NN}(\omega,\tilde{k}) + I_{N\Delta}(\omega,\tilde{k}) \tag{22}$$

is defined via eqs. (3c,15), and

$$\Delta_c(\omega,\tilde{k}) = (\Delta_o(\omega,\tilde{k}) + G_c(\tilde{k}))/\varepsilon(\omega,\tilde{k}) \qquad (23)$$

is the correlated pion propagator. Equation (21) allows us to calculate the growth rate of collective fields via Γ_{col} and the scattering rate Γ_{scat} in non-equilibrium systems, eq. (1). A further decomposition of Γ_{scat} is possible noting that the integrand vanishes unless $I(\omega)I(-\omega) \neq 0$. Then

$$\Gamma_{scat} = \Gamma_{NN} + \Gamma_{N\Delta} + \Gamma_{\Delta\Delta} \qquad (24)$$

where

$$\begin{Bmatrix} \Gamma_{NN} \\ \Gamma_{N\Delta} \\ \Gamma_{\Delta\Delta} \end{Bmatrix} = \int \frac{3Vd^4k}{(2\pi)^4} \begin{Bmatrix} 2\ I_{NN}(\omega) I_{NN}(-\omega) \\ 4\ I_{NN}(\omega) I_{N\Delta}(-\omega) \\ 2\ I_{N\Delta}(\omega) I_{N\Delta}(-\omega) \end{Bmatrix} P(\omega,k) |\Delta_o + G_c|^2 \quad , \qquad (25)$$

and the polarization form factor P is

$$P(\omega,\tilde{k}) = \frac{-\log(1 - 4\, I(\omega)\ I(-\omega) |\Delta_c|^2)}{4\, I(\omega)\ I(-\omega) |\Delta_o + G_c|^2} \quad . \qquad (26)$$

Γ_{NN} is the effective elastic NN → NN scattering rate, while $\Gamma_{N\Delta}$ and $\Gamma_{\Delta\Delta}$ are the effective inelastic NN → NΔ and NN → ΔΔ rates in the medium. In the low density limit, $\Pi_{NN} + \Pi_{N\Delta} \to 0 \Rightarrow P(\omega,\tilde{k}) \to 1$, and Γ_{ij} reduce to rates calculated with free space cross sections, $d\sigma^o$, i.e.

$$\Gamma_{ij}/V \xrightarrow[\rho \to 0]{} \Gamma^o_{ij}/V \equiv \rho^2 < \sigma^o_{NN \to ij}\ v_{rel} > \quad . \qquad (27)$$

Diagrammatically, only the third term in Fig. VII contributes to Γ_{ij} in the low density limit, giving $d\sigma^o \propto |\Delta_o + G_c|^2$. At high densities effective two body (elastic and inelastic) cross sections, $d\sigma_{eff}$, can be derived[7] from eq. (25) giving

$$d\sigma_{eff} = P(\omega,\tilde{k})\ d\sigma^o \quad , \qquad (28)$$

where $(\omega,\tilde{k})$ are the energy-momentum transfers in the process. Therefore, $P(\omega,\tilde{k})$ contains the density and configuration dependence of the effective cross sections in the medium. For systems close to <u>equilibrium</u>, P reduces to[7]

$$P(\omega,\tilde{k}) \approx \frac{1}{|\varepsilon(\omega,\tilde{k})|^2} \quad , \qquad (29)$$

as is found in the kinetic theory of plasmas.[12] The important point to note about eq. (28) is that the existence of collective instabilities implies that there exist certain critical values of $(\omega_c, \tilde{k}_c)$ such that $P(\omega_c, \tilde{k}_c) \to \infty$ and hence $d\sigma_{eff} \to \infty$ if the energy-momentum transfer $(\omega_c, \tilde{k}_c)$ is kinematically allowed. This is known as critical scattering phenomena and is extensively discussed in Ref. (7). Thus the presence of the polarization factor in eq. (28) leads to enhanced scattering rates if instabilities are present.

As an example of the kind of enhancements pionic instabilities lead to, $P(\omega,\tilde{k}) = d\sigma_{eff}/d\sigma^o$ is plotted in Fig. VIII for $p_{cm} = 4m_\pi$ in eq. (1). This figure is taken from Ref. 7 and corresponds to the elastic ($\omega = 0$) scattering of a nucleon of momentum $\tilde{p}_{cm}$ with another of momentum $-\tilde{p}_{cm}$ in the medium. Kinematically, $\tilde{k}$ is constrained by $k = 2\, p_{cm} \cos\theta_\pi$. Logarithmic divergencies of $d\sigma_{eff}$ at $k \approx 1.5$ and $2.0\ m_\pi$ arise when kinematically allowed values of (k,θ_π) lie on the boundary of region I of unstable pion modes (see Fig. XIV of Ref. 7 and Fig. Va here). Figure VIII illustrates then critical scattering phenomena for large momentum transfers that arise as a result of pionic instabilities.

The integrated scattering rates are given in Table I for a variety of lab kinetic energies, $T_L \sim (0.4 - 1.5)$ GeV/nucleon. It must be emphasized that the spirit of these calculations is to obtain only order of magnitude estimates of the effects of pionic instabilities on these rates. We cannot expect to predict absolute rates with such a simple model. Nevertheless, the ratios of effective rates Γ^{eff}_{ij} to free rates Γ^o_{ij} do indicate the magnitude of enhancements that can arise due to collective phenomena. The rates in table I were obtained by integrating numerically eq. (25) up to momentum transfers $k = 8\ m_\pi$. The free rates Γ^o_{ij} were obtained from eq. (25) by setting $P(\omega,\tilde{k}) = 1$. To set a scale for the absolute magnitudes of Γ_{ij}, note that a 20 mb cross section in eq. (27) would give $\Gamma_{ij}/V \approx 0.25\ m_\pi^4$. The essential point to note in tables IA,B is that both the elastic and inelastic scattering rates are enhanced by factors $\sim (2 - 4)$ due to pionic instabilities. Further details of these calculations will be given elsewhere.

IV. Summary

Model calculations of dense, excited nuclear matter expected in heavy ion collisions indicate that in both thermal[4] and non-equilibrium[7] extremes pionic instabilities can be expected. The typical excitation energies involved in these high energy ($\sim$ 1 GeV/nuc) collisions are not too large to prevent such instabilities. Furthermore, the spontaneous phonon pair creation rates $\gamma(\tilde{k})$ were shown to be sufficiently large for these instabilities to develop during the short collision times. In the non-equilibrium case finite frequency instabilities (regions II,III) were found as well as zero frequency (condensate) instabilities (region I). The total $\pi^+\pi^-$ and $\pi^o\pi^o$ phonon pair creation rate $\Gamma_{col} = \langle\gamma\rangle\, V/V^\pi_{crit} \equiv \Gamma_o + \Gamma_{\pi'}$ is given in table IC, with Γ_o being the

rate for zero frequency pairs and Γ_π, being the rate for finite frequency pairs. We noted also the short wavelengths $2\pi/k_c \sim (3 - 5)$ fm of these pion modes as being essential for such instabilities to develop in the finite size nuclear systems involved.

Then through the calculation of the complex correlation energy, the effect of pionic instabilities on the dynamics was studied. The main result is that critical scattering phenomena leads to enhancements of both elastic and inelastic scattering rates by factors $\sim 2 - 4$. We can now assess the relative importance of the two effects mentioned at the beginning of section III. The ratio $\Gamma_{col}/\Gamma_{scat}$ of rates in eq. (21) provides a measure of which effect dominates. This ratio is given table IC. Note that $\Gamma_{col}/\Gamma_{scat} < 1$ in all cases indicating that the scattering rates are greater than the growth rates of collective fields. Therefore, the dynamics is dominated by two body collisions involving density dependent interactions, eq. (28). The reduction by 2 - 4 of the effective nucleon mean free path in the medium is therefore expected to lead to more rapid thermalization, indicating that a hydrodynamic description[5,6,13] of the dynamics would be appropriate.[7]

Finally, we comment on the implication of the enhancement of $\Gamma^{eff}_{N\Delta}$ in the medium in connection with real pion production. It is tempting to assume that a factor of 2 enhancement of the $NN \to N\Delta$ rate would lead to twice as many pion being observed in the lab. However, the final number of pions observed depends not only on the production rate $\Gamma_{N\Delta}$ but also sensitively on the absorption rates of pions. Therefore, to estimate real pion production rates, the effects of pionic instabilities on pion absorption rates must also be investigated. Such an investigation is currently in progress.

References

*This work was done with support from the U.S. Energy Research and Development Administration.

1. A. B. Migdal, O. A. Markin, I. I. Mishustin, Sov. Phys. JETP 39 (1974) 212

2. G. E. Brown, W. Weise, Phys. Reports 27C (1976) 1

3. O. Buneman, Phys. Rev. 115 (1959) 503

4. V. Ruck, M. Gyulassy, W. Greiner, Z. Physik A277 (1976) 391

5. H. G. Baumgart, J. U. Schott, Z. Sakamoto, E. Schopper, H. Stöcker, J. Hofmann, W. Scheid, W. Greiner, Z. Physik A273 (1975) 359

6. M. I. Sobel, P. J. Siemens, J. P. Bondorf, H. A. Bethe, Nucl. Phys. A251 (1975) 502

7. M. Gyulassy, W. Greiner, Ann. Phys. (in press)

8. W. A. Mann et al., Phys. Rev. Lett. 31 (1973) 844

9. P. A. Schreiner, F. V. Hippel, Phys. Rev. Lett. 30 (1973) 339

10. G. E. Brown, W. Weise, Phys. Rep. C22 (1975) 279

11. S. O. Bäckman, W. Weise, Phys. Lett. 55B (1975) 1;
G. Baym, G. E. Brown, Nucl. Phys. A247 (1975) 395

12. H. W. Wyld, D. Pines, Phys. Rev. 127 (1962) 1851

13. A. A. Amsden, F. H. Harlow, J. R. Nix, Los Alamos preprint
LA-UR-77-31 (1977)

Table Caption:

I. Collective Γ_{col} and scattering Γ_{ij} rates in non-equilibrium nuclear matter at various lab energies T_L.[ij] The $NN \to NN$ rates (A), $NN \to N\Delta$ rates (B), and spontaneous $\pi^+\pi^-$, $\pi^o\pi^o$ phonon pair creation rates (C) were calculated with eqs. (21,25). The enhancements of the scattering rates due to pionic instabilities are given by σ_{eff}/σ_o in A and B. The ratio $\Gamma_{col}/\Gamma_{scat}$ in C measures the importance of phonon pair production as compared to the modification of the scattering rates on the dynamics.

Figure Captions

I. Range of densities and temperatures where pion condensation is likely (shaded). T_{crit} is taken from Ref. (4) for $g = 0.5$. Curves AB and BC illustrate the compression and decompression phases in heavy ion collisions.

II. Initial non-equilibrium momentum distribution in heavy ion collisions.

III a) Pion propagator Δ in a nuclear medium.

b) Polarization operator Π including nucleon particle-hole and Δ_{33} - nucleon hole intermediate states as well as correlations.

IV. a) Contour plot for the rates $\gamma(k_\pi, \theta_\pi)$ of spontaneous $\pi^+\pi^-$ or $\pi^o\pi^o$ phonon pair creation in non-equilibrium nuclear matter, eq. (1), for $p_{cm} = 2.0\ m_\pi$. Contours correspond to multiples of $0.1\ m_\pi$ ($\approx 2 \times 10^{22}$ sec^{-1}). The angle θ_π is that between $\tilde{k}_\pi$ and $\tilde{p}_{cm}$. Zero frequency (Re $\omega_c = 0$) pionic instabilities occur in region I. Finite frequency (Re $\omega_c \neq 0$) instabilities occur in regions II, III.

b) Same as IVa but for $p_{cm} = 3.0\ m_\pi$.

V. a) Same as IVa but for $p_{cm} = 4.0\ m_\pi$.

b) Same as Va but with large correlation parameter $g = 0.6$.

VI. a) Same as IVa but for $p_{cm} = 5.0\ m_\pi$.

b) For $p_{cm} = 6.0\ m_\pi$.

VII. Series of ring diagrams included in the Random Phase Approximation for the correlation energy density $\mathcal{M}_{RPA}$ in eq. (18).

VIII. Ratio of the effective $d\sigma_{eff}$, to the free, $d\sigma_o$, elastic $(NN \to NN)$ differential cross sections as a function of momentum transfer k as calculated via eq. (28). (Taken from Fig. XIb of Ref. 7). This illustrates critical scattering phenomena due to pionic instabilities.

Table I

A. Elastic Scattering Rates

T_L(GeV/N)	p_{cm}/m_π	$\Gamma^{eff}_{NN}/V(m_\pi^4)$	$\Gamma^{o}_{NN}/V(m_\pi^4)$	$\sigma^{el}_{eff}/\sigma^{el}_{o}$
0.38	3	0.37	0.09	4.1
0.67	4	0.31	0.08	3.9
1.04	5	0.27	0.07	3.9
1.50	6	0.22	0.06	3.7

B. Inelastic Scattering Rates

T_L(GeV/N)	p_{cm}/m_π	$\Gamma^{eff}_{N\Delta}/V(m_\pi^4)$	$\Gamma^{o}_{N\Delta}/V(m_\pi^4)$	$\sigma^{in}_{eff}/\sigma^{in}_{o}$
0.38	3	0.24	0.06	4.0
0.67	4	0.58	0.28	2.1
1.04	5	0.72	0.42	1.7
1.50	6	0.64	0.39	1.6

C. Collective Rates

T_L(GeV/N)	p_{cm}/m_π	$\Gamma_{col}/V(m_\pi^4)$	$\Gamma_{\pi'}/\Gamma_o$	$\Gamma_{col}/\Gamma_{scat}$
0.38	3	0.21	0.47	0.34
0.67	4	0.18	0.47	0.20
1.04	5	0.25	0.50	0.25
1.50	6	0.59	3.20	0.69

Fig. 1

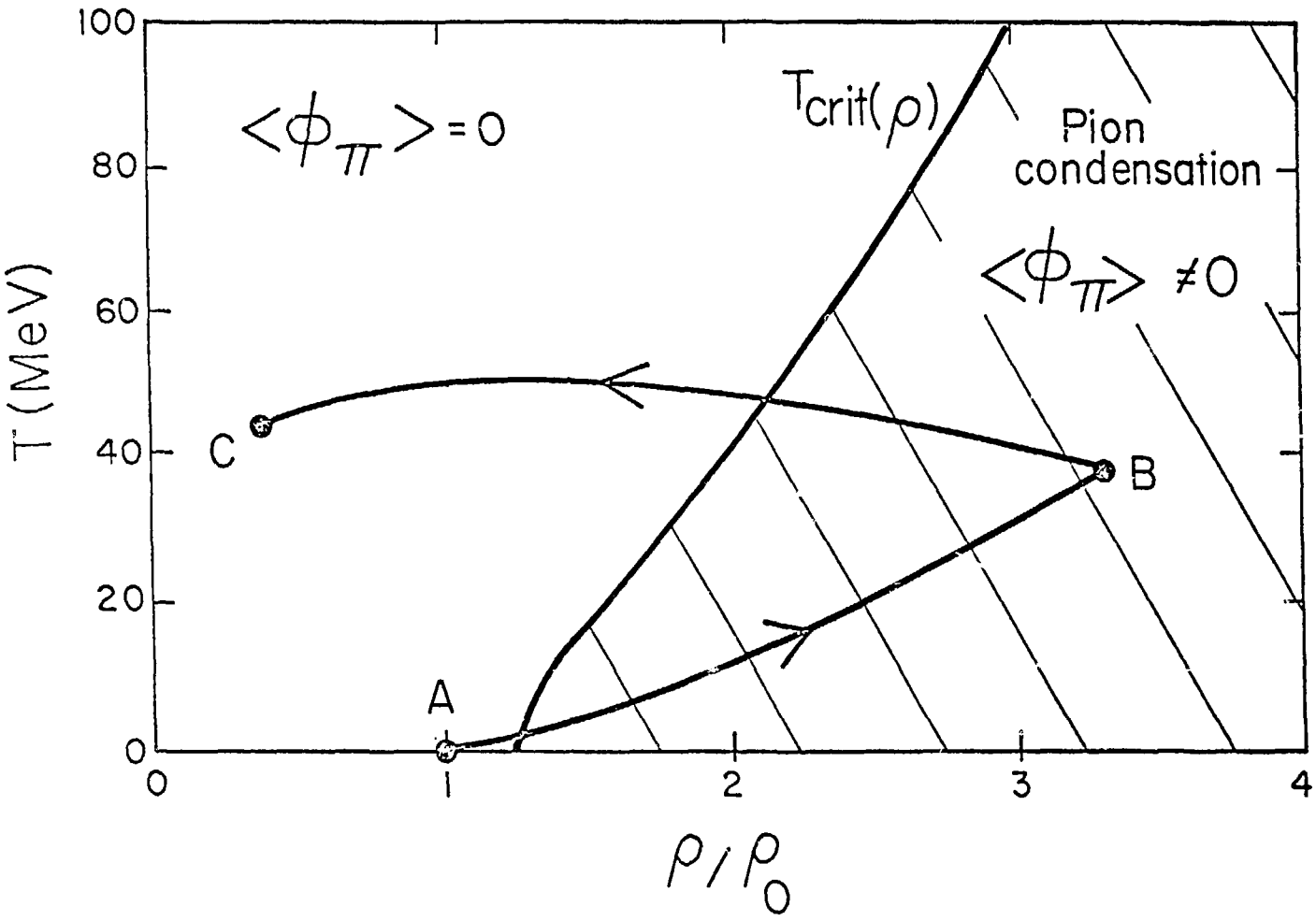

XBL776-1092

Fig. II

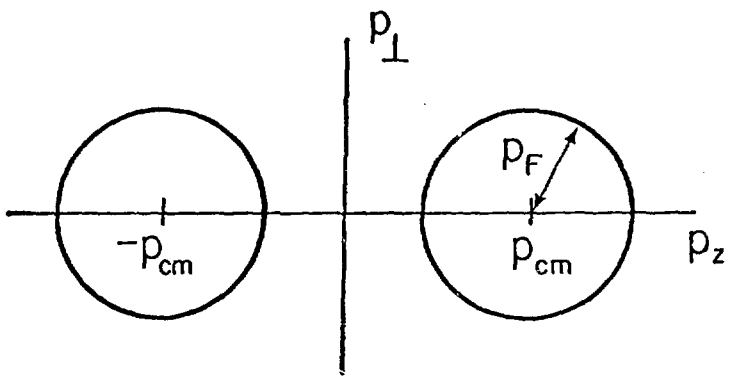

XBL776-1091

Fig. III

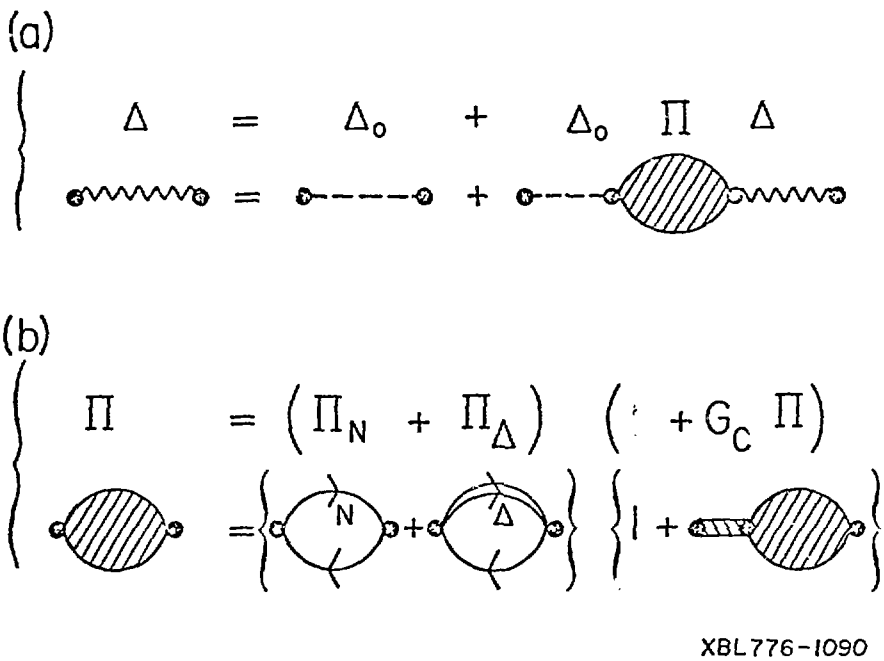

XBL776-1090

Fig. IV

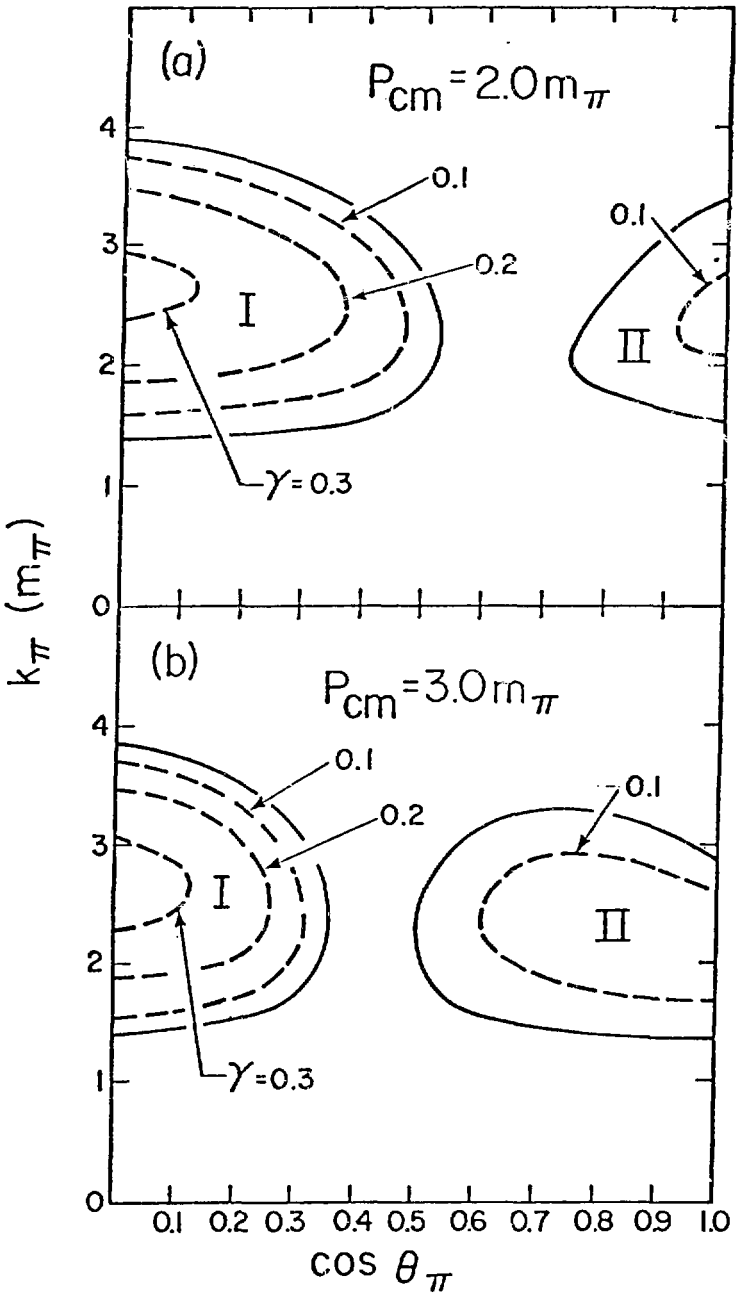
(a)
$P_{cm} = 2.0 m_\pi$
0.1
0.2
0.1
I
II
$\gamma = 0.3$
(b)
$P_{cm} = 3.0 m_\pi$
0.1
0.2
0.1
I
II
$\gamma = 0.3$
k_π (m_π)
0 1 2 3 4
0.1 0.2 0.3 0.4 0.5 0.6 0.7 0.8 0.9 1.0
cos θ_π

Fig. V

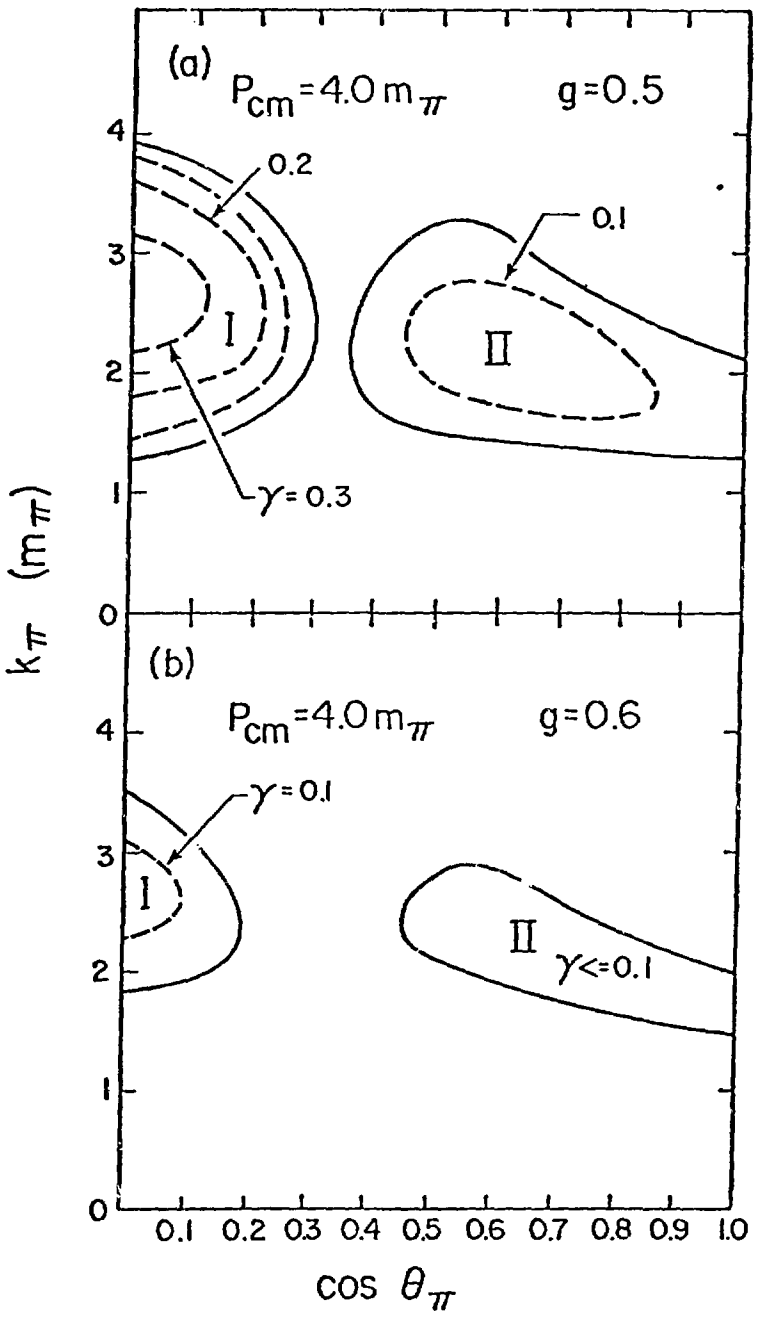

XBL-1093

Fig. VI

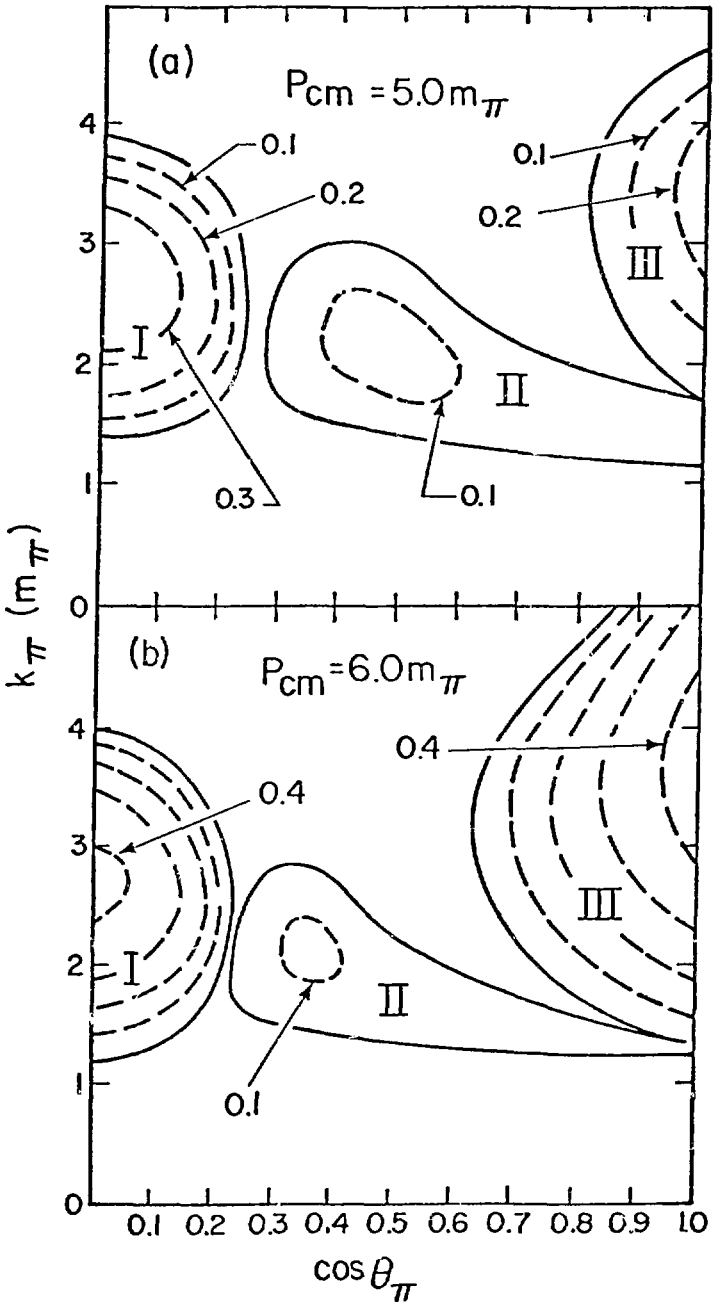

XBL776-1095

Fig. VII

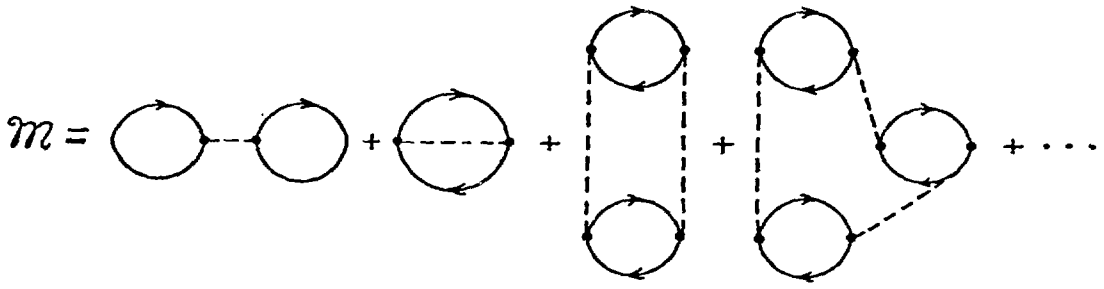

Fig. VIII

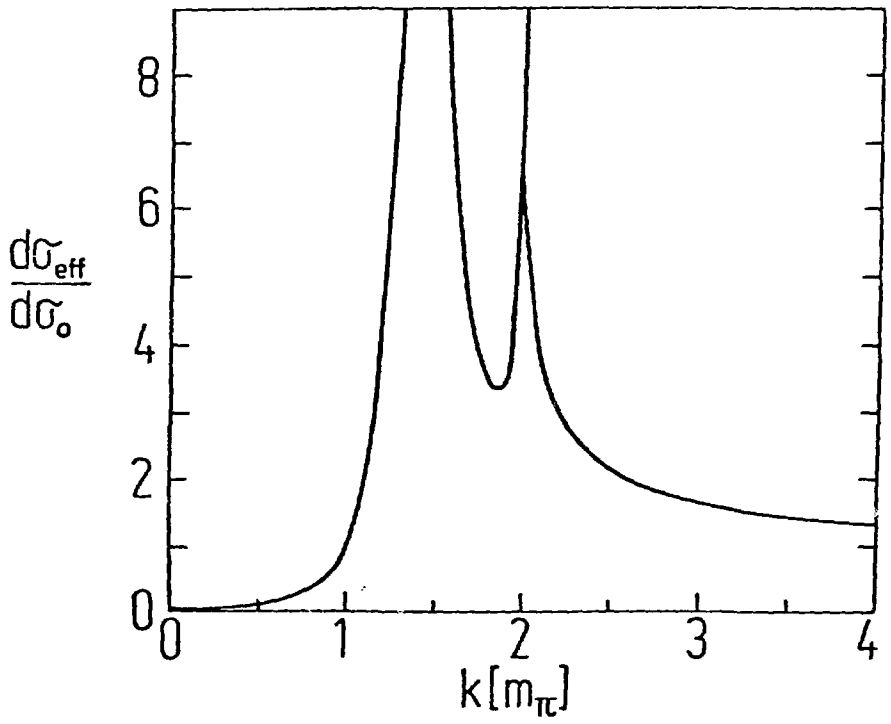

XBL 772-7475

QUANTUM STATISTICAL DESCRIPTION OF HEAVY ION COLLISIONS+)

S. Ayik and W. Nörenberg

Institut für Theoretische Physik der Universität and
Max-Planck-Institut für Kernphysik, Heidelberg

The aim of the statistical description for deeply inelastic collisions of heavy ions is to derive an adequate transport theory from a microscopic formulation. This may be achieved by considering the Liouville equation in the Wigner representation. This representation transforms the density matrix of the composite system to the Wigner function which is the quantum mechanical analogue of the classical phase space distribution function. We generalize the quantum statistical formulation of ref. [1] by considering the Liouville equation in the Wigner representation. This way we include the relative motion of the colliding ions and derive a generalized master equation [2]. The Wigner function is especially useful for describing the deeply inelastic processes in the classical limit. In this limit, it becomes the joint probability distribution for the relative distance and the relative momentum and gives the occupation probability of internal states. This generalized master equation is useful only if the basis representation has been chosen in a way that allows for a Markoff approximation. Deeply inelastic collisions are mainly dominated by the interactions of many degrees of freedom. This allows us to assume stochastic properties of the coupling matrix elements of the interaction which leads to the Markoff approximation. In addition we consider the classical limit of the relative motion. The results can be given by two coupled equations. One equation is the classical equation for the relative motion with friction. The other is the master equation for the internal motion. The explicit form of friction tensor and transition probability are given [1,2].

1. W. Nörenberg, Z.Physik A274(1975)241 and A276(1976)84
2. S. Ayik, Phys.Lett. 63B(1976)22
   S. Ayik and W. Nörenberg, to be published

+) Work supported by the "Bundesministerium für Forschung und Technologie", Bonn.

DEEP INELASTIC COLLISIONS AND FUSION STUDIED ON THE $^{40}Ar+^{197}Au$ SYSTEM

m.Berlanger[+], f.Hanappe[+], c.Ngô, j.Péter and b.Tamain

Institut de Physique Nucléaire BP n°1 91406 Orsay France

We investigated the Ar+Au system at two different bombarding energies 201 and 248 MeV. The mass and the energy of the products have been measured at different angles. Mass distributions exhibit two components separated at the low bombarding and partly merging into each other at high bombarding energy. One of them can be attributed to fission following complete fusion, the other one is centered around mass 40 and corresponds to deep inelastic products. These two different mechanisms correspond to different time scales. Angular distributions $\frac{d^2\sigma}{d\theta dM}$ are peaked a little bit forward the grazing angle for products close to the projectile and, when the mass transfer increases, becomes constant. For deep inelastic collisions the mass transfer occurs in the way predicted using potential energy considerations, but the small FWHM and the slight shift of the position of the maximum of these distributions indicates a short contact time. Due to the increase of the temperature, the FWHM of the mass distribution of deep inelastic products increases with the bombarding energy. The mean total kinetic energy studied as a function of the detection angle shows the influence of statistical fluctuations at backward angles. One also observes for this system that the relaxation time connected with the mass asymmetry degree of freedom is larger than the one associated to the energy damping. Complete fusion cross sections measurements were also done at 183, 189 and 195 MeV which allowed to draw the excitation function for this process. Calculations of the fusion cross section using the concept of critical distance are in agreement with the data.

[+]Université libre de Bruxelles, Bruxelles, Belgique.

RELATIVISTIC EQUATIONS-OF-MOTION CALCULATIONS OF HIGH-ENERGY HEAVY-ION COLLISIONS†

A. R. Bodmer[+], A. D. MacKellar[*], and C. N. Panos[+], Argonne National Laboratory, Argonne, Ill. 60439

When heavy ions collide at high energies it is reasonable to treat the collision in a classical microscopic approximation. For small impact parameters, the central densities produced during overlap are high enough to produce significant correlation effects. Under these conditions it is meaningful to treat the collisions with a classical microscopic equations-of motion approach. Nonrelativistic calculations have been made using this approach[1,2]). We have extended these calculations to include relativistic effects to order v^2/c^2. The NN potential is the sum of a short-range repulsion due to vector-meson exchange and a longer-range attraction due to scalar-meson exchange. The effects of retardation are then uniquely determined to order v^2/c^2 [3]). The parameters of the corresponding momentum-dependent potential are adjusted to fit the empirical total $\sin^2\theta$ weighted cross section as a function of energy by the use of classical relativistic two-body calculations. It is now necessary to calculate trajectories by the use of Hamilton's equations. Initial distributions for the individual nuclei have been prepared using methods similar to those described previously[1]). We have made preliminary calculations of the collisions of two nuclei, each with 20 nucleons, for specific initial distributions for these nuclei and for laboratory energies of 117, 300 and 500 MeV/nucleon. Even at the higher energies the effects of relativistic kinematics are rather minor, but the retardation corrections then give large and repulsive contributions to the potential energy when the two nuclei overlap appreciably. Central collisions are explosive in character even for these rather light nuclei. The collisions show a general similarity with the previously obtained nonrelativistic results for 50 nucleons on 50 nucleons[1]).

+Also University of Illinois at Chicago Circle, Chicago, Ill. 60680.
*Also University of Kentucky, Lexington, Ky. 40506
†Work performed in part under the auspices of USERDA, Div. of Physical Research.

1. A. R. Bodmer and C. N. Panos, Phys. Rev. C15(1977) 1342.
2. L. Wilets, E. M. Henley, M. Kraft, and A. D. MacKellar, to be published in Nuclear Physics.
3. See, e.g. J. Stachel and P. Havas, Phys. Rev. D13(1976) 1598, and references cited there for Hamiltonian and Lagrangian formulations which are Lorentz invariant to order v^2/c^2, and involve only particles interacting directly through potentials.

REGGE PARAMETERIZATION OF QUASI-ELASTIC TRANSFER AMPLITUDES*

B. V. Carlson and K. W. McVoy, Department of Physics, University of Wisconsin, Madison, WI 53706

Analyses of the partial-wave decompositions of a substantial number of DWBA and CCBA calculations for heavy-ion-induced quasi-elastic transfer reactions have clearly indicated that the ℓ-windows for these reactions are dominated by Regge poles, i.e., by poles at complex values of ℓ. Consequently, starting from a suggestion by Fuller,[1] we have constructed a parameterized partial-wave decomposition for transfer cross sections, of a DWBA form, with the ℓ-dependence of the "radial integrals" given by the Regge-pole form

$$I_{\ell_f \ell_i} = C \frac{(\ell_f - z)}{(\ell_i - p_i)(\ell_i - p_f)} \; e^{-[\frac{\ell_i + \ell_f}{2} - L_o]^2/\Delta^2} \qquad (1)$$

This is an 8-parameter form, in which p_i, p_f and z (pole and zero positions) are complex and c and L_o real parameters; Δ^2 is fixed at 150.

Least-square searches on angular distributions have produced excellent fits to quasi-elastic transfer data of both direct and multi-step character. Fig. (1) shows a fit to[2] $^{48}Ca(^{16}O,^{15}N)^{49}Sc$ ($3/2^-$, 3.09 MeV), which is not fit by a DWBA calculation, presumably because it is a multi-step reaction. Fig. (2) shows a fit to $^{74}Ge(^{18}O, ^{16}O)^{76}Ge(2^+, 0.56$ MeV), whose unusual angular distribution, according to the experimenters,[3] distinctly shows it to be a multistep process. The dip at 40°, in the Regge interpretation, is an interference between the surface waves generated by the two Regge poles.

*Supported in part by the National Science Foundation.

1) R. G. Fuller and O. Dragun, Phys. Rev. Lett. 22 (1974) 617.
2) D. G. Korar et al., Proc. of ANL Symp. on Heavy Ion Collisions, April 1976, Vol. II, 645.
3) P. D. Bond, H.J. Korner, M.C. Lemaire, D.J. Pisano and C.E. Thorn, BNL preprint, 1°77.

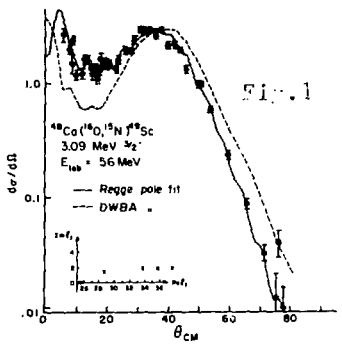

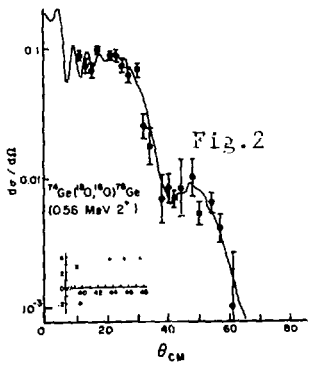

GAMMA-RAY MULTIPLICITIES IN DEEP INELASTIC COLLISIONS AND COMPLETE FUSION OF THE SYSTEM ^{40}Ar ^{197}Au.

M.A. Deleplanque, C. Gerschel, M. Ishihara*, C. Ngô, N. Perrin,
J. Péter, B. Tamain, L. Valentin,
Institut de Physique Nucléaire, B.P. n° 1, 91406 Orsay, France,
and D. Paya, Y. Sugiyama,
DPhN/MF, C.E.N.-Saclay, B.P. n° 2, 91190 Gif/Yvette, France
and M. Berlanger, F. Hanappe,
Phys. Nucl. Expérim., Université Libre de Bruxelles, Belgique.

We measured the gamma-ray multiplicity M_γ associated with the pairs of fission fragments and D.I.C. products in reactions induced by 225 MeV Ar ions on Au. Two 3x3" NaI detectors in the reaction plane and one out-of-plane detected the γ in coincidence with the products identified by their mass and kinetic energy.

Fusion-fission : The rate of initial orbital angular momentum transferred to the fragments depends only on the shape at the scission-point. The elongation of the system at this point is calculated from the measured kinetic energy (I). The critical value of initial ℓ-waves contributing to complete fusion is 68$\hbar$. That leads to calculated M_γ=6. The measured value is 8.5±1.5. The difference is due to the additional intrinsic angular momentum (8-16$\hbar$) probably induced by the bending modes.

Deep Inelastic Collisions : When the light products are within ±15 mass units of the projectile mass, the average M_γ is 7.5±1.5 and the maximum of the yrast bump on the gamma-ray energy spectrum is located at 1.2 MeV. It is impossible to fit these two values with the sticking hypothesis (M_γ = 15, E_γ = 0.7 MeV). As far as rolling is concerned these values are coherent together, but too low if we take incoming angular momenta in the range 68 to 75$\hbar$ as determined by (I). This would indicate a short contact time for the composite systems decaying at this angle, in agreement with the observed non-complete kinetic energy relaxation (I).

*on leave from I.P.C.R., Wako-Shi, Japan.

(I) M. Berlanger, F. Hanappe, C. Ngô, J. Péter, B. Tamain, this conference.

Approximate solution of Schrödinger's equation in a rotating frame

Hans Feldmeier
Technische Hochschule Darmstadt

A selfconsistent calculation for wavefunctions with axial symmetry in a rotating coordinate frame can be achieved by allowing the single particle wavefunctions to be of the form

$$\psi_\alpha(r,z,\varphi) = \hat{\psi}_\alpha(r,z)\, e^{i[n_\alpha\varphi + \chi(r,z,\varphi)]} \qquad \text{where}$$

$\hat{\psi}_\alpha(r,z)$ is a complex function and $\chi_\alpha(r,z,\varphi)$ is a real function of the form:

$$\chi_\alpha(r,z,\varphi) = \sum_{k=1}^{\infty} g_k^{(\alpha)}(r,z)\cos k\varphi + f_k^{(\alpha)}(r,z)\sin k\varphi$$

Variation of $\int_{t_1}^{t_2} \langle \Psi \,|\, i\hbar\frac{\partial}{\partial t} + \vec{\omega}\vec{L} - H \,|\, \Psi\rangle \, dt$

with respect to all $\hat{\psi}_\alpha, g_k^{(\alpha)}$ and $f_k^{(\alpha)}$ yields equations for these quantities which depend on the two variables r and z only.

For example when we restrict Ψ to a single Slaterdeterminant (TDHF) with all s.p. wavefunctions having the same phase χ, we get for the common phase

$$\chi(r,z,\varphi) = g(r,z)\cos\varphi \qquad \text{and} \qquad \vec{\nabla}(\rho\,\vec{\nabla}\chi) = \frac{m\vec{\omega}}{\hbar}(\vec{r}\times\vec{\nabla}\rho) \qquad (*)$$

where ρ is the single particle density and $\vec{\omega}$ the angular velocity of the frame which is perpendicular to the symmetry-axis (z-axis).
Variation with respect to $\hat{\psi}_\alpha$ provides the usual TDHF equations in two dimensions which are complemented by a rotational potential

$$V_{rot}(r,z) = \frac{1}{2\pi}\int_0^{2\pi} d\varphi \left\{ \frac{\hbar^2}{2m}(\vec{\nabla}\chi)^2 - \hbar\vec{\omega}(\vec{r}\times\vec{\nabla}\chi)\right\}$$

Calculating the expectation value of $\vec{L}$ we get $\langle\vec{L}\rangle = \hbar\int\rho(\vec{r}\times\vec{\nabla}\chi)\,d^3r$ and we obtain for the moment of inertia $I = \frac{1}{\vec{\omega}^2}\langle\vec{\omega}\vec{L}\rangle$ the $|\vec{\omega}|$ independent expression

$$I = \hbar\frac{\vec{\omega}}{|\vec{\omega}|}\int\rho\left(\vec{r}\times\vec{\nabla}\left(\frac{\chi}{|\vec{\omega}|}\right)\right)d^3r$$

The rotational energy turns out to be $E_{rot} = \frac{\hbar^2}{2m}\int\rho(\vec{\nabla}\chi)^2 d^3r$ which can be transformed using eq. (*) into $E_{rot} = \frac{1}{2}I\vec{\omega}^2$

Calculations of heavy ion reactions have been performed in the TDHF model using the above formalism. A more detailed discussion will be published.

BARRIER TOP RESONANCES AND PARTICLE TRANSFER REACTIONS*

W. A. Friedman, Physics Department, University of Wisconsin, Madison, WI 53706

It is recognized that particle transfer amplitudes are often dominated by two poles in angular momentum (Regge Poles). Furthermore, it has been established that one of these is associated with the entrance channel wave function and one with the exit channel wave function. In a recent paper we suggest that these poles arise from Barrier Top Resonances,[1] which yield ℓ-poles whose real part corresponds to the orbiting angular momentum (that ℓ for which the top of the angular momentum-Coulomb barrier coincides with the incoming energy). Such poles arise only when the internal absorption is strong and they have widths determined by the barrier curvature and imaginary potential at the barrier. They reflect the following simplification: Partial wave distorted waves for strong internal absorption see an effective potential which is essentially a one dimensional barrier of approximate parabolic shape. The wave functions for such potentials possess Barrier Top Resonances. With strong absorption the distorted waves near the nucleus are dominated by such resonances.

The ℓ-pole location (ℓ_o, Γ_ℓ) carries much of the same information as the channel optical potential, but it provides a more efficient phenomenological parametrization.

Each inelastic channel has similar barrier top resonances. When such channels are strongly coupled to the elastic channel the wave function acquires new or effective pole positions. A phenomenological approach discussed in another contribution to this conference capitalizes on this feature to fit differential cross sections with an amplitude having two adjustable ℓ-poles. DWBA results require elastic barrier top locations. CCBA results require slightly shifted pole positions.

*Supported in part by the National Science Foundation.

1. W. A. Friedman and C. J. Goebel, Annals of Physics 104 (1977) 145.

2. B. V. Carlson and K. W. McVoy, Contribution to this Conference.

The Collective Path in Adiabatic TDHF

K. Goeke, Inst. f. Kernphysik, KFA Jülich, D-5170 Jülich, West Germany

P.G. Reinhard, Inst. f. Kernphysik, Univ. Mainz, D-6500 Mainz, West Germany

Many large amplitude collective phenomena can be characterized by one (or several) collective coordinate $q = q(t)$ and the corresponding set of many body wave functions $|q\rangle$, i.e. the collective path. For obvious reasons the path must be determined together with the collective mass, $M_o(q)$, and the collective potential, $V_o(q)$, which can be achieved in the framework of an adiabatic TDHF theory[1,2]. One performs[2] a perturbation expansion of $i\dot{\rho} = [W,\rho]$ and of $\rho^2 = \rho$ for small velocities, i.e. $\rho \sim \rho_o(q) + p\rho_1(q) + p^2\rho_2(q) + \ldots$ Sorting the terms according to orders of p leads to[2]

$$[W_o - \partial_q V\hat{Q},\rho_o] = 0 \qquad M_o(q) = i\,\mathrm{Tr}(|\rho_o,\rho_1|\partial_q\rho_o) \qquad (1),(2)$$

$$[W_p + [W_o,\hat{P}],\rho_o] = -i[\hat{Q},\rho_o]/M_o \qquad (3)$$

with $\hat{Q},\hat{P}$ given by $\partial_q\rho = -i[\hat{P},\rho]$ and $\partial_p\rho = i[\hat{Q},\rho]$. The p^2-equation, which has been omitted gives a criterion[2] for the validity of ATDHF in that $\hat{Q}_2 = [\rho_2,\rho_o]$ should be small

$$[W_{Q_2}+[W_o,Q_2],\rho_o] = [\tfrac{1}{2}W_{QQ}+[W_Q,Q] - \partial_q\hat{Q}/M_o + \tfrac{1}{2}\hat{Q}\partial_q M_o^{-1},\rho_o]$$

with $W_{Q_2} = \mathrm{Tr}(v[Q_2,\rho_o])$ and $W_{QQ} = \mathrm{Tr}(v[\hat{Q},\hat{Q},\rho_o])$. There are several methods to solve eqs. (1)-(3) which correspond to standard procedures in solving differential equations[2]. (The ρ denotes the one body density matrix.)

References:

1) F. Villars, preprint MIT, 1976

2) K. Goeke and P.G. Reinhard, preprint Jülich, 1977

CALCULATION OF DIFFERENTIAL CROSS SECTIONS FOR DEEP INELASTIC COLLISIONS

p. Grangé and j. Richert

Laboratoire de Physique Nucléaire Théorique BP n°20 CRO 67037

Strasbourg-France

m. Berlanger[+], h. Hofmann[*] and c. Ngô

Institut de Physique Nucléaire, BP n°1 91406 Orsay, France.

As proposed in ref.1) we apply a Fokker Planck equation in phase space of the collective degrees to compute cross sections for deep inelastic reactions. In this approach, the distribution function for the collective degrees is a gaussian entirely determined by their first and second moments. The second moments which describe the statistical fluctuations of the collective degrees are entirely determined by the first one due to the fluctuation dissipation theorem. The first moments satisfy classical equations of motion including a friction force. They can be described using a classical phenomenological model. Such an approach, already used in ref.2) allows to compute $\frac{d^2\sigma}{d\theta dx}$ where x is the mass asymmetry degree of freedom. But there, because each fragments are kept spherical during the process, it was not possible to quantitatively reproduce the energy loss and therefore $\frac{d^3\sigma}{d\theta dx dE}$. We extend the model of ref.2) to the case where deformations in the exit channel are simulated using ref.3) for the classical model. It is then possible to compute absolute values of all quantities concerning mass exchange and energy damping. In addition, repartition of the spins of the fragments as a function of mass asymmetry is obtained which can directly be compared with γ multiplicity measurements.

1) H.Hofmann and P.J.Siemens, Nucl. Phys. A275 (1977) 464.

2) C.Ngô and H.Hofmann, Zeit. Phys. in press, see also H.Hofmann and C.Ngô, Phys. Lett. 65B (1976) 37.

3) K. Siwek-Wilczynska and J.Wilczynski, Nucl. Phys. A264 (1976) 115.

[+] Université Libre de Bruxelles, Bruxelles, Belgique.

[*] Physik Department der technischen Universität München, D8046 Garching B.R.D.

CENTRAL COLLISIONS OF RELATIVISTIC HEAVY IONS IN NUCLEAR EMULSION

H.H. Heckman, H.J. Crawford, D.E. Greiner, P.J. Lindstrom and L.W. Wilson
Lawrence Berkeley Laboratory and Space Sciences Laboratory
University of California, Berkeley, California 94720 U.S.A.

We are carrying out an experimental study on the angular and momentum distributions of fragments emitted from central collisions between emulsion nuclei (AgBr) and heavy-ion projectiles ^{4}He, ^{16}O and ^{40}Ar at beam momentum $5.72Z_B$ GeV/c. The criterion we have adopted for a central collision is one that exhibits an absence of projectile fragmentation, i.e., no beam-velocity fragments ($Z_F \geq 1$ from ^{4}He interactions, $Z_F \geq 2$ from ^{16}O and ^{40}Ar interactions) are produced within 5^{o} of the incident beam direction.

Production angles have been measured for all fragments having a restricted grain density $g \geq 2g_{min}$, corresponding to $E \leq 250$ MeV/A for singly charged particles. Range measurements have been made for fragment ranges ≤ 4 mm, equivalent to E = 31 MeV/A for protons (and ^{4}He). The experimental data are analyzed in terms of the Maxwell-Boltzmann distribution, from which estimates of the temperature τ and longitudinal velocity $\beta_{||}$ of the particle-emitting systems are made. The principal results of the experiment, to date, are: 1) the angular and momentum, i.e., range, distributions are, within the experimental errors, the same, independent of projectile; 2) the fitted parameters τ and $\beta_{||}$ are small, typically 6-7 MeV and 0.01-0.02, respectively; 3) no single pair of parameters τ and $\beta_{||}$ fit all data; and 4) the angular and momentum distributions are smooth, void of structure.

DISSIPATION AND THE NUCLEAR COLLECTIVE MODEL

Helmut Hofmann, Physik-Department, Technische Universität München, 8046 Garching, W-Germany

In a previous paper[1] it was shown how the cranking model for nuclear collection motion can be extended formally to treat dissipative processes at finite temperature. This was possible by applying the technique used to derive equations of motion for deeply inelastic heavy ion collisions[2]: quasistatic approach for describing the intrinsic system and linear response theory to compute the effective forces for the collective degrees.

As is well known, the cranking-model is an approximation which does not describe the nuclear motion self-consistently. So the question may be asked whether the friction coefficient is changed by requiring self-consistency. A hint for the answer may be found for the model case of harmonic vibrations. For one collective degree Q the Hamiltonian reads: $\hat{H} = \hat{H}_{int} + \kappa Q(t) \hat{F}$ If we explicitly allow for damped harmonic motion, the requirement $\langle \hat{F} \rangle_t = Q(t)$ leads to a modified dispersion relation with complex frequency solutions. In the low frequency limit the friction coefficient deduced in this way is identical to the one for the cranking model.

The postulation of damped collective motion needs a careful discussion of the meaning of irreversibility. The instrinsic excitation (due to collective motion) is primarily described by one particular response function:

$$\tilde{\chi}''(t) = -i \sum_{nm} \frac{e^{-\frac{E_m}{T}}}{Z} |F_{mn}|^2 \sin \Omega_{nm} t$$

A decaying behaviour of this function (indicating irreversible motion) can be expected only for times $t \lesssim \frac{\hbar}{\Gamma} \ll \frac{\hbar}{d}$. (Here d is an effective mean level spacing and $\frac{\hbar}{d}$ may be interpreted as a Poincaré recurrence time.) Thus, damped collective motion will be found only if a measuring device cuts off the times $t > \frac{\hbar}{\Gamma}$ - or, what is equivalent, does not allow a separation of the intrinsic energy better than an uncertainty I. (For this discussion we assume, that no other slow collective mode of the intrinsic system is excited.)

The magnitude of d depends on the physical situation we are studying and/or on the model for the intrinsic Hamiltonian H_{int}. For some situations p-h excitations might be sufficient (i.e. H_{int} can be represented by a shell model Hamiltonian) for other cases residual two-body interactions will be necessary to make the level spectrum complex enough.

1) H. Hofmann, Phys.Lett. 61B (1976) 423

2) For a summary and references to the original work see the invited talk: "Dissipation and fluctuations within a macroscopic treatment of heavy ion collisions" by Ch. Ngô.

FLUID DYNAMICS VERSUS TDHF

G. Holzwarth, Physik-Dept., Technische Universität München

A set of fluid-dynamical equations for the motion of a many-body system can be obtained by the requirement that at all times the system can be described by one pure state (as in TDHF) and on decomposition into phase and argument

$$\Psi(x_1 \ldots x_A, t) = \Phi(x_1 \ldots x_A, t) \exp i \frac{m}{h} S (x_1 \ldots x_A, t)$$

(Φ and S real) the phase S is restricted to single-particle form

$$S(x_1 \ldots x_A, t) = \sum_i \varphi(x_i, t).$$

In contrast to TDHF no assumptions about the correlations present in Φ are necessary. The resulting fluid-dynamical equations differ in basic respects from ordinary fluid dynamics: The intrinsic energy density e defined through

$$\langle \Phi H \Phi \rangle = \int \rho e \, d^3x$$

depends not only on the density ρ itself but contains important contributions from integrals and gradients of ρ. On the other hand, there is no dependence of e on parameters which in ordinary fluid dynamics characterize the local equilibrium ensemble. This fact has important consequences for the selection of shock conditions if discontinuities occur during motion of the fluid. Resulting compression ratios in slab collisions are in close agreement with TDHF results for c.m. energies up to about 50 MeV/particle. Further comparison is possible for small amplitude vibrations where it turns out that a non-equilibrium local momentum distribution in the state Φ is essential to obtain agreement with microscopic TDHF (or, equivalently, RPA) results, while ordinary fluid dynamics assuming locally a spherical Fermi surface leads to drastic disagreement for L = 2 resonances.

PION MULTIPLICITY DISTRIBUTIONS IN 2 GeV/NUCLEON HEAVY ION REACTIONS

B Jakobsson, R Kullberg and I Otterlund, Dept of Physics, Univ of Lund, Lund, Sweden. A Ruiz, Dept of Physics, Univ of Santander, Santander, Spain. J M Bolta and E Higon, Inst of Physics, Univ of Valencia, Valencia, Spain.

We have determined the charged pion multiplicity distributions in 2 GeV/nucleon ^{12}C and ^{16}O induced reactions in nuclear emulsions and compared them to the expected distributions from an individual nucleon-nucleon scattering model. By measuring the opacity with photometers for all candidates of relativistic fragments and the gap density of all other tracks we can obtain $N_{\pi^\pm}^{Em}$ which is:

$$N_{\pi^\pm}^{Em} = N_s - (Z_{inc} - \Sigma Z_{fr})$$

where N_s is the number of shower tracks ($E_{proton} < 400$ MeV), Z_{inc} and Z_{fr} the charge of the beam respectively multiply charged relativistic fragments.

The $N_{\pi^\pm}^{Em}$ distributions for ^{16}O-H,CNO,AgBr reactions are shown in Fig. 1 together with the results from individual nucleon-nucleon scattering calculations. In the model we determine the $P(\nu, n_{inc})$ probability distributions (ν = the number of scatterings for a nucleon, n_{inc} = the number of participating incident nucleons) by a Monte-Carlo and a Glauber calculation. The $\pi^\pm$ multiplicity distributions in each reaction step are determined from experimental nucleon-nucleon cross sections and phase-space generated inelasticity distributions. Furthermore Fermi motion and corrections for changing $N_{\pi^\pm}$ to $N_{\pi^\pm}^{Em}$ are introduced. Our conclusion from the discrepancies at large $N_{\pi^\pm}^{Em}$ is that there are indications of collective phenomena involved in the pion production in heavy ion interactions.

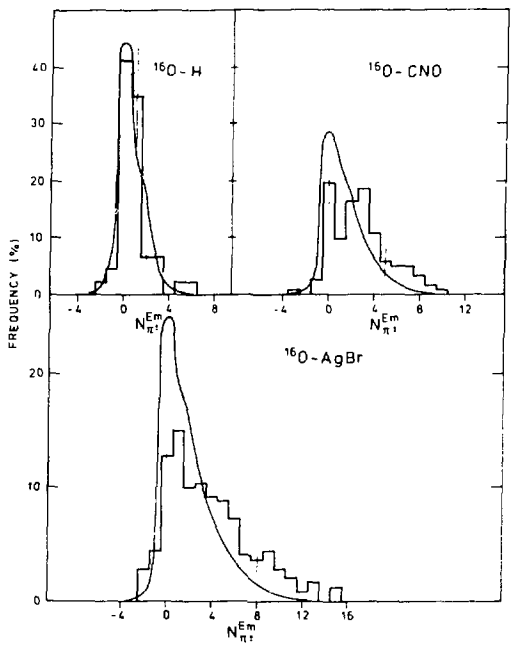

Fig.1. $\pi^\pm_{Em}$-multiplicity distributions in 2 GeV/nucleon ^{16}O induced reactions. Curves from individual nucleon-nucleon model.

^{20}Ne-W REACTIONS AT 340 MeV/NUCLEON STUDIED IN WIRE-LOADED NUCLEAR EMULSIONS

B Jakobsson and I Otterlund, Dept of Physics, Univ of Lund, Lund, Sweden.

We have used the combination of nuclear emulsions as 4π-detector and well defined wire-targets to study the target and projectile fragmentation of 340 MeV/nucleon ^{20}Ne-W reactions.[x] The first results from dE/dx and angular measurements indicate that the $d\sigma/d\Omega$ distributions for the largely ionising part of the tracks (black tracks - p,d,t $E \leq 44$ MeV/nucleon + ^{3}He, ^{4}He $E \leq 310$ MeV/nucleon + all heavier fragments) is well described by thermal emission from a slowly recoiling system in peripheral events. In central events however the $d\sigma/d\Omega$ distribution is much more anisotropic. An attempt to explain the complete distribution of black prongs by thermal emission + the fireball model [2] also including final state interactions from the idea of simple coalescense of nucleons [3] gives reasonable agreement however with a somewhat too large forward peaking compared to the experimental data.

[x]The method of laminating two emulsions over a grid of thin wires has been presented in Ref 1.

References

1 B Lindkvist, Nuclear Instr and Methods, 141 (1977) 511.
2 G D Westfall et al, Phys Rev Letters, 37 (1976) 1202.
3 H H Gutbrod et al, Phys Rev Letters, 37 (1976) 667.

ASPECTS OF TIME-DEPENDENT CALCULATIONS FOR HEAVY ION COLLISIONS*

K.-K. Kan and T. Tamura
Department of Physics, University of Texas, Austin, Texas, 78712

First, we point out that a limitation exists in applying the time-dependent Hartree-Fock (TDHF) method in collision processes, because certain degrees of freedom can only be treated classically. Before collision, where the two colliding nuclei have no interaction with each other, this classical aspect manifests itself in the fact that the TDHF wave function implies a wave packet for the relative distance between the centers of mass of the nuclei, which has a time-independent width. This is in contradiction with the well known fact of quantum mechanics that a free wave packet spreads out in space as time evolves. We note also the possibility that some other degrees of freedom may also behave classically during the collision process, and they may lead to some classical collective excitations in the final fragments.

This viewpoint affects our interpretation of the TDHF results. In particular, it makes the analysis of TDHF final states in terms of fully quantum mechanical stationary channel states unsuitable. Instead, we propose the use of "semi-classical channel states" which incorporate certain classical collective motions suggested by the behavior of the fragment itself. Investigation is made of the construction of the semi-classical channel states for one case of the one-dimensional slab collisions calculated by Bonche et al.[1)]

The classical aspect mentioned above also implies the necessity of going beyond the framework of TDHF, if a fully quantum mechanical calculation is sought. Along this line, we investigate a time-dependent version of the generator coordinate method (TDGC). In this method, the wave function of the system will be free from any classical behavior if the classical parameters involved are integrated out through the generator wave function. Before and after the collision, this generator wave function is naturally in the form of a wave packet.

In a time-dependent calculation, one has to restrict the calculation to finite region of space and a finite interval of time. In preparation for further studies in time-dependent methods such as TDGC, we therefore investigate the problem of extracting the cross section from a wave packet in a scattering process, in the face of this finite space time restriction. We find that even with this restriction, it is possible to obtain the cross section if a plane wave packet is used as the incident and if the scattered part of the wave function is calculated directly.

*Work supported by United States E.R.D.A.

1) P. Bonche, S. Koonin, and J.W. Negele, Phys. Rev. C13 (1976) 1226.

EXACT CALCULATION OF THE PENETRABILITY FOR A SIMPLE TWO-DIMENSIONAL POTENTIAL-ENERGY SURFACE REPRESENTING THE REACTION $^{100}Mo + {}^{100}Mo \rightarrow {}^{200}Po$

T. Kodama and R.A.M.S. Nazareth, Cen. Bras. Pesq. Fis., Rio de Janeiro
P. Möller and J. R. Nix, Los Alamos Scientific Laboratory*

In a study of the effect of the multidimensionality of the true potential-energy surface on the low-energy fusion cross section, we calculate exactly the penetrability for a simple two-dimensional barrier $V(r,\sigma)$. To be specific,

$$V(r,\sigma) = V_0 - \tfrac{1}{2}k_r r^2 + \tfrac{1}{2}k_1 \sigma^2 \quad , \text{ if } \quad r \geq r_1 \quad ,$$

and

$$V(r,\sigma) = V_0 - \tfrac{1}{2}k_r r^2 + \tfrac{1}{2}k_2 (\sigma - \sigma_0)^2 - \tfrac{1}{2}k_2 \sigma^2 \quad , \text{ if } \quad r < r_1 .$$

Here r is the distance between the centers of mass of the two halves of the system and σ is the elongation of each half about its center of mass. For the reaction $^{100}Mo + {}^{100}Mo \rightarrow {}^{200}Po$ our potential gives correctly the differences in height (22.83 MeV) and in σ (0.2143 R_0) between the maximum in the one-dimensional interaction barrier and the fission saddle point. For the true potential, stability with respect to positive σ-deformations is lost at a point where r is 0.231 R_0 larger and the energy is 9.82 MeV lower than for the maximum in the one-dimensional interaction barrier. This feature, as well as the occurrence of two misaligned fission and fusion valleys are reproduced by the simple potential $V(r,\sigma)$. For this two-dimensional potential we determine the penetrability by calculating exactly the amplitudes of the reflected and transmitted waves. The result is given in Fig. 1 (solid curve). The dashed curve is the result for the one-dimensional parabolic fusion barrier. Because the incident wave packet in the two-dimensional calculation is on the side of a steep hill near the top of the barrier, the calculated penetrability is substantially different from the result for a one-dimensional calculation. In particular, 10 MeV below the maximum in the one-dimensional fusion barrier the two-dimensional penetrability is 10^{10} times as large as the one-dimensional result. Also, for equal penetrability the slopes of the two curves are very different.

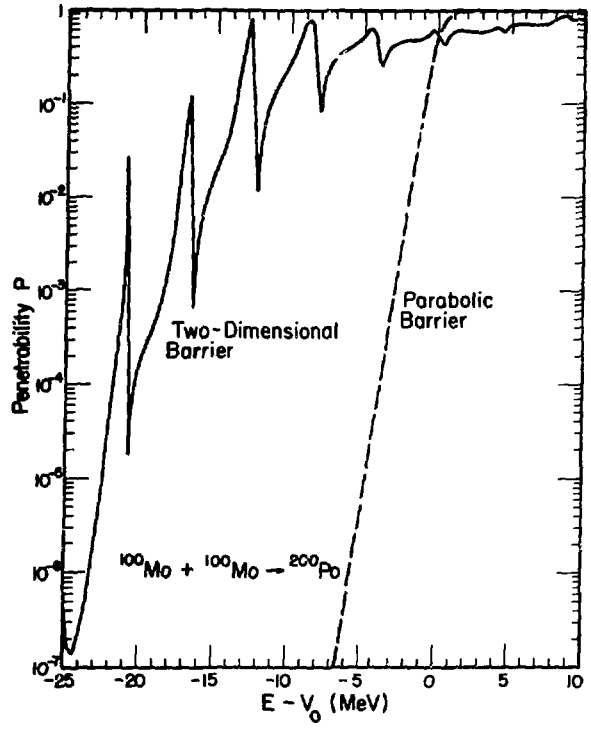

Figure 1

* Work performed under auspices of the U. S. ERDA.

ON THE SCATTERING THEORY OF DEFORMED ALIGNED HEAVY IONS

H.-J. Krappe, Hahn-Meitner-Institut, Berlin

H. Massmann, Facultad de Cientias, Univ. de Chile, Santiago/Chile

Recent successes in producing beams of highly polarized light alkali nuclei[1] motivated the investigation of this new experimental tool to determine heavy-ion interaction potentials. As a function of the orientation angles of the nuclear symmetry axis of a polarized, deformed ^{23}Na projectile we calculated the fusion excitation function and angular distribution for elastic scattering at energies slightly above the interaction barrier for the system $^{23}Na+^{58}Ni$. For such fairly light systems the nuclei are still well apart from each other at the interaction barrier. Therefore one can disregard the neck-formation degree of freedom and other polarization effects for distances larger than the interaction radius. For the same reason the reaction cross section consists predominantly of the fusion cross section.

As an adequate quantum mechanical description of this classical picture we use the ingoing-wave boundary condition model[2] with the boundary radius somewhat smaller than the interaction radius. As the boundary condition describes the disappearance of flux out of the elastic channel in this model the interaction potential between the nuclei can be assumed to be real. That reduces the number of free parameters considerably compared to usual optical potentials. The remaining real potential was derived from the generalized liquid-drop model[3], which completely determines all free parameters. Classical trajectory calculations for the system under consideration showed that the angular momentum transferred to the rotational degree of freedom of the projectile is only a small fraction of $\hbar$ for the ingoing part of the trajectory up to the point of closest approach. Also the rotation angle of the symmetry axis during the approach turned out to be only a few degrees. We have therefore considered the rotor to be frozen in.

The numerical calculation of the fusion and elastic scattering cross sections showed that the polarization effect can be as large as 20 % and should therefore be well observable. It depends on the quadrupole deformation as well as the diffuseness of the interaction potential and can therefore be used to check the assumed potential model or remove ambiguities of conventional optical potential fits.

1) E. Steffens, IEEE Trans. Nucl. Sci. NS-23 (1976) 1143
2) G. H. Rawitscher, Phys. Rev. Lett. 14 (1965) 150;
Phys. Rev. 135 (1964) B605; Nucl. Phys. 85 (1963) 337;
3) H. J. Krappe and R. Nix, Proc. Third IAEA Symposium on Physics and Chemistry of Fission, Rochester 1973, vol. 1 p. 159 (IAEA, Vienna 1974).

ON A GENERAL FORM OF THE MULTIPLE DIFFERENTIAL CROSS-SECTIONS IN DEEP INELASTIC COLLISIONS BETWEEN HEAVY IONS. (I)

Ch. LECLERCQ-WILLAIN[+]

Université Libre de Bruxelles, Physique Théorique CP229,
Bᴿᵈ du Triomphe, B 1050 Bruxelles, Belgium.

In a recent paper, [1], we have derived the general form of the energy averaged "macroscopic" cross section for deep inelastic collisions (D.I.C.) between heavy ions on the basis of semi-classical approximation. The coarse transition probability obtained by summing the energy averaged microscopic cross-sections over all final β channels which lie in a given interval $(a, \Delta a)$ of some measured macroscopic variables is

$$\frac{d^f Q^{b.I}}{d\omega_{a_1} da_1 \dots da_f} \Delta a = Q^{b.I}(a, \Delta a) = \sum_{\beta \in (a, \Delta a)} \frac{d\sigma_\beta^{b.I}}{d\Omega} \quad . \tag{1}$$

We have investigated the conditions for which this cross section is a function of probabilities only :

$$Q^{b.I}(a, \Delta a) = \frac{1}{\sin a_1} \mathcal{P}(a)\, \nu(a)\, \Delta a \quad .$$

The average quantities $\mathcal{P}(a)$, $\nu(a)$ are defined from a theory which does not involve a detailed knowledge of the dynamics on the microscopic scale. Using the terminology of statistical mechanics, we assume to known a classical time dependent distribution function $\mathcal{d}_0(\vec{A}, \vec{\pi}, t)$ of f_0 external macroscopic variables $\vec{A}$ and their conjugate momenta $\vec{\pi}$ [2]. If we introduce f commutative observables $\Omega_{\kappa=1,f}(\vec{A}, \vec{\pi})$ whose eigenvalues a_κ represent the macroscopic quantum numbers used to define the coarse cells (like the scattering angle, the masses, the charges or excitation energies); the probability density to find the system asymptotically at these values (a) is

$$\mathcal{P}(a) = \int d^{f_0}A \; d^{f_0}\pi \; \mathcal{H}_{\kappa=1}^{f} \delta(\Omega_\kappa - a_\kappa)\; \mathcal{d}_0(\vec{A}, \vec{\pi}, t = +\infty) \quad . \tag{3}$$

If A_1 is the deflection function θ_2 and Ω_1, the scattering angle ϑ, $\delta(\Omega_1 - a_1)$ can be written $\delta(\theta_2 - \eta a_1)$ using the classical relation $\theta_2 + 2\pi p = \eta\vartheta = \eta a_1 \pm \chi_1$ with $p = 0$. With the restriction to the scattering angle $\Omega_1 = a_1$, one can write for the density probability $\mathcal{P}(a)$ and the classical approximation $\bar{\nu}(a)$ of $\nu(a)$ in (2); the expressions:

$$\mathcal{P}(a) = \int d\theta\, \delta(\theta - \eta a_1) \int dt \;\; \mathcal{d}(\theta, t, a) \quad , \tag{4}$$

$$\bar{\nu}(a) = \int d\theta\, \delta(\theta - \eta a_1) \int dt\; \mathcal{d}(\theta, t, a)\, \nu(\theta, \theta', \theta'', t, a) \Big/ \int d\theta\, \delta(\theta - \eta a_1) \int \mathcal{d}(\theta, t, a) \tag{5}$$

where the classical distribution function

$$\mathcal{d}(\theta, t, a) = \int d\theta_2\, \delta(\theta - \theta_2) \int dp_{\theta_2}\, \delta(t - p e_{p_2}) \int dr\, dp_r\, d^{f-1}A\, d^{f-1}\pi \prod_{\kappa=2}^{f} \delta(\Omega_\kappa - a_\kappa)\, \mathcal{d}_0 \quad . \tag{6}$$

The function $\nu(\theta, \theta', \theta'', t, a)$ in (5) can be obtained by the stationary phase approximation (S.P.A.) and averaged over the incident beam energy. S.P.A. with sharp lower and upper angular momentum cut-offs is used to represent the effect of a sudden onset of direct and compound reactions, [1].

As it can easily be defined on the application forms [3] the average quantities $\bar{\mathcal{P}}(a)$ and $\nu(a)$, are function of the initial impact parameter b; so that the final distribution is obtained by summing all contributions like (2) over the values of this initial impact parameter. Using the b_j values deduced from the classical relation $\bar{\theta}(b, a_1 \dots a_f) = \eta a_1$ where $\bar{\vartheta}(b, a_1 \dots a_f)$ is the mean classical deflection function

$$\bar{\theta}(b, a_1 \dots a_f) = \int d\theta\; \theta \int \mathcal{d}(\theta, t, a) dt \Big/ \int \mathcal{d}\theta \int \mathcal{d}(\theta, t, a)\, dt \quad ,$$

one can write the multiple differential D.I.C. cross section on the form :

$$\frac{d^f Q^{b.I}}{d\omega_{a_1} da_1 \dots da_f} = \frac{1}{\sin a_1} \sum_j \int_{\frac{b_{j-1}+b_j}{2}}^{\frac{b_j+b_{j+1}}{2}} db \left| \frac{d\bar{\theta}(b, a_1 \dots a_f)}{db} \right| \mathcal{P}(a, b)\, \bar{\nu}(a, b) \quad .$$

[1] K. Dietrich and Ch. Leclercq-Willain, LBL-5815, Dec. 1976, to be published in Ann.Phys.(N.Y)

[2] H. Hofmann and P. Siemens, Nucl. Phys. A275 (1977) 464

[3] Ch. Leclercq-Willain and M. Baus-Baghdikian, (II) Contribution to this Conference.

[+] Maître de Recherches au F.N.R.S., Belgium.

SEMI-CLASSICAL ANGULAR, ENERGY AND MASS ASYMMETRY DISTRIBUTION IN DEEP INELASTIC COLLISIONS (II)

Ch. LECLERCQ-WILLAIN[+] and M. BAUS-BAGHDIKIAN[++]
Université Libre de Bruxelles, Physique Théorique CP229,
Bᴿᵈ du Triomphe, B 1050 Bruxelles, Belgium

We apply the statistical theory developed in I, [1], to the calculation of the differential scattering cross section of D.I.C. as a function of mass asymmetry, energy and scattering angle.

In (I.3) we introduce the observables Ω_κ to define the scattering angle ϑ, the azimuthal angle φ, the relative energy and the mass of the lightest ion

$$\Omega_1 \equiv \vartheta = a_1 \;,\quad \Omega_2 \equiv \varphi = a_2 \;,\quad \Omega_3 \equiv E = \frac{2p^2}{A(1-\alpha^2)} = a_3 \;,\quad \Omega_4 \equiv A_1 = \frac{A(1-\alpha)}{2} = a_4 \;.$$

$A = A_1 + A_2$ means the total mass number and $\alpha = A_2 - A_1$, the mass difference.

The density distribution function is defined by :

$$d(\theta,\ell,a) = \int d\alpha\, d\theta_2\, dp_1\, dp_{\theta_2}\, d\alpha\, dp_\alpha\, \delta(\theta-\theta_2)\,\delta(p\theta_2-\ell)\,\delta\left(\frac{2p^2}{A(1-\alpha^2)} - a_3\right) \delta\left(\frac{A(1-\alpha)}{2} - a_4\right) d_0(\bar\alpha,\bar p,\omega)\, d_0(\alpha, p_\alpha, \omega) \;. \tag{1}$$

The distribution functions d_0 are the Gaussian solutions of a F.P. equation with the assumption that the relative motion and the mass exchange are statistically uncorrelated. Using (1), the probability distribution (I.4) is

$$\mathcal{P}(a,b) = \int d\theta\, \delta(\theta-\eta a_1)\; C(a,b)\left(\frac{\pi}{\gamma_{\alpha\alpha}(b)}\right)^{1/2} e^{-\frac{\left(\left(1-\frac{2a_4}{A}\right)-\alpha^{el}(b)\right)^2}{4\gamma_{\alpha\alpha}(b)}}$$

$$e^{-\frac{\left(\theta-\theta^{el}(b)-\left(p_c(a,b)-p_\alpha^{el}(b)\right)\Gamma(a,b)\right)^2}{2\Delta(a,b)}} \tag{2}$$

$$p_c(a,b) = (2\pi a_3 - \frac{\ell^{el\,2}(b)}{\alpha^{el\,2}(b)})^{1/2} \quad \text{and the functions } \alpha^{el}(b),$$

$\theta^{el}(b)$, $p_\alpha^{el}(b)$, $\ell^{el}(b)$, $\alpha^{el}(b)$ are the first moments deduced from the classical equation of motion with conservative and dissipative forces [2]. All the functions of $(a_1 \dots a_f, b)$ in (2) are expressions involving the second moments of the d_0 distribution and b means the initial impact parameter.

The average classical angular function $\bar\nu(a,b)$ is obtained from (I.5) and (1).

In (2), the angular θ distribution is centered at

$$\bar\theta(a_1 \dots a_f, b) = \theta^{el}(b) - \left(p_c(a,b) - p_\alpha^{el}(b)\right)\Gamma(a,b) \tag{3}$$

For a defined value of $\bar\theta(a,b)$, the contribution to the differential cross section at the scattering angle a_1 is :

$$\frac{1}{\sin a_1}\, \mathcal{P}(a,b)\,.\,\bar\nu(a,b) \tag{4}$$

The main contributions are for impact parameter b_j deduced from the relation $\bar\theta(a_1 \dots a_f, b) = \eta a_1$.

For each b_j value the classical angular function $\bar\nu(a,b)$ (I.5) is calculated with the classical limits $\ell^{el}((b_{j-1}+b_j)/2)$ and $\ell^{el}((b_j+b_{j+1})/2)$ in the integral over ℓ. Summing all the contributions like (4), the D.I.C. multiple differential cross section is

$$\frac{d^4\sigma^{DI}}{d\cos a_1\, da_2\, da_3\, da_4} = \frac{1}{\sin a_1}\sum_j \int_{\bar\theta_{j-1}}^{\bar\theta_{j+1}} d\bar\theta\;\; \mathcal{P}(a,b)\;\bar\nu(a,b) \tag{5}$$

where $\bar\theta_{j-1} = \bar\theta\left(\frac{b_{j-1}+b_j}{2}\right)$ and $\bar\theta_{j+1} = \bar\theta\left(\frac{b_j+b_{j+1}}{2}\right)$.

These limits are replaced by $\bar\theta(b_\ell)$ if the interval defined by two successive b_j values contains a rainbow for $b = b_\ell$.

The expression (5) is equivalent to

$$\frac{d^4\sigma^{DI}}{d\cos a_1\, da_2\, da_3\, da_4} = \frac{1}{\sin a_1}\sum_j \int_{(b_{j-1}+b_j)/2}^{(b_j+b_{j+1})/2} db\,\left|\frac{d\bar\theta}{db}\right|\,\mathcal{P}(a,b)\;\bar\nu(a,b) \tag{6}$$

The energy distribution for all possible final masses at a scattering angle a_1 is defined by :

$$\frac{d^2\sigma^{DI}}{d\cos a_1\, da_3} = \frac{2\pi}{\sin a_1}\int da_4 \sum_j \int db\,\left|\frac{d\bar\theta}{db}\right|\;\mathcal{P}(a,b)\;\bar\nu(a,b).$$

If we describe the angular distribution whatever the final masses and energy may be, we use :

$$\frac{d\sigma^{DI}}{d\cos a_1} = \frac{2\pi}{\sin a_1}\int da_3 \int da_4 \sum_j \int db\,\left|\frac{d\bar\theta}{db}\right|\,\mathcal{P}(a,b)\;\bar\nu(a,b).$$

[1] Ch. Leclercq-Willain, Contribution to this Conference (I)

[2] H. Hofmann and P. Siemens, Nucl. Phys. A275 (1977) 464.

[+] Maître de Recherches F.N.R.S., Belgium.
[++] Chercheur agréé I.I.S.N., Belgium.

COULOMB EXCITATION EFFECTS ON HEAVY-ION ELASTIC SCATTERING

W. G. Love*, University of Georgia, Athens, Georgia 30602
T. Terasawa, University of Tokyo, Tokyo, Japan
G. R. Satchler, Oak Ridge National Lab.†, Oak Ridge, Tennessee 37830

We have constructed a polarization potential U_p for the effects of Coulomb excitation (CE) on elastic scattering. An adiabatic approximation is not used; indeed the real potential is negligible. Quadrupole CE of low states is the most important; these give a potential of the form $\mathrm{Im}U_p(r) = -W_p K(r)/r^5$. $K(r)$ is a local-energy correction factor for the slowing down of the ions in the Coulomb field; W_p is proportional to the B(E2) for the excitation. There are no adjustable parameters. The potential's validity was checked against exact coupled channel calculations. As is well known, the absorption due to CE may be very large for very heavy ion systems. For the examples in the figure, U_p was added to Woods-Saxon potentials U_o obtained[1] by fitting to elastic plus quasi-elastic data. The quasi-elastic contribution to the reaction cross section is very large; for example U_o by itself predicts $\sigma_A = 2.4$b for $^{40}Ar + ^{238}U$ whereas $U_o + U_p$ indicates $\sigma_A \approx 10$b. Further study is needed to see how estimates[1] of the contributions to σ_A of the non-quasi-elastic events such as fusion and deep inelastic will be affected by the presence of strong CE. At small angles where the nuclear potential is not felt, the sum of elastic and CE cross sections is closely equal to the Rutherford cross section. This suggests that fitting the sum of elastic and quasi-elastic data may be a reliable indicator of the remaining reaction cross section. However, a simple classical superposition is not valid at the larger angles so that this procedure will require some corrections.

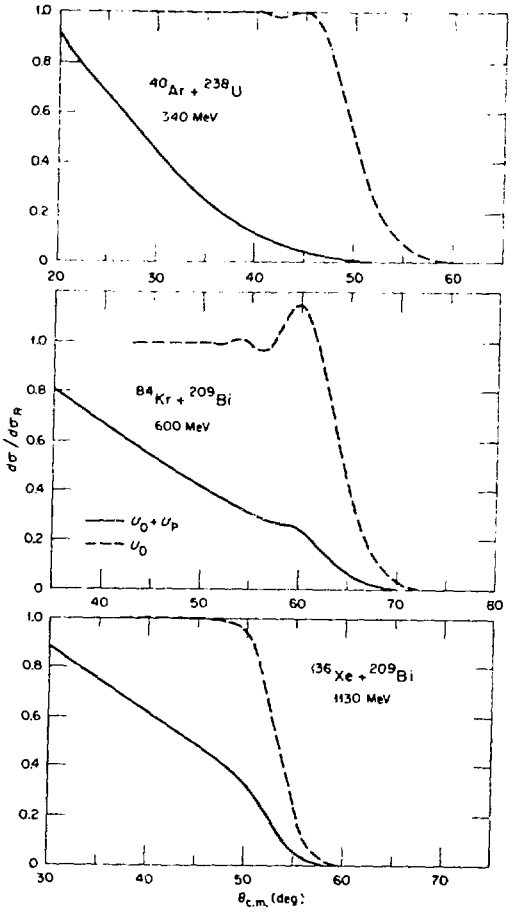

*Research supported in part by the National Science Foundation.

†Operated by Union Carbide Corp. for U.S.E.R.D.A.

[1] J.R. Birkelund, et al., Phys. Rev. C13 (1976) 133.

THE DEPENDENCE OF NUCLEAR ORBITING AND CHARGE EXCHANGE ON BOMBARDING ENERGY IN THE $^{144}Sm + ^{84}Kr$ REACTION*

A. Mignerey, D. Raich, K. Wolf, R. Boudrie, Argonne National Laboratory, Argonne, Illinois 60439

W. Schroder, J. Birkelund, J. Huizenga, University of Rochester, Rochester, New York 14627

V. E. Viola, University of Maryland, College Park, Maryland 20742

The dependence of nuclear orbiting and charge exchange on bombarding energy is studied using beams of ^{84}Kr ions at laboratory energies of 470, 595 and 720 MeV on a ^{144}Sm target. These energies correspond to 1.2, 1.5 and 1.8 times the Coulomb barrier, respectively. The angular distributions of the projectile-like products show large cross sections extending to small angles. This is consistent with orbiting or "negative angle scattering" in the 720 MeV case. But the nearly constant, large cross sections observed at low angles for the 595 MeV and 470 MeV cases are difficult to explain using the simple orbiting picture of Wilczynski.

It has been observed for projectile energies of 8.5 MeV/nucleon that the variances of the charge distributions σ_Z^2 broaden with increasing total kinetic energy loss, E_{LOSS}, and appear to follow a universal curve, independent of projectile-target combination.[1] The 720 MeV case also corresponds to 8.5 MeV/nucleon ^{84}Kr and gives values of σ_Z^2 consistent with the previous results. In these cases the relative ion velocities v' in the entrance channel are the same within 10%. The surprising feature is that the 595 MeV and 470 MeV cases, which correspond to reductions in v' by 20% and 50% respectively, follow the same universal curve, for exit channel energies well above the Coulomb barrier. Using a statistical model, σ_Z^2 is a measure of the number of protons exchanged in the interaction. Assuming the number of steps in the nucleon exchange process is given by $(A/Z)\sigma_Z^2$, values of 9 to 11 MeV are derived for the energy loss per exchange Δ, for E_{LOSS} from 10 to 90 MeV. The apparent independence of Δ on relative velocity v' is consistent with an initial, fast mechanism involving energy dissipation and mass transport, such as a rapid collective motion resulting in formation of a neck between the two nuclei.

*Work supported by USERDA.

1. J. R. Huizenga, *et al.*, Phys. Rev. Lett. 37 (1976) 885.

POSSIBLE STATIC DEFORMATION EFFECTS IN ^{84}Kr- AND ^{86}Kr-INDUCED REACTIONS ON TARGETS OF ^{144}Sm AND ^{154}Sm*

D. G. Raich, A. C. Mignerey, K. L. Wolf, R. L. Boudrie,† C. T. Roche
Argonne National Laboratory

W. U. Schröder, J. R. Birkelund, J. R. Huizenga
University of Rochester

V. E. Viola
University of Maryland

As previously reported[1] there is an appreciable difference between the angular distributions of products from Kr-ion induced reactions on ^{144}Sm and ^{154}Sm. We have studied this apparent static deformation effect at laboratory bombarding energies of 470, 600, and 720 MeV, corresponding to 1.2, 1.5, and 1.8 times the interaction barrier. The difference is most pronounced at the lowest projectile energy, where the differential cross-section $d\sigma/d\theta_{cm}$ of krypton-like products at angles forward of the grazing angle is nearly twice as large from reactions on highly deformed ^{154}Sm as from those on spherical ^{144}Sm. The enhanced cross-section is associated primarily with reactions from which the products are emitted at the relatively low (fully relaxed) total kinetic energies typical of strongly damped collisions. We can rule out the possibility that this effect is due to a fusion-fission mechanism because the yield at very backward angles is, with both targets, very small ($\sigma_{cf} < 300$ mb). Despite the difference in angular distributions, the widths of the product charge distributions are the same at a given center-of-mass deflection angle θ_{cm}. The results are interpreted in terms of interaction time differences in a nuclear diffusion model, where θ_{cm} gives a good indication of the interaction time.

Although the angular distributions for both targets are more similar at the two higher bombarding energies, in all cases the quasi-elastic peak is lower, broader, and shifted slightly forward in angle with a ^{154}Sm target. A quantitative understanding of this effect, and of the increased forward-angle yield at bombarding energies near the interaction barrier, should yield information on the shape of the deformed nuclear potential near the nuclear surface. Since the wavelength of the relative motion is small ($\lambda\!\!\!^{-} \approx 0.1$ fm here), interactions are calculated in a semiclassical model involving a deformed potential. Appreciable orientation-dependent differences in the ion-ion potential occur for a deformed nucleus relative to a spherical one, which qualitatively explain the observed effects.

*Work supported by USERDA.
†Present address: Los Alamos National Laboratory.
[1] R. L. Boudrie, *et al.*, Bull. Am. Phys. Soc. 21 (1976) 969.

Equilibration in Relativistic Collisions of Nuclear Matter.

J. Randrup and S.E. Koonin[+], NORDITA and the Niels Bohr Institute, DK-2100 Copenhagen, Denmark.

In order to study the equilibration process in relativistic nuclear collisions, we consider the collision of two interpenetrating spatially uniform systems of nuclear matter. For this case we derive a Boltzmann-like equation which treats exactly the relativistic kinematics and the exclusion principle; the nucleon-nucleon scatterings are based on the experimental cross sections. This dynamical equation is solved numerically for the evolution of the momentum space distribution from disjoint target and projectile Fermi spheres to a single thermal distribution for bombarding energies of 250 MeV, 400 MeV, 1.05 GeV, and 2.1 GeV per nucleon. The spectrum of emitted nucleons and their correlation are obtained as a function of the interaction time. The extent to which these quantities reflect the equilibration dynamics is explored.

At early interaction times the primary nucleon-nucleon collisions populate in momentum space a spherical shell connecting the two initial Fermi distributions. This is a consequence of four-momentum conservation in each binary collision. This structure is also reflected in the two-nucleon azimutal angle correlation function, which peaks strongly in the back-to-back direction. As equilibration proceeds, subsequent binary collisions degrade this early "shell" structure to a thermal distribution by filling in the hollow interior of the primary shell. In concert with this process, the structure in the correlation function relaxes quickly. At lower bombarding energies ($E/A \lesssim 1$ GeV), the spectra of the emitted nucleons are therefore not very well suited to probe the details of the dynamics. The time required to reach thermal equilibrium is found to be about 10 fm/c rather independently of the bombarding energy although the results at higher energies are expected to change when meson production is included.

+) Permanent address: CalTech, Pasadena, Calif., USA.

Unique Quantization of Adiabatic TDHF

P.G. Reinhard, Inst. f. Kernphysik, Univ. Mainz, D-6500 Mainz, West Germany

K. Goeke, Inst. f. Kernphysik, KFA Jülich, D-5170 Jülich, West Germany

The ATDHF theory[1] provides a prescription for the classical Hamiltonian $\mathcal{H}_c = p^2/2M_o + V_o$ of a large amplitude collective motion along a collective path $\langle x_i|q\rangle$ and its dynamical generalization $\langle x_i|qp\rangle \tilde{=} (1+ip\hat{Q})\langle x_i|q\rangle$. Assuming a grouping of the 3A coordinates x_i into a collective coordinate Q and intrinsic coordinates ξ_i one defines[1] the quantized collective Hamiltonian H_c as that quantity which remains after averaging over all ξ_i: $\mathcal{H}_c(p,q) = \int dQ \langle pq|Q\rangle H_c(Q,P)\langle Q|pq\rangle$. The $\langle Q|pq\rangle$ must have the structure $\langle Q|pq\rangle = (1+ipQ)\langle Q|q\rangle$ so that we can determine $\langle Q|q\rangle$ by identifying the moments $\int dx_i \langle q|x_i\rangle \hat{Q}^n \langle x_i|q\rangle = \int dQ \langle q|Q\rangle Q^n \langle Q|Q\rangle$. If $\langle Q|q\rangle$ are Gaussian with a width β, then one can defold[1] $\mathcal{H}_c$ obtaining e.g.

$$H_c = \frac{1}{4}\left[P^2\,\frac{1}{2M} + P\,\frac{1}{M}\,P + \frac{1}{2M}\,P^2\right] + V \qquad P = -i\,\frac{d}{dQ} \tag{1}$$

$$V = V_o - \frac{1}{4\beta}\,V_o'' - \frac{\beta}{4M_o} \tag{2}$$

The $M = M_o$ and the correction terms in (2) correct for the zero point motion. Eq. (1) is by no means an assumption. One can choose any other kinetic energy which would just give rise to additional subtraction terms in (2). The $\hat{Q}$ is explicitly provided by ATDHF[1].

Reference:

1) K. Goeke and P.G. Reinhard, peprint Jülich, 1977, and these proceedings

INCLUSION OF CORRELATIONS TO THE TDHF-METHOD

P. Schuck, Institut Laue-Langevin, Grenoble, France

It is well known that the TDHF equations correspond to the collisionless Vlassov equation. We want to show here how one formally can include collisions and correlations in the case of nuclear physics. We start out from the exact equation of motion for the density matrix:

$$i\frac{\delta}{\delta t}\rho^{t}_{pp'} = \left(\frac{p^2}{2m} - \frac{p'^2}{2m}\right)\rho^{t}_{pp'} + \frac{1}{2}\sum_{p_2p_3} w_{pp_1p_2p_3} \langle D| e^{iHt}\psi^{+}_{p'}\psi^{+}_{p_1}\psi_{p_3}\psi_{p_2}e^{-iHt}|D\rangle$$

$$- \frac{1}{2}\sum_{p_1p_2p_3} \langle D| e^{iHt}\psi^{+}_{p_2}\psi^{+}_{p_3}\psi_{p_1}\psi_{p}e^{-iHt}|D\rangle\, w_{p_3p_2p_2p'}$$

with $\rho^{t}_{pp'} = \langle D|\exp iHt\ \psi^{+}_{p'}\psi_{p}\ \exp -iHt|D\rangle$ and w the anti-symmetrized two body interaction. The initial state $|D\rangle$ is possibly the solution of a static HF calculation and in any case not the exact wave function; ρ would otherwise be time-independent since the exact Hamiltonian H of the system is supposed not to be time-dependent. Assuming that the exact evolution of the wavepacket $|\psi(t)\rangle = e^{-iHt}|D\rangle$ can be approximated at all times by a Slater determinant reduces eq.(1) to the usual TDHF equations. The question how to go beyond this approximation can be answered in introducing the one body Green's function $G^{t\,t'}_{pp'} = -i\langle D|T\{\psi_{p}(t)\psi^{+}_{p'}(t')\}|D\rangle$ where the time-dependence of the operators is determined by the exact Hamiltonian and the relation with the density is $\rho^{t}_{pp'} = -i\lim_{t'\to t+0} G^{t\,t'}_{pp'}$. The difference to the usual is the fact that this Green function is no longer translationally invariant with respect to time because we are dealing with wavepackets. Nevertheless it can be shown that one can derive a Dyson equation

$$(\omega - p^2/2m)G^{t\,t'}_{pp'} = \delta_{pp'}\delta(t-t') + \sum_{p_1}\int_{-\infty}^{+\infty} dt_1\, M^{t\,t_1}_{pp_1}\, G^{t_1t'}_{p_1p'}$$

with a mass operator not translationally invariant in time but otherwise defined in the same way as its invariant counterpart; the only difference being that the usually static quantities like single particle energies and densities depend now on time. The lowest order part of M is given by the time-dependent HF potential. The generalized equation of motion for the density is then given by

$$i\frac{\delta}{\delta t}\rho^{t}_{pp'} = (p^2/2m - p'^2/2m)\rho^{t}_{pp'} + \sum_{p_1}\int dt_1\left[M^{tt_1}_{pp_1}\, G^{t_1t_+}_{p_1p'} - G^{tt_1}_{pp_1}\, M^{t_1t_+}_{p_1p'}\right]$$

where $t_+ = t+0$. The above equation is in principle an exact equation and is besides the fact that all quantities are not translationally invariant in time the same as for example the one derived by Kadanoff and Baym. We are now in a position to derive approximations which go beyond TDHF in applying the usual many body formalism; for example from the second order contribution of the mass operator we can derive a Boltzmann collision integral and arrive at the equation $i\dot{\rho} - [H^{HF}(\rho),\rho] = I(\rho)$. Besides the Boltzmann collision integral generalizations of it as well as all other current approximations for the mass operator as for example particle vibration coupling are conceivable.

ENERGY DISSIPATION IN FISSION[+]

H. Schultheis[*] and R. Schultheis[*], Inst. Theor. Phys., Univ. Tübingen, D-74 Tübingen, W. Germany

The dissipation of energy in fission has been studied in a number of different approaches with contradictory results. In this work we derive limiting conditions for the internal excitation energy at scission by relating the potential energy of the system to the experimental post-scission data. Numerical results have been determined for the spontaneous fission of ^{252}Cf and for the thermal neutron induced fission of ^{235}U by taking into account a two-spheroid scission configuration with diffuse surface, nuclear interaction and Coulomb excitation effects. The results indicate low dissipation. The internal plus non-translational collective excitation energy at scission is found to be at most 8 MeV.

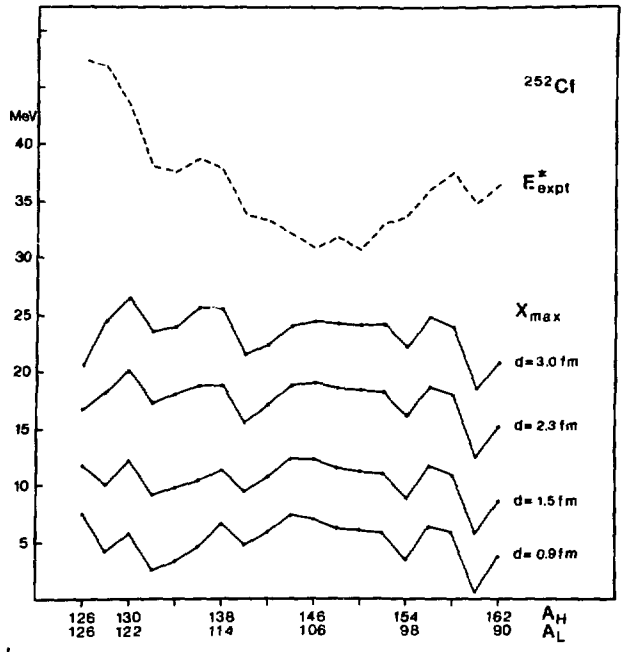

The figure shows the calculated upper bounds X_{max} of the internal plus vibrational plus rotational excitation energy per fragment pair at a number of separations d between the half-density surfaces of the fragments. With increasing separation X_{max} approaches the total fragment excitation energy E^{*}_{expt}.

[+] Supported in part by the Bundesministerium für Forschung und Technologie

[*] present address: Department of Physics and Astronomy, University of Maryland, College Park, Md. 20742

MANY-NUCLEON CORRELATIONS IN ^{32}S +

H. Schultheis*, R. Schultheis* and K. Wildermuth, Inst. Theor. Phys., Univ. Tübingen, D-74 Tübingen, West Germany
A. Faessler** and F. Grümmer, IKP, KFA Jülich, W. Germany

Long-range many-nucleon correlations in ^{32}S have been studied using soft-core potentials (Brink-Boeker B_1 and Volkov V_1) and alpha-particle-model wave functions. The energy has been minimized by restricting the cluster positions to configurations with substructures like $^{16}O - ^{16}O$, $^{16}O - ^{12}C - \alpha$ and $\alpha - ^{12}C - ^{12}C - \alpha$.

We find two separate valleys in the potential energy landscape that are associated with different types of correlations in the wave function and two local energy minima that are analogous to the ground state and isomeric state of actinide nuclei: The minimum at larger deformation (i.e. larger quadrupole moment and larger rms radius) is associated with an $^{16}O - ^{16}O$ "fragment" substructure whereas no such substructure is found in the ground state minimum of ^{32}S. A transition from one valley to the other is energetically favourable already for small deformations. The corresponding rearrangement between the ground-state type of wave function and the $^{16}O - ^{16}O$ wave function occurs rather rapidly: It is associated with only small changes in the quadrupole moment and rms radius.

+ Supported in part by the Bundesministerium für Forschung und Technologie

* Present address: Department of Physics and Astronomy, University of Maryland, College Park, Md. 20742

** Present address: Department of Physics, State University of New York, Stony Brook, NY 11794

THE CONTINUUM IN HEAVY-ION REACTIONS†

D. K. Scott, M. Bini*, C. K. Gelbke, D. L. Hendrie, J. L. Laville**,
J. Mahoney, M. C. Mermaz***, and C. Olmer
Lawrence Berkeley Laboratory, Berkeley, CA 94720

Heavy-ion reactions are often dominated by the excitation of the continuum. At low energies ($\lesssim$10 MeV/A), the continuum is attributed to direct or multistep reactions,[1] which develop from quasi-elastic to deeply-inelastic processes depending on the degree of equilibration[2]. Peripheral collisions at relativistic energies also lead to a continuum which has been explained as projectile fragmentation[3]. We have studied the transition between these extreme viewpoints by reactions of ^{16}O on ^{208}Pb at energies up to 20 MeV/A and we have compared these results with data[3] at 2.1 GeV/A.

The energy spectra at 20 MeV/A and 2.1 GeV/A are dominated by the Fermi motion of the fragment in the projectile. However it is not possible from the energy spectra alone to distinguish between a fast liberation of the cluster and a slow decay of the excited projectile[4]. Both the spectra and the isotope yields are consistent with emission of a fragment at a temperature between 7 and 8 MeV, which is close to the separation energy of a nucleon. Higher temperatures would lead to an explosion of the fragment. At energies below 10 MeV/A, temperature has also been a useful concept for understanding yields of isotopes emitted from a partially-equilibrated dinuclear system[5]. Temperatures of 2 MeV are typical, varying with incident energy as $\sqrt{E_{CM}-V_{Coul}}$. Our results suggest that, between 10 MeV/A and 20 MeV/A, the variation with energy is more rapid or that the dominant reaction mechanism changes abruptly. The temperature approaches 7 or 8 MeV at 20 MeV/A, with little subsequent change at relativistic energies. This approach to the continuum energy spectra could be a useful means of studying the evolution of the reaction mechanism.

†Work performed under the auspices of the U. S. Energy Research and Development Administration.

1) K. Katori, T. Ishigami, and M. Toyama, Symposium on Macroscopic Features of Heavy-Ion Collisions (Argonne 1976) Vol. 2, p. 625.
2) J. Wilczynski, Phys. Lett. 47B (1973) 484.
3) D. E. Greiner, P. J. Lindstrom, H. H. Heckman, B. Cork, and F. Bieser, Phys. Rev. Lett. 35 (1975) 152.
4) A. S. Goldhaber, Phys. Lett. 53B (1974) 306.
5) V. V. Volkov, Sov. J. Nucl. Phys. 6 (1976) 420.

*NATO Fellow, on leave from University of Florence, Italy.
**On leave from CNRS, Caen, France.
***On leave from CEN, Saclay, France.

Theory of Strongly Damped Collisions with Transfer as a Random Process

A. Sherman and D. Sperber*, Rensselaer Polytechnic Institute, Troy, New York, M. I. Sobel+, Brooklyn College, Brooklyn, New York and J. P. Bondorf, Niels Bohr Institute, Copenhagen.

The purpose of this model is to suggest a dynamical model for heavy ion collisions which incorporates the effect of the considerable transfer, as observed experimentally. Previously, transfer and dynamics have been studied independently. Presently the transfer is included as a random process. During the time target and projectile interact strongly transfer with a probability of 1/2 in both directions is allowed at specified time intervals. If there is no transfer the integration of the equation of motion continues, if transfer occurs the potentials are adjusted and the integration continues. The equations of motion are integrated many times for a number of impact parameters. Even for one impact parameter the random transfer leads to a distribution of the scattering angle, mass, charge and final energy. The effect is enhanced when many impact parameters are included. Very good agreement is obtained with experiments[1,2] of the RAMM group for Kr + Bi at 600 MeV and Xi + Bi at 1130 MeV. The feedback of the transfer on the dynamics is demonstrated. A comparison with diffusion theory is made. The effects of correlations and isospin equilibration are discussed.

*Supported by United States Energy and Development Agency

+Partially supported by a grant from the City University and a NATO Fellowship.

1) K. L. Wolf et al. Phys. Rev. Lett. 33, 1105 (1974).

2) W. U. Shroder et al. Phys. Rev. Lett. 36, 514 (1976).

ANALYSIS OF RELAXATION PHENOMENA IN DEEPLY INELASTIC HEAVY ION COLLISIONS+)

G. Wolschin and W. Nörenberg

Institut für Theoretische Physik der Universität and
Max-Planck-Institut für Kernphysik, Heidelberg

The transfer of mass, as well as the dissipation of relative kinetic energy and relative angular momentum in deeply inelastic heavy ion collisions have been studied as functions of time. Angular momentum dependent mean interaction times are calculated in a classical model. To determine the angle of rotation of the composite system, a parametrized deflection function is constructed from the experimental angular distribution via the classical relation between the cross-section and the deflection function. Both energy and angular momentum dissipation as inferred from the experimental energy loss are taken into account in the calculation of the interaction time. The model is applied to determine mass transport coefficients from experimental mass, or element distributions. The resulting mass drift and diffusion coefficients v_A ,D_A are accurate within less than 30%. They compare well with the systematics obtained from the microscopic transport theory [1], as well as with other recent experimental results [2,3]. The experimental relation between energy loss and variance of the element distribution 4 is used to determine both the rate of kinetic energy, and angular momentum dissipation [5].

1 W. Nörenberg, Z. Physik A274(1975)241 and A276(1976)84
S. Ayik, B. Schürmann and W. Nörenberg, Z. Physik A277 (1976)299 and A279(1976)145

2 L.G. Moretto and R. Schmitt, European Conference on Nuclear Physics with Heavy Ions, Caen (1976), J. Phys. C5(1976)109

3 W.U. Schröder et al., preprint 1977

4 J.R. Huizenga et al., Phys.Rev.Lett. 37(1976)885

5 G. Wolschin and W. Nörenberg, Proc. Int. Workshop on Gross Properties of Nuclei and Nuclear Excitations V, Hirschegg 1977 and Z. Physik, to be published

+ Work supported by the "Gesellschaft für Schwerionenforschung", Darmstadt, and by the "Bundesministerium für Forschung und Technologie", Bonn.

The Mass Transfer in the Collision ^{238}U-^{238}U

S. Yamaji, K.H. Ziegenhain, H.J. Fink, W. Greiner
Institut für Theoretische Physik, Universität Frankfurt, Germany
W. Scheid, Institut für Theoretische Physik, Universität Giessen, Germany

The mass transfer in heavy-ion collisions can be treated with the collective fragmentation coordinate which is defined by the ratio of nucleon numbers $\eta=(A_1-A_2)/(A_1+A_2)$ when the nuclei are seperated. When the nuclei overlap, the coordinate becomes continuous and is defined by the ratio $\eta=(V_1-V_2)/(V_1+V_2)$ of nuclear volumes. The Hamiltonian for the scattering of two nuclei contains the kinetic energies of the relative motion and mass transfer motion and the potential $V(R,\eta)$ which is depicted in Fig.1 for A=476 nucleons. The potential is assumed to depend on temperature which smoothes the shell effects out (dashed curves in Fig.1). The relative motion is treated classically whereas the mass transfer probability is computed with the wave function $\psi(\eta,t)$ solving the time-dependent Schrödinger equation which depends on the relative coordinate $\vec{R}(t)$. In Fig.2 we present the time evolution of the ^{238}U-^{238}U scattering for various sharing ratios f of the thermal excitation energy to the energy loss in the radial motion which is caused by friction. The times T are given in units of 10^{-23} sec. For small values of f an appreciable amount of mass is transferred to the region of superheavy nuclei ($\eta\approx 0.3$).

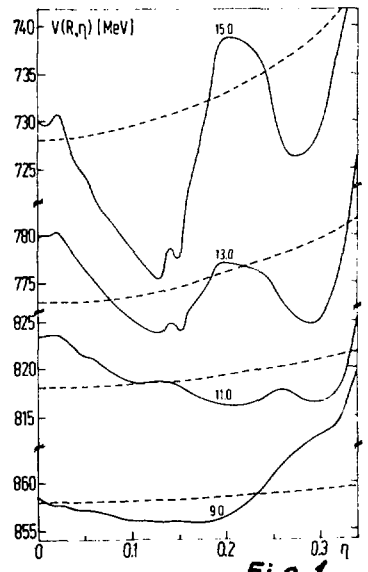

Fig.1

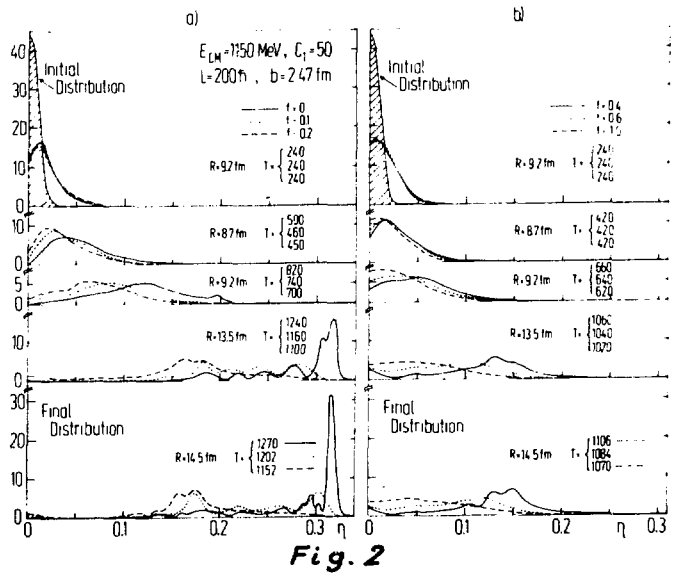

Fig. 2

SCHROEDINGER EQUATION OF A DISSIPATIVE CRANKING POTENTIAL

Kunio YASUE
Department of Physics, Nagoya University, Nagoya, Japan

Recently the cranking model has been brought into new consideration by Hofmann[1] with the aim to approach to nuclear dissipative phenomena such as heavy-ion collisions. He derived a thermodynamical equation with respect to the shape of a mean nuclear potential caused by the cranking model as follows:

$$m(Q,T)\ddot{Q} = -(\frac{\partial F}{\partial Q})_T - \gamma(Q,T)\dot{Q}, \tag{1}$$

where $Q(t)$ characterizes the shape, $F=F(Q,T)$ denotes a free energy of the system, T a temperature of the system and m and γ represent "inertia" coefficient and "friction" coefficient respectively.

However, Eq.(1) is purely classical, so that it seems desirable for us to derive its quantum theoretical version in order to treat such nuclear phenomena. Since the system is dissipative, the conventional procedure based upon the Hamiltonian formalism is not possible.

Hence, following the stochastic quantization method used in our previous papers[2)3)], we can derive the corresponding non-linear Schrödinger equation

$$i\hbar\frac{\partial}{\partial t}\psi = [-\frac{\hbar^2}{2m}\frac{\partial^2}{\partial Q^2} + F + \frac{i\gamma}{2m}\hbar\cdot\log\frac{\bar{\psi}}{\psi}]\psi, \tag{2}$$

under the assumption that m and γ are slowly varying variables, where $\psi = \psi(Q,t)$ denotes a probability amplitude and $\hbar$ Planck's constant divided by 2π.

References 1) H. Hofmann, Phys. Lett. 61 B (1976) 423.
2) K. Yasue, J. Stat. Phys. 16 (1977) 113.
3) K. Yasue, Phys. Lett. 64 B (1976) 239.

POLARIZATION OF NUCLEAR WAVE FUNCTIONS IN HEAVY ION REACTIONS

L. A. Charlton, G. Delic, N. K. Glendenning, K. Pruess
Lawrence Berkeley Laboratory, Berkeley, CA 94720

Most direct reactions between heavy ions can be interpreted in terms of a transition between shell model states of the isolated nuclei with the transition amplitude calculated in DWBA or, when important multiple step transitions through low-lying collective states are important, in CCBA. There are some experimental measurements however that cannot be so interpreted.[1] They exhibit a systematic discrepancy with the three features, 1) for weakly bound states the angular distribution is shifted toward smaller angles than expected, 2) the shift grows with decreasing binding for a sequence of levels in the same nucleus, 3) the magnitude of the shift decreases as the bombarding energy increases. These three features are expected if the weakly bound state is modified by the field of the other nucleus.[2] To assess whether the magnitude of the effect produced by such a wave function polarization is comparable to that observed, we have employed the two-center shell model to generate polarized states[3] in ^{209}Bi as a function of distance of the polarizing nucleus ^{11}B. Transitions to these states are computed in DWBA. The trend of growing shift with decreasing binding is reproduced as is the approximate magnitude of the shift ($\sim$15°). The calculation can be understood as the lowest order approximation to a dynamical process involving transitions through a large number of high-lying states in the Bi nucleus.[4]

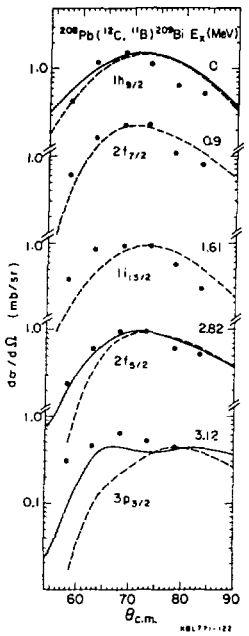

Fig. 1. Cross sections to a sequence of states showing systematic growth of discrepancy of DWBA (dashed) and improvement due to polarization of the wave function.

1) K. S. Toth et al., Phys. Rev. C14, (1976) 1471.

2) G. Delic, K. Pruess, L. A. Charlton, and N. K. Glendenning, Phys. Letters (in press) and Argonne Symposium on Macroscopic Features of Heavy Ion Collisions II (1976) 723.

3) P. Lichtner, K. Pruess, this conference.

4) K. Pruess, this conference.

CALCULATIONS OF SINGLE PARTICLE POLARIZATION USING A REALISTIC TWO-CENTER SHELL MODEL

P. Lichtner, University of Maryland, College Park, Md. 20742, and
K. Pruess, Lawrence Berkeley Laboratory, Berkeley, Ca. 94720.

It has been proposed recently that, in "slow" nucleus-nucleus collisions, the single particle states which participate in quasielastic reactions will be modified or polarized due to the proximity of the approaching nucleus and its force field.[1), 2)] We have estimated the time evolution of polarization within a simple two-state approximation and have found that typical direct interaction times often allow for strong polarization to develop. Extending the work of ref. 3) we have investigated the polarization of single particle states in the adiabatic (= static nuclei) limit, using a realistic two-center Woods-Saxon potential.

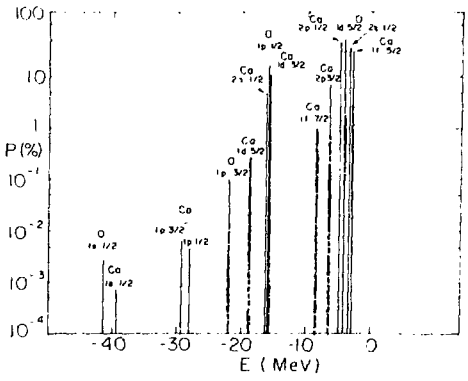

An example of our results is displayed in the figure. It shows the polarization of neutron states in the system $^{40}Ca + ^{16}O$ ($\Omega = 1/2$- components; Ω is the projection of angular momentum on the internuclear line) at grazing distance R = 10 fm. The polarization is here defined as the total probability of the non-asymptotic components.

The polarization is seen to generally increase with decreasing binding. Superimposed on this trend are resonance effects, when two levels in the colliding nuclei are close.

References.

1) K. Pruess and P. Lichtner, Nucl. Phys. A269(1976)252.

2) G. Delic, K. Pruess, L.A. Charlton, and N.K. Glendenning, in press in Phys. Lett. and preprint LBL - 5074.

3) K. Pruess, Nucl. Phys. A278(1977)124.

ADIABATIC APPROXIMATION FOR TWO-STEP PROCESSES IN HEAVY-ION INDUCED TRANSFER REACTIONS.

K. Pruess, Lawrence Berkeley Laboratory, Berkeley, Ca. 94720.

Rearrangement reactions involving polarized single particle states can be viewed as indirect processes via a large number of excited intermediate states, each of which contributes weakly and coherently.[1] Restricting ourselves to two-step processes the amplitude for any one of the indirect transitions can be written in a rather obvious notation as

$$T_{\alpha\to\beta'\to\beta} = \langle \chi_\beta^{(-)} | (\phi_\beta | \hat{V}_\beta | \phi_{\beta'}) \, G_{\beta'}^{(+)} \, (\phi_{\beta'} | \hat{V}_\alpha | \phi_\alpha) | \chi_\alpha^{(+)} \rangle \qquad (1)$$

α and β denote entrance and exit channel partitions, respectively, and other quantum numbers. For one-nucleon transfer the intermediate internal motion state $\phi_{\beta'}$ differs from ϕ_β in that the transferred nucleon is in an excited state (bound or unbound) with energy $\varepsilon_{\beta'}$. $G_{\beta'}^{(+)} = (E_{\beta'}^{(+)} - H_\beta)^{-1}$ is the Green's operator for the intermediate channel β' in which the relative motion energy is $E_{\beta'} = E - \varepsilon_{\beta'}$. $H_\beta = T_\beta + U_\beta$ is the optical model Hamiltonian appropriate for the exit channel. Round brackets indicate integration over internal coordinates.

T may be decomposed into two parts, $T = T^P + T^Q$, by inserting an identity operator in the form $1 = P + Q$ to the left of $G_{\beta'}^{(+)}$ into eq. (1). P is a projection operator which is expressed in terms of eigenstates $|E_i,\lambda\rangle$ of H_β and is chosen to contain only states with (adiabaticity condition)

$$|E_i - E_\beta| \quad < \quad |\varepsilon_\beta - \varepsilon_{\beta'}| \qquad (2)$$

Expanding $G_{\beta'}^{(+)}$ in a straightforward way T^P can be written in the form of an "adiabatic series"

$$T^P_{\alpha\to\beta'\to\beta} = \sum_{n=0}^{\infty} \langle \chi_\beta^{(-)} | \frac{(\phi_\beta | \hat{V}_\beta | \phi_{\beta'})}{\varepsilon_\beta - \varepsilon_{\beta'}} P \left[\frac{H_\beta - E_\beta}{\varepsilon_\beta - \varepsilon_{\beta'}} \right]^n (\phi_{\beta'} | \hat{V}_\alpha | \phi_\alpha) | \chi_\alpha^{(+)} \rangle \qquad (3)$$

The zeroth-order term (n=0) is the adiabatic or static limit. It has the form of a one-step transfer amplitude to a "polarized" state with the polarization amplitude identical to the familiar expression obtained in first order stationary perturbation theory.[1] Higher order terms are small and converge fast if the (local) momentum in $\chi_\beta^{(-)}$ is small and/or if the matrix element $(\phi_\beta | \hat{V}_\beta | \phi_{\beta'})$ varies slowly as a function of the relative motion vector $\underset{\sim}{r}_\beta$. Numerical examples show that $\hat{V}_\beta$ preferably induces transitions with small momentum exchange. Hence the cutoff eq. (2) is not severe for many relevant intermediate states, and T^P as given by eq. (3) may actually often be a good approximation for the whole T.

References.

1) K. Pruess, Nucl. Phys. A278(1977)124.

LIST OF PARTICIPANTS

AGASSI, D., Max-Planck Institut für Kernphysik, Postfach 103980, Heidelberg, West Germany
ALONSO, C. T., L-32, Lawrence Livermore Lab., P. O. Box 808, Livermore, CA 94550
ARVIEU, R., Institut des Sciences Nucléaires, B.P. 257, 38044 Grenoble, France
AYIK, S., Institut für Theoretische Physik, der Universität, Philosophenweg 19, 6900 Heidelberg, West Germany
BERLANGER, M., Physique Nucléaire Experimentale, CP 229, Université Libre de Bruxelles, Bd du Triomphe, B-1050, Bruxelles, Belgium
BODMER, A. R., Physics Div., Argonne National Lab., Argonne, IL 60439
BOHIGAS, O., Institut Physique Nucléaire, B.P. N° 1, 91406 Orsay, France
BUENERD, M., Institut des Sciences Nucléaires, B.P. 257, 38044 Grenoble, France
CLEARY, T. P., Physics Div., Oak Ridge National Lab., Oak Ridge, TN 37830
COLE, A. J., Institut des Sciences Nucléaires, B.P. 257, 38044 Grenoble, France
CORDELL, K., Dept. of Physics, Univ. of Virginia, Charlottesville, VA 22903
CUSSON, R. Y., Dept. of Physics, Duke Univ., Durham, NC 27706
DAVIES, K. T. R., Physics Div., Oak Ridge National Lab., Oak Ridge, TN 37830
DAYRAS, R., Physics Div., Oak Ridge National Lab., Oak Ridge, TN 37830
DELEPLANQUE, M. A., Bldg. 70-A, Lawrence Berkeley Lab., Berkeley, CA 94720
DIVADEENAM, M., Bldg. 197, Brookhaven National Lab., Upton, L.I., NY 11973
FRIEDMAN, W. A., Dept. of Physics, Univ. of Wisconsin, Madison, WI 53706
GLENDENNING, N. K., Lawrence Berkeley Lab., Berkeley, CA 94720
GOBBI, A., GSI, Postfach 541, 6100 Darmstadt, West Germany
GREINER, W., Institut für Theoretische Physik, der Universität Frankfurt Robert-Mayer-Str. 8-10, D-6000 Frankfurt/Main, West Germany
GRIFFIN, J. J., Dept. of Physics, Univ. of Maryland, College Park, MD 20740
GUTBROD, H. H., Lawrence Berkeley Lab., Berkeley, CA 94720
GYULASSY, M., Nuclear Science Div., Lawrence Berkeley Lab., Berkeley, CA 94720
HALBERT, E., Physics Div., Oak Ridge National Lab., Oak Ridge, TN 37830
HALBERT, M. L., Physics Div., Oak Ridge National Lab., Oak Ridge, TN 37830
HECKMAN, H. H., Lawrence Berkeley Lab., Berkeley, CA 94720
HOFMANN, H., Physik Dept., der TUM, James Franck Strasse, 8046 Garching, West Germany
HOLUB, R., USBM, Bldg. 20, Denver Federal Center, Denver, CO 80225
HOLZWARTH, G., Technical University Munich, 8046 Garching, West Germany
HUIZENGA, J. R., Nuclear Structure Research Lab., Dept. of Physics, Univ. of Rochester, Rochester, NY 14627
KAN, K. K., Dept. of Physics, Univ. of Texas, Austin, TX 78712

KO, C. M., Cyclotron Lab., Dept. of Physics, Michigan State Univ., East Lansing, MI 48824
KRAPPE, H. J., Hahn-Meitner-Institut, Glienicker Str. 100, 1000 Berlin 39, West Germany
KRIEGER, S. J., Dept. of Physics, Univ. of Illinois at Chicago Circle, Chicago, IL 60439
LECLERCQ-WILLAIN, C., Physique Théorique - CP 229, Campus de la Plaine U.L.B., Université Libre de Bruxelles, Bd. du Triomphe, B-1050 Brussels, Belgium
LICHTNER, P., Dept. of Physics, Univ. of Maryland, College Park, MD 20740
MacKELLAR, A. D., Dept. of Physics, Univ. of Kentucky, Lexington, KY 40506
MAGUIRE, C. F., Dept. of Physics, Vanderbilt Univ., Nashville, TN 37235
MAHER, J. V., Dept. of Physics, Univ. of Pittsburgh, Pittsburgh, PA 15260
MARUHN, J. A., Physics Div., Oak Ridge National Lab., Oak Ridge, TN 37830
MARUHN, V., Physics Div., Oak Ridge National Lab., Oak Ridge, TN 37830
McGRORY, J. B., Physics Div., Oak Ridge National Lab., Oak Ridge, TN 37830
MÖLLER, P., MS-452, Los Alamos Scientific Lab., Los Alamos, NM 87545
NATOWITZ, J. B., Cyclotron Inst., Texas A & M Univ., College Station, TX 77843
NEGELE, J. W., Rm. 6-302, M.I.T., Cambridge, MA 02139
NGÔ, C., Institut de Physique Nucléaire, B.P. N° 1, 91406 Orsay, France
NOACK, C., Dept. of Physics, Univ. of Bremen, P. O. Box 330440, D-2800 Bremen, West Germany
OBENSHAIN, F. E., Physics Div., Oak Ridge National Lab., Oak Ridge, TN 37830
PINKSTON, W. T., Vanderbilt Univ., Box 1807, Station B, Nashville, TN 37235
PLASIL, F., Physics Div., Oak Ridge National Lab., Oak Ridge, TN 37830
PRUESS, K., Nuclear Science Div., Lawrence Berkeley Lab., Berkeley, CA 94720
RAICH, D. G., Bldg. 200, Argonne National Lab., 9700 South Cass Ave., Argonne, IL 60439
RANDRUP, J., NORDITA, Blegdamsvej 17, DK-2100 Copenhagen Ø, Denmark
SAGE, K. A., Dept. of Physics, Duke Univ., Durham, NC 27706
SARANTITES, D. G., Dept. of Chemistry, Washington Univ., St. Louis, MO 63130
SATCHLER, G. R., Physics Div., Oak Ridge National Lab., Oak Ridge, TN 37830
SCHEID, W., Institut für Theoretische Physik, Universität Giessen, 63 Giessen, West Germany
SCHOPPER, E., Institut für Kernphysik, der Universität, August-Euler-Strasse 6, 6 Frankfurt/Main 90, West Germany
SCHUCK, P., Institut M. V. Laue - P. Langevin, Av. des Martyrs, B.P. 156 X, 38042 Grenoble Cedex, France
SCHULTHEIS, H., Dept. of Physics & Astronomy, Univ. of Maryland, College Park, MD 20742

SCHULTHEIS, R., Dept. of Physics & Astronomy, Univ. of Maryland, College Park, MD 20742
SCHUSSLER, F., C.E.N. de Grenoble, Ave. des Martyrs, 38041 Grenoble, France
SCOTT, D. K., Bldg. 88, Lawrence Berkeley Lab., 1 Cyclotron Road, Berkeley, CA 94720
SMITH, R. K., Dept. of Physics, Duke Univ., Durham, NC 27706
SPERBER, D., Dept. of Physics, Rensselaer Polytechnic Inst., Troy, NY 12181
STELSON, P. H., Physics Div., Oak Ridge National Lab., Oak Ridge, TN 37830
STOKSTAD, R. G., Physics Div., Oak Ridge National Lab., Oak Ridge, TN 37830
THORNTON, S. T., Dept. of Physics, Univ. of Virginia, McCormick Rd., Charlottesville, VA 22901
VIGDOR, S. E., Dept. of Physics, Indiana Univ., Bloomington, IN 47401
VRBA, J. A., Dept. of Physics, Univ. of Tennessee, Knoxville, TN 37916
WEIDENMÜLLER, H., Max-Planck Institut für Kernphysik, P. O. Box 103980, Heidelberg, West Germany
WELTON, T. A., Physics Div., Oak Ridge National Lab., Oak Ridge, TN 37830
WOLF, K. L., D-200, Argonne National Lab., 9700 S. Cass Ave., Argonne, IL 60439
ZOHNI, O., Nuclear Structure Research Lab., Univ. of Rochester, Rochester, NY 14627
ZUCKER, A., Oak Ridge National Lab., P. O. Box X, Oak Ridge, TN 37830

GOMEZ del CAMPO, J., Physics Div., Oak Ridge National Lab., Oak Ridge, TN 37830
SHAPIRA, D., Physics Div., Oak Ridge National Lab., Oak Ridge, TN 37830

AUTHOR INDEX

☆ U.S. GOVERNMENT PRINTING OFFICE: 1977-748-189/235